Top Quark Physics at the LHC:
top quark pair precision measurements and associated production with additional bosons

HABILITATIONSSCHRIFT

vorgelegt von
Dr. Carmen Diez Pardos

eingereicht bei der Naturwissenschaftlich-Technischen Fakultät
der Universität Siegen

Siegen 2021

INTRODUCTION

Elementary particle physics aims to understand the smallest constituents of matter and their interactions. Our current knowledge is best described by the Standard Model (SM) of particle physics [1–4]. There are two types of fundamental particles in nature: fermions and bosons. Matter is composed of twelve fermions. They have spin 1/2, which means they obey the Pauli exclusion principle. Each of these fermions has its own antiparticle, which has the same mass, but opposite quantum numbers. The twelve fermions comprise three generations of leptons: the electron, the muon and the tau, each with a counterpart neutrino; and three generations quarks, each with two different flavours: up and down, charm and strange, and top and bottom. Quarks have additionally colour charge and come in three colours. The only known difference among the generations is the increasing fermion mass. Forces are mediated through the exchange of particles: photons for the electromagnetic force, the Z and W bosons for the weak force, and gluons for the strong force.

The SM is a quantum field theory. The interactions are described by the gauge symmetry group $SU(3)_C \times SU(2)_L \times U(1)_Y$. The $SU(3)_C$ symmetry describes Quantum Chromodynamics (QCD), the strong interaction; a theory of the interactions of particles which carry colour charge: the quarks and gluons. The latter are the eight massless particles mediating the interaction. The term $SU(2)_L \times U(1)_Y$ describes the unification of the weak and the electromagnetic interactions. Before the electroweak symmetry breaking, $SU(2)_L$ is mediated by three weak isospin, massless bosons W^μ, and $U(1)_Y$ by a weak hypercharge massless boson, B^0. The weak hypercharge relates the electrical charge and the third component of the weak isospin. After the symmetry breaking, these gauge bosons are recombined and give rise to the massive mediators of the weak force (W^+, W^-, Z) and the massless photon γ, carrier of the electromagnetic interaction. This process required the introduction of a scalar field, the Higgs field, and its spin-0 boson, the Higgs boson. Otherwise, for reasons of invariance, mass terms for the gauge fields or the fermions are not allowed.

The understanding of the basic components of matter is a century old effort. However, great advancements have been accomplished in this field in the last 60 years as a result of the interplay between new colliders, improved experimental techniques, and theoretical insights. Every particle predicted by the SM has been observed, for instance the electroweak bosons W and Z in 1983, the top quark in 1995, and the tau neutrino in 2000. A fundamental breakthrough was the discovery of the missing piece, the Higgs boson, at the Large Hadron Collider (LHC) at CERN in 2012 [5,6]. Despite the success of the SM in describing most of the experimental data, it is not an ultimate theory of fundamental interactions, since, e.g. it does not include the gravitational interaction. The nature of neutrinos, whether they are Dirac or Majorana particles, and the mechanism of their mass generation are also unknown. Other profound questions that remain unanswered by the SM are the origin of the charge-parity (CP) violation, responsible for the matter-antimatter asymmetry in the universe, why QCD seems to preserve CP-symmetry, and the electroweak hierarchy problem or why the electroweak scale, $\mathcal{O}(10^2 \text{ GeV})$, is much lighter than the Planck scale, $\mathcal{O}(10^{19} \text{ GeV})$. Similarly, the origin of Dark Matter, which can only be answered by the presence of physics phenomena beyond the SM (BSM), is still unknown.

The LHC and its main experiments are built to shed light on the unsolved questions, reaching the TeV energy scale, where many of the extensions of the SM predict the existence of new physics phenomena. The LHC was designed to provide proton beams with

an energy of 7 TeV yielding a centre-of-mass energy ($\sqrt{s}$) of 14 TeV and with an instantaneous luminosity of 10^{34}cm^{-2}s^{-1}. This centre-of-mass energy provides parton-parton collisions up to energies of about 1 TeV, which together with the very high collision rate, favours the study of the production of rare particles. During the first running phases the centre-of-mass energies of proton-proton collisions were 7 TeV (2010-2011), 8 TeV (2012) and 13 TeV (2015-2018). The total data sets collected by the ATLAS [7] and CMS [8] experiments correspond to about 5, 20, and 140 fb^{-1} of integrated luminosity at $\sqrt{s} = 7$, 8, and 13 TeV, respectively. The physics programme of the LHC comprises two general objectives: first, to perform precision measurements of SM quantities and second, to directly discover new physics phenomena BSM. With the data recorded up to now no sign of new physics has been found. However, very stringent limits have been set on parameters of BSM theories.

As part of this quest to scrutinise the SM and look for possible deviations, the focus of the research summarised in this thesis is the top quark, the heaviest fundamental particle known to date with a mass of 173.1 ± 0.9 GeV [9]. It was discovered by the CDF and D0 Collaborations at the Fermilab Tevatron, using proton-antiproton collisions at $\sqrt{s} = 1.8$ TeV [10,11]. Owing to its large mass, the decay time of the top quark is significantly smaller than the time scale of hadronisation, and top quarks decay before forming bound states. This allows studying the properties of an unconfined quark, such as its polarisation [12] and charge [13], and to directly measure the mass of the top quark from the invariant mass of its decay products [14]. Furthermore, the value of the mass of the top quark provides a natural hard scale for testing the validity of perturbative QCD. The coupling of the top quark to the Higgs field (Yukawa coupling, y_t) is predicted to be much larger than that of any other fermion. The top quark is expected to play a relevant role in the electroweak symmetry breaking. Moreover, the relationship between the masses of the top quark, the W boson, and the Higgs boson is predicted by the SM. Hence measurements of these masses allow probing its self-consistency. Additionally, the top quark provides a probe for BSM physics since in many scenarios of new physics it is expected to couple to new particles.

The absence of new physics signals in the LHC data recorded so far suggests that new physics might only be directly manifested at an energy scale that is larger than the scales probed at the LHC. In this case, the new states could be only produced virtually at the LHC. These virtual effects can be accommodated, for instance, by adding higher-dimensional operators in the SM Lagrangian like in what is known as an Effective Field Theory. Top quark observables are expected to be sensitive to several of these new operators [15].

This thesis concerns in particular the study of top quark physics using data from both the CMS and ATLAS experiments. This includes precision measurements related to top quark pair ($t\bar{t}$) production and the top quark mass, and searches and measurements for associated production of $t\bar{t}$ with a Higgs boson ($t\bar{t}$H) or a photon ($t\bar{t}\gamma$). The measurements comprise results with the data collected at 7 and 8 TeV (Run 1) and at 13 TeV (Run 2). With millions of top quarks produced, the intrinsic properties and decay mechanisms can be studied in detail. Progress in experimental and theoretical methods contributed to reach unprecedented precision in the comparison of data and SM predictions. Experimental advances have also allowed to observe for the first time the production of top quarks with additional bosons.

Top quarks at the LHC

Top quarks are mostly produced in pairs via the strong interaction in hadron colliders. At the LHC energies, the dominant mechanism is gluon-gluon fusion, corresponding to about 85% of the generation process at $\sqrt{s} = 13$ TeV. Top quarks can also be produced singly, via the electroweak interaction. The three modes of single top quark production are t-channel, tW associated production, and s-channel. Top quarks decay almost exclusively via the t $\to$ bW and it is the decays of the W bosons into a lepton and a neutrino or a pair of quarks that defines the final state. Therefore, $t\bar{t}$ signatures can be classified according to the combinatorics of the W boson decays. Thus, $t\bar{t}$ final states include events with one lepton, one neutrino and four jets, out of which two stem from a b quark, referred to as b jets (single-lepton channel); with two leptons, two neutrinos and two b jets (dilepton channel), or with six jets, out of which two are b jets (all-hadronic channel). Despite the low branching ratio, dilepton channels are extensively exploited because they can be experimentally identified with high purity. They are the main final states considered in the measurements presented here.

Physics analyses: from raw data to measurement

In the following the general analysis strategy and main steps of several physics analyses are discussed. A key element to all of them is the correct identification of the events coming from the physics process under study and the separation of these events from those arising from background processes that mimic the signature of the signal in the data. Monte Carlo (MC) event generators are used to estimate the expected amount of signal and background events in data. Additionally, estimates based on data using control regions are typically used either when the MC estimate is not reliable or for validation purposes. In analyses with a high signal purity, an optimised event selection is typically enough to enhance the signal events while suppressing background events. However, if the number of signal events is very small compared to the background processes and/or the kinematic properties of the events are very similar, multivariate analysis techniques are required. These techniques allow the combination of the full event information to build an optimal discriminator between signal and background events. The signal fraction in the data is then obtained by counting events or using advanced statistical methods such as profile likelihood fits. For analyses aiming to study not only the production rate (the cross section) of the process but the properties of the top quarks (e.g. its mass or kinematic properties) event reconstruction techniques are employed to identify which of the measured objects correspond to the parton level objects arising from the decay of the top quarks. Another element often used in measurements where observed distributions are compared to calculations is an unfolding procedure to correct the data for detector effects. This allows comparing the results among experiments and existing or future higher-order calculations.

Top quark identification

The ATLAS [7] and CMS [8] detectors (and typically any hadron collider detector) consist of tracking detectors, electromagnetic and hadron calorimeters, and muon detectors. Strong magnetic fields are provided by superconducting magnets, which bend the trajectory of charged particles. Their momenta are determined by identifying the curvature of their trajectories in the magnetic fields. Particle energies are determined in a destructive measurement from electromagnetic and hadronic showers in the calorimeters.

The raw signals of the different subdetectors are processed to reconstruct the basic analysis objects such as electrons, muons, and jets. Top quark measurements require a good understanding of all physics objects as the products of top quark decays involve - depending on the decay mode - the presence of high momentum isolated leptons, missing transverse momentum owing to the neutrinos that escape detection ($\not{E}_T$), and highly energetic jets. Jets originating from bottom quarks are identified through b-tagging techniques.

Monte Carlo simulations

Monte Carlo event generators, interfaced with detailed detector simulations, are used to model experimental effects, such as reconstruction and selection efficiencies as well as detector resolutions. They are tools to simulate the QCD dynamics at the different energy scales of an event. The partonic scattering is calculated in perturbation theory using numerical methods, the subsequent emission of soft and collinear partons is simulated using parton shower generators. Soft processes such as multiple parton interactions, hadronisation, and hadron decays are described with phenomenological models. The detector simulation is performed with Geant 4 [16]. Typical event generators are MadGraph5_aMC@NLO [17] and Powheg [18–20] which are used for instance to calculate $t\bar{t}$ and $t\bar{t}H$ matrix elements at up to next-to-leading order (NLO) accuracy in QCD. They are matched to the parton shower MC generators Pythia [21, 22] or Herwig [23, 24].

Event selection and efficiency measurements

The first event selection step is performed by the multilevel trigger system. The first level is implemented at hardware level in custom-made electronics while the subsequent levels are implemented at software level on large computing farms. The main trigger paths used in top quark physics select one or more isolated electrons or muons above a threshold in transverse momentum (p_T), yielding a very efficient selection of leptonic $t\bar{t}$ topologies. The following steps to select signal events and reject background processes are based on the kinematic properties of the top quark decay objects, such as p_T and pseudorapidity of leptons and jets and global event variables, as $\not{E}_T$ and additional requirements on heavy-quark content.

A fundamental piece of any physics analysis is therefore the determination of the efficiency of the reconstruction, trigger, and selection of the objects involved. To improve the description of the data by the simulation correction factors for detector effects are applied. The methods based on data used to determine lepton and trigger efficiencies I contributed to are shortly described in the following. The evaluation of the efficiency directly from data avoids depending on MC simulation and introducing biases due to detector behaviour mismodelling.

The first method referred to as 'Tag and Probe' is based on dilepton events from Z boson decays, where one lepton is required to pass stringent criteria to select the event and the second one is used to determine the efficiency. It is widely used to measure single lepton trigger and identification efficiencies. Leptons coming from Z boson decays are kinematically similar to those arising from W boson decays, so they are well suited for efficiency measurement in top quark topologies. The method exploits the clear selection of $Z \rightarrow \ell\ell$ candidates and takes into account the possible presence of background events remaining in the selected sample. The efficiency of dilepton triggers or combination of triggers is alternatively measured in data using triggers that require $\not{E}_T$ or jets in the event, which are uncorrelated to the triggers used in the analysis and allow to select events in an unbiased way. The efficiency is computed as the fraction of those events

where the triggers of interest fired over the total number of events that fulfill the offline requirements. The method, further developed in the context of Ref. [P11], was used as cross check measurement for the central measurements provided by the CMS Collaboration and in multiple measurements involving top quark topologies, such as Refs. [25, 26, P7].

Multivariate analysis techniques

After the event selection, the classification of events as signal- or background-like is often performed using machine learning (ML) techniques. Supervised ML methods use signal and background MC simulations to *train* an algorithm to distinguish both processes based on non-linear combinations of several input variables, such as the kinematic properties of jets and charged leptons, the b-tagging probability, invariant masses, and angular correlations of combinations of jets and leptons in $t\bar{t}$ topologies. The first methods used in top quark physics in Run 1 were boosted decision trees (BDTs) while artificial neural networks (ANNs) are increasingly being applied in the measurements at $\sqrt{s} = 13$ TeV, in addition to applications in object identification and reconstruction. The exploitation of ML techniques helps to fully profit from the potential of the data and was crucial in the recent observations of several processes in the last years, most notably $t\bar{t}H$ [P3].

Top quark kinematic reconstruction

The purpose of the kinematic reconstruction is to estimate the four vectors of the $t\bar{t}$ system and the top quarks based on those of the identified jets, leptons, and $\not{E}_{T}$, while account for detector resolution effects. The top quark reconstruction faces problems such as underdetermined kinematic properties due to unmeasured neutrinos, and the combinatorics of assigning jets to partons from the top quark decay (the bottom quarks from the top quark decays and the light-flavour quarks from the hadronic W-boson decays). In the case of the dilepton channel the kinematic reconstruction corresponds to solving the equation of the neutrino momenta, for which several constraints need to be imposed. In the method described in Ref. [27], which is applied and adapted if necessary in Refs. [P5, P6, P8, P14], the following constraints are imposed: the balance of the transverse momentum of the two neutrinos; the W-boson invariant mass of 80.4 GeV; and the equality of the top and antitop quark masses. The remaining ambiguities are resolved by prioritising those event solutions with two or one b-tagged jets over solutions using jets without b tags. The efficiency of the kinematic reconstruction is measured to be above 90% in most regions of phase space. In $t\bar{t}$ events with additional jets, the algorithm correctly identifies the two jets coming from the $t\bar{t}$ decay in about 70% of the cases [P6]. Multivariate analysis approaches can also be employed to identify the reconstructed physics objects that most likely come from the decay of the $t\bar{t}$ system, which allows as well to study the properties of the additional QCD radiation, first exploited in Ref. [P6].

Signal extraction: maximum-likelihood fit

The simplest method to measure the cross section of a process is to count the number of events that pass the event selection, subtract the expected number of background events, and correct by the efficiency and acceptance, and finally scale by the total luminosity of the data set. However, in order to increase the sensitivity to the signal by reducing the dependence on the background estimates and improving the precision of the measurement, binned profile likelihood fits are exploited in many of the results discussed in the following, e.g. [P1, P2, P5]. The expected signal and background distributions are modelled in the fit by template histograms constructed from the simulated samples and the

sum of signal and background contributions is fitted to the data. The likelihood function consists of Poisson terms for the event yields and prior functions for the background normalisation and further nuisance parameters that represent the systematic uncertainties: $\mathcal{L} = \prod_i P\left(N^i_{\text{data}} | N^i_{\text{signal}}(\vec{\theta}) + N^i_{\text{bkg}}(\vec{\theta})\right) \times \prod_t P_{\hat{\theta}_t}(\hat{\theta}_t | \theta_t)$, where N^i_{data}, N^i_{signal}, and N^i_{bkg} are the observed number of events in data, the predicted number of signal events, and the estimated number of background events in bin i of the corresponding distribution. The vector $\vec{\theta}$ represents the nuisance parameters, θ_t, that describe the sources of systematic uncertainties and $P_{\hat{\theta}_t}$ denotes the prior probability density function for each nuisance parameter that represents the prior knowledge of the parameter. The normalisation of the signal process is a free parameter. Events are typically divided in categories with different signal and background composition, correlating processes and their uncertainties where appropriate. In this way, the different background fraction in the different categories helps to constrain the uncertainties of the various processes and increases the overall sensitivity. The parameter of interest is measured by profiling the nuisance parameters and minimising $-2\ln\mathcal{L}$ [28].

UNFOLDING TECHNIQUES

Physics quantities reconstructed with a collider detector and the theoretical calculations of observables can only be compared if effects from the trigger and reconstruction efficiencies and resolutions, which yield to migrations of events and statistical correlations among neighbouring bins, are corrected in data in a procedure known as unfolding. Mathematically, the relation between the reconstructed (N_{reco}) and the *true* (N_{true}) quantities considering discrete distributions can be expressed as $N^i_{\text{reco}} = \sum_j A^{ij} N^j_{\text{true}} + N^j_{\text{bkg}}$ in each bin i of the measurement. A^{ij} represents the response matrix that corrects for migrations and efficiencies.

Obtaining the true distribution from the direct inversion of the matrix is an ill-posed problem, because the statistical fluctuations in data cannot be distinguished from the real spectrum without further assumptions. This leads to numerical instabilities in the matrix inversion and might introduce non-physical anticorrelations among neighboring bins. Thus, a smoothing prescription known as regularisation is applied. It requires a continuous and smooth transition between bins of the measured distribution. There are several approaches for regularisation, such as the Tikhonov regularisation, implemented for instance in the TUNFOLD package [29], and the regularisation by singular-value decomposition as in Ref. [30] exploited in the differential measurements discussed in Refs. [P6, P8, P9]. The regularisation level is determined using the averaged global correlation method [31]. An alternative method is an iterative matrix unfolding that uses Bayes' theorem [32] implemented in the ROOUNFOLD package [33]. The unfolding method relies on the Bayesian probability formula, starting from a given prior of the true-level distribution and iteratively updating it with the posterior distribution. This approach is followed in the differential cross section measurements of $t\bar{t}\gamma$ [P1]. Independently of the method, the binning, to keep bin-by-bin migrations small, and the level of regularisation are optimised for each distribution individually and the performance of the unfolding procedure is tested for possible biases from the choice of the model for signal simulation.

SYSTEMATIC UNCERTAINTIES

The high production rate of top quark pairs ensures that many measurements will have small statistical uncertainties. Therefore, systematic uncertainties typically limit the

precision of the results described in the following. The sources of systematic uncertainties considered arise from detector effects, as well as theoretical uncertainties. The large data sets collected allow accurate studies on the detector response, resulting in a precise understanding of the systematic uncertainties associated to the reconstruction efficiencies and energy and momentum measurements. Measurements are used to tune the MC simulations to improve the description of the data and reduce the systematic uncertainties related to the modelling [P12].

TOP QUARK PAIR PRODUCTION

INCLUSIVE AND DIFFERENTIAL CROSS SECTIONS

The first step towards the understanding of top quark physics is the measurement of the production rate of the dominant mechanism at the LHC, $t\bar{t}$ production. Measurements can be compared to calculations performed at next-to-next-to-leading order (NNLO) including resummation of soft gluon terms [34]. Final states with an electron and a muon are especially suited for precise $t\bar{t}$ cross section measurements due to the low contamination from background processes. Our first measurements at $\sqrt{s} = 8$ and 13 TeV within the CMS Collaboration were performed as counting experiments [P4, P11], meant to establish top quark production at the new scales. Once the detector performance is well understood and the amount of data collected result in measurements with a small statistical uncertainty, the cross sections are measured using statistical methods that allow constraining in situ the most relevant sources of systematic uncertainties as aforementioned. With this analysis strategy, using a binned likelihood fit to multi-differential final state distributions related to b jets and other jets in the event, the $t\bar{t}$ cross sections yield $173.6 \pm 2.1\,\text{(stat)}\,^{+4.5}_{-4.0}\,\text{(syst)} \pm 3.8\,\text{(lumi)}$ pb and $244.9 \pm 1.4\,\text{(stat)}\,^{+6.3}_{-5.5}\,\text{(syst)} \pm 6.4\,\text{(lumi)}$ pb [P5], corresponding to a precision of 3.6% at 7 TeV and 3.7% at 8 TeV. These and further measurements of the $t\bar{t}$ inclusive cross section by ATLAS and CMS in different decay channels [35–39] are in excellent agreement with the theory calculations.

The total uncertainty of the measurement is dominated by the uncertainty on the luminosity and those related to trigger and lepton efficiencies, which cannot be constrained in the fit. Precision measurements can be used to set indirect limits to BSM models as stated before. In particular, these results are used to constrain the cross section of pair production of the lightest supersymmetric partner of the top quark in the context of Supersymmetry models with R-parity conservation [40].

In order to further test the predictions of the SM the next natural step was to perform measurements differentially to study the production in regions of phase space. This kind of measurements are relevant to constrain SM parameters and in BSM searches. As an example, the distribution of the $t\bar{t}$ invariant mass is sensitive to the top quark mass and y_t [41, 42] and the value of the top quark mass [43, 44]. Deviations with respect to the expected spectrum could be a sign of, for example, the existence of an extended Higgs sector [45]. Absolute differential cross sections are defined as:

$$\frac{\mathrm{d}\sigma_{t\bar{t}}}{\mathrm{d}x_i} = \frac{\sum_j A_{ij}^{-1}(N_{\text{data}}^j - N_{\text{bkg}}^j)}{\Delta_x^i \mathcal{L}},$$

where j represents the bin index of the reconstructed variable x, i is the index of the corresponding generator-level bin, N_{data}^j is the number of data events in bin j, N_{bkg}^j is the number of estimated background events, $\mathcal{L}$ is the integrated luminosity, Δ_x^i is the bin

width, and A_{ij} represents the response matrix to correct for migrations and efficiencies, as described above.

The normalised differential cross sections are derived by dividing the absolute result by the total cross section obtained by integrating over all bins of the observable. Normalised differential cross sections allow only the comparison of the shape of the distributions, however they are more precise than the absolute results because several sources of systematic uncertainties cancel at least partially in the ratio.

The differential cross sections in our publication [P9] are measured as a function of the kinematic properties of leptons, jets, top quarks or antiquarks, and the $t\bar{t}$ system. In order to avoid additional model uncertainties due to the extrapolation of the measurement outside experimentally well-described phase space regions, the cross sections for the measured leptons and b jets are defined at the particle level with kinematic requirements similar to those applied at reconstruction level. Measurements as functions of top quark or $t\bar{t}$ quantities are extrapolated to the full phase space in order to allow comparison with fixed order QCD calculations. The results are compared to various SM predictions, finding overall good agreement with the SM. However, the measured top quark transverse momentum has been found to be lower than the predictions up to NLO accuracy in QCD perturbation theory, but better described by a prediction beyond NLO. These results [P9] were used to set constraints on the gluon parton distribution function (PDF) [46] and incorporated to PDF sets such as the NNPDF3.1.

Top quark pair production with additional hard jets

At the LHC energies, the fraction of $t\bar{t}$ events with additional hard jets in the final state ($t\bar{t}$+jets) is large, about half of the total number of events. The understanding of these processes is essential to test the validity and completeness of high order perturbative QCD calculations of multijet processes. In addition, an accurate theoretical description of the $t\bar{t}$+jets production process is crucial to measurements of processes with $t\bar{t}$ multijet final states, such as four top quark production [47] to which $t\bar{t}$+jets is a dominant background. Moreover, anomalous production of $t\bar{t}$+jets could be a sign of new physics BSM [48].

We performed first detailed studies of $t\bar{t}$+jets production with the data collected at $\sqrt{s} = 7$ TeV [P8], further extended with the larger data set at 8 TeV [P6]. The $t\bar{t}$ cross section is measured differentially as a function of jet multiplicity and characterised both in terms of the total number of jets in the event and the number of additional jets with respect to the leading-order hard-interaction final state. Several kinematic properties of the additional jets are also investigated. Kinematic reconstruction methods, introduced above, are used to identify the two b jets originating from the decay of the top quark and antiquark. We also investigated the jet activity arising from quark and gluon radiation produced in association with the $t\bar{t}$ system by determining the fraction of events that do not contain additional jets above a given threshold, first explored in Ref. [49]. The data are compared and found to be consistent with predictions from several perturbative QCD event generators with some discrepancies found at large jet multiplicities or certain regions of phase space. The results [P6] were employed to improve the simulation of $t\bar{t}$ production, in particular the parton shower tuning in PYTHIA8 [P12]. This improved tune was heavily used by the CMS Collaboration in the production of MC simulation samples at 13 TeV.

The publication using the data set collected at 8 TeV also includes the first differential cross sections as functions of the kinematic properties of the additional b jets from gluon splitting ($t\bar{t}b\bar{b}$). These processes constitute an irreducible non-resonant background to the production of $t\bar{t}$H events, where the Higgs boson decays to a bottom quark pair, because of its much larger cross section. The sources of uncertainties associated to the $t\bar{t}b\bar{b}$ modelling

are among the dominant ones. Therefore, measurements of $t\bar{t}$+jets and $t\bar{t}b\bar{b}$ production provide important information to reduce that uncertainty and also as reference to improve NLO QCD calculations and simulations, which currently provide predictions with 20%-30% precision (Ref. [50] and references herein). The $t\bar{t}b\bar{b}$ measurements rely on BDTs to distinguish the b quarks from the top quark decays from those from gluon splitting, which improves the separation of jets from $t\bar{t}$ decays and additional radiation compared to the kinematic reconstruction in topologies with many b-quark jets. The measurements are compared to an NLO calculation [51]. The prediction describes well the shape of the different distributions, while the inclusive cross section is about 30 % lower than the measured one, but compatible within the uncertainties, in agreement with previous observations [52]. Given the small $t\bar{t}b\bar{b}$ cross section of the processes, our measurements are limited by the statistical uncertainty of the data, while the measurements of the inclusive jet kinematic properties are limited mostly by the uncertainty on the jet energy scale.

Top quark mass

The top quark mass like the mass of any quark is not an observable but a fundamental parameter of the SM. Its value is not predicted but can be inferred from experimental measurements, either through direct measurements of the invariant mass of its decay products, or indirectly from the predicted dependence of other measured observables, such as the cross section.

Direct measurements of the top quark mass based on its reconstructed invariant mass have reached a precision at the per mille level [14, 53–56]. The current world average of direct measurements is $173.34 \pm 0.27(\text{stat}) \pm 0.71(\text{syst})$ GeV [57]. These measurements might be sensitive to the details of the MC generator used to derive the templates to model the $t\bar{t}$ signal, preventing a clear theoretical interpretation. The results are often interpreted as the value of the top quark mass parameter in the MC simulation that best describes the data. Indirect measurements from cross sections are typically less precise, however, they can be unambiguously interpreted in a well-defined renormalisation scheme, e.g. on-shell top quark pole mass. As an example, the inclusive cross section measurements in Ref. [P5] have been used to extract the top quark pole mass at NNLO accuracy with about 1.0% precision. Measurements of $t\bar{t}$ differential cross sections can be used to extract the top quark pole mass at NLO accuracy [58, 59]. The difference in the accuracy depends on the available calculations the measurements can be compared to. In Ref. [P14], we performed an alternative measurement of the top quark mass from an observable based on the invariant mass of the $t\bar{t}$+jet system, proposed in Ref. [60], allowing for a theoretically well defined interpretation of the extracted mass in terms of the top quark pole mass. The precision of the measurement is largely limited by the modelling uncertainties of the LO MC $t\bar{t}$ simulation available at that point. This was the first measurement exploiting the $t\bar{t}$ dilepton channel, measurements in the single-lepton channel are discussed in Refs. [61, 62].

Top quark production in association with bosons

The associated production of top quarks with additional bosons became accessible for the first time at the LHC owing to the large $\sqrt{s}$ and the size of the available data sets. Measurements of the $t\bar{t}H$ process are the first direct tests of y_t and measurements of $t\bar{t}$ production with neutral vector bosons (γ, Z boson) provide the opportunity to directly probe the electroweak couplings of the top quark. These measurements allow to access the

electric charge and the electroweak dipole moments of the top quark and, more generally, to constrain modifications of the structure of these couplings, as predicted in many BSM models. The impact of different new physics scenarios on these processes is discussed, e.g. in Refs. [63–68]. The publications in this thesis [P2, P3, P13, P15] and [P1] focus on the search for $t\bar{t}H$ and measurements of the $t\bar{t}\gamma$ process, respectively.

Searches and first direct observation of $t\bar{t}H$ production

Due to the large mass of the top quark, larger than the mass of the Higgs boson, the coupling between these particles can only be studied directly in their associated production, unlike the coupling between the Higgs boson and lighter particles that can be measured by studying the Higgs boson decay. The effects of the y_t coupling can be also inferred indirectly from Higgs boson production through gluon-gluon fusion and Higgs boson decay to a pair of photons through loops. However, $t\bar{t}H$ production is the best direct probe of the y_t coupling with minimal model dependence. Measurements of $t\bar{t}H$ production have the potential to distinguish the SM Higgs mechanism from alternative mechanisms to generate fermion mass. The observation of $t\bar{t}H$ and the measurement of the coupling were therefore amongst the major goals of the physics programme for the LHC Run 2. Its small SM cross section, a factor of about 2000 smaller than $t\bar{t}$ production, makes this a very difficult measurement. Several topologies depending on the Higgs boson and $t\bar{t}$ decays were exploited and optimised individually in order to maximise the sensitivity to the processes. The Higgs boson decays considered involved final states with photons, bottom quark-antiquark pairs or leptons via WW, ZZ, and $\tau\tau$ decays.

My research focused on dileptonic $t\bar{t}$ topologies and final states with a Higgs boson decay into a b-quark pair (H $\rightarrow$ b$\bar{\text{b}}$), which are particularly interesting since this decay channel has the largest branching fraction for a 125 GeV Higgs boson, and precisely defined couplings in both production (top quarks) and decay (b quarks) [P2, P13, P15]. However, as mentioned previously, this process is affected by the overwhelming background from $t\bar{t}$+jets and, especially, the irreducible background from $t\bar{t}b\bar{b}$. At the same time, the relatively poor jet-energy resolution and the huge combinatorial uncertainty in the event reconstruction required the application of multivariate analysis methods to discriminate signal from background processes. In the following only the measurements with the full 2016 data set [P2] are discussed. In the dilepton channel, BDTs and the output of a matrix element method [69, 70] are used as final discriminant depending on the category based on the number of b jets. In the single-lepton channel, ANNs are employed to perform a multiclassification of an event as either signal or any of five different $t\bar{t}$+jets background processes. Events are further categorised according the most-probable process that produced the event according to the ANN classifer, which is used as final discriminant. The results are obtained in terms of the $t\bar{t}H$ signal strength, which is defined as the ratio of the measured cross section over the SM prediction. The best-fit value from a combined profile likelihood fit of the discriminant templates to data in all categories yields $0.72 \pm 0.24(\text{stat}) \pm 0.38(\text{syst})$. It corresponds to an observed (expected) signal significance of 1.6 (2.2) standard deviations above the background-only hypothesis.

This result combined with previous searches at 7 and 8 TeV [P10] that I contributed to, and all other $t\bar{t}H$ analyses with 2016 data [71–74] yield the first observation of the $t\bar{t}H$ production process [P3]. An excess of events is observed with a significance of 5.2 standard deviations over the expectation from the background-only hypothesis. The combined best fit signal strength is $1.26^{+0.31}_{-0.26}$ for a Higgs boson mass of 125.09 GeV. The sensitivity of the combination is slightly dominated by systematic uncertainties, in particular the uncertainty in the inclusive $t\bar{t}H$ cross section, the $t\bar{t}b\bar{b}$ background prediction, the lepton

efficiencies and misidentification, b-tagging efficiencies, and the limited size of the simulated samples. The measured production rate is consistent with the SM prediction within one standard deviation. This measurement established the tree-level coupling of the Higgs boson to an up-type quark and was further confirmed by Ref. [75].

TOP QUARK PAIR PRODUCTION IN ASSOCIATION WITH A PHOTON

The study of the associated production of top quarks with a photon is a probe of the tγ electroweak coupling. Deviations in the spectra of differential cross sections as a function of p_{T} for example could be a hint to new physics through anomalous dipole moments of the top quark. Additionally, the process is expected to be sensitive to $t\bar{t}$ charge asymmetry (top quarks produced via initial quarks at the LHC are emitted in slightly different directions depending on its charge) or spin correlations [76].

The first evidence for the production of $t\bar{t}\gamma$ was reported by the CDF Collaboration [77], while the observation of the $t\bar{t}\gamma$ process was established by the ATLAS Collaboration with the data collected at $\sqrt{s} = 7$ [78]. Recently, efforts have concentrated on improving the precision of the measurements and extending the scope and range of the differential ones. Our results in Ref. [P1] comprise the first fiducial inclusive and differential cross-section measurements of the combined double-resonant $t\bar{t}\gamma$ and single-resonant tWγ production. The cross sections are measured at parton level to allow comparison with the first full computation of pp $\rightarrow$ bWbWγ at NLO in perturbation theory [79, 80]. The measurement is performed in the $e\mu$ channel. Similarly to the $t\bar{t}$ cross section, the fiducial inclusive cross section is measured using a profile likelihood fit. The result, $\sigma_{\mathrm{fid}} = 39.6 \pm 0.8\,(\mathrm{stat})\,^{+2.6}_{-2.2}\,(\mathrm{syst})\,\mathrm{fb}$, reaches a precision of about 6.3% and it is in good agreement with the dedicated theoretical calculation. The absolute and normalised differential cross sections are measured as functions of photon kinematic variables, angular variables related to the photon and the leptons, and angular separations between the two leptons in the event. The NLO calculations describe well the shape and the normalisation of the differential cross sections, while the LO MC simulations provide a poor description of angular distributions. The systematic uncertainty is dominated by modelling uncertainties associated to the $t\bar{t}\gamma$ LO MC simulations, another example that illustrates the importance of higher-order calculations and simulations to further improve the precision of the measurements.

SUMMARY AND OUTLOOK

The large $t\bar{t}$ data sets collected at the LHC up to now allowed detailed $t\bar{t}$ production cross section measurements as well as the observation of $t\bar{t}$ in association with additional bosons. The results are exploited to extract SM parameters like the mass of the top quark, as input to improve the MC simulations and PDF sets and in indirect searches for new phenomena. The expected luminosity delivered by the LHC, about 300 fb^{-1} by the end of Run 3 (2024) and up to 3000 fb^{-1} after the HL-LHC, will allow access to unexplored regions of phase space, the study of more complex signatures and the testing of more theoretical models, and might shed light on profound questions that can only be answered by the presence of physics phenomena BSM. Measurements limited by systematic uncertainties do not benefit automatically from larger data sets. The gain in precision measurements and, thus, the precision to determine SM parameters (mass, α_S, PDFs, etc.) and to constrain BSM parameters (e.g. in the context of EFT interpretations) will depend strongly on the improvements in the modelling of the physics processes, a better

understanding and reconstruction of the physics objects and ultimately the identification and separation of signal from background processes.

PERSONAL CONTRIBUTIONS

The author lists in publications within large collaborations in experimental high energy physics include all members of the corresponding collaboration. This acknowledges the fact that publications would not be possible without the collaborative effort of many individuals involved in the data taking, calibration of the detectors, etc. Therefore, as a former member of the CMS Collaboration and a current one of the ATLAS Collaboration, I am a co-author of more than 1000 papers in peer-reviewed journals as of October 2021. In this thesis, only the relevant publications where I was a main author or had direct contributions are listed (Refs. [P1]– [P11]), as well as preliminary publications that are not superseded by the corresponding journal publications (Refs. [P12]– [P16]). Preliminary results are peer-reviewed by three or four members of the Collaboration, who are appointed as editorial board, and by the convenors of the corresponding working groups. Before being published, the results are presented within the Collaboration which approves the publication. I was the editor or co-editor of the publications Refs. [P1, P2, P5, P6, P8, P9, P14], responsible of writing the publication, the coordination of the analysis team, supervision of students and addressing the review process. The number of collaborators working closely in the publications was typically up to 10 people from up to three or four different institutions, with the exception of publications related to $t\bar{t}H$ with about 20 active authors.

Additionally to being editor/co-editor, my contributions to those publications are listed in the following. I contributed to all the stages of the measurement and provided the final results and performed the statistical analysis in the dilepton channel presented in Ref. [P2]. I provided additional results and cross checks for the combination of $t\bar{t}H$ measurements [P3]. I contributed to different steps in the previous analyses carried out using the data collected in 2016 [P13] and in 2015 [P15], and I was involved in the $t\bar{t}H$ analysis at 8 TeV and 7 TeV [P10], contributing with measurements of trigger and lepton efficiencies, as well as charge misidentification. I am a main author of the publications of the $t\bar{t}$+jets measurements [P6, P8]. I performed the measurement of the differential cross and the gap fractions in the dilepton decay channel in both publications. These results constituted the first differential measurements of this kind at the LHC and were employed in Ref. [P12], for which I provided additional material. I worked at different stages of the measurements presented in Ref. [P9]. I performed the first sensitivity studies, optimisation of the selection and generation of the MC samples in Ref. [P14], which was then continued by a PhD student under my supervision.

Finally, among others, I was an author of a search for direct pair production of scalar top quark partners in the dilepton channel at 8 TeV [P7] and inclusive cross section measurements [P4, P5] by providing the efficiency corrections for the trigger selection and lepton identification used in the analyses and I was part of the editorial team of the internal documentation.

REFERENCES

[1] S. L. Glashow, *Partial Symmetries of Weak Interactions*, *Nucl. Phys.* **22** (1961) 579.

[2] A. Salam and J. C. Ward, *Electromagnetic and weak interactions*, *Phys. Rev. Lett.* **13** (1964) 168.

[3] S. Weinberg, *A model of leptons*, *Phys. Rev. Lett.* **19** (1967) 1264.

[4] S. L. Glashow, J. Iliopoulos and L. Maiani, *Weak interactions with lepton-hadron symmetry*, *Phys. Rev. D* **2** (1970) 1285.

[5] CMS Collaboration, *Observation of a new boson at a mass of 125 GeV with the CMS experiment at the LHC*, *Phys. Lett. B* **716** (2012) 30 [`1207.7235`].

[6] ATLAS Collaboration, *Observation of a new particle in the search for the Standard Model Higgs boson with the ATLAS detector at the LHC*, *Phys. Lett. B* **716** (2012) 1 [`1207.7214`].

[7] ATLAS Collaboration, *The ATLAS Experiment at the CERN Large Hadron Collider*, *JINST* **3** (2008) S08003.

[8] CMS Collaboration, *The CMS experiment at the CERN LHC*, *JINST* **3** (2008) S08004.

[9] PARTICLE DATA GROUP collaboration, *Review of Particle Physics*, *Phys. Rev. D* **98** (2018) 030001.

[10] D0 collaboration, *Observation of the top quark*, *Phys. Rev. Lett.* **74** (1995) 2632 [`hep-ex/9503003`].

[11] CDF collaboration, *Observation of top quark production in $\bar{p}p$ collisions*, *Phys. Rev. Lett.* **74** (1995) 2626 [`hep-ex/9503002`].

[12] CMS Collaboration, *Measurement of the top quark polarization and $t\bar{t}$ spin correlations using dilepton final states in proton–proton collisions at $\sqrt{s} = 13\,TeV$*, *Phys. Rev. D* **100** (2019) 072002 [`1907.03729`].

[13] ATLAS Collaboration, *Measurement of the top quark charge in pp collisions at $\sqrt{s} = 7\,TeV$ with the ATLAS detector*, *JHEP* **11** (2013) 031 [`1307.4568`].

[14] CMS Collaboration, *Measurement of the top quark mass in the all-jets final state at $\sqrt{s} = 13\,TeV$ and combination with the lepton+jets channel*, *Eur. Phys. J. C* **79** (2019) 313 [`1812.10534`].

[15] I. Brivio, S. Bruggisser, F. Maltoni, R. Moutafis, T. Plehn, E. Vryonidou et al., *O new physics, where art thou? A global search in the top sector*, *JHEP* **02** (2020) 131 [`1910.03606`].

[16] S. Agostinelli et al., GEANT4 – *a simulation toolkit*, *Nucl. Instrum. Meth. A* **506** (2003) 250.

[17] J. Alwall, R. Frederix, S. Frixione, V. Hirschi, F. Maltoni, O. Mattelaer et al., *The automated computation of tree-level and next-to-leading order differential cross sections, and their matching to parton shower simulations*, *JHEP* **07** (2014) 079 [1405.0301].

[18] P. Nason, *A new method for combining NLO QCD with shower Monte Carlo algorithms*, *JHEP* **11** (2004) 040 [hep-ph/0409146].

[19] S. Frixione, P. Nason and C. Oleari, *Matching NLO QCD computations with parton shower simulations: the POWHEG method*, *JHEP* **11** (2007) 070 [0709.2092].

[20] S. Alioli, P. Nason, C. Oleari and E. Re, *A general framework for implementing NLO calculations in shower Monte Carlo programs: the POWHEG BOX*, *JHEP* **06** (2010) 043 [1002.2581].

[21] T. Sjöstrand, S. Mrenna and P. Skands, *PYTHIA 6.4 physics and manual*, *JHEP* **05** (2006) 026 [hep-ph/0603175].

[22] T. Sjöstrand, S. Ask, J. R. Christiansen, R. Corke, N. Desai, P. Ilten et al., *An introduction to PYTHIA 8.2*, *Comput. Phys. Commun.* **191** (2015) 159 [1410.3012].

[23] M. Bahr et al., *Herwig++ physics and manual*, *Eur. Phys. J. C* **58** (2008) 639 [0803.0883].

[24] J. Bellm et al., *Herwig 7.0/Herwig++ 3.0 release note*, *Eur. Phys. J. C* **76** (2016) 196 [1512.01178].

[25] CMS Collaboration, *Observation of the Associated Production of a Single Top Quark and a W Boson in pp Collisions at $\sqrt{s} = 8\,TeV$*, *Phys. Rev. Lett.* **112** (2014) 231802 [1401.2942].

[26] CMS Collaboration, *Search for the production of four top quarks in the single-lepton and opposite-sign dilepton final states in proton-proton collisions at $\sqrt{s} = 13\,TeV$*, *JHEP* **2019** (2019) .

[27] D0 collaboration, *Measurement of the top quark mass using dilepton events*, *Phys. Rev. Lett.* **80** (1998) 2063 [hep-ex/9706014].

[28] G. Cowan, K. Cranmer, E. Gross and O. Vitells, *Asymptotic formulae for likelihood-based tests of new physics*, *Eur. Phys. J. C* **71** (2011) 1554 [1007.1727].

[29] S. Schmitt, *TUnfold: an algorithm for correcting migration effects in high energy physics*, *JINST* **7** (2012) T10003 [1205.6201].

[30] A. Höcker and V. Kartvelishvili, *SVD approach to data unfolding*, *Nucl. Instrum. Meth. A* **372** (1996) 469–481.

[31] F. James, *Statistical methods in experimental physics, 2nd edition.* World Scientific, 2006.

[32] G. D'Agostini, *A multidimensional unfolding method based on Bayes' theorem*, *Nucl. Instrum. Meth. A* **362** (1995) 487.

[33] T. Adye, *Unfolding algorithms and tests using RooUnfold*, in *Proceedings of the PHYSTAT 2011 Workshop, CERN-2011-006*, pp. 313–318, 2011, 1105.1160.

[34] M. Czakon and A. Mitov, *Top++: A program for the calculation of the top-pair cross-section at hadron colliders*, *Comput. Phys. Commun.* **185** (2014) 2930 [1112.5675].

[35] ATLAS Collaboration, *Measurement of the $t\bar{t}$ production cross-section and lepton differential distributions in eμ dilepton events from pp collisions at $\sqrt{s} = 13\,TeV$ with the ATLAS detector*, *Eur. Phys. J. C* **80** (2020) 528 [1910.08819].

[36] ATLAS Collaboration, *Measurement of the $t\bar{t}$ production cross-section using eμ events with b-tagged jets in pp collisions at $\sqrt{s} = 7$ and $8\,TeV$ with the ATLAS detector*, *Eur. Phys. J. C* **74** (2014) 3109 [1406.5375].

[37] ATLAS Collaboration, *Measurement of the $t\bar{t}$ production cross section in the τ + jets final state in pp collisions at $\sqrt{s} = 8\,TeV$ using the ATLAS detector*, *Phys. Rev. D* **95** (2017) 072003 [1702.08839].

[38] CMS Collaboration, *Measurement of the $t\bar{t}$ production cross section using events in the eμ final state in pp collisions at $\sqrt{s} = 13\,TeV$*, *Eur. Phys. J. C* **77** (2017) 172 [1611.04040].

[39] CMS Collaboration, *Measurement of the $t\bar{t}$ production cross section using events with one lepton and at least one jet in pp collisions at $\sqrt{s} = 13\,TeV$*, *JHEP* **09** (2017) 051 [1701.06228].

[40] G. R. Farrar and P. Fayet, *Phenomenology of the Production, Decay, and Detection of New Hadronic States Associated with Supersymmetry*, *Phys. Lett. B* **76** (1978) 575.

[41] CMS Collaboration, *Measurement of the top quark Yukawa coupling from $t\bar{t}$ kinematic distributions in the lepton+jets final state in proton–proton collisions at $\sqrt{s} = 13\,TeV$*, *Phys. Rev. D* **100** (2019) 072007 [1907.01590].

[42] CMS Collaboration, *Measurement of the top quark Yukawa coupling from $t\bar{t}$ kinematic distributions in the dilepton final state in proton–proton collisions at $\sqrt{s} = 13\,TeV$*, *Phys. Rev. D* **102** (2020) 092013 [2009.07123].

[43] CMS Collaboration, *Running of the top quark mass from proton–proton collisions at $\sqrt{s} = 13\,TeV$*, *Phys. Lett. B* **803** (2020) 135263 [1909.09193].

[44] CMS Collaboration, *Measurement of the jet mass distribution and top quark mass in hadronic decays of boosted top quarks in pp collisions at $\sqrt{s} = 13\,TeV$*, *Phys. Rev. Lett.* **124** (2020) 202001 [1911.03800].

[45] CMS Collaboration, *Search for heavy Higgs bosons decaying to a top quark pair in proton–proton collisions at $\sqrt{s} = 13\,TeV$*, *JHEP* **04** (2020) 171 [1908.01115].

[46] M. Czakon, N. P. Hartland, A. Mitov, E. R. Nocera and J. Rojo, *Pinning down the large-x gluon with nnlo top-quark pair differential distributions*, *JHEP* **2017** (2017) .

[47] A. Collaboration, *Measurement of the $t\bar{t}t\bar{t}$ production cross section in pp collisions at $\sqrt{s}$=13 tev with the atlas detector*, 2106.11683.

[48] M. I. Gresham, I.-W. Kim and K. M. Zurek, *Searching for Top Flavor Violating Resonances*, *Phys. Rev. D* **84** (2011) 034025 [1102.0018].

[49] ATLAS Collaboration, *Measurement of $t\bar{t}$ production with a veto on additional central jet activity in pp collisions at $\sqrt{s} = 7\,TeV$ using the ATLAS detector*, *Eur. Phys. J. C* **72** (2012) 2043 [1203.5015].

[50] F. Buccioni, S. Kallweit, S. Pozzorini and M. F. Zoller, *NLO QCD predictions for $t\bar{t}t\bar{b}$ production in association with a light jet at the LHC*, *JHEP* **2019** (2019) .

[51] M. V. Garzelli, A. Kardos and Z. Trócsányi, *Hadroproduction of $t\bar{t}b\bar{b}$ final states at LHC: predictions at NLO accuracy matched with parton shower*, *JHEP* **2015** (2015) .

[52] CMS Collaboration, *Measurement of the cross section ratio $\sigma_{t\bar{t}b\bar{b}}/\sigma_{t\bar{t}jj}$ in pp collisions at $\sqrt{s} = 8\,TeV$*, *Phys. Lett. B* **746** (2015) 132 [1411.5621].

[53] ATLAS Collaboration, *Measurement of the top quark mass in the $t\bar{t} \to lepton+jets$ channel from $\sqrt{s} = 8\,TeV$ ATLAS data and combination with previous results*, *Eur. Phys. J. C* **79** (2019) 290 [1810.01772].

[54] ATLAS Collaboration, *Top-quark mass measurement in the all-hadronic $t\bar{t}$ decay channel at $\sqrt{s} = 8\,TeV$ with the ATLAS detector*, *JHEP* **09** (2017) 118 [1702.07546].

[55] CMS Collaboration, *Measurement of the top quark mass using proton–proton data at $\sqrt{s} = 7$ and $8\,TeV$*, *Phys. Rev. D* **93** (2016) 072004 [1509.04044].

[56] CMS Collaboration, *Measurement of the top quark mass with lepton+jets final states using pp collisions at $\sqrt{s} = 13\,TeV$*, *Eur. Phys. J. C* **78** (2018) 891 [1805.01428].

[57] The ATLAS, CDF, CMS and D0 Collaborations, *First combination of Tevatron and LHC measurements of the top-quark mass*, 2014.

[58] ATLAS Collaboration, *Measurement of lepton differential distributions and the top quark mass in $t\bar{t}$ production in pp collisions at $\sqrt{s} = 8\,TeV$ with the ATLAS detector*, *Eur. Phys. J. C* **77** (2017) 804 [1709.09407].

[59] CMS Collaboration, *Measurement of $t\bar{t}$ normalised multi-differential cross sections in pp collisions at $\sqrt{s} = 13\,TeV$, and simultaneous determination of the strong coupling strength, top quark pole mass, and parton distribution functions*, *Eur. Phys. J. C* **80** (2020) 658 [1904.05237].

[60] S. Alioli, P. Fernandez, J. Fuster, A. Irles, S. Moch, P. Uwer et al., *A new observable to measure the top-quark mass at hadron colliders*, *The European Physical Journal C* **73** (2013) .

[61] ATLAS Collaboration, *Determination of the top-quark pole mass using $t\bar{t} + 1$-jet events collected with the ATLAS experiment in 7 TeV pp collisions*, *JHEP* **10** (2015) 121 [1507.01769].

[62] ATLAS Collaboration, *Measurement of the top-quark mass in $t\bar{t} + 1$-jet events collected with the ATLAS detector in pp collisions at $\sqrt{s} = 8\,TeV$*, *JHEP* **11** (2019) 150 [1905.02302].

16

[63] U. Baur, A. Juste, L. H. Orr and D. Rainwater, *Probing electroweak top quark couplings at hadron colliders*, *Phys. Rev. D* **71** (2005) 054013 [`hep-ph/0412021`].

[64] A. O. Bouzas and F. Larios, *Electromagnetic dipole moments of the top quark*, *Phys. Rev. D* **87** (2013) 074015 [`1212.6575`].

[65] R. Röntsch and M. Schulze, *Probing top-Z dipole moments at the LHC and ILC*, *JHEP* **08** (2015) 044 [`1501.05939`].

[66] M. Schulze and Y. Soreq, *Pinning down electroweak dipole operators of the top quark*, *Eur. Phys. J. C* **76** (2016) 466 [`1603.08911`].

[67] O. Bessidskaia Bylund, F. Maltoni, I. Tsinikos, E. Vryonidou and C. Zhang, *Probing top quark neutral couplings in the Standard Model Effective Field Theory at NLO in QCD*, *JHEP* **05** (2016) 052 [`1601.08193`].

[68] P.-F. Duan, Y. Zhang, Y. Wang, M. Song and G. Li, *Electroweak corrections to top quark pair production in association with a hard photon at hadron colliders*, *Phys. Lett.* **B766** (2017) 102 [`1612.00248`].

[69] K. Kondo, *Dynamical likelihood method for reconstruction of events with missing momentum. 1: Method and toy models*, *J. Phys. Soc. Jap.* **57** (1988) 4126.

[70] D0 collaboration, *A precision measurement of the mass of the top quark*, *Nature* **429** (2004) 638 [`hep-ex/0406031`].

[71] CMS Collaboration, *Measurements of Higgs boson properties in the diphoton decay channel in proton–proton collisions at $\sqrt{s} = 13\,TeV$*, *JHEP* **11** (2018) 185 [`1804.02716`].

[72] CMS Collaboration, *Measurements of properties of the Higgs boson decaying into the four-lepton final state in pp collisions at $\sqrt{s} = 13\,TeV$*, *JHEP* **11** (2017) 047 [`1706.09936`].

[73] CMS Collaboration, *Evidence for associated production of a Higgs boson with a top quark pair in final states with electrons, muons, and hadronically decaying τ leptons at $\sqrt{s} = 13\,TeV$*, *JHEP* **08** (2018) 066 [`1803.05485`].

[74] CMS Collaboration, *Search for $t\bar{t}H$ production in the all-jet final state in proton–proton collisions at $\sqrt{s} = 13\,TeV$*, *JHEP* **06** (2018) 101 [`1803.06986`].

[75] ATLAS Collaboration, *Observation of Higgs boson production in association with a top quark pair at the LHC with the ATLAS detector*, *Phys. Lett. B* **784** (2018) 173 [`1806.00425`].

[76] J. A. Aguilar-Saavedra, E. Álvarez, A. Juste and F. Rubbo, *Shedding light on the $t\bar{t}$ asymmetry: the photon handle*, *JHEP* **2014** (2014) .

[77] CDF collaboration, *Evidence for $t\bar{t}\gamma$ production and measurement of $\sigma_{t\bar{t}\gamma}/\sigma_{t\bar{t}}$*, *Phys. Rev. D* **84** (2011) 031104 [`1106.3970`].

[78] ATLAS Collaboration, *Observation of top-quark pair production in association with a photon and measurement of the $t\bar{t}\gamma$ production cross section in pp collisions at $\sqrt{s} = 7\,TeV$ using the ATLAS detector*, *Phys. Rev. D* **91** (2015) 072007 [`1502.00586`].

[79] G. Bevilacqua, H. B. Hartanto, M. Kraus, T. Weber and M. Worek, *Hard photons in hadroproduction of top quarks with realistic final states*, *JHEP* **10** (2018) 158 [1803.09916].

[80] G. Bevilacqua, H. Hartanto, M. Kraus, T. Weber and M. Worek, *Precise predictions for $t\bar{t}\gamma/t\bar{t}$ cross section ratios at the LHC*, *JHEP* **01** (2019) 188 [1809.08562].

LIST OF PUBLICATIONS

[P1] ATLAS Collaboration, *Measurements of inclusive and differential cross-sections of combined $t\bar{t}\gamma$ and $tW\gamma$ production in the eμ channel at 13 TeV with the ATLAS detector*, arXiv:2007.06946, JHEP 09 (2020) 049 → p. 21

[P2] CMS Collaboration, *Search for $t\bar{t}H$ production in the $H \to b\bar{b}$ decay channel with leptonic $t\bar{t}$ decays in proton-proton collisions at $\sqrt{s} = 13$ TeV*, arXiv:1804.03682, JHEP 1903 (2019) 026 → p. 50

[P3] CMS Collaboration, *Observation of $t\bar{t}H$ production*, arXiv:1804.02610, Phys. Rev. Lett. 120 (2018) 231801 → p. 92

[P4] CMS Collaboration, *Measurement of the top quark pair production cross section in proton-proton collisions at $\sqrt{s} = 13$ TeV*, arXiv:1510.05302, Phys. Rev. Lett. 116, 052002 (2016) → p. 98

[P5] CMS Collaboration, *Measurements of the inclusive top-quark pair production cross section in the eμ decay channel in pp collisions at $\sqrt{s} = 7$ and 8 TeV*, arXiv:1603.02303, JHEP 1608 (2016) 029 → p. 105

[P6] CMS Collaboration, *Measurement of $t\bar{t}$ production with additional jet activity, including b quark jets, in the dilepton decay channel using pp collisions at $\sqrt{s} = 8$ TeV*, arXiv:1510.03072, Eur. Phys. J. C 76 (2016) 379 → p. 140

[P7] CMS Collaboration, *Search for direct pair production of scalar top quarks in the single- and dilepton channels in proton-proton collisions at $\sqrt{s}=8$ TeV*, arXiv:1602.03169, JHEP 07 (2016) 027, Erratum: JHEP 09 (2016) 056 → p. 183

[P8] CMS Collaboration, *Measurement of jet multiplicity distributions in $t\bar{t}$ production in pp collisions at 7 TeV*, arXiv:1404.3171, Eur. Phys. J. C 74 (2014) 3014 → p. 213

[P9] CMS Collaboration, *Measurement of the differential cross section for top quark pair production in pp collisions at $\sqrt{s} = 8$ TeV*, arXiv:1505.04480, Eur. Phys. J. C 75 (2015) 542 → p. 230

[P10] CMS Collaboration, *Search for the associated production of the Higgs boson with a top-quark pair*, arXiv:1408.1682, JHEP 09 (2014) 087 → p. 256

[P11] CMS Collaboration, *Measurement of the $t\bar{t}$ production cross section in the dilepton channel in pp collisions at $\sqrt{s} = 8$ TeV*, arXiv:1312.7582, JHEP 02 (2014) 024 → p. 301

[P12] CMS Collaboration, *Investigations of the impact of the parton shower tuning in Pythia 8 in the modelling of $t\bar{t}$ at $\sqrt{s}=8$ and 13 TeV*, CMS-PAS-TOP-16-021 → p. 314

[P13] CMS Collaboration, *Search for $t\bar{t}H$ production in the $H \to b\bar{b}$ decay channel with 2016 pp collision data at $\sqrt{s}$=13 TeV*, CMS-PAS-HIG-16-038 (2016) → p. 355

[P14] CMS Collaboration, *Determination of the normalised invariant mass distribution of $t\bar{t}$+jet and extraction of the top quark mass*, CMS-PAS-TOP-13-006 (2016) → p. 387

[P15] CMS Collaboration, *Search for $t\bar{t}H$ production in the $H \to b\bar{b}$ decay channel with $\sqrt{s}$=13 TeV pp collisions at the CMS experiment*, CMS-PAS-HIG-16-004 (2016) → p. 406

[P16] CMS Collaboration, *First measurement of the differential cross section for $t\bar{t}$ production in the dilepton final state at $\sqrt{s} = 13$ TeV*, CMS-PAS-TOP-15-010 (2015) → p. 436

Disclaimer: The complete lists of authors of the CMS and ATLAS Collaborations which are included at the end of each journal publication can be found online. They have been removed in this thesis to reduce the size of the document and improve readability. (Each list corresponds to 15–20 pages.)

Measurements of inclusive and differential cross-sections of combined $t\bar{t}\gamma$ and $tW\gamma$ production in the $e\mu$ channel at 13 TeV with the ATLAS detector

The ATLAS collaboration

E-mail: atlas.publications@cern.ch

ABSTRACT: Inclusive and differential cross-sections for the production of top quarks in association with a photon are measured with proton-proton collision data corresponding to an integrated luminosity of 139 fb^{-1}. The data were collected by the ATLAS detector at the LHC during Run 2 between 2015 and 2018 at a centre-of-mass energy of 13 TeV. The measurements are performed in a fiducial volume defined at parton level. Events with exactly one photon, one electron and one muon of opposite sign, and at least two jets, of which at least one is b-tagged, are selected. The fiducial cross-section is measured to be $39.6^{+2.7}_{-2.3}$ fb. Differential cross-sections as functions of several observables are compared with state-of-the-art Monte Carlo simulations and next-to-leading-order theoretical calculations. These include cross-sections as functions of photon kinematic variables, angular variables related to the photon and the leptons, and angular separations between the two leptons in the event. All measurements are in agreement with the predictions from the Standard Model.

JHEP09(2020)049

Contents

1 Introduction

Precise measurements of top-quark production and decay properties provide crucial information for testing the predictions of the Standard Model (SM) and its possible extensions. In particular, the study of the associated production of a top-quark pair ($t\bar{t}$) with a high-energy photon probes the $t\gamma$ electroweak coupling. Furthermore, measurements of the inclusive and differential cross-sections of this process are of particular interest because these topologies are sensitive, for instance, to new physics through anomalous dipole moments of the top quark [1–3] and in the context of effective field theories [4].

First evidence for the production of $t\bar{t}$ in association with a photon ($t\bar{t}\gamma$) was reported by the CDF Collaboration [5], while the observation of the $t\bar{t}\gamma$ process was established by the ATLAS Collaboration in proton-proton (pp) collisions at $\sqrt{s} = 7$ TeV [6]. Both the ATLAS and CMS Collaborations measured the $t\bar{t}\gamma$ cross-section at $\sqrt{s} = 8$ TeV [7, 8].

First measurements of the inclusive and differential cross-sections at $\sqrt{s} = 13$ TeV were performed by the ATLAS Collaboration [9].

This paper presents a measurement of the fiducial inclusive and differential combined $t\bar{t}\gamma + tW\gamma$ production cross-sections in the final state with one electron and one muon, referred to as the $e\mu$ channel. Events where the electrons and muons arise from the leptonic decays of τ-leptons are considered as background. The measurement is performed using the full data set recorded at the LHC between 2015 and 2018 at a centre-of-mass energy of $\sqrt{s} = 13$ TeV and corresponding to an integrated luminosity of 139 fb^{-1}. The fiducial inclusive cross-section is measured using a profile likelihood fit to the distribution of S_{T}, defined as the scalar sum of all transverse momenta in the event, including leptons, photons, jets and missing transverse momentum. The differential cross-sections, absolute and normalised to unity, are measured in the same fiducial region as the inclusive cross-section, as functions of photon kinematic variables, angular variables related to the photon and the leptons, and angular separations between the two leptons in the event.

Compared to the previous $t\bar{t}\gamma$ ATLAS analysis with 13 TeV data [9], only the $e\mu$ channel is considered since it provides a clean final state with a small background contribution and, thus, no multivariate analysis techniques are needed to separate signal and background processes. Additionally, the cross-sections are measured at parton level rather than at particle level to allow comparison with the theory calculation in refs. [10, 11]. The calculation constitutes the first full computation for $t\bar{t}$ production with a hard final-state photon in hadronic collisions at next-to-leading order (NLO) in quantum chromodynamics (QCD), $pp \to bWbW\gamma$, including all resonant and non-resonant diagrams, interferences, and off-shell effects of the top quarks and the W bosons. Therefore, in this paper the combined cross-section of resonant $t\bar{t}\gamma$ and non-resonant $tW\gamma$ production is measured, referred to as signal in the following. Example Feynman diagrams at leading order in QCD for $t\bar{t}\gamma$ and $tW\gamma$ production are shown in figure 1.

The paper is organised as follows. The ATLAS detector is briefly introduced in section 2. Details of the event-simulation generators and their theoretical predictions are given in section 3. The event selection and the analysis strategy are presented in sections 4 and 5. The systematic uncertainties are described in section 6. The results for the fiducial inclusive and differential cross-sections are presented in sections 7 and 8, respectively. Finally, a summary is given in section 9.

2 ATLAS detector

ATLAS [12–14] is a multipurpose detector with a forward-backward symmetric cylindrical geometry with respect to the LHC beam axis.[1] The innermost layers consist of tracking detectors in the pseudorapidity range $|\eta| < 2.5$. This inner detector (ID) is surrounded

---

[1]ATLAS uses a right-handed coordinate system with its origin at the nominal interaction point (IP) in the centre of the detector and the z-axis along the beam pipe. The x-axis points from the IP to the centre of the LHC ring, and the y-axis points upwards. Cylindrical coordinates (r, ϕ) are used in the transverse plane, ϕ being the azimuthal angle around the z-axis. The pseudorapidity is defined in terms of the polar angle θ as $\eta = -\ln\tan(\theta/2)$. Angular distance is measured in units of $\Delta R \equiv \sqrt{(\Delta\eta)^2 + (\Delta\phi)^2}$.
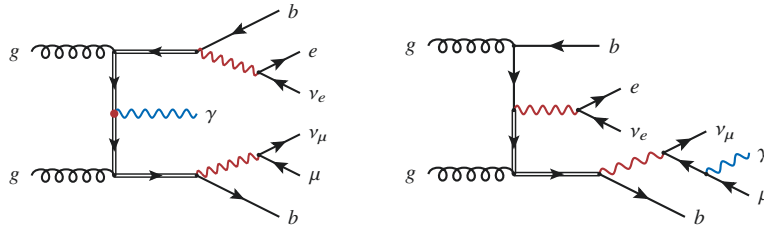
Figure 1. Example Feynman diagrams at leading order for $t\bar{t}\gamma$ (left) and $tW\gamma$ production (right) in the $e\mu$ channel. The top-quark mass resonances are marked with double-lined arrows, while W bosons are marked in red.

by a thin superconducting solenoid that provides a 2 T axial magnetic field. It is enclosed by the electromagnetic and hadronic calorimeters, which cover $|\eta| < 4.9$. The outermost layers of ATLAS consist of an external muon spectrometer within $|\eta| < 2.7$, incorporating three large toroidal magnetic assemblies with eight coils each. The field integral of the toroids ranges between 2.0 and 6.0 Tm for most of the acceptance. The muon spectrometer includes precision tracking chambers and fast detectors for triggering. A two-level trigger system [15] reduces the recorded event rate to an average of 1 kHz.

3 Signal and background modelling

The estimation of signal and background contributions relies on the modelling of these processes with simulated events produced with Monte Carlo (MC) event generators. The response of the ATLAS detector was simulated [16] with GEANT4 [17]. For some of the estimates of modelling uncertainties, the fast-simulation package ATLFAST-II was used instead of the full detector simulation. Additional pp interactions (pile-up) were generated with PYTHIA 8 [18, 19] using a set of tuned parameters called the A3 tune [20] and the NNPDF2.3LO parton distribution function (PDF) set [21]. Corrections to the pile-up profile, selection efficiencies, energy scales and resolutions derived from dedicated data samples are applied to the MC simulation to improve agreement with data.

This analysis uses both *inclusive* samples, in which processes were generated at matrix-element (ME) level without explicitly including a photon in the final state, and *dedicated* samples for certain processes, where photons were included in the ME-level generation step. Dedicated samples with a photon in the ME were generated for the $t\bar{t}\gamma$ and $tW\gamma$ final states, as well as for $V\gamma$ processes with additional jets. Here, V denotes either a W or a Z boson. Although no photons were generated at ME level in the inclusive samples, initial- and final-state radiation of photons is accounted for by the showering algorithm. Combining inclusive and dedicated samples for the modelling of processes might result in double-counting photon radiation in certain phase-space regions. As a consequence, a procedure to remove overlaps between the inclusive and dedicated samples was performed. Photon radiation simulated at ME level in dedicated samples achieves higher accuracy than the photon radiation in the showering algorithm. On the other hand, kinematic

requirements are applied to the kinematic properties of the photons at ME level in the dedicated samples. In the overlap-removal procedure, all events from the dedicated samples are kept while events from the inclusive samples are discarded if they contain a parton-level photon that fulfils the dedicated samples' kinematic requirements of $p_T(\gamma) > 15\,\mathrm{GeV}$ and $\Delta R(\gamma, \ell) > 0.2$, where $p_T(\gamma)$ is the photon's transverse momentum and $\Delta R(\gamma, \ell)$ is the angular distance between the photon and any charged lepton.

The dedicated sample for the $t\bar{t}\gamma$ signal process was simulated using the MAD-GRAPH5_aMC@NLO generator (v2.3.3) [22] and the NNPDF2.3LO PDF set at leading order (LO) in QCD. The events were generated as a doubly resonant $2 \to 7$ process, e.g. as $pp \to b\ell\nu b\ell\nu\gamma$, thus, diagrams where the photon is radiated from the initial state (in the case of quark-antiquark annihilation), intermediate top quarks, the b-quarks, and the intermediate W bosons, as well as the decay products of the W bosons, are included. To prevent divergences, the photon was required to have $p_T > 15$ GeV and $|\eta| < 5.0$ and the leptons to satisfy $|\eta| < 5.0$. The ΔR between the photon and any of the charged particles among the seven final-state particles were required to be greater than 0.2. The top-quark mass in this and all other samples was set to $172.5\,\mathrm{GeV}$. The renormalisation and the factorisation scales were set to $0.5 \times \sum_i \sqrt{m_i^2 + p_{T,i}^2}$, where the sum runs over all the particles generated from the ME calculation. The event generation was interfaced to PYTHIA 8 (v8.212) using the A14 tune [23] to model parton showers, hadronisation, fragmentation and the underlying event. Heavy-flavour hadron decays were modelled with EVTGEN [24]; this program was used for all samples, except for those generated using the SHERPA MC program [25, 26]. In the latter case, heavy-flavour decays were modelled directly with SHERPA.

Two dedicated samples for the $tW\gamma$ process were generated with the MAD-GRAPH5_aMC@NLO generator as well. The first one was produced at LO in the five-flavour scheme for the $2 \to 3$ process (e.g. $pp \to tW\gamma$) assuming a stable top quark. The second set of events was generated at LO as a $2 \to 6$ process (e.g. $pp \to b\ell\nu\ell\nu\gamma$) in the five-flavour scheme, where the photon is radiated from any other charged final-state particle. In the five-flavour scheme, the b-quarks are treated as massless and the LO representation of the process includes a b-quark in the initial state. The two sets of events are complementary and, once combined, provide a full simulation of the $tW\gamma$ process. Both samples make use of the NNPDF2.3LO PDF set and were interfaced to PYTHIA 8 (v8.212) for parton showering using the A14 tune. The photon was also required to have $p_T > 15$ GeV and $|\eta| < 5.0$ and to be separated by $\Delta R > 0.2$ from any parton. Although possible interference effects between $t\bar{t}\gamma$ and $tW\gamma$ are still missing in the simulated LO samples, the $tW\gamma$ process is treated as part of the signal in this analysis.

Events with $W\gamma$ and $Z\gamma$ final states (with additional jets) were simulated as dedicated samples. The $W\gamma$ processes were simulated with SHERPA 2.2.2 at NLO accuracy in QCD using the NNPDF3.0NNLO PDF set, whereas $Z\gamma$ events were generated with SHERPA 2.2.4 at LO in QCD with the same PDF set. The samples are normalised to the cross-sections given by the corresponding MC simulation. The SHERPA generator performs all steps of the event generation, from the hard process to the observable particles. All samples were

matched and merged by the SHERPA-internal parton showering based on Catani-Seymour dipoles [27, 28] using the MEPS@NLO prescription [29–31]. Virtual corrections for the NLO accuracy in QCD in the matrix element were provided by the OpenLoops library [32, 33].

Inclusive $t\bar{t}$ production processes were simulated at matrix-element level at NLO accuracy in QCD using POWHEG-BOX v2 [34–36]. The calculation used the NNPDF3.0NLO PDF set [37]. The parton shower was generated with PYTHIA 8 (v8.230), for which the A14 tune [38] was used. The $t\bar{t}$ events are normalised to a cross-section value calculated with the TOP++2.0 program at next-to-next-to-leading order (NNLO) in perturbative QCD, including soft-gluon resummation to next-to-next-to-leading-logarithm order (see ref. [39] and references therein).

Events with inclusive W- and Z-boson production in association with additional jets were simulated with SHERPA 2.2.1 [25, 26] at NLO in QCD. The NNPDF3.0NLO PDF set was used in conjunction with a dedicated tune provided by the SHERPA authors. The samples are normalised to the NNLO cross-section in QCD [40].

Events with two directly produced vector bosons, i.e. WW, WZ and ZZ, were generated with SHERPA versions 2.2.2 (purely leptonic decays) and 2.2.1 (all others) at LO in QCD. The NNPDF3.0NNLO PDF set was used in conjunction with a dedicated tune provided by the SHERPA authors. The samples are normalised to NLO accuracy cross-sections in QCD [41].

Events with a $t\bar{t}$ pair and an associated W or Z boson ($t\bar{t}V$) were simulated at NLO at the ME level with MADGRAPH5_aMC@NLO using the NNPDF3.0NLO PDF set. The ME generator was interfaced to PYTHIA 8 (v8.210), for which the A14 tune was used in conjunction with the NNPDF2.3LO PDF set. The samples are normalised to NLO in QCD and electroweak theory [42].

The background processes are sorted into three categories based on the origin of the reconstructed photon required in the event selection. The three are estimated from MC simulation by categorising events from all considered samples that are not classified as signal events. The MC simulations for all categories include processes without prompt photons such as $t\bar{t}$, W+jets, Z+jets, diboson and $t\bar{t}V$ production, as well as background processes with an additional prompt photon. The first category is labelled *h-fake* and contains any type of hadronic fakes that mimic a photon signature in the detector. This category includes not only photon signatures faked by hadronic energy depositions in the electromagnetic calorimeter, but also hadron decays involving photons, for example $\pi^0 \to \gamma\gamma$ decays. It also includes processes with a prompt photon, where the prompt photon is not reconstructed in the detector or does not pass the selection requirements, but a h-fake photon does. Studies performed with data-driven techniques following the approach described in ref. [9] show that possible data-driven corrections have a negligible effect on the distribution shapes of relevant observables. Possible differences in the total expected number of events are covered by a normalisation uncertainty as described in section 6. The second category is labelled *e-fake* and contains processes with an electron mimicking a photon signature in the calorimeter. Similarly to the h-fake category, this category includes contributions from processes without a prompt photon but with an e-fake photon, as well as processes with a prompt photon in the simulation but an e-fake photon in the reconstruction. This

category represents a minor background contribution. The third category is called *prompt γ background* and contains any type of background process with a prompt photon. The background contribution from $t\bar{t}$ production with a photon produced in an additional pp interaction in the same bunch crossing was found to be negligible. This was estimated by comparing the significance of the distance in z between the photon's origin and the primary vertex in data and simulation.

The $t\bar{t}\gamma$ and $tW\gamma$ events where one or both W bosons decay into τ-leptons, which then subsequently decay into e or μ, are categorised as *Other $t\bar{t}\gamma/tW\gamma$*, and not as $e\mu$ signal, following the definition of signal events in the theory calculation in refs. [10, 11]. Single-lepton events, where a second lepton is faked by hadronic energy depositions, are also included in the category *Other $t\bar{t}\gamma/tW\gamma$*. The contribution of $t\bar{t}\gamma$ single-lepton events was found to be negligible in the $e\mu$ final state in the previous measurement [9] and it is therefore estimated from the MC simulation.

4   Event selection

The data set used in this analysis corresponds to the 139 fb^{-1} of integrated luminosity collected with the ATLAS detector during the Run 2 period. Each event in data and simulation is required to have at least one reconstructed primary vertex with at least two associated reconstructed tracks. Furthermore, only events where at least one of the single-electron [43] or single-muon [44] triggers was fired are selected.

The main physics objects considered in this analysis are electrons, muons, photons, jets, b-jets and missing transverse momentum. Electrons are reconstructed from energy deposits in the electromagnetic calorimeter associated with reconstructed tracks in the ID system. They are identified with a combined likelihood technique [45] using a 'tight' working point, and are required to be isolated based on calorimeter and tracking quantities. The p_{T}- and η-dependent isolation criteria yield an efficiency of 90% for electrons with $p_{\mathrm{T}} = 25\,\mathrm{GeV}$ and 99% for those with $p_{\mathrm{T}} = 60\,\mathrm{GeV}$. The origin of the electron track has to be compatible with the primary vertex. Electrons are calibrated with the method described in ref. [45]. They are selected if they fulfil $p_{\mathrm{T}} > 25\,\mathrm{GeV}$ and $|\eta_{\mathrm{clus}}| < 2.47$, excluding the calorimeter barrel/endcap transition region $1.37 < |\eta_{\mathrm{clus}}| < 1.52$.[2]

Muons are reconstructed with an algorithm that combines the track segments in the various layers of the muon spectrometer and the tracks in the ID system. The reconstruction, identification and calibration methods are described in ref. [46]. Muons are required to be isolated according to track- and calorimeter-based criteria similar to those applied to electrons. Only muons with calibrated $p_{\mathrm{T}} > 25\,\mathrm{GeV}$ and $|\eta| < 2.5$ and passing 'medium' quality requirements are considered. The muon track is also required to originate from the primary collision vertex.

Photons are reconstructed from energy deposits in the central region of the electromagnetic calorimeters. If the cluster considered is not matched to any reconstructed track in the ID system, the photon candidate is classified as unconverted. If the cluster is matched with one or two reconstructed tracks that are consistent with originating from a photon

---

[2]η_{clus} denotes the pseudorapidity of the calorimeter cell cluster associated with the electron.

conversion and if, in addition, a conversion vertex can be found, the photon candidate is classified as converted. Both kinds of photons are considered in this analysis. Photons are reconstructed and identified as described in ref. [47] and their energies are calibrated with the method described in ref. [48]. They are subject to a tight isolation requirement defined as $E_T^{iso}\big|_{\Delta R<0.4} < 0.022 \cdot E_T(\gamma) + 2.45\,\text{GeV}$ in conjunction with $p_T^{iso}\big|_{\Delta R<0.2} < 0.05 \cdot E_T(\gamma)$, where E_T^{iso} refers to the calorimeter isolation within $\Delta R < 0.4$ around the direction of the photon candidate and p_T^{iso} is the track isolation within $\Delta R < 0.2$ [47]. Only photons with calibrated $E_T > 20\,\text{GeV}$ and $|\eta_{clus}| < 2.37$, excluding the calorimeter transition region $1.37 < |\eta_{clus}| < 1.52$, are considered.

Jets are reconstructed using the anti-k_t algorithm [49] in the FASTJET implementation [50] with a distance parameter $R = 0.4$. They are reconstructed from topological clusters of cells in the calorimeter [51]. The jet energy scale and jet energy resolution are calibrated using information from both simulation and data [52]. The jets are required to have $p_T > 25\,\text{GeV}$ and $|\eta| < 2.5$. Jets with a large contribution from pile-up vertices are identified with the *Jet Vertex Tagger* [53] and rejected.

The b-tagging algorithm (MV2c10) applied to the selected jets to identify those from b-quark hadronisation [54] labelled as b-jets is based on a boosted decision tree combining information from other algorithms using track impact parameters and secondary vertices, and a multi-vertex reconstruction algorithm. A working point with a selection efficiency of 85% on simulated $t\bar{t}$ events is used, corresponding to rejection factors of 3.1 and 35 for jets initiated by charm quarks and light-flavour partons, respectively. The flavour-tagging efficiency for b-jets, as well as for c-jets and light-flavour jets, is calibrated as described in ref. [55].

The reconstructed missing transverse momentum E_T^{miss} [56, 57] is computed as the negative vector sum over all reconstructed, fully calibrated physics objects, including photons, and the remaining unclustered energy, also called the *soft term*. The soft term is estimated from low-p_T tracks associated with the primary vertex but not with any reconstructed object.

An overlap-removal procedure is applied to avoid the reconstruction of the same energy clusters or tracks as different objects. First, electron candidates sharing their track with a muon candidate are removed and jets within a $\Delta R = 0.2$ cone around any remaining electron are excluded. Secondly, electrons within a $\Delta R = 0.4$ cone around any remaining jet are removed. If the distance between a jet and any muon candidate is $\Delta R < 0.4$, the muon candidate is discarded if the jet has more than two associated tracks, otherwise the jet is removed. Finally, photons within a $\Delta R = 0.4$ cone around any remaining electron or muon are removed and then jets within a $\Delta R = 0.4$ cone around any remaining photon are excluded.

The selected events must have exactly one electron and exactly one muon, each with $p_T > 25\,\text{GeV}$. At least one of these leptons has to be matched to a fired single-lepton trigger. Since the p_T threshold of the single-lepton triggers was increased over the different data-taking periods due to increased collisions rates, the offline p_T thresholds for these electrons and muons that are matched to a fired single-lepton trigger are chosen to be 25 GeV in 2015, 27 GeV in 2016, and 28 GeV in 2017 and 2018 in order to lie above the trigger thresholds. Electrons and muons must have opposite-sign charges and the $e\mu$

	Events
$t\bar{t}\gamma\ e\mu$	2391 ± 130
$tW\gamma\ e\mu$	$156 \pm\ \ 15$
Other $t\bar{t}\gamma/tW\gamma$	$279 \pm\ \ 15$
h-fake	$78 \pm\ \ 40$
e-fake	$23 \pm\ \ 12$
Prompt γ bkg.	$87 \pm\ \ 40$
Total	3014 ± 160
Data	3014

Table 1. Event yields before the profile likelihood fit of the signal and background processes to data after the full selection. All categories are estimated from MC simulation and include correction factors for detector effects as described in section 6. The combination of all $t\bar{t}\gamma$ and $tW\gamma$ categories is scaled to match the event yields in data. The quoted uncertainties correspond to the total statistical and systematic uncertainties (cf. section 6) added in quadrature.

invariant mass is required to be higher than 15 GeV. The event is required to have at least two jets and at least one of the jets must be b-tagged. In addition, all events must contain exactly one reconstructed photon fulfilling the condition that ΔR between the selected photon and any of the leptons is greater than 0.4.

The observed event yields after selection are listed in table 1 for the different signal and background categories described in section 3. The LO cross-section of the MC samples underestimates the expected number of signal events; therefore, for illustration purposes the combination of all $t\bar{t}\gamma$ and $tW\gamma$ categories is normalised to match the event yields in data. Correction factors for detector effects (described in section 6) are applied, when needed, to improve the description of the data by the simulation.

The modelling of signal and background processes is inspected through the comparison of distributions. A selection of these distributions showing a comparison between the MC simulation before the profile likelihood fit and data is presented in figure 2. The combination of all $t\bar{t}\gamma$ and $tW\gamma$ categories is normalised to match the event yields in data as done in table 1 to allow a comparison of the shapes of the kinematic variables. All systematic uncertainties that are introduced in section 6 are included in these distributions and their sum in quadrature, which assumes they are fully uncorrelated, is illustrated by the shaded error bands.

5   Analysis strategy

The inclusive and differential cross-sections are measured in the fiducial region described in section 5.1 and the same sources of background contributions and systematic uncertainties are considered. In the fiducial inclusive cross-section the S_{T} distribution is fitted and the post-fit background yields and systematic uncertainties are used to extract the signal cross-section, while no fit is performed for the determination of the differential cross-sections.
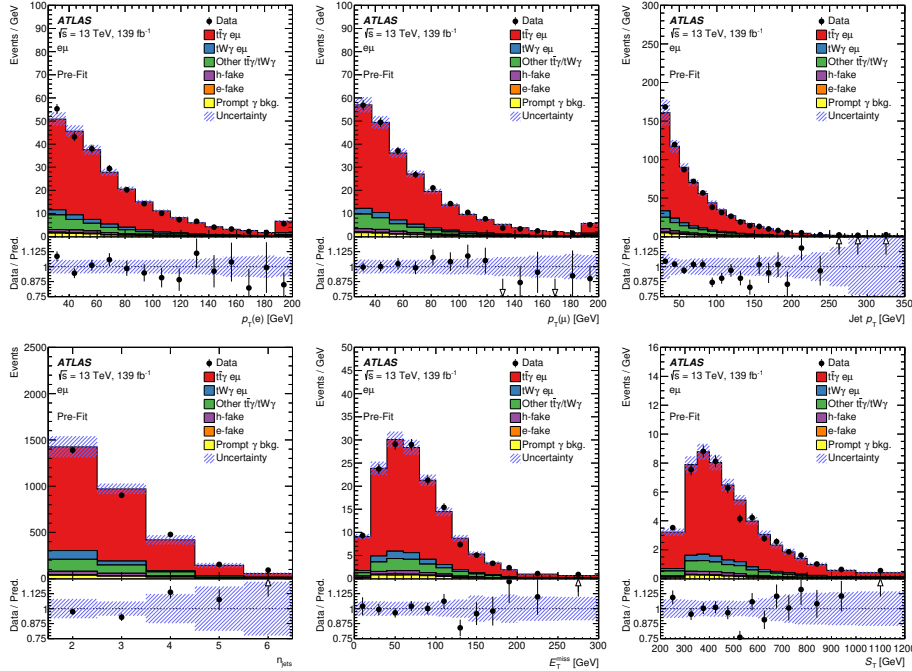
Figure 2. Distributions of the transverse momentum of the electron, the muon and all jets (top row), and the number of jets, $E_{\mathrm{T}}^{\mathrm{miss}}$ and S_{T} (bottom row) after event selection and before the profile likelihood fit. The combination of all $t\bar{t}\gamma$ and $tW\gamma$ categories is scaled to match the event yields in data. The shaded bands correspond to the statistical and systematic uncertainties (cf. section 6) added in quadrature. Overflow events are included in the last bin of each distribution. In the case of the S_{T} distribution, the underflow events are included in the first bin. The lower part of each plot shows the ratio of the data to the prediction.

5.1 Fiducial region definition

The cross-sections are reported at parton level in a fiducial region, defined by the kinematic properties of the signal process, in which all selected final-state objects are produced within the detector acceptance. This is done in a way that mimics the event selection as defined in the theoretical calculation. Objects at parton level are taken from the MC simulation history. Photons and leptons are selected as stable particles after final-state radiation. The leptons ($\ell = e, \mu$) must originate from W-boson decays and they are dressed with nearby photons within a cone of size of $\Delta R = 0.1$ around them and must have $p_{\mathrm{T}} > 25$ GeV and $|\eta| < 2.5$. Only events with exactly one electron and one muon are considered. Events with leptons originating from an intermediate τ-lepton in the top-quark decay chain are not considered. The b-jets at parton level in the calculation from refs. [10, 11] are jets clustered with the anti-k_t algorithm with a distance parameter of $R = 0.4$. Since showering and hadroni-

sation effects are not considered in this calculation, the jets correspond to the b-quarks from the top-quark decay (with an additional parton in the cases where the NLO real emission leads to a parton close by a b-quark). To mimic this definition in the LO MC simulation, parton-level b-jets are defined as follows. The anti-k_t algorithm with a distance parameter $R = 0.4$ is applied to all partons that are radiated from the two b-quarks (including the b-quarks themselves) and from the two initial partons. The jets that include a b-quark from the decay of a top quark are selected as b-jets. The event is kept if there are two b-jets satisfying $p_T > 25$ GeV and $|\eta| < 2.5$. Exactly one photon with $E_T > 20$ GeV and $|\eta| < 2.37$ is required. Photons are required to be isolated from nearby jets by imposing a modified cone approach as described in ref. [58], as it is also done in the theory calculation in refs. [10, 11], to ensure soft and collinear safety. The event is dropped if any of the following requirements is not fulfilled: $\Delta R(\gamma, \ell) > 0.4$, $\Delta R(e, \mu) > 0.4$, $\Delta R(b, b) > 0.4$ or $\Delta R(\ell, b) > 0.4$.

5.2 Fiducial inclusive cross-section

The fiducial inclusive cross-section is extracted using a binned profile likelihood fit to the full S_T distribution. The distribution of S_T provides good separation between signal and background and was found to be less sensitive to systematic uncertainties than other distributions considered, such as the jet multiplicity or the p_T of individual jets. The expected signal and background distributions are modelled in the fit using template distributions taken from the simulated samples. The parameter of interest, the fiducial cross-section σ_{fid}, is related to the number of signal events in bin i of the S_T distribution as:

$$N_i^s = L \times \sigma_{\text{fid}} \times C \times f_i^{S_T}.$$

The term L is the integrated luminosity, $f_i^{S_T}$ is the fraction of generated signal events falling into bin i of the S_T distribution after fiducial requirements are applied, and C is the correction factor for the signal efficiency ϵ and for migration into the fiducial region f_{out}, defined as follows:

$$f_{\text{out}} = \frac{N_{\text{reco}}^{\text{non-fid}}}{N_{\text{reco}}}, \qquad \epsilon = \frac{N_{\text{reco}}^{\text{fid}}}{N_{\text{MC}}^{\text{fid}}} \qquad \Rightarrow C = \frac{\epsilon}{1 - f_{\text{out}}} = \frac{N_{\text{reco}}}{N_{\text{MC}}^{\text{fid}}},$$

where N_{reco} is the number of simulated signal events passing the event selection described in section 4, $N_{\text{MC}}^{\text{fid}}$ is the corresponding number of signal events generated in the fiducial region defined in section 5.1, and $N_{\text{reco}}^{\text{fid}}$ and $N_{\text{reco}}^{\text{non-fid}}$ are the numbers of signal events that pass the event selection and are generated within and outside the fiducial region, respectively. The efficiency and outside migration are obtained from simulated $t\bar{t}\gamma$ and $tW\gamma$ events. The correction factor is estimated from the signal simulation to be $C = 0.462 \pm 0.002$ (statistical uncertainty only).

The likelihood function $\mathcal{L}$, based on Poisson statistics, is given by:

$$\mathcal{L} = \prod_i P \left(N_i^{\text{obs}} | N_i^s(\vec{\theta}) + \sum_b N_i^b(\vec{\theta}) \right) \times \prod_t G(0|\theta_t, 1),$$

where N_i^{obs}, N_i^s, and N_i^b are the observed number of events in data, the predicted number of signal events, and the estimated number of background events in bin i of the S_T distribution, respectively. The rates of those $t\bar{t}\gamma$ and $tW\gamma$ events not counted as part of the signal

– 10 –

and categorised as *Other $t\bar{t}\gamma/tW\gamma$* are scaled with the same parameter as the signal events in the fit, i.e. no independent production cross-section is assumed for these parts of the simulated $t\bar{t}\gamma/tW\gamma$ process. The vector $\vec{\theta}$, of components θ_t, represents the nuisance parameters that describe the sources of systematic uncertainties. Each nuisance parameter θ_t is constrained by a Gaussian distribution, $G(0|\theta_t, 1)$. The width of the Gaussian function corresponds to a change of ± 1 standard deviation of the corresponding quantity in the likelihood. For systematic uncertainties related to the finite number of simulated MC events, the Gaussian terms in the likelihood are replaced by Poisson terms. The cross-section is measured by profiling the nuisance parameters and minimising $-2\ln\mathcal{L}$ [59].

5.3 Absolute and normalised differential cross-sections

The measurements of the absolute and normalised differential cross-sections are performed as functions of the p_{T} and $|\eta|$ of the photon, and of angular variables between the photon and the leptons: ΔR between the photon and the closest lepton $\Delta R(\gamma, \ell)_{\mathrm{min}}$, as well as $\Delta\phi(\ell, \ell)$ and $|\Delta\eta(\ell, \ell)|$ between the two leptons. The kinematic properties of the photon are sensitive to the $t\gamma$ coupling. In particular, $\Delta R(\gamma, \ell)_{\mathrm{min}}$ is related to the angle between the top quark and the radiated photon, which could give insight into the structure of this coupling. The distributions of $\Delta\phi(\ell, \ell)$ and $|\Delta\eta(\ell, \ell)|$ are sensitive to the $t\bar{t}$ spin correlation. The corresponding distributions in data and SM simulations are compared in figure 3. The simulation describes reasonably well the data within the uncertainties although it favours smaller $\Delta R(\gamma, \ell)_{\mathrm{min}}$ and larger $\Delta\phi(\ell, \ell)$ values than the observed ones.

The data are corrected for detector resolution and acceptance effects to parton level in the fiducial phase space using an iterative matrix unfolding that uses Bayes' theorem [60] implemented in the RooUnfold package [61]. The differential cross-section is defined as:

$$\frac{\mathrm{d}\sigma}{\mathrm{d}X_k} = \frac{1}{L \times \Delta X_k \times \epsilon_k} \times \sum_j M_{jk}^{-1} \times (N_j^{\mathrm{obs}} - N_j^b) \times f_{e\mu,j} \times (1 - f_{\mathrm{out},j})\,.$$

The indices j and k represent the bin indices of the observable X at detector and parton levels, respectively. The variable N_j^{obs} is the number of observed events, and N_j^b is the number of estimated non-$t\bar{t}\gamma/tW\gamma$ background events (pre-fit) in bin j at detector level. The contribution from the *Other $t\bar{t}\gamma/tW\gamma$* category is taken into account by correcting the remaining number of observed events by the signal fraction, $f_{e\mu,j}$, defined as the ratio of the number of selected $t\bar{t}\gamma$ and $tW\gamma$ $e\mu$ events to the total number of selected $t\bar{t}\gamma$ and $tW\gamma$ events, as determined from simulation. This avoids the dependence on the signal cross-section used for the normalisation. The efficiency ϵ_k is the fraction of signal events generated at parton level in bin k of the fiducial region that are reconstructed and selected at detector level. The total integrated luminosity is denoted by L, and ΔX_k represents the bin width. The migration matrix M_{kj} describes the detector response and expresses the probability for an event in bin k at parton level to be reconstructed in bin j at detector level, calculated from events passing both the fiducial-region selection and the event selection. The outside-migration fraction $f_{\mathrm{out},j}$ is the fraction of signal events generated outside the fiducial region but reconstructed and selected in bin j at detector level. The normalised
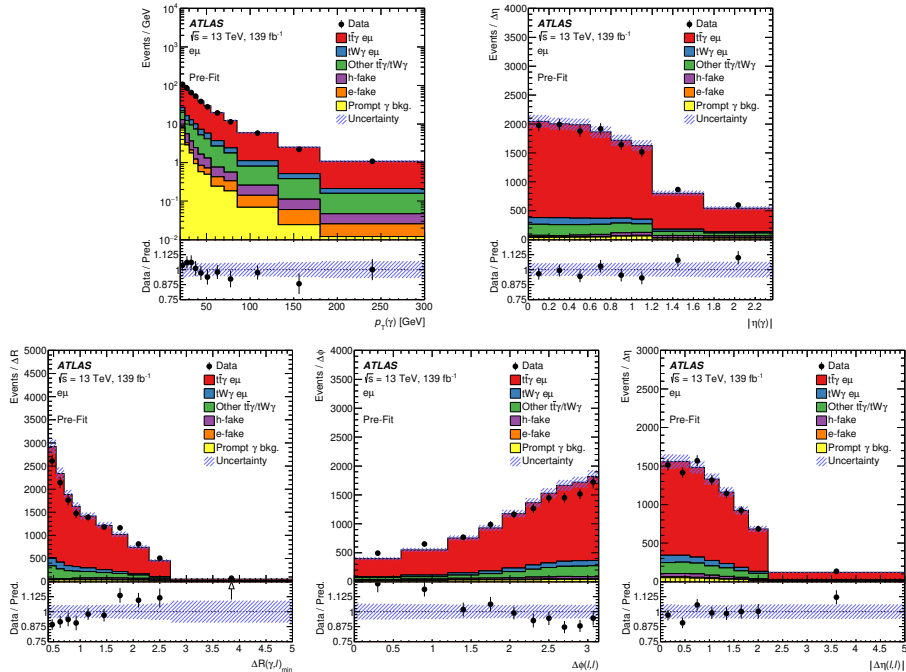
Figure 3. Distributions of the photon p_T and $|\eta|$ in the top row, and $\Delta R(\gamma, \ell)_{min}$, $\Delta\phi(\ell, \ell)$ and $|\Delta\eta(\ell, \ell)|$ in the bottom row after event selection and before the profile likelihood fit. The combination of all $t\bar{t}\gamma$ and $tW\gamma$ categories is scaled to match the event yields in data. The shaded bands correspond to the statistical and systematic uncertainties (cf. section 6) added in quadrature. When overflow events are present, they are included in the last bin of the distribution. The lower part of each plot shows the ratio of the data to the prediction.

differential cross-section is derived by dividing the absolute result by the total cross-section, obtained by integrating over all bins of the observable.

The signal MC samples are used to determine ϵ_k, $f_{\text{out},j}$, and M_{kj}. The unfolding method relies on the Bayesian probability formula, starting from a given prior of the parton-level distribution and iteratively updating it with the posterior distribution. The binning choices of the unfolded observables take into account the detector resolution and the expected statistical uncertainty. The bin width has to be larger than twice the resolution, and the statistical uncertainty is required to be around or below 10% across all bins, with the latter being the limiting factor in most of the cases. The resolution of the lepton and photon momenta is very high and, therefore, the fraction of events migrating from one bin to another is small. In all bins, the purity, defined as the fraction of reconstructed events that originate from the same bin at parton level, is larger than 80%, and it is above 90% for all observables except for the p_T of the photon. The number of iterations chosen is two, which provides good convergence of the unfolding distribution and a statistically stable result.
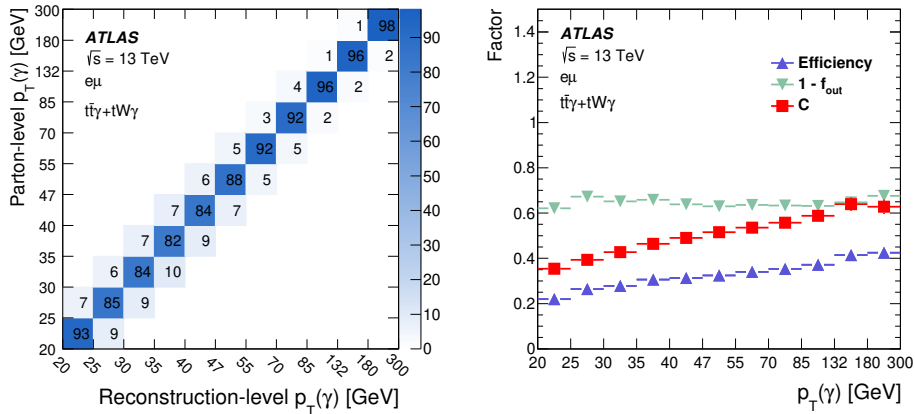
Figure 4. Left: migration matrix relating the photon p_T at the reconstruction and parton levels in the fiducial phase space, normalised by column and shown as percentages. Right: signal reconstruction and selection efficiency (ϵ), ($1 - f_{\text{out}}$) fraction and resulting C correction factor as a function of the photon p_T.

For illustration purposes, the migration matrix is presented in the left panel of figure 4, while the right panel shows the efficiency, outside-migration fraction and the resulting C correction factor obtained for the distribution of the photon p_T. The performance of the unfolding procedure is tested for possible biases from the choice of input model. It was verified that when reweighting the shape of the signal simulation by up to 50% bin-by-bin with respect to the nominal shape, the unfolding procedure based on the nominal response matrix reproduces the altered shapes.

6   Systematic uncertainties

Various systematic uncertainties arising from detector effects are considered, along with theoretical uncertainties. Signal and background predictions are both subject to these uncertainties.

6.1   Experimental uncertainties

Experimental systematic uncertainties affect the normalisation and shape of the distributions of the simulated signal and background samples. These include reconstruction and identification efficiency uncertainties, as well as uncertainties in the energy and momentum scale and resolution for the reconstructed physics objects in the analysis, including leptons, photons, jets and E_T^{miss}. In addition, uncertainties in the flavour-tagging of jets, the jet vertex tagger (JVT) discriminant, the integrated luminosity value and the pile-up simulation are considered.

The photon identification and isolation efficiencies as well as the efficiencies of the lepton reconstruction, identification, isolation, and trigger in the MC samples are all corrected

– 13 –

using scale factors to match the corresponding values in data. Similarly, corrections to the lepton and photon momentum scale and resolution are applied in simulation [46, 48]. All these corrections, which are p_T and η dependent, are varied within their uncertainties.

The jet energy scale (JES) uncertainty is derived using a combination of simulations, test-beam data and *in situ* measurements [52]. Additional contributions from jet-flavour composition, η-intercalibration, punch-through, single-particle response, calorimeter response to different jet flavours, and pile-up are taken into account, resulting in 30 uncorrelated JES uncertainty subcomponents, of which 29 are non-zero in a given event depending on the type of simulation used. The most relevant JES uncertainties are related to the pile-up correction (*JES pile-up correction*) and modelling aspects of the in situ calibration (*JES in situ calibration*). The jet energy resolution (JER) in simulation is smeared by the measured JER uncertainty [62] split into eight uncorrelated sources. The uncertainty associated with the JVT discriminant is obtained by varying the efficiency correction factors (labelled *jet vertex tagging* in the results, cf. figure 5).

The uncertainties related to the b-jet tagging calibration are determined separately for b-jets, c-jets and light-flavour jets [63–65]. For each jet category, the uncertainties are decomposed into several uncorrelated components. The corrections are varied by their measured uncertainties.

The uncertainties associated with energy scales and resolutions of photons, leptons and jets are propagated to the E_T^{miss}. Additional uncertainties originate from the modelling of its soft term [66].

The uncertainty in the combined 2015–2018 integrated luminosity is 1.7% [67], obtained using the LUCID-2 detector [68] for the primary luminosity measurements.

The uncertainty associated with the modelling of pile-up in the simulation is assessed by varying the pile-up reweighting in the simulation within its uncertainties.

6.2 Signal and background modelling uncertainties

The $t\bar{t}\gamma$ signal modelling uncertainties include the uncertainties owing to the choice of QCD scales, parton shower, amount of initial-state radiation (ISR), and PDF set. The effect of the QCD scale uncertainty is evaluated by varying the renormalisation and factorisation scales separately up and down by a factor of two from their nominal chosen values. The uncertainty from the parton shower and hadronisation ($t\bar{t}\gamma$ *PS model*) is estimated by comparing the $t\bar{t}\gamma$ nominal samples, produced with MADGRAPH5_aMC@NLO + PYTHIA 8, with an alternative sample interfaced to HERWIG 7 [69, 70]. The ISR uncertainty ($t\bar{t}\gamma$ *ISR*) is studied by comparing the nominal MADGRAPH5_aMC@NLO + PYTHIA 8 sample with the results of varying the A14 tune parameter for radiation [23]. The PDF uncertainty ($t\bar{t}\gamma$ *PDF*) is evaluated using the standard deviation in each bin of the respective distribution formed by the set of 100 replicas of the NNPDF set [21].

For the $tW\gamma$ process the uncertainties due to the choice of renormalisation and factorisation scales are also estimated by varying them up and down separately by a factor of two relative to the nominal sample value. A systematic uncertainty from the parton shower and hadronisation model is considered by comparing PYTHIA 8 and HERWIG 7 both interfaced

to MadGraph5_aMC@NLO. The $tW\gamma$ modelling uncertainties are treated as uncorrelated with the $t\bar{t}\gamma$ signal modelling uncertainties.

The $tW\gamma$ process was generated in the five-flavour scheme at leading order in QCD and one of the two b-quarks is not included in the matrix-element generation step. This b-quark, expected to be produced in the initial state through the PDF, is only found in a fraction of the events at parton level in the MC simulation. The fractions of generated $tW\gamma$ events without a second b-quark were found to be around 30% and 50% for the MC samples interfaced with HERWIG and PYTHIA, respectively. Therefore, an additional uncertainty associated with this possibly lost b-quark is assigned ($tW\gamma$ *parton definition*) as follows. Relative to the nominal $tW\gamma$ simulation, the parton-level event yields are doubled, assuming all b-jets are found, while the number of reconstructed events is kept constant. This leads to a variation of the correction factor C of 2.8%.

Several uncertainties in the modelling of $t\bar{t}$ processes, which give a dominant contribution to the h-fake and prompt γ background categories, are considered as shape-only uncertainties. The uncertainties associated with the parton shower and hadronisation are estimated by comparing the nominal simulation with alternative showering by HERWIG 7. Uncertainties in the modelling of final-state radiation are estimated by evaluating the effects of varying four different parameters in the POWHEG + PYTHIA 8 generator set-up described in the following. Uncertainties due to the renormalisation and factorisation scales are estimated by varying them up and down independently by a factor of two relative to the default scale choice. These scale variations are implemented with corresponding weights which are available as part of the nominal MC sample. Uncertainties due to the value of α_S used in the ISR parton shower modelling are estimated by comparing the nominal POWHEG + PYTHIA 8 simulation with alternative samples that correspond to higher and lower radiation parameter settings in the A14 tune, controlled by the *var3c* parameter in PYTHIA 8. This parameter is varied within its uncertainties corresponding to variations of $\alpha_S(m_Z)$ between 0.115 and 0.140. An additional ISR uncertainty is obtained by comparing the nominal sample with an additional one where the h_{damp} parameter, which controls the p_{T} of the first additional emission, is varied by a factor of two as supported by measurements reported in ref. [71].

In addition to those background modelling uncertainties, global normalisation uncertainties of 50% are assigned to the following three categories: h-fake photons, e-fake photons and prompt γ background [9] (*h-fakes*, *e-fakes*, and *prompt γ normalisation*).

6.3 Treatment of the systematic uncertainties in the measurements

As stated in section 5, the impact of systematic uncertainties on the fiducial inclusive cross-section measurement is taken into account via nuisance parameters in the likelihood function. The nuisance parameters $\vec{\theta}$ are profiled in the maximum-likelihood fit. Variations of the nuisance parameters can affect the rate of events as well as the shape of the S_{T} distribution. In the case of signal modelling uncertainties, the rate uncertainty is composed of variations of the efficiency ϵ and the fraction f_{out}. All MC samples used to evaluate signal modelling uncertainties are scaled to the same number of events in the fiducial phase space, $N_{\text{MC}}^{\text{fid}}$. The only uncertainty that is not included as a nuisance parameter in the profile

– 15 –

likelihood fit is the uncertainty from the $tW\gamma$ parton definition. This uncertainty does not affect the number of reconstructed events in the corresponding template in the profile likelihood fit. It comprises only an uncertainty in the number of generated events in the fiducial phase space. Thus, the $tW\gamma$ parton definition uncertainty is added in quadrature to the post-fit uncertainty of the profile likelihood fit.

To reduce the sensitivity to statistical fluctuations due to the limited number of events in the MC samples used in systematic variations, *smoothing* techniques are applied to the MC templates used to evaluate the signal and background modelling systematic uncertainties in the template fit. Additionally, the systematic uncertainties are symmetrised, taking the average of the up- and down-variation as the uncertainty. In the cases where both variations have the same sign or only one variation is available (e.g. the uncertainty from the parton shower and hadronisation signal modelling) the largest variation or the available one, respectively, is taken as both the up- and down-variations for the corresponding source. The ISR uncertainty suffers from statistical fluctuations in the available $t\bar{t}\gamma$ MC samples, so a more conservative approach is chosen for the symmetrisation. In this case, the largest of the two variations is taken and mirrored around the nominal prediction.

In the case of the differential cross-section measurements, each systematic uncertainty is determined individually in each bin of the measurement by varying the corresponding efficiency, resolution, and model parameter within its uncertainty. The same symmetrisation approach described for the fiducial inclusive cross-section is used for this measurement. For each variation, the measured differential cross-section is recalculated and the deviation from the nominal result per bin is taken as the systematic uncertainty. The overall uncertainty in the measurement is then derived by adding all contributions in quadrature, assuming the sources of systematic uncertainty to be fully uncorrelated.

Sources of systematic uncertainty relating only to the background prediction are evaluated by shifting the nominal distribution of the corresponding background process by its associated uncertainty. For the experimental uncertainties, the input is varied by the corresponding shift, which typically affects both the shape and normalisation of signal and background process distributions. The resulting distribution is unfolded and compared with the nominal unfolded distribution and the difference is assigned as an uncertainty. The systematic uncertainties due to signal modelling are evaluated by varying the signal corrections, i.e. the migration matrix M_{kj}, the efficiency ϵ_k and the fraction $f_{\mathrm{out},j}$, by the corresponding model parameter uncertainty and calculating the difference between the resulting unfolded distributions and the nominal ones.

7 Fiducial inclusive cross-section measurement

The number of signal events is extracted using a profile likelihood fit to the S_{T} distribution and is translated into the signal cross-section in the fiducial phase space given by the kinematic boundaries of the signal as described in section 5.

The best-fit values of the nuisance parameters ranked highest in impact are shown in figure 5 along with their impact on the result. Rate and shape uncertainties from the $t\bar{t}\gamma$ PS model and $t\bar{t}\gamma$ ISR variations are treated as separate nuisance parameters.

– 16 –

Category	Uncertainty
$t\bar{t}\gamma/tW\gamma$ modelling	3.8%
Background modelling	2.1%
Photons	1.9%
Luminosity	1.8%
Jets	1.6%
Pile-up	1.3%
Leptons	1.1%
Flavour-tagging	1.1%
MC statistics	0.4%
Soft term $E_{\mathrm{T}}^{\mathrm{miss}}$	0.2%
$tW\gamma$ parton definition	2.8%
Total syst.	6.3%

Table 2. Illustrative summary of the systematic uncertainties on the fiducial inclusive cross-section measurement grouped into different categories and their relative impact on the measurement (symmetrised). The categories '$t\bar{t}\gamma/tW\gamma$ modelling' and 'Background modelling' include all corresponding systematic uncertainties described in section 6.2. The '$tW\gamma$ parton definition' uncertainty is listed separately since it does not enter the profile likelihood fit directly as described in section 6.3. The category 'Photons' corresponds to the uncertainties related to photon identification and isolation as well as photon energy scale and resolution. 'Jets' includes the total uncertainty from the JES, JER and JVT discriminant, while the b-tagging-related uncertainties are given in a separate category ('Flavour-tagging'). The category 'Leptons' represents the uncertainties related to lepton identification, isolation and energy/momentum calibration.

This approach prevents pulls on the rate uncertainty due to differences in the shape of the S_{T} distribution between the data and simulation, in particular in the tail where the data overshoot the prediction and the fit compensates for this discrepancy by pulling the nuisance parameter of the $t\bar{t}\gamma$ PS model shape uncertainty. The impact of the individual nuisance parameters is evaluated as the difference between the reference best-fit value of the cross-section and the one obtained when fixing the corresponding nuisance parameter under scrutiny to its best-fit value and its $\pm$ one standard deviation ($\pm 1\sigma$). Table 2 shows the systematic uncertainties and their relative impact on the measurement of the fiducial inclusive cross-section. The effect of each category of uncertainties is calculated from the variance (σ^2) difference between the total uncertainty in the measured fiducial cross-section and the uncertainty from the fit with the corresponding nuisance parameters fixed to their fitted values. The uncertainties in the signal modelling, especially the rate uncertainties from the $t\bar{t}\gamma$ PS model and the ISR variation, have the largest impact on the result.

The distribution of the fitted S_{T} variable is shown in figure 6. The dashed band represents the post-fit uncertainties. The expected yields after the fit describe the data well.
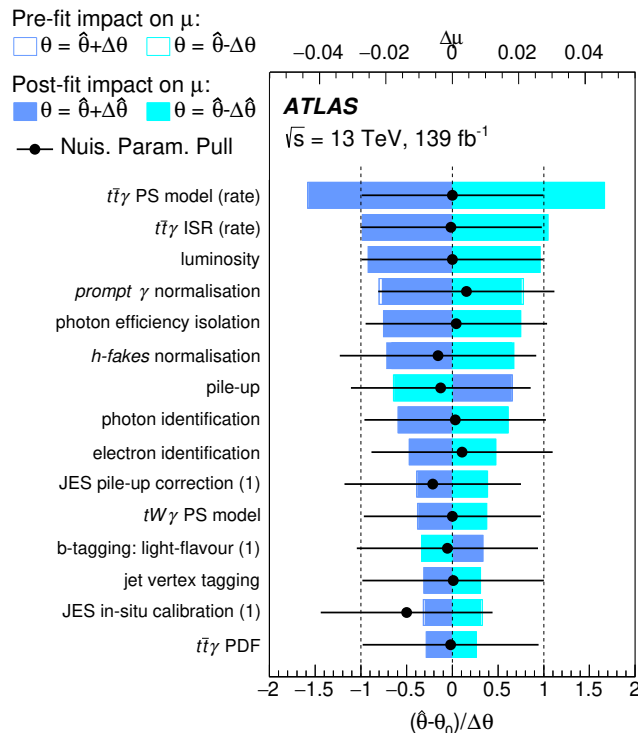
Figure 5. Ranking of the systematic uncertainties included in the profile likelihood fit used in the fiducial inclusive cross-section measurement. The blue and turquoise bands indicate the post-fit impact on the fit result, whereas the outlined blue and turquoise rectangles show the pre-fit impact. The difference between the two reflects the constraint of the nuisance parameter due to correlations in the fit. Most nuisance parameters are not or only marginally constrained. The impact is overlaid with the post-fit values of the nuisance parameters (pulls) shown by the black dots. The black lines represent the post-fit uncertainties normalised to the pre-fit uncertainties. For uncertainties parameterised with more than one nuisance parameter, the index (1) refers to the leading component.

Extrapolated to the fiducial phase space using the correction factor C, the fit result corresponds to a fiducial inclusive cross-section for the combined $t\bar{t}\gamma/tW\gamma$ process in the $e\mu$ channel of $\sigma_{\text{fid}} = 39.6 \pm 0.8\,(\text{stat})\,^{+2.6}_{-2.2}\,(\text{syst})\,\text{fb} = 39.6\,^{+2.7}_{-2.3}\,\text{fb}$. The measured cross-section is in good agreement with the dedicated theoretical calculation provided by the authors of refs. [10, 11], which predicts a value of $\sigma_{\text{fid}} = 38.50\,^{+0.56}_{-2.18}\,(\text{scale})\,^{+1.04}_{-1.18}\,(\text{PDF})\,\text{fb}$ for the chosen fiducial phase space using the CT14 PDF set [72]. The uncertainty in the theory prediction includes uncertainties owing to the scales and PDF. The PDF uncertainty is rescaled to the 68% CL. In the theoretical calculation, the renormalisation and factorisation scales are chosen as $1/4$ of the total transverse momentum of the system, defined as the scalar sum of the p_{T} of the leptons, b-jets, photon and the total missing p_{T} from the neutrinos. The
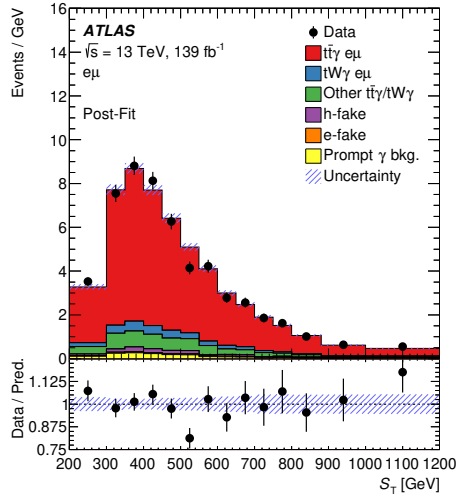
Figure 6. Post-fit distribution of the S_{T} variable. The uncertainty band represents the post-fit uncertainties. Underflow and overflow events are included in the first and last bins of the distribution, respectively. The lower part of the plot shows the ratio of the data to the prediction.

mass of the top quark is set to 173.2 GeV. The electroweak coupling in the calculation is derived from the Fermi constant G_μ and it is set to $\alpha_{G_\mu} \approx 1/132$, while it is $1/137$ for the leading emission. Further details can be found in ref. [10].

8 Differential cross-section measurements

The absolute differential cross-sections are shown in figure 7 while the normalised measured differential cross-sections are presented in figure 8. The cross-sections are compared with the NLO calculation in the same fiducial phase space and with the combination of the $t\bar{t}\gamma$ and $tW\gamma$ LO MADGRAPH5_aMC@NLO simulations interfaced with PYTHIA 8 and HERWIG 7, referred to as MG5_aMC+PYTHIA8 and MG5_aMC+HERWIG7 in the following plots and tables. The calculated χ^2/ndf values for the absolute and normalised cross-sections and their corresponding p-values are summarised in tables 3 and 4, quantifying the probability of compatibility between data and each of the predictions. The χ^2 values are calculated as:

$$\chi^2 = \sum_{j,k} (\sigma_{j,\mathrm{data}} - \sigma_{j,\mathrm{pred.}}) \cdot C_{jk}^{-1} \cdot (\sigma_{k,\mathrm{data}} - \sigma_{k,\mathrm{pred.}}),$$

where σ_{data} and $\sigma_{\mathrm{pred.}}$ are the unfolded and predicted differential cross-sections, C_{jk} is the covariance matrix of σ_{data}, calculated as the sum of the covariance matrix for the statistical uncertainty and the covariance matrices for the systematic uncertainties, and j and k are the binning indices of the distribution. The covariance matrix for each of the systematic uncertainties is estimated as $\sigma_j \times \sigma_k$, where σ_j and σ_k are the symmetrised

Predictions	$p_{\mathrm{T}}(\gamma)$		$|\eta(\gamma)|$		$\Delta R(\gamma,\ell)_{\min}$		$\Delta\phi(\ell,\ell)$		$|\Delta\eta(\ell,\ell)|$	
	χ^2/ndf	p-value	χ^2/ndf	p-value	χ^2/ndf	p-value	χ^2/ndf	p-value	χ^2/ndf	p-value
Theory NLO	6.1/11	0.87	4.5/8	0.81	11.7/10	0.31	5.8/10	0.83	6.2/8	0.62

Table 3. χ^2/ndf and p-values between the measured absolute cross-sections and the NLO calculation.

Predictions	$p_{\mathrm{T}}(\gamma)$		$|\eta(\gamma)|$		$\Delta R(\gamma,\ell)_{\min}$		$\Delta\phi(\ell,\ell)$		$|\Delta\eta(\ell,\ell)|$	
	χ^2/ndf	p-value	χ^2/ndf	p-value	χ^2/ndf	p-value	χ^2/ndf	p-value	χ^2/ndf	p-value
$t\bar{t}\gamma+tW\gamma$ (MG5_aMC+Pythia8)	6.3/10	0.79	7.3/7	0.40	20.1/9	0.02	30.8/9	<0.01	6.5/7	0.48
$t\bar{t}\gamma+tW\gamma$ (MG5_aMC+Herwig7)	5.3/10	0.87	7.7/7	0.36	18.9/9	0.03	31.6/9	<0.01	6.8/7	0.45
Theory NLO	6.0/10	0.82	4.5/7	0.72	13.5/9	0.14	5.8/9	0.76	5.6/7	0.59

Table 4. χ^2/ndf and p-values between the measured normalised cross-sections and various predictions from the MC simulation and the NLO calculation.

uncertainties for bin j and bin k of the unfolded distribution. In the case of the normalised differential cross-sections, the last bin is removed from the χ^2 calculation and the number of degrees of freedom is reduced by one.

The shape of the measured differential distributions is generally well described by both the LO MC predictions from MadGraph5_aMC@NLO and the NLO theory prediction. The latter tends to describe the shape of the measured distribution slightly better. The shapes of $\Delta R(\gamma,\ell)_{\min}$ and $\Delta\phi(\ell,\ell)$ are not perfectly modelled by the Mad-Graph5_aMC@NLO simulation, while the NLO prediction provides a better description of these distributions.

The systematic uncertainties of the unfolded distributions are decomposed into signal modelling uncertainties, experimental uncertainties, and background modelling uncertainties. The breakdown of the categories of systematic uncertainties and the statistical one, which is the dominant source of uncertainty, is illustrated in figures 9 and 10 for the absolute and normalised differential cross-sections, respectively. The systematic uncertainty is dominated by the background and signal modelling.

9 Conclusions

Measurements of the fiducial inclusive production cross-section, as well as absolute and normalised differential production cross-sections, of the combined $t\bar{t}\gamma/tW\gamma$ process in the $e\mu$ decay channel are presented using pp collisions at a centre-of-mass energy of 13 TeV, corresponding to an integrated luminosity of 139 fb^{-1} recorded by the ATLAS detector at the LHC. For the estimation of efficiencies and acceptance corrections, a LO Monte Carlo simulation of the $2 \to 7$ process $pp \to e\nu\mu\nu bb\gamma$ was used for the $t\bar{t}\gamma$ part of the signal. The contribution from $tW\gamma$ was estimated from a combination of LO Monte Carlo simulations for the $2 \to 3$ process $pp \to tW\gamma$ and the $2 \to 6$ process $pp \to e\nu\mu\nu b\gamma$. The simulations include initial- and final-state radiation of the photon from all involved objects in the matrix element. The resonant top-quark production is taken into account in the
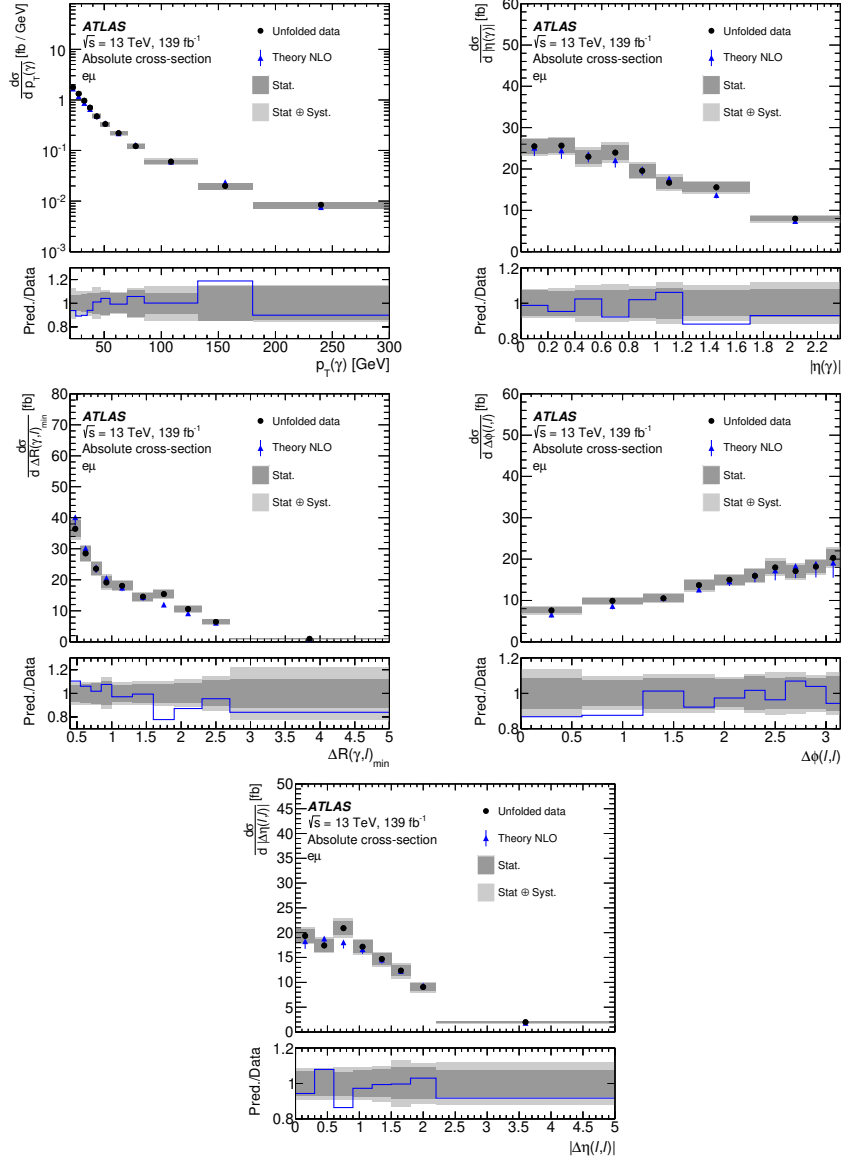
Figure 7. Absolute differential cross-section measured in the fiducial phase space as a function of the photon p_T, photon $|\eta|$, $\Delta R(\gamma, \ell)_{\text{min}}$, $\Delta\phi(\ell, \ell)$, and $|\Delta\eta(\ell, \ell)|$ (from left to right and top to bottom). Data are compared with the NLO calculation provided by the authors of refs. [10, 11]. The uncertainty in the calculation corresponds to the total scale and PDF uncertainties. The PDF uncertainty is rescaled to the 68% CL. The lower part of each plot shows the ratio of the prediction to the data.
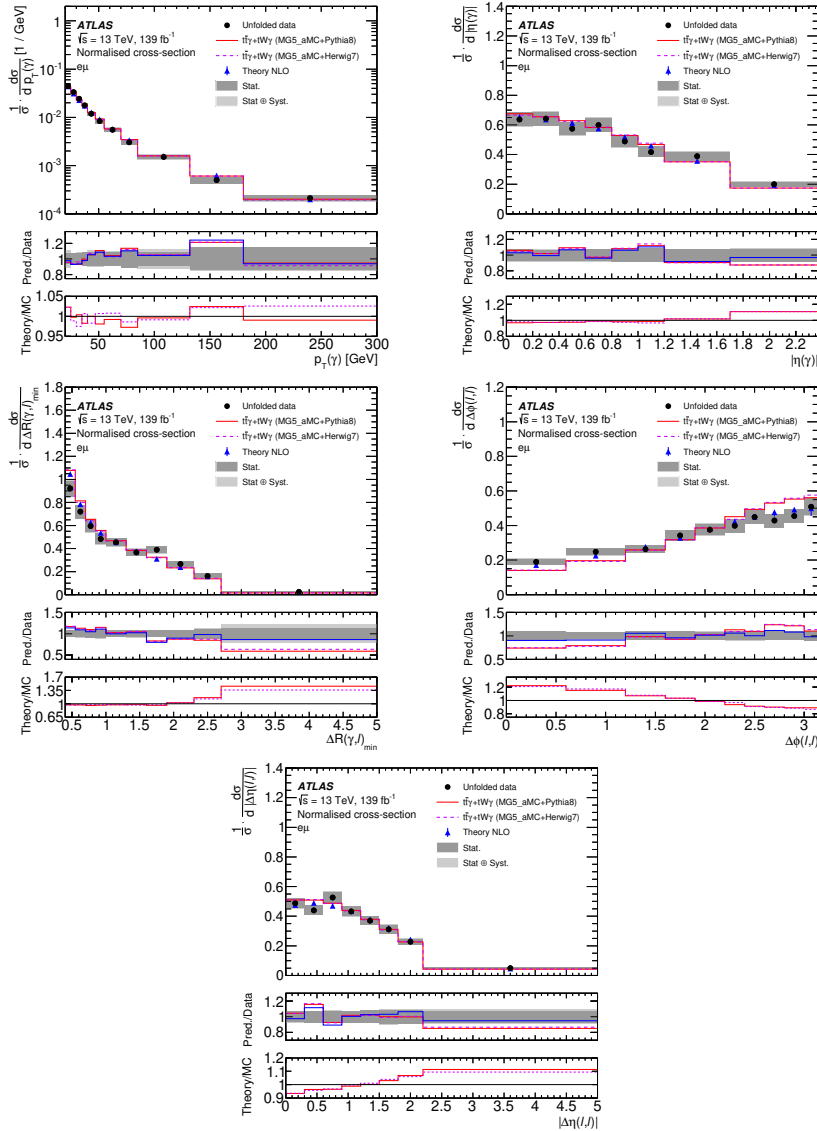
Figure 8. Normalised differential cross-section measured in the fiducial phase space as a function of the photon p_T, photon $|\eta|$, $\Delta R(\gamma, \ell)_{\min}$, $\Delta\phi(\ell, \ell)$, and $|\Delta\eta(\ell, \ell)|$ (from left to right and top to bottom). Data are compared with the NLO calculation provided by the authors of refs. [10, 11] and the MadGraph5_aMC@NLO simulation interfaced with Pythia 8 and Herwig 7. The uncertainty in the calculation corresponds to the total scale and PDF uncertainties. The PDF uncertainty is rescaled to the 68% CL. The lower parts of each plot show the ratio of the prediction to the data and the ratio of the NLO calculation to the MC simulations.
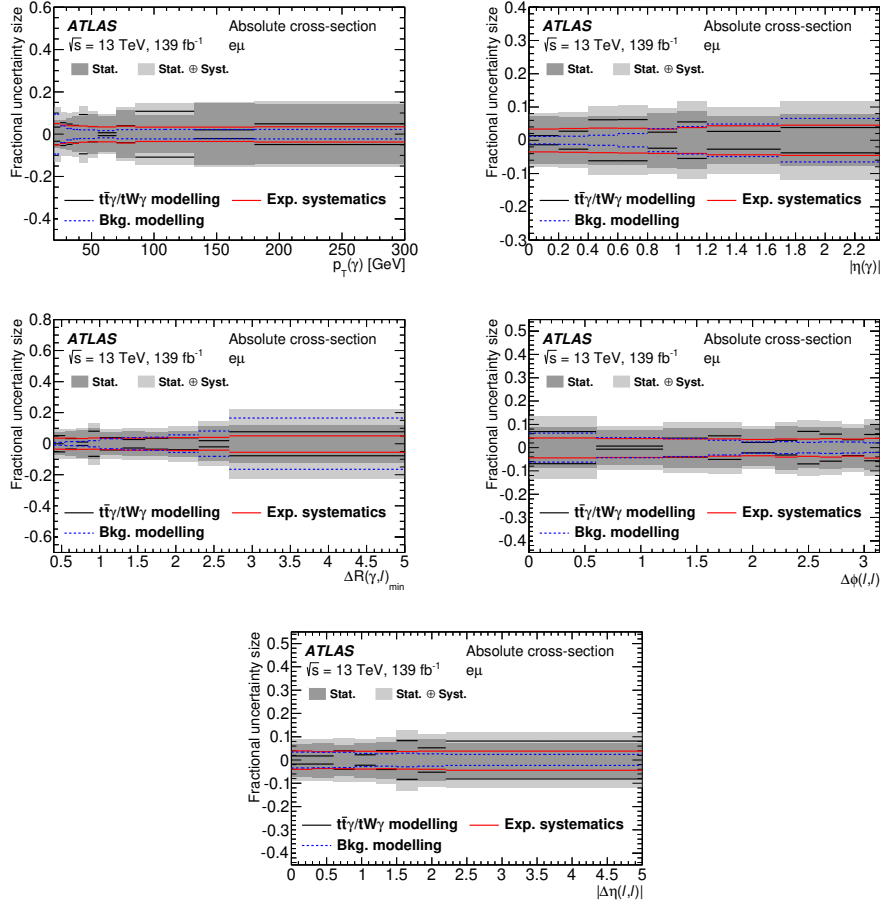
Figure 9. Contribution of each category of systematic uncertainties in each bin of the measurement of the absolute cross-sections as functions of the photon p_T, photon $|\eta|$, $\Delta R(\gamma, \ell)_{\min}$, $\Delta\phi(\ell, \ell)$ and $|\Delta\eta(\ell, \ell)|$.

simulation of $t\bar{t}\gamma$. Possible singly resonant production leading to the same final state is included in the simulation of the $tW\gamma$ process.

The results are compared with the prediction from the LO Monte Carlo simulations and also a dedicated NLO theory prediction which includes all off-shell contributions. The measured fiducial inclusive cross-section of $\sigma = 39.6^{+2.7}_{-2.3}$ fb is found to be in good agreement with the predicted NLO cross-section. All considered differential distributions are also found to be well described by the NLO theory prediction.
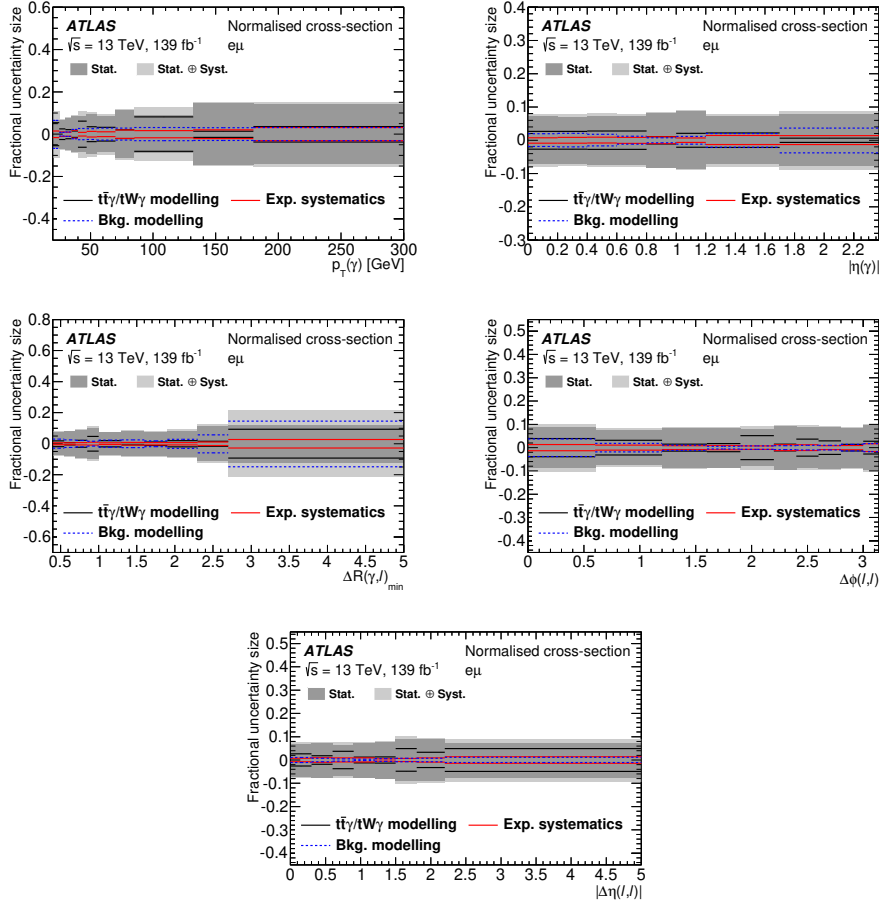
Figure 10. Contribution of each category of systematic uncertainties in each bin of the measurement of the normalised cross-sections as functions of the photon p_{T}, photon $|\eta|$, $\Delta R(\gamma, \ell)_{\mathrm{min}}$, $\Delta\phi(\ell, \ell)$ and $|\Delta\eta(\ell, \ell)|$ (from left to right and top to bottom).

Acknowledgments

References

[1] U. Baur, A. Juste, L.H. Orr and D. Rainwater, *Probing electroweak top quark couplings at hadron colliders*, *Phys. Rev. D* **71** (2005) 054013 [`hep-ph/0412021`] [INSPIRE].

[2] A.O. Bouzas and F. Larios, *Electromagnetic dipole moments of the top quark*, *Phys. Rev. D* **87** (2013) 074015 [`arXiv:1212.6575`] [INSPIRE].

[3] M. Schulze and Y. Soreq, *Pinning down electroweak dipole operators of the top quark*, *Eur. Phys. J. C* **76** (2016) 466 [`arXiv:1603.08911`] [INSPIRE].

[4] O. Bessidskaia Bylund, F. Maltoni, I. Tsinikos, E. Vryonidou and C. Zhang, *Probing top quark neutral couplings in the Standard Model effective field theory at NLO in QCD*, *JHEP* **05** (2016) 052 [`arXiv:1601.08193`] [INSPIRE].

[5] CDF collaboration, *Evidence for $t\bar{t}\gamma$ production and measurement of $\sigma_{t\bar{t}\gamma}/\sigma_{t\bar{t}}$*, *Phys. Rev. D* **84** (2011) 031104 [`arXiv:1106.3970`] [INSPIRE].

– 25 –

[6] ATLAS collaboration, *Observation of top-quark pair production in association with a photon and measurement of the $t\bar{t}\gamma$ production cross section in pp collisions at $\sqrt{s} = 7\,TeV$ using the ATLAS detector*, *Phys. Rev. D* **91** (2015) 072007 [`arXiv:1502.00586`] [ɪɴSPIRE].

[7] ATLAS collaboration, *Measurement of the $t\bar{t}\gamma$ production cross section in proton-proton collisions at $\sqrt{s} = 8\,TeV$ with the ATLAS detector*, *JHEP* **11** (2017) 086 [`arXiv:1706.03046`] [ɪɴSPIRE].

[8] CMS collaboration, *Measurement of the semileptonic $t\bar{t} + \gamma$ production cross section in pp collisions at $\sqrt{s} = 8\,TeV$*, *JHEP* **10** (2017) 006 [`arXiv:1706.08128`] [ɪɴSPIRE].

[9] ATLAS collaboration, *Measurements of inclusive and differential fiducial cross-sections of $t\bar{t}\gamma$ production in leptonic final states at $\sqrt{s} = 13\,TeV$ in ATLAS*, *Eur. Phys. J. C* **79** (2019) 382 [`arXiv:1812.01697`] [ɪɴSPIRE].

[10] G. Bevilacqua, H.B. Hartanto, M. Kraus, T. Weber and M. Worek, *Hard photons in hadroproduction of top quarks with realistic final states*, *JHEP* **10** (2018) 158 [`arXiv:1803.09916`] [ɪɴSPIRE].

[11] G. Bevilacqua, H.B. Hartanto, M. Kraus, T. Weber and M. Worek, *Precise predictions for $t\bar{t}\gamma/t\bar{t}$ cross section ratios at the LHC*, *JHEP* **01** (2019) 188 [`arXiv:1809.08562`] [ɪɴSPIRE].

[12] ATLAS collaboration, *The ATLAS experiment at the CERN Large Hadron Collider*, 2008 *JINST* **3** S08003 [ɪɴSPIRE].

[13] ATLAS collaboration, *ATLAS insertable B-layer technical design report*, Tech. Rep. CERN-LHCC-2010-013, CERN, Geneva, Switzerland (2010) [ATLAS-TDR-19] [*Addendum* CERN-LHCC-2012-009] [*Addendum* ATLAS-TDR-19-ADD-1].

[14] ATLAS IBL collaboration, *Production and integration of the ATLAS insertable B-layer*, 2018 *JINST* **13** T05008 [`arXiv:1803.00844`] [ɪɴSPIRE].

[15] ATLAS collaboration, *Performance of the ATLAS trigger system in* 2015, *Eur. Phys. J. C* **77** (2017) 317 [`arXiv:1611.09661`] [ɪɴSPIRE].

[16] ATLAS collaboration, *The ATLAS simulation infrastructure*, *Eur. Phys. J. C* **70** (2010) 823 [`arXiv:1005.4568`] [ɪɴSPIRE].

[17] GEANT4 collaboration, *GEANT4 — a simulation toolkit*, *Nucl. Instrum. Meth. A* **506** (2003) 250 [ɪɴSPIRE].

[18] T. Sjöstrand, S. Mrenna and P.Z. Skands, *PYTHIA 6.4 physics and manual*, *JHEP* **05** (2006) 026 [`hep-ph/0603175`] [ɪɴSPIRE].

[19] T. Sjöstrand et al., *An introduction to PYTHIA 8.2*, *Comput. Phys. Commun.* **191** (2015) 159 [`arXiv:1410.3012`] [ɪɴSPIRE].

[20] ATLAS collaboration, *The PYTHIA 8 A3 tune description of ATLAS minimum bias and inelastic measurements incorporating the Donnachie-Landshoff diffractive model*, Tech. Rep. ATL-PHYS-PUB-2016-017, CERN, Geneva, Switzerland (2016).

[21] J. Pumplin, D.R. Stump, J. Huston, H.L. Lai, P.M. Nadolsky and W.K. Tung, *New generation of parton distributions with uncertainties from global QCD analysis*, *JHEP* **07** (2002) 012 [`hep-ph/0201195`] [ɪɴSPIRE].

[22] J. Alwall et al., *The automated computation of tree-level and next-to-leading order differential cross sections, and their matching to parton shower simulations*, *JHEP* **07** (2014) 079 [`arXiv:1405.0301`] [ɪɴSPIRE].

[23] ATLAS collaboration, *ATLAS PYTHIA* 8 *tunes to* 7 *TeV datas*, Tech. Rep. ATL-PHYS-PUB-2014-021, CERN, Geneva, Switzerland (2014).

[24] D.J. Lange, *The EvtGen particle decay simulation package*, *Nucl. Instrum. Meth. A* **462** (2001) 152 [INSPIRE].

[25] T. Gleisberg et al., *Event generation with SHERPA* 1.1, *JHEP* **02** (2009) 007 [arXiv:0811.4622] [INSPIRE].

[26] S. Höche, F. Krauss, S. Schumann and F. Siegert, *QCD matrix elements and truncated showers*, *JHEP* **05** (2009) 053 [arXiv:0903.1219] [INSPIRE].

[27] T. Gleisberg and S. Höche, *Comix, a new matrix element generator*, *JHEP* **12** (2008) 039 [arXiv:0808.3674] [INSPIRE].

[28] S. Schumann and F. Krauss, *A parton shower algorithm based on Catani-Seymour dipole factorisation*, *JHEP* **03** (2008) 038 [arXiv:0709.1027] [INSPIRE].

[29] S. Höche, F. Krauss, M. Schönherr and F. Siegert, *A critical appraisal of NLO+PS matching methods*, *JHEP* **09** (2012) 049 [arXiv:1111.1220] [INSPIRE].

[30] S. Catani, F. Krauss, R. Kuhn and B.R. Webber, *QCD matrix elements + parton showers*, *JHEP* **11** (2001) 063 [hep-ph/0109231] [INSPIRE].

[31] S. Höche, F. Krauss, M. Schönherr and F. Siegert, *QCD matrix elements + parton showers: the NLO case*, *JHEP* **04** (2013) 027 [arXiv:1207.5030] [INSPIRE].

[32] F. Cascioli, P. Maierhöfer and S. Pozzorini, *Scattering amplitudes with open loops*, *Phys. Rev. Lett.* **108** (2012) 111601 [arXiv:1111.5206] [INSPIRE].

[33] A. Denner, S. Dittmaier and L. Hofer, *Collier: a fortran-based Complex One-Loop LIbrary in Extended Regularizations*, *Comput. Phys. Commun.* **212** (2017) 220 [arXiv:1604.06792] [INSPIRE].

[34] P. Nason, *A new method for combining NLO QCD with shower Monte Carlo algorithms*, *JHEP* **11** (2004) 040 [hep-ph/0409146] [INSPIRE].

[35] S. Frixione, P. Nason and C. Oleari, *Matching NLO QCD computations with parton shower simulations: the POWHEG method*, *JHEP* **11** (2007) 070 [arXiv:0709.2092] [INSPIRE].

[36] S. Alioli, P. Nason, C. Oleari and E. Re, *A general framework for implementing NLO calculations in shower Monte Carlo programs: the POWHEG BOX*, *JHEP* **06** (2010) 043 [arXiv:1002.2581] [INSPIRE].

[37] NNPDF collaboration, *Parton distributions for the LHC run II*, *JHEP* **04** (2015) 040 [arXiv:1410.8849] [INSPIRE].

[38] ATLAS collaboration, *Summary of ATLAS PYTHIA* 8 *tunes*, Tech. Rep. ATL-PHYS-PUB-2012-003, CERN, Geneva, Switzerland (2012).

[39] M. Czakon and A. Mitov, *Top++: a program for the calculation of the top-pair cross-section at hadron colliders*, *Comput. Phys. Commun.* **185** (2014) 2930 [arXiv:1112.5675] [INSPIRE].

[40] ATLAS collaboration, *Measurement of* $W^\pm$ *and* Z-*boson production cross sections in pp collisions at* $\sqrt{s} = 13$ *TeV with the ATLAS detector*, *Phys. Lett. B* **759** (2016) 601 [arXiv:1603.09222] [INSPIRE].

[41] J.M. Campbell and R. Ellis, *An update on vector boson pair production at hadron colliders*, *Phys. Rev. D* **60** (1999) 113006 [hep-ph/9905386] [INSPIRE].

[42] LHC Higgs Cross Section Working Group collaboration, *Handbook of LHC Higgs cross sections: 4. Deciphering the nature of the Higgs sector*, arXiv:1610.07922 [INSPIRE].

[43] ATLAS collaboration, *Performance of electron and photon triggers in ATLAS during LHC run 2*, *Eur. Phys. J. C* **80** (2020) 47 [arXiv:1909.00761] [INSPIRE].

[44] ATLAS collaboration, *Performance of the ATLAS muon triggers in run 2*, arXiv:2004.13447 [INSPIRE].

[45] ATLAS collaboration, *Electron and photon performance measurements with the ATLAS detector using the* 2015–2017 *LHC proton-proton collision data*, 2019 *JINST* **14** P12006 [arXiv:1908.00005] [INSPIRE].

[46] ATLAS collaboration, *Muon reconstruction performance of the ATLAS detector in proton-proton collision data at* $\sqrt{s} = 13\,TeV$, *Eur. Phys. J. C* **76** (2016) 292 [arXiv:1603.05598] [INSPIRE].

[47] ATLAS collaboration, *Measurement of the photon identification efficiencies with the ATLAS detector using LHC run* 2 *data collected in* 2015 *and* 2016, *Eur. Phys. J. C* **79** (2019) 205 [arXiv:1810.05087] [INSPIRE].

[48] ATLAS collaboration, *Electron and photon energy calibration with the ATLAS detector using* 2015–2016 *LHC proton-proton collision data*, 2019 *JINST* **14** P03017 [arXiv:1812.03848] [INSPIRE].

[49] M. Cacciari, G.P. Salam and G. Soyez, *The anti-k_t jet clustering algorithm*, *JHEP* **04** (2008) 063 [arXiv:0802.1189] [INSPIRE].

[50] M. Cacciari, G.P. Salam and G. Soyez, *FastJet user manual*, *Eur. Phys. J. C* **72** (2012) 1896 [arXiv:1111.6097] [INSPIRE].

[51] ATLAS collaboration, *Properties of jets and inputs to jet reconstruction and calibration with the ATLAS detector using proton-proton collisions at* $\sqrt{s} = 13\,TeV$, Tech. Rep. ATL-PHYS-PUB-2015-036, CERN, Geneva, Switzerland (2015).

[52] ATLAS collaboration, *Jet energy scale measurements and their systematic uncertainties in proton-proton collisions at* $\sqrt{s} = 13\,TeV$ *with the ATLAS detector*, *Phys. Rev. D* **96** (2017) 072002 [arXiv:1703.09665] [INSPIRE].

[53] ATLAS collaboration, *Tagging and suppression of pileup jets with the ATLAS detector*, Tech. Rep. ATLAS-CONF-2014-018, CERN, Geneva, Switzerland (2014).

[54] ATLAS collaboration, *Optimisation and performance studies of the ATLAS b-tagging algorithms for the* 2017–18 *LHC run*, Tech. Rep. ATL-PHYS-PUB-2017-013, CERN, Geneva, Switzerland (2017).

[55] ATLAS collaboration, *Measurements of b-jet tagging efficiency with the ATLAS detector using* $t\bar{t}$ *events at* $\sqrt{s} = 13\,TeV$, *JHEP* **08** (2018) 089 [arXiv:1805.01845] [INSPIRE].

[56] ATLAS collaboration, E_T^{miss} *performance in the ATLAS detector using* 2015–2016 *LHC pp collisions*, Tech. Rep. ATLAS-CONF-2018-023, CERN, Geneva, Switzerland (2018).

[57] ATLAS collaboration, *Performance of missing transverse momentum reconstruction with the ATLAS detector using proton-proton collisions at* $\sqrt{s} = 13\,TeV$, *Eur. Phys. J. C* **78** (2018) 903 [arXiv:1802.08168] [INSPIRE].

[58] S. Frixione, *Isolated photons in perturbative QCD*, *Phys. Lett. B* **429** (1998) 369 [hep-ph/9801442] [INSPIRE].

– 28 –

Search for $t\bar{t}H$ production in the $H \to b\bar{b}$ decay channel with leptonic $t\bar{t}$ decays in proton-proton collisions at $\sqrt{s} = 13$ TeV

JHEP03 (2019) 026

The CMS collaboration

E-mail: cms-publication-committee-chair@cern.ch

ABSTRACT: A search is presented for the associated production of a standard model Higgs boson with a top quark-antiquark pair ($t\bar{t}H$), in which the Higgs boson decays into a b quark-antiquark pair, in proton-proton collisions at a centre-of-mass energy $\sqrt{s} = 13$ TeV. The data correspond to an integrated luminosity of $35.9\,\text{fb}^{-1}$ recorded with the CMS detector at the CERN LHC. Candidate $t\bar{t}H$ events are selected that contain either one or two electrons or muons from the $t\bar{t}$ decays and are categorised according to the number of jets. Multivariate techniques are employed to further classify the events and eventually discriminate between signal and background. The results are characterised by an observed $t\bar{t}H$ signal strength relative to the standard model cross section, $\mu = \sigma/\sigma_{\text{SM}}$, under the assumption of a Higgs boson mass of 125 GeV. A combined fit of multivariate discriminant distributions in all categories results in an observed (expected) upper limit on μ of 1.5 (0.9) at 95% confidence level, and a best fit value of $0.72 \pm 0.24(\text{stat}) \pm 0.38(\text{syst})$, corresponding to an observed (expected) signal significance of 1.6 (2.2) standard deviations above the background-only hypothesis.

Contents

1 Introduction

The observation [1–3] of a Higgs boson with a mass of approximately 125 GeV [4, 5] at the CERN LHC marked the starting point of a broad experimental programme to determine the properties of the newly discovered particle. Decays into $\gamma\gamma$, ZZ, WW, and $\tau\tau$ final states have been observed, and there is evidence for the direct decay of the particle to the bottom quark-antiquark ($b\bar{b}$) final state [6–10]. The measured rates for various production and decay channels are consistent with the standard model (SM) expectations [11, 12], and the hypothesis of a spin-0 particle is favoured over other hypotheses [13, 14].

In the SM, the Higgs boson couples to fermions with a Yukawa-type interaction, with a coupling strength proportional to the fermion mass. Probing the coupling of the Higgs boson to the heaviest known fermion, the top quark, is therefore very important for testing the SM and for constraining various models of physics beyond the SM (BSM), some of which predict a different coupling strength than the SM. Indirect constraints on the coupling between the top quark and the Higgs boson are available from processes including virtual top quark loops, for example Higgs boson production through gluon-gluon fusion [11, 12],
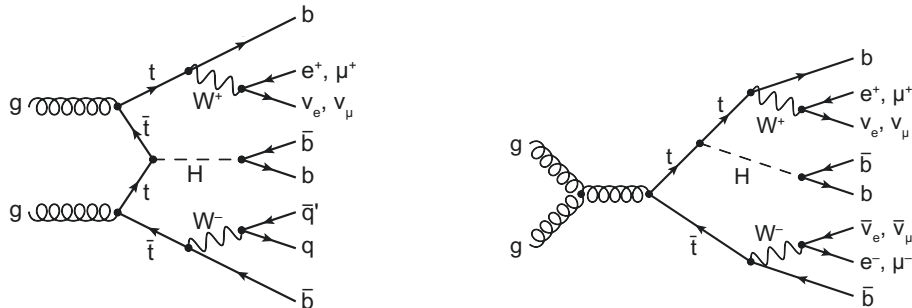
– 1 –

Figure 1. Representative leading-order Feynman diagrams for $t\bar{t}H$ production, including the subsequent decay of the Higgs boson into a b quark-antiquark pair, and the decay of the top quark-antiquark pair into final states with either one (single-lepton channel, left) or two (dilepton channel, right) electrons or muons.

as well as from production of four top quarks [15]. On the other hand, the associated production of a Higgs boson and a top quark-antiquark pair ($t\bar{t}H$ production) as illustrated by the Feynman diagrams in figure 1 is a direct probe of the Higgs boson coupling to fermions with weak isospin $+1/2$. The Higgs boson decay into $b\bar{b}$, also shown in figure 1, is experimentally attractive as a final state because it features the largest branching fraction of 0.58 ± 0.02 for a 125 GeV Higgs boson [16].

Several BSM physics scenarios predict a significantly enhanced production rate of events with $t\bar{t}H$ final states, while not modifying the branching fractions of Higgs boson decays by a measurable amount [17–26]. In this context, a measurement of the $t\bar{t}H$ production cross section has the potential to distinguish the SM Higgs mechanism of generating fermion masses from alternative ones.

Various dedicated searches for $t\bar{t}H$ production have been conducted during Run 1 of the LHC. The CMS Collaboration searches employed proton-proton (pp) collision data corresponding to an integrated luminosity of $5\,\text{fb}^{-1}$ at a centre-of-mass energy of $\sqrt{s} = 7\,\text{TeV}$ and $19.5\,\text{fb}^{-1}$ at $\sqrt{s} = 8\,\text{TeV}$. These searches have been performed by studying Higgs boson decays to b quarks, photons, and leptons using multivariate analysis (MVA) techniques, showing a mild excess of the observed $t\bar{t}H$ cross section relative to the SM expectation of $\mu = \sigma/\sigma_{\text{SM}} = 2.8 \pm 1.0$ [27]. A similar excess of $\mu = 2.1^{+1.4}_{-1.2}$ was observed in a search for $t\bar{t}H$ production in multilepton final states by the ATLAS Collaboration using data at $\sqrt{s} = 8\,\text{TeV}$, corresponding to an integrated luminosity of $20.3\,\text{fb}^{-1}$ [28]. The searches in the $H \to b\bar{b}$ decay channel were performed with several analysis techniques [27, 29, 30], yielding a most stringent observed (expected) upper limit on μ of 3.4 (2.2) at the 95% confidence level (CL).

The increased centre-of-mass energy of $\sqrt{s} = 13\,\text{TeV}$ results in a $t\bar{t}H$ production cross section 3.9 times larger than at $\sqrt{s} = 8\,\text{TeV}$ based on next-to-leading-order (NLO) calculations; while the cross section for the most important background, $t\bar{t}$ production, is increased by a factor of 3.3 [31], resulting in a more favourable signal-to-background ratio. The CMS Collaboration has performed searches in the all-jets [32] and multilepton [33]

– 2 –

final states with $35.9\,\mathrm{fb}^{-1}$ of data, achieving evidence for $\mathrm{t\bar{t}H}$ production with an observed (expected) significance of 3.2 (2.8) standard deviations in the latter case. Recently, the ATLAS Collaboration reported observed (expected) evidence for $\mathrm{t\bar{t}H}$ production with a significance of 4.2 (3.8) standard deviations, based on an integrated luminosity of $36.1\,\mathrm{fb}^{-1}$ and combining several Higgs boson decay channels [34]; in the $\mathrm{H}\to\mathrm{b\bar{b}}$ channel alone, an observed (expected) upper limit on μ of 2.0 (1.2) at 95% CL and a best fit value of $\mu = 0.84^{+0.64}_{-0.61}$ were obtained [35].

In this paper, a search for $\mathrm{t\bar{t}H}$ production in the $\mathrm{H}\to\mathrm{b\bar{b}}$ final state is presented that has been performed using $35.9\,\mathrm{fb}^{-1}$ of data recorded with the CMS detector at $\sqrt{s}=13\,\mathrm{TeV}$ in 2016. In the SM, the top quark is expected to decay into a W boson and a b quark almost exclusively. Hence different $\mathrm{t\bar{t}}$ decay modes can be identified according to the subsequent decays of the W bosons. The event selection is based on the decay topology of $\mathrm{t\bar{t}H}$ events in which the Higgs boson decays into $\mathrm{b\bar{b}}$ and the $\mathrm{t\bar{t}}$ decay involves at least one lepton, resulting in either $\ell\nu\,\mathrm{q\bar{q}'}\,\mathrm{b\bar{b}}$ (single-lepton) or $\ell^+\nu\,\ell^-\bar{\nu}\,\mathrm{b\bar{b}}$ (dilepton) $\mathrm{t\bar{t}}$ final states, where $\ell = \mathrm{e},\mu$ arising either from the prompt decay of a W boson or from leptonic τ decays. Analysis methods established in Run 1 [27, 29] have been significantly improved, and novel methods have been added. In particular, two multivariate techniques — namely boosted decision trees (BDTs) and the matrix element method (MEM) [36–40] — that utilise event information differently in order to discriminate signal from background events have been employed in combination. Since the two methods aim at separating signal from different background processes, their combined usage helps to obtain a better sensitivity. In addition, a new multivariate technique based on deep neural networks (DNNs) has been employed to separate signal from background events. The best fit value of the signal strength modifier μ is obtained from a combined profile likelihood fit of the classifier output distributions to the data, correlating processes and their uncertainties where appropriate.

This document is structured as follows. The CMS detector is described in section 2. In section 3, the simulated signal and background samples are described. The basic selection of analysis objects and events is discussed in section 4. The general analysis strategy and background estimation methods are introduced in section 5. The effect of systematic uncertainties is studied in section 6. Results of the analysis are presented in section 7, followed by a summary in section 8.

2 The CMS detector

The central feature of the CMS apparatus is a superconducting solenoid of 6 m internal diameter, providing a magnetic field of 3.8 T. Within the solenoid volume are a silicon pixel and strip tracker, a lead tungstate crystal electromagnetic calorimeter, and a brass and scintillator hadron calorimeter, each composed of a barrel and two endcap sections. Forward calorimeters extend the pseudorapidity (η) coverage provided by the barrel and endcap detectors. Muons are detected in gas-ionisation chambers embedded in the steel magnetic flux-return yoke outside the solenoid. A more detailed description of the CMS detector, together with a definition of the coordinate system used and the relevant kinematic variables, can be found in ref. [41]. Events of interest are selected using a two-tiered

trigger system [42]. The first level, composed of custom hardware processors, uses information from the calorimeters and muon detectors to select events, while the second level selects events by running a version of the full event reconstruction software optimised for fast processing on a farm of computer processors.

3 Simulation of signal and background

Several Monte Carlo event generators, interfaced with a detailed detector simulation, are used to model experimental effects, such as reconstruction and selection efficiencies, as well as detector resolutions. The CMS detector response is simulated using GEANT4 (v.9.4) [43].

For the simulation of the $t\bar{t}H$ signal sample, the NLO event generator POWHEG (v.2) [44–47] is used. Standard model backgrounds are simulated using POWHEG (v.2), PYTHIA (v.8.200) [48], or MADGRAPH5_aMC@NLO (v.2.2.2) [49], depending on the process. The value of the Higgs boson mass is assumed to be 125 GeV, while the top quark mass value is set to 172.5 GeV. The proton structure is described by the parton distribution functions (PDF) NNPDF3.0 [50].

The main background contribution originates from $t\bar{t}$ production, the production of W and Z/γ^* bosons with additional jets (referred to as W+jets and Z+jets, or commonly as V+jets), single top quark production (tW and t-channel production), diboson (WW, WZ, and ZZ) processes, and $t\bar{t}$ production in association with a W or Z boson (referred to as $t\bar{t}$+W and $t\bar{t}$+Z, or commonly as $t\bar{t}$+V). Both the $t\bar{t}$ and the single top quark processes in the t- and tW-channels are simulated with POWHEG [51, 52]. The s-channel single top quark processes, as well as V+jets and $t\bar{t}$+V processes are simulated at NLO with MADGRAPH5_aMC@NLO, where for the V+jets processes the matching of matrix-element (ME) jets to parton showers (PS) is performed using the FxFx [53] prescription. The PYTHIA event generator is used to simulate diboson events.

Parton showering and hadronisation are simulated with PYTHIA (v.8.200) for all signal and background processes. The PYTHIA CUETP8M2T4 [54] tune is used to characterise the underlying event in the $t\bar{t}H$ signal and $t\bar{t}$ and single top quark background processes, while the CUETP8M1 [55] tune is used for all other background processes.

For comparison with the observed distributions, the events in the simulated samples are normalised to the same integrated luminosity of the data sample, according to their predicted cross sections. These are taken from theoretical calculations at next-to-next-to-leading order (NNLO, for V+jets production), approximate NNLO (single top quark tW channel [56]), and NLO (single top quark t- and s-channels [57, 58], $t\bar{t}$+V production [59], and diboson production [60]). The $t\bar{t}H$ cross section of 507^{+35}_{-50} fb and Higgs boson branching fractions used in the analysis also correspond to NLO accuracy [16]. The $t\bar{t}$ simulated sample is normalised to the full NNLO calculation with resummation to next-to-next-to-leading-logarithmic accuracy [61–67], assuming a top quark mass value of 172.5 GeV and using the NNPDF3.0 PDF set. This sample is further separated into the following processes based on the flavour of additional jets that do not originate from the top quark decays in the event: $t\bar{t}$+$b\bar{b}$, defined at generator level as the events in which two additional b jets are generated within the acceptance requirements (see section 4), each of which originates from

– 4 –

one or more B hadrons; $t\bar{t}$+b, for which only one additional b jet within the acceptance originates from a single B hadron; $t\bar{t}$+2b, which corresponds to events with two additional B hadrons that are close enough in direction to produce a single b jet; $t\bar{t}$+c$\bar{c}$, for which events have at least one additional c jet within the acceptance and no additional b jets; $t\bar{t}$ + light flavour jets ($t\bar{t}$+lf), which corresponds to events that do not belong to any of the above processes. The $t\bar{t}$+b$\bar{b}$, $t\bar{t}$+b, $t\bar{t}$+2b, and $t\bar{t}$+c$\bar{c}$ processes are collectively referred to as $t\bar{t}$+hf in the following. This categorisation is important because the subsamples originate from different physics processes and have different systematic uncertainties.

Effects from additional pp interactions in the same bunch crossings (pileup) are modelled by adding simulated minimum-bias events (generated with PYTHIA v.8.212, tune CUETP8M1) to all simulated processes. The pileup multiplicity distribution in simulation is reweighted to reflect the luminosity profile of the observed pp collisions. Correction factors described in section 4 are applied to the simulation where necessary to improve the description of the data.

4 Object and event reconstruction

The event selection is optimised to identify events from the production of a Higgs boson in association with $t\bar{t}$ events, where the Higgs boson decays into b$\bar{b}$. Two $t\bar{t}$ decay modes are considered: the single-lepton mode ($t\bar{t} \rightarrow \ell\nu\,q\bar{q}'\,b\bar{b}$), where one W boson decays into a charged lepton and a neutrino, and the dilepton mode ($t\bar{t} \rightarrow \ell^+\nu\,\ell^-\bar{\nu}\,b\bar{b}$), where both W bosons decay into a charged lepton and a neutrino. These signatures imply the presence of isolated leptons ($\ell = $ e, μ), missing transverse momentum due to the neutrinos from W boson decays, and highly energetic jets originating from the final-state quarks. Jets originating from the hadronisation of b quarks are identified through b tagging techniques [68].

Online, events in the single-lepton channel were selected by single-lepton triggers which require the presence of one electron (muon) with a transverse momentum (p_T) threshold of $p_T > 27(24)$ GeV. Events in the dilepton channel were selected either by the single-lepton trigger (retaining events with an additional lepton) or by dilepton triggers that require the presence of two electrons or muons. The same-flavour dilepton triggers required two electrons with $p_T > 23$ and 12 GeV, or two muons with $p_T > 17$ and 8 GeV, respectively. The different-flavour dilepton triggers required either a muon with $p_T > 23$ GeV and an electron with $p_T > 12$ GeV, or an electron with $p_T > 23$ GeV and a muon with $p_T > 8$ GeV.

Events are reconstructed using a particle-flow (PF) technique [69], which combines information from all subdetectors to enhance the reconstruction performance by identifying individual particle candidates in pp collisions. An interaction vertex [70] is required within 24 cm of the detector centre along the beam line direction, and within 2 cm of the beam line in the transverse plane. Among all such vertices, the reconstructed vertex with the largest value of summed physics-object p_T^2 is taken to be the primary pp interaction vertex. The physics objects are the jets, clustered using a jet finding algorithm [71, 72] with the tracks assigned to the vertex as inputs, and the associated missing transverse momentum, taken as the negative vector sum of the p_T of those jets. All other interaction vertices are

– 5 –

considered as pileup vertices. Charged tracks identified as hadrons from pileup vertices are omitted in the subsequent event reconstruction.

The electron and muon candidates are required to be sufficiently isolated from nearby jet activity as follows. For each electron (muon) candidate, a cone of $\Delta R = 0.3\,(0.4)$ is constructed around the direction of the track at the event vertex, where ΔR is defined as $\sqrt{(\Delta\eta)^2 + (\Delta\phi)^2}$, and $\Delta\eta$ and $\Delta\phi$ are the distances in the pseudorapidity and azimuthal angle. Excluding the contribution from the lepton candidate, the scalar p_T sum of all particle candidates inside the cone consistent with arising from the chosen primary event vertex is calculated. The neutral component from pileup interactions is subtracted event-by-event, based on the average transverse energy deposited by neutral particles in the event in the case of electrons, and half the transverse momentum carried by charged particles identified to come from pileup vertices in the case of muons. A relative isolation discriminant I_{rel} is defined as the ratio of this sum to the p_T of the lepton candidate. Electron candidates are selected if they have values of $I_{rel} < 0.06$, while muons are selected if they fulfil the requirement $I_{rel} < 0.15$ in the single-lepton channel and $I_{rel} < 0.25$ in the dilepton channel. In addition, electrons from identified photon conversions are rejected [73]. To further increase the purity of muons originating from the primary interaction and to suppress misidentified muons or muons from decay-in-flight processes, additional quality criteria, such as a minimal number of hits associated with the muon track, are required in both the silicon tracker and the muon system [74].

For the single-lepton channel, events are selected containing exactly one energetic, isolated lepton (e or μ), which is required to have $p_T > 30\,(26)$ GeV in the case of the electron (muon), and $|\eta| < 2.1$. Electron candidates in the transition region between the barrel and endcap calorimeters, $1.4442 < |\eta| < 1.5560$, are excluded. The flavour of the lepton must match the flavour of the trigger that accepted the event (e.g. if an electron is identified, the single-electron trigger must have accepted the event). For the dilepton channel, events are required to have a pair of oppositely charged energetic leptons (e$^+$e$^-$, $\mu^\pm$e$^\mp$, $\mu^+\mu^-$). The lepton with the highest p_T out of the pair is required to have $p_T > 25$ GeV, and the other lepton $p_T > 15$ GeV; both leptons are required to fulfil the requirement $|\eta| < 2.4$, excluding electrons in the transition region. The flavours of the lepton pair must match the flavour of the trigger that accepted the event. The events are unambiguously classified as e$^+$e$^-$, $\mu^\pm$e$^\mp$, or $\mu^+\mu^-$, depending on the type of the selected lepton pair, and there is no overlap with the other channels under study. The invariant mass of the selected lepton pair, $m_{\ell\ell}$, is required to be larger than 20 GeV to suppress events from heavy-flavour resonance decays and low-mass Drell-Yan processes. In the same-flavour channels, events are also rejected if $76 < m_{\ell\ell} < 106$ GeV, thereby suppressing further contribution from Z+jets events. In both the single- and dilepton channel, events with additional isolated leptons with $p_T > 15$ GeV and $|\eta| < 2.4$ are excluded from further analysis.

The missing transverse momentum vector $\vec{p}_T^{\,miss}$ is defined as the projection of the negative vector sum of the momenta of all reconstructed PF objects in an event on the plane perpendicular to the beams. Its magnitude is referred to as p_T^{miss}. Events are required to fulfil $p_T^{miss} > 20$ GeV in the single-lepton and $p_T^{miss} > 40$ GeV in the dilepton same-flavour channels to further suppress background contribution.

– 6 –

Jets are reconstructed from the PF particle candidates using the anti-k_T clustering algorithm [71] with a distance parameter of 0.4, as implemented in FASTJET [72]. Charged hadrons that are associated to pileup vertices are discarded from the clustering. The jet energy is corrected for the remaining neutral-hadron pileup component in a manner similar to that used to find the energy within the lepton isolation cone [75]. Jet energy corrections are also applied as a function of jet p_T and η [76] to data and simulation. All reconstructed jets in the single-lepton channel and the two jets leading in p_T in the dilepton channel are required to satisfy $|\eta| < 2.4$ and $p_T > 30$ GeV. Other jets in the dilepton channel are selected if $p_T > 20$ GeV. Events are selected if they contain at least four jets in the single-lepton channel or at least two jets in the dilepton channel.

Jets originating from the hadronisation of b quarks are identified using a combined secondary vertex algorithm (CSVv2) [68], which provides a b tagging discriminant by combining identified secondary vertices and track-based lifetime information. A discriminant value is chosen such that the probability of tagging jets originating from light-flavour quarks (u, d, or s) or gluons is about 1%, and the corresponding efficiency for tagging jets from b (c) quarks is $\approx$65% (10%). The shape of the CSVv2 discriminant distribution in simulation is corrected by scale factors to better describe the data. This correction is derived separately for light-flavour and b jets with a tag-and-probe approach. Control samples enriched in events with a Z boson and exactly two jets where a b jet veto is applied are used to obtain the correction for light-flavour jets. The correction for b jets is estimated using a sample enriched in $t\bar{t}$ events with no additional jets [68]. For c jets, the data-to-simulation scale factor is set to unity with an uncertainty twice the one of the correction for b jets. Events are required to have at least two (one) b-tagged jets in the single-lepton (dilepton) channels.

Event yields observed in data and predicted by the simulation after this selection (referred to as baseline selection in the following) are listed in table 1 for the single-lepton and dilepton channels. The corresponding jet and b-tagged jet multiplicity distributions are shown in figures 2 and 3, respectively. The $t\bar{t}H$ signal includes H $\to$ b$\bar{b}$ and all other Higgs boson decay modes. Background contributions from QCD multijet production, estimated using a low-p_T^{miss} control region in data, have been found to be negligible in this analysis.

5   Analysis strategy and event classification

In both the single-lepton and dilepton channels, events with at least four jets of which at least three are b-tagged are selected among those passing the baseline selection described in section 4. These events are then further divided into categories with varying signal purity and different background composition. In each category, combinations of several multivariate discriminants are optimised to separate signal from background. The signal is extracted in a simultaneous template fit of the discriminant output obtained from the simulation to the data across all the categories, correlating processes and their uncertainties where appropriate. In this way, the different background composition in the different categories helps to constrain the uncertainties of the different processes and increases the overall sensitivity of the search.

– 7 –

Process	SL channel	DL channel
$t\bar{t}$+lf	$463\,658 \pm 174$	$241\,032 \pm 99$
$t\bar{t}$+c$\bar{c}$	$76\,012 \pm 70$	$24\,550 \pm 32$
$t\bar{t}$+b	$22\,416 \pm 38$	$5\,979 \pm 16$
$t\bar{t}$+2b	$9\,052 \pm 24$	$1\,785 \pm 9$
$t\bar{t}$+b$\bar{b}$	$10\,897 \pm 27$	$1\,840 \pm 9$
Single t	$25\,215 \pm 166$	$12\,206 \pm 125$
V+jets	$12\,309 \pm 58$	$5\,684 \pm 209$
$t\bar{t}$+V	$2\,457 \pm 12$	$2\,570 \pm 23$
Diboson	449 ± 14	430 ± 15
Total bkg.	$622\,466 \pm 263$	$296\,077 \pm 266$
$t\bar{t}$H	$1\,232 \pm 2$	314.0 ± 0.9
Data	$610\,556$	$283\,942$

Table 1. Event yields observed in data and predicted by the simulation after the baseline selection requirements in the single-lepton (SL) and dilepton (DL) channels. The $t\bar{t}$H signal includes H $\to$ b$\bar{b}$ and all other Higgs boson decay modes. The quoted uncertainties are statistical only.

Several methods that classify events as signal- or background-like were explored to achieve optimal sensitivity: DNNs and BDTs, combined with a MEM. In the DNN approach, the jet multiplicity and the DNN classification output, described below, are used for the event categorisation ("jet-process categories"). In the BDT approach, events are divided into categories based on their jet and b-tagged jet multiplicity ("jet-tag categories"). The approach that provided the best expected sensitivity in each channel, evaluated on fits to simulated data, was chosen for obtaining the final result from data. Therefore, in the single-lepton channel the DNN approach is used, while in the dilepton channel a BDT+MEM classification is chosen. The methods and the corresponding categorisation are illustrated in figure 4 and described in the following.

In the single-lepton channel, events are separated depending on the jet multiplicity into three categories with $(4\,\text{jets}, \geq 3\,\text{b tags})$, $(5\,\text{jets}, \geq 3\,\text{b tags})$, and $(\geq 6\,\text{jets}, \geq 3\,\text{b tags})$. Dedicated multi-classification DNNs [77] are trained in each jet multiplicity category to separate signal and each of the five $t\bar{t}$+jets background processes $t\bar{t}$+b$\bar{b}$, $t\bar{t}$+2b, $t\bar{t}$+b, $t\bar{t}$+c$\bar{c}$, or $t\bar{t}$+lf.

The DNN training is performed using simulated $t\bar{t}$H and $t\bar{t}$+jets events as signal and background, respectively. The overall set of events is split into a training set (30%), an independent set (20%) for validation and optimisation of the DNN configuration (hyper parameters), such as the number of nodes per layer, and a set that is reserved for the fit to the data (50%). The hyper parameters and input variables are detailed in appendix A.

The training is conducted in two stages. In the first stage, a DNN is trained to predict which of the reconstructed physics objects originate from the expected underlying hard
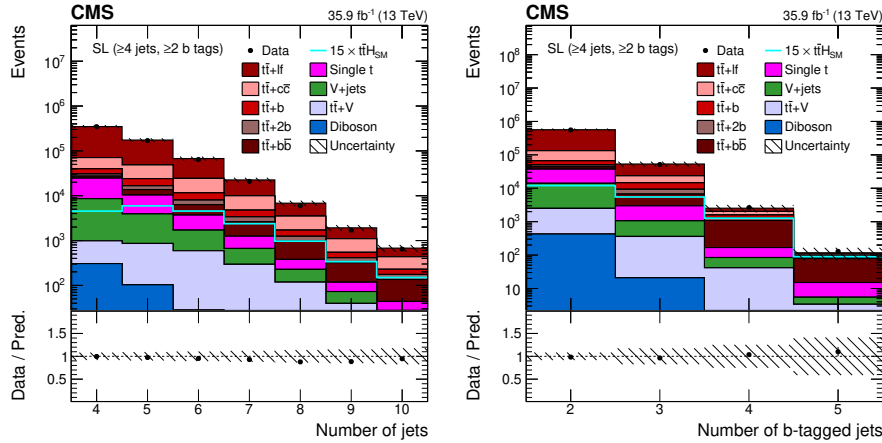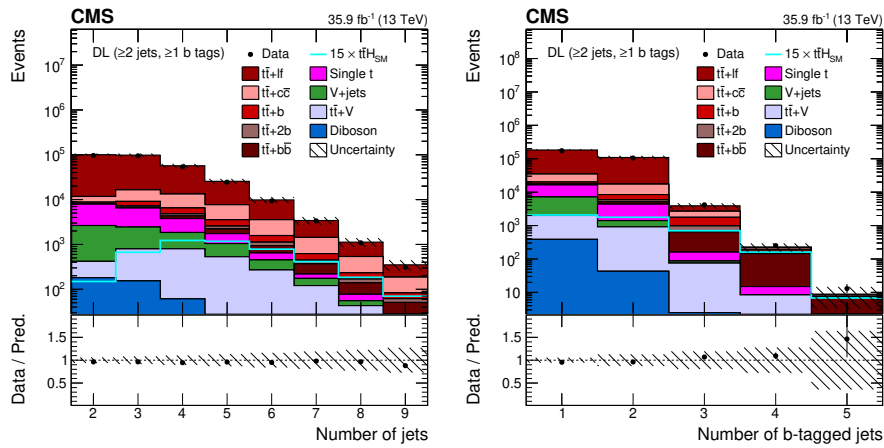
– 8 –

Figure 2. Jet (left) and b-tagged jet (right) multiplicity in the single-lepton (SL) channel after the baseline selection. The expected background contributions (filled histograms) are stacked, and the expected signal distribution (line), which includes H → b$\bar{\text{b}}$ and all other Higgs boson decay modes, is superimposed. Each contribution is normalised to an integrated luminosity of $35.9\,\text{fb}^{-1}$, and the signal distribution is additionally scaled by a factor of 15 for better visibility. The hatched uncertainty bands correspond to the total statistical and systematic uncertainties (excluding uncertainties that affect only the normalisation of the distribution) added in quadrature. The distributions observed in data (markers) are overlayed. The last bin includes overflow events. The lower plots show the ratio of the data to the background prediction.
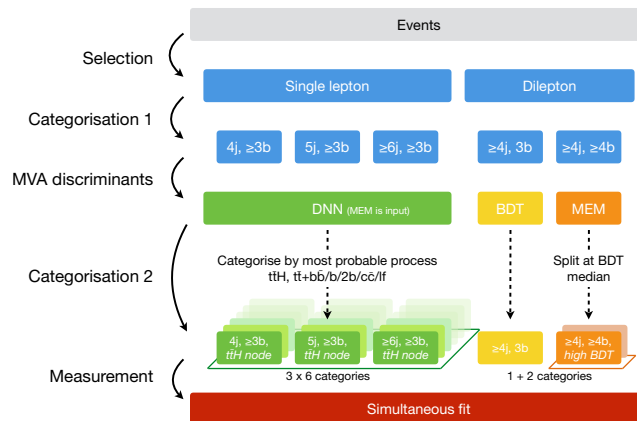
process, such as for example the b quark jet from the decay of a top quark. In the second stage, the initial network is extended by adding hidden layers, which take as input the variables and the output values of the first stage, and the resulting network is trained to predict the physics process of an event. The values obtained in the output nodes of the second stage are normalised to unity using a "softmax" function [77], and, as a result, can be interpreted as probabilities describing the likelihood of the event being a t$\bar{\text{t}}$H signal or one of the five t$\bar{\text{t}}$+jets background processes. Events are divided into subcategories of the most probable process according to this DNN classification. Thus, there are in total 18 jet-process categories in the single-lepton channel. In each of the jet-process categories, the DNN classifier output distribution of the node that matches the process category is used as the final discriminant.

The DNNs utilise input variables related to kinematic properties of individual objects, event shape, and the jet CSVv2 b tagging discriminant, and additionally the MEM discriminant output, described in the following.

The MEM discriminant is constructed as the ratio of the probability density values for the signal (t$\bar{\text{t}}$H) and background (t$\bar{\text{t}}$+b$\bar{\text{b}}$) hypotheses, following the algorithm described in ref. [29]. Each event is assigned a probability density value computed from the four-momenta of the reconstructed particles, which is based on the leading order scattering amplitudes for the t$\bar{\text{t}}$H and t$\bar{\text{t}}$+b$\bar{\text{b}}$ processes and integrated over the particle-level quanti-

Figure 3. Jet (left) and b-tagged jet (right) multiplicity in the dilepton (DL) channel after the baseline selection. The expected background contributions (filled histograms) are stacked, and the expected signal distribution (line), which includes $H \to b\overline{b}$ and all other Higgs boson decay modes, is superimposed. Each contribution is normalised to an integrated luminosity of $35.9\,\mathrm{fb}^{-1}$, and the signal distribution is additionally scaled by a factor of 15 for better visibility. The hatched uncertainty bands correspond to the total statistical and systematic uncertainties (excluding uncertainties that affect only the normalisation of the distribution) added in quadrature. The distributions observed in data (markers) are overlayed. The last bin includes overflow events. The lower plots show the ratio of the data to the background prediction.

Figure 4. Illustration of the analysis strategy.

60

ties that are either unknown or poorly measured. The probability density functions are constructed at leading order, assuming gluon-gluon fusion production both for signal and background processes as it represents the majority of the event rate. In each event, the four jets that are most likely to originate from b quarks are considered explicitly as candidates for the b quarks from the decay of the Higgs boson and the top quarks. All permutations of jets, regardless of their b tagging discriminant, are considered when associating the b-quark-like jets to the top quark or Higgs boson decays in the matrix element. The four b-like jets are selected using a likelihood ratio criterion as follows. The likelihoods are computed under either the hypothesis that four jets or that two jets in the event originate from b quarks, based on the expected b tagging discriminant probability densities from simulation. The used ratio is computed as the four-b-jets likelihood, normalised to the sum of the four- and the two-b-jets likelihoods. When computing the MEM in the single-lepton channel, up to four additional light jets, ordered in p_T, are permuted over as candidates for the light quarks from the hadronic decay of the W boson.

In the dilepton channel, events are separated into two jet-tag categories with $(\geq 4\,\text{jets}, 3\,\text{b tags})$ and $(\geq 4\,\text{jets}, \geq 4\,\text{b tags})$. In each jet-tag category, a dedicated BDT is trained to separate signal from background processes. The BDTs utilise input variables related to kinematic properties of individual objects, event shape, and the jet CSVv2 b tagging discriminant, similar as the DNNs, but no MEM information. The training is performed using simulated $t\bar{t}H$ and $t\bar{t}$+jets events as signal and background, respectively, which are weighted to achieve equal yields of signal and background events. In order to avoid a biased performance estimate, the events are separated in half for training and validation. The specific BDT boosting method used is the stochastic gradient boost [36, 78], available as part of the TMVA package [38]. The choice of the BDT architecture and the input variables was optimised with a procedure based on the particle swarm algorithm [79, 80], selecting the configuration and set of variables that yields the highest discrimination power. They are detailed in appendix A.

In the $(\geq 4\,\text{jets}, 3\,\text{b tags})$ category, the BDT output distribution is used as the final discriminant. The $(\geq 4\,\text{jets}, \geq 4\,\text{b tags})$ category is further divided into two subcategories, one with small values of the BDT output (background-like) and one with large output values (signal-like). The division is taken at the median of the BDT output distribution for simulated signal events. In each subcategory, the MEM discriminant output is used as the final discriminant. The high BDT output subcategory is expected to be enhanced with signal events and residual $t\bar{t}$+b$\bar{b}$ background events, and the MEM discriminant achieves by construction particularly powerful additional separation against the $t\bar{t}$+b$\bar{b}$ background contributions. The choice of the median contributes to a robust result by ensuring a sufficient number of events in each subcategory. Including the low b tag multiplicity and the low BDT output subcategories into the fit constrains the background contributions and systematic uncertainties for each of the different event topologies. Thus, there are in total three categories in the dilepton channel.

In summary, in the single-lepton channel events are subdivided into 18 jet-process categories and the DNN output distribution of the most probable process is used as the final discriminant. In the dilepton channel events are subdivided into three jet-tag categories and either the BDT or MEM output distribution is used as the final discriminant.

– 11 –

6 Systematic uncertainties

In table 2, all sources of systematic uncertainties considered in the analysis are listed. They affect either the rate of the signal or background processes, or the discriminant shape, or both. In the last case, the rate and shape effects are treated as entirely correlated and are varied simultaneously. The uncertainties are taken into account via nuisance parameters in the final fit procedure described in section 7, where the effects from the same source are treated as fully correlated among the different categories. The impact of the uncertainties on the final result is discussed in section 7.

The uncertainty in the integrated luminosity estimate is 2.5% [81]. The trigger efficiency in the single-lepton channel and the electron and muon identification efficiency uncertainties are estimated by comparing variations in measured efficiency between data and simulation using a high-purity sample of Z boson decays. In the dilepton channel, the trigger efficiency is measured in data with a method based on triggers that are uncorrelated with those used in the analysis, in particular based on p_T^{miss} requirements. These uncertainties are found to be small, typically below 1–2%. Effects of the uncertainty in the distribution of the number of pileup interactions are evaluated by varying the total inelastic cross section used to predict the number of pileup interactions in the simulated events by $\pm 4.6\%$ from its nominal value [82]. The uncertainty due to the limited knowledge of the jet energy scale (resolution) is determined by variations of the energy scale (resolution) correction of all jets in the signal and background predictions by one standard deviation. In the case of the jet energy scale uncertainty, these variations are divided into 26 sources, which include uncertainties owing to the extrapolation between samples of different jet-flavour composition and the presence of pileup collisions in the derivation of the corrections [76]. The effect of each source is evaluated individually. The uncertainty of the CSVv2 b tagging scale factors is evaluated by applying alternative scale factors based on varying the following systematic effects [68] by one standard deviation, separately for the different jet flavours: the contamination of background processes in the control samples, the jet energy scale uncertainty — which is correlated with the overall jet energy scale uncertainty — and the statistical uncertainty in the scale factor evaluation. The impact of the statistical uncertainty is parameterised as the sum of two contributions: one term with linear dependence on the b tagging discriminant value, allowing an overall tilt of the discriminant distribution, and another term with quadratic dependence, allowing an overall shift of the discriminant distribution.

Theoretical uncertainties of the cross sections used to predict the rates of various processes are propagated to the yield estimates. All rates are estimated using cross sections with at least NLO accuracy, which have uncertainties arising primarily from PDFs and the choice of factorisation and renormalisation scales (both in the ME and the PS). The cross section uncertainties are each separated into their PDF and scale components (renorm./fact. scales) and are correlated where appropriate between processes. For example, the PDF uncertainties for background processes originating primarily from gluon-gluon initial states are treated as 100% correlated. The PDF uncertainty of the $t\bar{t}H$ signal production is treated separately from the background processes.

The $t\bar{t}+b\bar{b}$ process, and to lesser extent the $t\bar{t}+2b$, $t\bar{t}+b$, and $t\bar{t}+c\bar{c}$ production, represent important sources of irreducible background. Neither previous measurements of

Source	Type	Remarks
Integrated luminosity	rate	Signal and all backgrounds
Lepton identification/isolation	shape	Signal and all backgrounds
Trigger efficiency	shape	Signal and all backgrounds
Pileup	shape	Signal and all backgrounds
Jet energy scale	shape	Signal and all backgrounds
Jet energy resolution	shape	Signal and all backgrounds
b tag hf fraction	shape	Signal and all backgrounds
b tag hf stats (linear)	shape	Signal and all backgrounds
b tag hf stats (quadratic)	shape	Signal and all backgrounds
b tag lf fraction	shape	Signal and all backgrounds
b tag lf stats (linear)	shape	Signal and all backgrounds
b tag lf stats (quadratic)	shape	Signal and all backgrounds
b tag charm (linear)	shape	Signal and all backgrounds
b tag charm (quadratic)	shape	Signal and all backgrounds
Renorm./fact. scales ($t\bar{t}$H)	rate	Scale uncertainty of NLO $t\bar{t}$H prediction
Renorm./fact. scales ($t\bar{t}$)	rate	Scale uncertainty of NNLO $t\bar{t}$ prediction
Renorm./fact. scales ($t\bar{t}$+hf)	rate	Additional 50% rate uncertainty of $t\bar{t}$+hf predictions
Renorm./fact. scales (t)	rate	Scale uncertainty of NLO single t prediction
Renorm./fact. scales (V)	rate	Scale uncertainty of NNLO W and Z prediction
Renorm./fact. scales (VV)	rate	Scale uncertainty of NLO diboson prediction
PDF (gg)	rate	PDF uncertainty for gg initiated processes except $t\bar{t}$H
PDF (gg $t\bar{t}$H)	rate	PDF uncertainty for $t\bar{t}$H
PDF ($q\bar{q}$)	rate	PDF uncertainty of $q\bar{q}$ initiated processes ($t\bar{t}$+W,W,Z)
PDF (qg)	rate	PDF uncertainty of qg initiated processes (single t)
μ_R scale ($t\bar{t}$)	shape	Renormalisation scale uncertainty of the $t\bar{t}$ ME generator (POWHEG), same for additional jet flavours
μ_F scale ($t\bar{t}$)	shape	Factorisation scale uncertainty of the $t\bar{t}$ ME generator (POWHEG), same for additional jet flavours
PS scale: ISR ($t\bar{t}$)	rate	Initial state radiation uncertainty of the PS (for $t\bar{t}$ events), jet multiplicity dependent rate uncertainty, independent for additional jet flavours
PS scale: FSR ($t\bar{t}$)	rate	Final state radiation uncertainty (for $t\bar{t}$ events), jet multiplicity dependent rate uncertainty, independent for additional jet flavours
ME-PS matching ($t\bar{t}$)	rate	NLO ME to PS matching, *hdamp* [54] (for $t\bar{t}$ events), jet multiplicity dependent rate uncertainty, independent for additional jet flavours
Underlying event ($t\bar{t}$)	rate	Underlying event (for $t\bar{t}$ events), jet multiplicity dependent rate uncertainty, independent for additional jet flavours
NNPDF3.0NLO ($t\bar{t}$H, $t\bar{t}$)	shape	Based on the NNPDF replicas, same for $t\bar{t}$H and additional jet flavours
Bin-by-bin event count	shape	Statistical uncertainty of the signal and background prediction due to the limited sample size

Table 2. Systematic uncertainties considered in the analysis, their corresponding type (affecting rate or shape of the distributions), and additional remarks.

– 13 –

t̄t+hf production [83–86] nor higher-order theoretical calculations can currently constrain the normalisation of these contributions to better than 35% accuracy [87, 88]. The shape of the final discriminant distributions as well as important input variable distributions of the sum of the t̄t+bb̄, t̄t+2b, and t̄t+b processes obtained with the nominal t̄t simulation were compared to those obtained from a 4-flavour scheme SHERPA (v.2.2.2) [89] t̄t+bb̄ simulation combined with OPENLOOPS (v.1.3.1) [90]. The shapes agree within the statistical precision. Therefore, an additional 50% rate uncertainty is assigned to each of the t̄t+hf processes to account also for differences in the phase space with respect to ref. [86]. Moreover, the robustness of the fit model was verified using simulated toy data, which were sampled from the templates of the fit model. The background templates were modified in the following ways to sample the toy data: increasing the normalisation of the t̄t+bb̄ background template by 30% in accordance with the results in ref. [86] or replacing the sum of the templates of the t̄t+bb̄, t̄t+2b, and t̄t+b processes obtained with the nominal t̄t simulation by those obtained from the 4-flavour scheme SHERPA plus OPENLOOPS mentioned above. In each case, a fit of the nominal model to the toy data is performed as described in section 7, including the full set of systematic uncertainties. The injected signal is recovered within a few percent, well within the uncertainties assigned to these processes.

The uncertainty arising from the missing higher-order terms in the simulation with POWHEG of the t̄t+jets process at the ME level is assessed by varying the renormalisation and factorisation scales in the simulation up and down by factors of two with respect to the nominal values, using event weights obtained directly from the generator. At the PS level, the corresponding uncertainty is estimated by varying the parameters controlling the amount of initial- and final-state radiation independently by factors of 0.5 and 2 [91]. These sources of uncertainties are treated as uncorrelated. The uncertainty originating from the scheme used to match the ME level calculation to the PS simulation is derived by comparing the reference t̄t+jets simulation with two samples with varied *hdamp* parameter [54], which controls the ME and PS matching and effectively regulates the high-p_T radiation. The effect on the final discriminators owing to uncertainties in the underlying event tune of the t̄t+jets event generator are estimated using simulations with varied parameters with respect to those used to derive the CUETP8M2T4 tune in the default setup. The event count in the additional samples required to estimate the modelling uncertainties was small and induced changes to the discriminant distributions comparable in size to the statistical fluctuations of the additional samples. For this reason, the uncertainties were estimated conservatively as the changes in the rates of the different t̄t subprocesses independently for different jet multiplicities. If the statistical uncertainty owing to the size of the simulated samples was larger than the rate change, the former was assigned as uncertainty. The derived rate uncertainties were then correlated between jet multiplicities to account for migration effects and are treated as uncorrelated among the t̄t subprocesses. Possible shape variations of the final discriminant distributions due to the PDF uncertainty have been estimated by evaluating the PDF replicas provided with the NNPDF set [50]. The impact of the mismodelling of the top quark p_T spectrum in the t̄t simulation [92] was found to be negligible.

The impact of statistical fluctuations in the signal and background prediction due to the limited number of simulated events is accounted for using the Barlow-Beeston approach described in refs. [93, 94].

	pre-fit (post-fit) yields					
Process	$t\bar{t}H$ node	$t\bar{t}+b\bar{b}$ node	$t\bar{t}+2b$ node	$t\bar{t}+b$ node	$t\bar{t}+c\bar{c}$ node	$t\bar{t}+lf$ node
$t\bar{t}+lf$	1249 (962)	727 (572)	1401 (1090)	1035 (823)	2909 (2296)	8463 (6829)
$t\bar{t}+c\bar{c}$	298 (458)	232 (359)	428 (678)	251 (400)	686 (1068)	1022 (1652)
$t\bar{t}+b$	253 (356)	215 (311)	370 (530)	326 (484)	308 (437)	469 (683)
$t\bar{t}+2b$	124 (96)	77 (62)	317 (254)	90 (73)	100 (79)	134 (108)
$t\bar{t}+b\bar{b}$	139 (137)	191 (192)	149 (140)	105 (103)	119 (114)	133 (128)
Single t	96 (96)	117 (109)	167 (162)	93 (96)	231 (232)	304 (307)
V+jets	37 (37)	76 (74)	48 (46)	27 (27)	97 (89)	69 (69)
$t\bar{t}+V$	13 (13)	6 (6)	12 (11)	6 (6)	10 (10)	16 (16)
Diboson	4 (4)	5 (5)	0.9 (0.8)	0.6 (0.7)	2 (2)	4 (4)
Total bkg.	2213 (2158)	1645 (1688)	2892 (2911)	1935 (2012)	4462 (4328)	10614 (9795)
± tot unc.	±508 (±58)	±415 (±53)	±588 (±89)	±402 (±67)	±1051 (±120)	±2359 (±270)
$t\bar{t}H$	27 (21)	9 (7)	16 (12)	7 (5)	9 (7)	16 (13)
± tot unc.	±4 (±3)	±1 (±1)	±2 (±2)	±1 (±1)	±1 (±1)	±2 (±2)
Data	2125	1793	2896	2027	4366	9693

Table 3. Observed and expected event yields per jet-process category (node) in the single-lepton channel with 4 jets and at least 3 b tags, prior to the fit to data (after the fit to data). The quoted uncertainties denote the total statistical and systematic components.

7 Results

The numbers of events selected in the jet-process categories of the single-lepton channel and in the jet-tag categories of the dilepton channel, before and after the fit of the signal strength modifier and the nuisance parameters, are listed in tables 3–6. The final discriminants in some example categories in the single-lepton channel and the three dilepton categories before and after the fit to data are displayed in figures 5–6 and figures 7–8, respectively. All final discriminants in the single-lepton channel before and after the fit to data are displayed in appendices B and C.

The signal strength modifier $\mu = \sigma/\sigma_{SM}$ of the $t\bar{t}H$ production cross section is determined in a simultaneous binned maximum likelihood fit to the data across all analysis categories. The fit procedure takes into account systematic uncertainties that modify the shape and normalisation of the final discriminant distributions, as described in section 6. The best fit values of the nuisance parameters are within 1 standard deviation of the prior uncertainty for more than 95% of the total number of nuisance parameters. The best fit values of the 20 parameters ranked highest in impact are presented in figure 9. As expected, the fit constrains the nuisance parameters related to the conservatively assigned 50% prior uncertainties on the $t\bar{t}+hf$ cross section to 40–60% of the prior. A few other nuisance parameters that are related to jet energy scale and b tagging uncertainties are constrained up to a factor of 50%. These constraints are not due to conservatively assigned prior uncertainties but are attributed to the fact that events are selected according to different, large multiplicities of jets and b-tagged jets, thus increasing the sensitivity of the

– 15 –

	pre-fit (post-fit) yields					
Process	t$\bar{\text{t}}$H node	t$\bar{\text{t}}$+b$\bar{\text{b}}$ node	t$\bar{\text{t}}$+2b node	t$\bar{\text{t}}$+b node	t$\bar{\text{t}}$+c$\bar{\text{c}}$ node	t$\bar{\text{t}}$+lf node
t$\bar{\text{t}}$+lf	785 (570)	647 (467)	830 (604)	683 (525)	1148 (848)	4903 (3697)
t$\bar{\text{t}}$+c$\bar{\text{c}}$	336 (455)	341 (469)	445 (633)	264 (382)	552 (756)	1207 (1726)
t$\bar{\text{t}}$+b	257 (351)	290 (399)	355 (494)	321 (477)	219 (301)	494 (692)
t$\bar{\text{t}}$+2b	136 (104)	128 (99)	324 (253)	89 (73)	85 (65)	184 (143)
t$\bar{\text{t}}$+b$\bar{\text{b}}$	266 (251)	410 (397)	224 (207)	150 (143)	144 (132)	228 (212)
Single t	62 (63)	82 (84)	98 (96)	45 (58)	114 (113)	189 (193)
V+jets	25 (23)	54 (53)	34 (31)	11 (12)	46 (41)	54 (51)
t$\bar{\text{t}}$+V	20 (20)	14 (13)	17 (16)	7 (7)	11 (10)	25 (24)
Diboson	1 (1)	3 (3)	0.4 (0.4)	— (—)	0.6 (0.4)	3 (3)
Total bkg.	1889 (1838)	1969 (1985)	2326 (2332)	1570 (1676)	2320 (2268)	7287 (6742)
± tot unc.	±459 (±57)	±485 (±70)	±489 (±71)	±334 (±47)	±597 (±79)	±1655 (±219)
t$\bar{\text{t}}$H	53 (41)	21 (17)	20 (15)	8 (6)	11 (8)	28 (22)
± tot unc.	±7 (±6)	±3 (±3)	±2 (±2)	±1 (±1)	±1 (±1)	±3 (±3)
Data	1848	2040	2299	1690	2302	6918

Table 4. Observed and expected event yields per jet-process category (node) in the single-lepton channel with 5 jets and at least 3 b tags, prior to the fit to data (after the fit to data). The quoted uncertainties denote the total statistical and systematic uncertainty.

	pre-fit (post-fit) yields					
Process	t$\bar{\text{t}}$H node	t$\bar{\text{t}}$+b$\bar{\text{b}}$ node	t$\bar{\text{t}}$+2b node	t$\bar{\text{t}}$+b node	t$\bar{\text{t}}$+c$\bar{\text{c}}$ node	t$\bar{\text{t}}$+lf node
t$\bar{\text{t}}$+lf	1982 (1381)	1280 (897)	852 (595)	916 (661)	243 (172)	50 (36)
t$\bar{\text{t}}$+c$\bar{\text{c}}$	1150 (1415)	998 (1230)	636 (805)	444 (567)	115 (147)	16 (19)
t$\bar{\text{t}}$+b	549 (705)	575 (746)	314 (409)	253 (338)	28 (35)	4 (5)
t$\bar{\text{t}}$+2b	306 (233)	282 (215)	372 (293)	78 (62)	10 (8)	1 (0.8)
t$\bar{\text{t}}$+b$\bar{\text{b}}$	834 (769)	1156 (1082)	299 (266)	145 (129)	17 (15)	3 (2)
Single t	110 (116)	146 (145)	92 (82)	53 (53)	4 (4)	3 (3)
V+jets	38 (37)	78 (76)	34 (30)	10 (9)	7 (6)	0.6 (0.6)
t$\bar{\text{t}}$+V	80 (75)	58 (54)	31 (28)	11 (11)	4 (4)	0.4 (0.4)
Diboson	0.9 (0.9)	0.5 (0.5)	0.4 (0.4)	0.4 (0.4)	— (—)	— (—)
Total bkg.	5049 (4733)	4575 (4447)	2629 (2509)	1911 (1831)	429 (392)	77 (67)
± tot unc.	±1216 (±186)	±1156 (±142)	±603 (±80)	±422 (±65)	±107 (±14)	±18 (±3)
t$\bar{\text{t}}$H	142 (108)	53 (40)	24 (18)	10 (7)	2.1 (1.5)	0.30 (0.23)
± tot unc.	±19 (±15)	±8 (±6)	±3 (±2)	±1 (±1)	±0.2 (±0.2)	±0.03 (±0.03)
Data	4822	4400	2484	1852	422	76

Table 5. Observed and expected event yields per jet-process category (node) in the single-lepton channel with at least 6 jets and at least 3 b tags, prior to the fit to data (after the fit to data). The quoted uncertainties denote the total statistical and systematic uncertainty.
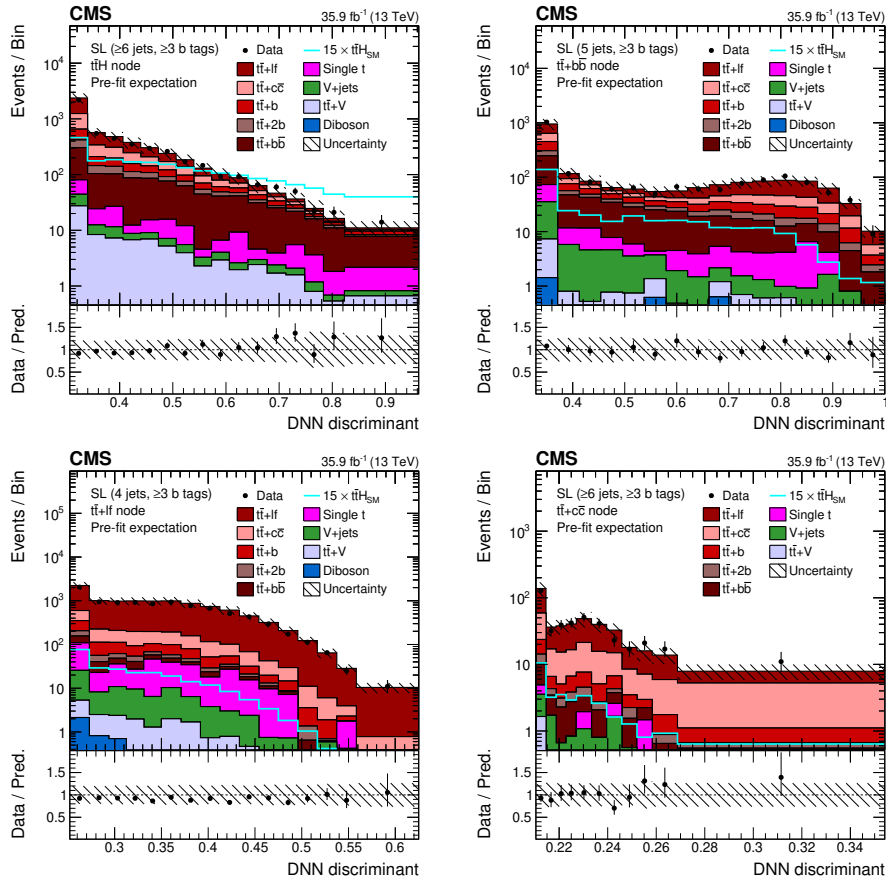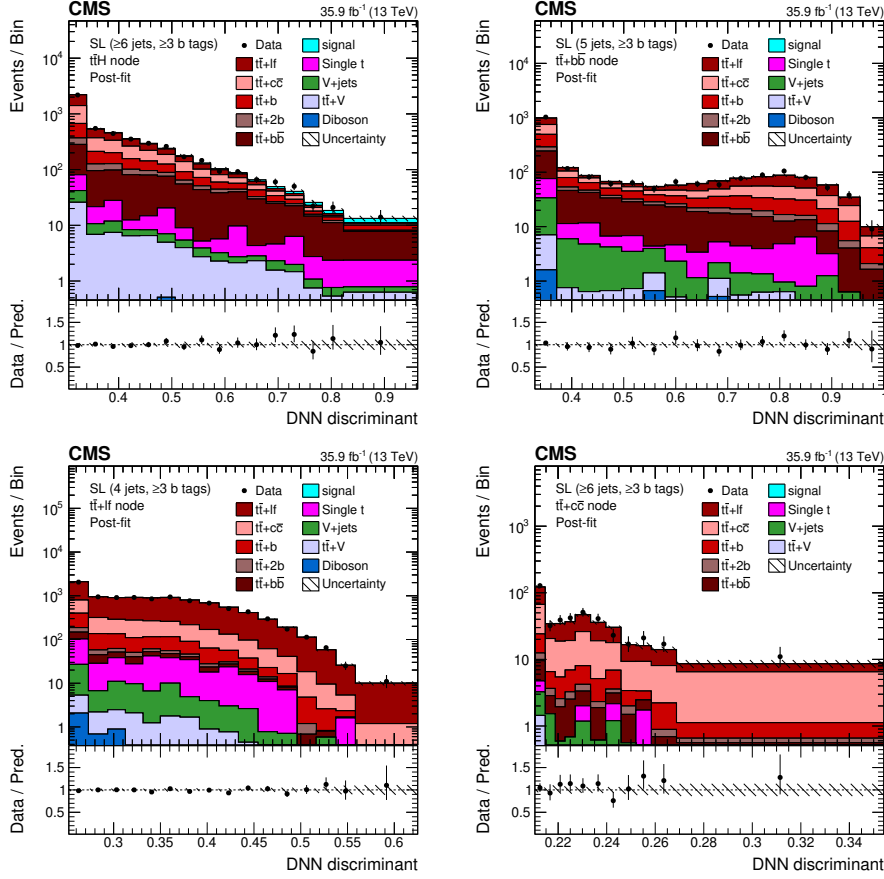
Figure 5. Final discriminant shapes in the single-lepton (SL) channel before the fit to data: DNN discriminant in the jet-process categories with ≥6 jets-t$\bar{\text{t}}$H (upper left); 5 jets-t$\bar{\text{t}}$+b$\bar{\text{b}}$ (upper right); 4 jets-t$\bar{\text{t}}$+lf (lower left); and ≥6 jets-t$\bar{\text{t}}$+c$\bar{\text{c}}$ (lower right). The expected background contributions (filled histograms) are stacked, and the expected signal distribution (line), which includes H → b$\bar{\text{b}}$ and all other Higgs boson decay modes, is superimposed. Each contribution is normalised to an integrated luminosity of 35.9 fb^{-1}, and the signal distribution is additionally scaled by a factor of 15 for better visibility. The hatched uncertainty bands include the total uncertainty of the fit model. The distributions observed in data (markers) are overlayed. The first and the last bins include underflow and overflow events, respectively. The lower plots show the ratio of the data to the background prediction.
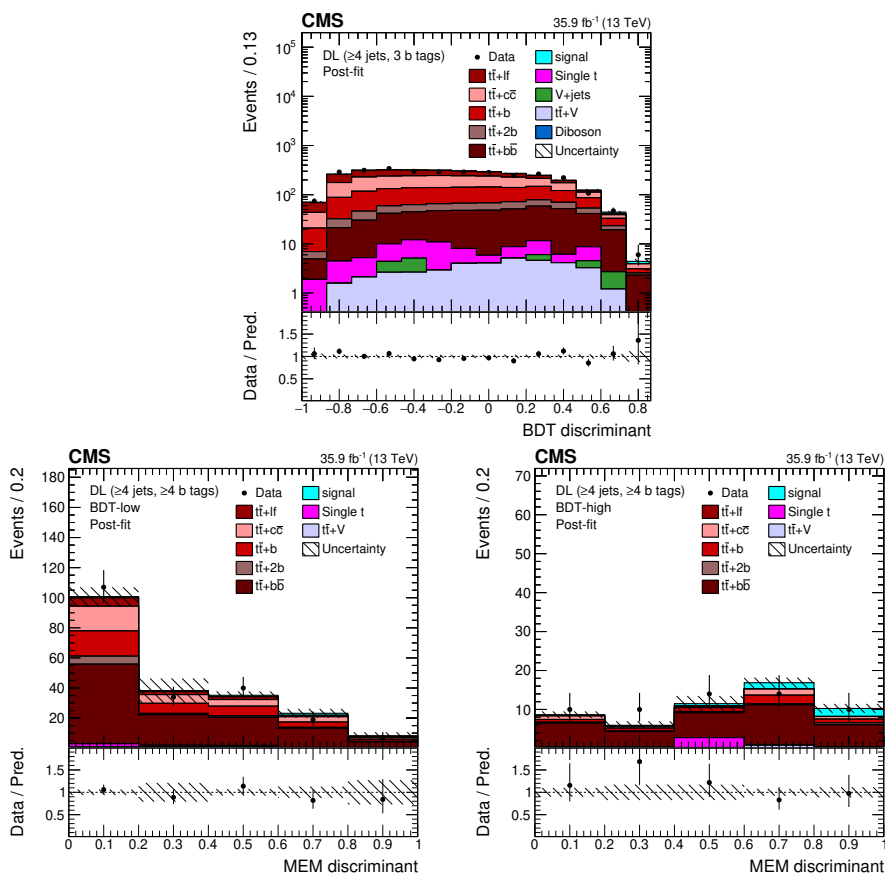
– 17 –
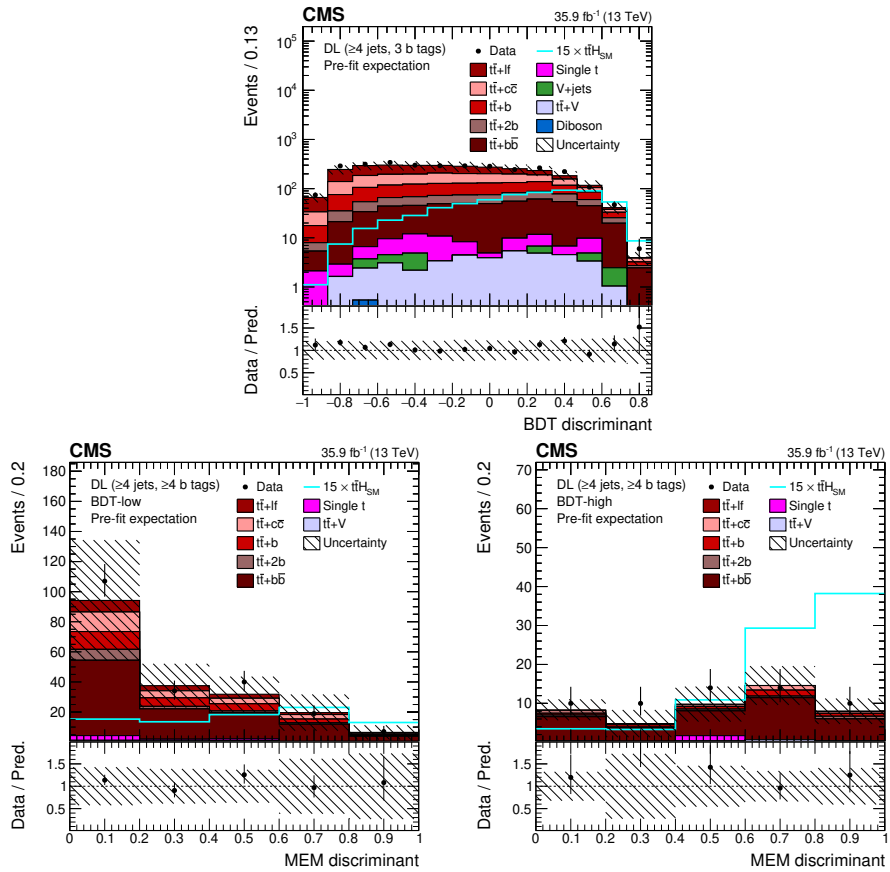
Figure 6. Final discriminant shapes in the dilepton (DL) channel before the fit to data: BDT discriminant in the analysis category with (≥ 4 jets, 3 b tags) (upper row) and MEM discriminant in the analysis categories with (≥ 4 jets, ≥ 4 b tags) (lower row) with low (left) and high (right) BDT output. The expected background contributions (filled histograms) are stacked, and the expected signal distribution (line), which includes $H \rightarrow b\bar{b}$ and all other Higgs boson decay modes, is superimposed. Each contribution is normalised to an integrated luminosity of $35.9\,\mathrm{fb}^{-1}$, and the signal distribution is additionally scaled by a factor of 15 for better visibility. The hatched uncertainty bands include the total uncertainty of the fit model. The distributions observed in data (markers) are overlayed. The first and the last bins include underflow and overflow events, respectively. The lower plots show the ratio of the data to the background prediction.

| | pre-fit (post-fit) yields | | | |
Process	$\geq$ 4 jets, 3 b tags	$\geq$ 4 jets, $\geq$ 4 b tags		
		BDT-low		BDT-high
$t\bar{t}$+lf	845 (637)	16 (11)		0.7 (0.5)
$t\bar{t}$+c$\bar{c}$	712 (966)	25 (31)		3 (4)
$t\bar{t}$+b	546 (747)	26 (35)		4 (6)
$t\bar{t}$+2b	252 (196)	11 (8)		2 (1)
$t\bar{t}$+b$\bar{b}$	439 (415)	103 (109)		33 (32)
Single t	47 (51)	5 (3)		1 (2)
V+jets	10 (8)	— (—)		— (—)
$t\bar{t}$+V	40 (38)	4 (4)		2 (2)
Diboson	0.9 (0.7)	— (—)		— (—)
Total bkg.	2893 (3058)	190 (201)		46 (48)
$\pm$ tot unc.	$\pm$705 ($\pm$98)	$\pm$67 ($\pm$10)		$\pm$17 ($\pm$3)
$t\bar{t}$H	42 (32)	6 (5)		6 (5)
$\pm$ tot unc.	$\pm$6 ($\pm$5)	$\pm$1 ($\pm$1)		$\pm$1 ($\pm$1)
Data	3077	207		58

Table 6. Observed and expected event yields per jet-tag category in the dilepton channel, prior to the fit to data (after the fit to data). The quoted uncertainties denote the total statistical and systematic uncertainty.

analysis to changes of the jet energy scale and b tagging efficiency, e.g. by their effect on the event yield per analysis category. Furthermore, the impact on μ of the most relevant sources of uncertainty is shown in figure 9, which is computed as the difference of the nominal best fit value of μ and the best fit value obtained when fixing the nuisance parameter under scrutiny to its best fit value plus/minus its post-fit uncertainty. In particular, the 20 parameters with the highest impact are shown, excluding nuisance parameters describing the statistical uncertainties due to the size of the simulated samples. The nuisance parameters with the highest impact are related to the uncertainty in the $t\bar{t}$+hf and signal cross sections, as well as in the b tagging scale factors.

The obtained best fit value of μ is $0.72\pm0.24\,(\text{stat})\pm0.38\,(\text{syst})$ with a total uncertainty of ±0.45. This corresponds to an observed (expected) significance of 1.6 (2.2) standard deviations above the background-only hypothesis. The observed and predicted event yields in all the bins of the final discriminants, ordered by the pre-fit expected signal-to-background ratio (S/B) are shown in figure 10 (left). The best fit values in each analysis channel separately and in the combination are listed in table 7 and displayed in figure 10 (right).

The contributions of the statistical and various systematic uncertainties to the uncertainty in μ are listed in table 8. The statistical uncertainty is evaluated by fixing all nuisance parameters to their post-fit values. The impact of the systematic uncertainties is evaluated

Figure 7. Final discriminant shapes in the single-lepton (SL) channel after the fit to data: DNN discriminant in the jet-process categories with ≥6 jets-t̄tH (upper left); 5 jets-t̄t+bb̄ (upper right); 4 jets-t̄t+lf (lower left); and ≥6 jets-t̄t+cc̄ (lower right). The hatched uncertainty bands include the total uncertainty after the fit to data. The distributions observed in data (markers) are overlayed. The first and the last bins include underflow and overflow events, respectively. The lower plots show the ratio of the data to the post-fit background plus signal distribution.

by repeating the fit fixing only the nuisance parameters related to the uncertainty under scrutiny to their post-fit values and subtracting the obtained uncertainty in quadrature from the total uncertainty of the fit where no parameters are fixed. The total uncertainty of the full fit (0.45) is different from the quadratic sum of the listed contributions because of correlations between the nuisance parameters.

The total uncertainty of 0.45 is dominated by contributions from systematic effects, while the statistical component is 0.24. The largest contributions originate from the theo-

Figure 8. Final discriminant shapes in the dilepton (DL) channel after the fit to data: BDT discriminant in the analysis category with $(\geq 4\,\text{jets}, 3\,\text{b tags})$ (upper row) and MEM discriminant in the analysis categories with $(\geq 4\,\text{jets}, \geq 4\,\text{b tags})$ (lower row) with low (left) and high (right) BDT output. The hatched uncertainty bands include the total uncertainty after the fit to data. The distributions observed in data (markers) are overlayed. The first and the last bins include underflow and overflow events, respectively. The lower plots show the ratio of the data to the post-fit background plus signal distribution.
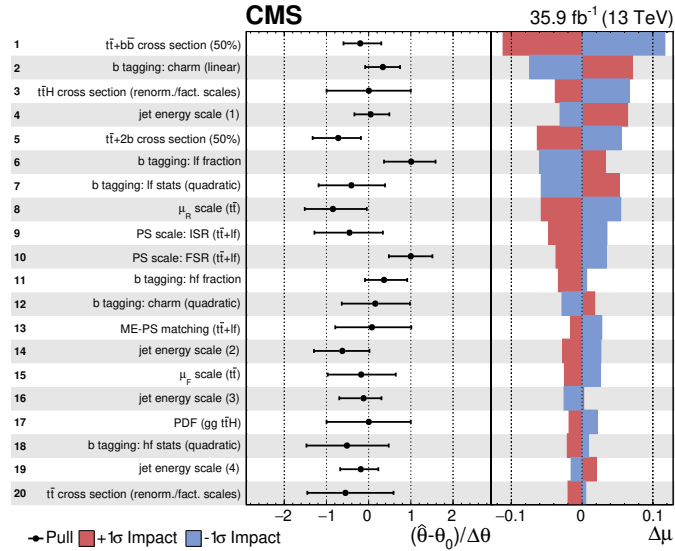
Figure 9. Post-fit pull and impact on the signal strength μ of the nuisance parameters included in the fit, ordered by their impact. Only the 20 highest ranked parameters are shown, not including nuisance parameters describing the uncertainty due to the size of the simulated samples. The four highest-ranked nuisance parameters related to the jet energy scale uncertainty sources are shown as indicated in parentheses. The pulls of the nuisance parameters (black markers) are computed relative to their pre-fit values θ_0 and uncertainties $\Delta\theta$. The impact $\Delta\mu$ is computed as the difference of the nominal best fit value of μ and the best fit value obtained when fixing the nuisance parameter under scrutiny to its best fit value $\hat{\theta}$ plus/minus its post-fit uncertainty (coloured areas).

| Channel | 95% CL upper limit | | Best-fit μ |
	observed	expected	$\pm$tot ($\pm$stat $\pm$ syst)
Single-lepton	1.75	$1.03^{+0.44}_{-0.29}$	$0.84^{+0.52}_{-0.50}\left(^{+0.27}_{-0.26}\ ^{+0.44}_{-0.43}\right)$
Dilepton	2.34	$2.48^{+1.17}_{-0.76}$	$-0.24^{+1.21}_{-1.12}\left(^{+0.63}_{-0.60}\ ^{+1.04}_{-0.95}\right)$
Combined	1.51	$0.92^{+0.39}_{-0.26}$	$0.72^{+0.45}_{-0.45}\left(^{+0.24}_{-0.24}\ ^{+0.38}_{-0.38}\right)$

Table 7. Best fit value of the signal strength modifier μ and the observed and median expected 95% CL upper limits in the single-lepton and the dilepton channels as well as the combined results. The one standard deviation confidence intervals of the expected limit and the best fit value are also quoted, split into the statistical and systematic components in the latter case.
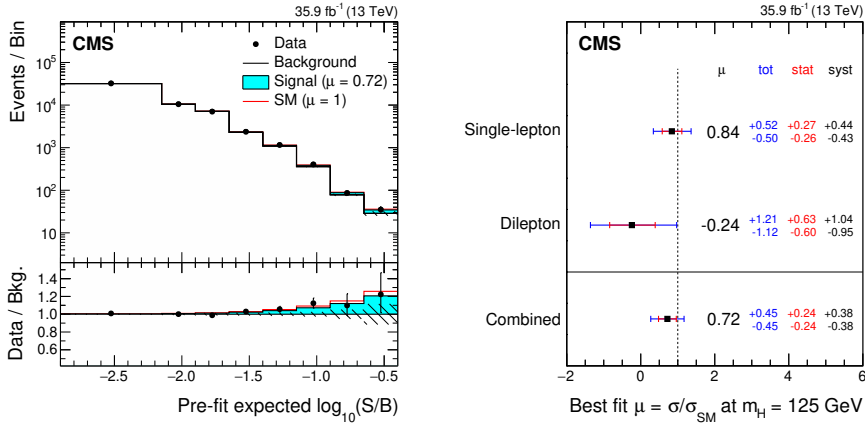
Figure 10. Bins of the final discriminants as used in the fit (left), reordered by the pre-fit expected signal-to-background ratio (S/B). Each of the shown bins includes multiple bins of the final discriminants with similar S/B. The fitted signal (cyan) is compared to the expectation for the SM Higgs boson $\mu = 1$ (red). Best fit values of the signal strength modifiers μ (right) with their 68% expected confidence intervals (outer error bar), also split into their statistical (inner error bar) and systematic components.

retical uncertainties amounting to $+0.28/-0.29$, where the $t\bar{t}+hf$ modelling uncertainties have a major contribution. Experimental uncertainties amount to $+0.15/-0.16$, dominated by the b tagging related uncertainties. Systematic uncertainties due to the size of the various simulated samples used to model the background and signal templates are at the same order and amount to $+0.14/-0.15$.

An upper limit on μ under the background-only hypothesis is also determined, using a modified frequentist CL_S procedure [95, 96] with the asymptotic method [97]. When combining all categories and channels, an observed (expected) upper limit at 95% CL on μ of 1.5 (0.9) is obtained. The observed and expected upper limits in each channel and in the combination are listed in table 7 and visualised in figure 11.

In addition, the statistical analysis has been performed using the jet-process categorisation and DNN output in both channels and their combination, as well as using the jet-tag categorisation and the BDT or MEM in both channels. The results obtained in each channel and the combination are compatible within 1.7 standard deviations or better, evaluated using a jackknife procedure [98]. This serves as an important cross check and validation of the complex analysis methods.

8 Summary

A search for the associated production of a Higgs boson and a top quark-antiquark pair ($t\bar{t}H$) is performed using pp collision data recorded with the CMS detector at a centre-of-mass energy of 13 TeV in 2016, corresponding to an integrated luminosity of $35.9\,\text{fb}^{-1}$. Candidate events are selected in final states compatible with the Higgs boson decaying into

Uncertainty source	$\pm\Delta\mu$ (observed)	$\pm\Delta\mu$ (expected)
Total experimental	$+0.15/-0.16$	$+0.19/-0.17$
b tagging	$+0.11/-0.14$	$+0.12/-0.11$
jet energy scale and resolution	$+0.06/-0.07$	$+0.13/-0.11$
Total theory	$+0.28/-0.29$	$+0.32/-0.29$
$t\bar{t}$+hf cross section and parton shower	$+0.24/-0.28$	$+0.28/-0.28$
Size of the simulated samples	$+0.14/-0.15$	$+0.16/-0.16$
Total systematic	$+0.38/-0.38$	$+0.45/-0.42$
Statistical	$+0.24/-0.24$	$+0.27/-0.27$
Total	$+0.45/-0.45$	$+0.53/-0.49$

Table 8. Contributions of different sources of uncertainties to the result for the fit to the data (observed) and to the expectation from simulation (expected). The quoted uncertainties $\Delta\mu$ in μ are obtained by fixing the listed sources of uncertainties to their post-fit values in the fit and subtracting the obtained result in quadrature from the result of the full fit. The statistical uncertainty is evaluated by fixing all nuisance parameters to their post-fit values. The quadratic sum of the contributions is different from the total uncertainty because of correlations between the nuisance parameters.
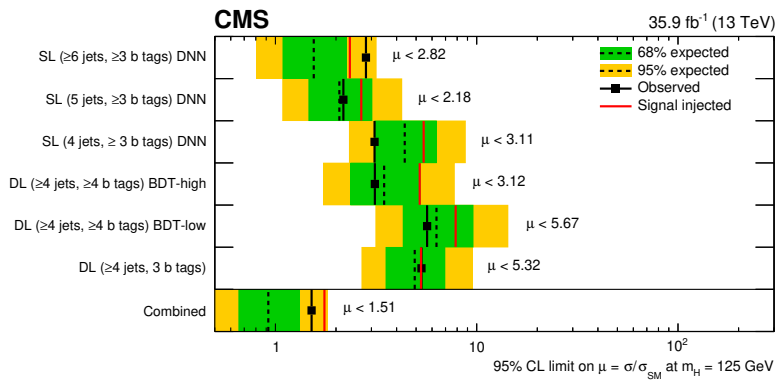
Figure 11. Median expected (dashed line) and observed (markers) 95% CL upper limits on μ. The inner (green) band and the outer (yellow) band indicate the regions containing 68 and 95%, respectively, of the distribution of limits expected under the background-only hypothesis. Also shown is the limit that is expected in case a SM $t\bar{t}$H signal ($\mu = 1$) is present in the data (solid red line).

– 24 –

a b quark-antiquark pair and the single-lepton and dilepton decay channels of the $t\bar{t}$ system. Selected events are split into mutually exclusive categories according to their $t\bar{t}$ decay channel and jet content. In each category a powerful discriminant is constructed to separate the $t\bar{t}$H signal from the dominant $t\bar{t}$+jets background, based on several multivariate analysis techniques (boosted decision trees, matrix element method, and deep neural networks). An observed (expected) upper limit on the $t\bar{t}$H production cross section μ relative to the SM expectations of $1.5\,(0.9)$ at 95% confidence level is obtained. The best fit value of μ is $0.72 \pm 0.24\,(\mathrm{stat}) \pm 0.38\,(\mathrm{syst})$. These results correspond to an observed (expected) significance of $1.6\,(2.2)$ standard deviations above the background-only hypothesis.

Acknowledgments

– 25 –

A BDT and DNN input variables and configuration

All input variables used in the DNNs and BDTs are listed in tables 9–11.

Variable	Definition	SL (4 jets, $\geq$ 3 b tags)	SL (5 jets, $\geq$ 3 b tags)	SL ($\geq$ 6 jets, $\geq$ 3 b tags)	DL ($\geq$ 4 jets, 3 b tags)	DL ($\geq$ 4 jets, $\geq$ 4 b tags)
p_T(jet 1)	p_T of the highest-p_T jet	+	+	-	-	-
η(jet 1)	η of the highest-p_T jet	-	+	+	-	-
d(jet 1)	b tagging discriminant of the highest-p_T jet	+	+	+	-	-
p_T(jet 2)	p_T of the second highest-p_T jet	-	+	-	-	-
η(jet 2)	η of the second highest-p_T jet	+	+	+	-	-
d(jet 2)	b tagging discriminant of the second highest-p_T jet	+	+	+	-	-
p_T(jet 3)	p_T of the third highest-p_T jet	-	+	-	-	-
η(jet 3)	η of the third highest-p_T jet	+	+	+	-	-
d(jet 3)	b tagging discriminant of the third highest-p_T jet	+	+	+	-	-
p_T(jet 4)	p_T of the fourth highest-p_T jet	+	+	-	-	-
η(jet 4)	η of the fourth highest-p_T jet	+	+	+	-	-
d(jet 4)	b tagging discriminant of the fourth highest-p_T jet	+	-	+	-	-
p_T(lep 1)	p_T of the highest-p_T lepton	-	+	+	-	-
η(lep 1)	η of the highest-p_T lepton	+	-	+	-	-
d_j^{avg}	average b tagging discriminant value of all jets	+	+	+	-	-
d_b^{avg}	average b tagging discriminant value of b-tagged jets	+	+	+	+	+
d_{non-b}^{avg}	average b tagging discriminant value of non-b-tagged jets	-	-	-	+	+
$\frac{1}{N_b}\sum_b^{N_b}\left(d - d_b^{avg}\right)^2$	squared difference between the b tagging discriminant value of a b-tagged jet and the average b tagging discriminant values of all b-tagged jets, summed over all b-tagged jets	+	+	+	-	-
d_j^{max}	maximal b tagging discriminant value of all jets	+	+	+	-	-
d_b^{max}	maximal b tagging discriminant value of b-tagged jets	+	+	+	-	-
d_j^{min}	minimal b tagging discriminant value of all jets	+	+	+	-	-
d_j^{min}	minimal b tagging discriminant value of b-tagged jets	+	+	+	-	-
d_2	second highest b tagging discriminant value of all jets	+	+	+	-	-

Table 9. Input variables used in the DNNs or BDTs in the different categories of the single-lepton and dilepton channels. Variables used in a specific multivariate method and analysis category are denoted by a "+" and unused variables by a "−". (Continued in tables 10 and 11.)

– 27 –

Variable	Definition	SL (4 jets, ≥ 3 b tags)	SL (5 jets, ≥ 3 b tags)	SL (≥ 6 jets, ≥ 3 b tags)	DL (≥ 4 jets, 3 b tags)	DL (≥ 4 jets, ≥ 4 b tags)
$N_\text{b}(\text{tight})$	number of b-tagged jets at a working point with a 0.1% probability of tagging gluon and light-flavour jets	+	+	+	-	-
BLR	likelihood ratio discriminating between 4 b quark jets and 2 b quark jets events	+	+	+	-	-
$\text{BLR}^{\text{trans}}$	transformed BLR defined as $\ln[\text{BLR}/(1.0 - \text{BLR})]$	+	+	+	-	-
$\Delta R_{\text{j,j}}^{\min}$	ΔR between the two closest jets	+	+	+	-	-
$\Delta R_{\text{b,b}}^{\min}$	ΔR between the two closest b-tagged jets	+	+	+	-	-
$\Delta R_{\text{j,j}}^{\max}$	ΔR between the two jets furthest apart	-	+	-	-	-
$\Delta R_{\text{b,b}}^{\max}$	ΔR between the two b-tagged jets furthest apart	-	-	+	-	-
$\Delta \eta_{\text{j,j}}^{\max}$	$\Delta \eta$ between the two jets furthest apart in η	-	-	-	-	+
$\Delta \eta_{\text{b,b}}^{\max}$	$\Delta \eta$ between the two b-tagged jets furthest apart in η	-	-	-	+	+
$\Delta \eta_{\text{b,b}}^{\text{avg}}$	average $\Delta \eta$ between b-tagged jets	-	-	+	-	-
$\Delta R_{\text{b,b}}^{\text{avg}}$	average ΔR between b-tagged jets	-	+	+	-	-
$\Delta R_{\text{j,b}}^{\text{avg}}$	average ΔR between jets of which at least one is b-tagged	-	-	-	+	-
$\Delta R_{\text{lep,j}}^{\min\Delta R}$	ΔR between lepton and closest jet	+	+	-	-	-
$\Delta R_{\text{lep,b}}^{\min\Delta R}$	ΔR between lepton and closest b-tagged jet	-	+	+	-	-
$m_{\text{lep,b}}^{\min\Delta R}$	mass of lepton and closest b-tagged jet	+	+	+	-	-
$m_{\text{b,b}}^{\min\Delta R}$	mass of closest b-tagged jets	+	+	+	-	+
$m_{\text{j,b}}^{\min\Delta R}$	mass of closest jets of which at least one is b-tagged	-	-	-	+	-
$m_{\text{b,b}}^{\max\text{ mass}}$	maximal mass of pairs of b-tagged jets	-	-	-	+	+
$p_{\text{T b,b}}^{\min\Delta R}$	combined p_T of closest b-tagged jets	-	-	-	+	-
$p_{\text{T j,b}}^{\min\Delta R}$	combined p_T of closest jets of which at least one is b-tagged	-	-	-	-	+
$m_{\text{j}}^{\text{avg}}$	average mass of all jets	+	+	+	-	-
$(m^2)_{\text{b}}^{\text{avg}}$	average squared mass of all b-tagged jets	+	-	+	-	-
$m_{\text{b,b}}^{\text{closest to 125}}$	mass of pair of b-tagged jets closest to $125\,\text{GeV}$	-	+	+	-	-
$N^{\text{j,b}}$	number of pairs of jets (with at least one b-tagged jet) with an invariant mass within 110–$140\,\text{GeV}$	-	-	-	+	+
MEM	matrix element method discriminant	+	+	+	-	-

Table 10. Continued from table 9 and continued in table 11.

Variable	Definition	SL (4 jets, $\geq$ 3 b tags)	SL (5 jets, $\geq$ 3 b tags)	SL ($\geq$ 6 jets, $\geq$ 3 b tags)	DL ($\geq$ 4 jets, 3 b tags)	DL ($\geq$ 4 jets, $\geq$ 4 b tags)
H_T^j	scalar sum of jet p_T	-	+	-	+	-
H_T^b	scalar sum of b-tagged jet p_T	+	+	+	-	-
A^j	$\frac{3}{2}\lambda_3$ where λ_i are the eigenvalues of the momentum tensor built with jets [99]	-	+	+	-	-
A^b	$\frac{3}{2}\lambda_3$ where λ_i are the eigenvalues of the momentum tensor built with b-tagged jets [99]	+	+	+	-	-
C^j	H_T^j divided by the sum of the energies of all jets	-	-	+	-	-
C^b	H_T^b divided by the sum of the energies of all b-tagged jets	-	-	+	-	+
S^j	$\frac{3}{2}(\lambda_2 + \lambda_3)$ where λ_i are the eigenvalues of the momentum tensor built with jets [99]	+	+	+	-	-
S^b	$\frac{3}{2}(\lambda_2 + \lambda_3)$ where λ_i are the eigenvalues of the momentum tensor built with b-tagged jets [99]	-	+	+	-	-
S_T^j	$\frac{2\lambda_2}{\lambda_2+\lambda_1}$ where λ_i are the eigenvalues of the momentum tensor built with jets [99]	+	+	+	-	-
S_T^b	$\frac{2\lambda_2}{\lambda_2+\lambda_1}$ where λ_i are the eigenvalues of the momentum tensor built with b-tagged jets [99]	+	+	+	-	-
I^b	a measure of how spherical or linear in $r - \phi$ space b-tagged jets are in the event	-	-	-	+	-
H_2	second Fox-Wolfram moment [100]	-	+	-	-	-
H_3	third Fox-Wolfram moment [100]	+	+	-	-	-
H_3^b	third Fox-Wolfram moment calculated with b-tagged jets [100]	-	-	-	-	+
R_3	ratio of Fox-Wolfram moments H_3/H_0 [100]	-	-	-	+	-
H_4	fourth Fox-Wolfram moment [100]	+	-	+	-	-

Table 11. Continued from table 10.

Category	N_{trees}	shrinkage	bagging fraction	N_{cuts}	depth
($\geq 4\,$jets, $3\,$b tags)	955	0.022	0.42	30	2
($\geq 4\,$jets, $\geq 4\,$b tags)	638	0.006	0.41	42	2

Table 12. Configuration of the BDTs used in the dilepton channel.

The BDTs employed in the dilepton channel were trained using the stochastic gradient boost method [36, 78], available as part of the TMVA package [38]. The number of trees (N_{trees}), the learning rate (shrinkage), the fraction of events used for the training of an individual tree (bagging fraction), the granularity of the cuts at each node splitting (N_{cuts}), and the number of node splittings per tree (depth) are listed in table 12.

The DNNs used in the single-lepton channel comprise two layers with 100 nodes each in each of the two network stages. Overtraining is suppressed by random node dropout with a probability of 30% and an L2 weight normalisation factor of 10^{-5}. All networks are optimised using the ADAM optimiser with a learning rate of 10^{-4}, and the ELU activation function is used to add non-linearity to the response of the network [77].

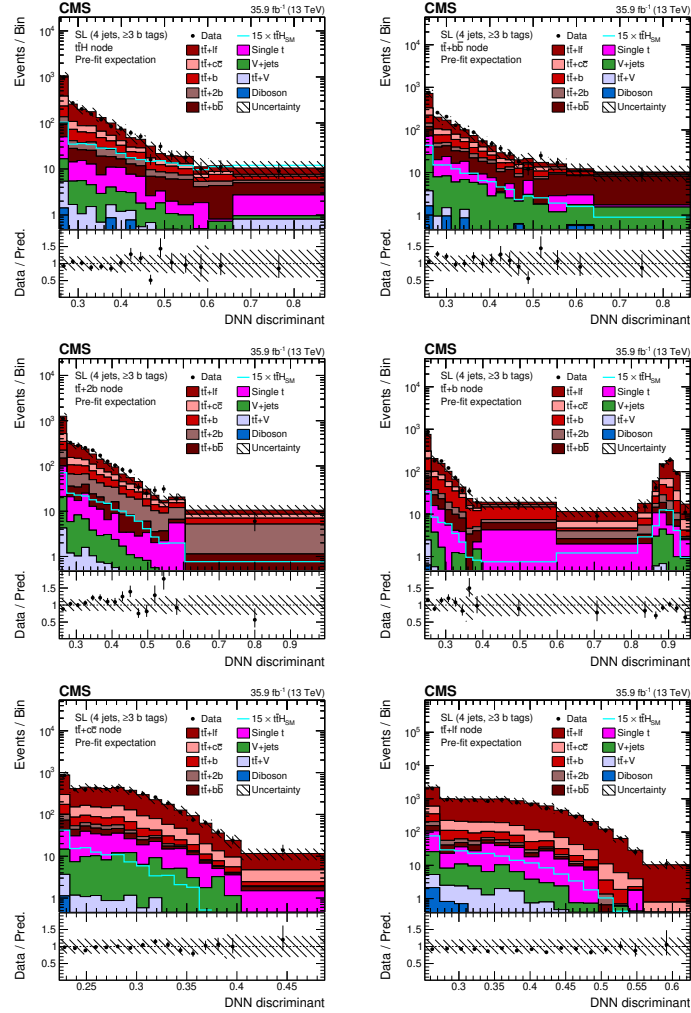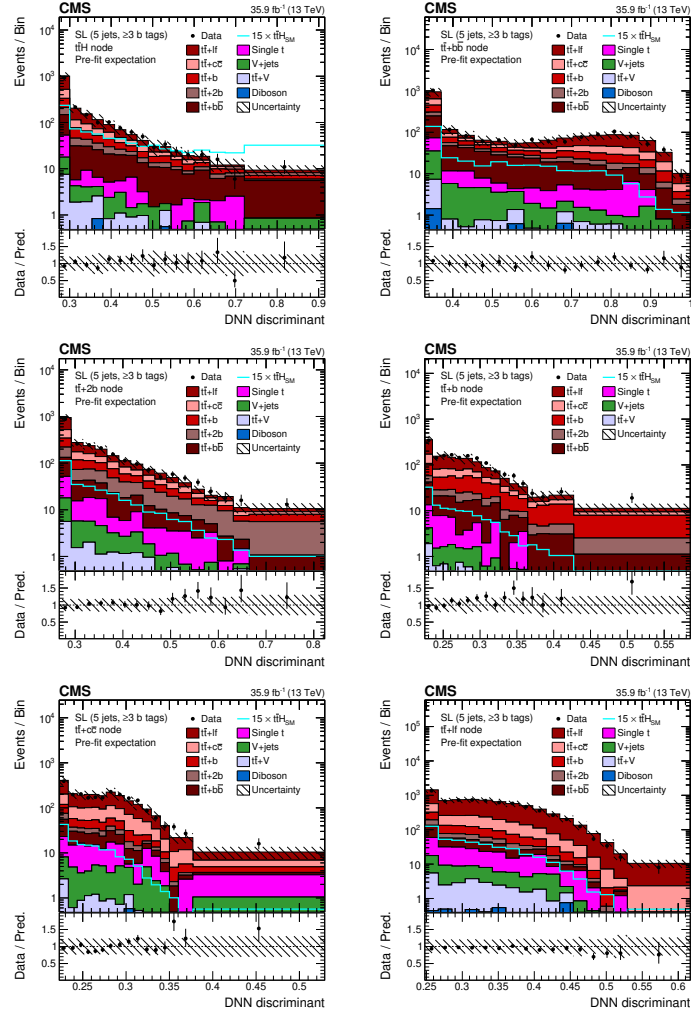## B Pre-fit discriminant shapes (single-lepton channel)

Figure 12. Final discriminant (DNN) shapes in the single-lepton (SL) channel before the fit to data, in the jet-process categories with (4 jets, ≥ 3 b tags) and (from upper left to lower right) t$\bar{\text{t}}$H, t$\bar{\text{t}}$+b$\bar{\text{b}}$, t$\bar{\text{t}}$+2b, t$\bar{\text{t}}$+b, t$\bar{\text{t}}$+c$\bar{\text{c}}$, and t$\bar{\text{t}}$+lf. The expected background contributions (filled histograms) are stacked, and the expected signal distribution (line), which includes H → b$\bar{\text{b}}$ and all other Higgs boson decay modes, is superimposed. Each contribution is normalised to an integrated luminosity of 35.9 fb^{-1}, and the signal distribution is additionally scaled by a factor of 15 for better visibility. The hatched uncertainty bands include the total uncertainty of the fit model. The first and the last bins include underflow and overflow events, respectively. The lower plots show the ratio of the data to the background prediction.
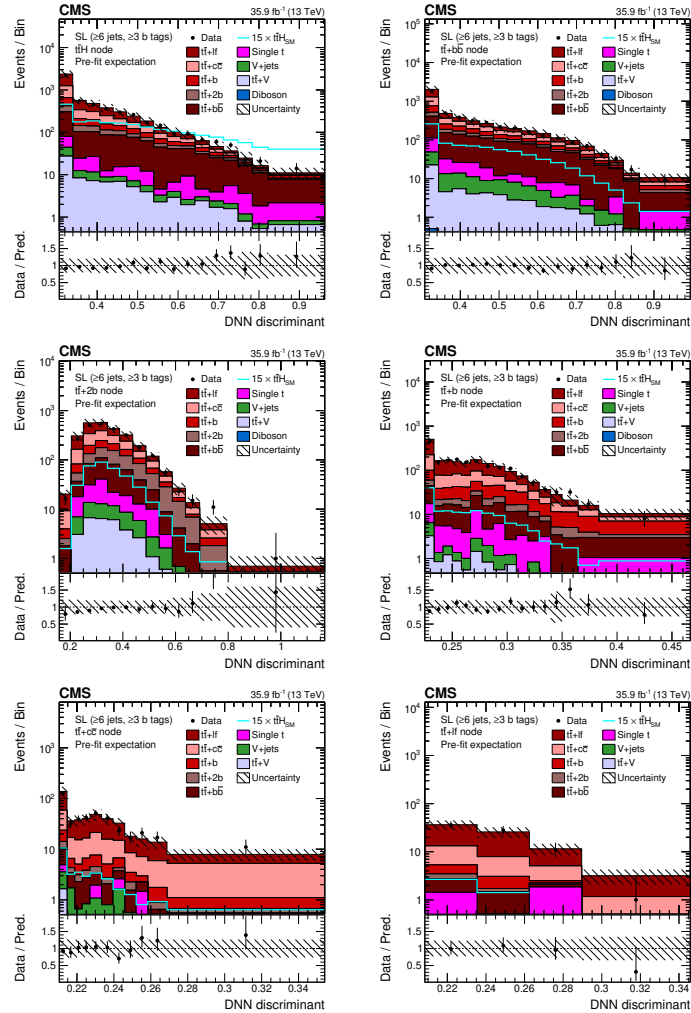
Figure 13. Final discriminant (DNN) shapes in the single-lepton (SL) channel before the fit to data, in the jet-process categories with (5 jets, ≥ 3 b tags) and (from upper left to lower right) $t\bar{t}H$, $t\bar{t}+b\bar{b}$, $t\bar{t}+2b$, $t\bar{t}+b$, $t\bar{t}+c\bar{c}$, and $t\bar{t}+lf$. The expected background contributions (filled histograms) are stacked, and the expected signal distribution (line), which includes $H \to b\bar{b}$ and all other Higgs boson decay modes, is superimposed. Each contribution is normalised to an integrated luminosity of $35.9\,\mathrm{fb}^{-1}$, and the signal distribution is additionally scaled by a factor of 15 for better visibility. The hatched uncertainty bands include the total uncertainty of the fit model. The first and the last bins include underflow and overflow events, respectively. The lower plots show the ratio of the data to the background prediction.
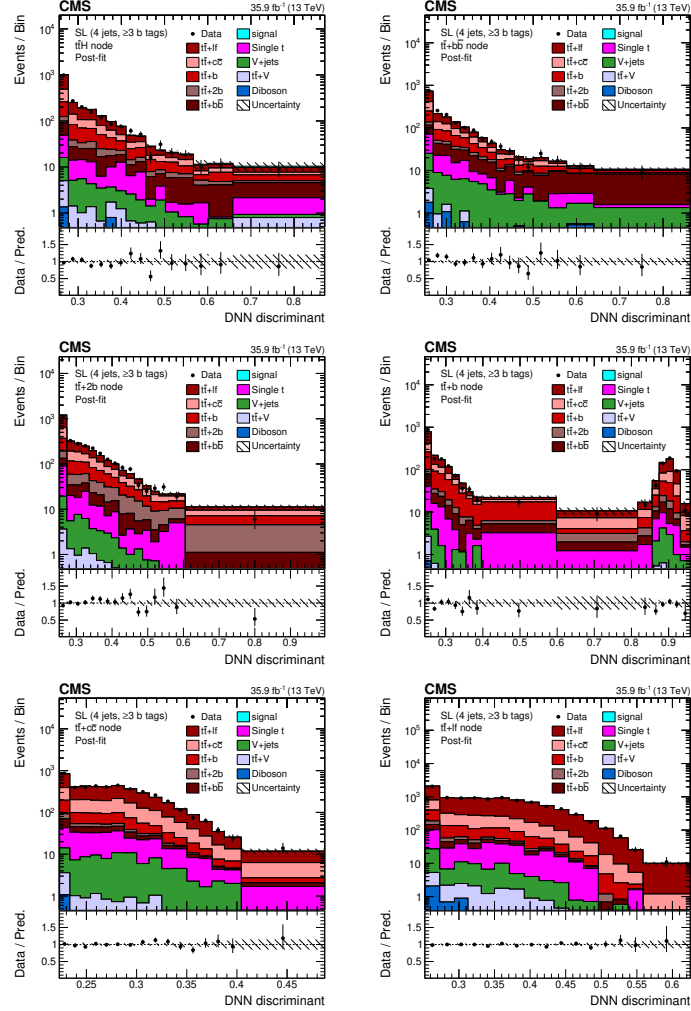
Figure 14. Final discriminant (DNN) shapes in the single-lepton (SL) channel before the fit to data, in the jet-process categories with (≥ 6 jets, ≥ 3 b tags) and (from upper left to lower right) $t\bar{t}H$, $t\bar{t}+b\bar{b}$, $t\bar{t}+2b$, $t\bar{t}+b$, $t\bar{t}+c\bar{c}$, and $t\bar{t}+lf$. The expected background contributions (filled histograms) are stacked, and the expected signal distribution (line), which includes $H \rightarrow b\bar{b}$ and all other Higgs boson decay modes, is superimposed. Each contribution is normalised to an integrated luminosity of $35.9\,\text{fb}^{-1}$, and the signal distribution is additionally scaled by a factor of 15 for better visibility. The hatched uncertainty bands include the total uncertainty of the fit model. The first and the last bins include underflow and overflow events, respectively. The lower plots show the ratio of the data to the background prediction.

– 33 –

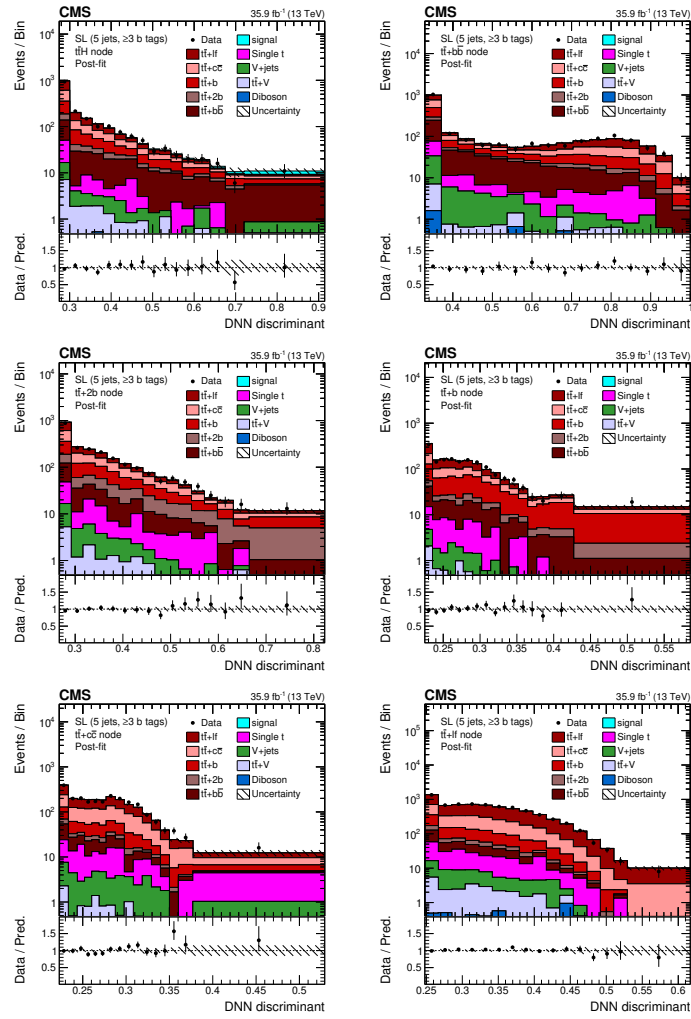**Figure 15**. Final discriminant (DNN) shapes in the single-lepton (SL) channel after the fit to data, in the jet-process categories with $(4\,\text{jets}, \geq 3\,\text{b tags})$ and (from upper left to lower right) $t\bar{t}H$, $t\bar{t}+b\bar{b}$, $t\bar{t}+2b$, $t\bar{t}+b$, $t\bar{t}+c\bar{c}$, and $t\bar{t}+lf$. The error bands include the total uncertainty after the fit to data. The first and the last bins include underflow and overflow events, respectively. The lower plots show the ratio of the data to the post-fit background plus signal distribution.
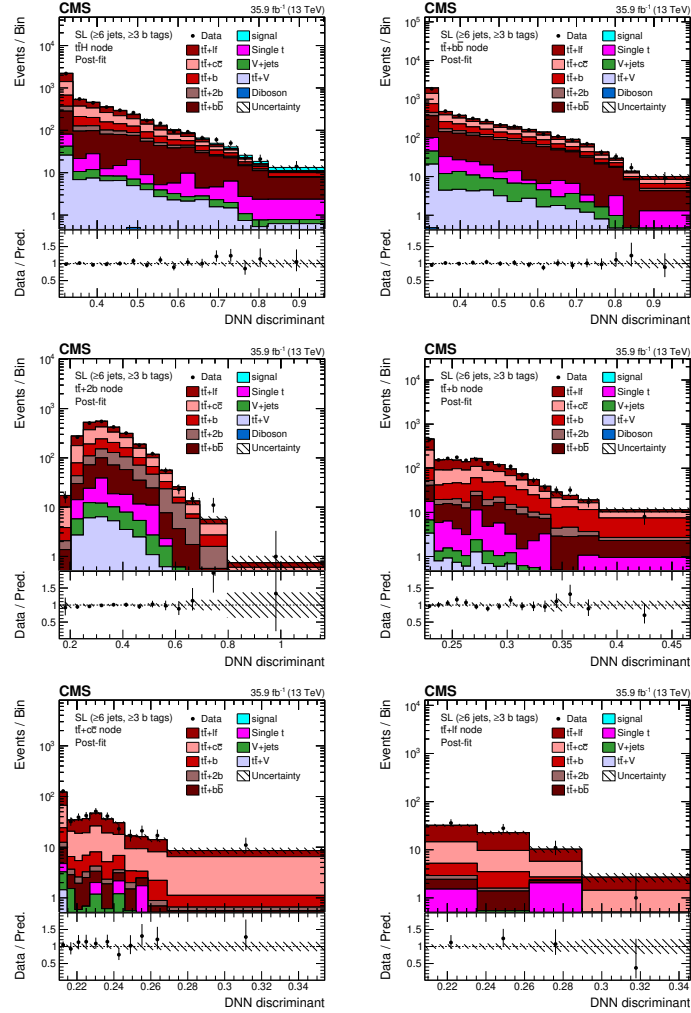
C   Post-fit discriminant shapes (single-lepton channel)

Figure 16. Final discriminant (DNN) shapes in the single-lepton (SL) channel after the fit to data, in the jet-process categories with (5 jets, $\geq$ 3 b tags) and (from upper left to lower right) $t\bar{t}H$, $t\bar{t}+b\bar{b}$, $t\bar{t}+2b$, $t\bar{t}+b$, $t\bar{t}+c\bar{c}$, and $t\bar{t}+lf$. The error bands include the total uncertainty after the fit to data. The first and the last bins include underflow and overflow events, respectively. The lower plots show the ratio of the data to the post-fit background plus signal distribution.

Figure 17. Final discriminant (DNN) shapes in the single-lepton (SL) channel after the fit to data, in the jet-process categories with (≥ 6 jets, ≥ 3 b tags) and (from upper left to lower right) $t\bar{t}H$, $t\bar{t}+b\bar{b}$, $t\bar{t}+2b$, $t\bar{t}+b$, $t\bar{t}+c\bar{c}$, and $t\bar{t}+lf$. The error bands include the total uncertainty after the fit to data. The first and the last bins include underflow and overflow events, respectively. The lower plots show the ratio of the data to the post-fit background plus signal distribution.

Open Access. This article is distributed under the terms of the Creative Commons Attribution License ([CC-BY 4.0](#)), which permits any use, distribution and reproduction in any medium, provided the original author(s) and source are credited.

– 36 –

References

[1] ATLAS collaboration, *Observation of a new particle in the search for the Standard Model Higgs boson with the ATLAS detector at the LHC*, *Phys. Lett.* **B 716** (2012) 1 [arXiv:1207.7214] [INSPIRE].

[2] CMS collaboration, *Observation of a new boson at a mass of 125 GeV with the CMS experiment at the LHC*, *Phys. Lett.* **B 716** (2012) 30 [arXiv:1207.7235] [INSPIRE].

[3] CMS collaboration, *A new boson with a mass of 125 GeV observed with the CMS experiment at the Large Hadron Collider*, *Science* **338** (2012) 1569 [INSPIRE].

[4] ATLAS and CMS collaborations, *Combined measurement of the Higgs boson mass in pp collisions at $\sqrt{s} = 7$ and 8 TeV with the ATLAS and CMS experiments*, *Phys. Rev. Lett.* **114** (2015) 191803 [arXiv:1503.07589] [INSPIRE].

[5] CMS collaboration, *Measurements of properties of the Higgs boson decaying into the four-lepton final state in pp collisions at $\sqrt{s} = 13$ TeV*, *JHEP* **11** (2017) 047 [arXiv:1706.09936] [INSPIRE].

[6] CMS collaboration, *Evidence for the direct decay of the 125 GeV Higgs boson to fermions*, *Nature Phys.* **10** (2014) 557 [arXiv:1401.6527] [INSPIRE].

[7] ATLAS collaboration, *Evidence for the Higgs-boson Yukawa coupling to tau leptons with the ATLAS detector*, *JHEP* **04** (2015) 117 [arXiv:1501.04943] [INSPIRE].

[8] CMS collaboration, *Observation of the Higgs boson decay to a pair of τ leptons with the CMS detector*, *Phys. Lett.* **B 779** (2018) 283 [arXiv:1708.00373] [INSPIRE].

[9] ATLAS collaboration, *Evidence for the $H \to b\bar{b}$ decay with the ATLAS detector*, *JHEP* **12** (2017) 024 [arXiv:1708.03299] [INSPIRE].

[10] CMS collaboration, *Evidence for the Higgs boson decay to a bottom quark-antiquark pair*, *Phys. Lett.* **B 780** (2018) 501 [arXiv:1709.07497] [INSPIRE].

[11] ATLAS collaboration, *Measurements of Higgs boson production and couplings in diboson final states with the ATLAS detector at the LHC*, *Phys. Lett.* **B 726** (2013) 88 [*Erratum ibid.* **B 734** (2014) 406] [arXiv:1307.1427] [INSPIRE].

[12] CMS collaboration, *Precise determination of the mass of the Higgs boson and tests of compatibility of its couplings with the Standard Model predictions using proton collisions at 7 and 8 TeV*, *Eur. Phys. J.* **C 75** (2015) 212 [arXiv:1412.8662] [INSPIRE].

[13] ATLAS collaboration, *Evidence for the spin-0 nature of the Higgs boson using ATLAS data*, *Phys. Lett.* **B 726** (2013) 120 [arXiv:1307.1432] [INSPIRE].

[14] CMS collaboration, *Constraints on the spin-parity and anomalous HVV couplings of the Higgs boson in proton collisions at 7 and 8 TeV*, *Phys. Rev.* **D 92** (2015) 012004 [arXiv:1411.3441] [INSPIRE].

[15] CMS collaboration, *Search for Standard Model production of four top quarks with same-sign and multilepton final states in proton-proton collisions at $\sqrt{s} = 13$ TeV*, *Eur. Phys. J.* **C 78** (2018) 140 [arXiv:1710.10614] [INSPIRE].

[16] LHC HIGGS CROSS SECTION WORKING GROUP collaboration, *Handbook of LHC Higgs cross sections: 4. Deciphering the nature of the Higgs sector*, arXiv:1610.07922 [INSPIRE].

[17] G. Burdman, M. Perelstein and A. Pierce, *Large Hadron Collider tests of a little Higgs model*, *Phys. Rev. Lett.* **90** (2003) 241802 [*Erratum ibid.* **92** (2004) 049903] [hep-ph/0212228] [INSPIRE].

[18] T. Han, H.E. Logan, B. McElrath and L.-T. Wang, *Phenomenology of the little Higgs model*, *Phys. Rev.* **D 67** (2003) 095004 [hep-ph/0301040] [INSPIRE].

[19] M. Perelstein, M.E. Peskin and A. Pierce, *Top quarks and electroweak symmetry breaking in little Higgs models*, *Phys. Rev.* **D 69** (2004) 075002 [hep-ph/0310039] [INSPIRE].

[20] H.-C. Cheng, I. Low and L.-T. Wang, *Top partners in little Higgs theories with T-parity*, *Phys. Rev.* **D 74** (2006) 055001 [hep-ph/0510225] [INSPIRE].

[21] H.-C. Cheng, B.A. Dobrescu and C.T. Hill, *Electroweak symmetry breaking and extra dimensions*, *Nucl. Phys.* **B 589** (2000) 249 [hep-ph/9912343] [INSPIRE].

[22] M. Carena, E. Ponton, J. Santiago and C.E.M. Wagner, *Light Kaluza Klein states in Randall-Sundrum models with custodial* SU(2), *Nucl. Phys.* **B 759** (2006) 202 [hep-ph/0607106] [INSPIRE].

[23] R. Contino, L. Da Rold and A. Pomarol, *Light custodians in natural composite Higgs models*, *Phys. Rev.* **D 75** (2007) 055014 [hep-ph/0612048] [INSPIRE].

[24] G. Burdman and L. Da Rold, *Electroweak symmetry breaking from a holographic fourth generation*, *JHEP* **12** (2007) 086 [arXiv:0710.0623] [INSPIRE].

[25] C.T. Hill, *Topcolor: top quark condensation in a gauge extension of the Standard Model*, *Phys. Lett.* **B 266** (1991) 419 [INSPIRE].

[26] A. Carmona, M. Chala and J. Santiago, *New Higgs production mechanism in composite Higgs models*, *JHEP* **07** (2012) 049 [arXiv:1205.2378] [INSPIRE].

[27] CMS collaboration, *Search for the associated production of the Higgs boson with a top-quark pair*, *JHEP* **09** (2014) 087 [*Erratum ibid.* **10** (2014) 106] [arXiv:1408.1682] [INSPIRE].

[28] ATLAS collaboration, *Search for the associated production of the Higgs boson with a top quark pair in multilepton final states with the ATLAS detector*, *Phys. Lett.* **B 749** (2015) 519 [arXiv:1506.05988] [INSPIRE].

[29] CMS collaboration, *Search for a Standard Model Higgs boson produced in association with a top-quark pair and decaying to bottom quarks using a matrix element method*, *Eur. Phys. J.* **C 75** (2015) 251 [arXiv:1502.02485] [INSPIRE].

[30] ATLAS collaboration, *Search for the Standard Model Higgs boson produced in association with top quarks and decaying into $b\bar{b}$ in pp collisions at $\sqrt{s} = 8\,TeV$ with the ATLAS detector*, *Eur. Phys. J.* **C 75** (2015) 349 [arXiv:1503.05066] [INSPIRE].

[31] LHC HIGGS CROSS SECTION WORKING GROUP collaboration, *Handbook of LHC Higgs cross sections: 1. Inclusive observables*, arXiv:1101.0593 [INSPIRE].

[32] CMS collaboration, *Search for $t\bar{t}H$ production in the all-jet final state in proton-proton collisions at $\sqrt{s} = 13\,TeV$*, *JHEP* **06** (2018) 101 [arXiv:1803.06986] [INSPIRE].

[33] CMS collaboration, *Evidence for associated production of a Higgs boson with a top quark pair in final states with electrons, muons and hadronically decaying τ leptons at $\sqrt{s} = 13\,TeV$*, *JHEP* **08** (2018) 066 [arXiv:1803.05485] [INSPIRE].

[34] ATLAS collaboration, *Evidence for the associated production of the Higgs boson and a top quark pair with the ATLAS detector*, *Phys. Rev.* **D 97** (2018) 072003 [`arXiv:1712.08891`] [InSPIRE].

[35] ATLAS collaboration, *Search for the Standard Model Higgs boson produced in association with top quarks and decaying into a $b\bar{b}$ pair in pp collisions at $\sqrt{s} = 13\,TeV$ with the ATLAS detector*, *Phys. Rev.* **D 97** (2018) 072016 [`arXiv:1712.08895`] [InSPIRE].

[36] T.J. Hastie, R.J. Tibshirani and J.H. Friedman, *The elements of statistical learning: data mining, inference and prediction*, second edition, Springer series in statistics, Springer, New York, NY, U.S.A. (2013) [ISBN:978-0-387-84857-0].

[37] P.C. Bhat, *Multivariate analysis methods in particle physics*, *Ann. Rev. Nucl. Part. Sci.* **61** (2011) 281 [InSPIRE].

[38] A. Höcker et al., *TMVA — toolkit for multivariate data analysis*, `PoS(ACAT)040` [`physics/0703039`] [InSPIRE].

[39] K. Kondo, *Dynamical likelihood method for reconstruction of events with missing momentum. 1: method and toy models*, *J. Phys. Soc. Jap.* **57** (1988) 4126 [InSPIRE].

[40] D0 collaboration, *A precision measurement of the mass of the top quark*, *Nature* **429** (2004) 638 [`hep-ex/0406031`] [InSPIRE].

[41] CMS collaboration, *The CMS experiment at the CERN LHC*, 2008 *JINST* **3** S08004 [InSPIRE].

[42] CMS collaboration, *The CMS trigger system*, 2017 *JINST* **12** P01020 [`arXiv:1609.02366`] [InSPIRE].

[43] GEANT4 collaboration, *GEANT4: a simulation toolkit*, *Nucl. Instrum. Meth.* **A 506** (2003) 250 [InSPIRE].

[44] P. Nason, *A new method for combining NLO QCD with shower Monte Carlo algorithms*, *JHEP* **11** (2004) 040 [`hep-ph/0409146`] [InSPIRE].

[45] S. Frixione, P. Nason and C. Oleari, *Matching NLO QCD computations with parton shower simulations: the POWHEG method*, *JHEP* **11** (2007) 070 [`arXiv:0709.2092`] [InSPIRE].

[46] S. Alioli, P. Nason, C. Oleari and E. Re, *A general framework for implementing NLO calculations in shower Monte Carlo programs: the POWHEG BOX*, *JHEP* **06** (2010) 043 [`arXiv:1002.2581`] [InSPIRE].

[47] H.B. Hartanto, B. Jager, L. Reina and D. Wackeroth, *Higgs boson production in association with top quarks in the POWHEG BOX*, *Phys. Rev.* **D 91** (2015) 094003 [`arXiv:1501.04498`] [InSPIRE].

[48] T. Sjöstrand et al., *An introduction to PYTHIA 8.2*, *Comput. Phys. Commun.* **191** (2015) 159 [`arXiv:1410.3012`] [InSPIRE].

[49] J. Alwall et al., *The automated computation of tree-level and next-to-leading order differential cross sections and their matching to parton shower simulations*, *JHEP* **07** (2014) 079 [`arXiv:1405.0301`] [InSPIRE].

[50] NNPDF collaboration, *Parton distributions for the LHC run II*, *JHEP* **04** (2015) 040 [`arXiv:1410.8849`] [InSPIRE].

– 39 –

[51] S. Alioli, P. Nason, C. Oleari and E. Re, *NLO single-top production matched with shower in POWHEG: s- and t-channel contributions*, *JHEP* **09** (2009) 111 [*Erratum ibid.* **02** (2010) 011] [arXiv:0907.4076] [InSPIRE].

[52] E. Re, *Single-top Wt-channel production matched with parton showers using the POWHEG method*, *Eur. Phys. J.* **C 71** (2011) 1547 [arXiv:1009.2450] [InSPIRE].

[53] R. Frederix and S. Frixione, *Merging meets matching in MC@NLO*, *JHEP* **12** (2012) 061 [arXiv:1209.6215] [InSPIRE].

[54] CMS collaboration, *Investigations of the impact of the parton shower tuning in PYTHIA 8 in the modelling of $t\bar{t}$ at $\sqrt{s} = 8$ and 13 TeV*, CMS-PAS-TOP-16-021, CERN, Geneva, Switzerland (2016).

[55] CMS collaboration, *Event generator tunes obtained from underlying event and multiparton scattering measurements*, *Eur. Phys. J.* **C 76** (2016) 155 [arXiv:1512.00815] [InSPIRE].

[56] N. Kidonakis, *Two-loop soft anomalous dimensions for single top quark associated production with a W^- or H^-*, *Phys. Rev.* **D 82** (2010) 054018 [arXiv:1005.4451] [InSPIRE].

[57] M. Aliev, H. Lacker, U. Langenfeld, S. Moch, P. Uwer and M. Wiedermann, *HATHOR: HAdronic Top and Heavy quarks crOss section calculatoR*, *Comput. Phys. Commun.* **182** (2011) 1034 [arXiv:1007.1327] [InSPIRE].

[58] P. Kant et al., *HatHor for single top-quark production: updated predictions and uncertainty estimates for single top-quark production in hadronic collisions*, *Comput. Phys. Commun.* **191** (2015) 74 [arXiv:1406.4403] [InSPIRE].

[59] F. Maltoni, D. Pagani and I. Tsinikos, *Associated production of a top-quark pair with vector bosons at NLO in QCD: impact on $t\bar{t}H$ searches at the LHC*, *JHEP* **02** (2016) 113 [arXiv:1507.05640] [InSPIRE].

[60] J.M. Campbell, R.K. Ellis and C. Williams, *Vector boson pair production at the LHC*, *JHEP* **07** (2011) 018 [arXiv:1105.0020] [InSPIRE].

[61] M. Cacciari, M. Czakon, M. Mangano, A. Mitov and P. Nason, *Top-pair production at hadron colliders with next-to-next-to-leading logarithmic soft-gluon resummation*, *Phys. Lett.* **B 710** (2012) 612 [arXiv:1111.5869] [InSPIRE].

[62] P. Bärnreuther, M. Czakon and A. Mitov, *Percent level precision physics at the Tevatron: first genuine NNLO QCD corrections to $q\bar{q} \to t\bar{t} + X$*, *Phys. Rev. Lett.* **109** (2012) 132001 [arXiv:1204.5201] [InSPIRE].

[63] M. Czakon and A. Mitov, *NNLO corrections to top-pair production at hadron colliders: the all-fermionic scattering channels*, *JHEP* **12** (2012) 054 [arXiv:1207.0236] [InSPIRE].

[64] M. Czakon and A. Mitov, *NNLO corrections to top pair production at hadron colliders: the quark-gluon reaction*, *JHEP* **01** (2013) 080 [arXiv:1210.6832] [InSPIRE].

[65] M. Beneke, P. Falgari, S. Klein and C. Schwinn, *Hadronic top-quark pair production with NNLL threshold resummation*, *Nucl. Phys.* **B 855** (2012) 695 [arXiv:1109.1536] [InSPIRE].

[66] M. Czakon, P. Fiedler and A. Mitov, *Total top-quark pair-production cross section at hadron colliders through $O(\alpha_S^4)$*, *Phys. Rev. Lett.* **110** (2013) 252004 [arXiv:1303.6254] [InSPIRE].

[67] M. Czakon and A. Mitov, *Top++: a program for the calculation of the top-pair cross-section at hadron colliders*, *Comput. Phys. Commun.* **185** (2014) 2930 [arXiv:1112.5675] [INSPIRE].

[68] CMS collaboration, *Identification of heavy-flavour jets with the CMS detector in pp collisions at* 13 *TeV*, 2018 *JINST* **13** P05011 [arXiv:1712.07158] [INSPIRE].

[69] CMS collaboration, *Particle-flow reconstruction and global event description with the CMS detector*, 2017 *JINST* **12** P10003 [arXiv:1706.04965] [INSPIRE].

[70] CMS collaboration, *Description and performance of track and primary-vertex reconstruction with the CMS tracker*, 2014 *JINST* **9** P10009 [arXiv:1405.6569] [INSPIRE].

[71] M. Cacciari, G.P. Salam and G. Soyez, *The anti-k_t jet clustering algorithm*, *JHEP* **04** (2008) 063 [arXiv:0802.1189] [INSPIRE].

[72] M. Cacciari, G.P. Salam and G. Soyez, *FastJet user manual*, *Eur. Phys. J.* **C 72** (2012) 1896 [arXiv:1111.6097] [INSPIRE].

[73] CMS collaboration, *Performance of electron reconstruction and selection with the CMS detector in proton-proton collisions at* $\sqrt{s} = 8$ *TeV*, 2015 *JINST* **10** P06005 [arXiv:1502.02701] [INSPIRE].

[74] CMS collaboration, *Performance of the CMS muon detector and muon reconstruction with proton-proton collisions at* $\sqrt{s} = 13$ *TeV*, 2018 *JINST* **13** P06015 [arXiv:1804.04528] [INSPIRE].

[75] M. Cacciari, G.P. Salam and G. Soyez, *The catchment area of jets*, *JHEP* **04** (2008) 005 [arXiv:0802.1188] [INSPIRE].

[76] CMS collaboration, *Jet energy scale and resolution in the CMS experiment in pp collisions at* 8 *TeV*, 2017 *JINST* **12** P02014 [arXiv:1607.03663] [INSPIRE].

[77] I. Goodfellow, Y. Bengio and A. Courville, *Deep learning*, http://www.deeplearningbook.org, MIT Press, U.S.A. (2016).

[78] J.H. Friedman, *Stochastic gradient boosting*, *Comput. Stat. Data Anal.* **38** (2002) 367.

[79] J. Kennedy and R. Eberhart, *Particle swarm optimization*, in *Proceedings of ICNN '95 — International Conference on Neural Networks*, volume 4, IEEE, (1995), pg. 1942.

[80] K. El Morabit, *A study of the multivariate analysis of Higgs boson production in association with a top quark-antiquark pair in the boosted regime at the CMS experiment*, master's thesis, EKP-2016-00035, Karlsruher Institut für Technologie (KIT), Germany (2015).

[81] CMS collaboration, *CMS luminosity measurements for the* 2016 *data taking period*, CMS-PAS-LUM-17-001, CERN, Geneva, Switzerland (2017).

[82] ATLAS collaboration, *Measurement of the inelastic proton-proton cross section at* $\sqrt{s} = 13$ *TeV with the ATLAS detector at the LHC*, *Phys. Rev. Lett.* **117** (2016) 182002 [arXiv:1606.02625] [INSPIRE].

[83] CMS collaboration, *Measurement of the cross section ratio* $\sigma_{t\bar{t}b\bar{b}}/\sigma_{t\bar{t}jj}$ *in pp collisions at* $\sqrt{s} = 8$ *TeV*, *Phys. Lett.* **B 746** (2015) 132 [arXiv:1411.5621] [INSPIRE].

[84] ATLAS collaboration, *Measurements of fiducial cross-sections for* $t\bar{t}$ *production with one or two additional b-jets in pp collisions at* $\sqrt{s} = 8$ *TeV using the ATLAS detector*, *Eur. Phys. J.* **C 76** (2016) 11 [arXiv:1508.06868] [INSPIRE].

Observation of *t̄tH* Production

A. M. Sirunyan *et al.*[*]

(CMS Collaboration)

The observation of Higgs boson production in association with a top quark-antiquark pair is reported, based on a combined analysis of proton-proton collision data at center-of-mass energies of $\sqrt{s} = 7$, 8, and 13 TeV, corresponding to integrated luminosities of up to 5.1, 19.7, and 35.9 fb^{-1}, respectively. The data were collected with the CMS detector at the CERN LHC. The results of statistically independent searches for Higgs bosons produced in conjunction with a top quark-antiquark pair and decaying to pairs of W bosons, Z bosons, photons, τ leptons, or bottom quark jets are combined to maximize sensitivity. An excess of events is observed, with a significance of 5.2 standard deviations, over the expectation from the background-only hypothesis. The corresponding expected significance from the standard model for a Higgs boson mass of 125.09 GeV is 4.2 standard deviations. The combined best fit signal strength normalized to the standard model prediction is $1.26^{+0.31}_{-0.26}$.

Proton-proton (pp) collisions at the CERN LHC, at the center-of-mass (c.m.) energies of $\sqrt{s} = 7$, 8, and 13 TeV, have allowed direct measurements of the properties of the Higgs boson [1–3]. In particular, the 13 TeV data collected so far by the ATLAS [4] and CMS [5] experiments have led to improved constraints on the couplings of the Higgs boson compared to those performed at the lower energies [6], permitting more precise consistency checks with the predictions of the standard model (SM) of particle physics [7–9]. Nonetheless, not all properties of the Higgs boson have been established, in part because of insufficiently large data sets. The lack of statistical precision can be partially overcome by combining the results of searches in different decay channels of the Higgs boson and at different c.m. energies. Among the properties that are not yet well established is the tree-level coupling of Higgs bosons to top quarks.

In this Letter, we present a combination of searches for the Higgs boson (H) produced in association with a top quark-antiquark pair ($t\bar{t}$), based on data collected with the CMS detector. Results from data collected at $\sqrt{s} = 13$ TeV [10–14] are combined with analogous results from $\sqrt{s} = 7$ and 8 TeV [15]. As a result of this combination, we establish the observation of $t\bar{t}H$ production. This constitutes the first confirmation of the tree-level coupling of the Higgs boson to top quarks.

A top quark decays almost exclusively to a bottom quark and a W boson, with the W boson subsequently decaying either to a quark and an antiquark or to a charged lepton and its associated neutrino. The Higgs boson exhibits a rich spectrum of decay modes that includes the decay to a bottom quark-antiquark pair, a $\tau^+\tau^-$ lepton pair, a photon pair, and combinations of quarks and leptons from the decay of intermediate on- or off-shell W and Z bosons. Thus, $t\bar{t}H$ production gives rise to a wide variety of final-state event topologies, which we consider in our analyses and in the combination of results presented below.

In the SM, the masses of elementary fermions are accounted for by introducing a minimal set of Yukawa interactions, compatible with gauge invariance, between the Higgs and fermion fields. Following the spontaneous breaking of electroweak symmetry [16–21], charged fermions of flavor f couple to H with a strength y_f proportional to the mass m_f of those fermions, namely $y_f = m_f/v$, where $v \approx 246$ GeV is the vacuum expectation value of the Higgs field. Measurements of the Higgs boson decay rates to down-type fermions (τ leptons and bottom quarks) agree with the SM predictions within their uncertainties [22,23]. However, the top quark Yukawa coupling (y_t) cannot be similarly tested from the measurement of a decay rate since on-shell top quarks are too heavy to be produced in Higgs boson decay. Instead, constraints on y_t can be obtained through the measurement of the $pp \to t\bar{t}H$ production process. Example tree-level Feynman diagrams for this process are shown in Fig. 1. To date, $t\bar{t}H$ production has eluded definite observation, although first evidence has been recently reported by the ATLAS [24] and CMS [10] Collaborations.

The overall agreement observed between the SM predictions and data for the rate of Higgs boson production
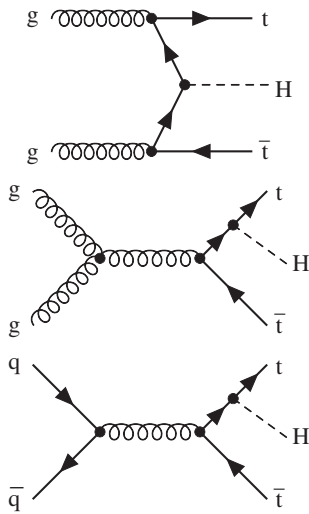

231801-1

FIG. 1.   Example tree-level Feynman diagrams for the $pp \rightarrow t\bar{t}H$ production process, with g a gluon, q a quark, t a top quark, and H a Higgs boson. For the present study, we consider Higgs boson decays to a pair of W bosons, Z bosons, photons, τ leptons, or bottom quark jets.

through gluon-gluon fusion and for the $H \rightarrow \gamma\gamma$ decay mode [6] suggests that the Higgs boson coupling to top quarks is SM-like, since the quantum loops in these processes include top quarks. However, non-SM particles in the loops could introduce terms that compensate for, and thus mask, other deviations from the SM. A measurement of the production rate of the tree-level $t\bar{t}H$ process can provide evidence for, or against, such new-physics contributions.

The central feature of the CMS apparatus is a superconducting solenoid of 6 m internal diameter, providing a magnetic field of 3.8 T. Within the solenoid volume are a silicon pixel and strip tracker, a lead tungstate crystal electromagnetic calorimeter, and a brass and scintillator hadron calorimeter, each composed of a barrel and two end cap sections. Forward calorimeters extend the pseudorapidity coverage provided by the barrel and end cap detectors. Muons are detected in gas-ionization chambers embedded in the steel flux-return yoke outside the solenoid. A detailed description of the CMS detector can be found in Ref. [5].

Events of interest are selected using a two-tiered trigger system [25] based on custom hardware processors and a farm of commercial processors running a version of the full reconstruction software optimized for speed. Offline, a particle-flow algorithm [26] is used to reconstruct and identify each particle in an event based on a combination of information from the various CMS subdetectors. Additional identification criteria are employed to improve

purities and define the final samples of candidate electrons, muons, hadronically decaying τ leptons (τ_h) [27,28], and photons. Jets are reconstructed from particle-flow candidates using the anti-k_T clustering algorithm [29] implemented in the FASTJET package [30]. Multivariate algorithms [31,32] are used to identify (tag) jets arising from the hadronization of bottom quarks (b jets) and discriminate against gluon and light flavor quark jets. The algorithms utilize observables related to the long lifetimes of hadrons containing b quarks and the relatively larger particle multiplicity and mass of b jets compared to light flavor quark jets. The τ_h identification is based on the reconstruction of the hadronic τ decay modes $\tau^- \rightarrow h^-\nu_\tau$, $h^-\pi^0\nu_\tau$, $h^-\pi^0\pi^0\nu_\tau$, and $h^-h^+h^-\nu_\tau$ (plus the charge conjugate reactions), where $h^\pm$ denotes either a charged pion or kaon. More details about the reconstruction procedures are given in Refs. [10–15].

The 13 TeV data employed for the current study were collected in 2016 and correspond to an integrated luminosity of up to 35.9 fb^{-1} [33]. The 7 and 8 TeV data, collected in 2011 and 2012, correspond to integrated luminosities of up to 5.1 and 19.7 fb^{-1} [34], respectively. The 13 TeV analyses are improved relative to the 7 and 8 TeV studies in that they employ triggers with higher efficiencies, contain improvements in the reconstruction and background-rejection methods, and use more precise theory calculations to describe the signal and the background processes. For the 7, 8, and 13 TeV data, the theoretical calculations of Ref. [35] for Higgs boson production cross sections and branching fractions are used to normalize the expected signal yields.

The event samples are divided into exclusive categories depending on the multiplicity and kinematic properties of reconstructed electrons, muons, τ_h candidates, photons, jets, and tagged b jets in an event. Samples of simulated events based on Monte Carlo event generators, with simulation of the detector response based on the GEANT4 [36] suite of programs, are used to evaluate the detector acceptance and optimize the event selection for each category. In the analysis of data, the background is, in general, evaluated from data control regions. When this is not feasible, either because the background process has a very small cross section or a control region depleted of signal events cannot be identified, the background is evaluated from simulation with a systematic uncertainty assigned to account for the known model dependence. Multivariate algorithms [37–41] based on deep neural networks, boosted decision trees, and matrix element calculations are used to reduce backgrounds.

At 13 TeV, we search for $t\bar{t}H$ production in the $H \rightarrow b\bar{b}$ decay mode by selecting events with at least three tagged b jets and with zero leptons [11], one lepton [12], or an opposite-sign lepton pair [12], where "lepton" refers to an electron or muon candidate. A search for $t\bar{t}H$ production in the $H \rightarrow \gamma\gamma$ decay mode is performed in events with two
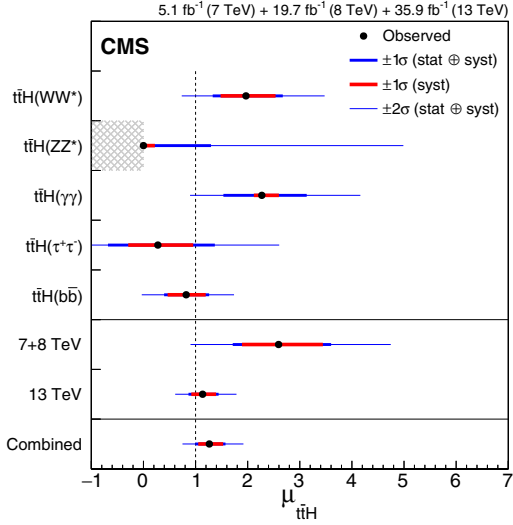
FIG. 2. Best fit value of the $t\bar{t}H$ signal strength modifier $\mu_{t\bar{t}H}$, with its 1 and 2 standard deviation confidence intervals (σ), for (upper section) the five individual decay channels considered, (middle section) the combined result for $7 + 8$ TeV alone and for 13 TeV alone, and (lower section) the overall combined result. The Higgs boson mass is taken to be 125.09 GeV. For the $H \to ZZ^*$ decay mode, $\mu_{t\bar{t}H}$ is constrained to be positive to prevent the corresponding event yield from becoming negative. The SM expectation is shown as a dashed vertical line.

reconstructed photons in combination with reconstructed electrons or muons, jets, and tagged b jets [13]. The signal yield is extracted from a fit to the diphoton invariant mass spectrum. Events with combinations of jets and tagged b jets and with two same-sign leptons, three leptons, or four leptons are used to search for $t\bar{t}H$ production in the $H \to \tau^+\tau^-$, WW^*, or ZZ^* decay modes [10,14], where in this case "lepton" refers to an electron, muon, or τ_h candidate (the asterisk denotes an off-shell particle). The searches in the different decay channels are statistically independent from each other. Analogous searches have been performed with the 7 and 8 TeV data [15].

The presence of a $t\bar{t}H$ signal is assessed by performing a simultaneous fit to the data from the different decay modes and also from the different c.m. energies as described below. A detailed description of the statistical methods can be found in Ref. [42]. The test statistic q is defined as the negative of twice the logarithm of the profile likelihood ratio [42]. Systematic uncertainties are incorporated through the use of nuisance parameters treated according to the frequentist paradigm. The ratio between the normalization of the $t\bar{t}H$ production process and its SM expectation [35], defined as the signal strength modifier $\mu_{t\bar{t}H}$, is a freely floating parameter in the fit. The SM expectation is evaluated assuming the combined ATLAS

and CMS value for the mass of the Higgs boson, which is 125.09 GeV [43]. We consider the five Higgs boson decay modes with the largest expected event yields, namely, $H \to WW^*$, ZZ^*, $\gamma\gamma$, $\tau^+\tau^-$, and $b\bar{b}$. Other Higgs boson decay modes and production processes, including $pp \to tH + X$ (or $\bar{t}H + X$), with X a light flavor quark or W boson, are treated as backgrounds and normalized using the predicted SM cross sections, subject to the corresponding uncertainties.

The measured values of the five independent signal strength modifiers, corresponding to the five decay channels considered, are shown in the upper section of Fig. 2 along with their 1 and 2 standard deviation confidence intervals obtained in the asymptotic approximation [44]. Numerical values are given in Table I. The individual measurements are seen to be consistent with each other within the uncertainties.

We also perform a combined fit, using a single signal strength modifier $\mu_{t\bar{t}H}$, that simultaneously scales the $t\bar{t}H$ production cross sections of the five decay channels considered, with all Higgs boson branching fractions fixed to their SM values [35]. Besides the five decay modes

TABLE I. Best fit value, with its uncertainty, of the $t\bar{t}H$ signal strength modifier $\mu_{t\bar{t}H}$, for the five individual decay channels considered, the combined result for $7 + 8$ TeV alone and for 13 TeV alone, and the overall combined result. The total uncertainties are decomposed into their statistical, experimental systematic, background theory systematic, and signal theory components. The numbers in parentheses are those expected for $\mu_{t\bar{t}H} = 1$.

				Uncertainty	
Parameter	Best fit	Statistical	Experimental	Background theory	Signal theory
$\mu_{t\bar{t}H}^{WW^*}$	$1.97^{+0.71}_{-0.64}$ $\left(^{+0.57}_{-0.54}\right)$	$^{+0.42}_{-0.41}$ $\left(^{+0.39}_{-0.38}\right)$	$^{+0.46}_{-0.42}$ $\left(^{+0.36}_{-0.34}\right)$	$^{+0.21}_{-0.21}$ $\left(^{+0.17}_{-0.17}\right)$	$^{+0.25}_{-0.12}$ $\left(^{+0.12}_{-0.03}\right)$
$\mu_{t\bar{t}H}^{ZZ^*}$	$0.00^{+1.30}_{-0.00}$ $\left(^{+2.89}_{-0.99}\right)$	$^{+1.28}_{-0.00}$ $\left(^{+2.82}_{-0.99}\right)$	$^{+0.20}_{-0.00}$ $\left(^{+0.51}_{-0.00}\right)$	$^{+0.04}_{-0.00}$ $\left(^{+0.15}_{-0.00}\right)$	$^{+0.09}_{-0.00}$ $\left(^{+0.27}_{-0.00}\right)$
$\mu_{t\bar{t}H}^{\gamma\gamma}$	$2.27^{+0.86}_{-0.74}$ $\left(^{+0.73}_{-0.64}\right)$	$^{+0.80}_{-0.72}$ $\left(^{+0.71}_{-0.64}\right)$	$^{+0.15}_{-0.09}$ $\left(^{+0.09}_{-0.04}\right)$	$^{+0.02}_{-0.01}$ $\left(^{+0.01}_{-0.00}\right)$	$^{+0.29}_{-0.13}$ $\left(^{+0.13}_{-0.05}\right)$
$\mu_{t\bar{t}H}^{\tau^+\tau^-}$	$0.28^{+1.09}_{-0.96}$ $\left(^{+1.00}_{-0.89}\right)$	$^{+0.86}_{-0.77}$ $\left(^{+0.83}_{-0.76}\right)$	$^{+0.64}_{-0.53}$ $\left(^{+0.54}_{-0.47}\right)$	$^{+0.10}_{-0.09}$ $\left(^{+0.09}_{-0.08}\right)$	$^{+0.20}_{-0.19}$ $\left(^{+0.14}_{-0.01}\right)$
$\mu_{t\bar{t}H}^{b\bar{b}}$	$0.82^{+0.44}_{-0.42}$ $\left(^{+0.44}_{-0.42}\right)$	$^{+0.23}_{-0.23}$ $\left(^{+0.23}_{-0.22}\right)$	$^{+0.24}_{-0.23}$ $\left(^{+0.24}_{-0.23}\right)$	$^{+0.27}_{-0.27}$ $\left(^{+0.26}_{-0.27}\right)$	$^{+0.11}_{-0.03}$ $\left(^{+0.11}_{-0.04}\right)$
$\mu_{t\bar{t}H}^{7+8\text{ TeV}}$	$2.59^{+1.01}_{-0.88}$ $\left(^{+0.87}_{-0.79}\right)$	$^{+0.54}_{-0.53}$ $\left(^{+0.51}_{-0.49}\right)$	$^{+0.53}_{-0.49}$ $\left(^{+0.48}_{-0.44}\right)$	$^{+0.55}_{-0.49}$ $\left(^{+0.50}_{-0.44}\right)$	$^{+0.37}_{-0.13}$ $\left(^{+0.14}_{-0.02}\right)$
$\mu_{t\bar{t}H}^{13\text{ TeV}}$	$1.14^{+0.31}_{-0.27}$ $\left(^{+0.29}_{-0.26}\right)$	$^{+0.17}_{-0.16}$ $\left(^{+0.16}_{-0.16}\right)$	$^{+0.17}_{-0.17}$ $\left(^{+0.17}_{-0.16}\right)$	$^{+0.13}_{-0.12}$ $\left(^{+0.13}_{-0.12}\right)$	$^{+0.14}_{-0.06}$ $\left(^{+0.11}_{-0.05}\right)$
$\mu_{t\bar{t}H}$	$1.26^{+0.31}_{-0.26}$ $\left(^{+0.28}_{-0.25}\right)$	$^{+0.16}_{-0.16}$ $\left(^{+0.15}_{-0.15}\right)$	$^{+0.17}_{-0.15}$ $\left(^{+0.16}_{-0.15}\right)$	$^{+0.14}_{-0.13}$ $\left(^{+0.13}_{-0.12}\right)$	$^{+0.15}_{-0.07}$ $\left(^{+0.11}_{-0.05}\right)$

considered, the signal normalizations for the Higgs boson decay modes to gluons, charm quarks, and $Z\gamma$, which are subleading and cannot be constrained with existing data, are scaled by $\mu_{t\bar{t}H}$. The results combining the decay modes at $7 + 8$ TeV, and separately at 13 TeV, are shown in the middle section of Fig. 2. The overall result, combining all decay modes and all c.m. energies, is shown in the lower section, with numerical values given in Table I. Table I includes a breakdown of the total uncertainties into their statistical and systematic components. The overall result is $\mu_{t\bar{t}H} = 1.26^{+0.31}_{-0.26}$, which agrees with the SM expectation $\mu_{t\bar{t}H} = 1$ within 1 standard deviation.

The principal sources of experimental systematic uncertainty in the overall result for $\mu_{t\bar{t}H}$ stem from the uncertainty in the lepton and b jet identification efficiencies and in the τ_h and jet energy scales. The background theory systematic uncertainty is dominated by modeling uncertainties in $t\bar{t}$ production in association with a W boson, a Z boson, or a pair of b or c quark jets. The dominant contribution to the signal theory systematic uncertainty arises from the finite accuracy in the SM prediction for the $t\bar{t}H$ cross section because of missing higher order terms and uncertainties in the proton parton density functions [35].

To highlight the excess of data over the expectation from the background-only hypothesis, we classify each event
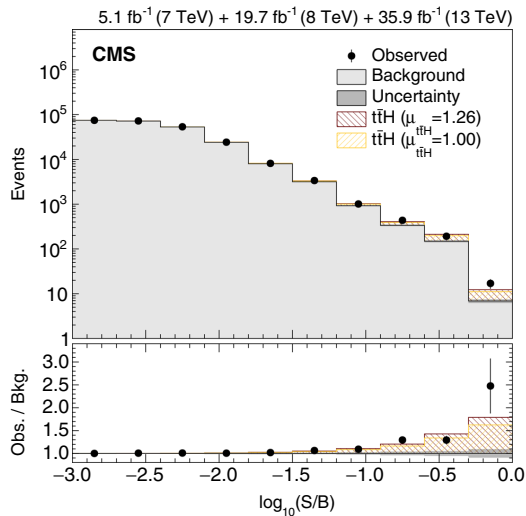

FIG. 3. Distribution of events as a function of the decimal logarithm of S/B, where S and B are the expected postfit signal (with $\mu_{t\bar{t}H} = 1$) and background yields, respectively, in each bin of the distributions considered in this combination. The shaded histogram shows the expected background distribution. The two hatched histograms, each stacked on top of the background histogram, show the signal expectation for the SM ($\mu_{t\bar{t}H} = 1$) and the observed ($\mu_{t\bar{t}H} = 1.26$) signal strengths. The lower panel shows the ratios of the expected signal and observed results relative to the expected background.

that enters the combined fit by the ratio S/B, where S and B are the expected postfit signal (with $\mu_{t\bar{t}H} = 1$) and background yields, respectively, in each bin of the distributions considered in the combination. The distribution of $\log_{10}(S/B)$ is shown in Fig. 3. The main sensitivity at high values of S/B is given by events selected in the $H \to \gamma\gamma$ analysis with a diphoton mass around 125 GeV and by events selected in the $H \to \tau^+\tau^-$, $H \to WW^*$, and $H \to b\bar{b}$ analyses with high values of the multivariate discriminating variables used for the signal extraction. A broad excess of events in the rightmost bins of this distribution is observed, consistent with the expectation for $t\bar{t}H$ production with a SM-like cross section.

The value of the test statistic q as a function of $\mu_{t\bar{t}H}$ is shown in Fig. 4, with $\mu_{t\bar{t}H}$ based on the combination of decay modes described above for the combined fit. The results are shown for the combination of all decay modes at $7 + 8$ TeV and at 13 TeV, separately, and for all decay modes at all c.m. energies. To quantify the significance of the measured $t\bar{t}H$ yield, we compute the probability of the background-only hypothesis (p value) as the tail integral of the test statistic using the overall combination evaluated at $\mu_{t\bar{t}H} = 0$ under the asymptotic approximation [45]. This corresponds to a significance of 5.2 standard deviations for a one-tailed Gaussian distribution. The expected significance for a SM Higgs boson with a mass of 125.09 GeV, evaluated through use of an Asimov data set [45], is 4.2 standard deviations.

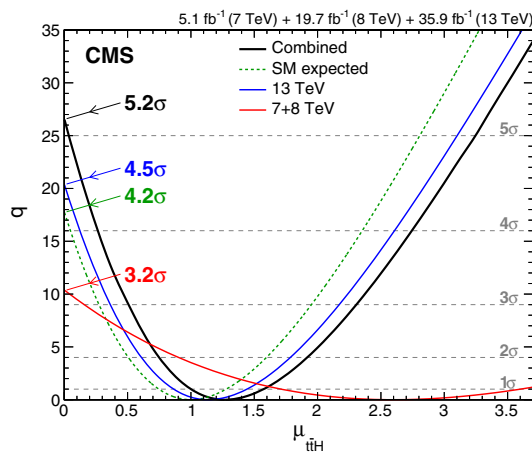In summary, we have reported the observation of $t\bar{t}H$ production with a significance of 5.2 standard deviations

FIG. 4. Test statistic q, described in the text, as a function of $\mu_{t\bar{t}H}$ for all decay modes at $7 + 8$ TeV and at 13 TeV, separately, and for all decay modes at all c.m. energies. The expected SM result for the overall combination is also shown. The horizontal dashed lines indicate the p values for the background-only hypothesis obtained from the asymptotic distribution of q, expressed in units of the number of standard deviations.

above the background-only hypothesis, at a Higgs boson mass of 125.09 GeV. The measured production rate is consistent with the standard model prediction within one standard deviation. In addition to comprising the first observation of a new Higgs boson production mechanism, this measurement establishes the tree-level coupling of the Higgs boson to the top quark, and hence to an up-type quark.

[1] ATLAS Collaboration, Observation of a new particle in the search for the standard model Higgs boson with the ATLAS detector at the LHC, Phys. Lett. B **716**, 1 (2012).

[2] CMS Collaboration, Observation of a new boson at a mass of 125 GeV with the CMS experiment at the LHC, Phys. Lett. B **716**, 30 (2012).

[3] CMS Collaboration, Observation of a new boson with mass near 125 GeV in pp collisions at $\sqrt{s} = 7$ and 8 TeV, J. High Energy Phys. 06 (2013) 081.

[4] ATLAS Collaboration, The ATLAS experiment at the CERN large hadron collider, J. Instrum. **3**, S08003 (2008).

[5] CMS Collaboration, The CMS experiment at the CERN LHC, J. Instrum. **3**, S08004 (2008).

[6] ATLAS and CMS Collaborations, Measurements of the Higgs boson production and decay rates and constraints on its couplings from a combined ATLAS and CMS analysis of the LHC pp collision data at $\sqrt{s} = 7$ and 8 TeV, J. High Energy Phys. 08 (2016) 045.

[7] S. L. Glashow, Partial-symmetries of weak interactions, Nucl. Phys. **22**, 579 (1961).

[8] S. Weinberg, A Model of Leptons, Phys. Rev. Lett. **19**, 1264 (1967).

[9] Abdus Salam, Weak and electromagnetic interactions, in *Elementary Particle Physics: Relativistic Groups and Analyticity*, edited by N. Svartholm (Almqvist & Wiksells, Stockholm, 1968), p. 367.

[10] CMS Collaboration, Evidence for associated production of a Higgs boson with a top quark pair in final states with electrons, muons, and hadronically decaying τ leptons at $\sqrt{s} = 13$ TeV, arXiv:1803.05485 [J. High Energy Phys. (to be published)].

[11] CMS Collaboration, Search for ttH in all-jet final states in proton-proton collisions at $\sqrt{s} = 13$ TeV, arXiv:1803.06986 [J. High Energy Phys. (to be published)].

[12] CMS Collaboration, Search for $t\bar{t}H$ production in the $H \to b\bar{b}$ decay channel with leptonic $t\bar{t}$ decays in proton-proton collisions at $\sqrt{s} = 13$ TeV, arXiv:1804.03682 [J. High Energy Phys. (to be published)].

[13] CMS Collaboration, Measurements of Higgs boson properties in the diphoton decay channel in proton-proton collisions at $\sqrt{s} = 13$ TeV, arXiv:1804.02716 [J. High Energy Phys. (to be published)].

[14] CMS Collaboration, Measurements of properties of the Higgs boson decaying into the four-lepton final state in pp collisions at $\sqrt{s} = 13$ TeV, J. High Energy Phys. 11 (2017) 047.

[15] CMS Collaboration, Search for the associated production of the Higgs boson with a top-quark pair, J. High Energy Phys. 09 (2014) 087.

[16] P. W. Higgs, Broken symmetries, massless particles and gauge fields, Phys. Lett. **12**, 132 (1964).

[17] F. Englert and R. Brout, Broken Symmetry and the Mass of Gauge Vector Mesons, Phys. Rev. Lett. **13**, 321 (1964).

[18] P. W. Higgs, Broken Symmetries and the Masses of Gauge Bosons, Phys. Rev. Lett. **13**, 508 (1964).

[19] G. S. Guralnik, C. R. Hagen, and T. W. B. Kibble, Global Conservation Laws and Massless Particles, Phys. Rev. Lett. **13**, 585 (1964).

[20] P. W. Higgs, Spontaneous symmetry breakdown without massless bosons, Phys. Rev. **145**, 1156 (1966).

[21] T. W. B. Kibble, Symmetry breaking in non-Abelian gauge theories, Phys. Rev. **155**, 1554 (1967).

[22] CMS Collaboration, Observation of the Higgs boson decay to a pair of τ leptons, Phys. Lett. B **779**, 283 (2018).

[23] CMS Collaboration, Evidence for the Higgs boson decay to a bottom quark-antiquark pair, Phys. Lett. B **780**, 501 (2018).

[24] ATLAS Collaboration, Evidence for the associated production of the Higgs boson and a top quark pair with the ATLAS detector, Phys. Rev. D **97**, 072003 (2018).

[25] CMS Collaboration, The CMS trigger system, J. Instrum. **12**, P01020 (2017).

[26] CMS Collaboration, Particle-flow reconstruction and global event description with the CMS detector, J. Instrum. **12,** P10003 (2017).

[27] CMS Collaboration, Reconstruction and identification of τ lepton decays to hadrons and ν_τ at CMS, J. Instrum. **11,** P01019 (2016).

[28] CMS Collaboration, Performance of Reconstruction and Identification of Tau Leptons in their Decays to Hadrons and Tau Neutrino in LHC Run-2, CMS Physics Analysis Summary CMS-PAS-TAU-16-002 CERN, 2016, https://cds.cern.ch/record/2196972.

[29] M. Cacciari, G. P. Salam, and G. Soyez, The anti-k_T jet clustering algorithm, J. High Energy Phys. 04 (2008) 063.

[30] M. Cacciari, G. P. Salam, and G. Soyez, FastJet user manual, Eur. Phys. J. C **72,** 1896 (2012).

[31] CMS Collaboration, Identification of b-quark jets with the CMS experiment, J. Instrum. **8,** P04013 (2013).

[32] CMS Collaboration, Identification of heavy-flavour jets with the CMS detector in pp collisions at 13 TeV, arXiv:1712.07158 [J. Instrum. (to be published)].

[33] CMS Collaboration, CMS Luminosity Measurements for the 2016 Data Taking Period, CMS Physics Analysis Summary CMS-PAS-LUM-17-001 CERN, 2017, https://cds.cern.ch/record/2257069.

[34] CMS Collaboration, CMS Luminosity Based on Pixel Cluster Counting—Summer 2013 Update, CMS Physics Analysis Summary CMS-PAS-LUM-13-001 CERN, 2013, https://cds.cern.ch/record/1598864.

[35] LHC Higgs Cross Section Working Group, Handbook of LHC Higgs Cross Sections: 4. Deciphering the Nature of the Higgs Sector, CYRM-2017-002 CERN, 2016.

[36] S. Agostinelli *et al.* (GEANT4 Collaboration), GEANT4—a simulation toolkit, Nucl. Instrum. Methods Phys. Res., Sect. A **506,** 250 (2003).

[37] I. Goodfellow, Y. Bengio, and A. Courville, *Deep Learning* (MIT Press, Cambridge, MA, 2016).

[38] J. Therhaag, A. Hoecker, P. Speckmeyer, E. von Toerne, and H. Voss, TMVA—toolkit for multivariate data analysis, in *Proceedings, Int'l Conf. on Computational Methods in Science and Engineering, 2009, ICCMSE2009*, Vol. 1504 (ICCMSE, 2012), p. 1013.

[39] V. M. Abazov *et al.* (D0 Collaboration), A precision measurement of the mass of the top quark, Nature (London) **429,** 638 (2004).

[40] V. M. Abazov *et al.* (D0 Collaboration), Helicity of the W boson in lepton + jets $t\bar{t}$ events, Phys. Lett. B **617,** 1 (2005).

[41] CMS Collaboration, Search for a standard model Higgs boson produced in association with a top-quark pair and decaying to bottom quarks using a matrix element method, Eur. Phys. J. C **75,** 251 (2015).

[42] ATLAS Collaboration, CMS Collaboration, LHC Higgs Combination Group, Procedure for the LHC Higgs Boson Search Combination in Summer 2011, Technical Report CMS-NOTE-2011-005, ATL-PHYS-PUB-2011-11 2011, https://cds.cern.ch/record/1379837.

[43] ATLAS and CMS Collaborations, Combined Measurement of the Higgs Boson Mass in pp Collisions at $\sqrt{s} = 7$ and 8 TeV with the ATLAS and CMS Experiments, Phys. Rev. Lett. **114,** 191803 (2015).

[44] CMS Collaboration, Precise determination of the mass of the Higgs boson and tests of compatibility of its couplings with the standard model predictions using proton collisions at 7 and 8 TeV, Eur. Phys. J. C **75,** 212 (2015).

[45] G. Cowan, K. Cranmer, E. Gross, and O. Vitells, Asymptotic formulae for likelihood-based tests of new physics, Eur. Phys. J. C **71,** 1554 (2011); Erratum, Eur. Phys. J. C **73,** 2501 (2013).

A. M. Sirunyan,[1] A. Tumasyan,[1] W. Adam,[2] F. Ambrogi,[2] E. Asilar,[2] T. Bergauer,[2] J. Brandstetter,[2] M. Dragicevic,[2] J. Erö,[2] A. Escalante Del Valle,[2] M. Flechl,[2] R. Frühwirth,[2,b] V. M. Ghete,[2] J. Hrubec,[2] M. Jeitler,[2,b] N. Krammer,[2] I. Krätschmer,[2] D. Liko,[2] T. Madlener,[2] I. Mikulec,[2] N. Rad,[2] H. Rohringer,[2] J. Schieck,[2,b] R. Schöfbeck,[2] M. Spanring,[2] D. Spitzbart,[2] A. Taurok,[2] W. Waltenberger,[2] J. Wittmann,[2] C.-E. Wulz,[2,b] M. Zarucki,[2] V. Chekhovsky,[3] V. Mossolov,[3] J. Suarez Gonzalez,[3] E. A. De Wolf,[4] D. Di Croce,[4] X. Janssen,[4] J. Lauwers,[4] M. Pieters,[4] M. Van De Klundert,[4] H. Van Haevermaet,[4] P. Van Mechelen,[4] N. Van Remortel,[4] S. Abu Zeid,[5] F. Blekman,[5] J. D'Hondt,[5] I. De Bruyn,[5] J. De Clercq,[5] K. Deroover,[5] G. Flouris,[5] D. Lontkovskyi,[5] S. Lowette,[5] I. Marchesini,[5] S. Moortgat,[5] L. Moreels,[5] Q. Python,[5] K. Skovpen,[5] S. Tavernier,[5] W. Van Doninck,[5] P. Van Mulders,[5] I. Van Parijs,[5] D. Beghin,[6] B. Bilin,[6] H. Brun,[6] B. Clerbaux,[6] G. De Lentdecker,[6] H. Delannoy,[6] B. Dorney,[6] G. Fasanella,[6] L. Favart,[6] R. Goldouzian,[6] A. Grebenyuk,[6] A. K. Kalsi,[6] T. Lenzi,[6] J. Luetic,[6] N. Postiau,[6] E. Starling,[6] L. Thomas,[6] C. Vander Velde,[6] P. Vanlaer,[6] D. Vannerom,[6] Q. Wang,[6] T. Cornelis,[7] D. Dobur,[7] A. Fagot,[7] M. Gul,[7] I. Khvastunov,[7,c] D. Poyraz,[7] C. Roskas,[7] D. Trocino,[7] M. Tytgat,[7] W. Verbeke,[7] B. Vermassen,[7] M. Vit,[7] N. Zaganidis,[7] H. Bakhshiansohi,[8] O. Bondu,[8] S. Brochet,[8] G. Bruno,[8] C. Caputo,[8] P. David,[8] C. Delaere,[8] M. Delcourt,[8] B. Francois,[8] A. Giammanco,[8] G. Krintiras,[8] V. Lemaitre,[8] A. Magitteri,[8] A. Mertens,[8] M. Musich,[8] K. Piotrzkowski,[8] A. Saggio,[8] M. Vidal Marono,[8] S. Wertz,[8] J. Zobec,[8] F. L. Alves,[9] G. A. Alves,[9] L. Brito,[9] M. Correa Martins Junior,[9] G. Correia Silva,[9] C. Hensel,[9] A. Moraes,[9] M. E. Pol,[9] P. Rebello Teles,[9] E. Belchior Batista Das Chagas,[10] W. Carvalho,[10] J. Chinellato,[10,d] E. Coelho,[10] E. M. Da Costa,[10] G. G. Da Silveira,[10,e]

P H Y S I C A L   R E V I E W   L E T T E R S

Measurement of the Top Quark Pair Production Cross Section in Proton-Proton Collisions at $\sqrt{s} = 13$ TeV

V. Khachatryan *et al.*[*]

(CMS Collaboration)

The top quark pair production cross section is measured for the first time in proton-proton collisions at $\sqrt{s} = 13$ TeV by the CMS experiment at the CERN LHC, using data corresponding to an integrated luminosity of 43 pb^{-1}. The measurement is performed by analyzing events with at least one electron and one muon of opposite charge, and at least two jets. The measured cross section is $746 \pm 58(\text{stat}) \pm 53(\text{syst}) \pm 36(\text{lumi})$ pb, in agreement with the expectation from the standard model.

The measurement of $t\bar{t}$ production at a center-of-mass energy not previously accessed has great discovery potential for physics beyond the standard model (SM), because new phenomena can significantly enhance the $t\bar{t}$ cross section. The increased energy also allows for a test of the production mechanism, dominated at the CERN LHC by gluon-gluon fusion, and of the validity of the theory of quantum chromodynamics (QCD). Furthermore, top quark production is an important source of background in many searches for physics beyond the SM, and its accurate evaluation is important. Previously, large samples of top quark events were collected in proton-proton collisions at the LHC at $\sqrt{s} = 7$ and 8 TeV and used to study $t\bar{t}$ production in different final states by the ATLAS [1–11] and CMS [12–20] collaborations.

This Letter presents the first measurement of the $t\bar{t}$ production cross section $\sigma_{t\bar{t}}$ at $\sqrt{s} = 13$ TeV, utilizing data corresponding to an integrated luminosity of 43 pb^{-1} recorded by the CMS experiment. In the SM, top quarks are produced predominantly in $t\bar{t}$ pairs via the strong interaction, and each top quark decays almost exclusively to a W boson and a b quark. For this study, we select events that contain at least one electron and one muon of opposite charge, and at least two jets.

The central feature of the CMS detector [21] is a superconducting solenoid of 6 m internal diameter, providing a magnetic field of 3.8 T. A silicon pixel and strip tracker, a lead tungstate crystal electromagnetic calorimeter (ECAL), and a brass and scintillator hadron calorimeter, each composed of a barrel and two endcap sections, are located within the solenoid volume. Muons are measured in gas-ionization detectors embedded in the steel flux-return

yoke outside the solenoid. A two-tier trigger system selects the most interesting pp collisions for offline analysis. A more detailed description of the CMS detector, together with a definition of its coordinate system and kinematic variables, can be found in Ref. [21].

We use several Monte Carlo (MC) generator programs to simulate signal and background processes. The next-to-leading-order (NLO) POWHEG (v2) [22,23] generator is used to generate $t\bar{t}$ signal events, assuming a top quark mass of $m_t = 172.5$ GeV [24]. We utilize the NNPDF3.0 NLO [25] parton distribution functions (PDF) in the MC calculations. The events are interfaced to PYTHIA (v8.205) [26,27] with the CUETP8M1 tune [28,29] to simulate parton showering, hadronization, and the underlying event. An alternative sample is obtained using the HERWIG++ (v2.7.1) [30] program to model the parton shower. Another sample of $t\bar{t}$ events is generated using MG5_AMC@NLO (v5_2.2.2) [31] and MADSPIN [32] generators, and again PYTHIA (v8.205) for parton showering, hadronization, and the underlying event. The MC generators have been validated by comparing to unfolded differential distributions of $t\bar{t}$ production at $\sqrt{s} = 8$ TeV [33].

Background events are simulated by the MG5_AMC@NLO (v5_2.2.2) generator for $W +$ jets production and Drell–Yan (DY) quark-antiquark annihilation into lepton-antilepton pairs through virtual photon or Z boson exchange, with normalization taken from data. Associated top quark and W boson production (tW) is simulated using POWHEG (v1) [34,35] and PYTHIA (v8.205), and is normalized to the approximate next-to-next-to-leading-order (NNLO) cross section [36]. The contributions from WW, WZ and ZZ (referred to as VV) processes are simulated with PYTHIA (v8.205), and normalized to their NLO cross sections [37]. All other backgrounds are estimated from control samples extracted from collision data. The simulated samples include additional interactions per bunch crossing (pileup). On average, about 20 collisions per bunch crossing are present in our data.

---

[*]Full author list given at the end of the article.

The SM prediction for the $t\bar{t}$ production cross section at $\sqrt{s} = 13$ TeV is calculated with the TOP++ program [38] at NNLO in perturbative QCD, including soft-gluon resummation at next-to-next-to-leading-log order (NNLL) [39–44], assuming $m_t = 172.5$ GeV. The result is $\sigma_{t\bar{t}}^{\text{NNLO+NNLL}} = 832^{+20}_{-29}(\text{scale}) \pm 35(\text{PDF} + \alpha_s)$ pb. The expected yields for signal in all figures and tables are normalized to this value. The first uncertainty reflects uncertainties in the factorization and renormalization scales, μ_F and μ_R. The second uncertainty, associated with the PDFs and strong coupling constant α_s, is obtained by following the PDF4LHC prescription [45,46] using the MSTW2008 68% C.L. NNLO [47,48], CT10 NNLO [49,50], and NNPDF2.3 5f FFN [51] PDF sets.

At the trigger level, events are required to contain one electron and one muon, where the electron has transverse momentum $p_T > 12$ GeV and the muon has $p_T > 17$ GeV, or the electron has $p_T > 17$ GeV and the muon has $p_T > 8$ GeV. Offline, particle candidates are reconstructed with the CMS particle-flow (PF) algorithm [52,53]. The PF algorithm reconstructs and identifies each individual particle using an optimized combination of information from the various elements of the CMS detector.

Events are selected to contain one electron [54] and one muon [55] of opposite charge, both of which are required to have $p_T > 20$ GeV and $|\eta| < 2.4$ (but excluding electrons within a small region of $|\eta|$ between the barrel and endcap sections of the ECAL). The electron and muon candidates are required to be sufficiently isolated from nearby jet activity as follows. For each electron and muon candidate, a cone of $\Delta R = 0.3$ and $\Delta R = 0.4$, respectively, is constructed around the direction of the track at the event vertex, where ΔR is defined as $\sqrt{(\Delta\eta)^2 + (\Delta\phi)^2}$, and $\Delta\eta$ and $\Delta\phi$ are the distances in pseudorapidity and azimuthal angle. Excluding the contribution from the lepton candidate, the scalar sum of the p_T of all particle candidates that are inside ΔR and are consistent with arising from the chosen primary event vertex is calculated to define a relative isolation discriminant, I_{rel}, through the ratio of this sum to the p_T of the lepton candidate. The neutral-particle contribution to I_{rel} is corrected for pileup based on the average energy density deposited by neutral particles in the event. This corresponds to an average p_T from pileup determined event-by-event that is subtracted from the summed scalar p_T in the isolation cone. An electron and muon candidate is selected if they have respective values of $I_{\text{rel}} < 0.11$ and $I_{\text{rel}} < 0.12$.

In events with more than one pair of leptons passing the above selection, the two leptons of opposite charge and different flavor with the largest p_T are selected for further study. Events with τ leptons contribute to the measurement only if they decay to electrons or muons that satisfy the selection requirements, and are included in the MC simulations.

The efficiency of the lepton selection is measured using a "tag-and-probe" method in same-flavor dilepton events enriched in Z boson candidates, as described in Refs. [19,56]. Differences in the event topology with respect to $t\bar{t}$ production are accounted for as a systematic uncertainty. In the current data set, the measured values for the combined identification and isolation efficiencies are typically 92% for muons and 77% for electrons. Based on a comparison of lepton selection efficiencies in data and simulation, the event yield in simulation is corrected using p_T- and η-dependent data-to-simulation scale factors (SF) to provide consistency with data. They have average values of 1.00 for muons and 0.96 for electrons.

Candidate events with dilepton invariant masses of $m_{e\mu} < 20$ GeV are removed to suppress backgrounds, mainly from low-mass DY processes. Jets are reconstructed from the PF particle candidates using the anti-k_T clustering algorithm [57] with a distance parameter of 0.4, optimized for the running conditions at higher center-of-mass energy. The jet energy is corrected for pileup in a manner similar to that used to find the energy within the lepton isolation cone. Jet energy corrections are also applied as a function of jet p_T and η [58] to data and simulation. Events are required to have at least two reconstructed jets with $p_T > 30$ GeV and $|\eta| < 2.4$.

Backgrounds in this analysis arise primarily from tW, DY, and VV events in which at least two leptons are produced. Background yields from tW and VV events are estimated from simulation. The $e^{\pm}\mu^{\mp}$ DY background normalization is estimated from data using the "$R_{\text{out/in}}$" method [19,59,60], where events with e^+e^- and $\mu^+\mu^-$ final states are explored as follows. A data-to-simulation normalization factor is estimated from the number of events within the Z boson mass window in data, and extrapolated to the number of events outside the Z mass window with corrections based on control regions in data enriched in DY events. This factor is found to be $1.04 \pm 0.16(\text{stat})$.

Other background sources, such as $t\bar{t}$ or $W +$ jets events with decays into one lepton and jets, can contaminate the signal sample if a jet is incorrectly reconstructed as a lepton, or an event contains a lepton from the decay of bottom or charm hadrons. These are grouped into the nonprompt-lepton category, together with contributions that can arise, for example, from the decays of mesons, photon conversions to e^+e^- pairs in the material of the detector, or effects from detector resolution. The non-prompt-lepton background is estimated from an extrapolation of a control region of same-sign (SS) dilepton events to the signal region of opposite-sign (OS) dileptons. The SS control region is defined using the same criteria as used for the nominal signal region, except requiring $e\mu$ pairs of the same charge. The SS dilepton events predominantly contain at least one misidentified lepton. Other SM processes, such as DY, tW, VV and $t\bar{t}$ dilepton production have significantly smaller contributions, and are estimated using
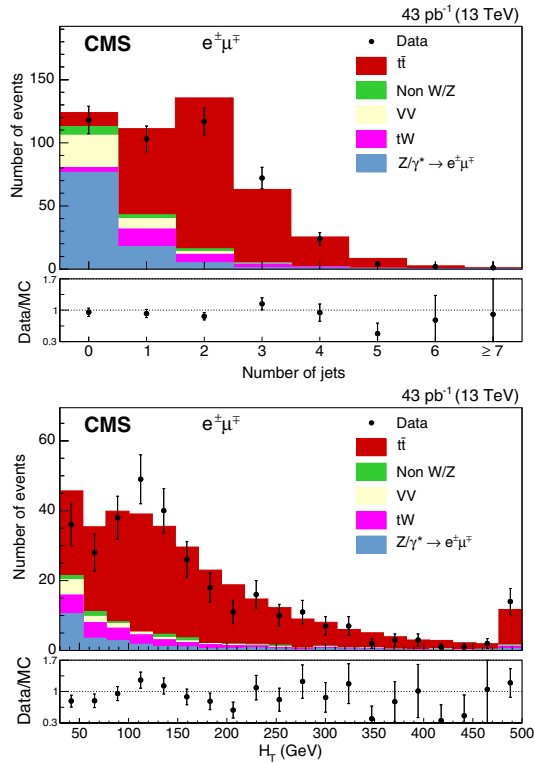
FIG. 1.   The distributions in (top) the jet multiplicity, and (bottom) H_T in events passing the dilepton criteria. The expected distributions for $t\bar{t}$ signal and individual backgrounds are shown after implementing data-based corrections; the last bin contains the overflow events. The ratios of data to the sum of the expected yields are given at the bottom of each panel.
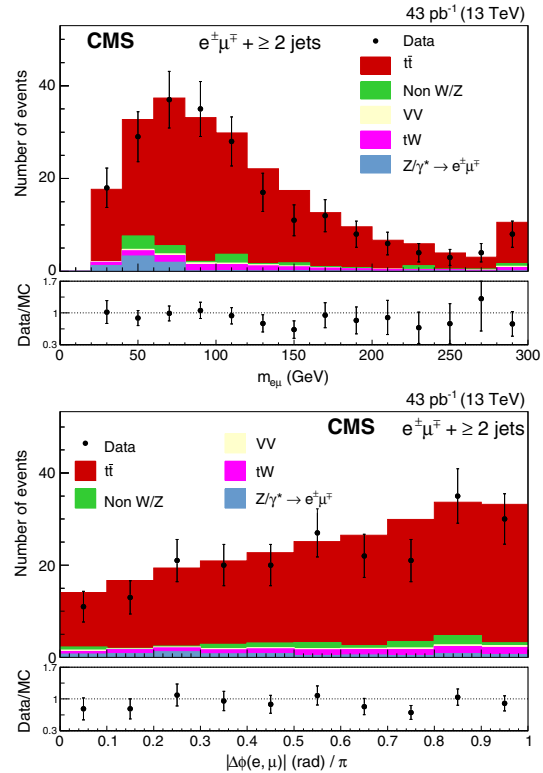
FIG. 2.   The distributions in (top) the dilepton invariant mass, and (bottom) the difference in the azimuthal angle between the two leptons after all selections. The last bin in (top) contains the overflow events. The ratios of data to the sum of the expected yields are given at the bottom of each panel.

simulation. The scaling from the SS control region in data to the signal region is performed using an extrapolation factor, extracted from MC simulation, given by the ratio of the number of OS events with misidentified leptons to the number of SS events with misidentified leptons. From the eight same-sign events observed in data, the expected contamination of 1.7 ± 0.4 events due to DY, tW, VV and $t\bar{t}$ dilepton production is subtracted, and the result is multiplied by the OS to SS ratio of 1.4 ± 0.3 to obtain an estimate of 8.5 ± 4.4 nonprompt lepton events contaminating the signal, including statistical and systematic uncertainties. This agrees with predictions from MC simulations of semileptonic $t\bar{t}$ and $W + $ jets events.

Figure 1 (top) shows the multiplicity of jets and (bottom) the scalar p_T sum of all jets (H_T) for events passing the dilepton criteria. Agreement is observed between data and the predictions for signal and background.

After requiring at least two jets, we obtain the plots presented in Fig. 2, where (top) shows the distribution in

the invariant dilepton mass $m_{e\mu}$, which is sensitive to the existence of a new heavy object decaying into a $t\bar{t}$ pair. Figure 2 (bottom) shows the difference in azimuthal angle between the two leptons, $\Delta\phi(e, \mu)$, and explores the correlation between the t and $\bar{t}$ spins [61–66]. For both distributions, data are in agreement with the SM expectations.

The dominant uncertainty is due to the preliminary integrated luminosity, which is estimated from x-y beam-beam scans performed in July 2015 utilizing the methods of Ref. [67]. The resulting uncertainty in the integrated luminosity is 4.8%.

Smaller uncertainties arise from the measured trigger efficiency, and the lepton identification and isolation efficiencies. After the offline dilepton selection, the trigger efficiency is measured in data to be $(91 \pm 4)\%$ using triggers based on the p_T imbalance in the event. This efficiency is applied to the MC simulations and the uncertainty is taken as a global uncertainty. The uncertainties on the electron and muon identification and isolation

efficiencies are estimated by changing the p_T- and η-dependent SF values by one standard deviation ($\pm 1\sigma$). The modeling of lepton energy scales is studied using $Z \rightarrow ee$ and $\mu\mu$ events in data and in simulation, yielding an uncertainty in the electron energy scale of 1%, and in the muon energy scale of 0.5%. The impact of the uncertainty in the jet energy scale (JES) is estimated by changing the p_T—and η-dependent JES SF by $\pm 1\sigma$, and the uncertainty in jet energy resolution (JER) uncertainty is estimated through similar η-dependent $\pm 1\sigma$ changes in the JER SF. The maximum of each of the deviations is taken as the uncertainty.

The distribution of the number of vertices per beam crossing is compared between data and simulation. The results indicate agreement of the total pp inelastic cross section within 10%. The result of varying this cross section by $\pm 10\%$ for all MC samples is used to obtain the systematic uncertainty due to pileup.

Theory uncertainties on $t\bar{t}$ production involve the systematic bias related to the missing higher-order diagrams in POWHEG, and is estimated through studies of the signal acceptance by changing the renormalization and factorization scales in POWHEG simultaneously within the range $[\mu/2, 2\mu]$ ($\mu = \mu_R = \mu_F$). In addition, the predictions of the NLO generators MG5_AMC@NLO (v5_2.2.2) and POWHEG are compared for $t\bar{t}$ production, where both use PYTHIA (v8.205) for hadronization, parton showering, and simulation of the underlying event. The uncertainty arising from the hadronization model mainly affects the JES and the fragmentation of jets. The uncertainty in the JES already contains a contribution from the uncertainty in the hadronization. The hadronization uncertainty is also determined by comparing samples of events generated with POWHEG, where the hadronization is either modeled with PYTHIA (v8.205) or HERWIG++ (v2.7.1). This also includes differences in parton showering, and the underlying event, and is called $t\bar{t}$ modeling uncertainty. All theory uncertainties on $t\bar{t}$ production are taken as the maximum difference found in the results. The uncertainty from the choice of PDF is determined by reweighting the sample of simulated $t\bar{t}$ events according to the 26 CT10 NLO [49,50] and the 100 NNPDF3.0 sets [25] of PDF uncertainties.

An uncertainty of 30% in cross sections for tW and VV backgrounds are taken from measurements [68–76]. For DY production, a global cross section uncertainty of 15% is applied, which is derived from the variation of the SF for events passing the dilepton criteria and events passing all selection cuts. The systematic uncertainty in the estimated nonprompt lepton background is given mainly by the systematic uncertainty in the ratio of OS to SS events with misidentified leptons in the MC simulations. We checked how well the simulation models the production of misidentified leptons by examining additional control regions, with the observed discrepancy used to assign an uncertainty of 23% to the method.

TABLE I.   Summary of individual contributions to the systematic uncertainty in the $\sigma_{t\bar{t}}$ measurement. The uncertainties are given in pb, and as relative uncertainties. The separate total systematic uncertainty without integrated luminosity, the part attributed to the integrated luminosity, and the statistical contributions are added in quadrature to obtain the total uncertainty.

Source	$\Delta\sigma_{t\bar{t}}$ (pb)	$\Delta\sigma_{t\bar{t}}/\sigma_{t\bar{t}}$ (%)
Trigger efficiencies	33	4.4
Lepton efficiencies	25	3.4
Lepton energy scale	< 1	≤ 0.1
Jet energy scale	11	1.5
Jet energy resolution	< 1	≤ 0.1
Pileup	5.2	0.7
QCD scales	1.4	0.2
NLO generator of $t\bar{t}$ signal	14	1.9
Modeling of $t\bar{t}$ signal	13	1.8
PDF	18	2.4
Single top tW background	13	1.8
VV background	3.5	0.5
Drell-Yan background	4.1	0.5
Nonprompt leptons background	7.6	1.0
Total systematic (w/o luminosity)	53	7.2
Integrated luminosity	36	4.8
Statistical uncertainty	58	7.8
Total	87	12

Table I summarizes the magnitude of the statistical and systematic uncertainties from different sources contributing to the $t\bar{t}$ production cross section. All sources of uncertainties are added in quadrature.

Table II shows the total number of events observed in data, together with the total number of background events expected from simulation or estimated from data. The mean acceptance multiplied by the selection efficiency and the branching fraction, as estimated from simulation at $m_t = 172.5$ GeV, is $\epsilon = (0.60 \pm 0.04)\%$, including statistical and systematic uncertainties. The measured fiducial cross section for $t\bar{t}$ production with two leptons (one electron and one muon) in the range $p_T > 20$ GeV and $|\eta| < 2.4$ is $\sigma_{t\bar{t}}^{\text{fid}} = 12.4 \pm 1.0(\text{stat}) \pm 1.0(\text{syst}) \pm 0.6(\text{lumi})$ pb. After applying all corrections, the inclusive

TABLE II.   The number of $e\mu$ events after final event selection expected for background, and observed in data. The uncertainties represent the statistical and systematic components added in quadrature.

Source	Number of events $e^{\pm}\mu^{\mp}$
Drell–Yan	6.9 ± 1.2
Nonprompt leptons	8.5 ± 4.4
tW	10.9 ± 3.4
VV	2.7 ± 0.9
Total background	29.1 ± 5.7
Data	220

cross section is measured to be $\sigma_{t\bar{t}} = 746 \pm 58(\text{stat}) \pm 53(\text{syst}) \pm 36(\text{lumi})$ pb.

A linear parametrization of the acceptance dependence on m_t in the range 169.5–175.5 GeV results in a cross section reduction of $\approx 0.7\%$ at $m_t = 173.34$ GeV, the current world average of the top quark mass [24].

In an alternative analysis, the selected sample is split into events with 0, 1, 2, and > 2 b quark jets, and 0, 1, 2, and > 2 additional light-flavor or gluon jets (i.e., not identified as b quark jets). Jets are identified as b quark jets using the combined secondary vertex (CSV) algorithm [77]. A maximum likelihood fit of the yields in different input samples is performed to extract simultaneously $\sigma_{t\bar{t}}$ and the b tagging efficiency. Systematic uncertainties are implemented through nuisance parameters [78]. This result is within 1% of the nominal analysis.

Figure 1 in the Supplemental Material [79] presents a summary of results for $\sigma_{t\bar{t}}$ from the combination of the Tevatron measurements at 1.96 TeV [80], from CMS measurements at $\sqrt{s} = 7$ and 8 TeV [14,19], and from the measurement presented here at $\sqrt{s} = 13$ TeV, compared to the NNLO + NNLL predictions as a function of $\sqrt{s}$ for $p\bar{p}$ and pp collisions [44].

In summary, the first measurement of the $t\bar{t}$ production cross section in proton-proton collisions at $\sqrt{s} = 13$ TeV is presented for events containing an electron-muon pair and at least two jets. The measurement is obtained through an event-counting analysis based on a data sample corresponding to an integrated luminosity of 43 pb^{-1}. The result is $\sigma_{t\bar{t}} = 746 \pm 58(\text{stat}) \pm 53(\text{syst}) \pm 36(\text{lumi})$ pb, with a total relative uncertainty of 12%. This measurement is consistent with the SM prediction of $\sigma_{t\bar{t}}^{\text{NNLO+NNLL}} = 832^{+40}_{-46}$ pb for a top quark mass of 172.5 GeV.

---

[1] ATLAS Collaboration, Measurement of the top pair production cross section in 8 TeV proton-proton collisions using kinematic information in the lepton + jets final state with ATLAS, Phys. Rev. D **91**, 112013 (2015).

[2] ATLAS Collaboration, Differential top-antitop cross-section measurements as a function of observables constructed from final-state particles using pp collisions at $\sqrt{s} = 7$ TeV in the ATLAS detector, J. High Energy Phys. 06 (2015) 100.

[3] ATLAS Collaboration, Measurement of the $t\bar{t}$ production cross-section as a function of jet multiplicity and jet transverse momentum in 7 TeV proton-proton collisions with the ATLAS detector, J. High Energy Phys. 01 (2015) 020.

[4] ATLAS Collaboration, Simultaneous measurements of the $t\bar{t}$, and Z/$\gamma^* \to \tau\tau$ production cross sections in pp collisions at $\sqrt{s} = 7$ TeV with the ATLAS detector, Phys. Rev. D **91**, 052005 (2015).

[5] ATLAS Collaboration, Measurements of normalized differential cross sections for $t\bar{t}$ production in pp collisions at $\sqrt{s} = 7$ TeV using the ATLAS detector, Phys. Rev. D **90**, 072004 (2014).

[6] ATLAS Collaboration, Measurement of the $t\bar{t}$ production cross-section using $e\mu$ events with b-tagged jets in pp collisions at $\sqrt{s} = 7$ and 8 TeV with the ATLAS detector, Eur. Phys. J. C **74**, 3109 (2014).

[7] ATLAS Collaboration, Measurement of the $t\bar{t}$ production cross section in the $\tau +$ jets channel using the ATLAS detector, Eur. Phys. J. C **73**, 2328 (2013).

[8] ATLAS Collaboration, Measurement of the top quark pair cross section with ATLAS in pp collisions at $\sqrt{s} = 7$ TeV using final states with an electron or a muon and a hadronically decaying τ lepton, Phys. Lett. B **717**, 89 (2012).

[9] ATLAS Collaboration, Measurement of $t\bar{t}$ production with a veto on additional central jet activity in pp collisions at $\sqrt{s} = 7$ TeV using the ATLAS detector, Eur. Phys. J. C **72**, 2043 (2012).

[10] ATLAS Collaboration, Measurement of the cross section for top-quark pair production in pp collisions at $\sqrt{s} = 7$ TeV with the ATLAS detector using final states with two high-p_{T} leptons, J. High Energy Phys. 05 (2012) 059.

[11] ATLAS Collaboration, Measurement of the top quark pair production cross-section with ATLAS in the single lepton channel, Phys. Lett. B **711**, 244 (2012).

[12] CMS Collaboration, Measurement of the differential cross section for top quark pair production in pp collisions at $\sqrt{s} = 8$ TeV, Eur. Phys. J. C **75**, 542 (2015).

[13] CMS Collaboration, Measurement of the $t\bar{t}$ production cross section in pp collisions at $\sqrt{s} = 8$ TeV in dilepton final states containing one τ lepton, Phys. Lett. B **739**, 23 (2014).

[14] CMS Collaboration, Measurement of the $t\bar{t}$ production cross section in the dilepton channel in pp collisions at $\sqrt{s} = 8$ TeV, J. High Energy Phys. 02 (2014) 024.

[15] CMS Collaboration, Measurement of the $t\bar{t}$ production cross section in the all-jet final state in pp collisions at $\sqrt{s} = 7$ TeV, J. High Energy Phys. 05 (2013) 065.

[16] CMS Collaboration, Measurement of the $t\bar{t}$ production cross section in the $\tau +$ jets channel in pp collisions at $\sqrt{s} = 7$ TeV, Eur. Phys. J. C **73**, 2386 (2013).

[17] CMS Collaboration, Measurement of the $t\bar{t}$ production cross section in pp collisions at $\sqrt{s} = 7$ TeV with lepton + jets final states, Phys. Lett. B **720**, 83 (2013).

[18] CMS Collaboration, Measurement of differential top-quark-pair production cross sections in pp colisions at $\sqrt{s} = 7$ TeV, Eur. Phys. J. C **73**, 2339 (2013).

[19] CMS Collaboration, Measurement of the $t\bar{t}$ production cross section in the dilepton channel in pp collisions at $\sqrt{s} = 7$ TeV, J. High Energy Phys. 11 (2012) 067.

[20] CMS Collaboration, Measurement of the $t\bar{t}$ production cross section in pp collisions at $\sqrt{s} = 7$ TeV in dilepton final states containing a τ, Phys. Rev. D **85**, 112007 (2012).

[21] CMS Collaboration, The CMS experiment at the CERN LHC, J. Instrum. **3**, S08004 (2008).

[22] S. Frixione, P. Nason, and C. Oleari, Matching NLO QCD computations with parton shower simulations: The POWHEG method, J. High Energy Phys. 11 (2007) 070.

[23] S. Alioli, P. Nason, C. Oleari, and E. Re, A general framework for implementing NLO calculations in shower Monte Carlo programs: The POWHEG BOX, J. High Energy Phys. 06 (2010) 043.

[24] ATLAS, CDF, CMS and D0 collaborations, First combination of Tevatron and LHC measurements of the top-quark mass, arXiv:1403.4427.

[25] F. Demartin, S. Forte, E. Mariani, J. Rojo, and A. Vicini, Impact of parton distribution function and α_S uncertainties on Higgs boson production in gluon fusion at hadron colliders, Phys. Rev. D **82**, 014002 (2010).

[26] T. Sjöstrand, S. Mrenna, and P. Skands, PYTHIA 6.4 physics and manual, J. High Energy Phys. 05 (2006) 026.

[27] T. Sjöstrand, S. Ask, J. R. Christiansen, R. Corke, N. Desai, P. Ilten, S. Mrenna, S. Prestel, C. O. Rasmussen, and P. Skands, An introduction to PYTHIA 8.2, Comput. Phys. Commun. **191**, 159 (2015).

[28] CMS Collaboration, Report No. CMS-PAS-GEN-14-001, 2014, https://cds.cern.ch/record/1697700.

[29] P. Skands, S. Carrazza, and J. Rojo, Tuning PYTHIA 8.1: The Monash 2013 tune, Eur. Phys. J. C **74**, 3024 (2014).

[30] M. Bähr, S. Gieseke, M. A. Gigg, D. Grellscheid, K. Hamilton, O. Latunde-Dada, S. Plätzer, P. Richardson, M. H. Seymour, A. Sherstnev, and B. R. Webber, Herwig + + physics and manual, Eur. Phys. J. C **58**, 639 (2008).

[31] J. Alwall, R. Frederix, S. Frixione, V. Hirschi, F. Maltoni, O. Mattelaer, H. S. Shao, T. Stelzer, P. Torrielli, and M. Zaro, The automated computation of tree-level and next-to-leading order differential cross sections, and their matching to

parton shower simulations, J. High Energy Phys. 07 (2014) 079.

[32] P. Artoisenet, R. Frederix, O. Mattelaer, and R. Rietkerk, Automatic spin-entangled decays of heavy resonances in Monte Carlo simulations, J. High Energy Phys. 03 (2013) 015.

[33] CMS Collaboration, Measurement of $t\bar{t}$ production with additional jet activity, including b quark jets, in the dilepton channel using pp collisions at $\sqrt{s} = 8$ TeV, arXiv: 1510.03072.

[34] S. Alioli, P. Nason, C. Oleari, and E. Re, NLO single-top production matched with shower in POWHEG: s- and t-channel contributions, J. High Energy Phys. 09 (2009) 111.

[35] E. Re, Single-top Wt-channel production matched with parton showers using the POWHEG method, Eur. Phys. J. C **71**, 1547 (2011).

[36] N. Kidonakis, in *Proceedings, Helmholtz International Summer School on Physics of Heavy Quarks and Hadrons (HQ 2013)* (Verlag Deutsches Elektronen-Synchrotron, Hamburg, 2014), p. 139.

[37] J. M. Campbell and R. K. Ellis, MCFM for the Tevatron and the LHC, Nucl. Phys. B, Proc. Suppl. **205–206**, 10 (2010).

[38] M. Czakon and A. Mitov, Top + +: A program for the calculation of the top-pair cross-section at hadron colliders, Comput. Phys. Commun. **185**, 2930 (2014).

[39] M. Beneke, P. Falgari, S. Klein, and C. Schwinn, Hadronic top-quark pair production with NNLL threshold resummation, Nucl. Phys. **B855**, 695 (2012).

[40] M. Cacciari, M. Czakon, M. Mangano, A. Mitov, and P. Nason, Top-pair production at hadron colliders with next-to-next-to-leading logarithmic soft-gluon resummation, Phys. Lett. B **710**, 612 (2012).

[41] P. Baernreuther, Michal Czakon, and Alexander Mitov, Percent-Level-Precision Physics at the Tevatron: Next-to-Next-to-Leading Order QCD Corrections to $q\bar{q} \rightarrow t\bar{t} + X$, Phys. Rev. Lett. **109**, 132001 (2012).

[42] M. Czakon and A. Mitov, NNLO corrections to top-pair production at hadron colliders: The all-fermionic scattering channels, J. High Energy Phys. 12 (2012) 054.

[43] M. Czakon and A. Mitov, NNLO corrections to top pair production at hadron colliders: The quark-gluon reaction, J. High Energy Phys. 01 (2013) 080.

[44] M. Czakon, P. Fiedler, and A. Mitov, Total Top-Quark Pair-Production Cross Section at Hadron Colliders Through $O(\alpha_S^4)$, Phys. Rev. Lett. **110**, 252004 (2013).

[45] M. Botje *et al.*, The PDF4LHC Working Group Interim Recommendations, arXiv:1101.0538.

[46] S. Alekhin *et al.*, The PDF4LHC Working Group Interim Report, arXiv:1101.0536.

[47] A. D. Martin, W. J. Stirling, R. S. Thorne, and G. Watt, Parton distributions for the LHC, Eur. Phys. J. C **63**, 189 (2009).

[48] A. D. Martin, W. J. Stirling, R. S. Thorne, and G. Watt, Uncertainties on α_s in global PDF analyses and implications for predicted hadronic cross sections, Eur. Phys. J. C **64**, 653 (2009).

[49] H.-L. Lai, M. Guzzi, J. Huston, Z. Li, P. M. Nadolsky, J. Pumplin, and C. P. Yuan, New parton distributions for collider physics, Phys. Rev. D **82**, 074024 (2010).

[50] J. Gao, M. Guzzi, J. Huston, H.-L. Lai, Z. Li, P. Nadolsky, J. Pumplin, D. Stump, and C. P. Yuan, CT10 next-to-next-to-leading order global analysis of QCD, Phys. Rev. D **89,** 033009 (2014).

[51] R. D. Ball *et al.* (NNPDF), Parton distributions with LHC data, Nucl. Phys. **B867,** 244 (2013).

[52] CMS Collaboration, Report No. CMS-PAS-PFT-09-001, 2009, http://cdsweb.cern.ch/record/1194487.

[53] CMS Collaboration, Report No. CMS-PAS-PFT-10-001, 2010, http://cdsweb.cern.ch/record/1247373.

[54] CMS Collaboration, Performance of electron reconstruction and selection with the CMS detector in proton-proton collisions at $\sqrt{s} = 8$ TeV, J. Instrum. **10,** P06005 (2015).

[55] CMS Collaboration, The performance of the CMS muon detector in proton-proton collisions at $\sqrt{s} = 7$ TeV at the LHC, J. Instrum. **8,** P11002 (2013).

[56] CMS Collaboration, Measurements of inclusive W and Z cross sections in pp collisions at $\sqrt{s} = 7$ TeV, J. High Energy Phys. 01 (2011) 080.

[57] M. Cacciari, G. P. Salam, and G. Soyez, The anti-k_t jet clustering algorithm, J. High Energy Phys. 04 (2008) 063.

[58] CMS Collaboration, Determination of jet energy calibration and transverse momentum resolution in CMS, J. Instrum. **6,** P11002 (2011).

[59] CMS Collaboration, Measurement of the $t\bar{t}$ production cross section and the top quark mass in the dilepton channel in pp collisions at $\sqrt{s} = 7$ TeV, J. High Energy Phys. 07 (2011) 049.

[60] CMS Collaboration, First measurement of the cross section for top-quark pair production in proton-proton collisions at $\sqrt{s} = 7$ TeV, Phys. Lett. B **695,** 424 (2011).

[61] G. Mahlon and S. J. Parke, Spin correlation effects in top quark pair production at the LHC, Phys. Rev. D **81,** 074024 (2010).

[62] W. Bernreuther and Z.-G. Si, Top quark spin correlations and polarization at the LHC: Standard model predictions and effects of anomalous top chromo moments, Phys. Lett. B **725,** 115 (2013).

[63] ATLAS Collaboration, Measurement of Spin Correlation in Top-Antitop Quark Events and Search for Top Squark Pair Production in pp Collisions at $\sqrt{s} = 8$ TeV Using the ATLAS Detector, Phys. Rev. Lett. **114,** 142001 (2015).

[64] ATLAS Collaboration, Measurements of spin correlation in top-antitop quark events from proton-proton collisions at $\sqrt{s} = 7$ TeV using the ATLAS detector, Phys. Rev. D **90,** 112016 (2014).

[65] ATLAS Collaboration, Observation of Spin Correlation in $t\bar{t}$ Events from pp Collisions at $\sqrt{s} = 7$ TeV using the ATLAS Detector, Phys. Rev. Lett. **108,** 212001 (2012).

[66] CMS Collaboration, Measurements of $t\bar{t}$ Spin Correlations and Top-Quark Polarization Using Dilepton Final States in

pp Collisions at $\sqrt{s} = 7$ TeV, Phys. Rev. Lett. **112,** 182001 (2014).

[67] CMS Collaboration, Report No. CMS-PAS-LUM-13-001, 2013, http://cdsweb.cern.ch/record/1643269.

[68] CMS Collaboration, Measurement of the W^+W^- and ZZ production cross sections in pp collisions at $\sqrt{s} = 8$ TeV, Phys. Lett. B **721,** 190 (2013).

[69] CMS Collaboration, Measurement of the W^+W^- cross section in pp collisions at $\sqrt{s} = 7$ TeV and limits on anomalous $WW\gamma$ and WWZ couplings, Eur. Phys. J. C **73,** 2610 (2013).

[70] CMS Collaboration, Measurement of W^+W^- production and search for the Higgs boson in pp collisions at $\sqrt{s} = 7$ TeV, Phys. Lett. B **699,** 25 (2011).

[71] CMS Collaboration, Measurement of the sum of WW and WZ production with W + dijet events in pp collisions at $\sqrt{s} = 7$ TeV, Eur. Phys. J. C **73,** 2283 (2013).

[72] CMS Collaboration, Measurement of the ZZ production cross section and search for anomalous couplings in $2\ell 2\ell'$ final states in pp collisions at $\sqrt{s} = 7$ TeV, J. High Energy Phys. 01 (2013) 063.

[73] CMS Collaboration, Measurement of the single-top-quark t-channel cross section in pp collisions at $\sqrt{s} = 7$ TeV, J. High Energy Phys. 12 (2012) 035.

[74] ATLAS Collaboration, Measurement of the WW cross section in $\sqrt{s} = 7$ TeV pp collisions with the ATLAS detector and limits on anomalous gauge couplings, Phys. Lett. B **712,** 289 (2012).

[75] ATLAS Collaboration, Measurement of the $W^\pm Z$ production cross section and limits on anomalous triple gauge couplings in proton-proton collisions at $\sqrt{s} = 7$ TeV with the ATLAS detector, Phys. Lett. B **709,** 341 (2012).

[76] ATLAS Collaboration, Measurement of the ZZ Production Cross Section and Limits on Anomalous Neutral Triple Gauge Couplings in Proton-Proton Collisions at $\sqrt{s} = 7$ TeV with the ATLAS Detector, Phys. Rev. Lett. **108,** 041804 (2012).

[77] CMS Collaboration, Identification of b-quark jets with the CMS experiment, J. Instrum. **8,** P04013 (2013).

[78] D. A. S. Fraser, N. Reid, and A. C. M. Wong, Inference for bounded parameters, Phys. Rev. D **69,** 033002 (2004).

[79] See Supplemental Material at http://link.aps.org/supplemental/10.1103/PhysRevLett.116.052002 for a figure of top-quark pair production cross section measurements as a function of the center-of-mass energy.

[80] CDF and D0 Collaborations, Combination of measurements of the top-quark pair production cross section from the Tevatron Collider, Phys. Rev. D **89,** 072001 (2014).

V. Khachatryan,[1] A. M. Sirunyan,[1] A. Tumasyan,[1] W. Adam,[2] E. Asilar,[2] T. Bergauer,[2] J. Brandstetter,[2] E. Brondolin,[2] M. Dragicevic,[2] J. Erö,[2] M. Flechl,[2] M. Friedl,[2] R. Frühwirth,[2,b] V. M. Ghete,[2] C. Hartl,[2] N. Hörmann,[2] J. Hrubec,[2] M. Jeitler,[2,b] V. Knünz,[2] A. König,[2] M. Krammer,[2,b] I. Krätschmer,[2] D. Liko,[2] T. Matsushita,[2] I. Mikulec,[2] D. Rabady,[2,c] B. Rahbaran,[2] H. Rohringer,[2] J. Schieck,[2,b] R. Schöfbeck,[2] J. Strauss,[2] W. Treberer-Treberspurg,[2] W. Waltenberger,[2]

104

Measurement of the $t\bar{t}$ production cross section in the eμ channel in proton-proton collisions at $\sqrt{s} = 7$ and 8 TeV

The CMS collaboration

E-mail: cms-publication-committee-chair@cern.ch

ABSTRACT: The inclusive cross section for top quark pair production is measured in proton-proton collisions at $\sqrt{s} = 7$ and 8 TeV, corresponding to 5.0 and 19.7 fb^{-1}, respectively, with the CMS experiment at the LHC. The cross sections are measured in the electron-muon channel using a binned likelihood fit to multi-differential final state distributions related to identified b quark jets and other jets in the event. The measured cross section values are $173.6 \pm 2.1\,(\text{stat})^{+4.5}_{-4.0}\,(\text{syst}) \pm 3.8\,(\text{lumi})$ pb at $\sqrt{s} = 7$ TeV, and $244.9 \pm 1.4(\text{stat})^{+6.3}_{-5.5}(\text{syst}) \pm 6.4\,(\text{lumi})$ pb at $\sqrt{s} = 8$ TeV, in good agreement with QCD calculations at next-to-next-to-leading-order accuracy. The ratio of the cross sections measured at 7 and 8 TeV is determined, as well as cross sections in the fiducial regions defined by the acceptance requirements on the two charged leptons in the final state. The cross section results are used to determine the top quark pole mass via the dependence of the theoretically predicted cross section on the mass, giving a best result of $173.8^{+1.7}_{-1.8}$ GeV. The data at $\sqrt{s} = 8$ TeV are also used to set limits, for two neutralino mass values, on the pair production of supersymmetric partners of the top quark with masses close to the top quark mass.

JHEP08(2016)029

Contents

1 Introduction

The study of top quark pair ($t\bar{t}$) production in proton-proton (pp) collisions at the CERN LHC provides an important test of the standard model (SM). The total production cross section, $\sigma_{t\bar{t}}$, can be accurately predicted by quantum chromodynamics (QCD) calculations at next-to-next-to-leading order (NNLO). A measurement of $\sigma_{t\bar{t}}$ can thus provide constraints on essential ingredients in the calculation, such as the top quark mass, the proton

parton distribution functions (PDFs), and the strong coupling α_{s}. Furthermore, deviations from these predictions can be an indication of physics beyond the SM. For example, in supersymmetric (SUSY) models, $\mathrm{t\bar{t}}$ pairs may appear as decay products of heavier new particles, increasing the $\mathrm{t\bar{t}}$ yields.

Studies of the $\mathrm{t\bar{t}}$ production cross section, as well as dedicated searches for deviations from the SM predictions, have been performed in recent years by the ATLAS and CMS collaborations using a variety of production and decay channels [1–22]. So far, all results are consistent with the SM.

This paper presents a new measurement of $\sigma_{\mathrm{t\bar{t}}}$ in pp collisions at centre-of-mass energies of 7 and 8 TeV. The measurement is performed in the eμ channel, where each W boson from the top quark decays into a charged lepton and a neutrino. Compared to the previous CMS analyses in the dilepton channel at 7 TeV [8] and 8 TeV [1], the new measurement is performed using the complete CMS data samples recorded in the years 2011 and 2012, with integrated luminosities of 5.0 and 19.7 fb^{-1} at $\sqrt{s} = 7$ and 8 TeV, respectively. The restriction to the eμ channel provides a pure $\mathrm{t\bar{t}}$ event sample owing to the negligible contamination from Z/γ^* processes with same-flavoured leptons in the final state. The event selection is based on the kinematic properties of the leptons. An improved cross section extraction method is used, performing a template fit of the signal and background contributions to multi-differential binned distributions related to the multiplicity of b quark jets (referred to as b jets in the following) and the multiplicity and transverse momenta of other jets in the event. The results obtained with this method (referred to as the "reference method" in the following) are cross-checked with an analysis performed using an event counting method.

The cross section is first determined in a fiducial ("visible") range, $\sigma_{\mathrm{t\bar{t}}}^{\mathrm{vis}}$, defined by requirements on the transverse momentum and pseudorapidity of the electron and muon. The results are then extrapolated to obtain the cross section in the full phase space, $\sigma_{\mathrm{t\bar{t}}}$, with an additional assessment of the extrapolation uncertainties. The ratio of the cross sections at the two centre-of-mass energies is also presented. The measurements of $\sigma_{\mathrm{t\bar{t}}}$ at 7 and 8 TeV are used to determine, together with the NNLO prediction [23], the top quark pole mass. Following a previous CMS analysis [24], the mass is determined via the dependence of the theoretically predicted cross section on the top quark mass.

The data are also used to constrain the cross section of pair production of the lightest supersymmetric partner of the top quark, the top squark, in the context of SUSY models with R-parity conservation [25]. The study focuses on models predicting the decay of top squarks into a top quark and a neutralino, $\widetilde{\mathrm{t}} \to \mathrm{t}\widetilde{\chi}_1^0$, and the three-body decay, $\widetilde{\mathrm{t}} \to \mathrm{bW}\widetilde{\chi}_1^0$, with the neutralino assumed to be the lightest supersymmetric particle (LSP) [26]. The pair production and the subsequent decays of the top squarks can lead to a final state that is very similar to the SM $\mathrm{t\bar{t}}$ events. The search is performed with the 8 TeV data, looking for an excess of the observed event yields of $\mathrm{t\bar{t}}$ events with respect to the SM predictions. Exclusion limits are set with 95% confidence level (CL) for the SUSY signal strength as a function of the top squark mass for two neutralino mass hypotheses. Previous measurements setting exclusion limits in a similar regime can be found in [14, 27].

This paper is structured as follows. Section 2 contains a brief description of the CMS detector, followed by details of the event simulation and theoretical calculations for the $\mathrm{t\bar{t}}$

cross section are given in section 3. The event selection and the definitions of the visible and total cross sections are given in sections 4 and 5, respectively. The methods used to measure the cross section are explained in section 6 and the systematic uncertainties are described in section 7. The measured $t\bar{t}$ production cross sections are reported in section 8, with the extraction of the top quark mass presented in section 9. The search for SUSY is described in section 10 and a summary is provided in section 11.

2   The CMS detector

The central feature of the CMS apparatus is a superconducting solenoid of 6 m internal diameter, providing a magnetic field of 3.8 T. Within the solenoid volume are a silicon pixel and strip tracker, a lead tungstate crystal electromagnetic calorimeter (ECAL), and a brass and scintillator hadron calorimeter (HCAL), each composed of a barrel and two endcap sections. Extensive forward calorimetry complements the coverage provided by the barrel and endcap detectors. Muons are measured in gas-ionisation detectors embedded in the steel flux-return yoke outside the solenoid. A more detailed description of the CMS detector, together with a definition of the coordinate system used and the relevant kinematic variables, can be found in ref. [28].

The particle-flow (PF) [29, 30] event algorithm reconstructs and identifies each individual particle with an optimised combination of information from the various elements of the CMS detector. The energy of photons is directly obtained from the ECAL measurement. The energy of electrons is determined from a combination of the electron momentum at the primary interaction vertex as determined by the tracker, the energy of the corresponding ECAL cluster, and the energy sum of all bremsstrahlung photons spatially compatible with originating from the electron track. The energy of muons is obtained from the curvature of the corresponding track. The energy of charged hadrons is determined from a combination of their momentum measured in the tracker and the matching ECAL and HCAL energy deposits, corrected for zero-suppression effects and for the response function of the calorimeters to hadronic showers. Finally, the energy of neutral hadrons is obtained from the corresponding corrected ECAL and HCAL energy.

3   Event simulation and theoretical calculations

Experimental effects, related to the event reconstruction and choice of selection criteria, together with the detector resolution, are modelled using Monte Carlo (MC) event generators interfaced with a detailed detector simulation. Unless specified, the same generators and parton shower models are used for the samples at 7 and 8 TeV.

The $t\bar{t}$ sample is simulated using the MADGRAPH event generator (v. 5.1.5.11) [31], which implements the relevant matrix elements at tree level with up to three additional partons. The MADSPIN [32] package is used to incorporate spin correlation effects. The value of the top quark mass is fixed to 172.5 GeV and the proton structure is described by the CTEQ6L1 [33] PDF set. The generated events are subsequently processed with PYTHIA (v. 6.426) [34] for parton showering and hadronisation, and the MLM prescription [35] is

used for matching of matrix-element jets to parton showers. Decays of τ leptons are handled with TAUOLA (v. 2.75) [36]. An additional $t\bar{t}$ signal sample, which is used to determine specific model uncertainties of the measurement, is obtained with the next-to-leading-order (NLO) generator POWHEG (v. 1.0 r1380) [37] and also interfaced with PYTHIA. In POWHEG, the value of the top quark mass is also set to 172.5 GeV, and the CT10 [38] PDF set is used to describe the proton structure. The PYTHIA Z2* tune, derived from the Z1 tune [39], is used to characterise the underlying event in the $t\bar{t}$ samples at 7 and 8 TeV. The Z1 tune uses the CTEQ5L PDF set, whereas Z2* adopts CTEQ6L. The propagation of the generated particles through the CMS detector and the modelling of the detector response is performed using GEANT4 (v. 9.4) [40].

Only $t\bar{t}$ pair decays into $e^{\pm}\mu^{\mp} + X$ in the final state are considered signal, including intermediate leptonic τ decays. The remaining $t\bar{t}$ decay modes are considered background processes and referred to as "$t\bar{t}$ bkg.".

The other SM background samples are simulated with MADGRAPH (without the MAD-SPIN package), POWHEG, or PYTHIA, depending on the process. The main background contributions originate from the production of W and Z/γ^* bosons with additional jets (referred to in the following as W+jets and Drell-Yan (DY), respectively), single top quark tW channel, diboson (WW, WZ, and ZZ, referred to as VV in the following), $t\bar{t}$ production in association with a Z, W, or γ boson (referred to as $t\bar{t}$V in the following), and QCD multijet events. The W+jets, DY, and $t\bar{t}$V samples are simulated with MADGRAPH with up to two additional partons in the final state. The POWHEG [41, 42] generator is used for simulating single top quark production, while PYTHIA is used to simulate diboson and QCD multijet events. Parton showering and hadronisation are also simulated with PYTHIA in all the background samples. The PYTHIA Z2* tune is used to characterise the underlying event in the background samples at $\sqrt{s} = 8$ TeV, while the Z2 tune [43] is used at $\sqrt{s} = 7$ TeV.

The simulated samples are normalised according to their expected total cross sections for integrated luminosities of 5.0 (19.7) fb^{-1} for $\sqrt{s} = 7$ (8) TeV. The expected cross sections are obtained from NNLO calculations for W+jets [44] and DY [45] processes, NLO+next-to-next-to-leading-log (NNLL) calculations for top quark tW or $\bar{t}$W channel [46], NLO calculations for VV [47], $t\bar{t}$+W [48], and $t\bar{t}$+Z [49] processes, and leading-order (LO) calculations for QCD multijet events [34].

A number of additional pp simulated hadronic interactions (pileup) are added to each simulated event to reproduce the multiple interactions in each bunch crossing in the data taking. The pileup events are generated using PYTHIA. Scale factors (SFs) described in section 4 are applied when needed to improve the description of the data by the simulation.

Calculations of the $\sigma_{t\bar{t}}$ at full NNLO accuracy in perturbative QCD, including the resummation of NNLL soft-gluon terms [50], are used to normalise the $t\bar{t}$ simulated samples and to extract the top quark pole mass. Assuming a top quark mass of 172.5 GeV, the predicted cross sections are:

$$\sigma_{t\bar{t}} = 177.3^{+4.7}_{-6.0}\,(\text{scale}) \pm\ \ 9.0\,(\text{PDF}+\alpha_s)\,\text{pb}, \quad \text{at } \sqrt{s} = 7\,\text{TeV and}$$
$$\sigma_{t\bar{t}} = 252.9^{+6.4}_{-8.6}\,(\text{scale}) \pm 11.7\,(\text{PDF}+\alpha_s)\,\text{pb}, \quad \text{at } \sqrt{s} = 8\,\text{TeV}.$$

The first uncertainty is an estimate of the effect of missing higher-order corrections and is determined by independent variations of the factorisation and renormalisation scales, μ_F and μ_R, by factors of two, up and down from their default values (the top quark mass). The second uncertainty is associated with variations in α_s and the PDF, following the PDF4LHC prescription with the MSTW2008 68% CL NNLO, CT10 NNLO, and NNPDF2.3 5f FFN PDF sets (as detailed in refs. [51, 52] and references therein, as well as in refs. [53–55]). These values were calculated using the Top++2.0 program [50]. The ratio of the cross sections at 7 and 8 TeV computed with NNPDF2.3, $R_{\mathrm{t\bar{t}}}^{\mathrm{NNLO}} = \sigma_{\mathrm{t\bar{t}}}(8\,\mathrm{TeV})/\sigma_{\mathrm{t\bar{t}}}(7\,\mathrm{TeV})$, is $1.437 \pm 0.001\,(\mathrm{scale}) \pm 0.006\,(\mathrm{PDF}) \pm 0.001\,(\alpha_\mathrm{s})$ [56].

4 Event selection

At trigger level, events are required to have one electron and one muon. For the 8 TeV data set one of the two leptons is required to have $p_\mathrm{T} > 17\,\mathrm{GeV}$ and the other $p_\mathrm{T} > 8\,\mathrm{GeV}$. For the 7 TeV data set both leptons are required to have $p_\mathrm{T} > 10\,\mathrm{GeV}$ or to fulfil the same criterion as for the 8 TeV data set. The eµ trigger efficiency is measured in data with a method based on triggers that are uncorrelated with those used in the analysis [1, 57]. In particular, the triggers require jets or missing transverse energy, which is defined as the magnitude of the projection, on the plane perpendicular to the beam direction, of the vector sum of the momenta of all reconstructed particles in an event. The trigger efficiency for events containing an eµ pair passing all selection criteria is approximately 96% at 7 TeV and 93% at 8 TeV. Using the eµ trigger efficiency measured in data, the corresponding efficiencies in the simulation are corrected by η-dependent SFs, which have an average value of 0.99 at 7 TeV and 0.97 at 8 TeV.

An interaction vertex [58] is required within 24 cm of the detector centre along the beam line direction, and within 2 cm of the beam line in the transverse plane. Among all such vertices, the primary vertex of an event is identified as the one with the largest value of the scalar sum of the p_T^2 of the associated tracks.

Leptons are required to have $p_\mathrm{T} > 20\,\mathrm{GeV}$ and $|\eta| < 2.4$. The lepton-candidate tracks are required to originate from the primary vertex.

Lepton candidates are required to be isolated from other PF candidates in the event. For each electron [59] or muon [60] candidate, a cone with $\Delta R = 0.3$ or 0.4, respectively, is constructed around the track direction at the primary vertex. Here ΔR is defined as $\Delta R = \sqrt{(\Delta\eta)^2 + (\Delta\phi)^2}$, where $\Delta\eta$ and $\Delta\phi$ are the differences in pseudorapidity and azimuthal angle (in radians) between any PF candidate and the lepton track direction. The scalar sum of the p_T of all PF candidates contained within the cone is calculated, excluding the contribution from the lepton candidate itself. All charged PF candidates not associated with the chosen primary vertex are assumed to arise from pileup events, and are excluded from the calculation of the p_T deposited in the cone. The neutral component is also corrected for pileup effects. The relative isolation discriminant, I_rel, is defined as the ratio of this sum to the p_T of the lepton candidate. An electron candidate is selected if $I_\mathrm{rel} < 0.10$; the corresponding requirement for muons is $I_\mathrm{rel} < 0.12$.

The efficiency of the lepton selection is measured using a "tag-and-probe" method in dilepton events enriched with Z boson candidates [8, 61]. The measured values for the

– 5 –

combined identification and isolation efficiencies are typically 80% for electrons and 90% for muons. The lepton identification efficiencies in simulation are corrected to the measured values in data by p_T and η dependent SFs, which have values in the range 0.97–0.99. From all events that contain oppositely charged lepton pairs, events are selected if the lepton pair with the largest value of the scalar sum of the p_T corresponds to an eμ pair. Candidate events with eμ invariant masses $m_{e\mu} < 20\,\mathrm{GeV}$ are removed to reduce the contamination from QCD multijet processes. This selection is referred to as "eμ selection".

Jets are reconstructed using the anti-k_T clustering algorithm [62] with a distance parameter $R = 0.5$. The algorithm uses the PF candidates as input objects. To minimise the impact of pileup, charged particle candidates not associated with the primary vertex are excluded. The jet energy is corrected for pileup in a manner similar to the correction of the total energy inside the lepton isolation cone. Additional jet energy corrections are also applied as a function of the jet p_T and η [63]. Jets are selected if they have $p_T > 30\,\mathrm{GeV}$ and $|\eta| < 2.4$ and the angular distance between them and the selected leptons satisfies $\Delta R(\mathrm{jet}, \mathrm{lepton}) > 0.5$.

As the $t\bar{t}$ events are expected to contain mainly jets from the hadronisation of b quarks, requiring the presence of b jets can reduce background from events without b quarks. Jets are identified as b jets (b-tagged) using the combined secondary vertex algorithm [64]. The discriminator threshold chosen for the reference method to extract the cross section corresponds to an identification efficiency for b jets of about 50% and a misidentification (mistag) probability of about 10% for c quark jets and 0.1% for light-flavour jets (u, d, s, and gluons). A looser discriminator threshold is chosen for the event counting method such that the efficiency is about 70% for jets originating from b quarks and 20% for c quark jets, while the probability of mistagging for jets originating from light flavours is around 1% [64]. For the reference method there are no constraints on the number of jets and b-tagged jets in the event.

Figures 1 and 2 show for the 7 and 8 TeV data and simulations, respectively, the p_T and η distributions of the highest (leading) and second-highest (subleading) p_T lepton from the selected eμ pair, after the eμ selection is applied. The data are compared to the expected distributions for the $t\bar{t}$ signal and individual backgrounds, which are derived from MC simulated samples. The contributions from QCD multijet, W+jets, and $t\bar{t}$ background processes arise from events where at least one jet is incorrectly reconstructed as a lepton or a lepton that does not originate from a prompt W or Z boson decay fulfils the selection criteria. These contributions are referred to as "non W/Z" background.

In general, the sum of the estimated contributions provides an adequate description of the data, within uncertainties. However, as observed previously [57], the simulation is seen to have a somewhat harder p_T spectrum than measured. The impact on the measurement is accounted for by including an additional modelling uncertainty.

Figure 3 shows the number of b-tagged jets in events passing the eμ selection at 7 and 8 TeV. It should be noted that the size of the uncertainties in figures 1–3 does not reflect those in the final measurements, which are constrained by the likelihood fit described in section 6.1. Good agreement is observed between data and the sum of the expected yields.
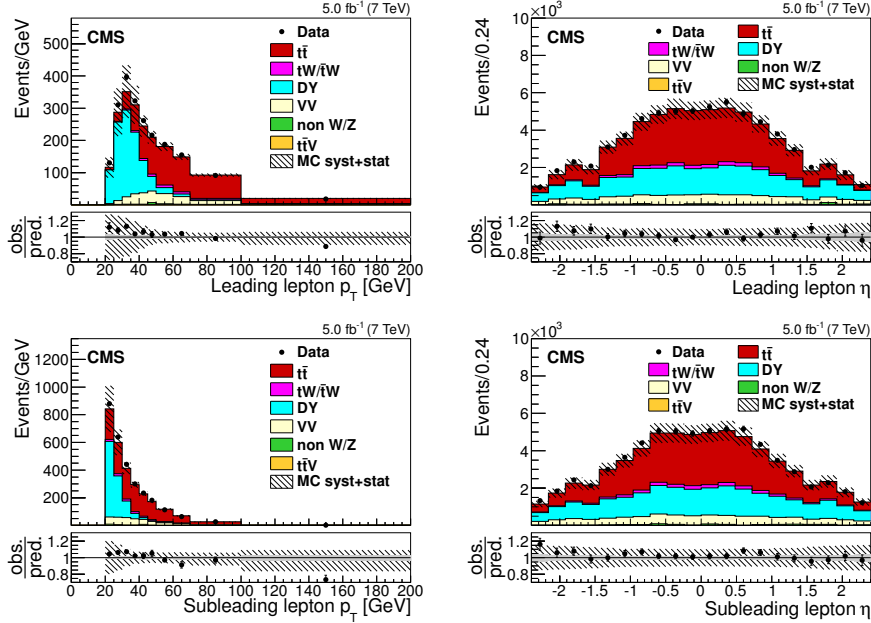
Figure 1. Distributions of p_T (left) and η (right) of the leading (top) and subleading (bottom) leptons, after the eμ selection, for the 7 TeV data. The last bin of the p_T distributions includes the overflow events. The hatched bands correspond to the total uncertainty in the sum of the predicted yields. The ratios of data to the sum of the predicted yields are shown at the bottom of each plot. Here, an additional solid gray band represents the contribution from the statistical uncertainty in the MC simulation. The contributing systematic uncertainties are discussed in section 7.

5 Cross section definitions

The $t\bar{t}$ production cross sections are first measured in a fiducial range, defined within the kinematic acceptance of the $t\bar{t}$ decay particles that are reconstructable in the detector. This avoids the need for extrapolating the cross sections into the unmeasured kinematic phase space of these particles. In this analysis the fiducial range is defined by the p_T and η requirements on the electron and muon in the final state. The visible cross section, $\sigma_{t\bar{t}}^{\text{vis}}$, is defined for events containing an oppositely charged eμ pair from the decay chain $t \to Wb \to \ell\nu b$ (including $W \to \tau\nu \to \ell\nu\nu\nu$) and with both leptons satisfying $p_T > 20\,\text{GeV}$ and $|\eta| < 2.4$. This visible cross section is then extrapolated to obtain the cross section for $t\bar{t}$ production at parton level in the full phase space using the formula

$$\sigma_{t\bar{t}} = \frac{\sigma_{t\bar{t}}^{\text{vis}}}{A_{e\mu}}. \tag{5.1}$$

Here, $A_{e\mu}$ denotes the acceptance defined as the fraction of all $t\bar{t}$ events fulfilling the above selection criteria for the visible cross section. The acceptance is determined from the
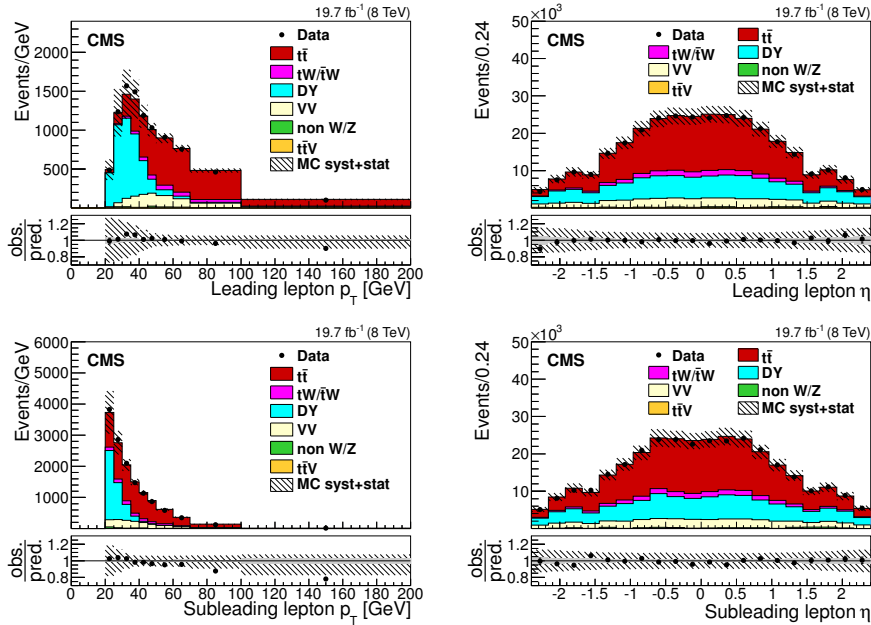
Figure 2. Distributions of p_T (left) and η (right) of the leading (top) and subleading (bottom) leptons, after the eμ selection, for the 8 TeV data. The last bin of the p_T distributions includes the overflow events. The hatched bands correspond to the total uncertainty in the sum of the predicted yields. The ratios of data to the sum of the predicted yields are shown at the bottom of each plot. Here, an additional solid grey band represents the contribution from the statistical uncertainty in the MC simulation. The contributing systematic uncertainties are discussed in section 7.

Figure 3. Number of b-tagged jets after the eμ selection for 7 TeV (left) and 8 TeV (right). The hatched bands correspond to the total uncertainty in the sum of the predicted yields. The ratios of data to the sum of the predicted yields are shown at the bottom of each plot. Here, an additional solid grey band represents the contribution from the statistical uncertainty in the MC simulation. The contributing systematic uncertainties are discussed in section 7.
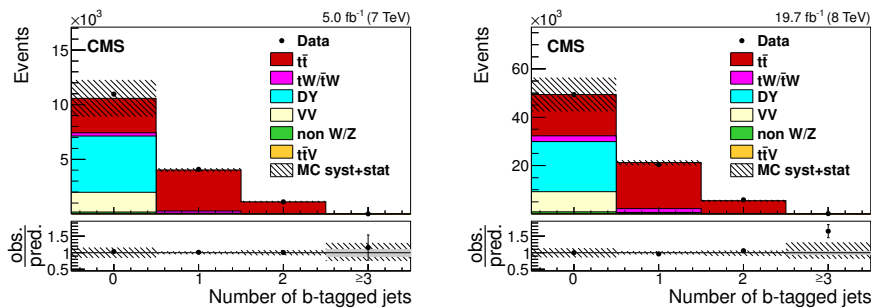
– 8 –

simulated $t\bar{t}$ signal sample, and includes the leptonic branching fraction of the W bosons of 10.86% [65].

6 Analysis methods for the measurement of the cross section

Two methods are used to measure the $t\bar{t}$ production cross section. The reference method is a binned likelihood fit to multi-differential final state distributions, performed in categories of number of additional and b-tagged jets, as described in section 6.1. In addition, an analysis is performed using an event counting technique, as explained in section 6.2.

6.1 Binned likelihood fit

An extended binned likelihood fit is applied to determine $\sigma_{t\bar{t}}^{\mathrm{vis}}$. The expected signal and background distributions are modelled in the fit by template histograms constructed from the simulated samples. The free parameters in the fit are $\sigma_{t\bar{t}}^{\mathrm{vis}}$, the background normalisation parameters $\vec{\omega} = (\omega_1, \omega_2, \ldots, \omega_K)$ for the K sources of backgrounds, and the M nuisance parameters $\vec{\lambda} = (\lambda_1, \lambda_2, \ldots, \lambda_M)$, representing sources of systematic uncertainties other than the background normalisation, such as the jet energy scale and the trigger efficiency. The likelihood function L, based on Poisson statistics, is given by

$$L = \prod_i \left(\exp\left[-\mu_i\right] \mu_i^{n_i} / n_i! \right) \prod_{k=1}^{K} \pi(\omega_k) \prod_{m=1}^{M} \pi(\lambda_m). \tag{6.1}$$

Here, i denotes the bin index of the chosen final state distribution, and μ_i and n_i are the expected and observed event numbers in bin i. The terms $\pi(\omega_k)$ and $\pi(\lambda_m)$ denote prior probability density functions for the background and the other nuisance parameters, representing the prior knowledge of these parameters. The Poisson expectation values μ_i can be further decomposed as

$$\mu_i = s_i(\sigma_{t\bar{t}}^{\mathrm{vis}}, \vec{\lambda}) + \sum_{k=1}^{K} b_{k,i}^{\mathrm{MC}}(\vec{\lambda}) \left(1 + \gamma_k \omega_k\right). \tag{6.2}$$

Here, s_i denotes the expected number of $t\bar{t}$ signal events, which depends on $\sigma_{t\bar{t}}^{\mathrm{vis}}$ and the nuisance parameters $\vec{\lambda}$. The quantity $b_{k,i}^{\mathrm{MC}}$ represents the nominal template prediction of background events from source k in bin i, and γ_k its estimated relative global normalisation uncertainty. In this analysis the background normalisation parameters ω_k and the other nuisance parameters λ_m are defined such that each prior can be represented by a unit normal distribution, unless mentioned otherwise.

A suitable differential distribution for the likelihood fit is the number of selected b-tagged jets in the event. The probability to reconstruct and identify one of the two b jets from the decaying $t\bar{t}$ pair is nearly independent of the probability to reconstruct and identify the other b jet. Because of the large mass of the top quark, the kinematic properties of the two b jets are determined to a large extent by the nearly independent decay topologies of the t and $\bar{t}$, and strong kinematic acceptance correlations arise only for extreme production topologies, such as for $t\bar{t}$ pairs with a large Lorentz boost.

Under the assumption of the independence of the probabilities to identify the b jets, it is possible to express the number of expected signal events with exactly one (s_1), and exactly two (s_2) b-tagged jets using binomial probabilities [14]:

$$s_1 = s_{e\mu}\, 2\epsilon_b(1 - C_b\epsilon_b), \tag{6.3}$$

$$s_2 = s_{e\mu}\, \epsilon_b^2 C_b. \tag{6.4}$$

Here, $s_{e\mu}$ is the total number of events after the eμ selection and can be written as $s_{e\mu} = \mathcal{L}\sigma_{t\bar{t}}^{vis}\epsilon_{e\mu}$, with $\mathcal{L}$ being the integrated luminosity and $\epsilon_{e\mu}$ the efficiency for events to pass the eμ selection. The parameter ϵ_b comprises the total efficiency that a b jet is reconstructed within the kinematic acceptance and b-tagged. The quantity C_b corrects for the small correlations between the tagging of the two b jets and can be expressed as $C_b = 4s_{e\mu}s_2/(s_1 + 2s_2)^2$.

The remaining signal events with zero or more than two b-tagged jets are considered in a third category:

$$s_0 = s_{e\mu}\left[1 - 2\epsilon_b(1 - C_b\epsilon_b) - C_b\epsilon_b^2\right]. \tag{6.5}$$

In ref. [14], two equations similar to eqs. (6.3), (6.4) are directly solved for the $t\bar{t}$ production cross section and ϵ_b. In the present analysis, eqs. (6.3), (6.4) are used together with eq. (6.5) in the template fit. The quantities $\epsilon_{e\mu}$, ϵ_b, and C_b are directly determined from the $t\bar{t}$ signal simulation, expressing ϵ_b as $(s_1 + 2s_2)/2s_{e\mu}$, and parametrised as a function of the nuisance parameters $\vec{\lambda}$. The nominal values for the 8 TeV simulated $t\bar{t}$ signal are $\epsilon_{e\mu} = 0.51$, $\epsilon_b = 0.36$, and $C_b = 0.99$, and the values for the 7 TeV sample are similar. The use of these equations facilitates an accurate modelling of the expected signal rates as a function of the nuisance parameters, i.e. avoiding mismodelling effects that could arise from approximating the dependences as linear functions.

In order to improve the sensitivity of the fit, the events are further categorised into four classes of multiplicity of additional jets in the event (zero, one, two, and three or more additional jets). This leads, together with the three classes of b-tagged jets, to 12 different categories in total. Additional jets must be non-b-tagged jets. In case there is no additional jet, the corresponding event yields are directly used in the likelihood fit, otherwise events are further categorised into bins of the p_T of the least energetic additional jet in the event.

The signal subcategory probabilities, background rates, and values of $\epsilon_{e\mu}$, ϵ_b, and C_b are obtained from simulation and depend on the nuisance parameters $\vec{\lambda}$. Each relevant dependency of a quantity on a parameter λ_m is modelled by a second-order polynomial, that is constructed from evaluating the quantity at three values $\lambda_m = 0, 1, -1$, corresponding to the nominal value of the parameter and to ± 1 standard deviation (σ) variations. For a few sources of uncertainty, only one exact variation is possible, e.g. when there are only two variants of signal generators available that differ in a certain uncertainty source such as the matrix element calculation; in such cases, a linear function is chosen to model the dependence of the quantity on the respective λ_m. For several nuisance parameters representing systematic modelling uncertainties in the measurement, a box prior is chosen instead of the standard unit normal prior, with a value of 0.5 between -1 and $+1$ and zero elsewhere. Such priors are chosen for the following uncertainties (discussed in section 7.2):
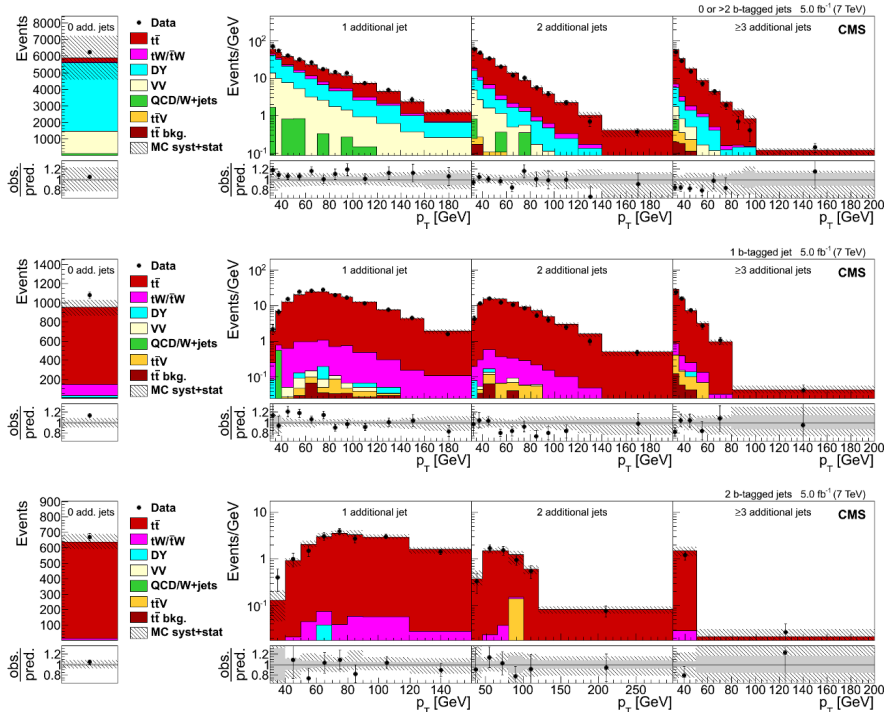
Figure 4. Total event yield for zero additional non-b-tagged jets (left) and p_T of the non-b-tagged jet with the lowest p_T in the event (right) for events with one, two, and at least three additional non-b-tagged jets, and with zero or more than two (top row), one (middle row), and two (bottom row) b-tagged jets at $\sqrt{s} = 7$ TeV. The last bin of the p_T distributions includes the overflow events. The hatched bands correspond to the sum of statistical and systematic uncertainties in the event yield for the sum of signal and background predictions. The ratios of data to the sum of the predicted yields are shown at the bottom of each plot. Here, an additional solid grey band represents the contribution from the statistical uncertainty in the MC simulation.

renormalisation and factorisation scales, jet-parton matching scale, top quark p_T modelling, colour reconnection, underlying event, and matrix element generator.

The likelihood fit is finally performed using the function $\chi^2 = -2 \ln L$, where L is the likelihood function given in eq. (6.1). The MINUIT [66] program is used to minimise this χ^2 as function of the free fit parameters $\sigma_{t\bar{t}}$, $\vec{\omega}$, and $\vec{\lambda}$. The fit uncertainty in $\sigma_{t\bar{t}}$ is determined using MINOS, the profile likelihood algorithm which is part of MINUIT. Figures 4 and 5 show the multi-differential distributions used in the fit. A reasonably good agreement is found between data and expectations before the fit.

Figures 6 and 7 compare the data with the simulation after the simultaneous fit at 7 and 8 TeV. The uncertainty bands are calculated taking into account the full correlation matrix. The description of the data by the simulation has improved with the fit. The best
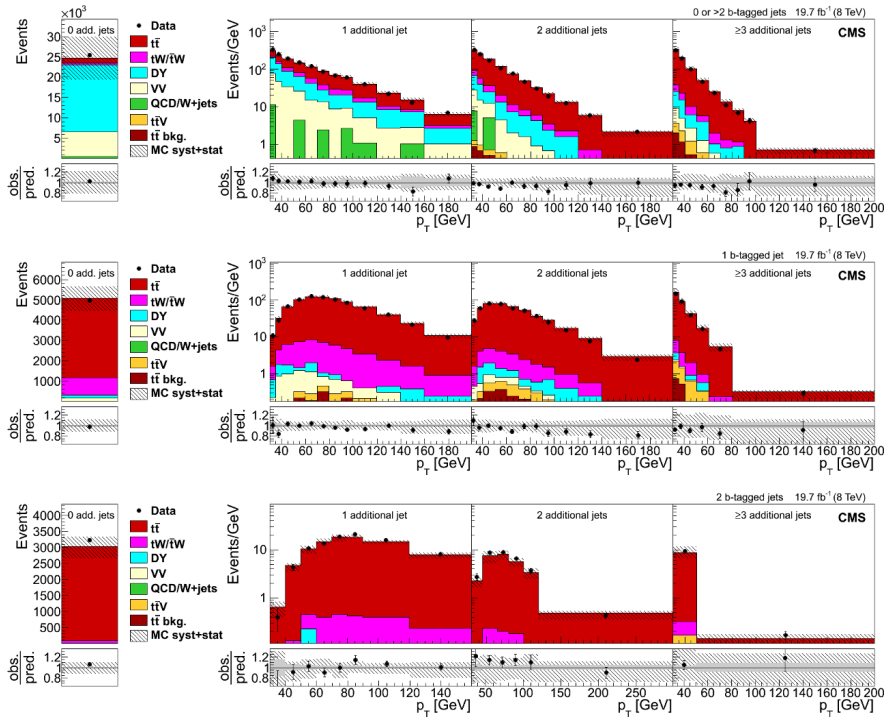
Figure 5. Total event yield for zero additional non-b-tagged jets (left) and p_{T} of the additional non-b-tagged jet with the lowest p_{T} in the event (right) for events with one, two, and at least three additional non-b-tagged jets, and with zero or more than two (top row), one (middle row), and two (bottom row) b-tagged jets at $\sqrt{s} = 8$ TeV. The last bin of the p_{T} distributions includes the overflow events. The hatched bands correspond to the sum of statistical and systematic uncertainties in the event yield for the sum of signal and background predictions. The ratios of data to the sum of the predicted yields are shown at the bottom of each plot. Here, an additional solid grey band represents the contribution from the statistical uncertainty in the MC simulation.

fit values of the nuisance parameters correspond to variations that are for most cases within 1σ of the prior uncertainties, about 98% of the cases. The maximum observed variation is about 1.9σ, corresponding to the uncertainty in the mistag SFs, see section 7. Other uncertainties with variations between 1 and 1.5σ are two components of the jet energy scale corrections and the statistical component of the b tagging SFs.

The fiducial $t\bar{t}$ production cross sections at $\sqrt{s} = 7$ and 8 TeV are determined simultaneously. For each centre-of-mass energy, a likelihood is defined as in eq. (6.1), respective χ^2 functions are constructed, and the sum of both χ^2 functions is minimised. Correlations between systematic uncertainties are fully taken into account (see section 7.3).
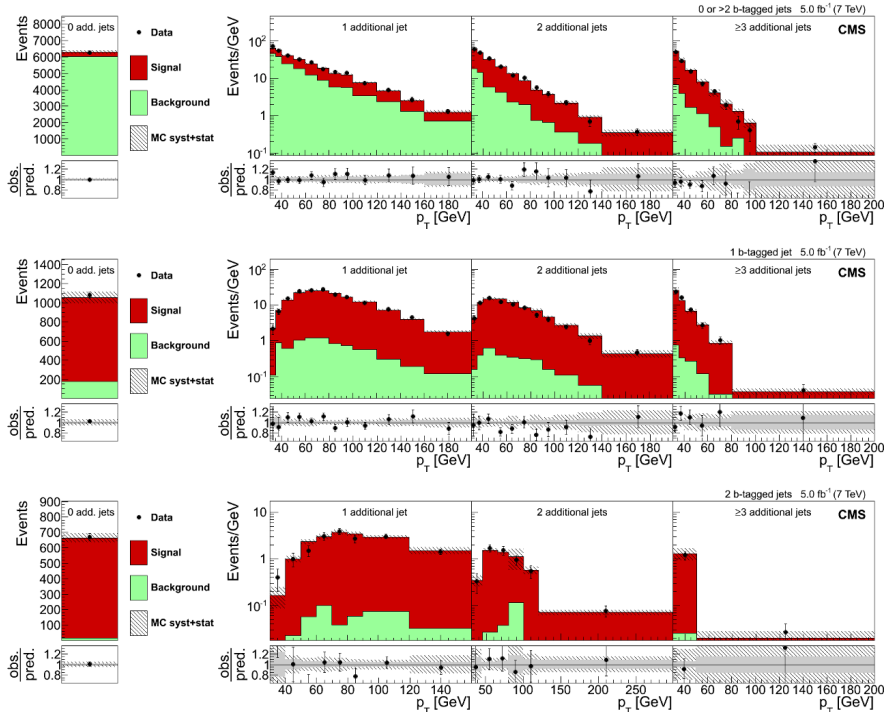
Figure 6. Fitted total event yield for zero additional non-b-tagged jets (left) and p_T of the non-b-tagged jet with the lowest p_T in the event (right) for events with one, two, and at least three additional non-b-tagged jets, and with zero or more than two (top row), one (middle row), and two (bottom row) b-tagged jets at $\sqrt{s} = 7$ TeV. The last bin of the p_T distributions includes the overflow events. The hatched bands correspond to the sum of statistical and systematic uncertainties in the event yield for the sum of signal and background predictions after the fit, and include all correlations. The ratios of data to the sum of the predicted yields are shown at the bottom of each plot. Here, an additional solid grey band represents the contribution from the statistical uncertainty in the MC simulation.

6.2   Event counting method

The $t\bar{t}$ production cross section is also measured by applying an event counting method similar to the one used in a previous measurement [1]. This method provides a cross-check of the reference method.

In this analysis, events are counted after applying the eμ selection described in section 4 with additional requirements that help to further suppress the background contribution: the presence of at least two jets is required, of which at least one has to be b-tagged. Compared with ref. [1], tighter requirements on lepton isolation and identification, as well as on b tagging, are applied to further reduce the background contribution.

Techniques based on control samples in data are used to estimate the background contribution arising from DY and from non W/Z events. The contributions of the remaining
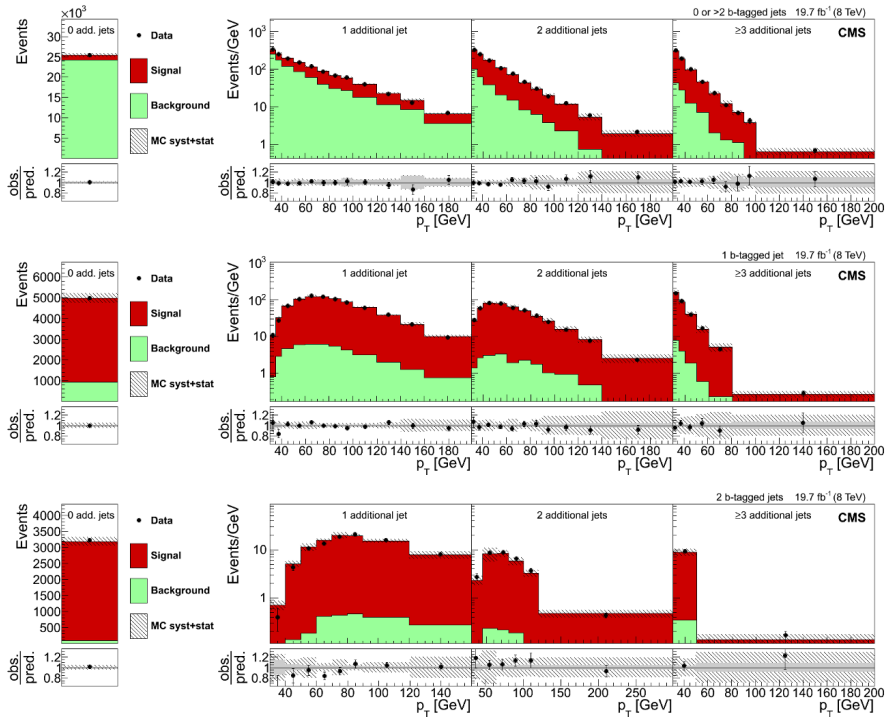
Figure 7. Fitted total event yield for zero additional non-b-tagged jets (left) and p_T of the non-b-tagged jet with the lowest p_T in the event (right) for events with one, two, and at least three additional non-b-tagged jets, and with zero or more than two (top row), one (middle row), and two (bottom row) b-tagged jets at $\sqrt{s} = 8$ TeV. The last bin of the p_T distributions includes the overflow events. The hatched bands correspond to the sum of statistical and systematic uncertainties in the event yield for the sum of signal and background predictions after the fit, and include all correlations. The ratios of data to the sum of the predicted yields are shown at the bottom of each plot. Here, an additional solid grey band represents the contribution from the statistical uncertainty in the MC simulation.

background processes are estimated from simulation. The DY contribution is estimated using the "$R_{\text{out/in}}$" method [1], in which events with e^+e^- and $\mu^+\mu^-$ final states are used to obtain a normalisation factor. This is estimated from the number of events within the Z boson mass window in data, and extrapolated to the number of events outside the Z mass window with corrections based on control regions in data enriched in DY events. The contribution to the background originating from non W/Z boson events is estimated by subtracting the same-sign prompt-lepton contributions from the same-sign event yields in data and multiplying by the ratio of opposite-sign over same-sign events. This ratio, originating from non-prompt lepton backgrounds, is taken from simulation.

Table 1 shows the total number of events observed in data and the numbers of expected signal and background events fulfilling all selection criteria. For both data sets, a good agreement between data and expected number of events is observed.

– 14 –

Source	Number of eμ events	
	7 TeV	8 TeV
DY	$22 \pm 3 \pm 3$	$173 \pm 25 \pm 26$
Non W/Z	$51 \pm 5 \pm 15$	$146 \pm 10 \pm 44$
Single top quark (tW)	$204 \pm 3 \pm 61$	$1034 \pm 3 \pm 314$
VV	$7 \pm 1 \pm 2$	$35 \pm 2 \pm 11$
$t\bar{t}V$	$12 \pm 1 \pm 3$	$84 \pm 1 \pm 26$
Total background	$296 \pm 6 \pm 63$	$1472 \pm 27 \pm 319$
$t\bar{t}$ dilepton signal	$5008 \pm 15 \pm 188$	$24440 \pm 44 \pm 956$
Data	4970	25441

Table 1. Number of selected events for the event counting method for the 7 and 8 TeV data sets. The results are given for the individual sources of background, $t\bar{t}$ signal, and data. The two uncertainties quoted correspond to the statistical and systematic components (cf. section 7), respectively.
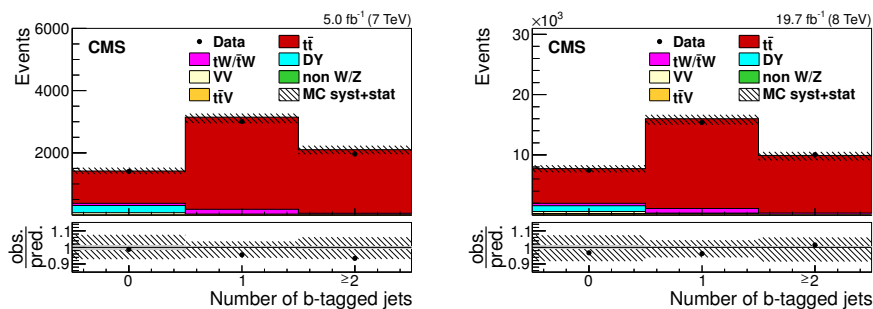

Figure 8. Comparison of the b jet multiplicity distributions in the eμ channel for 7 (left) and 8 (right) TeV between the data and simulation for events fulfilling the eμ selection and the requirement of having at least two jets. The hatched bands correspond to the sum of statistical and systematic uncertainties in the event yield for the signal and background predictions. The ratios of data to the predicted yields are shown at the bottom of each plot. Here, an additional solid grey band represents the contribution from the statistical uncertainty in the MC simulation.

Figure 8 shows the b jet multiplicity in events passing the full event selection, except for the b jet requirement, for data collected at 7 and 8 TeV. In both cases the total predicted yields provide a good description of the measured distributions.

The cross section $\sigma_{t\bar{t}}$ is determined from the number of data events after background subtraction, and dividing by the integrated luminosity of the data sample and by the product of detector and kinematical acceptance, selection efficiency, as estimated from simulation for a top quark mass of 172.5 GeV, and branching fraction of the selected $t\bar{t}$ dilepton final state.

– 15 –

7 Systematic uncertainties

The measurement of the top quark pair production cross section is affected by systematic uncertainties that originate from detector effects and from theoretical assumptions. Each source of systematic uncertainty is assessed individually by suitable variations of the MC simulations or by varying parameter values within their estimated uncertainties in the analysis. Each source is represented by a nuisance parameter, which is fitted together with $\sigma_{t\bar{t}}^{\text{vis}}$, as described in section 6. For the event counting method, the same sources of systematic uncertainty are evaluated following the procedure in ref. [1].

7.1 Experimental uncertainties

The uncertainty in the dilepton trigger ("Trigger") and lepton identification efficiencies ("Lepton ID/isolation") are estimated by varying the SFs within their uncertainties, which are in the range of 1–2%.

The lepton energies ("Lepton energy scale") are corrected separately for electrons [59] and for muons [67]. Their scales are varied by 0.15% for electrons and 0.3% for muons.

The uncertainty due to the limited knowledge of the jet energy scale ("JES") is determined by variations of the jet energy in bins of p_{T} and η [63]. For the reference method, these variations are divided into 27 sources and the effect of each source is evaluated individually. For the event counting method, the total variation is used to determine the uncertainty.

The uncertainty due to the limited accuracy of the jet energy resolution ("JER") is determined by changing the simulated JER by $\pm2.5\%$, $\pm4\%$, and $\pm5\%$, for jets with $|\eta| < 1.7$, $1.7 < |\eta| < 2.3$, and $|\eta| > 2.3$, respectively [63].

For the normalisation of each background source, an uncertainty of $\pm30\%$ is assumed. In the case of the single top quark background ("tW/$\bar{\text{t}}$W"), the variation covers the uncertainty in the absolute rate, including uncertainties due to PDFs. The same global variation is applied to the other dominant background contribution, DY. The predicted cross section has an uncertainty of $\approx5\%$, including PDF uncertainties. The variation used here additionally covers the observed differences in heavy-flavour composition between data and simulation in dedicated CMS analyses and is also suggested by estimates based on data [4, 8].

The uncertainties due to the b tagging efficiency ("b tag") and misidentification rate ("Mistag") are determined by varying the b tagging SFs of the b jets or the light-flavour jets, respectively, by the uncertainties quoted in ref. [64]. For the reference method, the b tagging uncertainties are divided into 19 individual sources, some of them are correlated to other systematic uncertainties, such as JER or pileup. The remaining sources are evaluated individually.

The effect of pileup events ("Pileup") is evaluated by weighting the inelastic pp cross section in simulation to the minimum bias cross section determined in data. The pileup model estimates the mean number of additional pp interactions to be about 9 events for the data collected at 7 TeV and 21 for the data collected at 8 TeV. These estimates are based on the total inelastic pp cross sections at $\sqrt{s} = 7$ (8) TeV, which are determined to be 73.5

(69.4) mb, following the measurement described in ref. [68]. The systematic uncertainty is determined by varying the cross sections within their uncertainty, $\pm 8\%$ at 7 TeV and $\pm 5\%$ at 8 TeV.

The uncertainty in the luminosity ("Luminosity") measurement is 2.2% [69] at 7 TeV and 2.6% [70] at 8 TeV.

7.2 Theoretical uncertainties

The impact of theoretical assumptions in the modelling is determined by repeating the analysis and replacing the standard MadGraph $t\bar{t}$ simulation by dedicated simulation samples with varied parameters.

The uncertainty in modelling of the hard-production process ("Q^2 scale") is assessed through a simultaneous variation of renormalisation and factorisation scales in the Mad-Graph sample by factors of 2 and 0.5 relative to their common nominal value, which is set to the $\mu_{\rm F}^2 = \mu_{\rm R}^2 = Q^2$ scale of the hard process. In MadGraph, it is defined by $Q^2 = m_{\rm t}^2 + \Sigma p_{\rm T}^2$, where the sum is over all additional final state partons in the matrix element calculations.

The impact of the choice of the scale that separates the description of jet production through matrix elements or parton shower ("ME/PS matching") in MadGraph is studied by changing its reference value of 20 GeV to 40 GeV and to 10 GeV.

The effect of the matrix-element generator choice on the measurement is evaluated by using powheg [37, 41, 42] for the $t\bar{t}$ simulation instead of MadGraph ("MadGraph vs powheg").

The flavour-dependent hadronisation uncertainty ("Hadronisation (JES)") is part of the JES uncertainty and comes from differences in the jet energy response for different jet flavours. It is estimated by the differences between using simulations with the Lund fragmentation model in pythia and cluster fragmentation model in herwig++ [71] and is evaluated for each jet flavour independently. An additional uncertainty included in this source is the uncertainty in the b quark fragmentation tune. This is evaluated by varying the Bowler-Lund b quark fragmentation model in tune Z2* to describe the results by ALEPH [72] and DELPHI [73] for the b quark fragmentation functions. Another uncertainty included in this source is the uncertainty in the semileptonic branching fraction of B hadrons, varied between 10.05% and 11.27%, which is the range of the measurements from B^0/B^+ decays and their uncertainties [65].

Differential cross section measurements [57] have shown that the $p_{\rm T}$ of the top quark is softer than predicted by the nominal MadGraph simulation used to measure the cross section. To account for this effect, the difference between the result obtained with the nominal simulation and using the MadGraph prediction reweighted to describe the measured top quark $p_{\rm T}$ spectrum is taken as a systematic uncertainty ("Top quark $p_{\rm T}$ modelling").

The uncertainties from ambiguities in modelling colour reconnection effects ("Colour reconnection") are estimated by comparing simulations of an underlying event tune including colour reconnection to a tune without it, the Perugia 2011 (P11) and P11 noCR tunes [74].

– 17 –

The uncertainty in the modelling of the underlying event ("Underlying event") is estimated by evaluating the relative variations of two different P11 PYTHIA tunes with respect to the standard P11 tune: the mpiHi and the TeV tunes with higher and lower underlying event activity, respectively.

The uncertainty from the choice of PDFs ("PDF") is determined by reweighting the sample of simulated $t\bar{t}$ events according to the 52 CT10 error PDF sets [38], scaled to 68% CL.

7.3 Correlations between systematic uncertainties for the measurements at 7 and 8 TeV

A number of systematic uncertainties affect the measurements at $\sqrt{s} = 7$ and 8 TeV similarly, while others are completely decoupled. In this analysis, systematic uncertainties are treated as either uncorrelated, partially correlated, or fully correlated between the two measurements. For fully correlated systematic uncertainties, common nuisance parameters are used in the simultaneous likelihood fit to the two data sets. For each partially correlated systematic uncertainty source, three nuisance parameters are introduced, one for each data set for the uncorrelated part and one common parameter for the correlated part. The degree of correlation is modelled by the parameter ρ. The uncertainties of the correlated and the two uncorrelated parameters are taken to be fractions ρ and $\sqrt{1 - \rho^2}$, respectively, of the uncertainty of the original nuisance parameter. The ρ values assumed for this analysis are listed in table 2.

For experimental sources, the same procedures are usually employed at the two centre-of-mass energies for calibration and determination of uncertainties. Also, the same MC generators are used for the modelling of background processes. Hence, these uncertainties are treated as 100% correlated, however for each source a (usually small) uncorrelated component arises from statistical fluctuations in the data or simulated samples. The resulting correlation coefficients are estimated to be 0.9 for several sources and 0.8 for the "Trigger" and "Mistag" sources. For the "Pileup" source a relatively small correlation of 0.5 is assumed because of the largely different beam conditions at the two energies.

From the uncertainties related to the JES, the flavour components ("JES: flavour"), owing to the comparison between different hadronisation models, and components related to the extrapolation from $Z \to \ell\ell$ kinematic acceptance to the full phase space using MC simulation ("JES: absolute extrapolation") are taken as fully correlated. The JES sources related to pileup ("JES: pileup") are treated as uncorrelated, because of different procedures used for the uncertainty assessment at the two energies, as well as the remaining terms ("JES: other"). The JES component of the b tagging uncertainties is fitted independently, assigning a correlation coefficient of 0.2 that reflects the amount of correlated JES uncertainty sources.

All modelling uncertainties are assumed to be fully correlated between the two centre-of-mass energies, including the three remaining JES parts. The integrated luminosity uncertainties are treated as fully uncorrelated, to account for the different beam conditions and specific effects associated to each measurement. It has been checked that variations of the assumed correlations within reasonable ranges lead to negligible changes of the extracted cross sections.

– 18 –

Uncertainty source	ρ
Trigger	0.8
Electron ID	0.9
Electron energy scale	0.9
Muon ID	0.9
Muon energy scale	0.9
JES: flavour	1
JES: pileup	0
JES: absolute extrapolation	1
JES: other	0
Jet energy resolution	0.9
Each background	0.9
b-tag (JES)	0.2
b-tag (stat)	0
b-tag (syst)	1
Mistag	0.8
Pileup	0.5
μ_{R}, μ_{F} scales	1
ME/PS matching	1
MadGraph vs powheg	1
b quark fragmentation tune	1
B hadron semileptonic branching fraction	1
Top quark p_{T} modelling	1
Colour reconnection	1
Underlying event	1
PDF	1
Integrated luminosity	0

Table 2. Assumed correlations ρ between systematic uncertainties for the 7 and 8 TeV data sets. If $\rho = 0$, the uncertainties are treated as uncorrelated between the two sets.

7.4 Final uncertainties

The total uncertainties in the fiducial cross sections, as obtained with the binned likelihood fit (section 6.1), are $^{+3.6}_{-3.4}$ % at 7 TeV and $^{+3.7}_{-3.4}$ % at 8 TeV. The impact of the sources of systematic uncertainties in this total uncertainty are listed in table 3. These are estimated by removing groups of uncertainties one at a time and gauging the difference in quadrature on the total uncertainty. Significant contributions to the total uncertainty spread over many different sources of experimental and modelling uncertainties with "Lumi", "Lepton ID/isolation", "Trigger", and "DY" being the four largest sources. The observed shifts of the fitted background or other nuisance parameters compared to their assumed uncertainty before the fit are in general small, indicating a consistent fit.

Source	Uncertainty [%]	
	7 TeV	8 TeV
Trigger	1.3	1.2
Lepton ID/isolation	1.5	1.5
Lepton energy scale	0.2	0.1
Jet energy scale	0.8	0.9
Jet energy resolution	0.1	0.1
tW/$\bar{\text{t}}$W	1.0	0.6
DY	1.4	1.3
t$\bar{\text{t}}$ bkg.	0.1	0.1
t$\bar{\text{t}}$V	0.1	0.1
Diboson	0.2	0.6
W+jets/QCD	0.1	0.2
b-tag	0.5	0.5
Mistag	0.2	0.1
Pileup	0.3	0.3
μ_R, μ_F scales	0.3	0.6
ME/PS matching	0.1	0.1
MADGRAPH vs POWHEG	0.4	0.5
Hadronisation (JES)	0.7	0.7
Top quark p_T modelling	0.3	0.4
Colour reconnection	0.1	0.2
Underlying event	0.1	0.1
PDF	0.2	0.3
Integrated luminosity	2.2	2.6
Statistical	1.2	0.6

Table 3. Illustrative summary of the individual contributions to the total uncertainty in the visible t$\bar{\text{t}}$ cross section measurements.

8   Cross section measurement

The results of the t$\bar{\text{t}}$ cross section measurements in pp collisions at 7 and 8 TeV are presented in the fiducial range and in the full phase space.

8.1   Fiducial cross section

The fiducial cross sections are defined for t$\bar{\text{t}}$ production with events containing an oppositely charged eμ pair with both leptons having $p_\text{T} > 20$ GeV and $|\eta| < 2.4$. The measured cross sections, using the binned likelihood fit extraction method (section 6) and assuming a top

Source	Uncertainty [%]	
	7 TeV	8 TeV
Total (visible)	$+3.6$ -3.4	$+3.7$ -3.4
Q^2 scale (extrapol.)	$+0.1$ -0.4	$+0.2$ -0.1
ME/PS matching (extrapol.)	$+0.1$ -0.1	$+0.3$ -0.3
Top quark p_{T} (extrapol.)	$+0.5$ -0.3	$+0.6$ -0.3
PDF (extrapol.)	$+0.1$ -0.1	$+0.1$ -0.1
Total	$+3.6$ -3.5	$+3.7$ -3.5

Table 4. Individual contributions to the systematic uncertainty in the total $t\bar{t}$ cross section measurements. The total systematic uncertainties in the fiducial cross sections $\sigma_{t\bar{t}}^{\mathrm{vis}}$ are given in the row "Total (visible)", and those in the full phase space cross section $\sigma_{t\bar{t}}$ in the row "Total".

quark mass of 172.5 GeV, are

$$\sigma_{t\bar{t}}^{\mathrm{vis}} = 3.03 \pm 0.04\,(\mathrm{stat})^{+0.08}_{-0.07}\,(\mathrm{syst}) \pm 0.07\,(\mathrm{lumi})\,\mathrm{pb}, \quad \text{at } \sqrt{s} = 7\,\mathrm{TeV \ and}$$

$$\sigma_{t\bar{t}}^{\mathrm{vis}} = 4.23 \pm 0.02\,(\mathrm{stat})^{+0.11}_{-0.09}\,(\mathrm{syst}) \pm 0.11\,(\mathrm{lumi})\,\mathrm{pb}, \quad \text{at } \sqrt{s} = 8\,\mathrm{TeV}.$$

The uncertainties are due to statistical fluctuations, combined experimental and theoretical systematic effects on the measurement, and the uncertainty in the measurement of the integrated luminosity. A summary of the systematic uncertainties is presented in table 3.

8.2 Full phase space cross section

The full phase space (total) cross sections for $t\bar{t}$ production are calculated from the fiducial cross section results by dividing $\sigma_{t\bar{t}}^{\mathrm{vis}}$ by the acceptance, as in eq. (5.1). The quantity $A_{\mathrm{e\mu}}$ is determined from the $t\bar{t}$ signal MC simulation. As it depends on the exact theoretical model used in the event generation part of the simulation, it is parametrised as a function of the same nuisance parameters that were used for the modelling uncertainties (section 7) in the binned likelihood fit extraction of the fiducial cross sections. The fitted values of these nuisance parameters are used to obtain the best estimates of $A_{\mathrm{e\mu}}$, 1.745×10^{-2} at 7 TeV and 1.728×10^{-2} at 8 TeV, which are used for the determination of the nominal values of $\sigma_{t\bar{t}}$. In order to determine the uncertainty in the phase space extrapolation modelled by $A_{\mathrm{e\mu}}$, each relevant nuisance parameter is iteratively varied from the fitted value by the $\pm 1\sigma$ values before the fit, while all other nuisance parameters are kept at their fitted values. The resulting variations of $A_{\mathrm{e\mu}}$ are taken as an additional extrapolation uncertainty. The sources that are considered here are "μ_{R} and μ_{F} scales", "ME/PS matching", "Top quark p_{T} modelling", and "PDF" (see section 7), and the individual uncertainties in $\sigma_{t\bar{t}}$ from these sources are added in quadrature. The resulting systematic uncertainties are listed in table 4.

The measurements of $\sigma_{t\bar{t}}$ at the two centre-of-mass energies are

$$\sigma_{t\bar{t}} = 173.6 \pm 2.1 \,(\text{stat})^{+4.5}_{-4.0} \,(\text{syst}) \pm 3.8 \,(\text{lumi}) \,\text{pb}, \quad \text{at } \sqrt{s} = 7 \,\text{TeV and}$$

$$\sigma_{t\bar{t}} = 244.9 \pm 1.4 \,(\text{stat})^{+6.3}_{-5.5} \,(\text{syst}) \pm 6.4 \,(\text{lumi}) \,\text{pb}, \quad \text{at } \sqrt{s} = 8 \,\text{TeV}.$$

After adding the uncertainties in quadrature, the resulting total uncertainties are 6.2 pb (3.6%) at $\sqrt{s} = 7$ TeV and 9.1 pb (3.7%) at $\sqrt{s} = 8$ TeV.

The results obtained with the method based on event counting (see section 6.2) are

$$\sigma_{t\bar{t}} = 165.9 \pm 2.5 \,(\text{stat}) \pm \; 6.2 \,(\text{syst}) \pm 3.6 \,(\text{lumi}) \,\text{pb}, \quad \text{at } \sqrt{s} = 7 \,\text{TeV and}$$

$$\sigma_{t\bar{t}} = 241.1 \pm 1.6 \,(\text{stat}) \pm 10.0 \,(\text{syst}) \pm 6.3 \,(\text{lumi}) \,\text{pb}, \quad \text{at } \sqrt{s} = 8 \,\text{TeV}.$$

As expected, the statistical and systematic uncertainties are slightly larger than those obtained with the reference method. The results of the two methods are in agreement.

The cross section measurements agree with previous results [1, 4, 8, 14, 15, 21, 22]. They constitute the most precise CMS measurements of $\sigma_{t\bar{t}}$ to date and have a similar precision to the most precise ATLAS result [14], obtained in the same decay channel. For both centre-of-mass energies, the predicted cross sections at NNLO (see section 3) are in good agreement with the measurements.

The ratio of cross sections using the results obtained with the reference analysis amounts to

$$R_{t\bar{t}} = \sigma_{t\bar{t}}(8 \,\text{TeV})/\sigma_{t\bar{t}}(7 \,\text{TeV}) = 1.41 \pm 0.06.$$

Here, the correlated uncertainty obtained from the simultaneous likelihood fit (section 6) of the fiducial cross sections at the two centre-of-mass energies is fully taken into account as well as the correlated uncertainty on the acceptances arising from model uncertainties, which are assumed to be fully correlated between the two energies. The total relative uncertainty of the ratio is 4.2%, indicating a partial cancellation of systematic uncertainties. The predicted ratio at NNLO (see section 3) is consistent with the measurement.

9 Determination of the top quark pole mass

The full phase space cross sections are used to determine the top quark pole mass (m_t) via the dependence of the theoretically predicted cross section on m_t and comparing it to the measured cross section. For this purpose, the cross section fit and the extrapolation to the full phase space (see sections 6 and 8.2) are repeated for three different hypotheses for the top quark mass parameter in the MC simulation (m_t^{MC}): 169.5, 172.5, and 175.5 GeV. For each mass value a sample of simulated $t\bar{t}$ events, generated with the corresponding m_t^{MC} value, is used in the fit as a signal model. The dependence of the distributions used in the fit on detector effects is evaluated individually for each mass value. Their dependence on modelling uncertainties varies little over the studied mass range and is thus taken from the nominal mass value ($m_t^{\text{MC}} = 172.5$ GeV). The obtained cross section dependence on the mass can be parametrised as an exponential function:

$$\sigma_{t\bar{t}}(7 \,\text{TeV}, m_t^{\text{MC}}) = \exp\left[-0.1718\,(m_t^{\text{MC}}/\text{GeV} - 178.5)\right] + 170.9 \,\text{pb},$$

$$\sigma_{t\bar{t}}(8 \,\text{TeV}, m_t^{\text{MC}}) = \exp\left[-0.1603\,(m_t^{\text{MC}}/\text{GeV} - 185.4)\right] + 237.0 \,\text{pb}.$$

To express the measured dependence as a function of m_t instead of m_t^MC, the difference between m_t and m_t^MC needs to be accounted for. This is estimated to be of the order of 1 GeV [75]. Therefore, an additional uncertainty $\Delta_{m_\mathrm{t}\pm}$ in the obtained cross section dependence is introduced. It is evaluated by shifting the measured dependence by ± 1 GeV in m_t^MC and recording the difference in $\sigma_{\mathrm{t}\bar{\mathrm{t}}}$. For the determination of m_t, this contribution to the total uncertainty is almost negligible. In consequence, the measurements of $\sigma_{\mathrm{t}\bar{\mathrm{t}}}$ can be represented by Gaussian likelihoods as a function of m_t of the form

$$L_\mathrm{exp}(m_\mathrm{t}, \sigma_{\mathrm{t}\bar{\mathrm{t}}}) = \exp\left[\frac{\left(\sigma_{\mathrm{t}\bar{\mathrm{t}}}(m_\mathrm{t}) - \sigma_{\mathrm{t}\bar{\mathrm{t}}}\right)^2}{-2(\Delta^2 + \Delta_{m_\mathrm{t}\pm}^2)}\right], \tag{9.1}$$

where Δ represents the total uncertainty in each of the cross section measurements and $\sigma_{\mathrm{t}\bar{\mathrm{t}}}(m_\mathrm{t})$ the measured dependence of the cross section on m_t.

The predicted dependence of $\sigma_{\mathrm{t}\bar{\mathrm{t}}}$ on the top quark pole mass at NNLO+NNLL is determined with TOP++, employing different PDF sets (NNPDF3.0 [76], CT14 [77], and MMHT2014 [78]) with $\alpha_\mathrm{s} = 0.118 \pm 0.001$. Additionally, uncertainties of 1.79% at 7 TeV and 1.72% at 8 TeV are assigned to the predicted cross section values to account for the uncertainty in the LHC beam energy [79]. The predicted $\sigma_{\mathrm{t}\bar{\mathrm{t}}}$ is represented by an asymmetric Gaussian function with width $\Delta_{\mathrm{p},\pm}$, comprising PDF, α_s, and the beam energy uncertainty summed in quadrature. This function is convolved with a box function to account for the uncertainty in the renormalisation and factorisation scales in the prediction [24]. The result of the convolution is given as

$$L_\mathrm{pred}(m_\mathrm{t}, \sigma_{\mathrm{t}\bar{\mathrm{t}}}) = \frac{1}{C(m_\mathrm{t})}\left(\mathrm{erf}\left[\frac{\sigma_{\mathrm{t}\bar{\mathrm{t}}}^{(\mathrm{h})}(m_\mathrm{t}) - \sigma_{\mathrm{t}\bar{\mathrm{t}}}}{\sqrt{2}\Delta_{\mathrm{p},+}}\right] - \mathrm{erf}\left[\frac{\sigma_{\mathrm{t}\bar{\mathrm{t}}}^{(\mathrm{l})}(m_\mathrm{t}) - \sigma_{\mathrm{t}\bar{\mathrm{t}}}}{\sqrt{2}\Delta_{\mathrm{p},-}}\right]\right), \tag{9.2}$$

where $\sigma_{\mathrm{t}\bar{\mathrm{t}}}^{(\mathrm{h})}$ and $\sigma_{\mathrm{t}\bar{\mathrm{t}}}^{(\mathrm{l})}$ denote the upper and lower predicted cross section values, respectively, from variations of the renormalisation and factorisation scales. The normalisation factor $C(m_\mathrm{t})$ assures that $\max(L_\mathrm{pred}) = 1$ for any fixed m_t.

Figure 9 shows the likelihoods for the predicted $\mathrm{t}\bar{\mathrm{t}}$ cross section employing NNPDF3.0 and the measurement of $\sigma_{\mathrm{t}\bar{\mathrm{t}}}$ at $\sqrt{s} = 7$ and 8 TeV as a function of m_t. The product of the two likelihoods is used to fit the mass value by maximizing the likelihood simultaneously with respect to m_t and $\sigma_{\mathrm{t}\bar{\mathrm{t}}}$. The extracted top quark pole masses using different PDF sets are listed in table 5. The contributions from uncertainties in the CT14 PDF set are scaled to a 68% CL.

Finally, a weighted average is calculated, taking into account all systematic uncertainty correlations between the measured cross sections at 7 and 8 TeV, and assuming 100% correlated uncertainties for the theoretical predictions at the two energies. The resulting top quark pole masses are listed in table 6 and are in good agreement with each other and previous measurements [14, 24].

	$m_{\rm t}\,[\,{\rm GeV}\,]$	
	7 TeV	8 TeV
NNPDF3.0	$173.5^{+1.9}_{-2.0}$	$174.2^{+2.0}_{-2.2}$
MMHT2014	$173.9^{+2.0}_{-2.1}$	$174.4^{+2.1}_{-2.3}$
CT14	$174.1^{+2.2}_{-2.4}$	$174.6^{+2.3}_{-2.5}$

Table 5. Top quark pole mass at NNLO+NNLL extracted by comparing the measured $t\bar{t}$ production cross section at 7 and 8 TeV with predictions employing different PDF sets.

	$m_{\rm t}\,[\,{\rm GeV}\,]$
NNPDF3.0	$173.8^{+1.7}_{-1.8}$
MMHT2014	$174.1^{+1.8}_{-2.0}$
CT14	$174.3^{+2.1}_{-2.2}$

Table 6. Combined top quark pole mass at NNLO+NNLL extracted by comparing the measured $t\bar{t}$ production cross section with predictions employing different PDF sets.
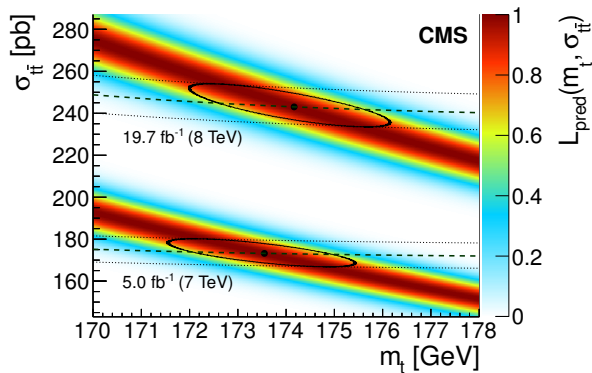
Figure 9. Likelihood for the predicted dependence of the $t\bar{t}$ production cross section on the top quark pole mass for 7 and 8 TeV determined with TOP++, employing the NNPDF3.0 PDF set. The measured dependences on the mass are given by the dashed lines, their 1σ-uncertainties are represented by the dotted lines. The extracted mass at each value of $\sqrt{s}$ is indicated by a black point, with its 1σ-uncertainty constructed from the continuous contour, corresponding to $-2\Delta\log(L_{\rm pred}L_{\rm exp}) = 1$.
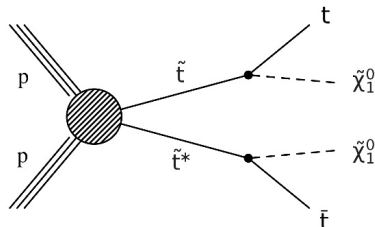
Figure 10. Diagram displaying the top squark pair production at the LHC in the decay mode where each top squark decays to a top quark and a neutralino $\widetilde{\chi}_1^0$.

10 Limits on top squark pair production

The SUSY models are predicated on the existence of partners for SM particles. A light top squark could contribute to the cancellation of the quadratic divergences in the Higgs mass loop corrections [26]. SUSY scenarios with a neutralino as LSP and a nearly mass-degenerate top squark provide one theoretically possible way to account for the observed relic abundance of dark matter [80, 81]. There are therefore strong motivations to search for a top squark with a mass close to, or even below, the TeV scale.

In the following, a SUSY model with R-parity conservation is considered, where top squarks are pair-produced via the strong interaction. The top squark decays into a top quark and the LSP, considered here as the lightest neutralino $\widetilde{\chi}_1^0$. A simplified model is used, where the parameters are the top squark and neutralino masses [82, 83]. The branching fraction of top squark into a top quark and a neutralino is assumed to be 100%, and the top quark polarisation is assumed to be fully right-handed. A diagram of the process is shown in figure 10.

Top squark pair production with the top squarks decaying into a top quark and a neutralino could produce final states very similar to the one from $t\bar{t}$ production but with additional missing transverse energy. If the difference between the masses of the top squark and the neutralino is close to the top quark mass, the events would have similar topologies to the SM $t\bar{t}$ events. In such situations, direct top squark searches have low sensitivity because of the overwhelming $t\bar{t}$ background. However, from a very precise $t\bar{t}$ cross section measurement, top squark pair events can be searched for by looking for a small excess in the measured cross section compared to the SM expectation. The study presented here is complementary to the direct searches performed by CMS [84–86] and ATLAS [87–89], as it is more sensitive in a mass region, $m(\widetilde{t}) \approx m(\widetilde{\chi}_1^0) + m_t$, that is not accessible to conventional SUSY searches. Previous indirect searches in this mass region have been performed by the ATLAS collaboration [27, 90].

The 8 TeV data, analysed with the counting method (section 6.2), are used to derive upper limits on the production cross section for the top squark pair production for different top squark masses. The number of observed events in data is compared to the sum of SM $t\bar{t}$ and background events and the expected yields from top squark pair production.
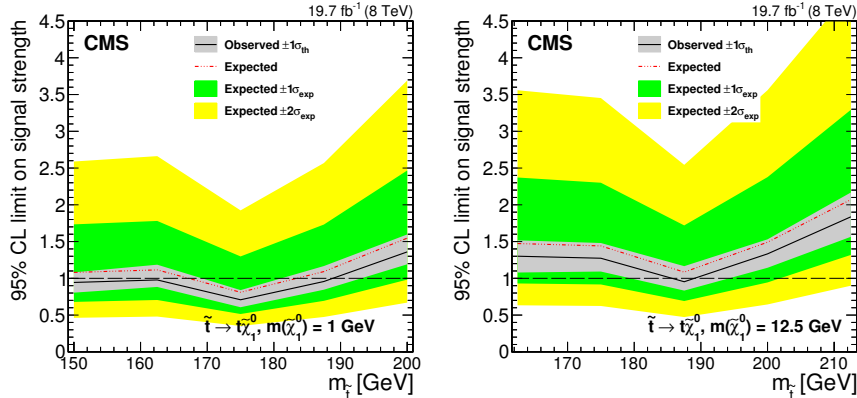
Figure 11. Expected and observed limits at 95% CL on the signal strength (see text) as a function of the top squark mass for neutralino masses of 1 GeV (left) and 12.5 GeV (right). The widest bands show the 68% and 95% CL ranges of the expected limit. The narrowest band quantifies the impact of the theoretical uncertainty in the cross section of the SUSY signal on the observed limit.

Top squark pair events generated with MADGRAPH with up to two associated partons are used for this study. The detector response is described using a fast simulation [91]. In order to account for differences with the full simulation of the CMS detector used for all other samples, a correction for the b tagging SFs is applied. Furthermore, a 10% uncertainty on the signal yields is added to account for the differences in lepton and trigger efficiencies between the fast and the full simulations. The signal samples are normalized according to the cross sections calculated at NLO+next-to-leading-logarithmic accuracy [92–96].

The 95% exclusion limits are calculated from Bayesian and modified CL_s techniques implemented in the THETA framework [97]. The yields of events given in table 1 (where $t\bar{t}$ MC events are normalised to the predicted NNLO cross section [23, 50]) are used, accounting for all the systematic uncertainties described in section 7. The uncertainty of 3.5% in the theoretical $t\bar{t}$ cross section is included to account for effects from renormalisation and factorisation scale and PDF uncertainties in the calculation [23].

The observed and expected limits on the mass of the top squark for neutralino masses of 1 and 12.5 GeV are shown in figure 11. The signal strength μ is defined as the ratio between the excluded cross section and the predicted one. Top squarks with masses below 189 GeV are excluded at 95% CL for the neutralino mass of 1 GeV, and in the range 185–189 GeV for the neutralino mass of 12.5 GeV.

The effect of the top quark polarisation on the final result is studied by calculating the exclusion limits assuming that the top quarks are 100% left-handed polarised. No significant differences are observed compared to the case of right-handed polarised top quarks.

11 Summary

A measurement of the inclusive $t\bar{t}$ production cross section in proton-proton collisions at the LHC is presented using the full 2011–2012 data samples of $5.0\,\mathrm{fb}^{-1}$ at $\sqrt{s} = 7\,\mathrm{TeV}$ and

19.7 fb^{-1} at $\sqrt{s} = 8$ TeV. The analysis is performed in the eμ channel using an improved cross section extraction method. The cross sections are determined with a binned likelihood fit to the p_T distribution of the non-b-tagged jet with the lowest p_T among the selected jets in the event, using categories of number of b-tagged and additional non-b-tagged jets. Assuming a top quark mass of 172.5 GeV, the results are

$$\sigma_{t\bar{t}} = 173.6 \pm 2.1 \,(\text{stat})^{+\,4.5}_{-\,4.0} \,(\text{syst}) \pm 3.8 \,(\text{lumi}) \,\text{pb}, \quad \text{at } \sqrt{s} = 7 \,\text{TeV and}$$
$$\sigma_{t\bar{t}} = 244.9 \pm 1.4 \,(\text{stat})^{+\,6.3}_{-\,5.5} \,(\text{syst}) \pm 6.4 \,(\text{lumi}) \,\text{pb}, \quad \text{at } \sqrt{s} = 8 \,\text{TeV},$$

in good agreement with recent NNLO QCD calculations. The ratio of the cross sections at the two different values of $\sqrt{s}$ is determined to be 1.41 ± 0.06. Moreover, the cross sections are measured in fiducial ranges defined by the transverse momentum and pseudorapidity requirements on the two charged leptons in the final state. The measurements constitute the most precise CMS results of $\sigma_{t\bar{t}}$ so far, and are competitive with recent ATLAS results [14].

The inclusive cross sections at 7 and 8 TeV are used to determine the top quark pole mass via the dependence of the theoretically predicted cross section on the mass, employing three different PDF sets. The values of the mass are consistent between the three sets. The most precise result, $173.8^{+1.7}_{-1.8}$ GeV, is obtained using the NNPDF3.0 PDF set.

The 8 TeV data are also used to constrain the cross section of pair production of supersymmetric top squarks with masses close to the top quark mass. No excess of event yields with respect to the SM prediction is found, and exclusion limits are presented as a function of the top squark mass for two different neutralino masses.

– 27 –

References

[1] CMS collaboration, *Measurement of the $t\bar{t}$ production cross section in the dilepton channel in pp collisions at $\sqrt{s} = 8\,TeV$, JHEP* **02** (2014) 024 [*Erratum ibid.* **1402** (2014) 102] [arXiv:1312.7582] [INSPIRE].

[2] CMS collaboration, *Measurement of the $t\bar{t}$ production cross section in pp collisions at $\sqrt{s} = 8\,TeV$ in dilepton final states containing one τ lepton, Phys. Lett.* **B 739** (2014) 23 [arXiv:1407.6643] [INSPIRE].

[3] CMS collaboration, *Measurement of the $t\bar{t}$ production cross section in the all-jets final state in pp collisions at $\sqrt{s} = 8\,TeV$, Eur. Phys. J.* **C 76** (2016) 128 [arXiv:1509.06076] [INSPIRE].

[4] CMS collaboration, *Measurement of the $t\bar{t}$ production cross section and the top quark mass in the dilepton channel in pp collisions at $\sqrt{s} = 7\,TeV$, JHEP* **07** (2011) 049 [arXiv:1105.5661] [INSPIRE].

[5] CMS collaboration, *Measurement of the $t\bar{t}$ production cross section in the all-jet final state in pp collisions at $\sqrt{s} = 7\,TeV$, JHEP* **05** (2013) 065 [arXiv:1302.0508] [INSPIRE].

[6] CMS collaboration, *Measurement of the top-antitop production cross section in the τ + jets channel in pp collisions at $\sqrt{s} = 7\,TeV$, Eur. Phys. J.* **C 73** (2013) 2386 [arXiv:1301.5755] [INSPIRE].

[7] CMS collaboration, *Measurement of the $t\bar{t}$ production cross section in pp collisions at $\sqrt{s} = 7\,TeV$ with lepton + jets final states, Phys. Lett.* **B 720** (2013) 83 [arXiv:1212.6682] [INSPIRE].

[8] CMS collaboration, *Measurement of the $t\bar{t}$ production cross section in the dilepton channel in pp collisions at $\sqrt{s} = 7\,TeV$, JHEP* **11** (2012) 067 [arXiv:1208.2671] [INSPIRE].

[9] CMS collaboration, *Measurement of the top quark pair production cross section in pp collisions at $\sqrt{s} = 7\,TeV$ in dilepton final states containing a τ, Phys. Rev.* **D 85** (2012) 112007 [arXiv:1203.6810] [INSPIRE].

[10] CMS collaboration, *Measurement of the $t\bar{t}$ production cross section in pp collisions at $7\,TeV$ in Lepton + jets events using b-quark jet identification, Phys. Rev.* **D 84** (2011) 092004 [arXiv:1108.3773] [INSPIRE].

[11] CMS collaboration, *Measurement of the top-antitop production cross section in pp collisions at $\sqrt{s} = 7\,TeV$ using the kinematic properties of events with leptons and jets, Eur. Phys. J.* **C 71** (2011) 1721 [arXiv:1106.0902] [INSPIRE].

[12] ATLAS collaboration, *Measurement of the top pair production cross section in $8\,TeV$ proton-proton collisions using kinematic information in the lepton+jets final state with ATLAS, Phys. Rev.* **D 91** (2015) 112013 [arXiv:1504.04251] [INSPIRE].

[13] ATLAS collaboration, *Simultaneous measurements of the $t\bar{t}$, W^+W^- and $Z/\gamma^* \rightarrow \tau\tau$ production cross-sections in pp collisions at $\sqrt{s} = 7\,TeV$ with the ATLAS detector, Phys. Rev.* **D 91** (2015) 052005 [arXiv:1407.0573] [INSPIRE].

[14] ATLAS collaboration, *Measurement of the $t\bar{t}$ production cross-section using $e\mu$ events with b-tagged jets in pp collisions at $\sqrt{s} = 7$ and $8\,TeV$ with the ATLAS detector, Eur. Phys. J.* **C 74** (2014) 3109 [arXiv:1406.5375] [INSPIRE].

[15] ATLAS collaboration, *Measurement of the cross section for top-quark pair production in pp collisions at $\sqrt{s} = 7\,TeV$ with the ATLAS detector using final states with two high-p_T leptons, JHEP* **05** (2012) 059 [arXiv:1202.4892] [INSPIRE].

[16] ATLAS collaboration, *Measurement of the ttbar production cross section in the τ + jets channel using the ATLAS detector*, *Eur. Phys. J.* **C 73** (2013) 2328 [arXiv:1211.7205] [InSPIRE].

[17] ATLAS collaboration, *Measurement of the top quark pair cross section with ATLAS in pp collisions at $\sqrt{s} = 7$ TeV using final states with an electron or a muon and a hadronically decaying τ lepton*, *Phys. Lett.* **B 717** (2012) 89 [arXiv:1205.2067] [InSPIRE].

[18] ATLAS collaboration, *Measurement of the top quark pair production cross-section with ATLAS in the single lepton channel*, *Phys. Lett.* **B 711** (2012) 244 [arXiv:1201.1889] [InSPIRE].

[19] ATLAS collaboration, *Measurement of the top quark pair production cross section in pp collisions at $\sqrt{s} = 7$ TeV in dilepton final states with ATLAS*, *Phys. Lett.* **B 707** (2012) 459 [arXiv:1108.3699] [InSPIRE].

[20] ATLAS collaboration, *Measurement of the top quark-pair production cross section with ATLAS in pp collisions at $\sqrt{s} = 7$ TeV*, *Eur. Phys. J.* **C 71** (2011) 1577 [arXiv:1012.1792] [InSPIRE].

[21] ATLAS collaboration, *Search for new phenomena in $t\bar{t}$ events with large missing transverse momentum in proton-proton collisions at $\sqrt{s} = 7$ TeV with the ATLAS detector*, *Phys. Rev. Lett.* **108** (2012) 041805 [arXiv:1109.4725] [InSPIRE].

[22] ATLAS collaboration, *Search for anomalous production of prompt like-sign muon pairs and constraints on physics beyond the standard model with the ATLAS detector*, *Phys. Rev.* **D 85** (2012) 032004 [arXiv:1201.1091] [InSPIRE].

[23] M. Czakon, P. Fiedler and A. Mitov, *Total top-quark pair-production cross section at hadron colliders through $O(\alpha_S^4)$*, *Phys. Rev. Lett.* **110** (2013) 252004 [arXiv:1303.6254] [InSPIRE].

[24] CMS collaboration, *Determination of the top-quark pole mass and strong coupling constant from the $t\bar{t}$ production cross section in pp collisions at $\sqrt{s} = 7$ TeV*, *Phys. Lett.* **B 728** (2014) 496 [arXiv:1307.1907] [InSPIRE].

[25] G.R. Farrar and P. Fayet, *Phenomenology of the production, decay and detection of new hadronic states associated with supersymmetry*, *Phys. Lett.* **B 76** (1978) 575 [InSPIRE].

[26] H.P. Nilles, *Supersymmetry, supergravity and particle physics*, *Phys. Rept.* **110** (1984) 1 [InSPIRE].

[27] ATLAS collaboration, *Measurement of spin correlation in top-antitop quark events and search for top squark pair production in pp collisions at $\sqrt{s} = 8$ TeV using the ATLAS detector*, *Phys. Rev. Lett.* **114** (2015) 142001 [arXiv:1412.4742] [InSPIRE].

[28] CMS collaboration, *The CMS experiment at the CERN LHC*, 2008 *JINST* **3** S08004 [InSPIRE].

[29] CMS collaboration, *Particle-flow event reconstruction in CMS and performance for jets, taus and MET*, CMS-PAS-PFT-09-001 (2009).

[30] CMS collaboration, *Commissioning of the particle-flow event reconstruction with the first LHC collisions recorded in the CMS detector*, CMS-PAS-PFT-10-001 (2010).

[31] J. Alwall et al., *The automated computation of tree-level and next-to-leading order differential cross sections and their matching to parton shower simulations*, *JHEP* **07** (2014) 079 [arXiv:1405.0301] [InSPIRE].

[32] P. Artoisenet, R. Frederix, O. Mattelaer and R. Rietkerk, *Automatic spin-entangled decays of heavy resonances in Monte Carlo simulations*, *JHEP* **03** (2013) 015 [arXiv:1212.3460] [InSPIRE].

– 30 –

[33] J. Pumplin, D.R. Stump, J. Huston, H.L. Lai, P.M. Nadolsky and W.K. Tung, *New generation of parton distributions with uncertainties from global QCD analysis*, *JHEP* **07** (2002) 012 [hep-ph/0201195] [INSPIRE].

[34] T. Sjöstrand, S. Mrenna and P.Z. Skands, *PYTHIA 6.4 physics and manual*, *JHEP* **05** (2006) 026 [hep-ph/0603175] [INSPIRE].

[35] M.L. Mangano, M. Moretti, F. Piccinini and M. Treccani, *Matching matrix elements and shower evolution for top-quark production in hadronic collisions*, *JHEP* **01** (2007) 013 [hep-ph/0611129].

[36] N. Davidson, G. Nanava, T. Przedzinski, E. Richter-Was and Z. Was, *Universal Interface of TAUOLA technical and physics documentation*, *Comput. Phys. Commun.* **183** (2012) 821 [arXiv:1002.0543] [INSPIRE].

[37] S. Alioli, P. Nason, C. Oleari and E. Re, *A general framework for implementing NLO calculations in shower Monte Carlo programs: the POWHEG BOX*, *JHEP* **06** (2010) 043 [arXiv:1002.2581] [INSPIRE].

[38] H.-L. Lai et al., *New parton distributions for collider physics*, *Phys. Rev.* **D 82** (2010) 074024 [arXiv:1007.2241] [INSPIRE].

[39] R. Field, *Early LHC underlying event data-findings and surprises*, in the proceedings of the 22nd *conference on hadron collider physics (HCP2010)*, August 23–27, Toronto, Canada (2010), arXiv:1010.3558 [INSPIRE].

[40] GEANT4 collaboration, S. Agostinelli et al., *GEANT4 — a simulation toolkit*, *Nucl. Instrum. Meth.* **A 506** (2003) 250 [INSPIRE].

[41] S. Alioli, P. Nason, C. Oleari and E. Re, *NLO single-top production matched with shower in POWHEG: s- and t-channel contributions*, *JHEP* **09** (2009) 111 [*Erratum ibid.* **02** (2010) 011] [arXiv:0907.4076] [INSPIRE].

[42] E. Re, *Single-top Wt-channel production matched with parton showers using the POWHEG method*, *Eur. Phys. J.* **C 71** (2011) 1547 [arXiv:1009.2450] [INSPIRE].

[43] R. Field, *Min-bias and the underlying event at the LHC*, *Acta Phys. Polon.* **B 42** (2011) 2631 [arXiv:1110.5530] [INSPIRE].

[44] K. Melnikov and F. Petriello, *The W boson production cross section at the LHC through $O(\alpha_s^2)$*, *Phys. Rev. Lett.* **96** (2006) 231803 [hep-ph/0603182] [INSPIRE].

[45] K. Melnikov and F. Petriello, *Electroweak gauge boson production at hadron colliders through $O(\alpha_s^2)$*, *Phys. Rev.* **D 74** (2006) 114017 [hep-ph/0609070] [INSPIRE].

[46] N. Kidonakis, *Two-loop soft anomalous dimensions for single top quark associated production with a W^- or H^-*, *Phys. Rev.* **D 82** (2010) 054018 [arXiv:1005.4451] [INSPIRE].

[47] J.M. Campbell, R.K. Ellis and C. Williams, *Vector boson pair production at the LHC*, *JHEP* **07** (2011) 018 [arXiv:1105.0020] [INSPIRE].

[48] J.M. Campbell and R.K. Ellis, *$t\bar{t}W^\pm$ production and decay at NLO*, *JHEP* **07** (2012) 052 [arXiv:1204.5678] [INSPIRE].

[49] M.V. Garzelli, A. Kardos, C.G. Papadopoulos and Z. Trócsányi, *$t\bar{t}\,W^\pm$ and $t\bar{t}Z$ hadroproduction at NLO accuracy in QCD with parton shower and hadronization effects*, *JHEP* **11** (2012) 056 [arXiv:1208.2665] [INSPIRE].

[50] M. Czakon and A. Mitov, *Top++: a program for the calculation of the top-pair cross-section at hadron colliders*, *Comput. Phys. Commun.* **185** (2014) 2930 [arXiv:1112.5675] [INSPIRE].

[51] M. Botje et al., *The PDF4LHC working group interim recommendations*, arXiv:1101.0538 [INSPIRE].

– 31 –

[52] S. Alekhin et al., *The PDF4LHC working group interim report*, arXiv:1101.0536 [INSPIRE].

[53] A.D. Martin, W.J. Stirling, R.S. Thorne and G. Watt, *Uncertainties on α_s in global PDF analyses and implications for predicted hadronic cross sections*, *Eur. Phys. J.* **C 64** (2009) 653 [arXiv:0905.3531] [INSPIRE].

[54] J. Gao et al., *CT10 next-to-next-to-leading order global analysis of QCD*, *Phys. Rev.* **D 89** (2014) 033009 [arXiv:1302.6246] [INSPIRE].

[55] R.D. Ball et al., *Parton distributions with LHC data*, *Nucl. Phys.* **B 867** (2013) 244 [arXiv:1207.1303] [INSPIRE].

[56] M. Czakon, M.L. Mangano, A. Mitov and J. Rojo, *Constraints on the gluon PDF from top quark pair production at hadron colliders*, *JHEP* **07** (2013) 167 [arXiv:1303.7215] [INSPIRE].

[57] CMS collaboration, *Measurement of the differential cross section for top quark pair production in pp collisions at $\sqrt{s} = 8\,TeV$*, *Eur. Phys. J.* **C 75** (2015) 542 [arXiv:1505.04480] [INSPIRE].

[58] CMS collaboration, *CMS tracking performance results from early LHC operation*, *Eur. Phys. J.* **C 70** (2010) 1165 [arXiv:1007.1988] [INSPIRE].

[59] CMS collaboration, *Performance of electron reconstruction and selection with the CMS detector in proton-proton collisions at $\sqrt{s} = 8\,TeV$*, 2015 *JINST* **10** P06005 [arXiv:1502.02701] [INSPIRE].

[60] CMS collaboration, *Performance of CMS muon reconstruction in pp collision events at $\sqrt{s} = 7\,TeV$*, 2012 *JINST* **7** P10002 [arXiv:1206.4071] [INSPIRE].

[61] CMS collaboration, *Measurements of inclusive W and Z cross sections in pp collisions at $\sqrt{s} = 7\,TeV$*, *JHEP* **01** (2011) 080 [arXiv:1012.2466] [INSPIRE].

[62] M. Cacciari, G.P. Salam and G. Soyez, *The anti-k_t jet clustering algorithm*, *JHEP* **04** (2008) 063 [arXiv:0802.1189] [INSPIRE].

[63] CMS collaboration, *Determination of jet energy calibration and transverse momentum resolution in CMS*, 2011 *JINST* **6** P11002 [arXiv:1107.4277] [INSPIRE].

[64] CMS collaboration, *Identification of b-quark jets with the CMS experiment*, 2013 *JINST* **8** P04013 [arXiv:1211.4462] [INSPIRE].

[65] PARTICLE DATA GROUP collaboration, K.A. Olive et al., *Review of particle physics*, *Chin. Phys.* **C 38** (2014) 090001 [INSPIRE].

[66] F. James and M. Roos, *Minuit: a system for function minimization and analysis of the parameter errors and correlations*, *Comput. Phys. Commun.* **10** (1975) 343 [INSPIRE].

[67] A. Bodek, A. van Dyne, J.Y. Han, W. Sakumoto and A. Strelnikov, *Extracting muon momentum scale corrections for hadron collider experiments*, *Eur. Phys. J.* **C 72** (2012) 2194 [arXiv:1208.3710] [INSPIRE].

[68] G. Antchev et al., *First measurement of the total proton-proton cross section at the LHC energy of $\sqrt{s} = 7\,TeV$*, *Europhys. Lett.* **96** (2011) 21002 [arXiv:1110.1395] [INSPIRE].

[69] CMS collaboration, *Absolute calibration of the luminosity measurement at CMS: winter 2012 update*, CMS-PAS-SMP-12-008 (2012).

[70] CMS collaboration, *CMS luminosity based on pixel cluster counting — Summer 2013 update*, CMS-PAS-LUM-13-001 (2013).

[71] M. Bähr et al., *HERWIG++ physics and manual*, *Eur. Phys. J.* **C 58** (2008) 639 [arXiv:0803.0883] [INSPIRE].

[72] ALEPH collaboration, A. Heister et al., *Study of the fragmentation of b quarks into B mesons at the Z peak*, *Phys. Lett.* **B 512** (2001) 30 [hep-ph/0106051] [INSPIRE].

[73] DELPHI collaboration, J. Abdallah et al., *A study of the b-quark fragmentation function with the DELPHI detector at LEP I and an averaged distribution obtained at the Z pole*, *Eur. Phys. J.* **C 71** (2011) 1557 [arXiv:1102.4748] [INSPIRE].

[74] P.Z. Skands, *Tuning Monte Carlo generators: the Perugia tunes*, *Phys. Rev.* **D 82** (2010) 074018 [arXiv:1005.3457] [INSPIRE].

[75] A. Buckley et al., *General-purpose event generators for LHC physics*, *Phys. Rept.* **504** (2011) 145 [arXiv:1101.2599] [INSPIRE].

[76] NNPDF collaboration, R.D. Ball et al., *Parton distributions for the LHC Run II*, *JHEP* **04** (2015) 040 [arXiv:1410.8849] [INSPIRE].

[77] S. Dulat et al., *New parton distribution functions from a global analysis of quantum chromodynamics*, *Phys. Rev.* **D 93** (2016) 033006 [arXiv:1506.07443] [INSPIRE].

[78] L.A. Harland-Lang, A.D. Martin, P. Motylinski and R.S. Thorne, *Parton distributions in the LHC era: MMHT 2014 PDFs*, *Eur. Phys. J.* **C 75** (2015) 204 [arXiv:1412.3989] [INSPIRE].

[79] J. Wenniger, *Energy calibration of the LHC beams at 4 TeV*, CERN-ATS-2013-040 (2013).

[80] C. Boehm, A. Djouadi and M. Drees, *Light scalar top quarks and supersymmetric dark matter*, *Phys. Rev.* **D 62** (2000) 035012 [hep-ph/9911496] [INSPIRE].

[81] C. Balázs, M. Carena and C.E.M. Wagner, *Dark matter, light stops and electroweak baryogenesis*, *Phys. Rev.* **D 70** (2004) 015007 [hep-ph/0403224] [INSPIRE].

[82] J. Alwall, P. Schuster and N. Toro, *Simplified models for a first characterization of new physics at the LHC*, *Phys. Rev.* **D 79** (2009) 075020 [arXiv:0810.3921] [INSPIRE].

[83] LHC New Physics Working Group collaboration, D. Alves, *Simplified models for LHC new physics searches*, *J. Phys.* **G 39** (2012) 105005 [arXiv:1105.2838] [INSPIRE].

[84] CMS collaboration, *Search for top-squark pair production in the single-lepton final state in pp collisions at $\sqrt{s} = 8$ TeV*, *Eur. Phys. J.* **C 73** (2013) 2677 [arXiv:1308.1586] [INSPIRE].

[85] CMS collaboration, *Searches for third-generation squark production in fully hadronic final states in proton-proton collisions at $\sqrt{s} = 8$ TeV*, *JHEP* **06** (2015) 116 [arXiv:1503.08037] [INSPIRE].

[86] CMS collaboration, *Search for direct pair production of scalar top quarks in the single- and dilepton channels in proton-proton collisions at $\sqrt{s} = 8$ TeV*, *JHEP* **07** (2016) 027 [arXiv:1602.03169] [INSPIRE].

[87] ATLAS collaboration, *Search for top squark pair production in final states with one isolated lepton, jets and missing transverse momentum in $\sqrt{s} = 8$ TeV pp collisions with the ATLAS detector*, *JHEP* **11** (2014) 118 [arXiv:1407.0583] [INSPIRE].

[88] ATLAS collaboration, *Search for direct pair production of the top squark in all-hadronic final states in proton-proton collisions at $\sqrt{s} = 8$ TeV with the ATLAS detector*, *JHEP* **09** (2014) 015 [arXiv:1406.1122] [INSPIRE].

[89] ATLAS collaboration, *Search for direct top-squark pair production in final states with two leptons in pp collisions at $\sqrt{s} = 8$ TeV with the ATLAS detector*, *JHEP* **06** (2014) 124 [arXiv:1403.4853] [INSPIRE].

[90] ATLAS collaboration, *ATLAS run 1 searches for direct pair production of third-generation squarks at the Large Hadron Collider*, *Eur. Phys. J.* **C 75** (2015) 510 [arXiv:1506.08616] [INSPIRE].

[91] CMS collaboration, *The fast simulation of the CMS detector at LHC*, *J. Phys. Conf. Ser.* **331** (2011) 032049 [ɪɴSPIRE].

[92] W. Beenakker, R. Hopker, M. Spira and P.M. Zerwas, *Squark and gluino production at hadron colliders*, *Nucl. Phys.* **B 492** (1997) 51 [hep-ph/9610490] [ɪɴSPIRE].

[93] A. Kulesza and L. Motyka, *Threshold resummation for squark-antisquark and gluino-pair production at the LHC*, *Phys. Rev. Lett.* **102** (2009) 111802 [arXiv:0807.2405] [ɪɴSPIRE].

[94] A. Kulesza and L. Motyka, *Soft gluon resummation for the production of gluino-gluino and squark-antisquark pairs at the LHC*, *Phys. Rev.* **D 80** (2009) 095004 [arXiv:0905.4749] [ɪɴSPIRE].

[95] W. Beenakker, S. Brensing, M. Krämer, A. Kulesza, E. Laenen and I. Niessen, *Soft-gluon resummation for squark and gluino hadroproduction*, *JHEP* **12** (2009) 041 [arXiv:0909.4418] [ɪɴSPIRE].

[96] W. Beenakker et al., *Squark and gluino hadroproduction*, *Int. J. Mod. Phys.* **A 26** (2011) 2637 [arXiv:1105.1110] [ɪɴSPIRE].

[97] T. Müller, J. Ott and J. Wagner-Kuhr, *THETA — A framework for template-based statistical modeling and inference*, http://theta-framework.org.

– 34 –

THE EUROPEAN
PHYSICAL JOURNAL C

CrossMark

Measurement of t̄t production with additional jet activity, including b quark jets, in the dilepton decay channel using pp collisions at $\sqrt{s} = 8$ TeV

CMS Collaboration[*]

CERN, 1211 Geneva 23, Switzerland

Abstract Jet multiplicity distributions in top quark pair (t̄t) events are measured in pp collisions at a centre-of-mass energy of 8 TeV with the CMS detector at the LHC using a data set corresponding to an integrated luminosity of 19.7 fb^{-1}. The measurement is performed in the dilepton decay channels (e$^+$e$^-$, $\mu^+\mu^-$, and e$^\pm\mu^\mp$). The absolute and normalized differential cross sections for t̄t production are measured as a function of the jet multiplicity in the event for different jet transverse momentum thresholds and the kinematic properties of the leading additional jets. The differential t̄tb and t̄tb̄b cross sections are presented for the first time as a function of the kinematic properties of the leading additional b jets. Furthermore, the fraction of events without additional jets above a threshold is measured as a function of the transverse momenta of the leading additional jets and the scalar sum of the transverse momenta of all additional jets. The data are compared and found to be consistent with predictions from several perturbative quantum chromodynamics event generators and a next-to-leading order calculation.

1 Introduction

Precise measurements of t̄t production and decay properties [1–9] provide crucial information for testing the expectations of the standard model (SM) and specifically of calculations in the framework of perturbative quantum chromodynamics (QCD) at high-energy scales. At the energies of the CERN LHC, about half of the t̄t events contain jets with transverse momentum (p_T) larger than 30 GeV that do not come from the weak decay of the t̄t system [5]. In this paper, these jets will be referred to as "additional jets" and the events as "t̄t+jets". The additional jets typically arise from initial-state QCD radiation, and their study provides an essential test of the validity and completeness of higher-order QCD calculations describing the processes leading to multijet events.

A correct description of these events is also relevant because t̄t+jets processes constitute important backgrounds in the searches for new physics. These processes also constitute a challenging background in the attempt to observe the production of a Higgs boson in association with a t̄t pair (t̄tH), where the Higgs boson decays to a bottom (b) quark pair (bb̄), because of the much larger cross section compared to the t̄tH signal. Such a process has an irreducible nonresonant background from t̄t pair production in association with a bb̄ pair from gluon splitting. Therefore, measurements of t̄t+jets and t̄tb̄b production can give important information about the main background in the search for the t̄tH process and provide a good test of next-to-leading-order (NLO) QCD calculations.

Here, we present a detailed study of the production of t̄t events with additional jets and b quark jets in the final state from pp collisions at $\sqrt{s} = 8$ TeV using the data recorded in 2012 with the CMS detector, corresponding to an integrated luminosity of 19.7 fb^{-1}. The t̄t pairs are reconstructed in the dilepton decay channel with two oppositely charged isolated leptons (electrons or muons) and at least two jets. The analysis follows, to a large extent, the strategy used in the measurement of normalized t̄t differential cross sections in the same decay channel described in Ref. [8].

The measurements of the absolute and normalized differential t̄t cross sections are performed as a function of the jet multiplicity for different p_T thresholds for the jets, in order to probe the momentum dependence of the hard-gluon emission. The results are presented in a visible phase space in which all selected final-state objects are produced within the detector acceptance and are thus measurable experimentally. The study extends the previous measurement at $\sqrt{s} = 7$ TeV [5], where only normalized differential cross sections were presented.

The absolute and normalized t̄t+jets production cross sections are also measured as a function of the p_T and pseudorapidity (η) [10] of the leading additional jets, ordered by p_T. The CMS experiment has previously published a mea-

[*] e-mail: cms-publication-committee-chair@cern.ch

Springer

surement of the inclusive $t\bar{t}b\bar{b}$ production cross section [11]. In the present analysis, the $t\bar{t}b\bar{b}$ and $t\bar{t}b$ (referred to as "$t\bar{t}b\bar{b}$ ($t\bar{t}b$)" in the following) cross sections are measured for the first time differentially as a function of the properties of the additional jets associated with b quarks, which will hereafter be called b jets. The $t\bar{t}b\bar{b}$ process corresponds to events where two additional b jets are generated in the visible phase space, while $t\bar{t}b$ represents the same physical process, where only one additional b jet is within the acceptance requirements. In cases with at least two additional jets or two b jets, the cross section is also measured as a function of the angular distance between the two jets and their dijet invariant mass. The results are reported both in the visible phase space and extrapolated to the full phase space of the $t\bar{t}$ system to facilitate the comparison with theoretical calculations.

Finally, the fraction of events that do not contain additional jets (gap fraction) is determined as a function of the threshold on the leading and subleading additional-jet p_T, and the scalar sum of all additional-jet p_T. This was first measured in Refs. [5,12].

The results are compared at particle level to theoretical predictions obtained with four different event generators: MADGRAPH [13], MC@NLO [14], POWHEG [15], and MG5_AMC@NLO [16], interfaced with either PYTHIA [17] or HERWIG [18], and in the case of POWHEG with both. Additionally, the measurements as a function of the b jet quantities are compared to the predictions from the event generator POWHEL [19].

This paper is structured as follows. A brief description of the CMS detector is provided in Sect. 2. Details of the event simulation generators and their theoretical predictions are given in Sect. 3. The event selection and the method used to identify the additional radiation in the event for both $t\bar{t}$+jets and $t\bar{t}b\bar{b}$ ($t\bar{t}b$) studies are presented in Sects. 4 and 5. The cross section measurement and the systematic uncertainties are described in Sects. 6 and 7. The results as a function of the jet multiplicity and the kinematic properties of the additional jets and b jets are presented in Sects. 8–10. The definition of the gap fraction and the results are described in Sect. 11. Finally, a summary is given in Sect. 12.

2 The CMS detector

The central feature of the CMS apparatus is a superconducting solenoid of 6 m internal diameter, providing a magnetic field of 3.8 T. Within the solenoid volume are a silicon pixel and strip tracker, a lead tungstate crystal electromagnetic calorimeter (ECAL), and a brass and scintillator hadron calorimeter, each composed of a barrel and two endcap sections. Extensive forward calorimetry complements the coverage provided by the barrel and endcap detectors. Muons are measured in gas-ionization detectors embedded in the

steel flux-return yoke outside the solenoid. A more detailed description of the CMS detector, together with a definition of the coordinate system used and the relevant kinematic variables, can be found in Ref. [10].

3 Event simulation and theoretical predictions

Experimental effects coming from event reconstruction, selection criteria, and detector resolution are modelled using Monte Carlo (MC) event generators interfaced with a detailed simulation of the CMS detector response using GEANT4 (v. 9.4) [20].

The MADGRAPH (v. 5.1.5.11) [13] generator calculates the matrix elements at tree level up to a given order in α_s. In particular, the simulated $t\bar{t}$ sample used in this analysis is generated with up to three additional partons. The MADSPIN [21] package is used to incorporate spin correlations of the top quark decay products. The value of the top quark mass is chosen to be $m_t = 172.5$ GeV, and the proton structure is described by the CTEQ6L1 [22] set of parton distribution functions (PDF). The generated events are subsequently processed with PYTHIA (v. 6.426) [17] for fragmentation and hadronization, using the MLM prescription for the matching of higher-multiplicity matrix element calculations with parton showers [23]. The PYTHIA parameters for the underlying event, parton shower, and hadronization are set according to the Z2* tune, which is derived from the Z1 tune [24]. The Z1 tune uses the CTEQ5L PDFs, whereas Z2* adopts CTEQ6L.

In addition to the nominal $t\bar{t}$ MADGRAPH sample, dedicated samples are generated by varying the central value of the renormalization (μ_R) and factorization (μ_F) scales and the matrix element/parton showering matching scale (jet-parton matching scale). These samples are produced to determine the systematic uncertainties in the measurement owing to the theoretical assumptions on the modelling of $t\bar{t}$ events, as well as for comparisons with the measured distributions. The nominal values of μ_R and μ_F are defined by the Q^2 scale in the event: $\mu_R^2 = \mu_F^2 = Q^2 = m_t^2 + \sum p_T^2(\text{jet})$, where the sum runs over all the additional jets in the event not coming from the $t\bar{t}$ decay. The samples with the varied scales use $\mu_R^2 = \mu_F^2 = 4Q^2$ and $Q^2/4$, respectively. For the nominal MADGRAPH sample, a jet-parton matching scale of 40 GeV is chosen, while for the varied samples, values of 60 and 30 GeV are employed, respectively. These scales correspond to jet-parton matching thresholds of 20 GeV for the nominal sample, and 40 and 10 GeV for the varied ones.

The POWHEG (v. 1.0 r1380) and MC@NLO (v. 3.41) generators, along with the CT10 [25] and CTEQ6M [22] PDFs, are used, respectively, for comparisons with the data. The POWHEG generator simulates calculations of $t\bar{t}$ production to full NLO accuracy, and is matched with two parton shower MC generators: the PYTHIA (v. 6.426) Z2* tune (designated

as PYTHIA6 in the following), and the HERWIG [18] (v. 6.520) AUET2 tune [26] (referred to as HERWIG6 in the following). The parton showering in PYTHIA is based on a transverse-momentum ordering of parton showers, whereas HERWIG uses angular ordering. The MC@NLO generator implements the hard matrix element to full NLO accuracy, matched with HERWIG (v. 6.520) for the initial- and final-state parton showers using the default tune. These two generators, POWHEG and MC@NLO, are formally equivalent up to the NLO accuracy, but they differ in the techniques used to avoid double counting of radiative corrections that may arise from interfacing with the parton showering generators.

The cross section as a function of jet multiplicity and the gap fraction measurements are compared to the NLO predictions of the POWHEG (v2) [15] and MG5_AMC@NLO [16] generators. The POWHEG (v2) generator is matched to the PYTHIA (v. 8.205) CUETP8M1 tune [27] (referred to as PYTHIA8), HERWIG6, and PYTHIA6. In these samples the HDAMP parameter of POWHEGBOX, which controls the matrix element and parton shower matching and effectively regulates the high-p_T radiation, is set to $m_t = 172.5$ GeV. The MG5_AMC@NLO generator simulates $t\bar{t}$ events with up to two additional partons at NLO, and is matched to the PYTHIA8 parton shower simulation using the FxFx merging prescription [28]. The top quark mass value used in all these simulations is also 172.5 GeV and the PDF set is NNPDF3.0 [29]. In addition, a $t\bar{t}$ MADGRAPH sample matched to PYTHIA8 for the parton showering and hadronization is used for comparisons with the data.

The $t\bar{t}b\bar{b}$ production cross sections are also compared with the predictions by the generator POWHEL [19] (HELAC-NLO [30] + POWHEGBOX [31]), which implements the full $t\bar{t}b\bar{b}$ process at NLO QCD accuracy, with parton shower matching based on the POWHEG NLO matching algorithm [15,32]. The events are further hadronized by means of PYTHIA (v. 6.428), using parameters of the Perugia 2011 C tune [33]. In the generation of the events, the renormalization and factorization scales are fixed to $\mu_R = \mu_F = H_T/4$, where H_T is the sum of the transverse energies of the final-state partons $(t, \bar{t}, b, \bar{b})$ from the underlying tree-level process, and the CT10 PDFs are used.

The SM background samples are simulated with MAD-GRAPH, POWHEG, or PYTHIA, depending on the process. The MADGRAPH generator is used to simulate $Z/\gamma*$ production (referred to as Drell–Yan, DY, in the following), $t\bar{t}$ production in association with an additional boson (referred to as $t\bar{t}+Z$, $t\bar{t}+W$, and $t\bar{t}+\gamma$), and W boson production with additional jets (W+jets in the following). Single top quark events (tW channel) are simulated using POWHEG. Diboson (WW, WZ, and ZZ) and QCD multijet events are simulated using PYTHIA. For the $t\bar{t}b$ and $t\bar{t}b\bar{b}$ measurements, the expected contribution from SM $t\bar{t}H$ processes, simulated with PYTHIA, is also considered, although the final state has not yet been observed.

For comparison with the measured distributions, the events in the simulated samples are normalized to an integrated luminosity of 19.7 fb^{-1} according to their predicted cross sections. These are taken from next-to-next-to-leading-order (NNLO) (W+jets [34] and DY [35]), NLO + next-to-next-to-leading logarithmic (NNLL) (single top quark tW channel [36]), NLO (diboson [37], $t\bar{t}+Z$ [38], $t\bar{t}+W$ [38], and $t\bar{t}+H$ [39]), and leading-order (LO) (QCD multijet [17]) calculations. The contribution of QCD multijet events is found to be negligible. The predicted cross section for the $t\bar{t}+\gamma$ sample is obtained by scaling the LO cross section obtained with the WHIZARD event generator [40] by an NLO/LO K-factor correction [41]. The $t\bar{t}$ simulated sample is normalized to the total cross section $\sigma_{t\bar{t}} = 252.9 \pm ^{6.4}_{8.6}$(scale) $\pm$ 11.7(PDF + α_s) pb, calculated with the TOP++2.0 program to NNLO in perturbative QCD, including soft-gluon resummation to NNLL order [42], and assuming $m_t = 172.5$ GeV. The first uncertainty comes from the independent variation of the factorization and renormalization scales, μ_R and μ_F, while the second one is associated with variations in the PDF and α_s, following the PDF4LHC prescription with the MSTW2008 68 % confidence level (CL) NNLO, CT10 NNLO, and NNPDF2.3 5f FFN PDF sets (see Refs. [43,44] and references therein and Refs. [45–47]).

A number of additional pp simulated hadronic interactions ("pileup") are added to each simulated event to reproduce the multiple interactions in each bunch crossing from the luminosity conditions in the real data taking. Correction factors for detector effects (described in Sects. 4 and 6) are applied, when needed, to improve the description of the data by the simulation.

4 Event reconstruction and selection

The event selection is based on the decay topology of the $t\bar{t}$ events, where each top quark decays into a W boson and a b quark. Only the cases in which both W bosons decayed to a charged lepton and a neutrino are considered. These signatures imply the presence of isolated leptons, missing transverse momentum owing to the neutrinos from W boson decays, and highly energetic jets. The heavy-quark content of the jets is identified through b tagging techniques. The same requirements are applied to select the events for the different measurements, with the exception of the requirements on the b jets, which have been optimized independently for the $t\bar{t}$+jets and $t\bar{t}b\bar{b}$ ($t\bar{t}b$) cases. The description of the event reconstruction and selection is detailed in the following.

Events are reconstructed using a particle-flow (PF) algorithm, in which signals from all subdetectors are combined [48,49]. Charged particles are required to originate from the primary collision vertex [50], defined as the vertex with the highest sum of p_T^2 of all reconstructed tracks associated

with it. Therefore, charged-hadron candidates from pileup events, i.e. originating from additional pp interactions within the same bunch crossing, are removed before jet clustering on an event-by-event basis. Subsequently, the remaining neutral-particle component from pileup events is accounted for through jet energy corrections [51].

Muon candidates are reconstructed from tracks that can be linked between the silicon tracker and the muon system [52]. The muons are required to have $p_T > 20$ GeV, be within $|\eta| < 2.4$, and have a relative isolation $I_{rel} < 0.15$. The parameter I_{rel} is defined as the sum of the p_T of all neutral and charged reconstructed PF candidates, except the muon itself, inside a cone of $\Delta R \equiv \sqrt{(\Delta\eta)^2 + (\Delta\phi)^2} < 0.3$ around the muon direction, divided by the muon p_T, where $\Delta\eta$ and $\Delta\phi$ are the difference in pseudorapidity and azimuthal angle between the directions of the candidate and the muon, respectively. Electron candidates are identified by combining information from charged-track trajectories and energy deposition measurements in the ECAL [53], and are required to be within $|\eta| < 2.4$, have a transverse energy of at least 20 GeV, and fulfill $I_{rel} < 0.15$ inside a cone of $\Delta R < 0.3$. Electrons from identified photon conversions are rejected. The lepton identification and isolation efficiencies are determined via a tag-and-probe method using Z boson events.

Jets are reconstructed by clustering the PF candidates, using the anti-k_T clustering algorithm [54,55] with a distance parameter of 0.5. The jet momentum is determined as the vectorial sum of all particle momenta in the jet, and is found in the simulation to be within 5 to 10 % of the true momentum over the entire p_T range and detector acceptance. Jet energy corrections are derived from the simulation, and are confirmed with in situ measurements with the energy balance of dijet and photon+jet events [56]. The jet energy resolution amounts typically to 15 % at 10 GeV and 8 % at 100 GeV. Muons and electrons passing less stringent requirements compared to the ones mentioned above are identified and excluded from the clustering process. Jets are selected in the interval $|\eta| < 2.4$ and with $p_T > 20$ GeV. Additionally, the jets identified as part of the decay products of the $t\bar{t}$ system (cf. Sect. 5) must fulfill $p_T > 30$ GeV. Jets originating from the hadronization of b quarks are identified using a combined secondary vertex algorithm (CSV) [57], which provides a b tagging discriminant by combining identified secondary vertices and track-based lifetime information.

The missing transverse energy ($\not{E}_T$) is defined as the magnitude of the projection on the plane perpendicular to the beams of the negative vector sum of the momenta of all reconstructed particles in an event [58]. To mitigate the effect of contributions from pileup on the $\not{E}_T$ resolution, we use a multivariate correction where the measured momentum is separated into components that originate from the primary and the other collision vertices [59]. This correction improves the $\not{E}_T$ resolution by $\approx$5 %.

Events are triggered by requiring combinations of two leptons (ℓ = e or μ), where one fulfills a p_T threshold of 17 GeV and the other of 8 GeV, irrespective of the flavour of the leptons. The dilepton trigger efficiencies are measured using samples selected with triggers that require a minimum $\not{E}_T$ or number of jets in the event, and are only weakly correlated to the dilepton triggers used in the analysis.

Events are selected if there are at least two isolated leptons of opposite charge. Events with a lepton pair invariant mass less than 20 GeV are removed to suppress events from heavy-flavour resonance decays, QCD multijet, and DY production. In the $\mu\mu$ and ee channels, the dilepton invariant mass is required to be outside a Z boson mass window of 91$\pm$15 GeV, and $\not{E}_T$ is required to be larger than 40 GeV.

For the $t\bar{t}$+jets selection, a minimum of two jets is required, of which at least one must be tagged as a b jet. A loose CSV discriminator value is chosen such that the efficiency for tagging jets from b (c) quarks is $\approx$85 % (40 %), while the probability of tagging jets originating from light quarks (u, d, or s) or gluons is around 10 %. Efficiency corrections, depending on jet p_T and η, are applied to account for differences in the performance of the b tagging algorithm between data and simulation.

For the $t\bar{t}b\bar{b}$ ($t\bar{t}b$) selection, at least three b-tagged jets are required (without further requirements on the minimum number of jets). In this case, a tighter discriminator value [57] is chosen to increase the purity of the sample. The efficiency of this working point is approximately 70 % (20 %) for jets originating from a b (c) quark, while the misidentification rate for light-quark and gluon jets is around 1 %. The shape of the CSV discriminant distribution in simulation is corrected to better describe the efficiency observed in the data. This correction is derived separately for light-flavour and b jets from a tag-and-probe approach using control samples enriched in events with a Z boson and exactly two jets, and $t\bar{t}$ events in the eμ channel with no additional jets [60].

5 Identification of additional radiation in the event

To study additional jet activity in the data, the identification of jets arising from the decay of the $t\bar{t}$ system is crucial. In particular, we need to identify correctly the two b jets from the top quark decays in events with more than two b jets. This is achieved by following two independent but complementary approaches: a kinematic reconstruction [61] and a multivariate analysis, optimized for the two cases under study, $t\bar{t}$+jets and $t\bar{t}b\bar{b}$ ($t\bar{t}b$), respectively. The purpose of the kinematic reconstruction is to completely reconstruct the $t\bar{t}$ system based on $\not{E}_T$ and the information on identified jets and leptons, taking into account detector resolution effects. This method is optimized for the case where the b jets in the event only arise from the decay of the top quark pair. The

multivariate approach is optimized for events with more b jets than just those from the $t\bar{t}$ system. This method identifies the two jets that most likely originated from the top quark decays, and the additional b jets, but does not perform a full reconstruction of the $t\bar{t}$ system. Both methods are described in the following sections.

5.1 Kinematic reconstruction in $t\bar{t}$+jets events

The kinematic reconstruction method was developed and used for the first time in the analysis from Ref. [8]. In this method the following constraints are imposed: $\not{E}_T$ is assumed to originate solely from the two neutrinos; the W boson invariant mass is fixed to 80.4 GeV [62]; and the top quark and antiquark masses are fixed to a value of 172.5 GeV. Each pair of jets and lepton-jet combination fulfilling the selection criteria is considered in the kinematic reconstruction. Effects of detector resolution are accounted for by randomly smearing the measured energies and directions of the reconstructed lepton and b jet candidates by their resolutions. These are determined from the simulation of signal events by comparing the reconstructed b jets and leptons matched to the generated b quarks and leptons from top quark decays. For a given smearing, the solution of the equations for the neutrino momenta yielding the smallest invariant mass of the $t\bar{t}$ system is chosen. For each solution, a weight is calculated based on the expected invariant mass spectrum of the lepton and b jet from the top quark decays at the parton level. The weights are summed over 100 randomly smeared reconstruction attempts, and the kinematics of the top quark and antiquark are calculated as a weighted average. Finally, the two jets and lepton-jet combinations that yield the maximum sum of weights are chosen for further analysis. Combinations with two b-tagged jets are chosen over those with a single b-tagged jet. The efficiency of the kinematic reconstruction, defined as the number of events with a solution divided by the total number of selected $t\bar{t}$+jets events, is approximately 94 %. The efficiency in simulation is similar to the one in data for all jet multiplicities. Events with no valid solution for the neutrino momenta are excluded from further analysis. In events with additional jets, the algorithm correctly identifies the two jets coming from the $t\bar{t}$ decay in about 70 % of the cases.

After the full event selection is applied, the dominant background in the eμ channel originates from other $t\bar{t}$ decay channels and is estimated using simulation. This contribution corresponds mostly to leptonic τ decays, which are considered background in the $t\bar{t}$+jets measurements. In the ee and $\mu\mu$ channels, the dominant background contribution arises from Z/γ*+jets production. The normalization of this background contribution is derived from data using the events rejected by the Z boson veto, scaled by the ratio of events failing and passing this selection, estimated from simulation [63].

The remaining backgrounds, including the single top quark tW channel, W+jets, diboson, and QCD multijet events, are estimated from simulation for all the channels.

In Fig. 1, the multiplicity distributions of the selected jets per event are shown for different jet p_T thresholds and compared to SM predictions. In this figure and the following ones, the $t\bar{t}$ sample is simulated using MADGRAPH+PYTHIA6, where only $t\bar{t}$ events with two leptons (e or μ) from the W boson decay are considered as signal. All other $t\bar{t}$ events, specifically those originating from decays via τ leptons, which are the dominant contribution, are considered as background. In the following figures, "Electroweak" corresponds to DY, W+jets, and diboson processes, and "$t\bar{t}$ bkg." includes the $t\bar{t}+\gamma$/W/Z events. The data are well described by the simulation, both for the low jet p_T threshold of 30 GeV and the higher thresholds of 60 and 100 GeV. The hatched regions in Figs. 1, 2 and 3 correspond to the uncertainties affecting the shape of the simulated signal and background events (cf. Sect. 6), and are dominated by modelling uncertainties in the former.

Additional jets in the event are defined as those jets within the phase space described in the event selection (cf. Sect. 4) that are not identified by the kinematic reconstruction to be part of the $t\bar{t}$ system. The η and p_T distributions of the additional jets with the largest and second largest p_T in the event (referred to as the leading and subleading additional jets in the following) are shown in Fig. 2. Three additional event variables are considered: the scalar sum of the p_T of all additional jets, H_T, the invariant mass of the leading and subleading additional jets, m_{jj}, and their angular separation, $\Delta R_{jj} = \sqrt{(\Delta\eta)^2 + (\Delta\phi)^2}$, where $\Delta\eta$ and $\Delta\phi$ are the pseudorapidity and azimuthal differences between the directions of the two jets. These distributions are shown in Fig. 3. The predictions from the simulation, also shown in the figures, describe the data within the uncertainties.

5.2 Identification of $t\bar{t}$ jets and additional jets in $t\bar{t}b\bar{b}$ events

The multivariate approach uses a boosted decision tree (BDT) to distinguish the b jets stemming from the $t\bar{t}$ system from those arising from additional radiation for final states with more than two b jets. This method is optimized for $t\bar{t}b\bar{b}$ topologies in the dilepton final state of the $t\bar{t}$ system. The BDT is set up using the TMVA package [64]. To avoid any dependence on the kinematics of the additional jets, and especially on the invariant mass of the two additional jets, the method identifies the jets stemming from the $t\bar{t}$ system by making use of properties of the $t\bar{t}$ system that are expected to be mostly insensitive to the additional radiation. The variables combine information from the two final-state leptons, the jets, and $\not{E}_T$. All possible pairs of reconstructed jets in an event are considered. For each pair, one jet is assigned to the
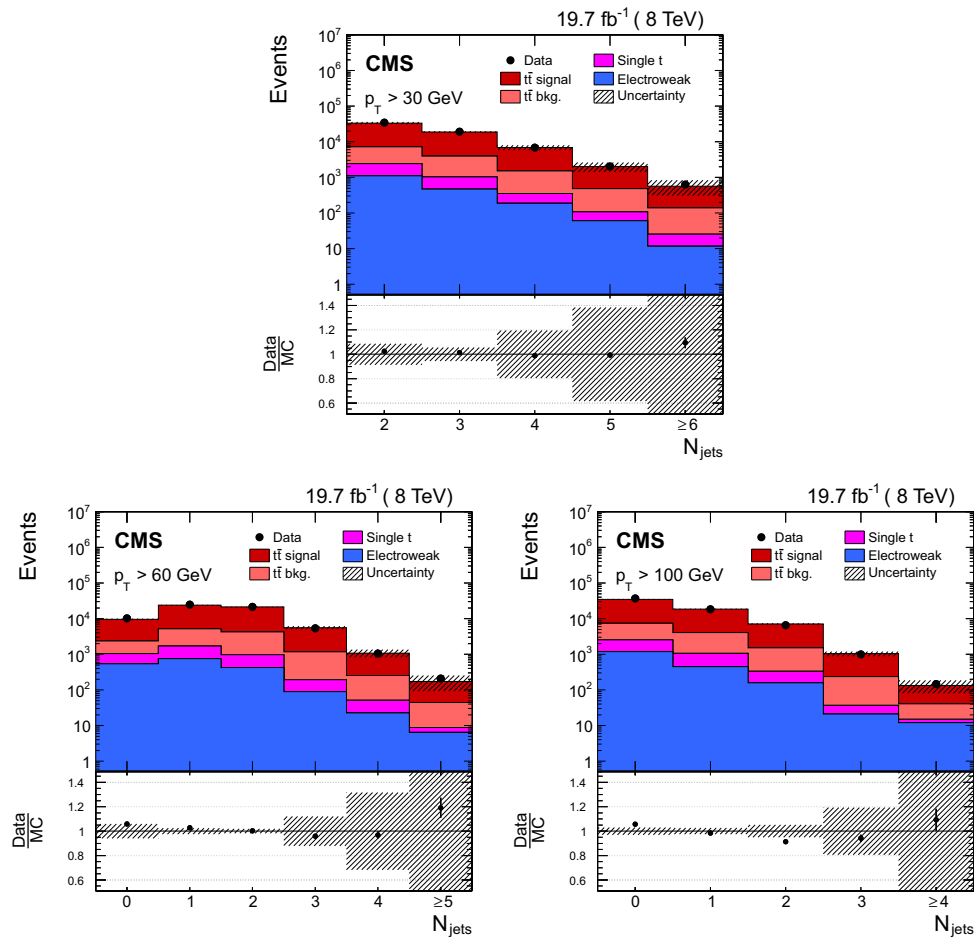
Fig. 1 Reconstructed jet multiplicity distribution after event selection in data (*points*) and from signal and background simulation (*histograms*) for all jets with p_T of at least 30 GeV (*top*), 60 GeV (*bottom left*), and 100 GeV (*bottom right*). The *hatched regions* correspond to the uncer- tainties affecting the shape of the distributions in the simulated signal $t\bar{t}$ events and backgrounds (cf. Sect. 6). The *lower plots* show the ratio of the data to the MC simulation prediction. Note that in all cases the event selection requires at least two jets with $p_T > 30$ GeV

b jet and the other to the $\bar{b}$ jet. This assignment is needed to define the variables used in the BDT and is based on the measurement of the charge of each jet, which is calculated from the charge and the momenta of the PF constituents used in the jet clustering. The jet in the pair with the largest charge is assigned to the $\bar{b}$, while the other jet is assigned to the b. The efficiency of this jet charge pairing is defined as the fraction of events where the assigned b and $\bar{b}$ are correctly matched to the corresponding generated b and $\bar{b}$ jets, and amounts to 68 %.

A total of twelve variables are included in the BDT. Some examples of the variables used are: the sum and difference of the invariant mass of the $b\ell^+$ and $\bar{b}\ell^-$ systems, $m^{b\ell^+} \pm m^{\bar{b}\ell^-}$;

the absolute difference in the azimuthal angle between them, $|\Delta\phi^{b\ell^+,\bar{b}\ell^-}|$; the p_T of the $b\ell^+$ and $\bar{b}\ell^-$ systems, $p_T^{b\ell^+}$ and $p_T^{\bar{b}\ell^-}$; and the difference between the invariant mass of the two b jets and two leptons and the invariant mass of the b$\bar{b}$ pair, $m^{b\bar{b}\ell^+\ell^-} - m^{b\bar{b}}$. The complete list of variables can be found in Appendix A. The main challenge with this method is the large number of possible jet assignments, given four genuine b jets and potential extra jets from additional radiation in each event. The basic methodology is to use the BDT discriminant value of each dijet combination as a measure of the probability that the combination stems from the t$\bar{t}$ system. The jets from the t$\bar{t}$ system are then identified as the pair with the highest BDT discriminant. From the remaining jets,
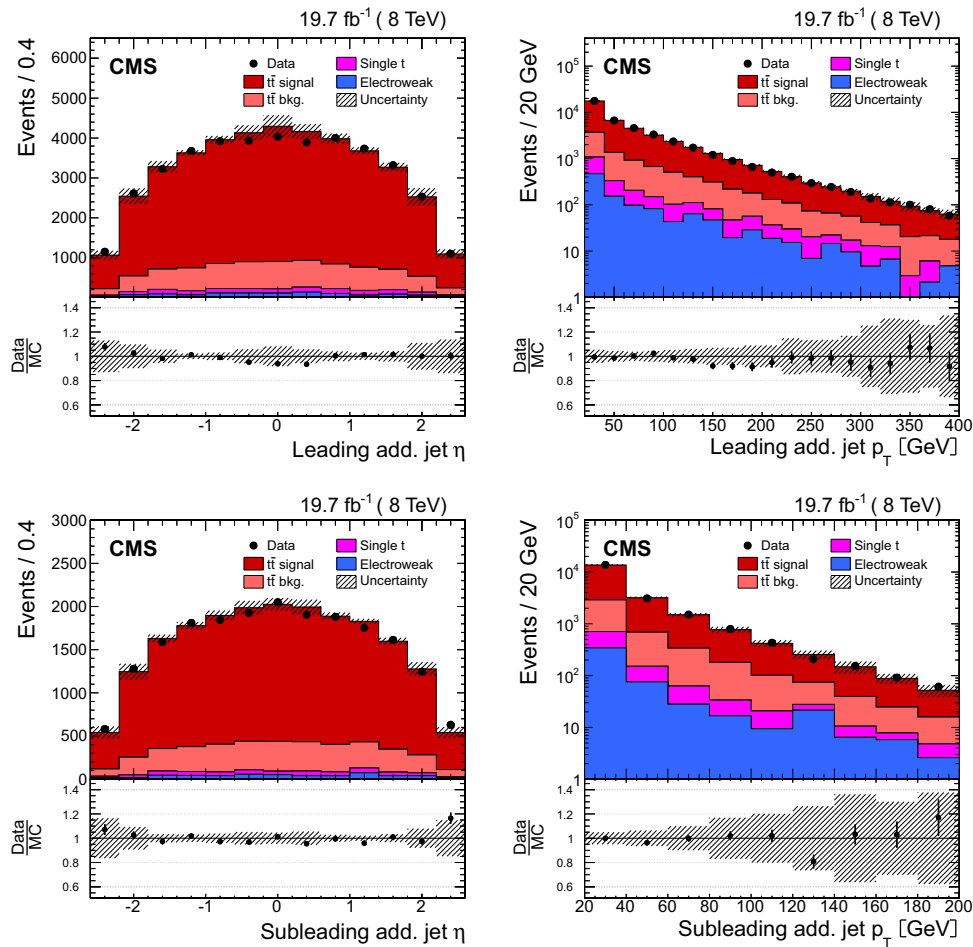
Fig. 2 Distribution of the η (*left*) and p_T (*right*) of the leading (*top row*) and subleading (*bottom row*) additional reconstructed jets in data (*points*) and from signal and background simulation (*histograms*). The *hatched regions* correspond to the uncertainties affecting the shape of the simulated distributions in the signal $t\bar{t}$ events and backgrounds (cf. Sect. 6). The *lower plots* show the ratio of the data to the MC simulation prediction

those b-tagged jets with the highest p_T are selected as being the leading additional ones.

The BDT training is performed on a large and statistically independent sample of simulated $t\bar{t}H$ events with the Higgs boson mass varied over the range 110–140 GeV. The $t\bar{t}b\bar{b}$ events are not included in the training to avoid the risk of overtraining owing to the limited number of events in the available simulated samples. The simulated $t\bar{t}H$ $(b\bar{b})$ sample is suited for this purpose since the four b jets from the decay of the $t\bar{t}$ system and the Higgs boson have similar kinematic distributions. Since it is significantly harder to identify the jets from the $t\bar{t}$ system in $t\bar{t}H$ events than in $t\bar{t}b\bar{b}$ events, where the additional b jets arise from initial- or final-state radiation,

a good BDT performance with $t\bar{t}H$ events implies also a good identification in $t\bar{t}b\bar{b}$ events. The distributions of the BDT discriminant in data and simulation are shown in Fig. 4 for all dijet combinations in an event, and for the combination with the highest weight that is assigned to the $t\bar{t}$ system. The subset "Minor bkg." includes all non-$t\bar{t}$ processes and $t\bar{t}+Z/W/\gamma$ events. There is good agreement between the data and simulation distributions within the statistical uncertainties.

The number of simulated events with correct assignments for the additional b jets in $t\bar{t}H$ events relative to the total number of events where those jets are selected and matched to the corresponding generator jets, is approximately 34 %. In $t\bar{t}b\bar{b}$ events, this fraction is about 40 %. This efficiency is
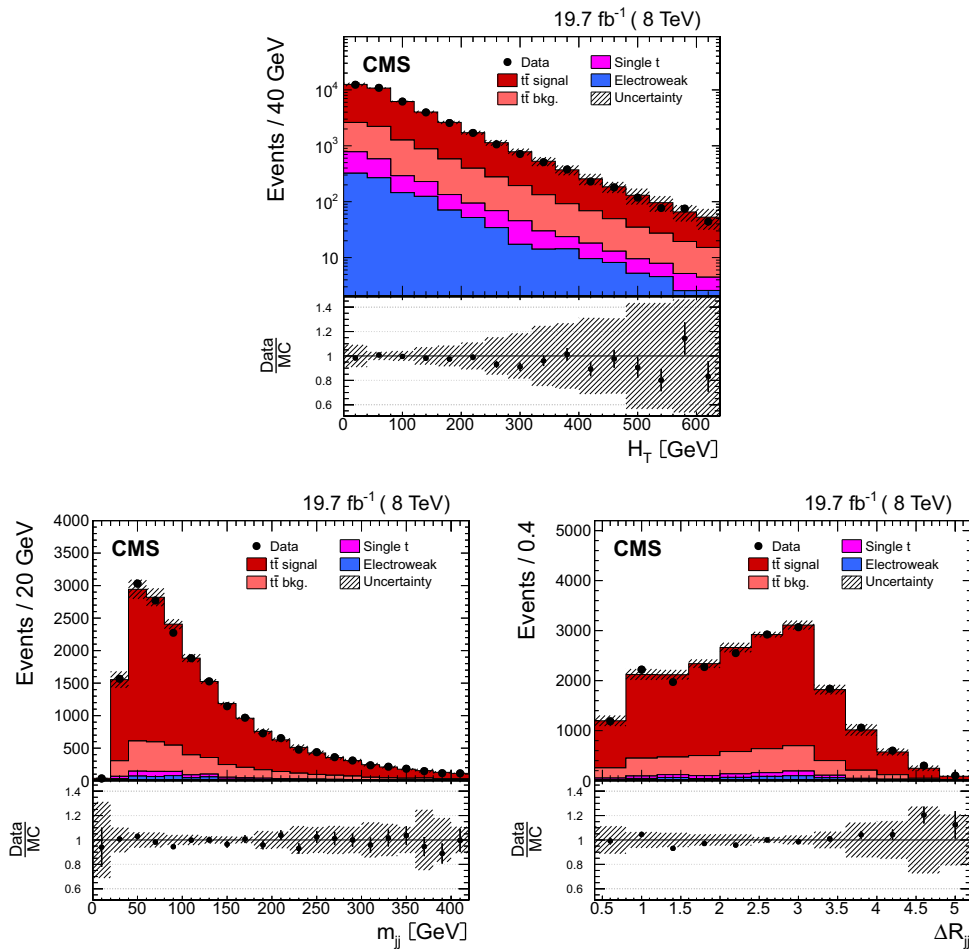
Fig. 3 Distribution of the scalar sum of the p_T of all additional jets H_T (*top*), the invariant mass of the leading and subleading additional jets m_{jj} (*bottom left*), and their angular distance ΔR_{jj} (*bottom right*) in data (*points*) and from signal and background simulation (*histograms*). The *hatched regions* correspond to the uncertainties affecting the shape of the distributions in the simulated signal $t\bar{t}$ events and backgrounds (cf. Sect. 6). The *lower plots* show the ratio of the data to the MC simulation prediction

high enough to allow the measurement of the $t\bar{t}$ cross section as a function of the kinematic variables of the additional b jets (the probability of selecting the correct assignments by choosing random combinations of jets is 17 % in events with four jets and 10 % in events with five jets). The relative increase in efficiency with respect to the use of the kinematic reconstruction for $t\bar{t}b\bar{b}$ is about 15 %. Additionally, the BDT approach improves the correlation between the generated and reconstructed variables, especially for the distribution of the invariant mass of the two leading additional b jets m_{bb} and their angular separation $\Delta R_{bb} = \sqrt{(\Delta\eta)^2 + (\Delta\phi)^2}$, where $\Delta\eta$ and $\Delta\phi$ are the pseudorapidity and azimuthal differences between the directions of the two b jets.

The expected fraction of events with additional b jets is not properly modelled in the simulation, in agreement with the observation of a previous CMS measurement [11]. This discrepancy between the MADGRAPH+PYTHIA simulation and data can be seen in the b jet multiplicity distribution, as shown in Fig. 5.

To improve the description of the data by the simulation, a template fit to the b-tagged jet multiplicity distribution is performed using three different templates obtained from simulation. One template corresponds to the $t\bar{t}b$ and $t\bar{t}b\bar{b}$ processes, defined at the generator level as the events where one or two additional b jets are generated within the acceptance requirements, $p_T > 20$ GeV and $|\eta| < 2.4$, (referred to as "$t\bar{t}$+HF").
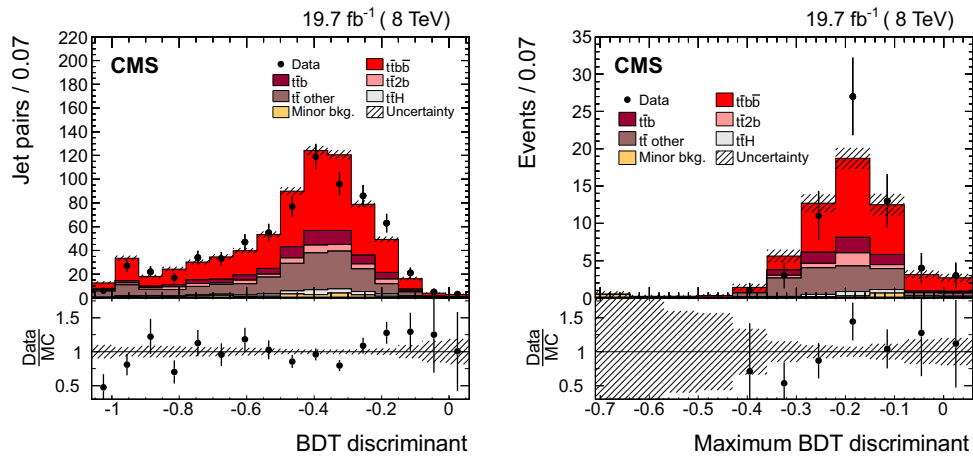
Fig. 4 The BDT discriminant of all dijet combinations in data (*points*) and from signal and background simulation (*histograms*) per event (*left*) and dijet combination with the highest discriminant per event (*right*) in events with at least four jets and exactly four b-tagged jets. The distributions include the correction obtained with the template fit to the

b-tagged jet multiplicity (cf. Sect. 5.2). The *hatched area* represents the statistical uncertainty in the simulated samples. "Minor bkg." includes all non-$t\bar{t}$ processes and $t\bar{t}+Z/W/\gamma$. The *lower plots* show the ratio of the data to the MC simulation prediction

Fig. 5 The pre-fit distribution of the b jet multiplicity in data (*points*) and from signal and background simulation (*histograms*) for events fulfilling the lepton selection criteria, having ≥2 jets, ≥1 b-tagged jet (*left*), and the post-fit distribution (*right*). The *hatched area* represents the sta-

tistical uncertainty in the simulated samples. "Minor bkg." includes all non-$t\bar{t}$ processes and $t\bar{t}+Z/W/\gamma$. The *lower plots* show the ratio of the data to the MC simulation prediction
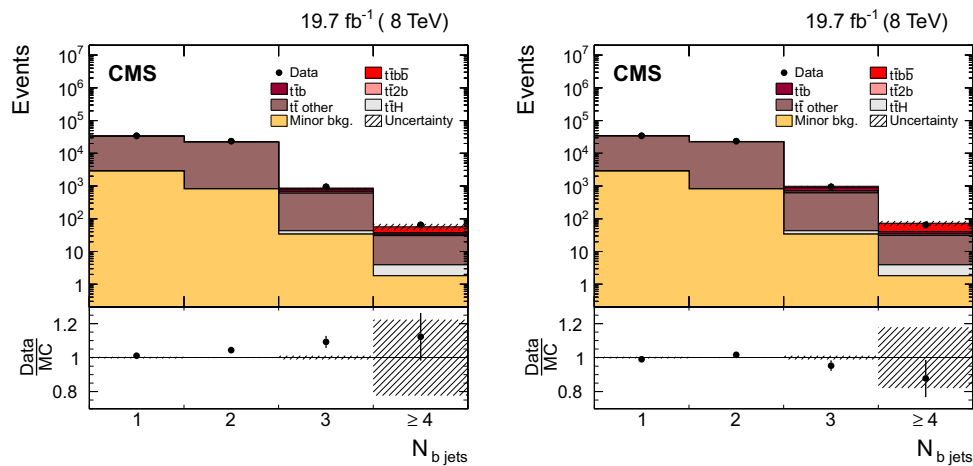
The $t\bar{t}b\bar{b}$ and $t\bar{t}b$ processes are combined into a single template because they only differ by the kinematic properties of the second additional b jet. Details about the definition of the b jets and the acceptance are given in Sect. 7. The second template includes the background contribution coming from $t\bar{t}c\bar{c}$ and $t\bar{t}+$light-jets events (referred to as "$t\bar{t}$ other"), where $t\bar{t}c\bar{c}$ events are defined as those that have at least one

c jet within the acceptance and no additional b jets. This contribution is not large enough to be constrained by data, therefore it is combined with the $t\bar{t}+$light-jets process in a single template. The third template contains the remaining background processes, including $t\bar{t}2b$, which corresponds to events with two additional b hadrons that are close enough in direction to produce a single b jet. This process, produced

by collinear g $\rightarrow$ b$\bar{\text{b}}$ splitting, is treated separately owing to the large theoretical uncertainty in its cross section and insufficient statistical precision to constrain it with data. The normalizations of the first two templates are free parameters in the fit. The third is fixed to the corresponding cross section described in Sect. 3, except for the cross section for the t$\bar{\text{t}}$2b process, which is corrected by a factor of $1.74^{+0.69}_{-0.74}$ [65]. The normalization factors obtained for the template fit correspond to 1.66 ± 0.43 (t$\bar{\text{t}}$+HF) and 1.00 ± 0.01 (t$\bar{\text{t}}$ other). Details about the uncertainties in those factors are presented in Sect. 6.1.1. The improved description of the b jet multiplicity can be seen in Fig. 5 (right).

Figure 6 (top) shows the p_{T} and $|\eta|$ distributions of the leading additional b jet, measured in events with at least three b-tagged jets (using the tighter discriminator value described in Sect. 4), after the full selection and including all corrections. The distributions of the p_{T} and $|\eta|$ of the second additional b jet in events with exactly four b-tagged jets, ΔR_{bb}, and m_{bb} are also presented. The dominant contribution arises from the t$\bar{\text{t}}$b$\bar{\text{b}}$ process. The t$\bar{\text{t}}$ decays into τ leptons decaying leptonically are included as signal to increase the number of t$\bar{\text{t}}$b and t$\bar{\text{t}}$b$\bar{\text{b}}$ events both in data and simulation. It has been checked that the distribution of the variables of relevance for this analysis do not differ between the leptons directly produced from W boson decays and the leptons from τ decays within the statistical uncertainties in the selected t$\bar{\text{t}}$b and t$\bar{\text{t}}$b$\bar{\text{b}}$ events. In general, the variables presented are well described by the simulation, after correcting for the heavy-flavour content measured in data, although the simulation tends to predict smaller values of ΔR_{bb} than the data. After the full selection, the dominant background contribution arises from dilepton t$\bar{\text{t}}$ events with additional light-quark, gluon, and c jets, corresponding to about 50 and 20 % of the total expected yields for the t$\bar{\text{t}}$b and t$\bar{\text{t}}$b$\bar{\text{b}}$ cases, respectively. Smaller background contributions come from single top quark production, t$\bar{\text{t}}$ in association with W or Z bosons, and t$\bar{\text{t}}$ events in the lepton+jets decay channels. The contribution from t$\bar{\text{t}}$H (b$\bar{\text{b}}$) is also small, amounting to 0.9 and 3 % of the total expected events for the t$\bar{\text{t}}$b and t$\bar{\text{t}}$b$\bar{\text{b}}$ distributions. The contribution from background sources other than top quark production processes such as DY, diboson, or QCD multijet is negligible.

6 Systematic uncertainties

Different sources of systematic uncertainties are considered arising from detector effects, as well as theoretical uncertainties. Each systematic uncertainty is determined individually in each bin of the measurement by varying the corresponding efficiency, resolution, or model parameter within its uncertainty, in a similar way as in the CMS previous measurement of the t$\bar{\text{t}}$ differential cross sections [8]. For each variation, the measured differential cross section is recalculated and

the difference with respect to the nominal result is taken as the systematic uncertainty. The overall uncertainty in the measurement is then derived by adding all contributions in quadrature, assuming the sources of systematic uncertainty to be fully uncorrelated.

6.1 Experimental uncertainties

The experimental sources of systematic uncertainty considered are the jet energy scale (JES), jet energy resolution (JER), background normalization, lepton trigger and identification efficiencies, b tagging efficiency, integrated luminosity, pileup modelling, and kinematic reconstruction efficiency.

The experimental uncertainty from the JES is determined by varying the energy scale of the reconstructed jets as a function of their p_{T} and η by its uncertainty [56]. The uncertainty from the JER is estimated by varying the simulated JER by its η-dependent uncertainty [56].

The uncertainty from the normalization of the backgrounds that are taken from simulation is determined by varying the cross section used to normalize the sample, see Sect. 3, by ± 30 %. This variation takes into account the uncertainty in the predicted cross section and all other sources of systematic uncertainty [5,8,66]. In the case of the tW background, the variation of ± 30 % covers the theoretical uncertainty in the absolute rate, including uncertainties owing to the PDFs. The contribution from the DY process, as determined from data, is varied in the normalization by ± 30 % [1,63].

The trigger and lepton identification efficiencies in simulation are corrected by lepton p_{T} and η multiplicative data-to-simulation scale factors. The systematic uncertainties are estimated by varying the factors by their uncertainties, which are in the range 1–2 %.

For the t$\bar{\text{t}}$+jets measurements, the b tagging efficiency in simulation is also corrected by scale factors depending on the p_{T} and η of the jet. The shape uncertainty in the b tagging efficiency is then determined by taking the maximum change in the shape of the p_{T} and $|\eta|$ distributions of the b jet, obtained by changing the scale factors. This is achieved by dividing the b jet distributions in p_{T} and $|\eta|$ into two bins at the median of the respective distributions. The b tagging scale factors for b jets in the first bin are scaled up by half the uncertainties quoted in Ref. [57], while those in the second bin are scaled down, and vice versa, so that a maximum variation is assumed and the difference between the scale factors in the two bins reflects the full uncertainty. The changes are made separately in the p_{T} and $|\eta|$ distributions, and independently for heavy-flavour (b and c) and light-flavour (s, u, d, and gluon) jets, assuming that they are all uncorrelated. A normalization uncertainty is obtained by varying the scale factors up and down by half the uncertainties. The total uncer-
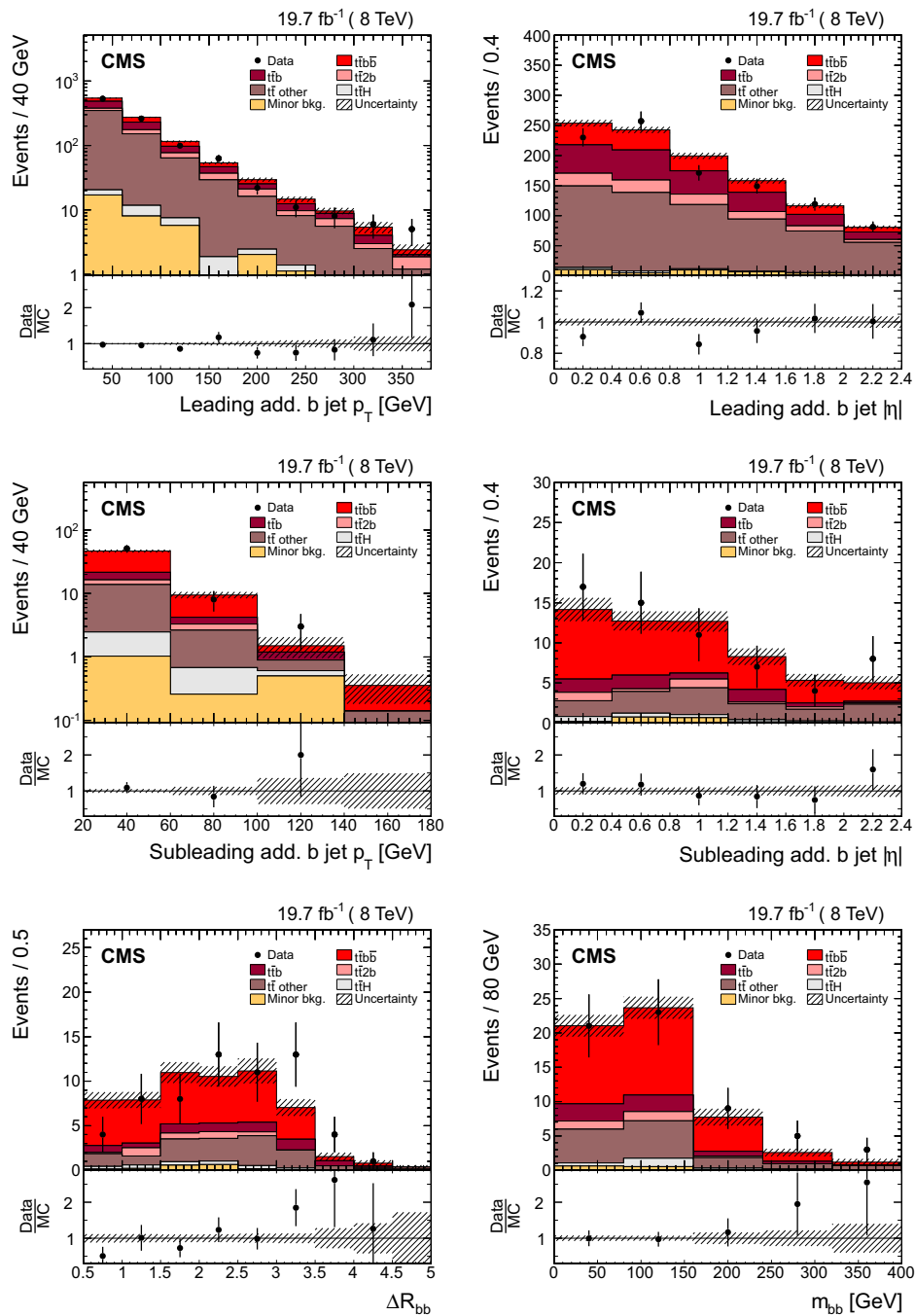
Fig. 6 Distributions of the leading additional b jet p_T (*top left*) and $|\eta|$ (*top right*), subleading additional b jet p_T (*middle left*) and $|\eta|$ (*middle right*), ΔR_{bb} (*bottom left*), and m_{bb} (*bottom right*) from data (*points*) and from signal and background simulation (*histograms*). The *hatched area* represents the statistical uncertainty in the simulated samples. "Minor bkg." includes all non-$t\bar{t}$ processes and $t\bar{t}+Z/W/\gamma$. The *lower plots* show the ratio of the data to the MC simulation prediction

tainty is obtained by summing in quadrature the independent variations.

The uncertainty in the integrated luminosity is 2.6 % [67]. The effect of the uncertainty in the level of pileup is estimated by varying the inelastic pp cross section in simulation by ±5 %.

The uncertainty coming from the kinematic reconstruction method is determined from the uncertainty in the correction factor applied to account for the small difference in efficiency between the simulation and data, defined as the ratio between the events with a solution and the total number of selected events.

6.1.1 Specific systematic uncertainties associated with the $t\bar{t}b\bar{b}$ ($t\bar{t}b$) measurements

In the $t\bar{t}b\bar{b}$ ($t\bar{t}b$) measurements, an additional uncertainty associated with the template fit to the b-tagged jet multiplicity distribution is considered. Since the input templates are known to finite precision, both the statistical and systematic uncertainties in the templates are taken into account. The considered systematic uncertainties that affect the shapes of the templates are those of the JES, the CSV discriminant scale factors following the method described in [60], the cross section of the $t\bar{t}c\bar{c}$ process, which is varied by ±50 % [60], and the uncertainty in the $t\bar{t}2b$ cross section. This is taken as the maximum between the largest uncertainty from the measurement described in Ref. [65] and the difference between the corrected cross section and the prediction by the nominal MADGRAPH simulation used in this analysis. This results in a variation of the cross section of about ±40 %. This uncertainty is included as a systematic uncertainty in the shape of the background template.

6.2 Model uncertainties

The impact of theoretical assumptions on the measurement is determined by repeating the analysis, replacing the standard MADGRAPH signal simulation by alternative simulation samples. The uncertainty in the modelling of the hard-production process is assessed by varying the common renormalization and factorization scale in the MADGRAPH signal samples up and down by a factor of two with respect to its nominal value of the Q in the event (cf. Sect. 3). Furthermore, the effect of additional jet production in MADGRAPH is studied by varying up and down by a factor of two the threshold between jet production at the matrix element level and via parton showering. The uncertainties from ambiguities in modelling colour reconnection (CR) effects are estimated by comparing simulations of an underlying-event (UE) tune including colour reconnection to a tune without it (Perugia 2011 and Perugia 2011 noCR tunes, described in Ref. [33]). The modelling of the UE is evaluated by comparing two different Perugia

11 (P11) PYTHIA tunes, mpiHi and TeV, to the standard P11 tune. The dependency of the measurement on the top quark mass is obtained using dedicated samples in which the mass is varied by ±1 GeV with respect to the default value used in the simulation. The uncertainty from parton shower modelling is determined by comparing two samples simulated with POWHEG and MC@NLO, using either PYTHIA or HERWIG for the simulation of the parton shower, underlying event, and hadronization. The effect of the uncertainty in the PDFs on the measurement is assessed by reweighting the sample of simulated $t\bar{t}$ signal events according to the 52 CT10 error PDF sets, at the 90 % CL [25].

Since the total uncertainty in the $t\bar{t}b$ and $t\bar{t}b\bar{b}$ production cross sections is largely dominated by the statistical uncertainty in the data, a simpler approach than for the $t\bar{t}$+jets measurements is chosen to conservatively estimate the systematic uncertainties: instead of repeating the measurement, the uncertainty from each source is taken as the difference between the nominal MADGRAPH+PYTHIA sample and the dedicated simulated sample at generator level. In the case of the uncertainty coming from the renormalization and factorization scales, the uncertainty estimated in the previous inclusive cross section measurement [11] is assigned.

6.3 Summary of the typical systematic uncertainties

Typical values of the systematic uncertainties in the absolute differential cross sections are summarized in Table 1 for illustrative purposes. They are the median values of the distribution of uncertainties over all bins of the measured variables. Details on the impact of the different uncertainties in the results are given in Sects. 8–11.

In general, for the $t\bar{t}$+jets case, the dominant systematic uncertainties arise from the uncertainty in the JES, as well as from model uncertainties such as the renormalization, factorization, and jet-parton matching scales and the hadronization uncertainties. For the $t\bar{t}b$ and $t\bar{t}b\bar{b}$ cross sections, the total uncertainty, including all systematic uncertainties, is only about 10 % larger than the statistical uncertainty. The experimental uncertainties with an impact on the normalization of the expected number of signal events, such as lepton and trigger efficiencies, have a negligible effect on the final cross section determination, since the normalization of the different processes is effectively constrained by the template fit.

7 Differential $t\bar{t}$ cross section

The absolute differential $t\bar{t}$ cross section is defined as:

$$\frac{d\sigma_{t\bar{t}}}{dx_i} = \frac{\sum_j A_{ij}^{-1}(N_{\text{data}}^j - N_{\text{bkg}}^j)}{\Delta_x^i \mathcal{L}}, \tag{1}$$

Table 1 Summary of the typical systematic uncertainties in the measurements of the $t\bar{t}$+jets and $t\bar{t}b\bar{b}$ ($t\bar{t}b$) absolute differential cross sections and their sources. The median of the distribution of uncertainties over all bins of each measured differential cross section is quoted

Relative systematic uncertainty (%)		
Source	$t\bar{t}$+jets	$t\bar{t}b\bar{b}$ ($t\bar{t}b$)
Experimental uncertainties		
Trigger efficiency	1.3	0.1
Lepton selection	2.2	0.1
Jet energy scale	6.8	11
Jet energy resolution	0.3	2.5
Background estimate	2.1	5.6
b tagging	0.5	12
Kinematic reconstruction	0.3	–
Pileup	0.3	1.7
Model uncertainties		
Fact./renorm. scale	2.7	8.0
Jet-parton matching scale	1.3	3.0
Hadronization	4.5	5.2
Top quark mass	1.4	2.0
PDF choice	0.3	0.9
Underlying event	1.0	2.9
Colour reconnection	1.3	1.9

where j represents the bin index of the reconstructed variable x, i is the index of the corresponding generator-level bin, N_{data}^j is the number of data events in bin j, N_{bkg}^j is the number of estimated background events, $\mathcal{L}$ is the integrated luminosity, and Δ_x^i is the bin width. Effects from detector efficiency and resolution in each bin i of the measurement are corrected by the use of a regularized inversion of the response matrix (symbolized by A_{ij}^{-1}) described in this section.

For the measurements of $t\bar{t}$+jets, the estimated number of background events from processes other than $t\bar{t}$ production ($N_{\text{non }t\bar{t}\text{ bkg}}$) is subtracted from the number of events in data (N). The contribution from other $t\bar{t}$ decay modes is taken into account by correcting the difference $N - N_{\text{non }t\bar{t}\text{ bkg}}$ by the signal fraction, defined as the ratio of the number of selected $t\bar{t}$ signal events to the total number of selected $t\bar{t}$ events, as determined from simulation. This avoids the dependence on the inclusive $t\bar{t}$ cross section used for normalization. For the $t\bar{t}b$ and $t\bar{t}b\bar{b}$ production cross sections, where the different $t\bar{t}$ contributions are fitted to the data, the expected contribution from all background sources is directly subtracted from the number of data events.

The normalized differential cross section is derived by dividing the absolute result, Eq. (1), by the total cross section, obtained by integrating over all bins for each observable. Because of the normalization, the systematic uncertainties that are correlated across all bins of the measurement, e.g. the uncertainty in the integrated luminosity, cancel out.

Effects from the trigger and reconstruction efficiencies and resolutions, leading to migrations of events across bin boundaries and statistical correlations among neighbouring bins, are corrected using a regularized unfolding method [8,68,69]. The response matrix A_{ij} that corrects for migrations and efficiencies is calculated from simulated $t\bar{t}$ events using MADGRAPH. The generalized inverse of the response matrix is used to obtain the unfolded distribution from the measured distribution by applying a χ^2 technique. To avoid nonphysical fluctuations, a smoothing prescription (regularization) is applied. The regularization level is determined individually for each distribution using the averaged global correlation method [70]. To keep the bin-to-bin migrations small, the width of bins in the measurements are chosen according to their purity and stability. The purity is the number of events generated and correctly reconstructed in a certain bin divided by the total number of reconstructed events in the same bin. The stability is the ratio of the number of events generated and reconstructed in a bin to the total number of events generated in that bin. The purity and stability of the bins are typically larger than 40–50 %, which ensures that the bin-to-bin migrations are small enough to perform the measurement. The performance of the unfolding procedure is tested for possible biases from the choice of the input model (the $t\bar{t}$ MADGRAPH simulation). It has been verified that by reweighting the $t\bar{t}$ simulation the unfolding procedure based on the nominal response matrix reproduces the altered shapes within the statistical uncertainties. In addition, $t\bar{t}$ samples simulated with POWHEG and MC@NLO are employed to obtain the response matrices used in the unfolding for the determination of systematic uncertainties of the model (Sect. 6.2). Therefore, possible effects from the unfolding procedure are already taken into account in the systematic uncertainties.

The differential cross section is reported at the particle level, where objects are defined as follows. Leptons from W boson decays are defined after final-state radiation, and jets are defined at the particle level by applying the anti-k_{T} clustering algorithm with a distance parameter of 0.5 [54] to all stable particles, excluding the decay products from W boson decays into $e\nu$, $\mu\nu$, and leptonic τ final states. A jet is defined as a b jet if it has at least one b hadron associated with it. To perform the matching between b hadrons and jets, the b hadron momentum is scaled down to a negligible value and included in the jet clustering (so-called ghost matching [51]). The b jets from the $t\bar{t}$ decay are identified by matching the b hadrons to the corresponding original b quarks. The measurements are presented for two different phase-space regions, defined by the kinematic and geometric attributes of the $t\bar{t}$ decay products and the additional jets. The visible phase space is defined by the following kinematic requirements:

– Leptons: $p_{\text{T}} > 20$ GeV, $|\eta| < 2.4$,

– b jets arising from top quarks: $p_T > 30$ GeV, $|\eta| < 2.4$,
– Additional jets and b jets: $p_T > 20$ GeV, $|\eta| < 2.4$.

The full phase space is defined by requiring only the additional jets or b jets be within the above-mentioned kinematic range, without additional requirements on the decay products of the $t\bar{t}$ system, and including the correction for the corresponding dileptonic branching fraction, calculated using the leptonic branching fraction of the W boson [62].

In the following sections, the $t\bar{t}$ differential cross section measured as a function of the jet multiplicity in the visible phase space and the results as a function of the kinematic variables of the additional jets in the event, measured in the visible and the full phase-space regions, are discussed. The absolute cross sections are presented as figures and compared to different predictions. The full results are given in tables in Appendix B, along with the normalized differential cross sections measurements.

8 Differential $t\bar{t}$ cross sections as a function of jet multiplicity

In Fig. 7, the absolute differential $t\bar{t}$ cross section is shown for three different jet p_T thresholds: $p_T > 30$, 60, and 100 GeV. The results are presented for a nominal top quark mass of 172.5 GeV. The lower part of each figure shows the ratio of the predictions from simulation to the data. The light and dark bands in the ratio indicate the statistical and total uncertainties in the data for each bin, which reflect the uncertainties for a ratio of 1.0. All predictions are normalized to the measured cross section in the range shown in the histogram, which is evaluated by integrating over all bins for each observable. The results are summarized in Table 2, together with the normalized cross sections. In general, the MADGRAPH generator interfaced with PYTHIA6, and POWHEG interfaced both with HERWIG6 and PYTHIA6, provide reasonable descriptions of the data. The MC@NLO generator interfaced with HERWIG6 does not generate sufficiently large jet multiplicities, especially for the lowest jet p_T threshold. The sensitivity of MADGRAPH to scale variations is investigated through the comparison of different renormalization, factorization, and jet-parton matching scales with respect to the nominal MADGRAPH simulation. Variations in the jet-parton matching threshold do not yield large effects in the cross section, while the shape and normalization are more affected by the variations in the renormalization and factorization scales, which lead to a slightly worse description of the data up to high jet multiplicities, compared to their nominal values.

In Fig. 8, the results are compared to the predictions from MADGRAPH and MG5_AMC@NLO interfaced with PYTHIA8, and the POWHEG generator with the HDAMP parameter set to $m_t = 172.5$ GeV (labelled POWHEG ($h_{damp} = m_t$)

in the legend), interfaced with PYTHIA6, PYTHIA8, and HERWIG6. The MADGRAPH and MG5_AMC@NLO simulations interfaced with PYTHIA8 predict larger jet multiplicities than measured in the data for all the considered p_T thresholds. In general, no large deviations between data and the different POWHEG predictions are observed.

The total systematic uncertainty in the absolute differential cross section ranges between 6 to 30 %, while for the normalized cross section it varies from 2 % up to 20 % for the bins corresponding to the highest number of jets. In both cases, the dominant experimental systematic uncertainty arises from the JES, having a maximum value of 16 % for the absolute cross section bin with at least six jets and $p_T > 30$ GeV. Typical systematic uncertainty values range between 0.5 and 8 %, while the uncertainty in the normalized cross section is 0.5–4 %. Regarding the modelling uncertainties, the most relevant ones are the uncertainty in the renormalization and factorization scales and the parton shower modelling, up to 6 and 10 %, respectively. The uncertainties from the assumed top quark mass used in the simulation and the jet-parton matching threshold amount to 1–2 %. Other modelling uncertainties such as PDF, CR, and UE have slightly smaller impact. These uncertainties cancel to a large extent in the normalized results, with typical contributions below 0.5 %. The total contribution from the integrated luminosity, lepton identification, and trigger efficiency, which only affect the normalization, is 3.5 %. This contribution is below 0.1 % for every bin in the normalized results. The uncertainty from the estimate of the background contribution is around 2 % for the absolute cross sections and typically below 0.5 % for the normalized results.

9 Differential $t\bar{t}$ cross sections as a function of the kinematic variables of the additional jets

The absolute and normalized differential cross sections are measured as a function of the kinematic variables of the additional jets in the visible phase space defined in Sect. 7. The results are compared to predictions from four different generators: POWHEG interfaced with PYTHIA6 and HERWIG6, MC@NLO+HERWIG6, and MADGRAPH+PYTHIA6 with varied renormalization, factorization, and jet-parton matching scales. All predictions are normalized to the measured cross section over the range of the observable shown in the histogram in the corresponding figures.

The absolute differential cross sections as a function of the p_T of the leading and subleading additional jets and H_T, the scalar sum of the p_T of all additional jets in the event, are shown in Fig. 9. The total uncertainties in the absolute cross sections range from 8–14 % for the leading additional jet p_T and H_T, and up to 40 % for the subleading additional jet p_T, while the systematic uncertainties in the normalized cross
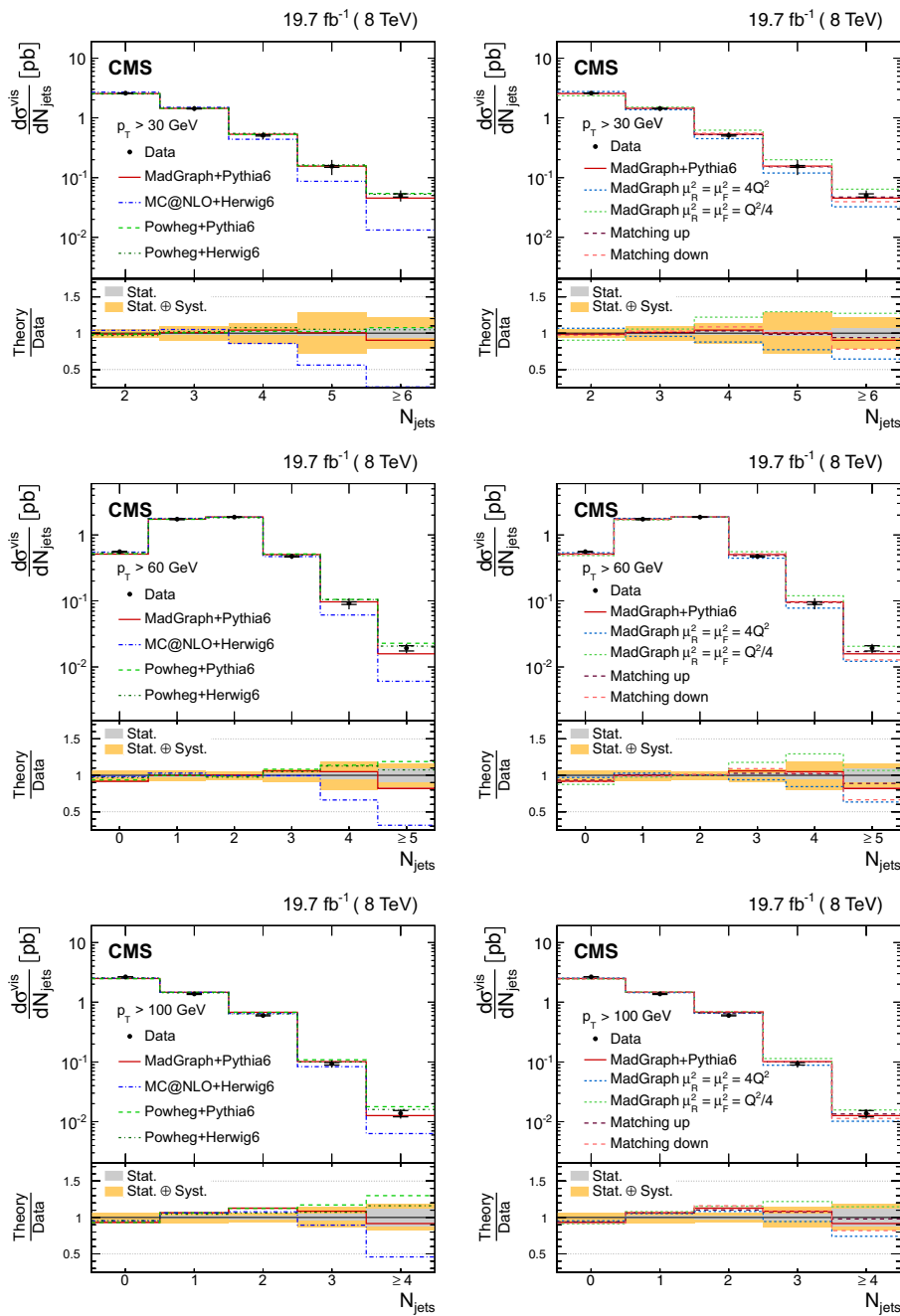
Fig. 7 Absolute differential $t\bar{t}$ cross sections as a function of jet multiplicity for jets with $p_T > 30$ GeV (*top row*), 60 GeV (*middle row*), and 100 GeV (*bottom row*). In the figures on the *left*, the data are compared with predictions from MADGRAPH interfaced with PYTHIA6, MC@NLO interfaced with HERWIG6, and POWHEG with PYTHIA6 and HERWIG6.

The figures on the *right* show the behaviour of the MADGRAPH generator with varied renormalization, factorization, and jet-parton matching scales. The *inner (outer) vertical bars* indicate the statistical (total) uncertainties. The *lower part of each plot* shows the ratio of the predictions to the data
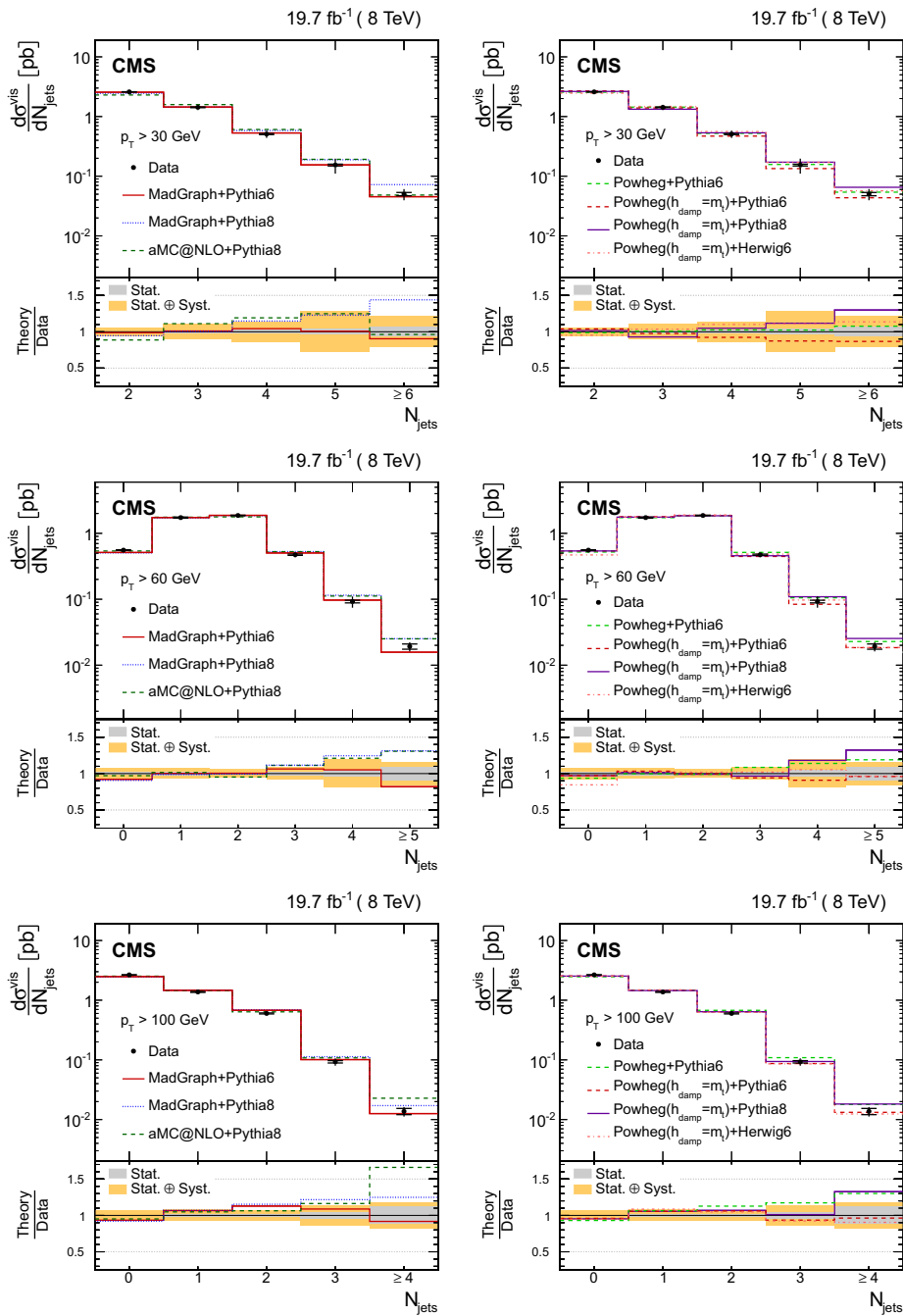
Fig. 8 Absolute differential $t\bar{t}$ cross sections as a function of jet multiplicity for jets with $p_T > 30$ GeV (*top row*), 60 GeV (*middle row*), and 100 GeV (*bottom row*). In the figures on the *left*, the data are compared with predictions from MADGRAPH interfaced with PYTHIA6 and PYTHIA8, and MG5_AMC@NLO interfaced with PYTHIA8. The figures on the *right* show the behaviour of the POWHEG generator without and with HDAMP set to m_t, matched with different versions and tunes of PYTHIA and HERWIG6. The *inner (outer) vertical bars* indicate the statistical (total) uncertainties. The *lower part of each plot* shows the ratio of the predictions to the data

Fig. 9 Absolute differential $t\bar{t}$ cross section as a function of p_T of the leading additional jet (*top*) and the subleading additional jet (*middle*), and H_T (*bottom*) in the visible phase space of the $t\bar{t}$ system and the additional jets. Data are compared to predictions from MadGraph+Pythia6, Powheg+Pythia6, Powheg+Herwig6, and MC@NLO+Herwig6 (*left*) and to MadGraph with varied renormalization, factorization, and jet-parton matching scales (*right*). The *inner (outer) vertical bars* indicate the statistical (total) uncertainties. The *lower part of each plot* shows the ratio of the predictions to the data
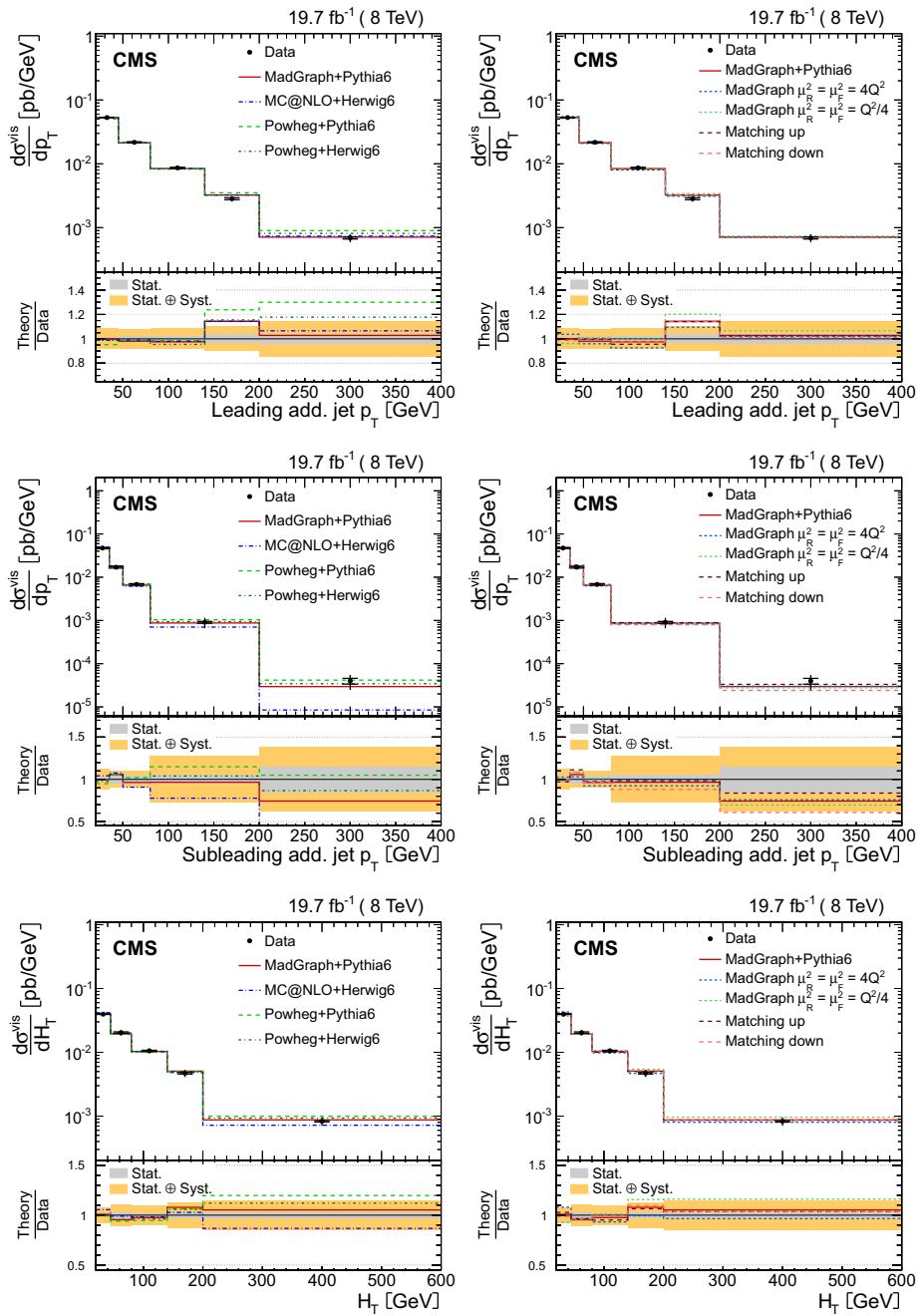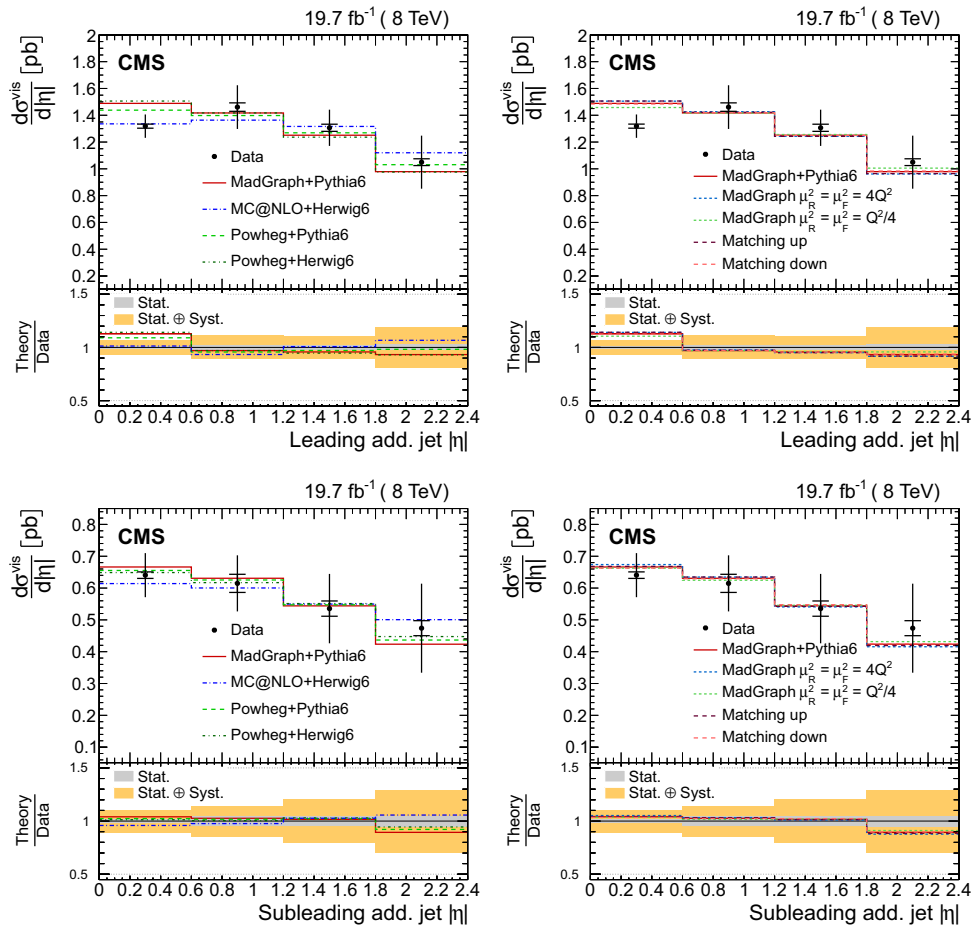
Fig. 10 Absolute differential $t\bar{t}$ cross section as a function of the $|\eta|$ of the leading additional jet (*top*) and the subleading additional jet (*bottom*) in the visible phase space of the $t\bar{t}$ system and the additional jets. Data are compared to predictions from MadGraph+Pythia6, Powheg+Pythia6, Powheg+Herwig6, and mc@nlo+Herwig6 (*left*) and to MadGraph with varied renormalization, factorization, and jet-parton matching scales (*right*). The *inner* (*outer*) *vertical bars* indicate the statistical (total) uncertainties. The *lower part of each plot* shows the ratio of the predictions to the data

sections for the bins with the larger number of events are about 3–4 %. The dominant sources of systematic uncertainties arise in both cases from model uncertainties, in particular the renormalization and factorization scales, and the parton shower modelling (up to 10 % for the absolute cross sections), and JES (3–6 % for the absolute cross sections). The typical contribution of other uncertainties such as the assumed top quark mass in the simulation, background contribution, etc., amounts to 1–3 % and 0.5–1.5 %, for the absolute and normalized cross sections, respectively.

In general, the simulation predictions describe the behaviour of the data for the leading additional jet momenta and H_T, although some predictions, in particular powheg,

favour a harder p_T spectrum for the leading jet. The mc@nlo+Herwig6 prediction yields the largest discrepancies. The varied MadGraph samples provide similar descriptions of the shape of the data, except for MadGraph with the lower $\mu_R = \mu_F$ scale, which worsens the agreement.

The results as a function of $|\eta|$ are presented in Fig. 10. The typical total systematic uncertainties in the absolute cross sections vary from 6.5–19 % for the leading additional jet and about 11–20 % for the subleading one. The uncertainty in the normalized cross section ranges from 1.5–9 % and 5–14 %, respectively. The shape of the $|\eta|$ distribution is well modelled by mc@nlo+Herwig6. The distributions from Mad-Graph and powheg yield a similar description of the data,
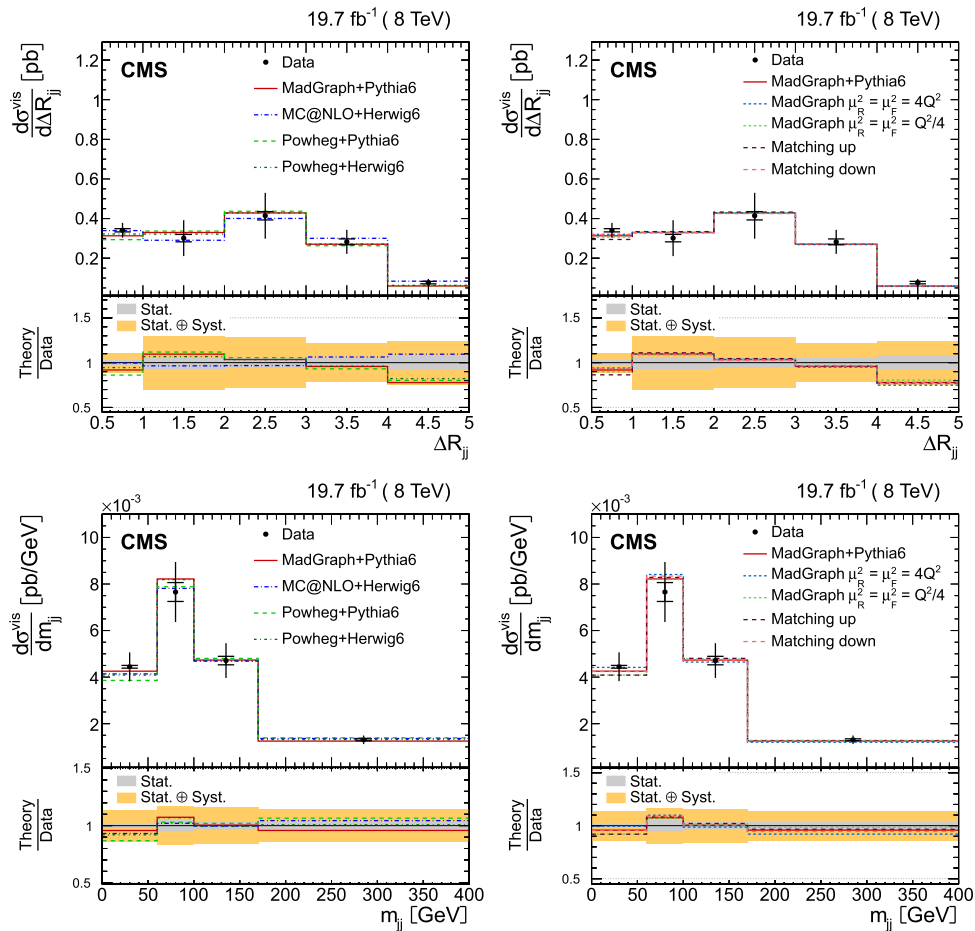
Fig. 11 Absolute differential $t\bar{t}$ cross section as a function of ΔR_{jj} between the leading and subleading additional jets (*top*) and their invariant mass, m_{jj} (*bottom*). Data are compared to predictions from MADGRAPH+PYTHIA6, POWHEG+PYTHIA6, POWHEG+HERWIG6, and MC@NLO+HERWIG6 (*left*) and to MADGRAPH with varied renormalization, factorization, and jet-parton matching scales (*right*). The *inner* (*outer*) *vertical bars* indicate the statistical (total) uncertainties. The *lower part of each plot* shows the ratio of the predictions to the data

being slightly more central than MC@NLO. Variations of the MADGRAPH parameters have little impact on these distributions.

The differential cross section is also measured as a function of the dijet angular separation ΔR_{jj} and invariant mass m_{jj} for the leading and subleading additional jets (Fig. 11). In general, all simulations provide a reasonable description of the distributions for both variables. All results are reported in Tables 3, 4 and 5 in Appendix B. Representative examples of the migration matrices are presented in Fig. 24 in Appendix C.

The absolute and normalized differential cross sections are also measured as a function of the kinematic variables of the additional jets and b jets in the event for the full

phase space of the $t\bar{t}$ system to facilitate comparison with theoretical calculations. In this case, the phase space is defined only by the kinematic requirements on the additional jets.

Figures 12 and 13 show the absolute cross sections as a function of the p_T and $|\eta|$ of the leading and subleading additional jets and H_T, while the results as a function of ΔR_{jj} and m_{jj} are presented in Fig. 14.

The total uncertainties range between 8–12 % for the leading jet p_T and H_T, 10 % at lower p_T and 40 % in the tails of distribution of the subleading jet p_T. The uncertainties for $|\eta|$ are 6–16 % and 10–30 % for the leading and subleading additional jets, respectively. The typical uncertainties in the cross section as a function of ΔR_{jj} and m_{jj}
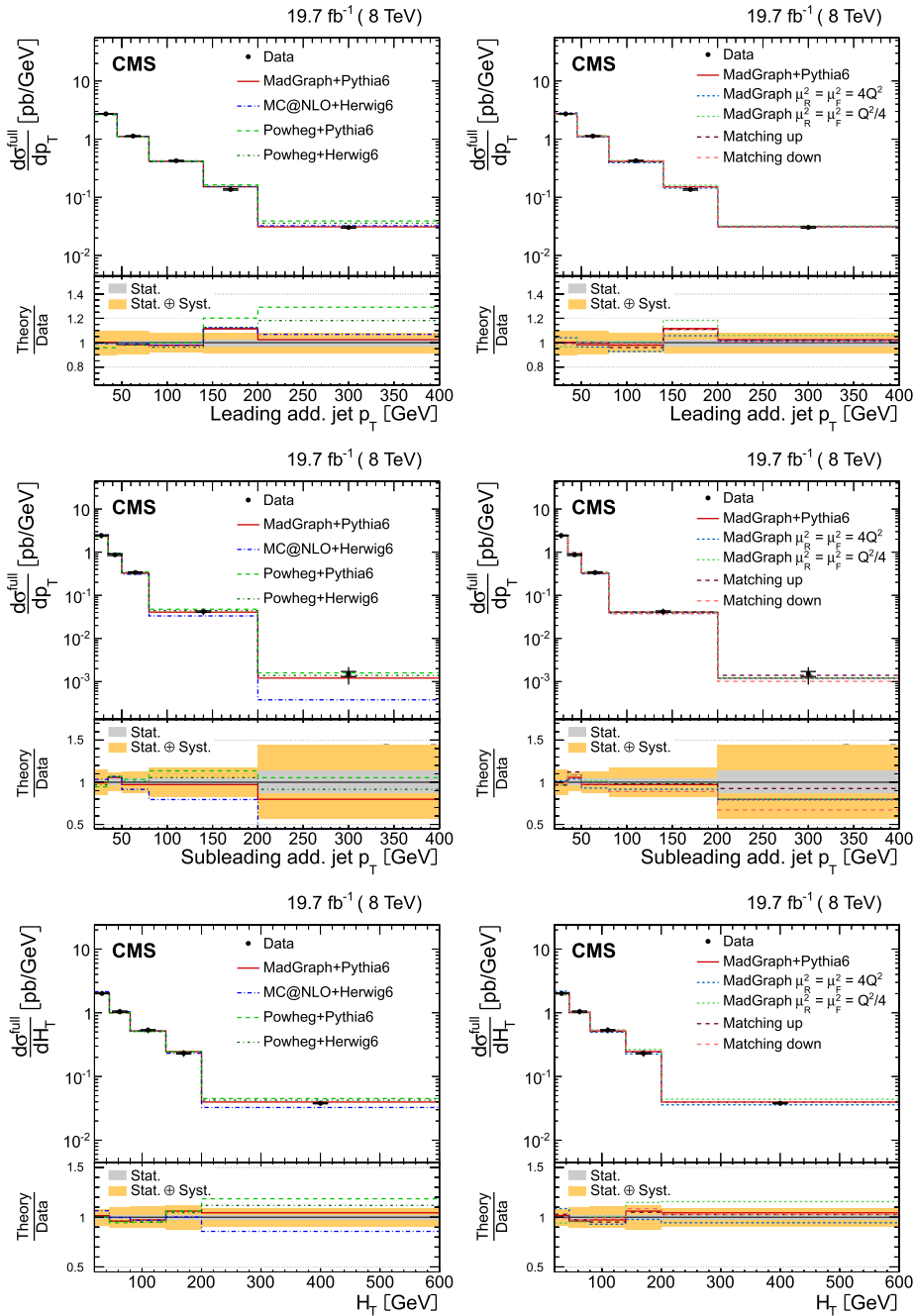
Fig. 12 Absolute differential $t\bar{t}$ cross section as a function of p_T of the leading additional jet (*top*) and the subleading additional jet (*middle*) and H_T (*bottom*) measured in the full phase space of the $t\bar{t}$ system, corrected for acceptance and branching fractions. Data are compared to predictions from MadGraph+Pythia6, Powheg+Pythia6, Powheg+Herwig6, and MC@NLO+Herwig6 (*left*) and to MadGraph with varied renormalization, factorization, and jet-parton matching scales (*right*). The *inner* (*outer*) *vertical bars* indicate the statistical (total) uncertainties. The *lower part of each plot* shows the ratio of the predictions to the data
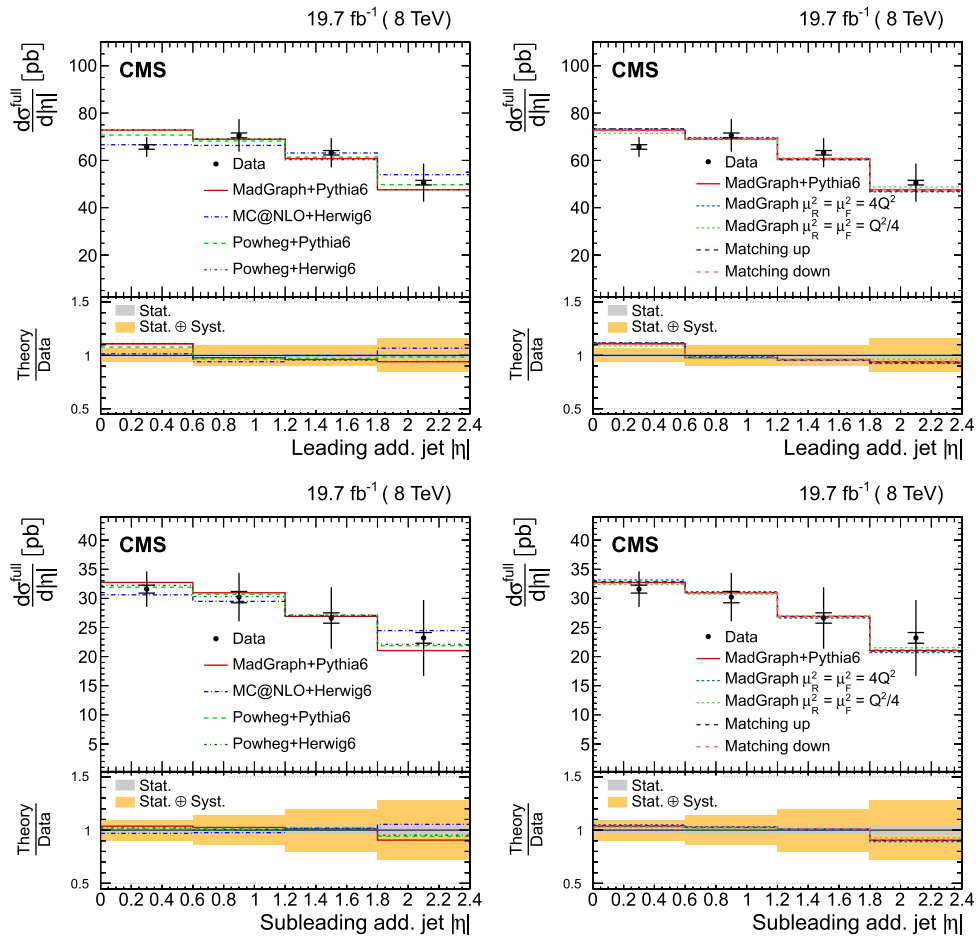
Fig. 13 Absolute differential $t\bar{t}$ cross section as a function of the $|\eta|$ of the leading additional jet (*top*) and the subleading additional jet (*bottom*) measured in the full phase space of the $t\bar{t}$ system, corrected for acceptance and branching fractions. Data are compared to predictions from MADGRAPH+PYTHIA6, POWHEG+PYTHIA6, POWHEG+HERWIG6, and MC@NLO+HERWIG6 (*left*) and to MADGRAPH with varied renormalization, factorization, and jet-parton matching scales (*right*). The *inner* (*outer*) *vertical bars* indicate the statistical (total) uncertainties. The *lower part of each plot* shows the ratio of the predictions to the data

are on the order of 10–20 %. The uncertainties are dominated by the JES, scale uncertainties, and shower modelling.

The numerical values are given in Tables 6, 7 and 8 of Appendix B, together with the normalized results. In the latter, the uncertainties are on average 2–3 times smaller than for the absolute cross sections, owing to the cancellation of uncertainties such as the integrated luminosity, lepton identification, and trigger efficiency, as well as a large fraction of the JES and model uncertainties, as discussed in Sect. 8. The dominant systematic uncertainties are still the model uncertainties, although they are typically smaller than for the absolute cross sections.

The shapes of the distributions measured in the full and visible phase-space regions of the $t\bar{t}$ system are similar, while the absolute differential cross sections are a factor of 2.2 larger than those in the visible phase space of the $t\bar{t}$ system (excluding the factor due to the leptonic branching fraction correction (4.54 ± 0.10) % [62]).

10 Differential $t\bar{t}b\bar{b}$ ($t\bar{t}b$) cross sections as a function of the kinematic variables of the additional b jets

Figure 15 shows the absolute $t\bar{t}$ differential cross sections in the visible phase space of the $t\bar{t}$ system and the additional b
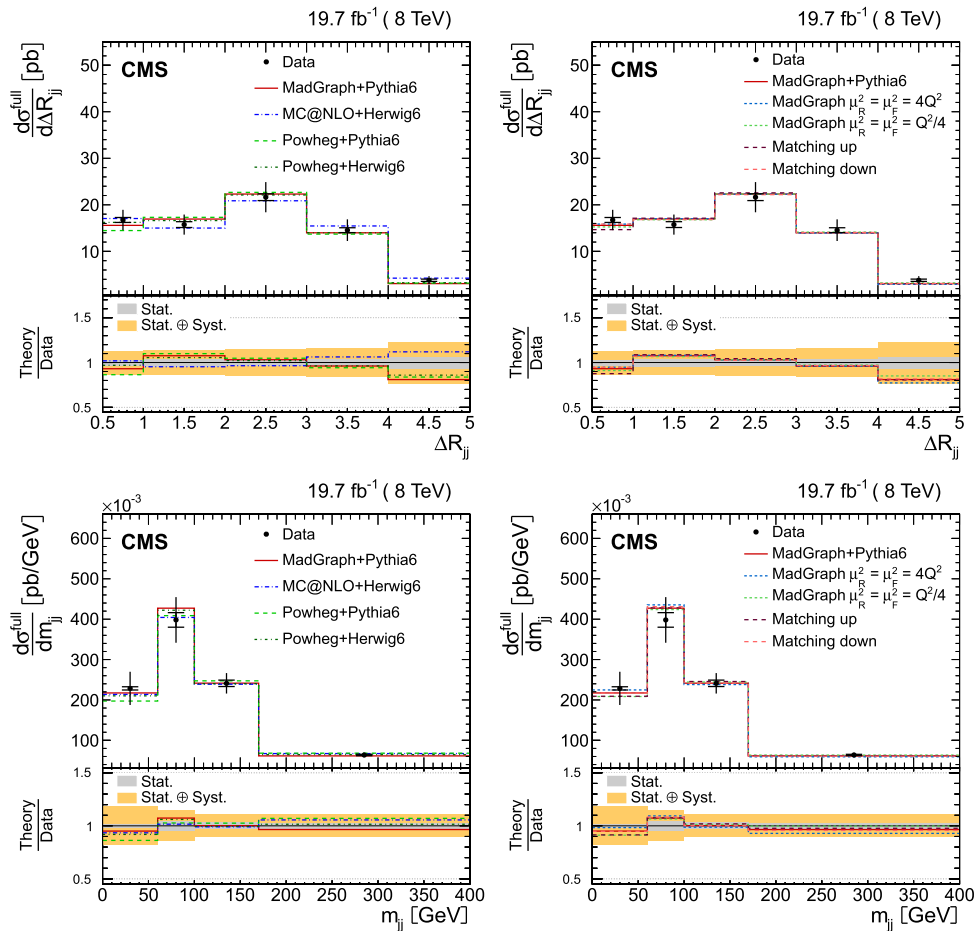
Fig. 14 Absolute differential $t\bar{t}$ cross section as a function of ΔR_{jj} between the leading and subleading additional jets (*top*) and their invariant mass, m_{jj} (*bottom*) measured in the full phase space of the $t\bar{t}$ system, corrected for acceptance and branching fractions. Data are compared to predictions from MADGRAPH+PYTHIA6, POWHEG+PYTHIA6,

POWHEG+HERWIG6, and MC@NLO+HERWIG6 (*left*) and to MADGRAPH with varied renormalization, factorization, and jet-parton matching scales (*right*). The *inner* (*outer*) *vertical bars* indicate the statistical (total) uncertainties. The *lower part of each plot* shows the ratio of the predictions to the data

jets as a function of the p_{T} and $|\eta|$ of the leading and subleading additional b jets, and ΔR_{bb} and m_{bb} of the two b jets. The uncertainties in the measured cross sections as a function of the b jet kinematic variables are dominated by the statistical uncertainties, with values varying from 20–100 %. The results are quantified in Tables 9 and 10 in Appendix B, together with the normalized results. The corresponding migration matrices between the reconstructed and particle levels for the kinematic properties of the additional b jets are presented in Fig. 25 in Appendix C for illustration purposes.

The dominant systematic uncertainties are the b tagging efficiency and JES, up to 20 % and 15 %, respectively. Other uncertainties have typical values on the order of or below 5 %.

The experimental sources of systematic uncertainties affecting only the normalization, which are constrained in the fit, have a negligible impact. The largest model uncertainty corresponds to that from the renormalization and factorization scales of 8 %. The effect of the assumed top quark mass and the PDF uncertainties have typical values of 1–2 %. On average, the inclusion of all the systematic uncertainties increases the total uncertainties by 10 %.

The measured distributions are compared with the MAD-GRAPH+PYTHIA6 prediction, normalized to the corresponding measured inclusive cross section in the same phase space. The measurements are also compared to the predictions from MC@NLO interfaced with HERWIG6 and from POWHEG with

Fig. 15 Absolute differential $t\bar{t}$ cross section measured in the visible phase space of the $t\bar{t}$ system and the additional b jets, as a function of the leading additional b jet p_T (*top left*) and $|\eta|$ (*top right*), subleading additional b jet p_T (*middle left*) and $|\eta|$ (*middle right*), the angular separation ΔR_{bb} between the two leading additional b jets (*bottom left*), and the invariant mass m_{bb} of the two b jets (*bottom right*). Data are compared with predictions from MADGRAPH interfaced with PYTHIA6, MC@NLO interfaced with HERWIG6, and POWHEG with PYTHIA6 and HERWIG6, normalized to the measured inclusive cross section. The *inner* (*outer*) *vertical bars* indicate the statistical (total) uncertainties. The *lower part of each plot* shows the ratio of the predictions to the data

PYTHIA6 and HERWIG6. The normalization factors applied to the MADGRAPH and POWHEG predictions are found to be about 1.3 for results related to the leading additional b jet. The predictions from both generators underestimate the $t\bar{t}b\bar{b}$ cross sections by a factor 1.8, in agreement with the results from Ref. [11]. The normalization factors applied to MC@NLO are approximately 2 and 4 for the leading and subleading additional b jet quantities, respectively, reflecting the observation that the generator does not simulate sufficiently large jet multiplicities. All the predictions have slightly harder p_T spectra for the leading additional b jet than the data, while they describe the behaviour of the $|\eta|$ and m_{bb} distributions within the current precision. The predictions favour smaller ΔR_{bb} values than the measurement, although the differences are in general within two standard deviations of the total uncertainty.

The $t\bar{t}b\bar{b}$ production cross sections are compared to the NLO calculation by POWHEL+PYTHIA6 in Fig. 16. In the figure, the prediction is normalized to the absolute cross section given by the calculation of $20.8\pm0.6\,(\text{stat})^{+7.9}_{-5.4}(\text{scale})$ fb. The prediction describes well the shape of the different distributions, while the predicted absolute $t\bar{t}b\bar{b}$ cross section is about 30 % lower than the measured one, but compatible within the uncertainties.

The absolute differential cross sections measured in the visible phase space of the additional b jets and the full phase space of the $t\bar{t}$ system are presented in Fig. 17 and given in Tables 11 and 12 of Appendix B. The results are corrected for acceptance and dileptonic branching fractions including τ leptonic decays (6.43 ± 0.14) % [62]. The results are compared to the same predictions as in Fig. 15, which are scaled to the measured cross section, obtained by integrating all the bins of the corresponding distribution. The normalization factor applied to the simulations is similar to the previous one for the results in the visible phase space of the $t\bar{t}$ system. The description of the data by the simulations is similar as well. The total measured $\sigma_{t\bar{t}b\bar{b}}$, as well as the agreement between the data and the simulation, is in agreement with the result obtained in Ref. [11]. In the full phase space, the inclusive $t\bar{t}b\bar{b}$ cross section at NLO given by POWHEL+PYTHIA6 corresponds to $62\pm1\,(\text{stat})^{+23}_{-17}(\text{scale})$ fb (excluding the dileptonic branching fraction correction). The comparison of the differential $t\bar{t}b\bar{b}$ cross section with the NLO calculation is presented in Fig. 18.

Differences between the kinematic properties of the additional jets and b jets are expected owing to the different production mechanisms [71] of both processes. The dominant production mechanism of pp $\rightarrow$ $t\bar{t}b\bar{b}$ is gluon-gluon (gg) scattering, while in the case of pp $\rightarrow$ $t\bar{t}jj$, the quark-gluon (qg) channel is equally relevant. The $|\eta|$ distributions of the additional b jets seem to be more central than the corresponding distributions of the additional jets, see Figs. 10 and 13. This difference can be attributed mainly to the contribution

of the production via the qg channel, which favours the emission of jets at larger $|\eta|$. The distributions of the differential cross section as a function of m_{bb} peak at smaller invariant masses than those as a function of m_{jj}, presented in Figs. 11 and 14, because of the larger contribution of the gg channel. Given the large uncertainties in the $t\bar{t}b\bar{b}$ measurements, no statistically significant differences can be observed in the shape of the p_T distributions of the additional b jets compared to the additional jets, shown in Figs. 9 and 12.

11 Additional jet gap fraction

An alternative way to investigate the jet activity arising from quark and gluon radiation is to determine the fraction of events that do not contain additional jets above a given p_T threshold [5,12]. A threshold observable, referred to as the gap fraction, is defined as:

$$f(p_T^j) = \frac{N(p_T^j)}{N_{\text{total}}}, \qquad (2)$$

where N_{total} is the total number of selected events and $N(p_T^j)$ is the number of events that do not contain at least j additional jets (apart from the two jets from the $t\bar{t}$ solution hypothesis) above a p_T threshold, with j corresponding to one or two jets. The measurements are presented as a function of the p_T of the leading and subleading additional jets, respectively.

A modified gap fraction can be defined as:

$$f(H_T) = \frac{N(H_T)}{N_{\text{total}}}, \qquad (3)$$

where $N(H_T)$ is the number of events in which the sum of the scalar p_T of the additional jets (H_T) is less than a certain threshold. In both cases, detector effects are unfolded using the MADGRAPH simulation to obtain the results at the particle level. The additional jets at the generator level are defined as all jets within the kinematic acceptance, excluding the two b jets originating from the b quarks from top quark decay (see Sect. 7). For each value of the p_T and H_T thresholds the gap fraction at the generator level is evaluated, along with the equivalent distributions after the detector simulation and analysis requirements. Given the high purity of the selected events, above 70 % for any bin for the leading additional jet p_T and H_T, and above 85 % for any bin for the subleading additional jets, a correction for detector effects is applied by following a simpler approach than the unfolding method used for other measurements presented here. The data are corrected to the particle level by applying the ratio of the generated distributions at particle level to the simulated ones at the reconstruction level, using the nominal MADGRAPH simulation.

The measured gap fraction distributions are compared to predictions from MADGRAPH interfaced with PYTHIA6,
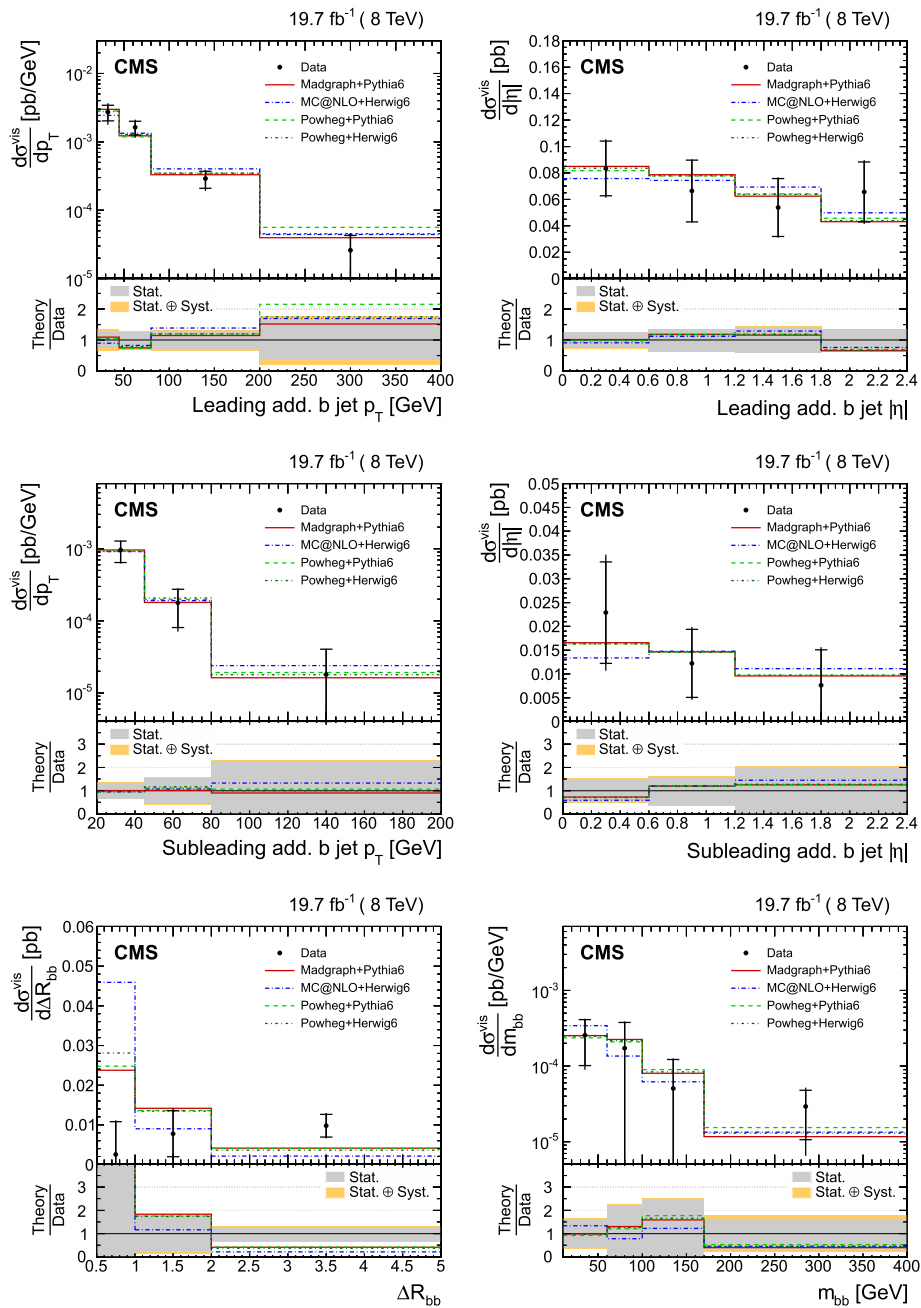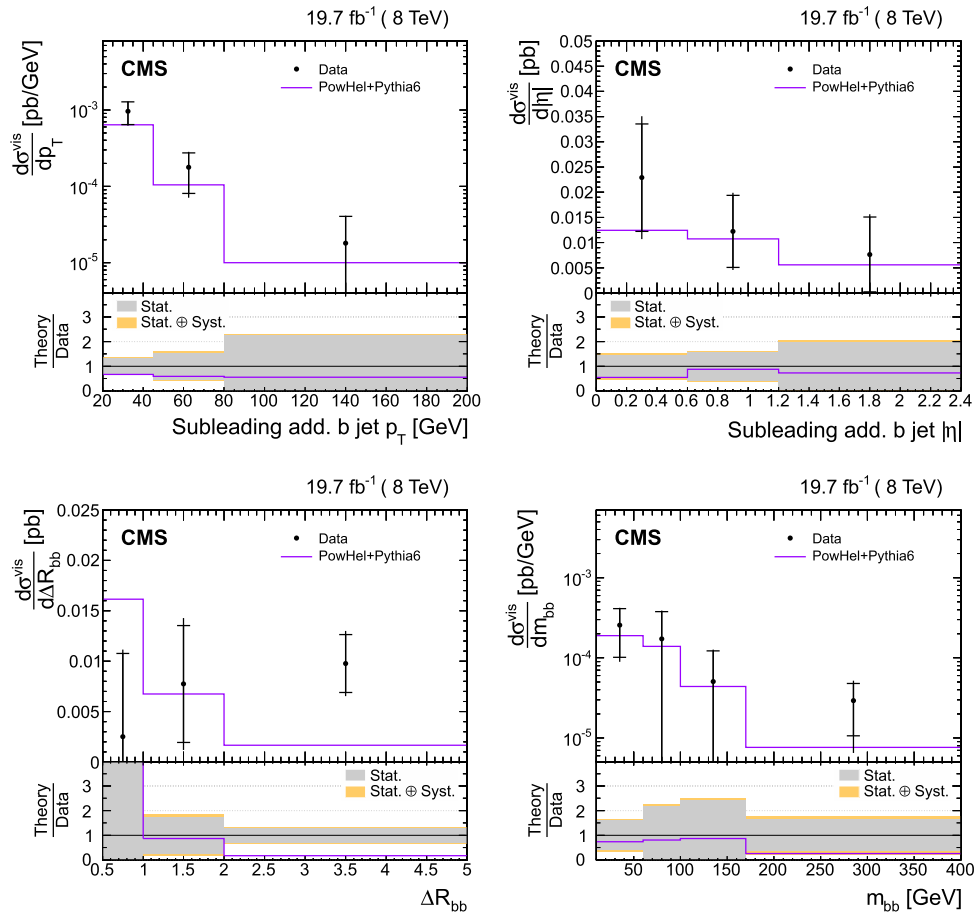
Fig. 16 Absolute differential $t\bar{t}$ cross section measured in the visible phase space of the $t\bar{t}$ system and the additional b jets, as a function of the second additional b jet p_T (*top left*) and $|\eta|$ (*top right*), the angular separation ΔR_{bb} between the two leading additional b jets (*bottom left*), and the invariant mass m_{bb} of the two b jets (*bottom right*). Data are compared with predictions from POWHEL+PYTHIA6. The *inner* (*outer*) *vertical bars* indicate the statistical (total) uncertainties. The *lower part of each plot* shows the ratio of the calculation to data

POWHEG6 interfaced with PYTHIA6 and HERWIG6, MC@NLO interfaced with HERWIG6, and to the MADGRAPH predictions with varied renormalization, factorization, and jet-parton matching scales. Figure 19 displays the gap fraction distribution as a function of the p_T of the leading and subleading additional jets, and H_T. The lower part of the figures shows the ratio of the predictions to the data. The light band indicates the total uncertainty in the data in each bin. The threshold, defined at the value where the data point is shown, is varied from 25 GeV (lower value compared to previous measurements [5]) to 190 GeV. In general, MADGRAPH interfaced with PYTHIA6 agrees with the data distributions of the three variables, while POWHEG interfaced with PYTHIA6 and HERWIG6 also provide a good description of the data,

though they tend to predict a lower gap fraction than the measured ones. The MC@NLO generator interfaced with HERWIG6 describes the data well as a function of the leading additional jet p_T. However, it predicts higher values of the gap fraction as a function of the subleading jet p_T and H_T. Modifying the renormalization and factorization scales in MADGRAPH worsens the agreement with data, while variations of the jet-parton matching threshold provide similar predictions as the nominal MADGRAPH simulation, in agreement with the results shown before.

The results are also compared in Fig. 20 with the recently available simulations, described in Sect. 3, matched to different versions of the parton showering models. The MADGRAPH and MG5_AMC@NLO generators interfaced with
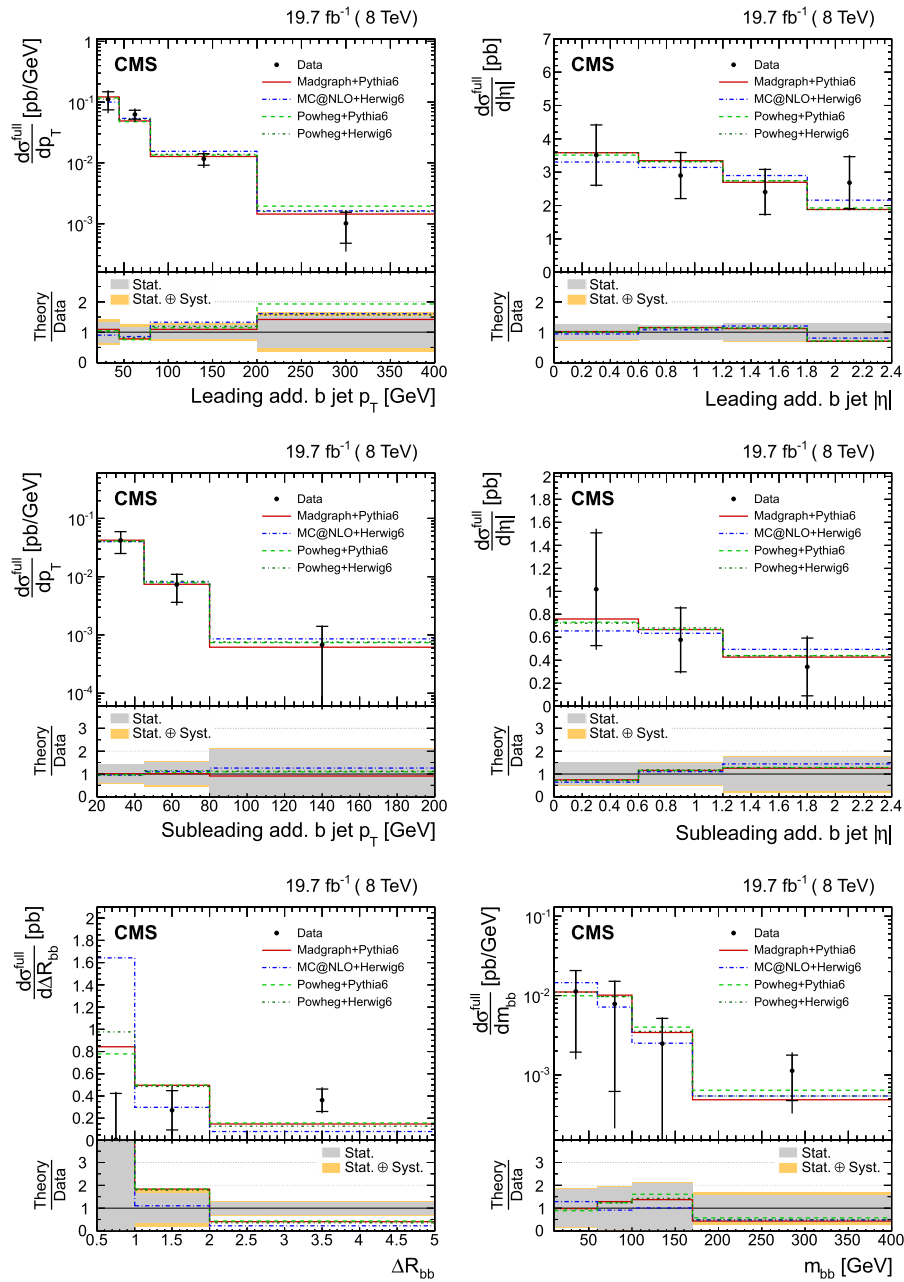
Fig. 17 Absolute differential $t\bar{t}$ cross section measured in the full phase space of the $t\bar{t}$ system, corrected for acceptance and branching fractions, and the visible phase space of the additional b jets, as a function of the leading additional b jet p_T (*top left*) and $|\eta|$ (*top right*), subleading additional b jet p_T (*middle left*) and $|\eta|$ (*middle right*), the angular separation ΔR_{bb} between the leading and subleading additional b jets (*bottom left*), and the invariant mass m_{bb} of the two b jets (*bottom right*).

Data are compared with predictions from MADGRAPH interfaced with PYTHIA6, MC@NLO interfaced with HERWIG6, and POWHEG intefarced with both PYTHIA6 and HERWIG6, normalized to the measured inclusive cross section. The *inner* (*outer*) *vertical bars* indicate the statistical (total) uncertainties. The *lower part of each plot* shows the ratio of the predictions to the data
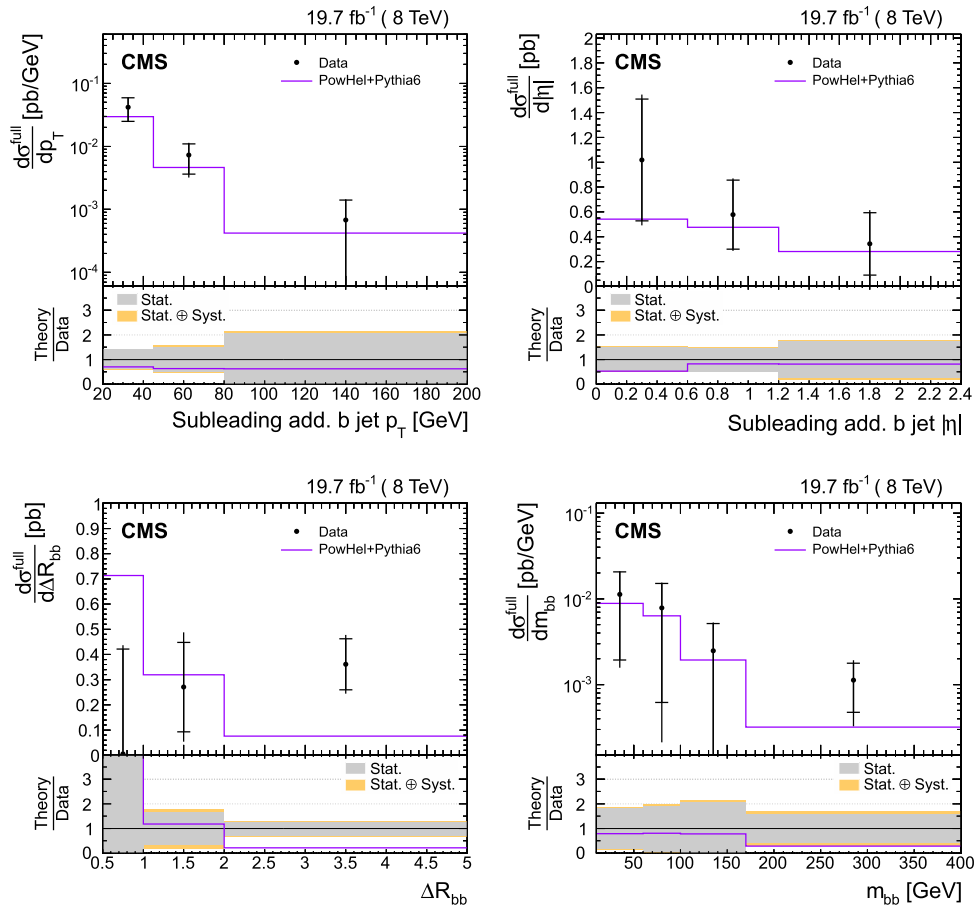
Fig. 18 Absolute differential $t\bar{t}$ cross section measured in the full phase space of the $t\bar{t}$ system, corrected for acceptance and branching fractions, and the additional b jets, as a function of the second additional b jet p_T (*top left*) and $|\eta|$ (*top right*), the angular separation ΔR_{bb} between the leading and subleading additional b jets (*bottom left*), and the invari-ant mass m_{bb} of the two b jets (*bottom right*). Data are compared with predictions from POWHEL+PYTHIA6. The *inner (outer) vertical bars* indicate the statistical (total) uncertainties. The *lower part of each plot* shows the ratio of the calculation to data

PYTHIA8 predict up to 10 % lower values of the gap fraction for all the variables, which reflects the fact that those simulations generate larger jet multiplicities, as discussed in Sect. 8. Within the uncertainties, the predictions of the POWHEG+PYTHIA8 simulation agree well with data, while the POWHEG generator (with HDAMP $= m_t$) interfaced with PYTHIA6 and HERWIG6 tends to overestimate and underestimate the measured values, respectively.

The gap fraction is also measured in different $|\eta|$ regions of the additional jets, with the results presented in Figs. 21, 22 and 23 as a function of the leading additional jet p_T, subleading additional jet p_T, and H_T, respectively. In general, the gap fraction values predicted by the simulations describe the data better in the higher $|\eta|$ ranges. The values given by MAD-GRAPH and POWHEG interfaced with PYTHIA6 are slightly

below the measured ones in the central region for the leading p_T jet and H_T, while MC@NLO+HERWIG6 yields higher values of the gap fraction. In the case of the subleading jet p_T, all predictions agree with the data within the uncertainties, except for MC@NLO+HERWIG6 in the more central regions. Variations of the jet-parton matching threshold do not have a noticeable impact on the gap fraction, while MADGRAPH with the varied renormalization and factorization scales provides a poorer description of the data.

The total systematic uncertainty in the gap fraction distributions is about 5 % for low values of the threshold (p_T or H_T) and decreases to <0.5 % for the highest values. The measurement of the gap fraction as a function of H_T has larger uncertainties because of the impact of the lower-momentum jets that have a significantly larger uncertainty, as discussed

Fig. 19 Measured gap fraction as a function of the leading additional jet p_T (*top row*), subleading additional jet p_T (*middle row*), and of H_T (*bottom row*). Data are compared to predictions from MadGraph, Powheg interfaced with Pythia and Herwig, and MC@NLO interfaced with Herwig (*left*), and to MadGraph with varied renormalization, factorization, and jet-parton matching scales (*right*). For each bin the threshold is defined at the value where the data point is placed. The *vertical bars* on the data points indicate the statistical uncertainty. The *shaded band* corresponds to the statistical and the total systematic uncertainty added in quadrature. The *lower part of each plot* shows the ratio of the predictions to the data
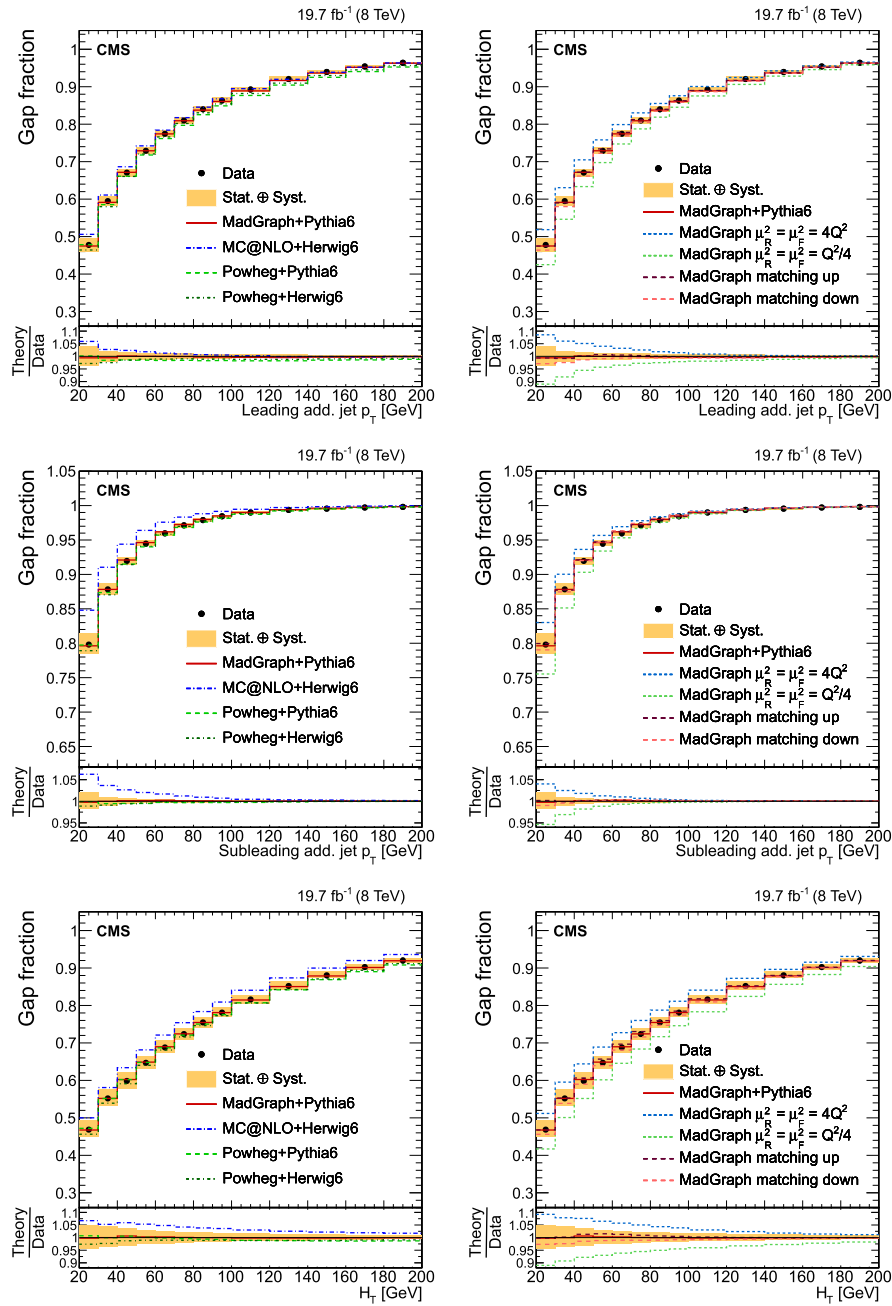
Fig. 20 Measured gap fraction as a function of the leading additional jet p_T (*top row*), subleading additional jet p_T (*middle row*), and of H_T (*bottom row*). Data are compared to predictions from MADGRAPH, interfaced with PYTHIA6 and PYTHIA8, and MG5_AMC@NLO interfaced with HERWIG6 (*left*), and to POWHEG interfaced with different versions of PYTHIA and HERWIG6 (*right*). For each bin the threshold is defined at the value where the data point is placed. The *vertical bars* on the data points indicate the statistical uncertainty. The *shaded band* corresponds to the statistical and the total systematic uncertainty added in quadrature. The *lower part of each plot* shows the ratio of the predictions to the data
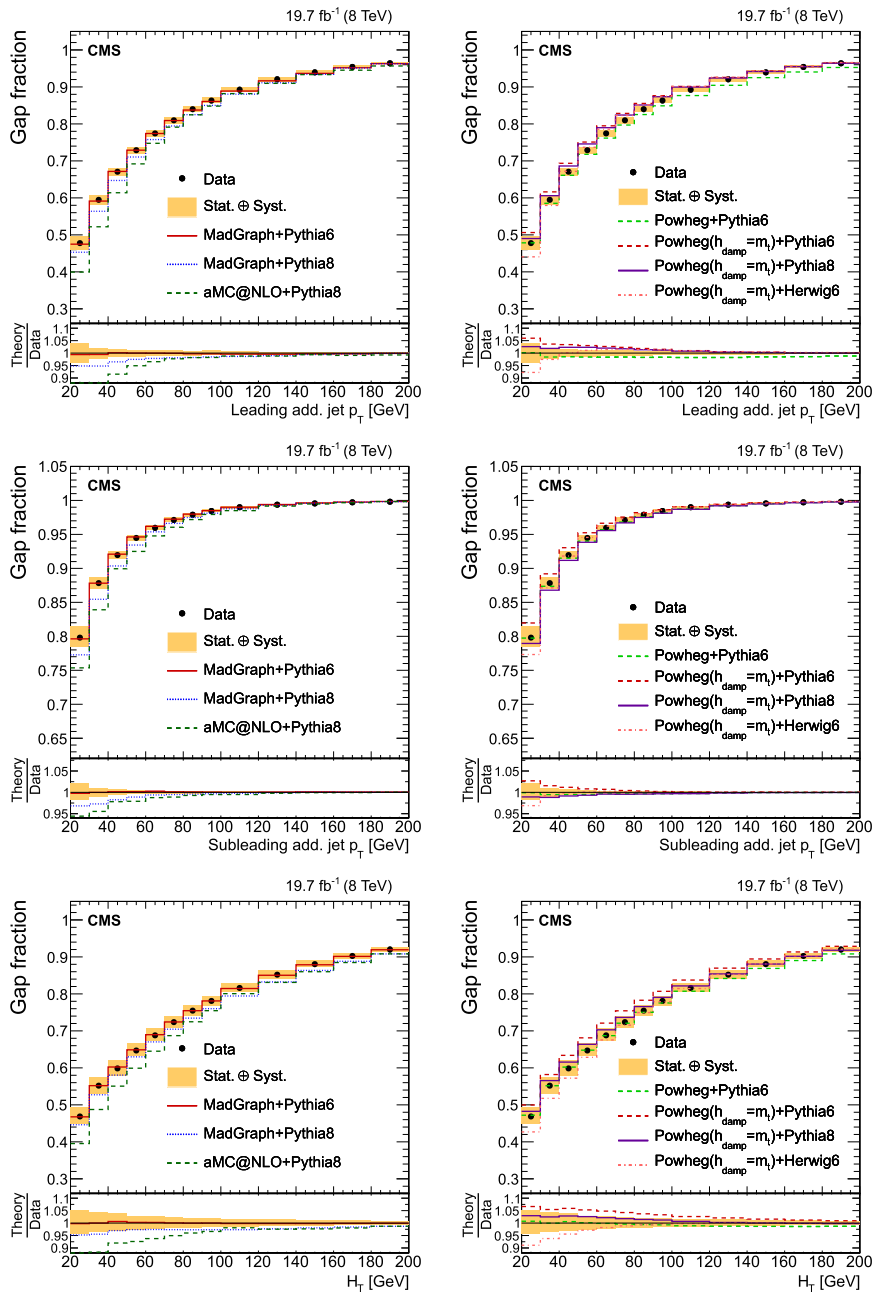
168

Fig. 21 Measured gap fraction as a function of the leading additional jet p_T in different η regions. Data are compared to predictions from MadGraph, Powheg interfaced with Pythia6 and Herwig6, and MC@NLO interfaced with Herwig6 (*left*) and to MadGraph with varied renormalization, factorization, and jet-parton matching scales (*right*). For each bin the threshold is defined at the value where the data point is placed. The *vertical bars* on the data points indicate the statistical uncertainty. The *shaded band* corresponds to the statistical uncertainty and the total systematic uncertainty added in quadrature. The *lower part of each plot* shows the ratio of the predictions to the data

Fig. 22 Measured gap fraction as a function of the subleading additional jet p_T in different $|\eta|$ regions. Data are compared to predictions from MadGraph, Powheg interfaced with Pythia6 and Herwig6, and MC@NLO interfaced with Herwig6 (*left*) and to MadGraph with varied with varied renormalization, factorization, and jet-parton matching scales (*right*). For each bin the threshold is defined at the value where the data point is placed. The *vertical bars* on the data points indicate the statistical uncertainty. The *shaded band* corresponds to the statistical uncertainty and the total systematic uncertainty added in quadrature. The *lower part of each plot* shows the ratio of the predictions to the data
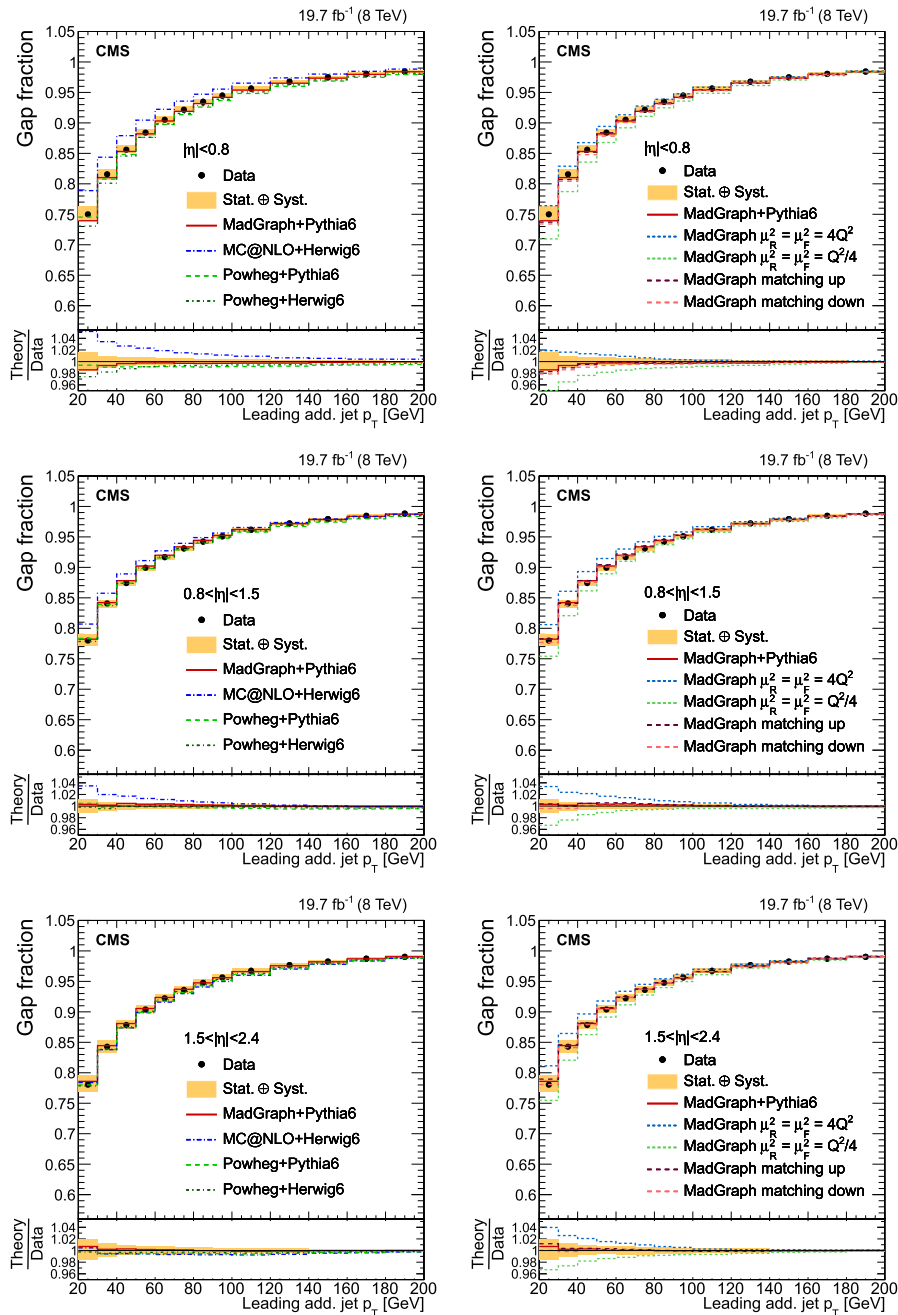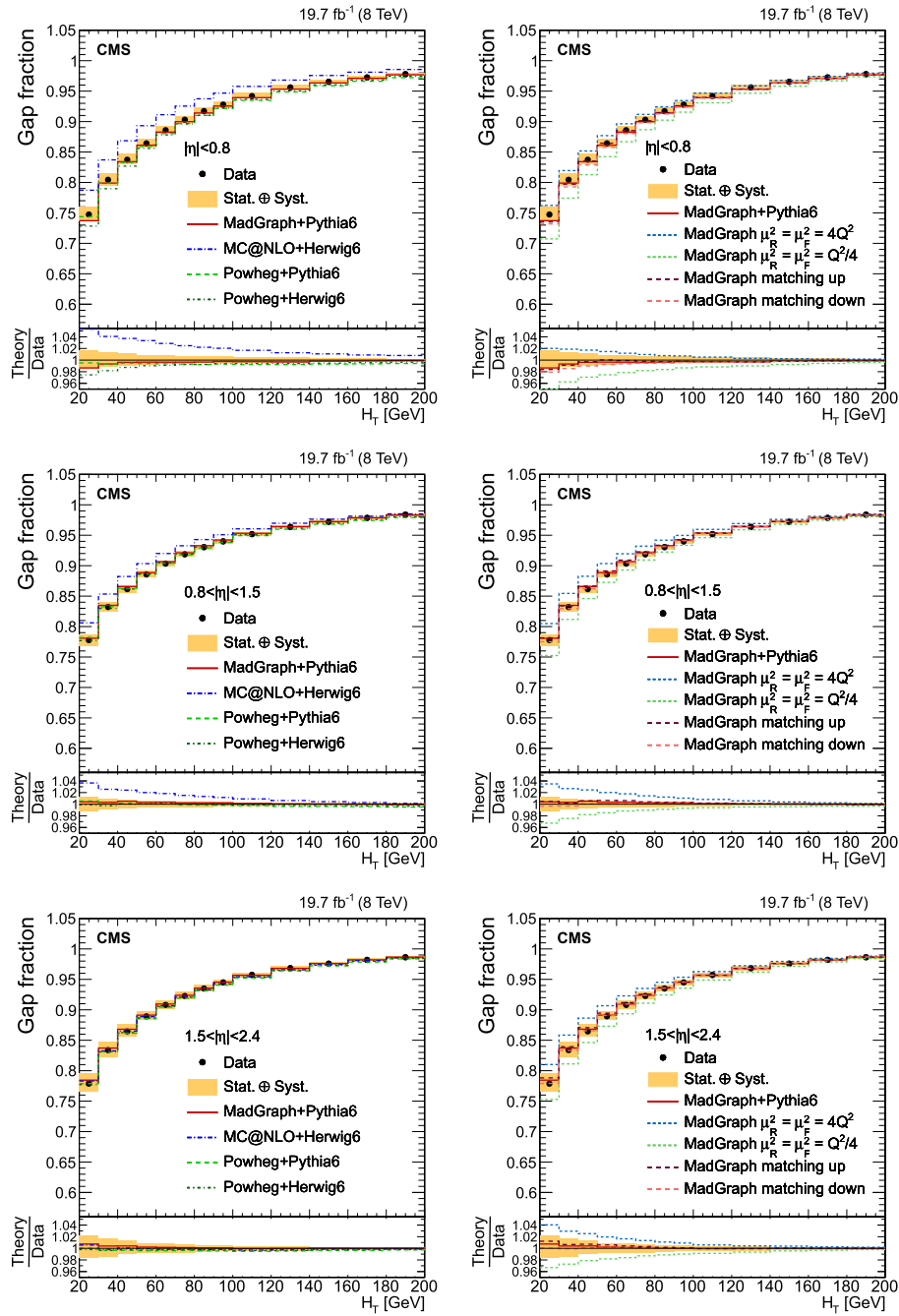
Fig. 23 Measured gap fraction as a function of H_T in different η regions. Results in data are compared to the nominal MADGRAPH signal sample, POWHEG and MC@NLO (*left*) and to the samples with varied renormalization, factorization, and jet-parton matching scales (*right*). For each bin the threshold is defined at the value where the data point is placed. The *vertical bars* on the data points indicate the statistical uncertainty. The *shaded band* corresponds to the statistical uncertainty and the total systematic uncertainty added in quadrature. The *lower part* of each *plot* shows the ratio of the predictions to the data
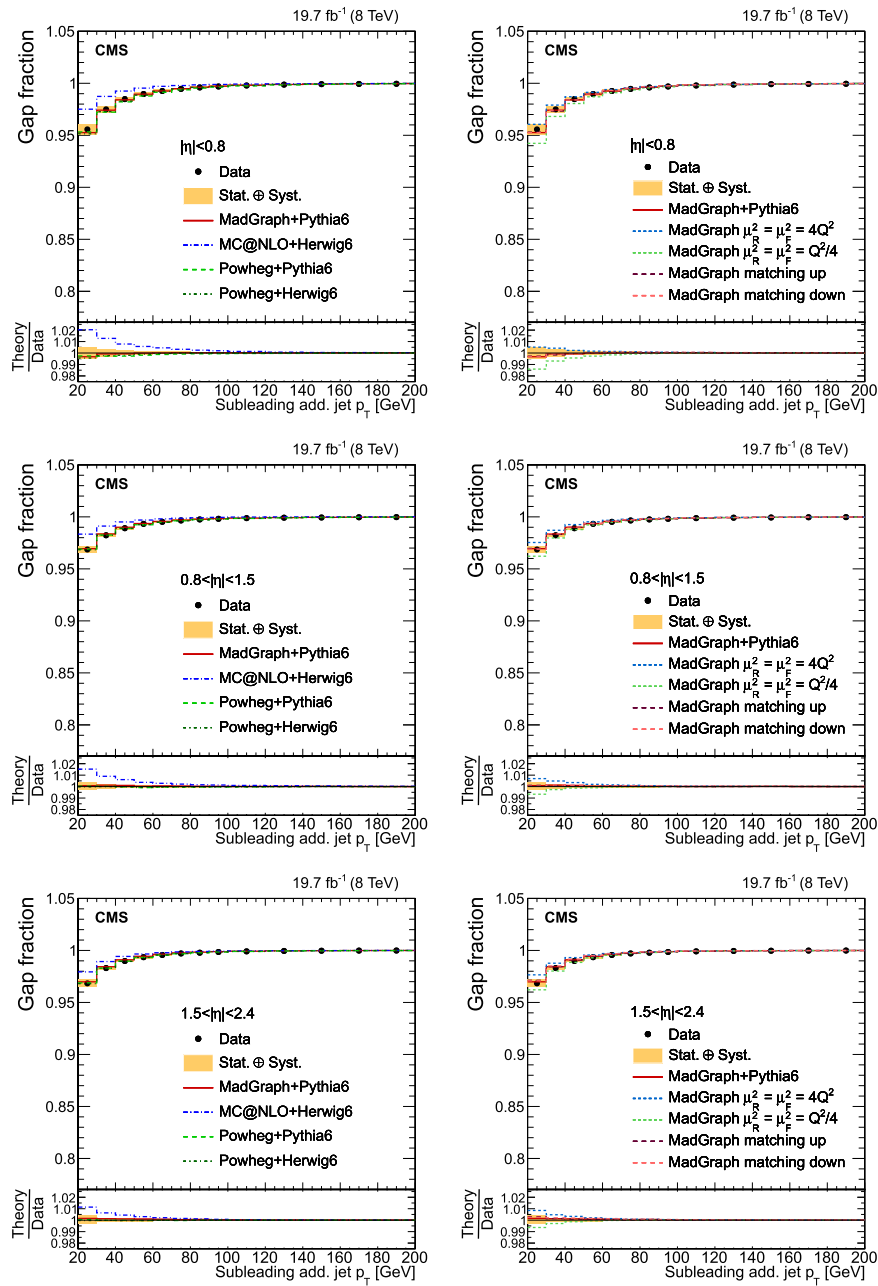
in Sect. 9. The uncertainty in JES is the dominant source of systematic uncertainty, corresponding to approximately 4 % for the smallest p_T and H_T values. Other sources with a smaller impact on the total uncertainty are the b tagging efficiency, JER, pileup, and the simulated sample used to correct the data to the particle level.

12 Summary

Measurements of the absolute and normalized differential top quark pair production cross sections have been presented using pp collisions at a centre-of-mass energy of 8 TeV, corresponding to an integrated luminosity of 19.7 fb^{-1}, in the dilepton decay channel as a function of the number of jets in the event, for three different jet p_T thresholds, and as a function of the kinematic variables of the leading and subleading additional jets. The results have been compared to the predictions from MADGRAPH interfaced with PYTHIA6, POWHEG interfaced with both PYTHIA6 and HERWIG6, MC@NLO interfaced with HERWIG6, and MADGRAPH samples with varied renormalization, factorization, and jet-parton matching scales. In general, all these generators are found to give a reasonable description of the data.

The MADGRAPH and POWHEG generators interfaced with PYTHIA6 describe the data well for all measured jet multiplicities; while MC@NLO interfaced with HERWIG6 generates lower multiplicities than observed for the lower-p_T thresholds. The prediction from MADGRAPH with varied renormalization and factorization scales does not provide an improved description of the data compared to the nominal simulation.

These results are also compared to the predictions from POWHEG with the HDAMP parameter set to the top quark mass interfaced with PYTHIA6, PYTHIA8, and HERWIG6, which provide a reasonable description of the data within the uncertainties, and the predictions from MADGRAPH and MG5_AMC@NLO interfaced with PYTHIA8, which generate higher jet multiplicities for all the p_T thresholds.

The measured kinematic variables of the leading and subleading additional jets are consistent with the various predictions. The simulations also describe well the data distributions of the leading additional jet p_T and H_T, although they tend to predict higher p_T values and more central values in η. MADGRAPH with varied parameters yields similar predictions, except for varying the renormalization and factorization scales, which tends to give higher H_T values. The MC@NLO generator predicts lower yields than observed for the subleading additional jet p_T.

The uncertainties in the measured $t\bar{t}b\bar{b}$ ($t\bar{t}b$) absolute and normalized differential cross sections as a function of the b jet kinematic variables are dominated by the statistical uncertainties. In general, the predictions describe well the shape of the measured cross sections as a function of the variables

studied, except for ΔR_{bb}, where they favour smaller values than the measurement. The predictions underestimate the total $t\bar{t}b\bar{b}$ cross section by approximately a factor of 2, in agreement with previous measurements [11]. The calculation by POWHEL [19] describes well the shape of the distributions, while the predicted absolute cross section is about 30 % lower, but compatible with the measurements within the uncertainties.

The gap fraction has been measured as a function of the p_T of the leading and subleading additional jets and H_T of the additional jets in different η ranges. For a given threshold value, the gap fraction as a function of H_T is lower than the gap fraction as a function of the p_T of the leading additional jet, showing that the measurement is probing multiple quark and gluon emission. Within the uncertainties, all predictions describe the gap fraction well as a function of the momentum of the first additional jet, while MC@NLO interfaced with HERWIG fails to describe the gap fraction as a function of the subleading additional jet p_T and H_T. In general, MADGRAPH with decreased renormalization and factorization scales more poorly describes the observed gap fraction, while varying the jet-parton matching threshold provides a similar description of the data. The MADGRAPH and MG5_AMC@NLO generators interfaced with PYTHIA8 predict lower values than measured. The POWHEG simulation with HDAMP = m_t interfaced with PYTHIA8 is consistent with the data, while the simulation interfaced with HERWIG6 and PYTHIA6 tends to worsen the comparison with the measurement.

In general, the different measurements presented are in agreement with the SM predictions as formulated by the various event generators, within their uncertainties. The correct description of $t\bar{t}$+jets production is important since it constitutes a major background in searches for new particles in several supersymmetric models and in $t\bar{t}H$ processes, where the Higgs boson decays into $b\bar{b}$. The $t\bar{t}b\bar{b}$ ($t\bar{t}b$) differential cross sections, measured here for the first time, also provide important information about the main irreducible background in the search for $t\bar{t}H$ ($b\bar{b}$).

A BDT variables

The variables used for the BDT are listed below. The candidate b jet is denoted with the superscript b in the following equations, while the candidate anti-b jet is denoted as $\bar{\mathrm{b}}$. Combinations of particles that are treated as a system by adding their four-momentum vectors are denoted without a comma, e.g. $\mathrm{b}\ell^+$ represents the b jet and the antilepton system. The angular separation $\Delta R = \sqrt{(\Delta\eta)^2 + (\Delta\phi)^2}$ and the azimuthal angular difference $\Delta\phi$ between the directions of two particles is designated using the two particle abbreviations in a superscript, separated by a comma.

One variable is the difference in the jet charges, c_{rel}, of the b and $\bar{\mathrm{b}}$ jets:

- $c_{\mathrm{rel}}^{\bar{\mathrm{b}}} - c_{\mathrm{rel}}^{\mathrm{b}}$

It is the only variable not directly related to the kinematical properties of the $\mathrm{t}\bar{\mathrm{t}}$ decay and the additional radiation. The values are by definition positive, as the jet with the highest charge is always assigned as the anti-b jet.

There are three angular variables:

- $0.5\,(|\Delta\phi^{\mathrm{b},\vec{p}_{\mathrm{T}}}| + |\Delta\phi^{\bar{\mathrm{b}},\vec{p}_{\mathrm{T}}}|)$
- $|\Delta\phi^{\mathrm{b}\ell^+,\bar{\mathrm{b}}\ell^-}|$
- $\Delta R^{\mathrm{b},\ell^+}$ and $\Delta R^{\bar{\mathrm{b}},\ell^-}$

Here, $\vec{p}_{\mathrm{T}}$ denotes the missing transverse momentum in an event. The angles are defined such that $-\pi \leq \Delta\phi \leq \pi$, and consequently the absolute values are within $[0, \pi]$.

Two variables are the p_{T} of the b jet ($\bar{\mathrm{b}}$ jet) and charged antilepton (lepton) systems:

- $p_{\mathrm{T}}^{\mathrm{b}\ell^+}$ and $p_{\mathrm{T}}^{\bar{\mathrm{b}}\ell^-}$

The remaining variables are based on the invariant or transverse masses of several particle combinations:

- $m^{\mathrm{b}\ell^+} + m^{\bar{\mathrm{b}}\ell^-}$
- $m^{\mathrm{b}\ell^+} - m^{\bar{\mathrm{b}}\ell^-}$
- $m^{\mathrm{b}\bar{\mathrm{b}}\ell^+\ell^-} - m^{\mathrm{b}\bar{\mathrm{b}}}$
- $m_{\mathrm{recoil}}^{\mathrm{jets}} - m^{\mathrm{b}\bar{\mathrm{b}}}$
- $0.5\,(m_{\mathrm{T}}^{\mathrm{b}\vec{p}_{\mathrm{T}}} + m_{\mathrm{T}}^{\bar{\mathrm{b}}\vec{p}_{\mathrm{T}}})$

For any pair of jets, the variable $m_{\mathrm{recoil}}^{\mathrm{jets}}$ is the invariant mass of all the other selected jets recoiling against this pair, i.e. all selected jets except these two.

B Summary tables of absolute and normalized cross section measurements

Table 2 Absolute (left) and normalized (right) differential $t\bar{t}$ cross sections as a function of the jet multiplicity (N_{jets}) for jets with $p_T > 30$ GeV (top), $p_T > 60$ GeV (middle), and $p_T > 100$ GeV (bottom), along with their statistical, systematic, and total uncertainties. The results are presented at the particle level in the visible phase space of the $t\bar{t}$ decay products and the additional jets

N_{jets}	$d\sigma^{vis}/dN_{jets}$ (pb)	Stat. (%)	Syst. (%)	Tot. (%)	$(1/\sigma^{vis})(d\sigma^{vis}/dN_{jets})$	Stat. (%)	Syst. (%)	Tot. (%)
$p_T > 30$ GeV								
2	2.59	0.6	5.8	5.8	5.38×10^{-1}	0.6	3.6	3.6
3	1.43	1.5	10	10	2.95×10^{-1}	1.2	3.8	4.0
4	5.1×10^{-1}	2.2	14	14	1.05×10^{-1}	2.1	9.3	9.5
5	1.5×10^{-1}	3.6	28	28	3.1×10^{-2}	3.5	28	29
≥ 6	5.0×10^{-2}	6.4	20	21	1.1×10^{-2}	6.2	16	17
$p_T > 60$ GeV								
0	5.56×10^{-1}	1.5	7.4	7.5	1.17×10^{-1}	2.0	5.9	6.2
1	1.73	2.0	6.8	7.1	3.67×10^{-1}	1.4	1.9	2.3
2	1.87	1.2	5.9	6.1	3.93×10^{-1}	1.0	1.8	2.1
3	4.73×10^{-1}	2.2	8.4	8.6	9.85×10^{-2}	2.1	3.7	4.3
4	9.2×10^{-2}	4.6	19	19	2.0×10^{-2}	4.4	18	18
≥ 5	1.9×10^{-2}	9.1	13	16	4.2×10^{-3}	8.7	9.2	13
$p_T > 100$ GeV								
0	2.66	0.6	6.1	6.2	5.59×10^{-1}	0.6	2.9	2.9
1	1.37	1.6	7.6	7.7	2.92×10^{-1}	1.3	4.5	4.6
2	6.00×10^{-1}	2.0	6.5	6.8	1.25×10^{-1}	1.8	2.0	2.7
3	9.29×10^{-2}	4.5	13	14	2.0×10^{-2}	4.4	13	14
≥ 4	1.37×10^{-2}	12	14	18	2.9×10^{-3}	11	13	17

Table 3 Absolute (left) and normalized (right) differential $t\bar{t}$ cross sections as a function of the p_T (p_T^{j1}) and the $|\eta|$ ($|\eta^{j1}|$) of the leading additional jet in the event (not coming from the top quark decay products), along with their statistical, systematic, and total uncertainties. The results are presented at the particle level in the visible phase space

p_T^{j1} bin range (GeV)	$d\sigma^{vis}/dp_T^{j1}$ (pb/GeV)	Stat. (%)	Syst. (%)	Tot. (%)	$(1/\sigma^{vis})(d\sigma^{vis}/dp_T^{j1})$ (GeV^{-1})	Stat. (%)	Syst. (%)	Tot. (%)
20, 45	5.30×10^{-2}	0.8	8.2	8.2	1.82×10^{-2}	0.8	2.8	2.9
45, 80	2.17×10^{-2}	2.2	7.7	8.0	7.44×10^{-3}	1.4	3.9	4.1
80, 140	8.64×10^{-3}	2.2	7.9	8.2	2.96×10^{-3}	2.1	4.9	5.3
140, 200	2.8×10^{-3}	3.4	9.3	10	9.78×10^{-4}	3.3	6.7	7.4
200, 400	6.9×10^{-4}	3.8	14	14	2.4×10^{-4}	3.5	14	14
$|\eta^{j1}|$ bin range (GeV)	$d\sigma^{vis}/d|\eta^{j1}|$ (pb)	Stat. (%)	Syst. (%)	Tot. (%)	$(1/\sigma^{vis})(d\sigma^{vis}/d|\eta^{j1}|)$	Stat. (%)	Syst. (%)	Tot. (%)
0, 0.6	1.32	1.2	6.5	6.6	4.27×10^{-1}	1.7	6.4	6.6
0.6, 1.2	1.5	2.2	11	11	4.77×10^{-1}	1.4	2.3	2.7
1.2, 1.8	1.3	2.0	10	10	4.20×10^{-1}	1.6	1.4	2.1
1.8, 2.4	1.1	2.4	19	19	3.42×10^{-1}	1.9	9.3	9.5

Table 4 Absolute (left) and normalized (right) differential $t\bar{t}$ cross sections as a function of the p_T (p_T^{j2}) and the $|\eta|$ ($|\eta^{j2}|$) of the subleading additional jet, along with their statistical, systematic, and total uncertainties. The results are presented at particle level in the visible phase space

p_T^{j2} bin range (GeV)	$d\sigma^{vis}/dp_T^{j2}$ (pb/GeVns)	Stat. (%)	Syst. (%)	Tot. (%)	$(1/\sigma^{vis})(d\sigma^{vis}/dp_T^{j2})$ (GeV^{-1})	Stat. (%)	Syst. (%)	Tot. (%)
20, 35	4.7×10^{-2}	2.6	12	12	3.68×10^{-2}	1.1	4.5	4.7
35, 50	1.7×10^{-2}	4.7	8.8	10	1.32×10^{-2}	2.7	5.6	6.3
50, 80	6.82×10^{-3}	4.3	8.5	9.6	5.30×10^{-3}	5.2	7.1	8.7
80, 200	9.0×10^{-4}	4.9	27	27	7.1×10^{-4}	4.6	25	26
200, 400	4.0×10^{-5}	15	35	38	2.7×10^{-5}	16	49	51
$|\eta^{j2}|$ bin range (GeV)	$d\sigma^{vis}/d|\eta^{j2}|$ (pb)	Stat. (%)	Syst. (%)	Tot. (%)	$(1/\sigma^{vis})(d\sigma^{vis}/d|\eta^{j2}|)$	Stat. (%)	Syst. (%)	Tot. (%)
0, 0.6	6.4×10^{-1}	1.6	11	11	4.69×10^{-1}	3.2	8.6	9.2
0.6, 1.2	6.2×10^{-1}	4.6	14	14	4.50×10^{-1}	2.9	5.2	6.0
1.2, 1.8	5.3×10^{-1}	4.5	20	20	3.99×10^{-1}	3.2	6.0	6.8
1.8, 2.4	4.7×10^{-1}	5.0	29	30	3.5×10^{-1}	3.8	14	14

Table 5 Absolute (left) and normalized (right) differential $t\bar{t}$ cross sections as a function of the invariant mass (m_{jj}) of the two leading additional jets in the event, the angle ΔR between them (ΔR_{jj}), and H_T, along with their statistical, systematic, and total uncertainties. The results are presented at the particle level in the visible phase space

m_{jj} bin range (GeV)	$d\sigma^{vis}/dm_{jj}$ (pb/GeV)	Stat. (%)	Syst. (%)	Tot. (%)	$(1/\sigma^{vis})(d\sigma^{vis}/dm_{jj})$ (GeV^{-1})	Stat. (%)	Syst. (%)	Tot. (%)
0, 60	4.4×10^{-3}	1.3	14	14	3.7×10^{-3}	2.4	13	13
60, 100	7.6×10^{-3}	5.3	16	17	6.33×10^{-3}	3.6	4.9	6.0
100, 170	4.7×10^{-3}	3.9	15	16	3.96×10^{-3}	2.8	4.9	5.6
170, 400	1.3×10^{-3}	3.2	14	14	1.08×10^{-3}	2.4	4.3	5.2
ΔR_{jj} bin range	$d\sigma^{vis}/d\Delta R_{jj}$ (pb)	Stat. (%)	Syst. (%)	Tot. (%)	$(1/\sigma^{vis})(d\sigma^{vis}/d\Delta R_{jj})$	Stat. (%)	Syst. (%)	Tot. (%)
0.5, 1.0	3.4×10^{-1}	2.4	11	11	2.8×10^{-1}	5.4	18	19
1.0, 2.0	3.0×10^{-1}	6.2	29	30	2.4×10^{-1}	3.8	9.2	10
2.0, 3.0	4.1×10^{-1}	5.1	28	28	3.29×10^{-1}	3.0	7.5	8.1
3.0, 4.0	2.8×10^{-1}	5.2	21	21	2.28×10^{-1}	3.5	7.2	8.0
4.0, 5.0	7.7×10^{-2}	8.1	23	24	6.0×10^{-2}	7.3	19	20
H_T bin range	$d\sigma^{vis}/dH_T$ (pb)	Stat. (%)	Syst. (%)	Tot. (%)	$(1/\sigma^{vis})(d\sigma^{vis}/dH_T)$	Stat. (%)	Syst. (%)	Tot. (%)
20, 45	3.96×10^{-2}	1.0	7.6	7.7	1.35×10^{-2}	0.9	3.6	3.7
45, 80	2.0×10^{-2}	2.6	10	11	6.91×10^{-3}	1.7	3.2	3.6
80, 140	1.06×10^{-2}	2.0	9.3	9.5	3.53×10^{-3}	1.9	2.6	3.3
140, 200	4.7×10^{-3}	2.7	13	13	1.62×10^{-3}	2.6	6.6	7.1
200, 600	8.3×10^{-4}	2.6	15	15	2.8×10^{-4}	2.3	11	12

Table 6 Absolute (left) and normalized (right) differential $t\bar{t}$ cross sections as a function of the p_T (p_T^{j1}) and the $|\eta|$ ($|\eta^{j1}|$) of the leading additional jet in the event (not coming from the top quark decay prod-ucts), along with their statistical, systematic, and total uncertainties. The results are presented at the particle level in the full phase space of the $t\bar{t}$ system, corrected for acceptance and branching fractions

p_T^{j1} bin range (GeV)	$d\sigma^{full}/dp_T^{j1}$ (pb/GeV)	Stat. (%)	Syst. (%)	Tot. (%)	$(1/\sigma^{full})(d\sigma^{full}/dp_T^{j1})$ (GeV^{-1})	Stat. (%)	Syst. (%)	Tot. (%)
20, 45	2.7	0.9	10	10	1.85×10^{-2}	0.7	2.3	2.4
45, 80	1.13	1.7	9.3	9.4	7.66×10^{-3}	1.3	3.4	3.6
80, 140	4.25×10^{-1}	1.8	7.6	7.8	2.88×10^{-3}	1.7	3.2	3.6
140, 200	1.36×10^{-1}	2.7	7.8	8.3	9.26×10^{-4}	2.6	4.4	5.1
200, 400	3.04×10^{-2}	3.0	7.8	8.4	2.07×10^{-4}	2.9	8.0	8.5
$|\eta^{j1}|$ bin range (GeV)	$d\sigma^{full}/d|\eta^{j1}|$ (pb)	Stat. (%)	Syst. (%)	Tot. (%)	$(1/\sigma^{full})(d\sigma^{full}/d|\eta^{j1}|)$	Stat. (%)	Syst. (%)	Tot. (%)
0, 0.6	65.7	1.4	6.2	6.4	4.37×10^{-1}	1.5	5.8	5.9
0.6, 1.2	70.6	1.4	9.6	9.8	4.72×10^{-1}	1.2	2.2	2.5
1.2, 1.8	63.2	1.5	9.6	9.8	4.19×10^{-1}	1.3	0.8	1.5
1.8, 2.4	51	1.9	16	16	3.38×10^{-1}	1.7	7.4	7.6

Table 7 Absolute (left) and normalized (right) differential $t\bar{t}$ cross sections as a function of the p_T (p_T^{j2}) and the $|\eta|$ ($|\eta^{j2}|$) of the subleading additional jet in the event (not coming from the top quark decay prod-ucts), along with their statistical, systematic, and total uncertainties. The results are presented at the particle level in the full phase space of the $t\bar{t}$ system, corrected for acceptance and branching fractions

p_T^{j2} bin range (GeV)	$d\sigma^{full}/dp_T^{j2}$ (pb/GeV)	Stat. (%)	Syst. (%)	Tot. (%)	$(1/\sigma^{full})(d\sigma^{full}/dp_T^{j2})$ (GeV^{-1})	Stat. (%)	Syst. (%)	Tot. (%)
20, 35	2.4	1.6	15	15	3.76×10^{-2}	0.9	3.9	4.0
35, 50	8.7×10^{-1}	4.0	10	11	1.33×10^{-2}	2.8	5.8	6.5
50, 80	3.4×10^{-1}	3.9	12	13	5.18×10^{-3}	4.3	5.5	7.0
80, 200	4.2×10^{-2}	4.0	17	18	6.5×10^{-4}	3.8	21	21
200, 400	1.5×10^{-3}	13	42	44	2.2×10^{-5}	14	52	54
$|\eta^{j2}|$ bin range (GeV)	$d\sigma^{full}/d|\eta^{j2}|$ (pb)	Stat. (%)	Syst. (%)	Tot. (%)	$(1/\sigma^{full})(d\sigma^{full}/d|\eta^{j2}|)$	Stat. (%)	Syst. (%)	Tot. (%)
0, 0.6	31.6	2.2	9.4	9.7	4.69×10^{-1}	2.9	9.1	9.5
0.6, 1.2	30	3.2	13	14	4.50×10^{-1}	2.4	4.4	5.0
1.2, 1.8	27	3.3	20	20	4.02×10^{-1}	2.7	5.7	6.3
1.8, 2.4	23	4.0	28	28	3.5×10^{-1}	3.4	13	13

Table 8 Absolute (left) and normalized (right) differential $t\bar{t}$ cross sections as a function of the invariant mass of the two first leading additional jets in the event (m_{jj}), the angle ΔR between them (ΔR_{jj}), and H_T, along with their statistical, systematic, and total uncertainties. The results are presented at the particle level in the full phase space of $t\bar{t}$ system, corrected for acceptance and branching fractions

m_{jj} bin range (GeV)	$d\sigma^{full}/dm_{jj}$ (pb/GeVns)	Stat. (%)	Syst. (%)	Tot. (%)	$(1/\sigma^{full})(d\sigma^{full}/dm_{jj})$ (GeV^{-1})	Stat. (%)	Syst. (%)	Tot. (%)
0, 60	2.3×10^{-1}	1.7	18	18	3.7×10^{-3}	2.4	13	13
60, 100	4.0×10^{-1}	5.0	13	14	6.47×10^{-3}	3.5	4.3	5.5
100, 170	2.4×10^{-1}	3.3	10	12	3.98×10^{-3}	2.9	4.2	5.1
170, 400	6.4×10^{-2}	2.7	10	10	1.04×10^{-3}	2.5	5.4	6.0
ΔR_{jj} bin range	$d\sigma^{full}/d\Delta R_{jj}$ (pb)	Stat. (%)	Syst. (%)	Tot. (%)	$(1/\sigma^{full})(d\sigma^{full}/d\Delta R_{jj})$	Stat. (%)	Syst. (%)	Tot. (%)
0.5, 1.0	17	3.2	13	13	2.6×10^{-1}	4.5	11.6	12
1.0, 2.0	16	4.0	13	14	2.45×10^{-1}	3.0	5.4	6.2
2.0, 3.0	22	3.4	15	15	3.35×10^{-1}	2.4	5.7	6.2
3.0, 4.0	15	3.6	16	16	2.27×10^{-1}	2.8	6.0	6.7
4.0, 5.0	3.8	6.5	22	23	5.8×10^{-2}	6.0	15	16

Table 8 continued

H_T bin range	$d\sigma^{full}/dH_T$ (pb)	Stat. (%)	Syst. (%)	Tot. (%)	$(1/\sigma^{full})(d\sigma^{full}/dH_T)$	Stat. (%)	Syst. (%)	Tot. (%)
20, 45	2.01	1.0	8.2	8.3	1.36×10^{-2}	0.9	2.7	2.8
45, 80	1.1	2.0	9.9	10	7.08×10^{-3}	1.5	2.0	2.5
80, 140	5.3×10^{-1}	1.7	11	11	3.56×10^{-3}	1.6	3.0	3.5
140, 200	2.3×10^{-1}	2.3	12	12	1.58×10^{-3}	2.2	4.7	5.1
200, 600	3.80×10^{-2}	2.0	9.2	9.4	2.56×10^{-4}	1.9	5.8	6.1

Table 9 Absolute (left) and normalized (right) differential $t\bar{t}$ cross sections as a function of the p_T and the $|\eta|$ of the leading ($p_T^{\,b1}$, $|\eta^{\,b1}|$) and subleading ($p_T^{\,b2}$, $|\eta^{\,b2}|$) additional b jet in the event (not coming from the top quark decay products), along with their statistical, systematic, and total uncertainties. The results are presented at particle level in the visible phase space

$p_T^{\,b1}$ bin range (GeV)	$d\sigma^{vis}/dp_T^{\,b1}$ (pb/GeVns)	Stat. (%)	Syst. (%)	Tot. (%)	$(1/\sigma^{vis})(d\sigma^{vis}/dp_T^{\,b1})$ (GeV^{-1})	Stat. (%)	Syst. (%)	Tot. (%)
20, 45	2.7×10^{-3}	25	23	35	1.6×10^{-2}	26	25	36
45, 80	1.6×10^{-3}	23	18	29	9.8×10^{-3}	23	19	30
80, 200	2.9×10^{-4}	28	19	34	1.8×10^{-3}	28	21	35
200, 400	2.6×10^{-5}	64	46	78	1.6×10^{-4}	62	46	78

$|\eta^{\,b1}|$ bin range (GeV)	$d\sigma^{vis}/d|\eta^{\,b1}|$ (pb)	Stat. (%)	Syst. (%)	Tot. (%)	$(1/\sigma^{vis})(d\sigma^{vis}/d|\eta^{\,b1}|)$	Stat. (%)	Syst. (%)	Tot. (%)
0, 0.6	8.3×10^{-2}	25	8	26	0.5	32	8	33
0.6, 1.2	6.6×10^{-2}	35	7	36	0.4	30	7	30
1.2, 1.8	5.4×10^{-2}	41	12	42	0.3	34	12	36
1.8, 2.4	6.6×10^{-2}	35	12	37	0.4	29	12	32

$p_T^{\,b2}$ bin range (GeV)	$d\sigma^{vis}/dp_T^{\,b2}$ (pb/GeV)	Stat. (%)	Syst. (%)	Tot. (%)	$(1/\sigma^{vis})(d\sigma^{vis}/dp_T^{\,b2})$ (GeV^{-1})	Stat. (%)	Syst. (%)	Tot. (%)
20, 45	9.6×10^{-4}	33	11	34	3.0×10^{-2}	18	8	20
45, 80	1.8×10^{-4}	54	24	60	5.5×10^{-3}	51	24	56
80, 200	1.8×10^{-5}	124	35	129	5.5×10^{-4}	128	35	132

$|\eta^{\,b2}|$ bin range (GeV)	$d\sigma^{vis}/d|\eta^{\,b2}|$ (pb)	Stat. (%)	Syst. (%)	Tot. (%)	$(1/\sigma^{vis})(d\sigma^{vis}/d|\eta^{\,b2}|)$	Stat. (%)	Syst. (%)	Tot. (%)
0, 0.6	2.3×10^{-2}	47	25	53	0.8	57	25	62
0.6, 1.2	1.2×10^{-2}	58	18	61	0.4	47	14	49
1.2, 2.4	7.6×10^{-3}	97	38	104	0.3	79	37	87

Table 10 Absolute (left) and normalized (right) differential $t\bar{t}$ cross sections as a function of the invariant mass of the two leading additional b jets in the event (m_{bb}) and the angle ΔR_{bb}, along with their statistical, systematic, and total uncertainties. The results are presented at particle level in the visible phase space

m_{bb} bin range (GeV)	$d\sigma^{vis}/dm_{bb}$ (pb/GeV)	Stat. (%)	Syst. (%)	Tot. (%)	$(1/\sigma^{vis})(d\sigma^{vis}/dm_{bb})$ (GeV^{-1})	Stat. (%)	Syst. (%)	Tot. (%)
10, 60	2.6×10^{-4}	60	24	65	8.2×10^{-3}	64	23	68
60, 100	1.7×10^{-4}	118	42	125	5.5×10^{-3}	104	41	112
100, 170	5.0×10^{-5}	142	49	151	1.6×10^{-3}	135	47	142
170, 400	2.9×10^{-5}	64	44	77	9.4×10^{-4}	66	45	80

ΔR_{bb} bin range	$d\sigma^{vis}/d\Delta R_{bb}$ (pb)	Stat. (%)	Syst. (%)	Tot. (%)	$(1/\sigma^{vis})(d\sigma^{vis}/d\Delta R_{bb})$	Stat. (%)	Syst. (%)	Tot. (%)
0.5, 1.0	2.5×10^{-3}	327	99	342	0.1	334	98	348
1.0, 2.0	7.7×10^{-3}	75	39	84	0.2	63	36	72
2.0, 5.0	9.8×10^{-3}	29	14	32	0.3	19	15	24

Table 11 Absolute (left) and normalized (right) differential $t\bar{t}$ cross sections as a function of the p_T and the $|\eta|$ of the leading (p_T^{b1}, $|\eta^{b1}|$) and subleading (p_T^{b2}, $|\eta^{b2}|$) additional b jet in the event (not coming from the top quark decay products), along with their statistical, systematic, and total uncertainties. The results are presented at particle level in the full phase space of the $t\bar{t}$ system, corrected for acceptance and branching fractions

p_T^{b1} bin range (GeV)	$d\sigma^{full}/dp_T^{b1}$ (pb/GeV)	Stat. (%)	Syst. (%)	Tot. (%)	$(1/\sigma^{full})(d\sigma^{full}/dp_T^{b1})$ (GeV^{-1})	Stat. (%)	Syst. (%)	Tot. (%)
20, 45	1.1×10^{-1}	33	25	41	1.7×10^{-2}	24	24	34
45, 80	6.3×10^{-2}	17	19	25	9.5×10^{-3}	19	19	27
80, 200	1.2×10^{-2}	22	20	29	1.8×10^{-3}	26	20	33
200, 400	1.0×10^{-3}	53	39	66	1.5×10^{-4}	55	39	67
$|\eta^{b1}|$ bin range (GeV)	$d\sigma^{full}/d|\eta^{b1}|$ (pb)	Stat. (%)	Syst. (%)	Tot. (%)	$(1/\sigma^{full})(d\sigma^{full}/d|\eta^{b1}|)$	Stat. (%)	Syst. (%)	Tot. (%)
0.0, 0.6	3.5	26	7	27	0.5	26	7	27
0.6, 1.2	2.9	24	6	25	0.4	23	6	24
1.2, 1.8	2.4	28	9	30	0.4	26	9	27
1.8, 2.4	2.7	29	10	31	0.4	26	10	28
p_T^{b2} bin range (GeV)	$d\sigma^{full}/dp_T^{b2}$ (pb/GeV)	Stat. (%)	Syst. (%)	Tot. (%)	$(1/\sigma^{full})(d\sigma^{full}/dp_T^{b2})$ (GeV^{-1})	Stat. (%)	Syst. (%)	Tot. (%)
20, 45	4.2×10^{-2}	40	10	42	3.0×10^{-2}	18	7	20
45, 80	7.3×10^{-3}	50	25	56	5.3×10^{-3}	57	24	62
80, 200	6.8×10^{-4}	108	35	113	4.9×10^{-4}	114	35	120
$|\eta^{b2}|$ bin range (GeV)	$d\sigma^{full}/d|\eta^{b2}|$ (pb)	Stat. (%)	Syst. (%)	Tot. (%)	$(1/\sigma^{full})(d\sigma^{full}/d|\eta^{b2}|)$	Stat. (%)	Syst. (%)	Tot. (%)
0.0, 0.6	1.0	48	18	52	0.7	46	18	50
0.6, 1.2	5.8×10^{-1}	48	15	50	0.4	41	12	43
1.2, 2.4	3.4×10^{-1}	73	29	79	0.3	66	29	72

Table 12 Absolute (left) and normalized (right) differential $t\bar{t}$ cross sections as a function of the invariant mass of the two leading additional b jets in the event (m_{bb}) and the angle ΔR_{bb}, along with their statistical, systematic, and total uncertainties. The results are presented at the particle level in the full phase space of the $t\bar{t}$ system, corrected for acceptance and branching fractions

| m_{bb} bin range (GeV)	$d\sigma^{full}/dm_{bb}$ (pb/GeV)	Stat. (%)	Syst. (%)	Tot. (%)	$(1/\sigma^{full})(d\sigma^{full}/dm_{bb})$ (GeV^{-1})	Stat. (%)	Syst. (%)	Tot. (%)
10, 60	1.1×10^{-2}	83	23	86	8.4×10^{-3}	69	23	73
60, 100	7.9×10^{-3}	92	31	97	5.8×10^{-3}	89	30	94
100, 170	2.5×10^{-3}	107	38	113	1.8×10^{-3}	111	35	117
170, 400	1.1×10^{-3}	58	41	71	8.4×10^{-4}	66	42	78
ΔR_{bb} bin range	$d\sigma^{full}/d\Delta R_{bb}$ (pb)	Stat. (%)	Syst. (%)	Tot. (%)	$(1/\sigma^{full})(d\sigma^{full}/d\Delta R_{bb})$	Stat. (%)	Syst. (%)	Tot. (%)
0.5, 1.0	5.5×10^{-3}	7508	2063	7786	4.1×10^{-3}	7506	2063	7784
1.0, 2.0	2.7×10^{-1}	65	46	80	2.0×10^{-1}	56	44	71
2.0, 5.0	3.6×10^{-1}	28	16	32	2.7×10^{-1}	22	16	28
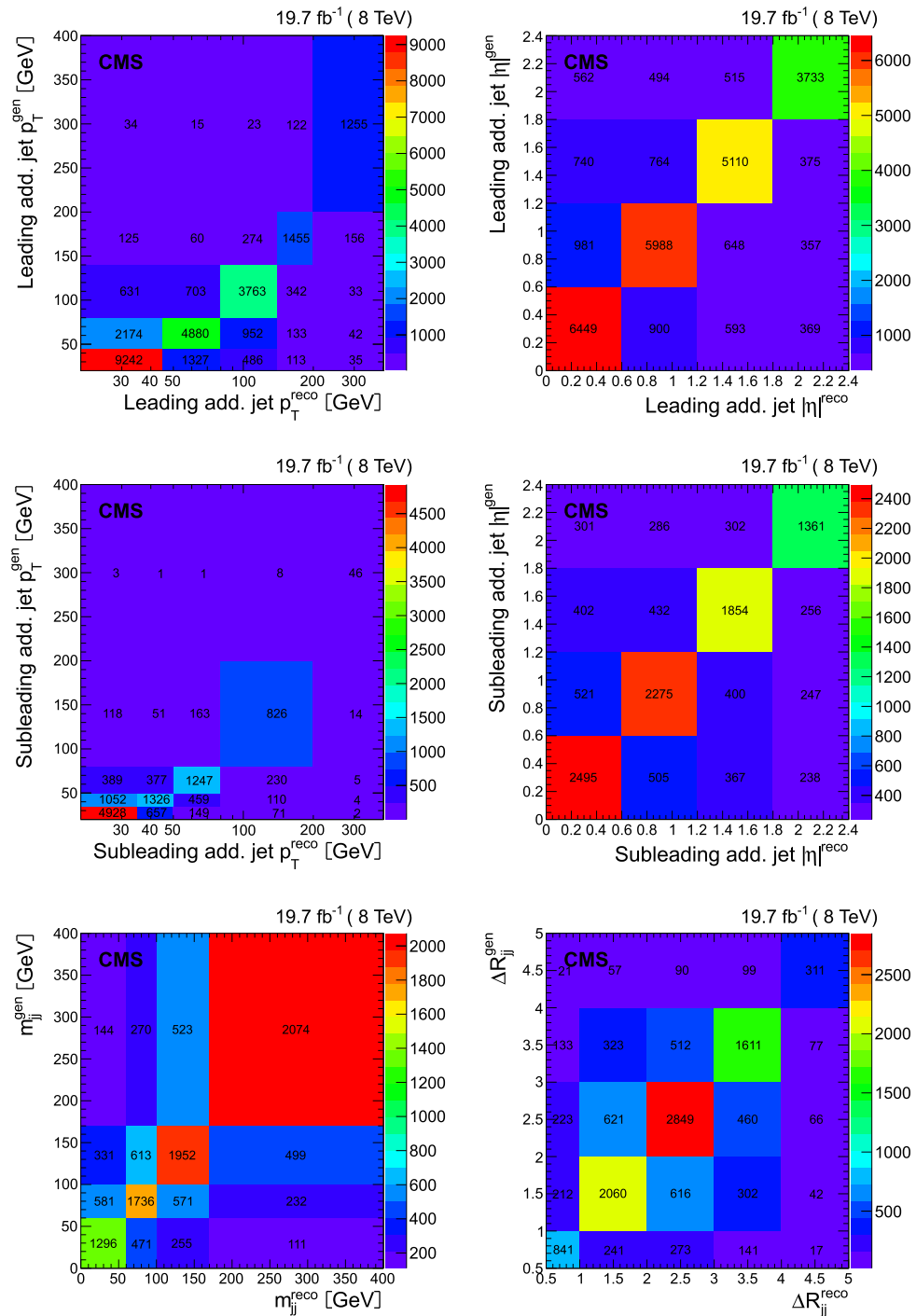
Fig. 24 The migration matrices relating the reconstructed level and the particle level in the visible phase space of the $t\bar{t}$ decay products and the additional jets for the p_T (*left*) and $|\eta|$ (*right*) of the leading (*top row*) and subleading (*middle row*) additional jets in the event, m_{jj} (*bottom left*) and ΔR_{jj} (*bottom right*). The matrices are obtained from simulated $t\bar{t}$ events using MADGRAPH+PYTHIA6
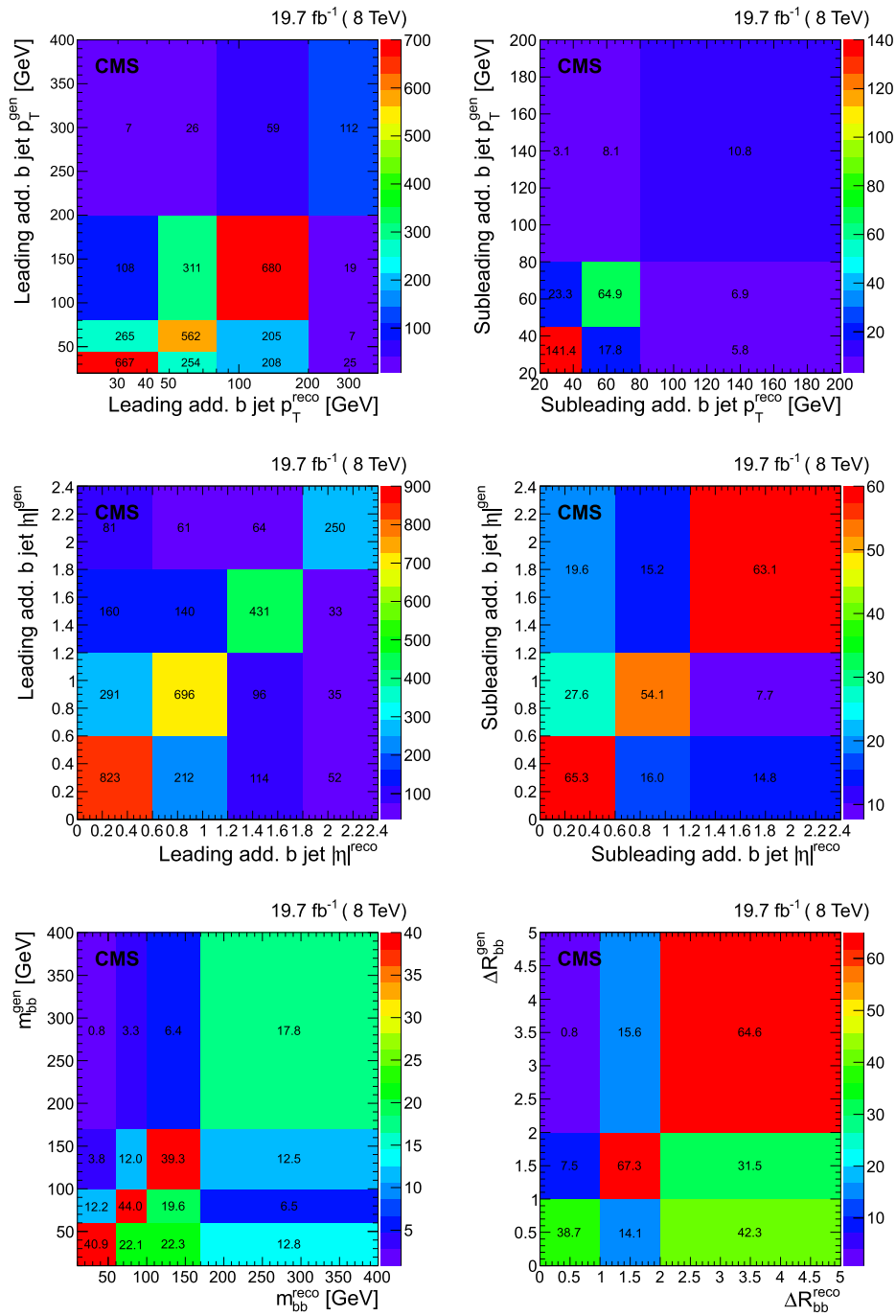
Fig. 25 The migration matrices relating the reconstructed level and the particle level in the visible phase space of the $t\bar{t}$ decay products and the additional jets for the p_T (*left*) and $|\eta|$ (*right*) of the leading (*top row*) and subleading (*middle row*) additional b jets in the event, m_{bb} (*bottom left*), and ΔR_{bb} (*bottom right*). The matrices are obtained from simulated $t\bar{t}$ events using MADGRAPH+PYTHIA6

C Migration matrices

The migration matrices relating the kinematic properties of the additional jets and b jets at the reconstruction level and particle level in the visible phase space of the $t\bar{t}$ decay products and the additional jets are presented in Figs. 24 and 25, respectively.

References

1. CMS Collaboration, Measurement of the $t\bar{t}$ production section in the dilepton channel in pp collisions at $\sqrt{s}$ = 8 TeV. JHEP **02**, 024 (2014). doi:10.1007/JHEP02(2014)024. arXiv:1312.7582 [Erratum: doi:10.1007/JHEP02(2014)102]

2. ATLAS Collaboration, Measurement of the $t\bar{t}$ production cross-section using $e\mu$ events with b-tagged jets in pp collisions at $\sqrt{s}$ = 7 and 8 TeV with the ATLAS detector. Eur. Phys. J. C**74**, 3109 (2014). doi:10.1140/epjc/s10052-014-3109-7. arXiv:1406.5375

3. CMS Collaboration, Measurement of differential top-quark pair production cross sections in pp collisions at $\sqrt{s}$ = 7 TeV. Eur. Phys. J. C **73**, 2339 (2013). doi:10.1140/epjc/s10052-013-2339-4. arXiv:1211.2220

4. ATLAS Collaboration, Measurements of top quark pair relative differential cross-sections with ATLAS in pp collisions at $\sqrt{s}$ = 7 TeV. Eur. Phys. J. C **73**, 2261 (2013). doi:10.1140/epjc/s10052-012-2261-1. arXiv:1207.5644

5. CMS Collaboration, Measurement of jet multiplicity distributions in $t\bar{t}$ production in pp collisions at $\sqrt{s}$ = 7 TeV. Eur. Phys. J. C **74**, 3014 (2014). doi:10.1140/epjc/s10052-014-3014-0. arXiv:1404.3171

6. ATLAS Collaboration, Measurements of normalized differential cross-sections for $t\bar{t}$ production in pp collisions at $\sqrt{s}$ = 7 TeV using the ATLAS detector. Phys. Rev. D **90**, 072004 (2014). doi:10.1103/PhysRevD.90.072004. arXiv:1407.0371

7. ATLAS Collaboration, Measurements of the production cross-section as a function of jet multiplicity and jet transverse momentum in 7 TeV proton–proton collisions with the ATLAS detector. JHEP **01**, 020 (2015). doi:10.1007/JHEP01(0215)020. arXiv:1407.0891

8. CMS Collaboration, Measurement of the differential cross section for top quark pair production cross section in pp collisions at $\sqrt{s}$ = 8 TeV. Eur. Phys. J. C **75**, 542 (2015). doi:10.1140/epjc/s10052-015-3709-x. arXiv:1505.04480

9. ATLAS Collaboration, Measurement of the top pair production cross section in 8 TeV proton–proton collisions using kinematic information in the lepton+jets final state with ATLAS. Phys. Rev. D **91**, 112013 (2015). doi:10.1103/PhysRevD.91.112013. arXiv:1504.04251

10. CMS Collaboration, The CMS experiment at the CERN LHC. JINST **3**, S08004 (2008). doi:10.1088/1748-0221/3/08/S08004

11. CMS Collaboration, Measurement of the cross section ratio $\sigma_{t\bar{t}b\bar{b}}/\sigma_{t\bar{t}jj}$ in pp collisions at $\sqrt{s}$ = 8 TeV. Phys. Lett. B **746**, 132 (2015). doi:10.1016/j.physletb.2015.04.060. arXiv:1411.5621

12. ATLAS Collaboration, Measurement of $t\bar{t}$ production with a veto on additional central jet activity in pp collisions at $\sqrt{s}$ = 7 TeV using the ATLAS detector. Eur. Phys. J. C **72** (2012) 2043. doi:10.1140/epjc/s10052-012-2043-9. arXiv:1203.5015

13. J. Alwall et al., MadGraph v5: going beyond. JHEP **06**, 128 (2011). doi:10.1007/JHEP06(2011)128. arXiv:1106.0522

14. S. Frixione, B.R. Webber, Matching NLO QCD computations and parton shower simulations. JHEP **06**, 029 (2002). doi:10.1088/1126-6708/2002/06/029. arXiv:hep-ph/0204244

15. S. Frixione, P. Nason, C. Oleari, Matching NLO QCD computations with Parton Shower simulations: the POWHEG method. JHEP **11**, 070 (2007). doi:10.1088/1126-6708/2007/11/070. arXiv:0709.2092

16. J. Alwall et al., The automated computation of tree-level and next-to-leading order differential cross sections, and their matching to parton shower simulations. JHEP **07**, 079 (2014). doi:10.1007/JHEP07(2014)079. arXiv:1405.0301

17. T. Sjöstrand, S. Mrenna, P.Z. Skands, PYTHIA 6.4 physics and manual. JHEP **05**, 026 (2006). doi:10.1088/1126-6708/2006/05/026. arXiv:hep-ph/0603175

18. G. Corcella et al., HERWIG 6: an event generator for hadron emission reactions with interfering gluons (including supersymmetric processes). JHEP **01**, 010 (2001). doi:10.1088/1126-6708/2001/01/010. arXiv:hep-ph/0011363

19. M.V. Garzelli, A. Kardos, Z. Trócsányi, Hadroproduction of $t\bar{t}b\bar{b}$ final states at LHC: predictions at NLO accuracy matched with parton shower. JHEP **03**, 083 (2015). doi:10.1007/JHEP03(2015)083. arXiv:1408.0266

20. GEANT4 Collaboration, GEANT4—a simulation toolkit. Nucl. Instrum. Methods A **506**, 250 (2003). doi:10.1016/S0168-9002(03)01368-8

21. P. Artoisenet, R. Frederix, O. Mattelaer, R. Rietkerk, Automatic spin-entangled decays of heavy resonances in Monte Carlo simulations. JHEP **03**, 015 (2013). doi:10.1007/JHEP03(2013)015. arXiv:1212.3460

22. J. Pumplin et al., New generation of parton distributions with uncertainties from global QCD analysis. JHEP **07**, 012 (2002). doi:10.1088/1126-6708/2002/07/012. arXiv:hep-ph/0201195

23. M.L. Mangano, M. Moretti, F. Piccinini, M. Treccani, Matching matrix elements and shower evolution for top-quark production in hadronic collisions. JHEP **01**, 013 (2007). doi:10.1088/1126-6708/2007/01/013. arXiv:hep-ph/0611129

24. R. Field, Early LHC underlying event data–findings and surprises, in *Hadron Collider Physics. Proceedings, 22nd Conference, HCP 2010, Toronto, Canada, August 23–27, 2010* (2010). arXiv:1010.3558

25. H.-L. Lai et al., New parton distributions for collider physics. Phys. Rev. D **82**, 074024 (2010). doi:10.1103/PhysRevD.82.074024. arXiv:1007.2241

26. ATLAS Collaboration, ATLAS tunes of PYTHIA 6 and PYTHIA 8 for MC11. Technical Report ATL-PHYS-PUB-2011-009 (2011)

27. R. Astalos et al., Proceedings of the sixth international workshop on multiple partonic interactions at the Large Hadron Collider (2015). arXiv:1506.05829

28. R. Frederix, S. Frixione, Merging meets matching in MC@NLO. JHEP **12**, 061 (2012). doi:10.1007/JHEP12(2012)061. arXiv:1209.6215

29. NNPDF Collaboration, Parton distributions for the LHC run II. JHEP **04**, 040 (2015). doi:10.1007/JHEP04(2015)040. arXiv:1410.8849

30. G. Bevilacqua et al., HELAC-NLO. Comput. Phys. Commun. **184**, 986 (2013). doi:10.1016/j.cpc.2012.10.033. arXiv:1110.1499

31. S. Alioli, P. Nason, C. Oleari, E. Re, A general framework for implementing NLO calculations in shower Monte Carlo programs: the POWHEG BOX. JHEP **06**, 043 (2010). doi:10.1007/JHEP06(2010)043. arXiv:1002.2581

32. P. Nason, A new method for combining NLO QCD with shower Monte Carlo algorithms. JHEP **11**, 040 (2004). doi:10.1088/1126-6708/2004/11/040. arXiv:hep-ph/0409146

33. P.Z. Skands, Tuning Monte Carlo generators: the Perugia tunes. Phys. Rev. D **82**, 074018 (2010). doi:10.1103/PhysRevD.82.074018. arXiv:1005.3457

34. K. Melnikov, F. Petriello, The W boson production cross section at the LHC through $O(\alpha_s^2)$. Phys. Rev. Lett. **96**, 231803 (2006). doi:10.1103/PhysRevLett.96.231803. arXiv:hep-ph/0603182

35. K. Melnikov, F. Petriello, Electroweak gauge boson production at hadron colliders through $O(\alpha_s^2)$. Phys. Rev. D **74**, 114017 (2006). doi:10.1103/PhysRevD.74.114017. arXiv:hep-ph/0609070

36. N. Kidonakis, Two-loop soft anomalous dimensions for single top quark associated production with W^- or H^-. Phys. Rev. D **82**, 054018 (2010). doi:10.1103/PhysRevD.82.054018. arXiv:hep-ph/1005.4451

37. J.M. Campbell, R.K. Ellis, C. Williams, Vector boson pair production at the LHC. JHEP **07**, 018 (2011). doi:10.1007/JHEP07(2011)018. arXiv:1105.0020

38. M.V. Garzelli, A. Kardos, C. Papadopoulos, Z. Trócsányi, $t\bar{t}W^\pm$ + $t\bar{t}Z$ hadroproduction at NLO accuracy in QCD with parton shower and hadronization effects. JHEP **11**, 056 (2012). doi:10.1007/JHEP11(2012)056. arXiv:1208.2665

39. S. Heinemeyer et al., Handbook of LHC Higgs cross sections: 3. Higgs properties. CERN Report CERN-2013-004 (2013). doi:10.5170/CERN-2013-004. arXiv:1307.1347

40. W. Kilian, T. Ohl, J. Reuter, WHIZARD: simulating multi-particle processes at LHC and ILC. Eur. Phys. J. C **71**, 1742 (2011). doi:10.1140/epjc/s10052-011-1742-y. arXiv:hep-ph/9905386

41. K. Melnikov, M. Schulze, A. Scharf, QCD corrections to top quark pair production in association with a photon at hadron colliders. Phys. Rev. D **83**, 074013 (2011). doi:10.1103/epjc/PhysRevD.83.074013. arXiv:1102.1967

42. M. Czakon, A. Mitov, Top++: a program for the calculation of the top-pair cross-section at hadron colliders. Comput. Phys. Commun. **185**, 2930 (2014). doi:10.1016/j.cpc.2014.06.021. arXiv:1112.5675

43. M. Botje et al., The PDF4LHC Working Group interim recommendations (2011). arXiv:1101.0538

44. S. Alekhin et al., The PDF4LHC Working Group interim report (2011). arXiv:1101.0536

45. A.D. Martin, W.J. Stirling, R.S. Thorne, G. Watt, Uncertainties on α_s in global PDF analyses and implications for predicted hadronic cross sections. Eur. Phys. J. C **64**, 653 (2009). doi:10.1140/epjc/s10052-009-1164-2. arXiv:0905.3531

46. J. Gao et al., CT10 next-to-next-to-leading order global analysis of QCD. Phys. Rev. D **89**, 033009 (2014). doi:10.1103/PhysRevD.89.033009. arXiv:1302.6246

47. NNPDF Collaboration, Parton distributions with LHC data. Nucl. Phys. B **867**, 244 (2013). doi:10.1016/j.nuclphysb.2012.10.003. arXiv:1207.1303

48. CMS Collaboration, Commissioning of the particle-flow event reconstruction with the first LHC collisions recorded in the CMS detector. CMS Physics Analysis Summary CMS-PAS-PFT-10-001 (2010)

49. CMS Collaboration, Particle-flow event reconstruction in CMS and performance for jets, taus, and MET. CMS Physics Analysis Summary CMS-PAS-PFT-09-001 (2009)

50. CMS Collaboration, Description and performance of track and primary-vertex reconstruction with the CMS tracker. JINST **9**, P10009 (2014). doi:10.1088/1748-0221/9/10/P10009. arXiv:1405.6569

51. M. Cacciari, G.P. Salam, G. Soyez, The catchment area of jets. JHEP **04**, 005 (2008). doi:10.1088/1126-6708/2008/04/005. arXiv:0802.1188

52. CMS Collaboration, Performance of CMS muon reconstruction in pp collision events at $\sqrt{s} = 7$ TeV. JINST **7**, P10002 (2012). doi:10.1088/1748-0221/7/10/P10002. arXiv:1206.4071

53. CMS Collaboration, Performance of electron reconstruction and selection with the CMS detector in proton–proton collisions at $\sqrt{s} = 8$ TeV. JINST **10**, P06005 (2015). doi:10.1088/1748-0221/10/06/P06005. arXiv:1502.02701

54. M. Cacciari, G.P. Salam, G. Soyez, The anti-k_t jet clustering algorithm. JHEP **04**, 063 (2008). doi:10.1088/1126-6708/2008/04/063. arXiv:0802.1189

55. M. Cacciari, G.P. Salam, G. Soyez, FastJet user manual. Eur. Phys. J. C **72**, 1896 (2012). doi:10.1140/epjc/s10052-012-1896-2. arXiv:1111.6097

56. CMS Collaboration, Determination of jet energy calibration and transverse momentum resolution in CMS. JINST **6**, P11002 (2011). doi:10.1088/1748-0221/6/11/P11002. arXiv:1107.4277

57. CMS Collaboration, Identification of b-quark jets with the CMS experiment. JINST **8**, P04013 (2013). doi:10.1088/1748-0221/8/04/P04013. arXiv:1211.4462

58. CMS Collaboration, Missing transverse energy performance of the CMS detector. JINST **6**, P09001 (2011). doi:10.1088/1748-0221/6/09/P09001. arXiv:1106.5048

59. CMS Collaboration, Performance of the CMS missing transverse momentum reconstruction in pp data at $\sqrt{s} = 8$ TeV. JINST **10**, P02006 (2015). doi:10.1088/1748-0221/10/02/P02006. arXiv:1411.0511

60. CMS Collaboration, Search for the associated production of the Higgs boson with a top-quark pair. JHEP **09**, 087 (2014). doi:10.1007/JHEP09(2014)087. arXiv:1408.1682 [Erratum: doi:10.1007/JHEP10(2014)106]

61. D0 Collaboration, Measurement of the top quark mass using dilepton events. Phys. Rev. Lett. **80**, 2063 (1998). doi:10.1103/PhysRevLett.80.2063. arXiv:hep-ex/9706014

62. Particle Data Group, K.A. Olive et al., Rev. Part. Phys. **38**, 090001 (2014). doi:10.1088/1674-1137/38/9/090001

63. CMS Collaboration, Measurement of the $t\bar{t}$ production cross section and the top quark mass in the dilepton channel in pp collisions at $\sqrt{s} = 7$ TeV. JHEP **07**, 049 (2011). doi:10.1007/JHEP07(2011)049. arXiv:1105.5661

64. H. Voss, A. Höcker, J. Stelzer, F. Tegenfeldt, TMVA, the toolkit for multivariate data analysis with ROOT, in *XIth International Workshop on Advanced Computing and Analysis Techniques in Physics Research (ACAT)*, p. 40 (2007). arXiv:physics/0703039

65. CMS Collaboration, Measurement of the cross section and angular correlations for associated production of a Z boson with b hadrons in pp collisions at $\sqrt{s} = 7$ TeV. JHEP **12**, 039 (2013). doi:10.1007/JHEP12(2013)039. arXiv:1310.1349

66. CMS Collaboration, Measurement of the $t\bar{t}$ production cross section in the dilepton channel in pp collisions at $\sqrt{s} = 7$ TeV. JHEP **11**, 067 (2012). doi:10.1007/JHEP11(2012)067. arXiv:1208.2671

67. CMS Collaboration, CMS luminosity based on pixel cluster counting—Summer 2013 update. CMS Physics Analysis Summary CMS-PAS-LUM-13-001 (2013)

68. A. Hoecker, V. Kartvelishvili, SVD approach to data unfolding. Nucl. Instrum. Methods A **372**, 469 (1996). doi:10.1016/0168-9002(95)01478-0. arXiv:hep-ph/9509307

69. V. Blobel, An unfolding method for high-energy physics experiments (2002). arXiv:hep-ex/0208022

70. F. James, Statistical Methods in Experimental Physics, 2nd edn. World Scientific, Singapore (2006)

71. G. Bevilacqua, M. Worek, On the ratio of $t\bar{t}b\bar{b}$ and $t\bar{t}jj$ cross sections at the CERN Large Hadron Collider. JHEP **07**, 135 (2014). doi:10.1007/JHEP07(2014)135. arXiv:1403.2046

Search for direct pair production of scalar top quarks in the single- and dilepton channels in proton-proton collisions at $\sqrt{s} = 8\,\text{TeV}$

The CMS collaboration

E-mail: cms-publication-committee-chair@cern.ch

Abstract: Results are reported from a search for the top squark $\widetilde{t}_1$, the lighter of the two supersymmetric partners of the top quark. The data sample corresponds to $19.7\,\text{fb}^{-1}$ of proton-proton collisions at $\sqrt{s} = 8\,\text{TeV}$ collected with the CMS detector at the LHC. The search targets $\widetilde{t}_1 \to b\widetilde{\chi}_1^\pm$ and $\widetilde{t}_1 \to t^{(*)}\widetilde{\chi}_1^0$ decay modes, where $\widetilde{\chi}_1^\pm$ and $\widetilde{\chi}_1^0$ are the lightest chargino and neutralino, respectively. The reconstructed final state consists of jets, b jets, missing transverse energy, and either one or two leptons. Leading backgrounds are determined from data. No significant excess in data is observed above the expectation from standard model processes. The results exclude a region of the two-dimensional plane of possible $\widetilde{t}_1$ and $\widetilde{\chi}_1^0$ masses. The highest excluded $\widetilde{t}_1$ and $\widetilde{\chi}_1^0$ masses are about $700\,\text{GeV}$ and $250\,\text{GeV}$, respectively.

JHEP07(2016)027

Contents

1 Introduction

Theories of supersymmetry (SUSY) predict the existence of a scalar partner for each standard model (SM) left-handed and right-handed fermion. When the symmetry is broken, the scalar partners acquire a mass different from their SM counterparts, the mass splitting between scalar mass eigenstates being dependent on the mass of the SM fermion. Because of the large mass of the top quark, the splitting between its chiral supersymmetric partners is potentially the largest among all supersymmetric quarks (squarks). As a result the lighter supersymmetric scalar partner of the top quark, the top squark ($\widetilde{t}_1$), could be the lightest squark. The search for a low mass top squark is of particular interest following the discovery of a Higgs boson [1–3], as a top squark with a mass in the TeV range would contribute substantially to the cancellation of the divergent loop corrections to the Higgs boson mass. SUSY scenarios with a neutralino ($\widetilde{\chi}_1^0$) as lightest supersymmetric particle (LSP) and a nearly degenerate-mass $\widetilde{t}_1$ provide one theoretically possible way to produce the observed relic abundance of dark matter [4, 5]; this further motivates the search for the $\widetilde{t}_1$ at the LHC.

In this paper we report two searches for direct top squark pair production with the CMS detector at $\sqrt{s} = 8\,\mathrm{TeV}$ with integrated luminosities of $19.5\,\mathrm{fb}^{-1}$ and $19.7\,\mathrm{fb}^{-1}$. Each search is based on the two decay modes shown in figure 1. The decay modes and the nomenclature we will use to refer to them are as follows:

$$\mathrm{pp} \to \widetilde{t}_1 \bar{\widetilde{t}}_1 \to t^{(*)} \bar{t}^{(*)} \widetilde{\chi}_1^0 \widetilde{\chi}_1^0 \qquad \text{(the ``tt'' decay mode);}$$

$$\mathrm{pp} \to \widetilde{t}_1 \bar{\widetilde{t}}_1 \to b\bar{b}\widetilde{\chi}_1^+ \widetilde{\chi}_1^- \to b\bar{b} W^{+(*)} W^{-(*)} \widetilde{\chi}_1^0 \widetilde{\chi}_1^0 \quad \text{(the ``bbWW'' decay mode).}$$

The tt and bbWW events both contain bottom quark jets (henceforth called b jets) and may contain charged leptons and neutrinos from $\mathrm{W}^{(*)}$ decay. The search strategies are therefore tailored to require either one lepton or two leptons, as well as at least one b jet and a minimum amount of transverse momentum imbalance. Throughout this paper the term "lepton" refers only to $\mathrm{e}^{\pm}$ and $\mu^{\pm}$. Previous searches for low mass top squarks in leptonic final states have been conducted by the D0, CDF, CMS, and ATLAS collaborations [6–12].

As shown in table 1, we categorize the decays of the $\widetilde{t}_1$ as 2-body or 3-body processes and as a function of the masses of the involved particles. In all cases we take the lightest neutralino $\widetilde{\chi}_1^0$ to be the LSP. For each decay mode we fix the corresponding $\widetilde{t}_1$ branching fraction to unity; the search is in all other respects designed to be as independent as possible of the details of any specific SUSY model. We explore a range of signal mass points for each decay mode under consideration. In the decay mode tt, the unknown masses are those of the $\widetilde{t}_1$ and the $\widetilde{\chi}_1^0$, while in the case of bbWW, a third unknown is the mass of the lightest chargino ($\widetilde{\chi}_1^{\pm}$). In the latter case we consider three possible mass assignments, labeled by the parameter $x = 0.25, 0.50, 0.75$; x is defined by

$$m(\widetilde{\chi}_1^{\pm}) = m(\widetilde{\chi}_1^0) + x\big[m(\widetilde{t}_1) - m(\widetilde{\chi}_1^0)\big]. \qquad (1.1)$$

In this paper we expand the result of our previous search in the single-lepton final state [12] by improving key aspects of the signal selection. Since the SM background

Kinematic conditions	Type of decay	Decay mode
$m(\mathrm{b}) + m(\mathrm{W}) + m(\widetilde{\chi}_1^0) \leq m(\widetilde{\mathrm{t}}_1)$ and $m(\widetilde{\mathrm{t}}_1) < m(\mathrm{t}) + m(\widetilde{\chi}_1^0)$	3-body decays (tt)	$\widetilde{\mathrm{t}}_1(\to \mathrm{t}^*\widetilde{\chi}_1^0) \to \mathrm{bW}\widetilde{\chi}_1^0$
$m(\mathrm{t}) + m(\widetilde{\chi}_1^0) \leq m(\widetilde{\mathrm{t}}_1)$	2-body decays (tt)	$\widetilde{\mathrm{t}}_1 \to \mathrm{t}\widetilde{\chi}_1^0$, with $\mathrm{t} \to \mathrm{bW}$
$m(\mathrm{b}) + m(\mathrm{W}) + m(\widetilde{\chi}_1^0) \leq m(\widetilde{\mathrm{t}}_1)$ and $m(\widetilde{\chi}_1^0) < m(\widetilde{\chi}_1^\pm) < m(\widetilde{\mathrm{t}}_1) - m(\mathrm{b})$	2-body decays (bbWW)	$\widetilde{\mathrm{t}}_1 \to \mathrm{b}\widetilde{\chi}_1^\pm$, with $\widetilde{\chi}_1^\pm \to \mathrm{W}^{(*)}\widetilde{\chi}_1^0$

Table 1. Kinematic conditions for the $\widetilde{\mathrm{t}}_1$ decay modes explored in this paper.
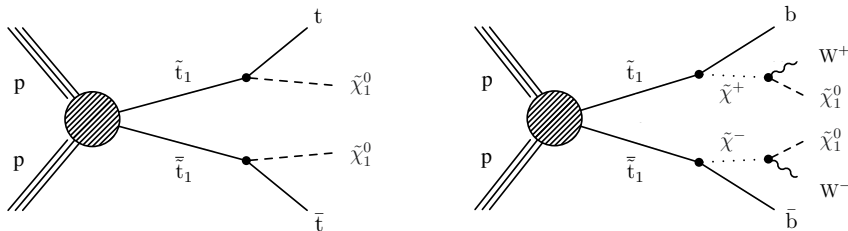
Figure 1. Top squark direct pair production at the LHC. Left: tt decay mode. Right: bbWW decay mode.

dominates the signal by several orders of magnitude and often has similar distributions for individual discriminating variables, a multivariate approach has been developed to exploit differences in the correlations among discriminating variables for signal and SM background. The background determination method has also been improved compared to ref. [12] in order to better control and correct the tail of the key transverse mass distribution. In addition to the single lepton search, we also report on a search in the dilepton mode, where the key discriminating variable is an M_{T2} variable [13]. The final result is based on a combination of the single lepton and dilepton searches.

2 The CMS detector

The central feature of the CMS apparatus is a superconducting solenoid that provides an axial magnetic field of $3.8\,\mathrm{T}$ for charged-particle tracking. Trajectories of charged particles are measured by a silicon pixel and strip tracker, covering $0 < \phi < 2\pi$ in azimuth and $|\eta| < 2.5$, where the pseudorapidity η is defined as $\eta = -\ln[\tan(\theta/2)]$; θ is the polar angle of the trajectory of the particle with respect to the counterclockwise beam direction. A crystal electromagnetic calorimeter and a brass/scintillator hadronic calorimeter surround the tracking detectors. The calorimeter measures the energy and direction of electrons, photons, and hadronic jets. Muons are measured in gas-ionization detectors embedded in the steel flux-return yoke outside the solenoid. The detector is nearly hermetic, allowing for momentum balance measurements in the plane transverse to the beam axis. Events are selected online by a two-level trigger system [14]. A more detailed description of the CMS detector can be found in ref. [15].

3 Samples, triggers, and reconstruction algorithms

3.1 Samples and trigger requirements

Events used for this search are selected initially by single-lepton and dilepton triggers. For the single-electron final state, the online selection requires the electron be isolated and have transverse momentum $p_T > 27\,\text{GeV}$; in subsequent offline analysis the reconstructed electron p_T is required to exceed $30\,\text{GeV}$. For the single-muon final state, two triggers are used, which both require $|\eta(\mu)| < 2.1$: a purely leptonic trigger requiring an isolated muon with $p_T > 24\,\text{GeV}$; and an additional mixed trigger requiring an isolated muon of $p_T > 17\,\text{GeV}$ together with three jets, each having $p_T > 30\,\text{GeV}$. The first trigger suffices for muons whose offline reconstructed p_T exceeds $26\,\text{GeV}$, while the second trigger allows the analysis to use muons with reconstructed p_T as low as $20\,\text{GeV}$; the additional jets are required in the analysis in any case. The dilepton triggers require either ee, $\mu\mu$, or eμ pairs. In each case, one lepton must satisfy $p_T > 17\,\text{GeV}$ and the other lepton must satisfy $p_T > 8\,\text{GeV}$. Trigger efficiencies are measured in data and applied to simulated events. The integrated luminosity, after data quality requirements, is $19.5 \pm 0.5\,\text{fb}^{-1}$ for the single-lepton states and $19.7 \pm 0.5\,\text{fb}^{-1}$ for the dilepton final states [16].

The SM background processes of relevance to this analysis are $t\bar{t}$, W+jets, $Z/\gamma^* \rightarrow \ell^+\ell^-$ (denoted Drell-Yan, or DY), single top, diboson, triboson, and $t\bar{t}$ + boson(s). They are simulated by the MadGraph [17] (v5.1.3.30) and powheg [18] event generators, with CTEQ6L1 [19] and CT10 [20] parton density functions (PDF) respectively. Simulated event samples with signal mass points chosen on a grid of $(m(\widetilde{t}_1), m(\widetilde{\chi}_1^0))$ values are generated, where the mass of the $\widetilde{t}_1$ varies between 100 and $1000\,\text{GeV}$, and the mass of the $\widetilde{\chi}_1^0$ varies between 0 and $700\,\text{GeV}$; as mentioned in section 1 (see eq. (1.1)), three different mass hierarchies are considered for the bbWW decay mode. The generation of signal samples is performed using MadGraph with CTEQ6L1 PDF. Parton shower and hadronization are simulated using pythia [21] (v6.4.26 for background and v6.4.22 for signal) with the tune Z2* [22]. All simulated events are propagated through the CMS detector model either with the Geant4 package [23], or, in the case of the signal samples, with a fast parametric simulation [24]. The next-to-leading-order (NLO) plus the next-to-leading-log (NLL) cross sections for top squark pair production are calculated with prospino [25–30].

To ensure agreement with data, simulated events are weighted so that the distribution of the number of proton-proton interactions per beam crossing agrees with that seen in data; they are additionally weighted by the trigger efficiency and the lepton identification and isolation efficiencies. For simulated $t\bar{t}$ samples, a p_T-dependent weight is applied to match the shape of the $d\sigma(pp \rightarrow t\bar{t} + X)/dp_T$ distribution observed in data. Signal events are weighted to account for the effect of initial state radiation [12].

3.2 Object reconstruction

In this search, all particle candidates are reconstructed with the particle-flow (PF) algorithm [31, 32], and additional criteria are then applied to select electrons, muons, jets, and b jets; the criteria are applied to both collision data and simulation samples.

The identification and measurement of the p_T of muons uses information provided by the silicon detector and the muon system [33]. We require the muon to have a 'tight' identification [33] with pseudorapidity $|\eta| < 2.1$ and $|\eta| < 2.4$ for the single-lepton and dilepton searches, respectively. The identification and energy measurement of the electrons uses information provided by the tracker and the electromagnetic calorimeter. Electron candidates are reconstructed in the tracker with the Gaussian-sum filter algorithm [34]. We require the electron to have a 'medium' identification [34] with pseudorapidity $|\eta| < 1.44$ and $|\eta| < 2.5$ for the single-lepton and dilepton searches, respectively. Both muon and electron identification demand that the lepton be isolated from the hadronic components of the event. We define an isolation variable for the leptons based on a scalar sum of transverse momenta, $\mathcal{P} \equiv \sum |\vec{p}_T|$, where the sum is taken over all PF candidates within a cone about the lepton of $\Delta R \equiv \sqrt{(\Delta\phi)^2 + (\Delta\eta)^2} = 0.3$, excluding the transverse momentum of the lepton itself, $p_T(\ell)$. In the single-lepton search we impose an upper limit on the absolute isolation, $\mathcal{P} < 5\,\text{GeV}$; for both searches we impose an upper limit on the relative isolation $\mathcal{P}/p_T(\ell) < 0.15$.

Jets are constructed by clustering all the PF candidates with the anti-k_T jet clustering algorithm [35], using a distance parameter $R = 0.5$. Contamination from additional pp interactions (pileup) is mitigated by discarding charged PF candidates that are incompatible with having originated from the estimated proton-proton collision point. The average pileup energy associated with neutral hadrons is computed event-by-event and subtracted from the jet energy and from the energy used when computing lepton isolation, i.e., a measure of the activity around the lepton. The energy subtracted is the average pileup energy per unit area (in $\Delta\eta \times \Delta\phi$) times the jet or isolation cone area [36, 37]. Candidate jets must be separated from selected leptons by $\Delta R > 0.4$. Relative and absolute jet energy corrections are applied to the raw jet momenta to establish a uniform jet response in $|\eta|$ and a calibrated response in jet p_T. We require the jets pass $p_T > 30\,\text{GeV}$ and $|\eta| < 2.4$. To tag jets originating from the hadronization of b quarks, we utilize the combined secondary vertex algorithm at its 'medium' operating point [38] with a corresponding efficiency for b jets of 65% and a mistag rate for light jets of 1%. Scale factors are applied to simulation samples to reproduce the efficiencies measured in the data.

As the decays of $\widetilde{t}_1$ are expected to yield neutralinos and neutrinos in their decay chain, genuine missing transverse momentum is expected in the final state of signal events. We define the missing transverse momentum by a sum over the transverse momenta of all PF candidates, $\vec{p}_T^{\text{miss}} \equiv -\sum \vec{p}_T$. All calibration corrections [39] have been applied to candidates used in the sum. The magnitude of the $\vec{p}_T^{\text{miss}}$ vector is denoted by $E_T^{\text{miss}} \equiv |\vec{p}_T^{\text{miss}}|$. We reject events where known detector effects or noise lead to anomalously large E_T^{miss} values.

4 Single-lepton search

In the single-lepton search, we consider only final states containing one lepton (e or μ only) and several jets.

4.1 Event selection

The preselection criteria are defined as follows:

- Exactly one identified and isolated lepton satisfying $p_T(\mu) > 20\,\mathrm{GeV}$ or $p_T(e) > 30\,\mathrm{GeV}$;

- A veto is applied against the presence of a second lepton by requiring that no additional isolated tracks or hadronically decaying τ lepton (τ_h) candidates [12] are present;

- The number of jets and number of b jets must satisfy $N(\mathrm{jets}) \geq 4$ and $N(\mathrm{b\ jets}) \geq 1$;

- $E_T^{\mathrm{miss}} > 80\,\mathrm{GeV}$;

- $M_T > 100\,\mathrm{GeV}$.

The transverse mass variable is defined by $M_T \equiv \sqrt{2E_T^{\mathrm{miss}} p_T(\ell)(1 - \cos\Delta\phi)}$, where $p_T(\ell)$ is the transverse momentum of the selected lepton and $\Delta\phi$ is the angular difference between the lepton $\vec{p}_T(\ell)$ and $\vec{p}_T^{\mathrm{miss}}$. The requirement on this variable suppresses events in which the source of the lepton and $\vec{p}_T^{\mathrm{miss}}$ is $W^\pm$ decay.

At the preselection level, the $t\bar{t}$ and W+jets backgrounds represent 90% and 7%, respectively, of the total expected background (see section 4.2). For the signal selection, we use a boosted decision tree (BDT) [40] to take advantage of the correlations among variables that discriminate between signal and background; figure 2 illustrates how a pair of kinematic variables correlate differently for a background process and signal. Compared to the approach of ref. [12], the signal selection is characterized mainly by the use of new variables, and a systematic search for the most reduced set of best-performing variables to be used as input to the BDT. Furthermore, because the discriminating power of each input varies across the $(m(\widetilde{t}_1), m(\widetilde{\chi}_1^0))$ mass plane, the latter is partitioned and a unique BDT is trained in each partition. The full list of variables (not all used in every BDT) is given below:

- E_T^{miss}: the presence of missing transverse momentum signals the possible production of a stable unseen object, such as the $\widetilde{\chi}_1^0$.

- $p_T(\ell)$: the correlation between the missing transverse momentum E_T^{miss} and the lepton transverse momentum $p_T(\ell)$ differs between signal, where genuine E_T^{miss} is due to two missing objects ($\widetilde{\chi}_1^0$), and $t\bar{t}$ and W+jets backgrounds where the E_T^{miss} is due to a single missing object (ν).

- $N(\mathrm{jets})$, $p_T(j_1)$, $p_T(b_1)$: these describe the multiplicity of selected jets and the p_T of the highest p_T jet and highest p_T b jet, respectively.

- M_{T2}^W: the distribution of this variable shows an edge at the top quark mass for $t\bar{t}$ events where both W bosons decay leptonically and one of the leptons is lost.

– 6 –

It is defined by minimizing the following over possible momentum vectors $\vec{p}_{T1}$ and $\vec{p}_{T2}$:

$$M_{T2}^{W} = \min \left\{ M_x \text{ consistent with:} \begin{bmatrix} \vec{p}_{T1} + \vec{p}_{T2} = \vec{p}_T^{\text{miss}}, & (p_1 + p_\ell)^2 \equiv p_2^2 = m(W)^2, \\ p_1^2 = 0, & (p_1 + p_\ell + p_{b_1})^2 = (p_2 + p_{b_2})^2 = M_x^2 \end{bmatrix} \right\}.$$
(4.1)

Here p_1 is the momentum of the neutrino associated with a successfully reconstructed lepton in one $W \to \ell\nu$ decay, and p_2 corresponds to an unreconstructed W whose two decay products (the lost lepton and the neutrino) escape detection. The momenta p_{b_1} and p_{b_2} are of the b jets with the highest (leading) and second-highest (sub-leading) p_T values, respectively. Including M_{T2}^{W} in the BDT reduces the contribution of the $t\bar{t}$ dilepton background.

- H_T: the scalar sum $H_T \equiv \sum |\vec{p}_T|$, summed over all jets with $p_T > 30\,\text{GeV}$, characterizes the hadronic component of the event. A related variable H_T^{frac} is defined by $H_T^{\text{frac}} \equiv \sum' |\vec{p}_T| / H_T$, where the terms in the numerator are restricted to jets of $p_T > 30\,\text{GeV}$ that lie in the same hemisphere as $\vec{p}_T^{\text{miss}}$.

- $\Delta R(\ell, b_1)$, $\Delta\phi(j_{1,2}, \vec{p}_T^{\text{miss}})$: two topological variables, $\Delta R(\ell, b_1)$ and $\Delta\phi(j_{1,2}, \vec{p}_T^{\text{miss}})$, are defined as follows: ΔR is the distance between the lepton and the leading b jet; and $\Delta\phi$ is the minimal angular difference between the $\vec{p}_T^{\text{miss}}$ vector and either the leading or sub-leading jet.

- χ_{had}^2: to characterize the kinematics of $t\bar{t}$ events we build a χ^2 variable comparing the invariant masses of the three- and two-jet systems to the mass of the top quark and W boson, respectively. It is defined as:

$$\chi_{\text{had}}^2 = \frac{(M_{j_1j_2j_3} - m(t))^2}{\sigma_{j_1j_2j_3}^2} + \frac{(M_{j_1j_2} - m(W))^2}{\sigma_{j_1j_2}^2},$$
(4.2)

where $M_{j_1j_2j_3}$ and $M_{j_1j_2}$ are, respectively the invariant mass of the three-jet system from the top quark and of the two jets posited to originate from W boson decay; $\sigma_{j_1j_2j_3}$ and $\sigma_{j_1j_2}$ are the uncertainties of these invariant masses. The $M_{j_1j_2j_3}$ value is calculated after imposing a $M_{j_1j_2} = m(W)$ constraint by kinematic fit, while $M_{j_1j_2}$ is the two-jet invariant mass before the fit. The jet assignments are made according to the b tag information: j3 must be tagged as a b quark if there are at least two b jets in the event, and j1 and j2 cannot be tagged unless there are at least three b jets in the event. This variable is used for the signal selection in the tt decay mode.

- $M(3\,\text{jet})$, $M(\ell b)$: finally, to kinematically disentangle the signal from the $t\bar{t}$ background, we construct two new invariant-mass variables that characterize the process where one $\tilde{t}_1$ decays into 3 jets and $\tilde{\chi}_1^0$ while the other decays into a b quark, lepton, neutrino, and $\tilde{\chi}_1^0$. In the case of the bbWW decay mode and the tt decay mode where no on-shell top quark is produced, i.e. $m(\tilde{t}_1) - m(\tilde{\chi}_1^0) < m(t)$, the $M(\ell b)$ distribution discriminates between $t\bar{t}$ and signal. The quantity $M(3\,\text{jet})$ is the invariant mass of the 3 jets among the 4 highest p_T jets which are the most back-to-back (according to angular difference) to the lepton. In the case of $t\bar{t}$ background, $M(3\,\text{jet})$ reconstructs
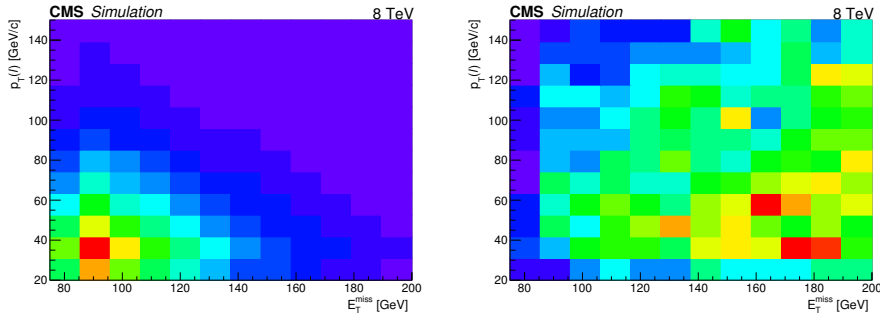
Figure 2. Distribution of the transverse momentum of the lepton versus the missing transverse energy at the preselection, for the simulated $t\bar{t}$ background (left) and for the bbWW decay mode ($x = 0.50$) of the signal with $m(\widetilde{t}_1)$-$m(\widetilde{\chi}_1^0) \geq 625\,\text{GeV}$ (right).

the mass of the top quark having decayed into 3 jets, modulo the limitations of the jet association. For the bbWW decay mode of the signal, it reconstructs an invariant mass different from $m(t)$, as no top quark is present in the final state. The quantity $M(\ell b)$ is defined as the invariant mass of the lepton and the b jet closest to it in ΔR.

Distributions of some of the variables used for the bbWW ($x = 0.75$) decay mode are illustrated in figure 3. The figure shows the distributions for both $t\bar{t}$ and signal samples; in the latter case four different kinematic possibilities are illustrated, distinguished by values of Δm:

$$\Delta m \equiv m(\widetilde{t}_1) - m(\widetilde{\chi}_1^0). \tag{4.3}$$

The figure shows clearly the evolution of the kinematic distributions as the mass difference between the lightest top squark and the LSP is varied. Differences in kinematic distributions may also be seen when comparing the tt and bbWW signal decay modes, and when varying the choice of x ($x = 0.25, 0.50, 0.75$) in the bbWW decay mode. In figure 4 we show distributions of some discriminating variables at the preselection level (but without the restriction on M_T) for both e and μ final states in data and simulated events. The figure shows good agreement between data and the total simulated background, within the uncertainties of the simulated events, which include the statistical uncertainty in the simulation samples quadratically added to the systematic uncertainty in the jet energy scale (JES).

As expected from the distributions shown in figure 3, different selection variables will exhibit different degrees of discriminating power, depending on the decay mode (tt or bbWW) and the relevant mass parameters (Δm or x) of the signal. To find the most discriminating variables, we test different sets of candidate BDT input variables, maximizing a figure of merit that compares the expected signal yield to the quadratic sum of the statistical and systematic uncertainties in the expected background yield. To keep the selection tool simple, a new variable is incorporated into the set of input variables only if it leads to a substantial increase in the figure of merit. The training of the BDT, together with this procedure for selecting variables, is then carried out separately for the different decay modes tt and bbWW ($x = 0.25, 0.50, 0.75$), and across six benchmark kinematic regions, defined
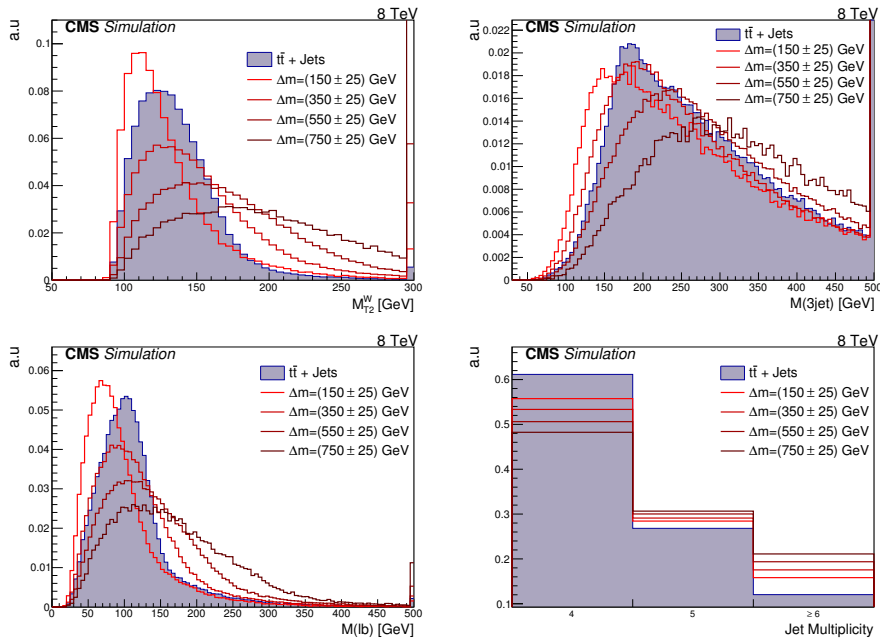
– 8 –

Figure 3. Distribution of some discriminating variables for the bbWW ($x = 0.75$) decay mode at the preselection level, for the main $t\bar{t}$ background and benchmark signal mass points grouped in bands of constant width $\Delta m = (150 \pm 25)$, (350 ± 25), (550 ± 25), and (750 ± 25) GeV. Distributions are normalized to the same area. From left to right and from top to bottom: M_{T2}^{W}, $M(3\,\text{jet})$, $M(\ell b)$ and $N(\text{jets})$.

as: $\Delta m = (150 \pm 25), (250 \pm 25), (350 \pm 25), (450 \pm 25), (550 \pm 25),$ and (650 ± 25) GeV. This partitioning allows us to take into account the evolution of the signal kinematics across the $(m(\widetilde{t}_1), m(\widetilde{\chi}_1^0))$ plane. The different BDT trainings are numbered from 1 to 6 to reflect the Δm regions in which they are trained.

The final sets of variables retained as input to the BDT are reported in table 2. Having been chosen with a quantitative assessment of the discriminating power of each variable, these represent the most reduced, while effective, sets of input variables to the BDT, for each decay mode and kinematic region. This represents a new feature of this search compared to ref. [12], where the BDT was trained with the same set of variables across different kinematic regions. Once the input variables to the BDT are determined, different BDTs are trained in each of the benchmark kinematic regions to build selection tools adapted to a kinematically varying signal. The simulation samples used for finding the best set of variables and training the BDT are statistically independent. This procedure is done for the tt and bbWW (different x values) decay modes. Using a more systematic approach for the definition of signal regions (SRs) than in ref. [12], we first consider which training is the best performing one in the $(m(\widetilde{t}_1), m(\widetilde{\chi}_1^0))$ plane. We observe that some
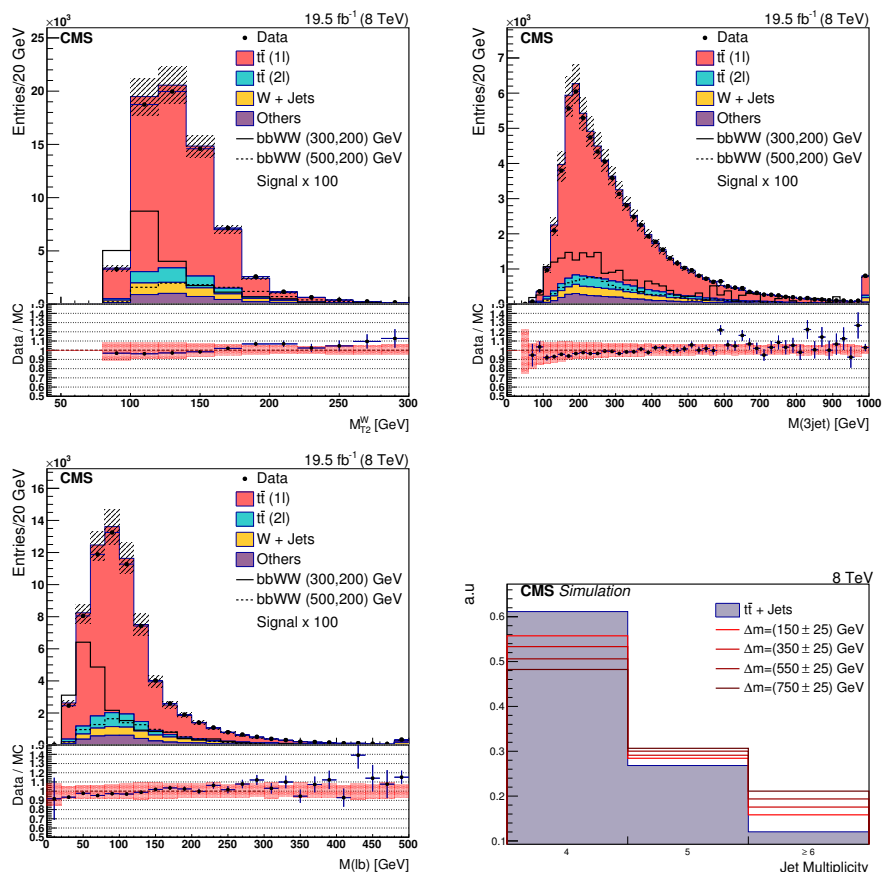
Figure 4. Distributions of different variables in both data and simulation, for both e and μ final states at the preselection level without the M_T requirement. From left to right: M_{T2}^W, $M(3\,\mathrm{jet})$, $M(\ell b)$ and $N(\mathrm{jets})$. The hatched region represents the quadratic sum of statistical and JES simulation uncertainties. The lower panel shows the ratio of data to total simulation background, with the red band representing the uncertainties mentioned in the text. Two signal mass points of the bbWW decay mode ($x = 0.75$) are represented by open histograms, dashed and solid, with their cross sections scaled by 100; the two mass points $(m(\widetilde{t}_1), m(\widetilde{\chi}_1^0))$ are (300, 200) and (500, 200) GeV.

BDTs are the best over a very limited part of the $(m(\widetilde{t}_1), m(\widetilde{\chi}_1^0))$ plane, so to simplify the final selection we retain BDT trainings that are observed to be the best performing over a large portion of the mass plane. The resulting SRs, defined as the chosen BDT training in the $(m(\widetilde{t}_1), m(\widetilde{\chi}_1^0))$ plane, are shown for all considered decay modes in figure 5.

With these SRs determined, the final selection is made by applying a minimum threshold to each BDT output as shown in figure 6. The thresholds are determined by minimizing

	$E_{\mathrm{T}}^{\mathrm{miss}}$	$p_{\mathrm{T}}(\ell)$	$M_{\mathrm{T2}}^{\mathrm{W}}$	$N(\mathrm{jets})$	$p_{\mathrm{T}}(\mathrm{j}_1)$	$p_{\mathrm{T}}(\mathrm{b}_1)$	H_{T}	$H_{\mathrm{T}}^{\mathrm{frac}}$	ΔR	$\Delta\phi$	χ^2_{had}	$M(\ell\mathrm{b})$	$M(3\,\mathrm{jet})$
tt:													
$\Delta m < m(\mathrm{t})$	✓	✓		✓		✓	✓		✓			✓	
$\Delta m \geq m(\mathrm{t})$	✓	✓	✓	✓	✓		✓		✓	✓	✓		
bbWW:													
$x = 0.25,\ 0.50$	✓	✓	✓	✓		✓			✓	✓		✓	✓
$x = 0.75$	✓	✓	✓	✓	✓		✓			✓		✓	✓

Table 2. Final selection variables chosen as input for the BDT training, as functions of the decay modes bbWW and tt, and kinematic regions. Column headings ΔR and $\Delta\phi$ refer to $\Delta R(\ell, \mathrm{b}_1)$ and $\Delta\phi(\mathrm{j}_{1,2}, \vec{p}_{\mathrm{T}}^{\,\mathrm{miss}})$.
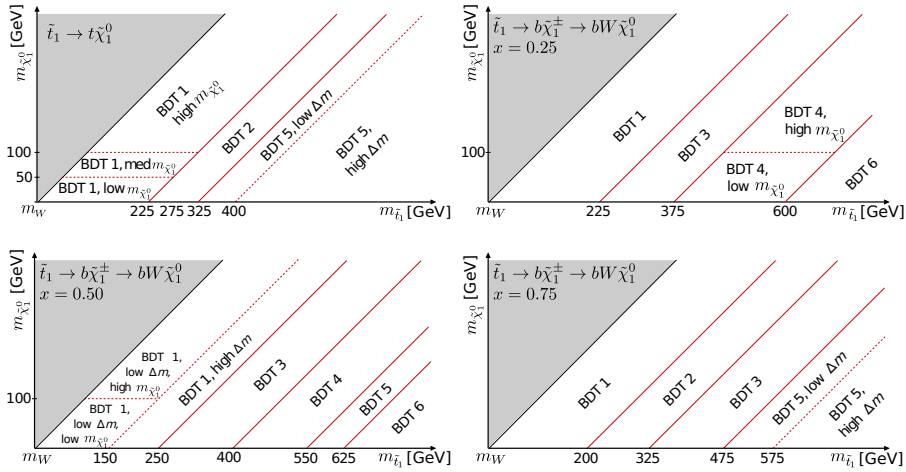
Figure 5. Signal regions (SRs) defined as functions of the chosen BDT trainings in the $(m(\tilde{\mathrm{t}}_1), m(\tilde{\chi}_1^0))$ plane for tt (top left), bbWW $x = 0.25$ (top right), 0.50 (bottom left), and 0.75 (bottom right) decay modes. The SRs are delimited by continuous red lines, and the final selections within the different SRs are delimited by dashed red lines. The attributes "low / high $\mathrm{m}(\tilde{\chi}_1^0)$" and "low / high Δm" indicate that in these regions different thresholds are applied for the same BDT training.

the expected upper limit cross section ($\sigma_{95}^{\mathrm{exp}}$) obtained from events remaining above the threshold, taking into account the predicted background (section 4.2). The final BDT trainings and selections are reported in figure 5 for all decay modes; within some SRs, the same BDT training is used with different threshold values, thus leading to different selections. On average the BDT selection suppresses the SM background by a factor $\sim\!10^3$ while reducing the signal only by a factor $\sim\!10$; the performance improves monotonically with increasing Δm.

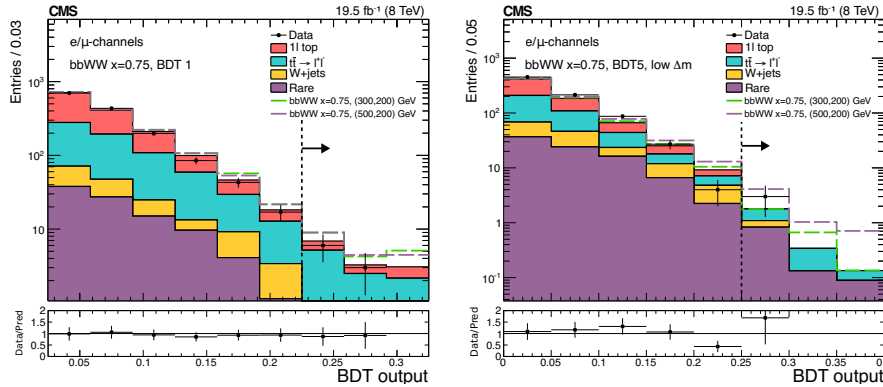**Figure 6**. The BDT output distributions of the bbWW ($x = 0.75$) decay mode in both final states at the preselection level for data and predicted background, with BDT1 > 0.025 (left) and BDT5 > 0 (right). Two representative signal mass points are shown: $(m(\widetilde{t}_1), m(\widetilde{\chi}_1^0)) = (300, 200)$ and $(500, 200)$ GeV. In each panel the final selection is indicated by the vertical black dashed line. The normalization and M_T correction (see section 4.2.2), computed in the tail of the BDT output, i.e. to the right of the dashed line, are here propagated to the full distribution. The uncertainties are statistical. The plots on the bottom represent the ratio of Data over the predicted background, where we quadratically add statistical uncertainties with the uncertainties on the scale factors.

4.2 Background estimation

The SM background processes in the single-lepton search can be divided into four categories. At preselection, the dominant contribution ($\sim 66\%$ of the total) is the $t\bar{t}$ production with one lepton; we include single top-quark production in this category and call the combination the "$t\bar{t} \to 1\ell$" component. The second most significant background (23%) comes from $t\bar{t}$ events with two leptons, where one lepton escapes detection; we will call this the "$t\bar{t} \to \ell\ell$" component. The third background (7%) is the production of W in association with jets, which we will denote "W+jets". Other backgrounds are labeled as "rare". We use data to estimate the event yields of the first three categories, starting with distributions obtained from simulation, and normalizing these with scale factors (SF) determined in control regions. The background is estimated using the formulae:

$$
\begin{aligned}
N_{\text{tail}}(t\bar{t} \to 1\ell) &= SF_0\, N_{\text{tail}}^{\text{MC}}(t\bar{t} \to 1\ell)\, SFR_{1\ell}, \\
N_{\text{tail}}(t\bar{t} \to \ell\ell) &= SF_{\ell\ell}\, N_{\text{tail}}^{\text{MC}}(t\bar{t} \to \ell\ell), \\
N_{\text{tail}}(\text{W+jets}) &= SF_0\, N_{\text{tail}}^{\text{MC}}(\text{W+jets})\, SFR_{\text{W}}.
\end{aligned}
\tag{4.4}
$$

The subscript *tail* refers to the region $M_T > 100$ GeV. The simulation yields at the final selection level ($N_{\text{tail}}^{\text{MC}}$) are corrected by normalization scale factors $SF_{\ell\ell}$ and SF_0 (defined in eq. (4.5) and (4.6)), determined in the M_T peak region $50 < M_T < 80$ GeV. The additional scale factor ratios, denoted $SFR_{1\ell}$ and SFR_{W}, are used to correct the tail of the M_T distribution, and are determined using a control region with zero b jets. The procedure accounts for the possibility of signal contamination in the different control regions. At the

final selection level the $t\bar{t} \to \ell\ell$ process represents an approximately constant proportion of the total background at ~60%, while the $t\bar{t} \to 1\ell$ and W+jets processes have varying proportions across the different selections within the remaining ~40%. Signal contamination is important only at low Δm, where it alters the background determination by up to 25%.

4.2.1 Normalization in the M_T peak

The scale factors $SF_{\ell\ell}$ and SF_0 are estimated to correct for the normalization in the M_T peak region and after the final selection on the output of the BDT. To calculate SF_0 we further require the second lepton veto, while $SF_{\ell\ell}$ is obtained without this veto. $SF_{\ell\ell}$ fixes the $t\bar{t} \to \ell\ell$ background normalization, while SF_0 sets the $t\bar{t} \to 1\ell$ and W+jets background normalizations. The scale factors are computed as follows:

$$SF_{\ell\ell} = \left(\frac{N(\mathrm{data}) - N^\mathrm{MC}(\mathrm{rare}) - N^\mathrm{MC}(\mathrm{signal})}{N^\mathrm{MC}(t\bar{t} \to 1\ell) + N^\mathrm{MC}(t\bar{t} \to \ell\ell) + N^\mathrm{MC}(\mathrm{W+jets})} \right), \tag{4.5}$$

$$SF_0 = \left(\frac{N(\mathrm{data}) - N^\mathrm{MC}(\mathrm{rare}) - N^\mathrm{MC}(\mathrm{signal}) - SF_{\ell\ell} N^\mathrm{MC}(t\bar{t} \to \ell\ell)}{N^\mathrm{MC}(t\bar{t} \to 1\ell) + N^\mathrm{MC}(\mathrm{W+jets})} \right). \tag{4.6}$$

The inclusion of the $N^\mathrm{MC}(\mathrm{signal})$ term accounts for possible signal contamination. At preselection we have: $SF_{\ell\ell} = (1.06 \pm 0.01)$ and $SF_0 = (1.05 \pm 0.01)$. At the final selection level, the deviation of these scale factors from unity is always within 10%.

4.2.2 Correction for the tail in the M_T distribution

To study the tail of the M_T distribution for different backgrounds, we enrich the data with the W+jets contribution by inverting the b-tagging criterion of the preselection. The left plot of figure 7 compares the data with background simulation, and shows some disagreement between the two for $M_\mathrm{T} > 100\,\mathrm{GeV}$. To correct this, we follow an approach based on template fits, which allows us to extract different correction factors for the $t\bar{t} \to 1\ell$ and the W+jets backgrounds, rather than assuming them to be equal as in ref. [12].

The template fit is performed using the invariant mass of the lepton and the jet with the highest b-tag discriminator. This variable, $M'_{\ell \mathrm{b}}$, is well modeled by the background simulation (see figure 8, left) and exhibits discriminating power between W+jets and $t\bar{t} \to 1\ell$ (figure 8, right). The contributions of the $t\bar{t} \to \ell\ell$ background, the rare backgrounds, and the signal, are taken from simulation and their normalizations are constrained within a 20% uncertainty during the template fit. The normalizations of the $t\bar{t} \to 1\ell$ and W+jets backgrounds are free parameters expressed in terms of scale factors SF. The fit is performed in a control region with zero b-tag jets, in two separate regions of the M_T distribution: the peak defined by $50 < M_\mathrm{T} < 80\,\mathrm{GeV}$, and the tail defined by $M_\mathrm{T} > 100\,\mathrm{GeV}$. We then extract the normalization independent ratios $SFR = SF_\mathrm{tail}/SF_\mathrm{peak}$ for $t\bar{t} \to 1\ell$ and for W+jets. Without any BDT signal selection and for a case of negligible signal contamination, the fit yields: $SFR_{t\bar{t} \to 1\ell} = (1.04 \pm 0.16)$ and $SFR_\mathrm{W} = (1.33 \pm 0.10)$. The right plot of figure 7 confirms the effectiveness of this correction.

Due to the low yields after the final selections, we loosen the requirements on the output of the BDT to keep 25% of the total yield when we extract the SFR values. The SFR ratios obtained for the different signal regions within a given decay mode (tt or bbWW)
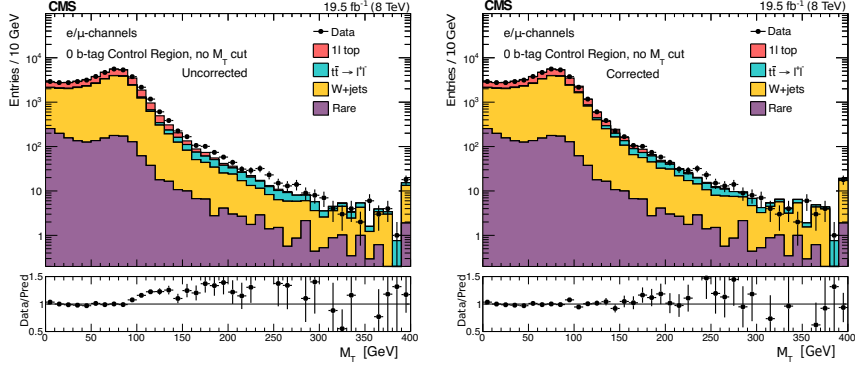
– 13 –

Figure 7. Full M_T distribution in the control region with zero b jets, without any extra signal selection. Left: without the tail correction factors applied; right: with SFR_W and $SFR_{1\ell}$ corrections applied. The plots on the bottom represent the ratio of Data over the predicted background.
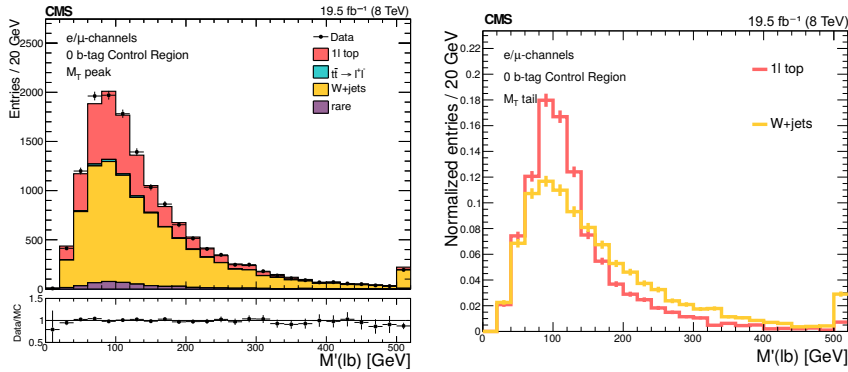
Figure 8. Left: comparison of data and simulation in the $M'_{\ell b}$ distributions for events with $50 < M_T < 80$ GeV and zero b jets. Right: shape comparison between $t\bar{t} \to 1\ell$ and W+jets for $M_T > 100$ GeV.

agree well with each other. We therefore set the final SFR factor for each decay mode to the average over the signal regions for that mode. The resulting SFR values for the tt and bbWW decay modes differ from one another, and also vary across the $(m(\tilde{t}_1), m(\tilde{\chi}_1^0))$ mass plane: $SFR_{1\ell}$ increases from 1.0 to 1.4 with increasing top squark mass, while SFR_W is stable around a mean value ~ 1.2 everywhere. In addition to the extraction of tail correction factors, we check in the control region with zero b jets that the distributions of all input variables in data are well described by the predicted background.

4.3 Systematic uncertainties

The sensitivity of this search is limited by uncertainties in both the background prediction and the acceptance and efficiency of the signal at the mass points under consideration. The

uncertainties are listed below.

4.3.1 Background

For systematic uncertainties affecting the predicted background:

- We study the impact of limited simulation statistics, generator scale variations, and JES uncertainty in the template fit method in the control region with zero b jets and no BDT selection. This leads to a global absolute uncertainty of 0.6 in $SFR_{1\ell}$ and 0.4 in SFR_{W}.

- The goodness of the $t\bar{t} \to \ell\ell$ background modeling is checked in two different control regions. The first uses events with exactly two leptons in the final state and a lower jet multiplicity ($N(\mathrm{jets}) \geq 2$) than that employed in the preselection; the second uses events with exactly one lepton, and an isolated track or τ_{h} candidate. The simulation prediction is compared with data in the M_{T} tail region of these control regions for each BDT selection. The comparison shows overall agreement and deviations are used to derive a relative systematic uncertainty, ranging from 20 to 80% depending on the selection.

- We check the modeling of the $N(\mathrm{jets})$ distribution in the $t\bar{t}$ background with a control region defined to have exactly two leptons and no requirement on M_{T}. The data/simulation scale factors are observed to be compatible with unity; therefore, no correction factor is used, but the deviations from unity are taken as systematic uncertainty. This leads to a flat 2% uncertainty, used for all the BDT selections.

- A 6% uncertainty for the modeling of the isolated track veto is applied to the fraction of $t\bar{t}$ dilepton background events that have a second e/μ or a one-prong τ_{h} decay in the acceptance. A 7% uncertainty for the modeling of the hadronic τ veto is only applied to the fraction of $t\bar{t}$ dilepton background events that have a τ_{h} in the acceptance.

- The $SF_{\ell\ell}$ and SF_0 normalization factors are varied within their statistical uncertainties and the variations are propagated as systematic uncertainties to the M_{T} peak regions.

- The statistical uncertainties in the simulation background samples are propagated to the systematic uncertainties in the backgrounds.

- The cross section of W+jets and rare backgrounds are conservatively varied by 50%, affecting the prediction of other background processes through $SF_{\ell\ell}$ and SF_0 (see equations of section 4.2); the cross section of the $t\bar{t}$ process is varied by 10%.

Table 3 gives a summary of the relative systematic uncertainties in the predicted total background yield at the preselection level, as well as their range of variation over the different top squark decay modes and BDT selections.

– 15 –

Source	Uncertainty (%) at preselection	Uncertainty (%) range over BDT selections
$SFR_{1\ell}$ uncertainty	16.4	0–24
SFR_W uncertainty	1.4	0–5
Modeling of M_T tail in $t\bar{t} \to \ell\ell$	1.6	7–39
Modeling of N(jets) in $t\bar{t}$	1.1	1–4
Modeling of the 2nd lepton veto	1.2	1–4
Normalization in M_T peak (data & MC stat)	0.7	3–37
Simulation statistics in SR	0.4	3–38
Cross section uncertainties	2.0	4–34
Total	16.8	23–58

Table 3. Summary of the relative systematic uncertainties in the total background, at the preselection level, and the range of variation over the BDT selections.

4.3.2 Signal

The statistical uncertainties in the signal samples are taken into account. The integrated luminosity is known [16] to a precision of 2.6% and the efficiencies of triggers (section 3.1) applied to the signal yield are known with a precision of 3%. The efficiencies for the identification and isolation of leptons are observed to be consistent within 5% for data and simulation; we take this difference as an uncertainty. The b-tagging efficiency has been varied within its uncertainties for b, c, and light flavor jets, leading to final yield uncertainties within 3% for all signal mass points. The systematic uncertainty in signal yield that is associated with the JES [41] is obtained by varying the jet energy scale within its uncertainty; the final uncertainties for all signal mass points are within 10%. Systematic uncertainties in the signal efficiency due to PDFs have been calculated [42–44], and are constant at ∼5%. The effect of the systematic uncertainty due to the modeling of ISR jets by the simulation is studied by deriving data/simulation scale factors that depend on N(jets). The maximum size of these uncertainties varies between 8 and 10% for different decay modes.

4.4 Summary of the single-lepton search

We develop a Δm-dependent signal selection tool with BDTs for the tt and bbWW decay modes. For each BDT selection shown in figure 5 we provide in table 4 the predicted background yield (without signal contamination) as well as the number of observed data events for the BDT selections. We do not observe any excess of data events compared to the predicted total background. The background composition varies as function of the different SRs of various decay modes. For the tt decay mode, the dominant background is $t\bar{t} \to \ell\ell$ (50-60% of the total background) across all SRs. For the bbWW x=0.25 decay mode, the dominant background is $t\bar{t} \to 1\ell$ for BDT3, BDT4, BDT6 (40-55%), and $t\bar{t} \to \ell\ell$ for BDT1 (58%). For the bbWW x=0.5 decay mode, the dominant background for BDT1 and BDT6 is $t\bar{t} \to \ell\ell$ (40-70%), while rare processes dominate for BDT4 and BDT5 (∼80%). For BDT3, $t\bar{t} \to \ell\ell$ and rare processes dominate with an equal proportion (∼ 33%). For

tt	BDT 1 Low $m(\widetilde{\chi}_1^0)$	BDT 1 Medium $m(\widetilde{\chi}_1^0)$	BDT 1 High $m(\widetilde{\chi}_1^0)$	BDT 2	BDT 5 Low Δm	BDT 5 High Δm
Background	363 ± 35	46 ± 16	19 ± 7	37 ± 13	6 ± 2	4 ± 2
Data	286	33	17	33	3	1

bbWW ($x = 0.25$)	BDT 1	BDT 3	BDT 4 Low $m(\widetilde{\chi}_1^0)$	BDT 4 High $m(\widetilde{\chi}_1^0)$	BDT 6
Background	42 ± 11	29 ± 7	20 ± 5	5 ± 2	6 ± 3
Data	27	23	19	5	6

bbWW ($x = 0.50$)	BDT 1 Low Δm Low $m(\widetilde{\chi}_1^0)$	BDT 1 Low Δm High $m(\widetilde{\chi}_1^0)$	BDT 1 High Δm	BDT 3	BDT 4	BDT 5	BDT 6
Background	14 ± 5	3 ± 2	91 ± 25	7 ± 2	0.8 ± 0.3	0.7 ± 0.4	3 ± 1
Data	16	1	85	4	1	2	5

bbWW ($x = 0.75$)	BDT 1	BDT 2	BDT 3	BDT 5 Low Δm	BDT 5 High Δm
Background	13 ± 4	23 ± 7	11 ± 3	2 ± 1	0.4 ± 0.2
Data	9	15	6	3	0

Table 4. Background prediction without signal contamination and observed data for the BDT selections. The total systematic uncertainties are reported for the predicted background.

the bbWW x=0.75 decay mode, $t\bar{t} \to \ell\ell$ is the dominant background (45–65%) for BDT1 to BDT3, while rare processes dominate for BDT5 (47–61%). In figure 6 we show the distribution of the BDT output for data and the predicted background (without signal contamination) for two trainings of the bbWW $x = 0.75$ case.

The signal contamination is taken into account by calculating a new estimation of the background in case of signal contamination (see eqs. (4.5) and (4.6)); this is done separately at each signal mass point in the $(m(\widetilde{t}_1), m(\widetilde{\chi}_1^0))$ plane, and for each of the signal regions defined in figure 5. For the calculation of limits (see section 6), the number of observed events in data and expected signal remain the same, while the expected background is modified to correct for signal contamination in the control regions. While the effect of this contamination is observed to be almost negligible at high Δm, it can modify the background estimate up to 25% at low Δm.

5 Dilepton search

5.1 Selection

For the three dilepton final states considered in this search ($e\mu$, ee, and $\mu\mu$), we define the preselection as follows:

- At least two oppositely charged leptons.

- For the leading and sub-leading lepton, we require $p_T > 20$ and $p_T > 10\,\text{GeV}$, respectively.

- For all lepton flavors: $M_{\ell^+\ell^-} > 20\,\text{GeV}$.

- If more than two lepton pairs are found that satisfy the above three requirements, the pair with the highest p_T is chosen.

- For ee, $\mu\mu$ channels: $|M_Z - M_{\ell^+\ell^-}| > 25\,\text{GeV}$ (Z boson veto) and $E_T^{\text{miss}} > 40\,\text{GeV}$.

- $N(\text{jets}) \geq 2$ and $N(\text{b jets}) \geq 1$.

At the preselection level, $t\bar{t}$ production with two leptons represents $\sim$90% of the total expected background.

In this search we separate the signal from the dileptonic $t\bar{t}$ background by constructing a transverse mass variable $M_{T2}^{\ell\ell}$ as defined in eq. (5.1). We begin with the two selected leptons ℓ_1 and ℓ_2. Under the assumption that the $\vec{p}_T^{\text{miss}}$ originates only from two neutrinos, we partition the $\vec{p}_T^{\text{miss}}$ into two hypothetical neutrinos with transverse momenta $\vec{p}_{T1}^{\text{miss}}$ and $\vec{p}_{T2}^{\text{miss}}$. We calculate the transverse mass M_T of the pairings of these hypothetical neutrinos with their respective lepton candidates and record the maximum of these two M_T. This process is repeated with other viable partitions of the $\vec{p}_T^{\text{miss}}$ until the minimum of these maximal M_T values is reached; this minimum is the $M_{T2}^{\ell\ell}$ for the event [13, 45]:

$$M_{T2}^{\ell\ell} = \min_{\vec{p}_{T1}^{\text{miss}} + \vec{p}_{T2}^{\text{miss}} = \vec{p}_T^{\text{miss}}} \left(\max \left[M_T(\vec{p}_T^{\ell_1}, \vec{p}_{T1}^{\text{miss}}), M_T(\vec{p}_T^{\ell_2}, \vec{p}_{T2}^{\text{miss}}) \right] \right). \qquad (5.1)$$

When constructed in this fashion, $M_{T2}^{\ell\ell}$ has the property that its distribution in $t\bar{t} \to \ell\ell$ events has a kinematic endpoint at $m(\text{W})$. The presence of additional invisible particles for the signal breaks the assumption that the $\vec{p}_T^{\text{miss}}$ arises from only two neutrinos; consequently, $M_{T2}^{\ell\ell}$ in dileptonic top squark events does not necessarily have an endpoint at $m(\text{W})$. The value of $m(\text{W})$ therefore dictates the primary demarcation between the control region $M_{T2}^{\ell\ell} < 80\,\text{GeV}$, and the general signal region $M_{T2}^{\ell\ell} > 80\,\text{GeV}$. The left plot of figure 9 shows the distribution of $M_{T2}^{\ell\ell}$ at the preselection level, where we observe its discriminating power for two representative signal mass points. The distribution of $M_{T2}^{\ell\ell}$ in top squark events, however, depends upon the signal mass point $(m(\widetilde{t}_1), m(\widetilde{\chi}_1^0))$, as can be observed on the right plot of figure 9.

The optimal threshold on $M_{T2}^{\ell\ell}$ for the final selection is thus dependent on the supersymmetric particle masses: using the background predictions from section 5.2 for the $M_{T2}^{\ell\ell}$ signal region, we iterate in 10 GeV steps through possible $M_{T2}^{\ell\ell}$ thresholds, from 80 GeV to 120 GeV; for each $(m(\widetilde{t}_1), m(\widetilde{\chi}_1^0))$ signal mass point, we pick the threshold that yields the lowest expected upper limit for the top squark production cross section, σ_{95}^{exp}.

5.2 Background prediction

For the $M_{T2}^{\ell\ell}$ signal regions used in this search, the dominant background is $t\bar{t}$. Other backgrounds also contribute, including DY, single-lepton events with an additional misidentified lepton (see section 5.2.3), and rare processes. The rare processes include single top quarks produced in association with a W boson; diboson production, including W or Z production with an associated photon; triple vector boson production; and $t\bar{t}$ production in association with one or two vector bosons. The normalization of the $t\bar{t}$ and DY backgrounds, and the normalization and shape of the misidentified lepton backgrounds, are evaluated from data
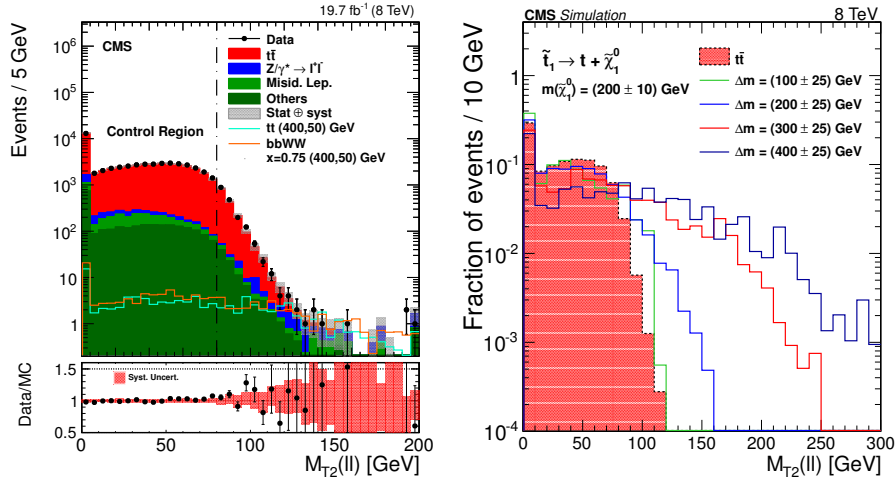
– 18 –

Figure 9. Left: data, expected background, and signal contributions in the $M_{T2}^{\ell\ell}$ distribution at the preselection level. Background processes are estimated as in section 5.2. The uncertainty bands are calculated from the full list of uncertainties discussed in section 5.4. The same signal mass point $(m(\tilde{t}_1), m(\tilde{\chi}_1^0)) = (400, 50)$ GeV is represented for the tt and bbWW ($x = 0.75$) decay modes. Right: $M_{T2}^{\ell\ell}$ distribution for the $t\bar{t}$ background and different signal mass points of the tt decay mode regrouped in constant Δm bands; distributions are normalized to the same area.

using control samples. The shapes of the $t\bar{t}$ and DY backgrounds, and the normalization and shapes of less common processes, are all estimated from the simulation. We perform a number of checks to validate the modeling of the $M_{T2}^{\ell\ell}$ distribution in our simulation (see section 5.3). For the background processes estimated from simulation, we apply the corrective scale factors mentioned in section 3.2.

5.2.1 $t\bar{t}$ estimation

The $t\bar{t} \to \ell\ell$ background represents about 90% of the events in the control region $M_{T2}^{\ell\ell} < 80$ GeV (see figure 9 left). We can therefore use this region to determine the normalization of the expected SM $t\bar{t}$ contribution in the signal region. To accomplish this, we first count the number of data events in the control region and subtract the simulation background contributions of all non-$t\bar{t}$ backgrounds; we then normalize it by the simulated $t\bar{t}$ yield in the control region. This procedure yields a scale factor of 1.024 ± 0.005. In this control region, the signal contamination relative to the expected $t\bar{t}$ contribution depends upon the Δm considered: while being completely negligible at high Δm, it can take values between 5% and 40% at low Δm, depending on Δm as well as the considered top squark decay mode.

5.2.2 Estimation of the Drell-Yan background

To estimate the contribution of DY events in the selected events, we use the Z-boson mass resonance in the $M_{\ell^+\ell^-}$ distribution for opposite charge and same flavor dilepton events.

From comparisons with data, we find that our simulation accurately models the Z mass line shape within systematic uncertainties. We can therefore calculate a normalization scale factor for simulated DY events by comparing the observed number of events inside the Z-veto region ($N_{\text{in}}^{\ell^+\ell^-}$) against the expected number of DY events calculated from the simulation ($N_{\text{in}}^{\text{DY}}$),

$$SF_{\text{DY}}^{\ell^+\ell^-} = \frac{\left(N_{\text{in}}^{\ell^+\ell^-} - 0.5 N_{\text{in}}^{\text{e}\mu} k_{\ell\ell}\right)}{N_{\text{in}}^{\text{DY}}}, \tag{5.2}$$

where the number of events with different flavor ($N_{\text{in}}^{\text{e}\mu}$) is subtracted to account for non-DY processes contaminating $N_{\text{in}}^{\ell^+\ell^-}$. The k-factors in eq. (5.2) account for different reconstruction efficiencies for electrons and muons. Using eq. (5.2), we calculate a scale factor of (1.43 ± 0.04) for $\mu\mu$ events and (1.46 ± 0.04) for ee events. To account for the contribution of eμ events originating from $Z \rightarrow \tau^+\tau^-$ decays, we estimate a scale factor of (1.44 ± 0.04) for eμ events by taking the geometric average of the scale factors for the same-flavor channels.

5.2.3 Misidentified lepton background estimation

The misidentified lepton background consists of events in which non-prompt leptons pass the identification criteria. The largest category of events falling in this group are semileptonic $t\bar{t}$ events and leptonically decaying W events where a jet, or a lepton within a jet, is misreconstructed as an isolated prompt lepton.

In order to have an estimation of this background from data, we first measure the lepton misidentification rate, which is the probability for a non-prompt lepton to pass the requirements of an isolated lepton. This is done by counting the rate at which leptons with relaxed identification ("loose" leptons) pass the "tight" selection requirements (see section 3.2). The measurement is performed in a data sample dominated by multijet events.

We then measure the prompt lepton rate, which is the efficiency for isolated and prompt leptons to pass selection requirements, in a data sample enriched in $Z \rightarrow \ell^+\ell^-$ events. As with the misidentification rate, the prompt rate is determined by counting the rate at which loose leptons pass tight selection requirements.

Both the measurements of the lepton misidentification rate and the prompt lepton rate are performed as functions of lepton p_{T} and $|\eta|$. For each dilepton event where both selected leptons pass at least the loose selection requirements, the measured misidentification and prompt rates directly translate into a weight for the event. These weights depend upon whether neither, one, or both loose leptons also passed the tight selection requirements. The shape and normalization of the misidentified lepton background is then extracted by first applying these derived weights to the data sample where both selected leptons pass at least the loose selection requirements, and then calculating the weighted distribution of relevant variables such as $M_{\text{T2}}^{\ell\ell}$. Once the background is determined, the number of events falling into the $M_{\text{T2}}^{\ell\ell}$ signal regions is found.

5.3 Checks of the $M_{\text{T2}}^{\ell\ell}$ shape

The search in the dileptonic final states requires a good understanding of the $M_{\text{T2}}^{\ell\ell}$ shape. In this section we provide a number of validation studies performed with simulation, with

– 20 –

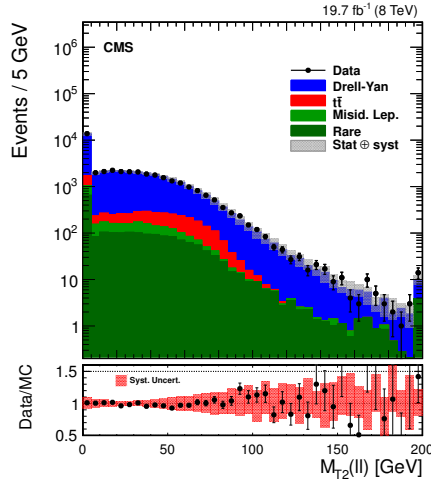**Figure 10**. Data and expected background contributions for the $M_{T2}^{\ell\ell}$ distribution in a control region enriched in $Z \to \ell\ell$ events. This control region is similar to the preselection, except that the Z boson veto and b jet requirements have been inverted. Background processes are estimated as in section 5.2. The uncertainty bands are calculated from the full list of uncertainties discussed in section 5.4.

comparisons to data in control regions.

One of the main factors determining the $M_{T2}^{\ell\ell}$ shape is the intrinsic resolution and energy scale of the input objects used in the $M_{T2}^{\ell\ell}$ calculation. From studies using $Z \to \ell\ell$ events, we confirm that the Gaussian core of the E_T^{miss} resolution function is sufficiently well-modeled by the simulation. These studies also confirm that the resolution and scale of the lepton $\vec{p}_T$ are both well-modeled in the simulation.

The intrinsic width of the intermediate W bosons in dileptonic $t\bar{t}$ events drives the shape of the $M_{T2}^{\ell\ell}$ distribution near the kinematic edge at 80 GeV. Comparisons of events with different generated W widths (between 289 MeV and 2.1 GeV) show that any systematic uncertainty in the W boson width has a negligible effect in the selected signal regions.

The final notable effect driving the $M_{T2}^{\ell\ell}$ shape is the category of events populating the tails of the E_T^{miss} resolution function. To confirm that this class of events is modeled in simulation with reasonable accuracy, we perform comparisons between data and simulation in a control region enriched in $Z \to \ell\ell$ events; this control region is obtained by inverting the Z boson veto and requiring zero reconstructed b jets. Figure 10 shows the $M_{T2}^{\ell\ell}$ distribution in this control region, illustrating that the data distribution, including expected events in the tail, is well-modeled by the simulation.

5.4 Systematic uncertainties

We present the dominant systematic uncertainties affecting the dilepton search.

5.4.1 Systematic uncertainties affecting the background and signal

The E_T^{miss} measurement, and subsequently the shape of the $M_{T2}^{\ell\ell}$ distribution, is affected by uncertainties in the lepton energy scale, the JES, the jet energy resolution, and the scale of the unclustered energy (objects with $p_T < 10\,\mathrm{GeV}$) in the event. We vary the four-vector momenta of the lepton and jets within their systematic uncertainties, and propagate the shifted $\vec{p}_T$ back into the E_T^{miss} and $M_{T2}^{\ell\ell}$ calculations. For the jet energy resolution uncertainty, we vary it within its uncertainty and propagate it back into the E_T^{miss} calculation. For the unclustered energy scale, we scale the total $\vec{p}_T$ of the unclustered energy by $\pm 10\%$ and propagate it back into the E_T^{miss} calculation.

As with the single-lepton search (see section 4.3), we also apply systematic uncertainties to account for the intrinsic statistical uncertainty in the simulation samples as well as any mismodeling by the simulation of the b-tagging efficiency, the lepton trigger efficiency, the lepton ID and isolation, and the limited modeling of ISR jets by the simulation. No substantial correlation has been observed between the value of $M_{T2}^{\ell\ell}$ and the size of these four systematic uncertainties.

5.4.2 Systematic uncertainties affecting only the background

For the two background normalizations ($t\bar{t}$ and DY), we account for the statistical uncertainty in the normalization. For the misidentified lepton background (see section 5.2.3), the two primary sources of systematic uncertainty are the statistical uncertainty in the measured rates of prompt and misidentified leptons, and any systematic uncertainty in the measurement of the misidentification rate. Combining these in quadrature yields a total systematic uncertainty of $\sim 75\%$ for the considered signal regions. For the diboson background processes, which are estimated from the simulation, we apply a conservative cross section uncertainty of 50%.

Table 5 displays the magnitude of the effect of the aforementioned systematic uncertainties (sections 5.4.1 and 5.4.2) on the background estimate for each of the considered signal regions.

5.4.3 Systematic uncertainties affecting only the signal

As in the single-lepton search, we account for the effect of PDF uncertainties in the signal efficiency. The resulting uncertainty in signal efficiency is found to be $\sim 4\%$ across all signal mass points.

5.5 Summary of the dilepton search

We have developed a signal selection based on the $M_{T2}^{\ell\ell}$ distribution. Table 6 presents the predicted backgrounds as well as the number of observed data events for all signal regions; we do not observe any excess of data events compared to the predicted total background. Top quark pair production dominates the composition of the total predicted background in the four signal regions with the lowest $M_{T2}^{\ell\ell}$ threshold, decreasing from 91 % to 45% with increasing threshold, while DY dominates in the last region ($\sim 38\%$). As with the single-lepton search, the signal contamination is also taken into account in the final interpretation of the results.

– 22 –

$M^{\ell\ell}_{\mathrm{T2}}$	Systematic uncertainties (%)										
	Stat.	ℓ ES	JES	Uncl.	JER	b tag	ℓ eff.	ISR	ML	σ	Total
$\geq$80 GeV	± 1	$^{+4}_{-5}$	$^{+2}_{-1}$	$^{+3}_{-1}$	$^{+3}_{-3}$	$^{+1}_{-0}$	$^{+1}_{-1}$	$^{+1}_{-1}$	$^{+1}_{-1}$	$^{+1}_{-1}$	$^{+7}_{-6}$
$\geq$90 GeV	± 2	$^{+6}_{-6}$	$^{+5}_{-2}$	$^{+7}_{-1}$	$^{+7}_{-4}$	$^{+2}_{-0}$	$^{+1}_{-1}$	$^{+0}_{-0}$	$^{+2}_{-2}$	$^{+1}_{-1}$	$^{+14}_{-9}$
$\geq$100 GeV	± 4	$^{+6}_{-5}$	$^{+9}_{-2}$	$^{+10}_{-1}$	$^{+12}_{-2}$	$^{+1}_{-1}$	$^{+1}_{-1}$	$^{+2}_{-1}$	$^{+3}_{-3}$	$^{+2}_{-2}$	$^{+20}_{-9}$
$\geq$110 GeV	± 7	$^{+9}_{-5}$	$^{+9}_{-1}$	$^{+4}_{-0}$	$^{+5}_{-0}$	$^{+1}_{-2}$	$^{+0}_{-0}$	$^{+3}_{-2}$	$^{+7}_{-7}$	$^{+5}_{-5}$	$^{+18}_{-13}$
$\geq$120 GeV	± 10	$^{+4}_{-5}$	$^{+12}_{-3}$	$^{+2}_{-0}$	$^{+5}_{-0}$	$^{+3}_{-1}$	$^{+0}_{-0}$	$^{+6}_{-4}$	$^{+12}_{-12}$	$^{+5}_{-5}$	$^{+22}_{-18}$

Table 5. The relevant sources of systematic uncertainty in the background estimate for each signal region used in the limit setting. From left to right, the systematic uncertainty sources are: lepton energy scale (ℓ ES), jet energy scale (JES), unclustered energy scale (Uncl.), $E^{\mathrm{miss}}_{\mathrm{T}}$ energy resolution from jets (JER), uncertainty in b tagging scale factors (b tag), lepton selection efficiency (ℓ eff.), ISR reweighting (ISR), the misidentified lepton estimate (ML), and the combined normalization uncertainty in the $t\bar{t}$, DY, and other electroweak backgrounds (σ).

$M^{\ell\ell}_{\mathrm{T2}}$ threshold	80 GeV	90 GeV	100 GeV	110 GeV	120 GeV
Data	1785	427	106	30	14
Expected background	1670 $^{+117}_{-104}$	410 $^{+55}_{-35}$	100 $^{+20}_{-8}$	31.8 $^{+5.8}_{-4.0}$	14.8 $^{+3.3}_{-2.7}$

Table 6. Data yields and background expectation for five different $M^{\ell\ell}_{\mathrm{T2}}$ threshold values. The asymmetric uncertainties quoted for the background indicate the total systematic uncertainty, including the statistical uncertainty in the background expectation.

6 Combination and final results

After applying all selections for the single-lepton and dilepton data sets, no evidence for direct top squark production is observed (see tables 4 and 6). We proceed to combine the results of the two searches. In this combination, no overlap is expected in the event selections of the two searches, and none is observed. Since the background predictions are primarily based on data in the two searches, the corresponding systematic uncertainties are taken to be uncorrelated. Systematic uncertainties affecting the expected signal, as well as those due to luminosity, b tagging, PDF, JES, and lepton identification and isolation, are treated as 100% correlated between the two searches.

We interpret the absence of excess in both single-lepton and dilepton searches in terms of a 95% confidence level (CL) exclusion of top squark pair production in the $(m(\widetilde{t}_1), m(\widetilde{\chi}^0_1))$ plane. A frequentist CL$_{\mathrm{S}}$ method [46–48] with a one-sided profile is used, taking into account the predicted background and observed number of data events, and the expected signal yield for all signal points. In this method, Poisson likelihoods are assigned to each of the single-lepton and dilepton yields, for each $(m(\widetilde{t}_1), m(\widetilde{\chi}^0_1))$ signal point, and multiplied to give the combined likelihood for both observations. The final yields of each analysis are taken from the signal region corresponding to the considered signal point. Systematic uncertainties are included as nuisance parameter distributions. A test statistic defined to be

the likelihood ratio between the background only and signal plus background hypotheses is used to set exclusion limits on top squark pair production; the distributions of these test statistics are constructed using simulated experiments. When interpreting the results for the tt and bbWW decay modes, we make the hypothesis of unit branching fractions, $\mathcal{B}(\widetilde{t}_1 \to t^{(*)}\widetilde{\chi}_1^0) = 1$ and $\mathcal{B}(\widetilde{t}_1 \to b\widetilde{\chi}_1^\pm) = 1$, respectively. The expected and observed limits, for which we combine the results of both searches and account for signal contamination, are reported in figure 11; the experimental uncertainties are reported on the expected contour, while the PDF uncertainty for the signal cross section, quadratically added to the systematic uncertainties in $2\mu_r$ and $\mu_r/2$ renormalization scales of the top squark pair production cross section, are reported on the observed contour.

For the tt decay mode, we reach sensitivity up to $m(\widetilde{t}_1) \sim 700\,\mathrm{GeV}$ for $\widetilde{\chi}_1^0$ mass up to $\sim 250\,\mathrm{GeV}$; there is a loss of sensitivity along the line $\Delta m = m(t)$, which delineates two different scenarios within the tt decay mode (see table 1) and where the signal acceptance drops dramatically. For the bbWW decay mode, the sensitivity reached in this study ranges from 600 to $\sim 700\,\mathrm{GeV}$ in $m(\widetilde{t}_1)$, depending on the values of $m(\widetilde{\chi}_1^0)$ and $m(\widetilde{\chi}_1^\pm)$; the sensitivity is greater in the case of a large $m(\widetilde{\chi}_1^\pm) - m(\widetilde{\chi}_1^0)$ mass difference as for $x = 0.75$, where the decay products of the two produced W bosons are more energetic. In the case of $x = 0.50$, there is a drop in sensitivity for $m(\widetilde{\chi}_1^\pm) - m(\widetilde{\chi}_1^0) \sim m(W)$, which corresponds to the limit in which the W boson is virtual. Because of the rather low threshold achievable in lepton p_T, sensitivity extends down to the kinematic limit $\Delta m \sim m(b) + m(W)$ for the bbWW $x = 0.50$ and 0.75 cases.

The final results are dominated by the single-lepton search, where the selection is based on a multivariate selection with new discriminating variables, which is adapted to the kinematics of expected signal events, and where the discriminating power of selection variables is quantitatively assessed. The new signal selection presented in this paper leads to the strengthening and further improvement of the results of ref. [12]. We now account for systematic uncertainties due to PDFs, and more thoroughly assess the effects of signal contamination. The combination with the dilepton search extends the sensitivity by $\sim 25\,\mathrm{GeV}$ in the tt decay mode in the $\Delta m \gtrsim m(t)$ region, and in the bbWW ($x = 0.50$) decay mode across the $m(\widetilde{\chi}_1^\pm) - m(\widetilde{\chi}_1^0) = m(W)$ region; it very moderately extends the sensitivity in the bbWW ($x = 0.75$) at both high $\widetilde{t}_1$ and $\widetilde{\chi}_1^0$ masses; no gain of sensitivity is observed in the bbWW ($x = 0.25$) case where the search is limited by the small $m(\widetilde{\chi}_1^\pm) - m(\widetilde{\chi}_1^0)$ mass difference, leaving a rather limited phase space to the decay products of the W boson. The signal contamination (see section 4.4) reduces the sensitivity of the search by 0–30 GeV depending on the decay mode and signal point under consideration. The limits are rather insensitive to the choice of hypothesis for the polarization of the interaction in the $t\widetilde{\chi}_1^0$ and $W\widetilde{\chi}_1^0\,\widetilde{\chi}_1^\pm$ couplings for the tt and bbWW decay modes, respectively.

7   Conclusions

Using up to $19.7\,\mathrm{fb}^{-1}$ of pp collision data taken at $\sqrt{s} = 8\,\mathrm{TeV}$, we search for direct top squark pair production in both single-lepton and dilepton final states. In both searches the standard model background, dominated by the $t\bar{t}$ process, is predicted using control sam-
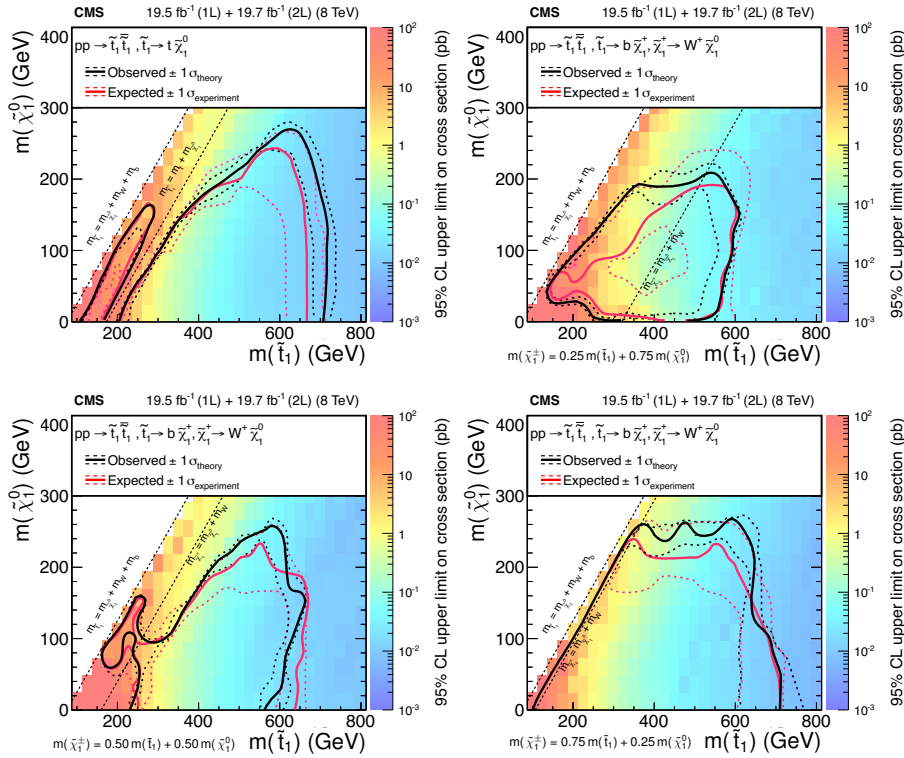
– 24 –

Figure 11. Exclusion limit at 95% CL obtained with a statistical combination of the results from the single-lepton and dilepton searches, for the tt (top left), bbWW $x = 0.25$ (top right), bbWW $x = 0.50$ (bottom left) and bbWW $x = 0.75$ (bottom right) decay modes. The red and black lines represent the expected and observed limits, respectively; the dotted lines represent in each case the $\pm 1\ \sigma$ variations of the contours. For all decay modes, we show the kinematic limit $m(\tilde{t}_1) = m(b) + m(W) + m(\tilde{\chi}_1^0)$ on the left side of the $(m(\tilde{t}_1), m(\tilde{\chi}_1^0))$ plane; for the tt decay mode, we show the $\Delta m = m(t)$ line; and for the bbWW decay mode, we show the $m(\tilde{\chi}_1^\pm) - m(\tilde{\chi}_1^0) = m(W)$ line.

ples in data. In this single-lepton search, we improve the results of ref. [12] by employing an upgraded multivariate tool for signal selection, fed by both kinematic and topological variables and specifically trained for different decay modes and kinematic regions. This systematic approach to the signal selection, where the discriminating power of each selection variable is quantitatively assessed, is a key feature of the single-lepton search. The background determination method has also been improved compared to ref. [12]. In the dilepton search the signal selection is based on the $M_{T2}^{\ell\ell}$ variable. In both searches, the effect of the signal contamination is accounted for. No excess above the predicted background is observed in either search. Simplified models (figure 1) are used to interpret the

results in terms of a region in the $(m(\widetilde{t}_1), m(\widetilde{\chi}_1^0))$ plane, excluded at 95% CL. We combine the results of both searches for maximal sensitivity; the sensitivity depends on the decay mode, and on the $(m(\widetilde{t}_1), m(\widetilde{\chi}_1^0))$ signal point. The highest excluded $\widetilde{t}_1$ and $\widetilde{\chi}_1^0$ masses are about 700 GeV and 250 GeV, respectively.

Acknowledgments

References

[1] ATLAS collaboration, *Observation of a new particle in the search for the Standard Model Higgs boson with the ATLAS detector at the LHC*, *Phys. Lett.* **B 716** (2012) 1 [arXiv:1207.7214] [INSPIRE].

[2] CMS collaboration, *Observation of a new boson at a mass of 125 GeV with the CMS experiment at the LHC*, *Phys. Lett.* **B 716** (2012) 30 [arXiv:1207.7235] [INSPIRE].

[3] CMS collaboration, *Combined results of searches for the standard model Higgs boson in pp collisions at $\sqrt{s} = 7$ TeV*, *Phys. Lett.* **B 710** (2012) 26 [arXiv:1202.1488] [INSPIRE].

[4] C. Boehm, A. Djouadi and M. Drees, *Light scalar top quarks and supersymmetric dark matter*, *Phys. Rev.* **D 62** (2000) 035012 [hep-ph/9911496] [INSPIRE].

[5] C. Balázs, M. Carena and C.E.M. Wagner, *Dark matter, light stops and electroweak baryogenesis*, *Phys. Rev.* **D 70** (2004) 015007 [hep-ph/0403224] [INSPIRE].

[6] D0 collaboration, V.M. Abazov et al., *Search for 3- and 4-body decays of the scalar top quark in $p\bar{p}$ collisions at $\sqrt{s} = 1.8$ TeV*, *Phys. Lett.* **B 581** (2004) 147 [INSPIRE].

– 27 –

[7] D0 collaboration, V.M. Abazov et al., *Search for pair production of the scalar top quark in muon+tau final states*, *Phys. Lett.* **B 710** (2012) 578 [arXiv:1202.1978] [INSPIRE].

[8] D0 collaboration, V.M. Abazov et al., *Search for the lightest scalar top quark in events with two leptons in pp̄ collisions at $\sqrt{s} = 1.96$ TeV*, *Phys. Lett.* **B 659** (2008) 500 [arXiv:0707.2864] [INSPIRE].

[9] CDF collaboration, T. Aaltonen et al., *Search for the supersymmetric partner of the top quark in pp̄ collisions at $\sqrt{s} = 1.96$ TeV*, *Phys. Rev.* **D 82** (2010) 092001 [arXiv:1009.0266] [INSPIRE].

[10] CDF collaboration, D. Acosta et al., *Search for the supersymmetric partner of the top quark in dilepton events from pp̄ collisions at $\sqrt{s} = 1.8$ TeV*, *Phys. Rev. Lett.* **90** (2003) 251801 [hep-ex/0302009] [INSPIRE].

[11] ATLAS collaboration, *ATLAS Run 1 searches for direct pair production of third-generation squarks at the Large Hadron Collider*, *Eur. Phys. J.* **C 75** (2015) 510 [arXiv:1506.08616] [INSPIRE].

[12] CMS collaboration, *Search for top-squark pair production in the single-lepton final state in pp collisions at $\sqrt{s} = 8$ TeV*, *Eur. Phys. J.* **C 73** (2013) 2677 [arXiv:1308.1586] [INSPIRE].

[13] M. Burns, K. Kong, K.T. Matchev and M. Park, *Using Subsystem MT2 for Complete Mass Determinations in Decay Chains with Missing Energy at Hadron Colliders*, *JHEP* **03** (2009) 143 [arXiv:0810.5576] [INSPIRE].

[14] CMS collaboration *CMS TriDAS project: Technical Design Report, Volume 1: The Trigger Systems*, CERN-LHCC-2000-038 (2000).

[15] CMS collaboration, *The CMS experiment at the CERN LHC*, 2008 *JINST* **3** S08004 [INSPIRE].

[16] CMS collaboration, *CMS Luminosity Based on Pixel Cluster Counting — Summer 2013 Update*, CMS-PAS-LUM-13-001 (2013).

[17] J. Alwall, M. Herquet, F. Maltoni, O. Mattelaer and T. Stelzer, *MadGraph 5: Going Beyond*, *JHEP* **06** (2011) 128 [arXiv:1106.0522] [INSPIRE].

[18] S. Frixione, P. Nason and G. Ridolfi, *A Positive-weight next-to-leading-order Monte Carlo for heavy flavour hadroproduction*, *JHEP* **09** (2007) 126 [arXiv:0707.3088] [INSPIRE].

[19] J. Pumplin, D.R. Stump, J. Huston, H.L. Lai, P.M. Nadolsky and W.K. Tung, *New generation of parton distributions with uncertainties from global QCD analysis*, *JHEP* **07** (2002) 012 [hep-ph/0201195] [INSPIRE].

[20] H.-L. Lai et al., *New parton distributions for collider physics*, *Phys. Rev.* **D 82** (2010) 074024 [arXiv:1007.2241] [INSPIRE].

[21] T. Sjöstrand, S. Mrenna and P.Z. Skands, *PYTHIA 6.4 Physics and Manual*, *JHEP* **05** (2006) 026 [hep-ph/0603175] [INSPIRE].

[22] CMS collaboration, *Study of the underlying event at forward rapidity in pp collisions at $\sqrt{s} = 0.9$, 2.76 and 7 TeV*, *JHEP* **04** (2013) 072 [arXiv:1302.2394] [INSPIRE].

[23] GEANT4 collaboration, S. Agostinelli et al., *GEANT4: A Simulation toolkit*, *Nucl. Instrum. Meth.* **A 506** (2003) 250 [INSPIRE].

[24] S. Abdullin et al., *The fast simulation of the CMS detector at LHC*, *J. Phys. Conf. Ser.* **331** (2012) 032049.

[25] W. Beenakker, R. Hopker and M. Spira, *PROSPINO: A Program for the production of supersymmetric particles in next-to-leading order QCD*, hep-ph/9611232 [ɪɴSPIRE].

[26] W. Beenakker, R. Höpker, M. Spira and P.M. Zerwas, *Squark and gluino production at hadron colliders*, *Nucl. Phys.* **B 492** (1997) 51 [hep-ph/9610490] [ɪɴSPIRE].

[27] A. Kulesza and L. Motyka, *Threshold resummation for squark-antisquark and gluino-pair production at the LHC*, *Phys. Rev. Lett.* **102** (2009) 111802 [arXiv:0807.2405] [ɪɴSPIRE].

[28] A. Kulesza and L. Motyka, *Soft gluon resummation for the production of gluino-gluino and squark-antisquark pairs at the LHC*, *Phys. Rev.* **D 80** (2009) 095004 [arXiv:0905.4749] [ɪɴSPIRE].

[29] W. Beenakker, S. Brensing, M. Krämer, A. Kulesza, E. Laenen and I. Niessen, *Soft-gluon resummation for squark and gluino hadroproduction*, *JHEP* **12** (2009) 041 [arXiv:0909.4418] [ɪɴSPIRE].

[30] W. Beenakker et al., *Squark and Gluino Hadroproduction*, *Int. J. Mod. Phys.* **A 26** (2011) 2637 [arXiv:1105.1110] [ɪɴSPIRE].

[31] CMS collaboration, *Particle-Flow Event Reconstruction in CMS and Performance for Jets, Taus and MET*, CMS-PAS-PFT-09-001 (2009).

[32] CMS collaboration, *Commissioning of the Particle-flow Event Reconstruction with the first LHC collisions recorded in the CMS detector*, CMS-PAS-PFT-10-001 (2010).

[33] CMS collaboration, *Performance of CMS muon reconstruction in pp collision events at $\sqrt{s} = 7\,TeV$*, 2012 *JINST* **7** P10002 [arXiv:1206.4071] [ɪɴSPIRE].

[34] CMS collaboration, *Performance of electron reconstruction and selection with the CMS detector in proton-proton collisions at $\sqrt{s} = 8\,TeV$*, 2015 *JINST* **10** P06005.

[35] M. Cacciari, G.P. Salam and G. Soyez, *The Anti-k_t jet clustering algorithm*, *JHEP* **04** (2008) 063 [arXiv:0802.1189] [ɪɴSPIRE].

[36] M. Cacciari and G.P. Salam, *Pileup subtraction using jet areas*, *Phys. Lett.* **B 659** (2008) 119 [arXiv:0707.1378] [ɪɴSPIRE].

[37] M. Cacciari, G.P. Salam and G. Soyez, *The catchment area of jets*, *JHEP* **04** (2008) 005 [arXiv:0802.1188] [ɪɴSPIRE].

[38] CMS collaboration, *Identification of b-quark jets with the CMS experiment*, 2013 *JINST* **8** P04013 [arXiv:1211.4462] [ɪɴSPIRE].

[39] CMS collaboration, *Performance of the CMS missing transverse momentum reconstruction in pp data at $\sqrt{s} = 8\,TeV$*, 2015 *JINST* **10** P02006.

[40] L. Rokach and O. Maimon, *Data mining with decision trees: theory and applications*, World Scientific Pub Co Inc., NewYork U.S.A. (2008).

[41] CMS collaboration, *Determination of jet energy calibration and transverse momentum resolution in CMS*, 2011 *JINST* **6** P11002 [arXiv:1107.4277] [ɪɴSPIRE].

[42] M. Botje et al., *The PDF4LHC Working Group Interim Recommendations*, arXiv:1101.0538 [ɪɴSPIRE].

[43] S. Alekhin et al., *The PDF4LHC Working Group Interim Report*, arXiv:1101.0536 [ɪɴSPIRE].

Regular Article - Experimental Physics

Measurement of jet multiplicity distributions in tt̄ production in pp collisions at $\sqrt{s} = 7\,\text{TeV}$

The CMS Collaboration[*]

CERN, 1211 Geneva 23, Switzerland

Abstract The normalised differential top quark-antiquark production cross section is measured as a function of the jet multiplicity in proton-proton collisions at a centre-of-mass energy of 7 TeV at the LHC with the CMS detector. The measurement is performed in both the dilepton and lepton+jets decay channels using data corresponding to an integrated luminosity of $5.0\,\text{fb}^{-1}$. Using a procedure to associate jets to decay products of the top quarks, the differential cross section of the tt̄ production is determined as a function of the additional jet multiplicity in the lepton+jets channel. Furthermore, the fraction of events with no additional jets is measured in the dilepton channel, as a function of the threshold on the jet transverse momentum. The measurements are compared with predictions from perturbative quantum chromodynamics and no significant deviations are observed.

1 Introduction

Precise measurements of the top quark-antiquark (tt̄) production cross section and top-quark properties performed at the CERN Large Hadron Collider (LHC) provide crucial information for testing the predictions of perturbative quantum chromodynamics (QCD) at large energy scales and in processes with multiparticle final states.

About half of the tt̄ events are expected to be accompanied by additional hard jets that do not originate from the decay of the tt̄ pair (tt̄ +jets). In this paper, these jets will be referred to as *additional jets*. These processes typically arise from either initial- or final-state QCD radiation, providing an essential handle to test the validity and completeness of higher-order QCD calculations of processes leading to multijet events. Calculations at next-to-leading order (NLO) are available for tt̄ production in association with one [1] or two [2] additional jets. The correct description of tt̄ +jets production is important to the overall LHC physics program since it constitutes an important background to processes with multijet final

states, such as associated Higgs-boson production with a tt̄ pair, with the Higgs boson decaying into a bb̄ pair, or final states predicted in supersymmetric theories. Anomalous production of additional jets accompanying a tt̄ pair could be a sign of new physics beyond the standard model [3].

This paper presents studies of the tt̄ production with additional jets in the final state using data collected in proton-proton (pp) collisions with centre-of-mass energy $\sqrt{s} = 7\,\text{TeV}$ with the Compact Muon Solenoid (CMS) detector [4]. The analysis uses data recorded in 2011, corresponding to a total integrated luminosity of $5.0 \pm 0.1\ \text{fb}^{-1}$. For the first time, the tt̄ cross section is measured differentially as a function of jet multiplicity and characterised both in terms of the total number of jets in the event, as well as the number of additional jets with respect to the leading-order hard-interaction final state. Kinematic properties of the additional jets are also investigated. The results are corrected for detector effects and compared at particle level with theoretical predictions obtained using different Monte Carlo (MC) event generators.

The differential cross sections as a function of jet multiplicity are measured in both the dilepton (ee, μμ, and eμ) and ℓ+jets (ℓ = e or μ) channels. For the dilepton channel, data containing two oppositely charged leptons and at least two jets in the final state are used, while for the ℓ+jets channel, data containing a single isolated lepton and at least three jets are used. Following the analysis strategy applied to the measurement of other tt̄ differential cross sections [5], the results are normalised to the inclusive cross section measured in situ, eliminating systematic uncertainties related to the normalisation. Lastly, the fraction of events that do not contain additional jets (*gap fraction*), first measured by ATLAS [6], is determined in the dilepton channel as a function of the threshold on the transverse momentum (p_T) of the leading additional jet and of the scalar sum of the p_T of all additional jets.

The measurements are performed in the visible phase space, defined as the kinematic region in which all selected final-state objects are produced within the detector accep-

* e-mail: cms-publication-committee-chair@cern.ch

tance. This avoids additional model uncertainties due to the extrapolation of the measurements into experimentally inaccessible regions of phase space.

The paper is structured as follows. A brief description of the CMS detector is provided in Sect. 2. Section 3 gives a description of the event simulation, followed by details of the object reconstruction and event selection in Sect. 4. A discussion of the sources of systematic uncertainties is given in Sect. 5. The measurement of the differential cross section is presented as a function of the jet multiplicity in Sect. 6 and as a function of the additional jet multiplicity in Sect. 7. The study of the additional jet gap fraction is described in Sect. 8. Finally, a summary is given in Sect. 9.

2 The CMS detector

The central feature of the CMS apparatus is a superconducting solenoid, 13 m in length and 6 m in diameter, which provides an axial magnetic field of 3.8 T. The bore of the solenoid is outfitted with various particle detection systems. Charged-particle trajectories are measured with silicon pixel and strip trackers, covering $0 \leq \phi < 2\pi$ in azimuth and $|\eta| < 2.5$ in pseudorapidity, where η is defined as $\eta = -\ln[\tan(\theta/2)]$, with θ being the polar angle of the trajectory of the particle with respect to the anticlockwise-beam direction. A lead tungstate crystal electromagnetic calorimeter (ECAL) and a brass/scintillator hadron calorimeter (HCAL) surround the tracking volume. The calorimetry provides excellent resolution in energy for electrons and hadrons within $|\eta| < 3.0$. Muons are measured up to $|\eta| < 2.4$ using gas-ionisation detectors embedded in the steel flux return yoke outside the solenoid. The detector is nearly hermetic, providing accurate measurements of any imbalance in momentum in the plane transverse to the beam direction. The two-level trigger system selects most interesting final states for further analysis. A detailed description of the CMS detector can be found in Ref. [4].

3 Event simulation

The reference simulated $t\bar{t}$ sample used in the analysis is generated with the MADGRAPH (v. 5.1.1.0) matrix element generator [7], with up to three additional partons. The generated events are subsequently processed using PYTHIA (v. 6.424) [8] to add parton showering using the MLM prescription [9] for removing the overlap in phase space between the matrix element and the parton shower approaches. The PYTHIA Z2 tune is used to describe the underlying event [10]. The top-quark mass is assumed to be $m_t = 172.5$ GeV. The proton structure is described by the CTEQ6L1 [11] parton distribution functions (PDFs).

The MADGRAPH generator is used to simulate W+jets and Z/γ^*+jets production. Single-top-quark events (s-, t-, and tW-channels) are simulated using POWHEG (r1380) [12–15]. Diboson (WW, WZ, and ZZ) and QCD multijet events are simulated using PYTHIA.

Additional $t\bar{t}$ and W+jets MADGRAPH samples are generated using different choices for the common factorisation and renormalisation scale ($\mu_F^2 = \mu_R^2 = Q^2$) and for the jet-parton matching threshold. These are used to determine the systematic uncertainties due to model uncertainties and for comparisons with the measured distributions. The nominal Q^2 scale is defined as $m_t^2 + \sum p_T^2(\text{jet})$. This is varied between $4Q^2$ and $Q^2/4$. For the reference MADGRAPH sample, a jet-parton matching threshold of 20 GeV is chosen, while for the up and down variations, thresholds of 40 and 10 GeV are used, respectively.

In addition to MADGRAPH, samples of $t\bar{t}$ events are generated with POWHEG and MC@NLO (v. 3.41) [16]. The CTEQ6M [11] PDF set is used in both cases. Both POWHEG and MC@NLO match calculations to full NLO accuracy with parton shower MC generators. For POWHEG, PYTHIA is chosen for hadronisation and parton shower simulation, with the same Z2 tune utilised for other samples. For MC@NLO, HERWIG (v. 6.520) [17] with the default tune is used.

For comparison with the measured distributions, the event yields in the simulated samples are normalised to an integrated luminosity of $5.0\,\text{fb}^{-1}$ according to their theoretical cross sections. These are taken from next-to-next-to-leading-order (NNLO) (W+jets and Z/γ^*+jets), NLO plus next-to-next-to-leading-log (NNLL) (single-top-quark s- [18], t- [19] and tW-channels [20]), NLO (diboson [21]), and leading-order (LO) (QCD multijet [8]) calculations. For the simulated $t\bar{t}$ sample, the full NNLO+NNLL calculation, performed with the TOP++ 2.0 program [22], is used. The PDF and α_S uncertainties are estimated using the PDF4LHC prescription [23,24] with the MSTW2008nnlo68cl [25], CT10 NNLO [26,27], and NNPDF2.3 5f FFN [28] PDF sets, and added in quadrature to the scale uncertainty to obtain a $t\bar{t}$ production cross section of $177.3^{+10.1}_{-10.8}$ pb (for a top-quark mass value of 172.5 GeV).

All generated samples are passed through a full detector simulation using GEANT4 [29], and the number of additional pp collisions (pileup) is matched to the real distribution as inferred from data.

4 Event reconstruction and selection

The event selection is based on the reconstruction of the $t\bar{t}$ decay products. The top quark decays almost exclusively into a W boson and a b quark. Only the subsequent decays of one or both W bosons to a charged lepton and a neutrino are considered here. Candidate events are required to contain

the corresponding reconstructed objects: isolated leptons and jets. The requirement of the presence of jets associated with b quarks or antiquarks (b jets) is used to increase the purity of the selected sample. The selection has been optimised independently in each channel to maximise the signal content and background rejection.

4.1 Lepton, jet, and missing transverse energy reconstruction

Events are reconstructed using a particle-flow (PF) technique [30,31], in which signals from all CMS sub-detectors are combined to identify and reconstruct the individual particle candidates produced in the pp collision. The reconstructed particles include muons, electrons, photons, charged hadrons, and neutral hadrons. Charged particles are required to originate from the primary collision vertex, defined as the vertex with the highest sum of transverse momenta of all reconstructed tracks associated to it. Therefore, charged hadron candidates from pileup events, i.e. originating from a vertex other than the one of the hard interaction, are removed before jet clustering on an event-by-event basis. Subsequently, the remaining neutral-hadron pileup component is subtracted at the level of jet energy correction [32].

Electron candidates are reconstructed from a combination of their track and energy deposition in the ECAL [33]. In the dilepton channel, they are required to have a transverse momentum $p_T > 20$ GeV, while in the ℓ+jets channel they are required to have $p_T > 30$ GeV. In both cases they are required to be reconstructed within $|\eta| < 2.4$, and electrons from identified photon conversions are rejected. As an additional quality criterion, a relative isolation variable I_{rel} is computed. This is defined as the sum of the p_T of all neutral and charged reconstructed PF candidates inside a cone around the lepton (excluding the lepton itself) in the η-ϕ plane with radius $\Delta R \equiv \sqrt{(\Delta \eta)^2 + (\Delta \phi)^2} < 0.3$, divided by the p_T of the lepton. In the dilepton (e+jets) channel, electrons are selected as isolated if $I_{rel} < 0.12$ (0.10).

Muon candidates are reconstructed from tracks that can be matched between the silicon tracker and the muon system [34]. They are required to have a transverse momentum $p_T > 20$ GeV within the pseudorapidity interval $|\eta| < 2.4$ in the dilepton channel, and to have $p_T > 30$ GeV and $|\eta| < 2.1$ in the ℓ+jets channel. Isolated muon candidates are selected by demanding a relative isolation of $I_{rel} < 0.20$ (0.125) in the dilepton (μ+jets) channel.

Jets are reconstructed by clustering the particle-flow candidates [35] using the anti-k_T algorithm with a distance parameter of 0.5 [36,37]. An offset correction is applied to take into account the extra energy clustered in jets due to pileup, using the FastJet algorithm [38] based on average pileup energy density in the event. The raw jet energies

are corrected to establish a relative uniform response of the calorimeter in η and a calibrated absolute response in p_T. Jet energy corrections are derived from the simulation, and are confirmed with in situ measurements with the energy balance of dijet and photon+jet events [35]. Jets are selected within $|\eta| < 2.4$ and with $p_T > 30$ (35) GeV in the dilepton (ℓ+jets) channel.

Jets originating from b quarks or antiquarks are identified with the Combined Secondary Vertex algorithm [39], which provides a b-tagging discriminant by combining secondary vertices and track-based lifetime information. The chosen working point used in the dilepton channel corresponds to an efficiency for tagging a b jet of about 80–85 %, while the probability to misidentify light-flavour or gluon jets as b jets (mistag rate) is around 10 %. In the ℓ+jets channel, a tighter requirement is applied, corresponding to a b-tagging efficiency of about 65–70 % with a mistag rate of 1 %. The probability to misidentify a c jet as b jet is about 40 % and 20 % for the working points used in the dilepton and ℓ+jets channels respectively [39].

The missing transverse energy (E_T^{miss}) is defined as the magnitude of the sum of the momenta of all reconstructed PF candidates in the plane transverse to the beams.

4.2 Event selection

Dilepton events are collected using combinations of triggers which require two leptons fulfilling p_T and isolation criteria. During reconstruction, events are selected if they contain at least two isolated leptons (electrons or muons) of opposite charge and at least two jets, of which at least one is identified as a b jet. Events with a lepton pair invariant mass smaller than 12 GeV are removed in order to suppress events from heavy-flavour resonance decays. In the ee and $\mu\mu$ channels, the dilepton invariant mass is required to be outside a Z-boson mass window of 91 ± 15 GeV (*Z-boson veto*), and E_T^{miss} is required to be larger than 30 GeV.

A kinematic reconstruction method [5] is used to determine the kinematic properties of the $t\bar{t}$ pair and to identify the two b jets originating from the decay of the top quark and antiquark. In the kinematic reconstruction the following constraints are imposed: the E_T^{miss} originated entirely from the two neutrinos; the reconstructed W-boson invariant mass of 80.4 GeV [40] and the equality of the reconstructed top quark and antiquark masses. The remaining ambiguities are resolved by prioritising those event solutions with two or one b-tagged jets over solutions using untagged jets. Finally, among the physical solutions, the solutions are ranked according to how the neutrino energies match with a simulated neutrino energy spectrum and the highest ranked one is chosen. The kinematic reconstruction yields no valid solution for about 11 % of the events. These are excluded

from further analysis. A possible bias due to rejected solutions has been studied and found to be negligible.

In the e+jets channel, events are triggered by an isolated electron with $p_T > 25$ GeV and at least three jets with $p_T > 30$ GeV. Events in the μ+jets channel are triggered by the presence of an isolated muon with $p_T > 24$ GeV fulfilling η requirements. Only triggered events that have exactly one high-p_T isolated lepton are retained in the analysis. In the e+jets channel, events are rejected if any additional electron is found with $p_T > 20$ GeV, $|\eta| < 2.5$, and relative isolation $I_{rel} < 0.20$. In the μ+jets channel, events are rejected if any electron candidate with $p_T > 15$ GeV, $|\eta| < 2.5$ and $I_{rel} < 0.20$ is reconstructed. In both ℓ+jets channels events with additional muons with $p_T > 10$ GeV, $|\eta| < 2.5$, and relative isolation $I_{rel} < 0.20$ are rejected. The presence of at least three reconstructed jets is required. At least two of them are required to be b-tagged.

Only $t\bar{t}$ events from the decay channel under study are considered as signal. All other $t\bar{t}$ events are considered as background, including those containing leptons from τ decays, which are the dominant contribution to this background.

4.3 Background estimation

After the full event selection is applied, the dominant background in the eμ channel comes from other $t\bar{t}$ decay modes, estimated using simulation. In the ee and $\mu\mu$ channels, it arises from Z/γ^*+jets production. The normalisation of this background contribution is derived from data using the events rejected by the Z-boson veto, scaled by the ratio of events failing and passing this selection estimated in simulation ($R_{out/in}$) [41]. The number of Z/γ^*+jets $\rightarrow$ ee/$\mu\mu$ events near the Z-boson peak, N_{Z/γ^*}^{in}, is given by the number of all events failing the Z-boson veto, N^{in}, after subtracting the contamination from non-Z/γ^*+jets processes. This contribution is extracted from eμ events passing the same selection, $N_{e\mu}^{in}$, and corrected for the differences between the electron and muon identification efficiencies using a correction factor k. The Z/γ^*+jets contribution is thus given by

$$N^{out} = R_{out/in} N_{Z/\gamma^*}^{in} = R_{out/in}(N^{in} - 0.5k N_{e\mu}^{in}) \qquad (1)$$

The factor k is estimated from $k^2 = N_{e\mu}/N_{ee}$ ($N_{e\mu}/N_{\mu\mu}$) for the $Z/\gamma^* \rightarrow e^+e^-$ ($\mu^+\mu^-$)+jets contribution, respectively. Here N_{ee} ($N_{\mu\mu}$) is the number of ee ($\mu\mu$) events in the Z-boson region, without the requirement on E_T^{miss}. The remaining backgrounds, including single-top-quark, W+jets, diboson, and QCD multijet events are estimated from simulation.

In the ℓ+jets channel, the main background contributions arise from W+jets and QCD multijet events, which are greatly suppressed by the b-tagging requirement. A procedure based on control samples in data is used to extract the QCD multijet background. The leptons in QCD multijet events are expected to be less isolated than leptons from other processes. Thus, inverting the selection on the lepton relative isolation provides a relatively pure sample of QCD multijet events in data. Events passing the standard event selection but with an I_{rel} between 0.3 and 1.0, and with at least one b-tagged jet are selected. The sample is divided in two: the sideband region (one b jet) and the signal region (≥ 2 b jets). The shape of the QCD multijet background is taken from the signal region, and the normalisation is determined from the sideband region. In the sideband region, the E_T^{miss} distribution of the QCD multijet model, other sources of background (determined from simulation), and the $t\bar{t}$ signal are fitted to data. The resulting scaling of QCD multijet background is applied to the QCD multijet shape from the signal region.

Since the initial state of LHC collision is enriched in up quarks with respect to down quarks, more W bosons are produced with positive charge than negative charge. In leptonic W-boson decays, this translates into a lepton charge asymmetry $\mathcal{A}$. Therefore, a difference between the number of events with a positively charged lepton and those with a negatively charged lepton ($\Delta\pm$) is observed. In data, this quantity ($\Delta\pm^{data}$) is proportional to the number of W+jets events when assuming that only the charge asymmetry from W-boson production is significant. The charge asymmetry has been measured by CMS [42] and found to be well described by the simulation, thus the simulated value can be used to extract the number of W+jets events from data: $N_{W+jets}^{data} = \Delta\pm^{data}/\mathcal{A}$. The correction factor on the W+jets normalisation, calculated before any b-tagging requirement, is between 0.81 and 0.92 depending on the W decay channel and the jet selection. Subsequently, b-tagging is applied to obtain the number of W+jets events in the signal region.

In addition, a heavy-flavour correction must be applied on the W+jets sample to account for the differences observed between data and simulation [43]. Using the matching between selected jets and generated partons, simulated events are classified as containing at least one b jet (W+bX), at least one c jet and no b jets (W+cX), or containing neither b jets nor c jets (W+light quarks). The rate of W+bX events is multiplied by 2 ± 1 and the rate of W+cX events is multiplied by $1^{+1.0}_{-0.5}$. No correction is applied to W+light-jets events. These correction factors are calculated in [43] in a phase space which is close to the one used in the analysis. The uncertainties in the correction factors are taken into account as systematic uncertainties. The total number of W+jets events is modified to conserve this number when applying the heavy-flavour corrections. The remaining backgrounds, originating from single-top-quark, diboson, and Z/γ^*+jets processes, are small and their contributions are estimated using simulation.
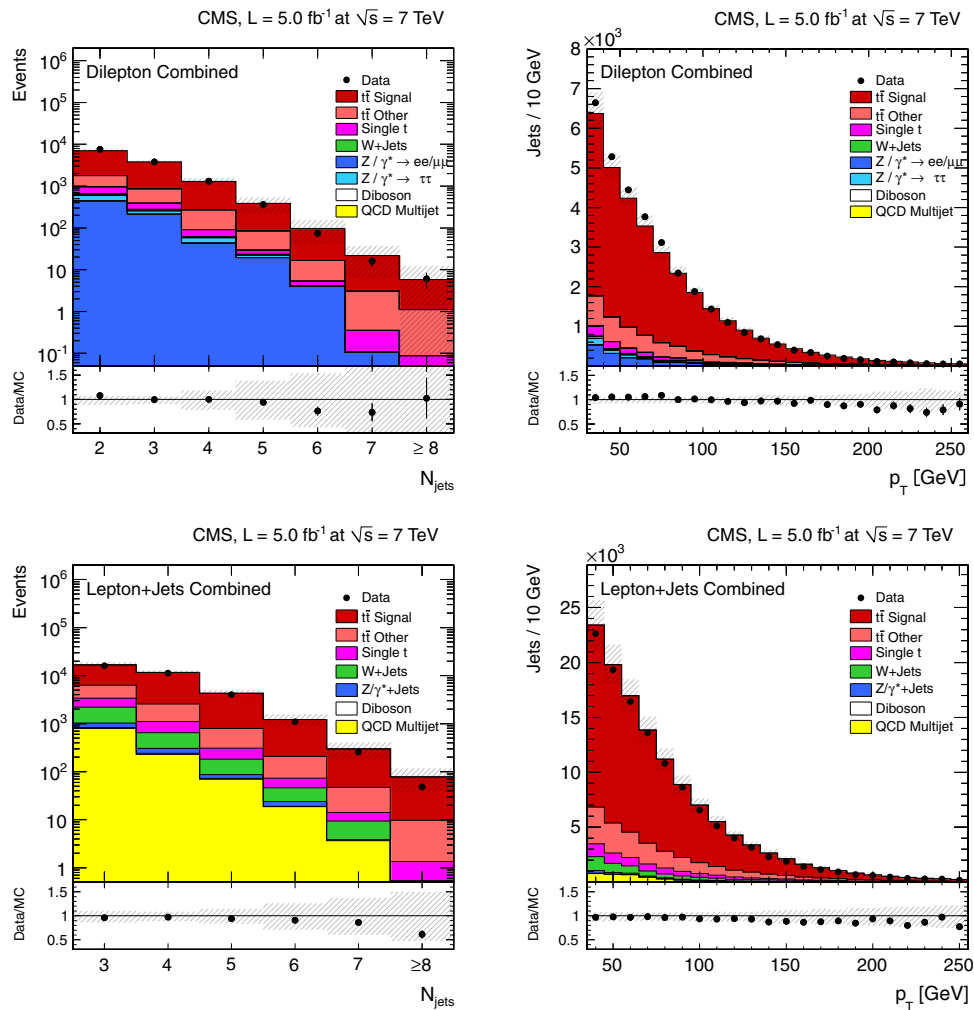
Fig. 1 Number of reconstructed jets (*left*) and jet p_T spectrum (*right*) after event selection in the dilepton channel for jets with $p_T > 30$ GeV (*top*), and in the ℓ+jets channel for jets with $p_T > 35$ GeV (*bottom*). The *hatched band* represents the combined effect of all sources of systematic uncertainty

The multiplicity and the p_T distributions of the selected reconstructed jets are shown for the dilepton and ℓ+jets channels in Fig. 1. Good agreement for the jet multiplicity is observed between data and simulation for up to 5 (6) jets in the dilepton (ℓ+jets) channels. For higher jet multiplicities, the simulation predicts slightly more events than observed in data. The modelling of the jet p_T spectrum in data is shifted towards smaller values, covered by the systematic uncertainties. The uncertainty from all systematic sources, which are described in Sect. 5, is determined by estimating their effect on both the normalisation and the shape. The size of these global uncertainties does not reflect those in the final mea-

surements, since they are normalised and, therefore, only affected by shape uncertainties.

5 Systematic uncertainties

Systematic uncertainties in the measurement arise from detector effects, background modelling, and theoretical assumptions. Each systematic uncertainty is investigated separately and estimated for each bin of the measurement by varying the corresponding efficiency, resolution, or scale within its uncertainty. For each variation, the measured nor-

malised differential cross section is recalculated, and the difference between the varied result and the nominal result in each bin is taken as systematic uncertainty. The overall uncertainty in the measurement is obtained by adding all contributions in quadrature. The sources of systematic uncertainty, described below, are assumed to be uncorrelated.

– **Jet energy** The impact of the jet energy scale (JES) [35] is determined by varying the p_T of all jets by the JES uncertainty, which is typically below 3 %. The uncertainty due to the jet energy resolution (JER) [44] is estimated by varying the nominal value by $\pm 1\sigma$.

– t$\bar{\text{t}}$ **model uncertainties** Uncertainties originating from theoretical assumptions on the renormalisation and factorisation scales, the jet-parton matching threshold, the hadronisation model, and the colour reconnection modelling [45], are determined by repeating the analysis, replacing the reference MADGRAPH signal simulation by other simulation samples. In particular, the impact of the former sources is assessed with MADGRAPH samples with the renormalisation and factorisation scales simultaneously varied from the nominal Q^2 values to $4Q^2$ and $Q^2/4$ and with jet-parton matching threshold varied to 40 and 10 GeV. The uncertainties from ambiguities in modeling colour reconnection effects are estimated by comparing simulations of an underlying event tune including colour reconnection to a tune without it (the Perugia 2011 and Perugia 2011 noCR tunes described in [46]). The hadronisation model uncertainty is estimated by comparing samples simulated with POWHEG and MC@NLO, using PYTHIA and HERWIG, respectively, for hadronisation. The uncertainty arising from the PDFs is assessed by reweighting the t$\bar{\text{t}}$ signal sample according to the 44 CTEQ66 error PDF sets, at 90 % confidence level. The effects of these variations are added in quadrature.

– **Background** The uncertainty due to the normalisation of the backgrounds that are taken from simulation is determined by varying the cross section by ± 30 % [47,48]. This takes into account the uncertainty in the predicted cross section and all other sources of systematic uncertainty.

In the dilepton channels, the contribution from Z/γ^*+jets processes as determined from data is varied in normalisation by ± 30 % [41].

In the ℓ+jets channels, the uncertainty in the W+jets background arises from the contamination of other processes with a lepton charge asymmetry when extracting the rate from data, and from the uncertainty in the heavy-flavour correction factors. The rate uncertainty is estimated to range from 10 to 20 %, depending on the channel. The model uncertainty is estimated using samples with varied renormalisation and factorisation scales and jet-parton

matching threshold.

The QCD multijet background modelling uncertainty arises from the choice of the relative isolation requirement on the anti-isolated lepton used for the extraction of the background from data, the influence of the contamination from other processes on the shape, and the extrapolation from the sideband to the signal region. The total uncertainty is about 15 % to more than 100 %, depending on the channel.

– **Other systematic uncertainties** The uncertainty associated with the pileup model is determined by varying the minimum bias cross section within its uncertainty of ± 8 %. Other uncertainties taken into account originate from lepton trigger, isolation, and identification efficiencies; b-jet tagging efficiency and misidentification probability; integrated luminosity [49]; and the kinematic reconstruction algorithm used in the dilepton channels.

In the dilepton channels, the total systematic uncertainty is about 3 % at low jet multiplicities, and increases to about 20 % in the bins with at least five jets. In the ℓ+jets channels, the total systematic uncertainty is about 6 % at the lowest jet multiplicity, and increases to 34 % for events with at least 8 jets.

The dominant systematic uncertainties for both dilepton and ℓ+jets channels arise from the JES (with typical values from 2 to 20 %, depending on the jet multiplicity bin and cross section measurement) and the signal model including hadronisation, renormalisation and factorisation scales and jet-parton matching threshold (from 3 to 30 %). The typical systematic uncertainty due to JER ranges from 0.2 to 3 %, b-tagging from 0.3 to 2 %, pileup from 0.1 to 1.4 %, and background normalisation from 1.6 to 3.8 %. The uncertainty from other sources is below 0.5 %. The remaining uncertainties on the model arise from PDF and colour reconnection, varying from 0.1 to 1.5 % and from 1 to 5.8 %, respectively. In all channels, the systematic uncertainty for larger jet multiplicities is dominated by the statistical uncertainty of the simulated samples that are used for the evaluation of modelling uncertainties.

6 Normalised differential cross section as a function of jet multiplicity

The differential t$\bar{\text{t}}$ production cross section as a function of the jet multiplicity is measured from the number of signal events after background subtraction and correction for the detector efficiencies and acceptances. The estimated number of background events arising from processes other that t$\bar{\text{t}}$ production ($N_{\text{non t}\bar{\text{t}} \text{BG}}$) is directly subtracted from the number of events in data (N). The contribution from other t$\bar{\text{t}}$ decay modes is

Table 1 Normalised differential $t\bar{t}$ production cross section as a function of the jet multiplicity for jets with $p_T > 30$ GeV in the dilepton channel. The statistical, systematic, and total uncertainties are also shown. The main experimental and model systematic uncertainties are displayed: JES and the combination of renormalisation and factorisation scales, jet-parton matching threshold, and hadronisation (in the table "Q^2/Match./Had.")

N_{jets}	$1/\sigma \, d\sigma/dN_{\text{jets}}$	Stat. (%)	Exp. Syst. (%)		Model Syst. (%)		Total (%)
			JES	Other	Q^2/Match./Had.	Other	
2	0.600	1.2	1.4	0.6	0.5	1.6	2.5
3	0.273	3.3	2.3	2.8	5.4	1.6	7.2
4	0.096	5.1	6.3	3.4	2.8	1.6	9.3
5	0.025	10.1	7.9	3.0	17.4	1.9	24.0
≥ 6	0.0013	23.8	14.2	2.8	24.3	2.1	37.1

Table 2 Normalised differential $t\bar{t}$ production cross section as a function of the jet multiplicity for jets with $p_T > 60$ GeV in the dilepton channel. The statistical, systematic, and total uncertainties are also shown. The main experimental and model systematic uncertainties are displayed: JES and the combination of renormalisation and factorisation scales, jet-parton matching threshold, and hadronisation (in the table "Q^2/Match./Had.")

N_{jets}	$1/\sigma \, d\sigma/dN_{\text{jets}}$	Stat. (%)	Exp. Syst. (%)		Model Syst. (%)		Total (%)
			JES	Other	Q^2/Match./Had.	Other	
0	0.158	3.4	7.0	5.7	2.7	1.6	10.1
1	0.397	4.0	4.9	2.0	3.3	1.9	7.6
2	0.350	2.6	3.2	3.3	3.5	1.7	6.6
3	0.079	5.2	3.4	3.0	5.8	1.6	9.2
4	0.0127	13.9	5.4	3.5	15.8	1.7	22.1
5	0.0020	30.9	4.8	3.6	15.5	1.6	35.1
≥ 6	0.00012	57.1	4.7	16.7	38.7	2.9	69.4

taken into account by correcting $N - N_{\text{non } t\bar{t} \text{ BG}}$ with the signal fraction, defined as the ratio of the number of selected $t\bar{t}$ signal events to the total number of selected $t\bar{t}$ events. This avoids the dependence on the inclusive $t\bar{t}$ cross section used for normalisation. The normalised differential cross section is derived by scaling to the total integrated luminosity and by dividing the corrected number of events by the cross section measured in situ for the same phase space. Because of the normalisation, those systematic uncertainties that are correlated across all bins of the measurement, and therefore only affect the normalisation, cancel out. In order to avoid additional uncertainties due to the extrapolation of the measurement outside of the phase space region probed experimentally, the differential cross section is determined in a visible phase space defined at the particle level by the kinematic and geometrical acceptance of the final-state leptons and jets.

The visible phase space at particle level is defined as follows. The charged leptons from the $t\bar{t}$ decays are selected with $|\eta| < 2.4$ in dilepton events and $|\eta| < 2.5\,(2.1)$ in e+jets (μ+jets) final states, $p_T > 20\,(30)$ GeV in the dilepton (ℓ+jets) channels. A jet is defined at the particle level in a similar way as described in Sect. 4 for the reconstructed jets, by applying the anti-k_T clustering algorithm to all stable particles (including neutrinos not coming from the hard interaction). Particle-level jets are rejected if the selected leptons are within a cone of $\Delta R = 0.4$ with respect to the jet, to avoid counting leptons misidentified as jets. A jet is defined as a b jet if it contains the decay products of a b hadron. The two b jets from the $t\bar{t}$ decay have to fulfill the kinematic requirements $|\eta| < 2.4$ and $p_T > 30\,(35)$ GeV in the dilepton (ℓ+jets) events. In the ℓ+jets channels, a third jet with the same properties is also required.

Effects from trigger and detector efficiencies and resolutions, leading to migrations of events across bin boundaries and statistical correlations among neighbouring bins, are corrected by using a regularised unfolding method [5,50,51]. A response matrix that accounts for migrations and efficiencies is calculated from simulated $t\bar{t}$ events using the reference MADGRAPH sample. The event migration in each bin is controlled by the purity (number of events reconstructed and generated in one bin divided by the total number of reconstructed events in that bin) and the stability (number of events reconstructed and generated in one bin divided by the total number of generated events in that bin). In these measurements, the purity and stability in the bins is typically 60 % or higher. The generalised inverse of the response matrix is used to obtain

Fig. 2 Normalised differential tt̄ production cross section as a function of the jet multiplicity for jets with $p_T > 30$ GeV (*top*) and $p_T > 60$ GeV (*bottom*) in the dilepton channel. The measurements are compared to predictions from MADGRAPH+PYTHIA, POWHEG+PYTHIA, and MC@NLO+HERWIG (*left*), as well as from MADGRAPH with varied renormalisation and factorisation scales, and jet-parton matching threshold (*right*). The *inner* (*outer*) *error bars* indicate the statistical (combined statistical and systematic) uncertainty. The *shaded band* corresponds to the combined statistical and systematic uncertainty

the unfolded distribution from the measured distribution by applying a χ^2 technique. To avoid non-physical fluctuations, a smoothing prescription (regularisation) is applied [5,52]. The unfolded data are subsequently corrected to take into account the acceptance in the particle level phase space.

The measured normalised differential cross sections are consistent among the different dilepton and ℓ+jets channels. The final results in the dilepton and ℓ+jets channels are obtained from the weighted average of the individual measurements, using the statistical uncertainty as the weight. The result from the combination of e+jets and μ+jets channels is defined for the pseudorapidity range $|\eta| < 2.1$, i.e. according

to the selection criterion of the μ+jets channel. The difference of this result to that for the pseudorapidity range $|\eta| < 2.5$ has been estimated to be less than 0.4 % in any of the bins of the jet multiplicity distribution. In the combination, the differences in the $|\eta|$-range between μ+jets and e+jets channels are therefore neglected.

The normalised differential tt̄ production cross section, $1/\sigma \, d\sigma/dN_{\text{jets}}$, as a function of the jet multiplicity, N_{jets}, is shown in Tables 1 and 2, and Fig. 2 for the dilepton channel and jets with $p_T > 30$ (60) GeV. For the ℓ+jets channel it is shown in Table 3 and Fig. 3 for jets with $p_T > 35$ GeV. In the tables, the experimental uncertainties are divided between
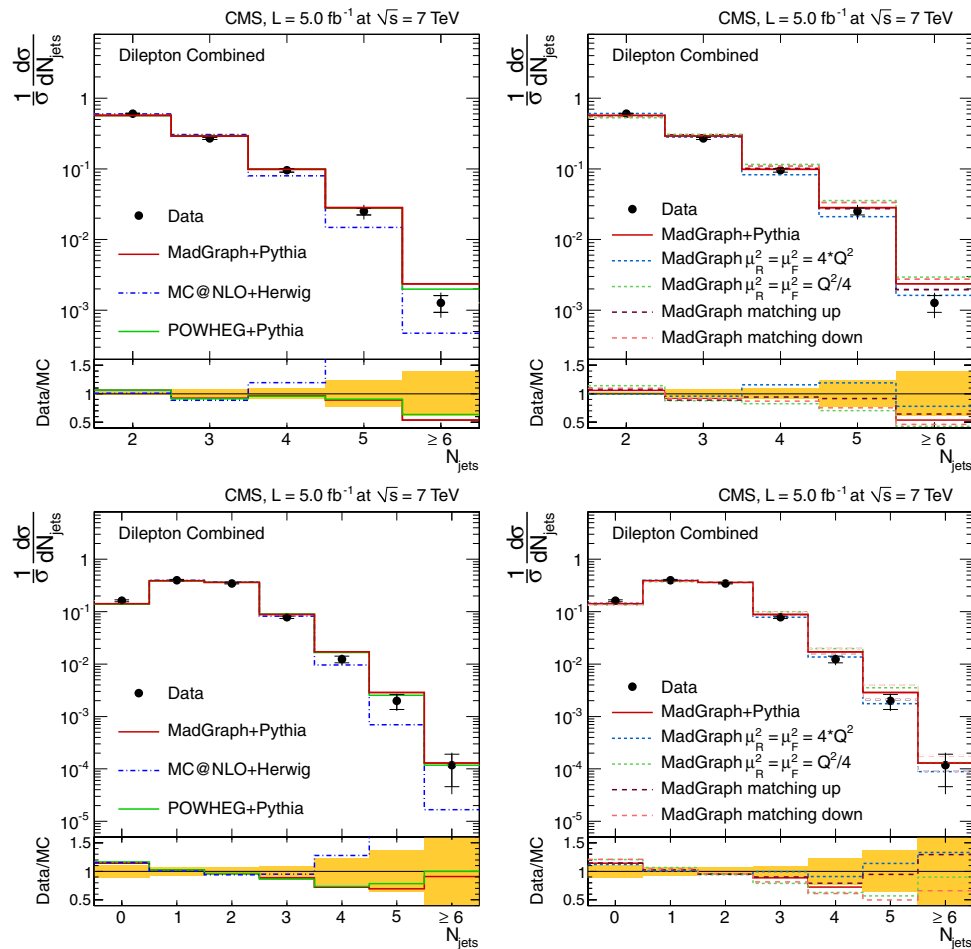
Table 3 Normalised differential $t\bar{t}$ production cross section as a function of the jet multiplicity for jets with $p_T > 35$ GeV in the ℓ+jets channel. The statistical, systematic, and total uncertainties are also shown. The main experimental and model systematic uncertainties are displayed: JES and the combination of renormalisation and factorisation scales, jet-parton matching threshold, and hadronisation (in the table "Q^2/Match./Had.")

N_{jets}	$1/\sigma\ \mathrm{d}\sigma/\mathrm{d}N_{\text{jets}}$	Stat. (%)	Exp. Syst. (%)		Model Syst. (%)		Total (%)
			JES	Other	Q^2/Match./Had.	Other	
3	0.453	0.9	3.8	2.2	3.8	1.3	6.1
4	0.372	1.2	1.8	1.8	3.2	1.4	4.5
5	0.130	2.7	5.6	2.0	7.5	1.8	10.2
6	0.0353	5.3	6.7	2.4	14.2	2.5	17.0
7	0.00841	10.5	10.7	3.3	19.1	4.3	24.9
≥ 8	0.00130	26.4	17.7	5.1	28.6	3.4	43.2

the dominant (JES) and other (JER, b-tagging, pileup, lepton identification, isolation, and trigger efficiencies, background contribution and integrated luminosity) contributions. The model uncertainties are also divided between the dominant (renormalisation and factorisation scales, jet-parton matching threshold, and hadronisation) and other (PDF and colour reconnection) contributions. The measurements are compared to the predictions from MADGRAPH and POWHEG, both interfaced with PYTHIA, and from MC@NLO interfaced with HERWIG.

The predictions from MADGRAPH+PYTHIA and POWHEG +PYTHIA are found to provide a reasonable description of the data. In contrast, MC@NLO+HERWIG generates fewer events in bins with large jet multiplicities. The effect of the variation of the renormalisation and factorisation scales and jet-parton matching threshold in MADGRAPH+PYTHIA is compared with the reference MADGRAPH+PYTHIA simulation. The choice of lower values for both these parameters seems to provide a worse description of the data for higher jet multiplicities.

7 Normalised differential cross section as a function of the additional jet multiplicity

The normalised differential $t\bar{t}$ production cross section is also determined as a function of the number of additional jets accompanying the $t\bar{t}$ decays in the ℓ+jets channel. This measurement provides added value to the one presented in Sect. 6 by distinguishing jets from the $t\bar{t}$ decay products and jets coming from additional QCD radiation. This is particularly interesting in final states with many jets.

For this measurement, the event selection follows the prescription discussed in Sect. 4, and requires at least four jets (in order to perform a full event reconstruction later) with $p_T > 30$ GeV and $|\eta| < 2.4$. The p_T requirement is lowered to gain more data and reduce the statistical uncertainty. The particle-level jets, defined as described in Sect. 6 but with

$p_T > 30$ GeV, are counted as additional jets if their distance to the $t\bar{t}$ decay products is $\Delta R > 0.5$. We consider the following objects as $t\bar{t}$ decay products: two b quarks, two light quarks from the hadronically decaying W boson, and the lepton from the leptonically decaying W boson; the neutrino is not included. The simulated $t\bar{t}$ events are classified into three categories according to the number of additional jets (0, 1, and ≥ 2) selected according to this definition. Figure 4 illustrates the contributions of $t\bar{t}$ events with 0, 1, and ≥ 2 additional jets to the number of reconstructed jets in the simulation.

A full event reconstruction of the $t\bar{t}$ system is performed in order to create a variable sensitive to additional jets, taking into account all possible jet permutations. The most likely permutation is determined using a χ^2 minimisation, where the χ^2 is given by:

$$\chi^2 = \left(\frac{m_{\text{W}^{\text{had}}}^{\text{rec}} - m_{\text{W}^{\text{had}}}^{\text{true}}}{\sigma_{\text{W}^{\text{had}}}} \right)^2$$
$$+ \left(\frac{m_{\text{t}^{\text{had}}}^{\text{rec}} - m_{\text{t}^{\text{had}}}^{\text{true}}}{\sigma_{\text{t}^{\text{had}}}} \right)^2 + \left(\frac{m_{\text{t}^{\text{lep}}}^{\text{rec}} - m_{\text{t}^{\text{lep}}}^{\text{true}}}{\sigma_{\text{t}^{\text{lep}}}} \right)^2,$$

where $m_{\text{t}^{\text{had}}}^{\text{rec}}$ and $m_{\text{t}^{\text{lep}}}^{\text{rec}}$ are the reconstructed invariant masses of the hadronically and the leptonically decaying top quark, respectively, and $m_{\text{W}^{\text{had}}}$ is the reconstructed invariant mass of the W boson from the hadronic top-quark decay. The parameters m^{true} and $\sigma_{\text{t}^{\text{had}}}$, $\sigma_{\text{t}^{\text{lep}}}$, and $\sigma_{\text{W}^{\text{had}}}$ are the mean value and standard deviations of the reconstructed mass distributions in the $t\bar{t}$ simulation. In each event, all jet permutations in which only b-tagged jets are assigned to b quarks are considered. The permutation with the smallest χ^2 value is chosen as the best hypothesis. For events containing the same number of reconstructed jets (N_{jets}) the variable $\sqrt{\chi^2}$ provides good discrimination between events classified as $t\bar{t} + 0$, 1, and ≥ 2 additional jets. The discrimination power is due to the sensitivity of the event reconstruction to the relation between N_{jets}

Fig. 4 Jet multiplicity distribution in simulated $t\bar{t}$ events in the ℓ+jets channel. The splitting into three categories, defined by the compatibility of the selected particle level jets with the $t\bar{t}$ decay partons is also shown (cf. Sect. 7)
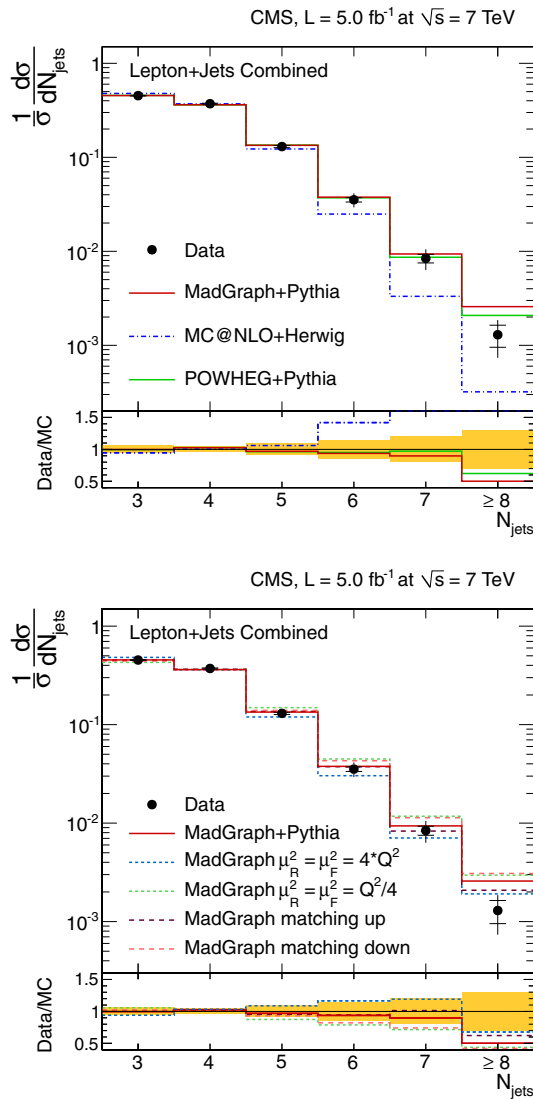
Fig. 3 Normalised differential $t\bar{t}$ production cross section as a function of jet multiplicity for jets with $p_T > 35$ GeV in the ℓ+jets channel. The measurement is compared to predictions from MADGRAPH+PYTHIA, POWHEG+PYTHIA, and MC@NLO+HERWIG (*top*), as well as from MADGRAPH with varied renormalisation and factorisation scales, and jet-parton matching threshold (*bottom*). The *inner* (*outer*) *error bars* indicate the statistical (combined statistical and systematic) uncertainty. The *shaded band* corresponds to the combined statistical and systematic uncertainty

and the number of additional jets $N_{\text{add. jets}}$. The best event reconstruction, thus providing a smaller $\sqrt{\chi^2}$, is achieved if the observation is close to $N_{\text{jets}} = 4 + N_{\text{add. jets}}$, where four is the expected number of jets from the $t\bar{t}$ decay partons. For instance, a $t\bar{t} + 1$ additional jet event with $N_{\text{jets}} = 4$ is likely
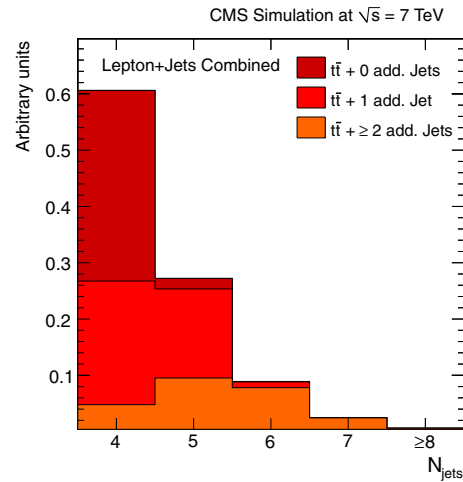
to get a large $\sqrt{\chi^2}$ value because one of the four jets from the $t\bar{t}$ decay partons is missing for a correct event reconstruction.

The measurement of the fractions of $t\bar{t}$ events with 0, 1, and ≥ 2 additional jets is performed using a binned maximum-likelihood fit of the $\sqrt{\chi^2}$ templates to data, simultaneously in both ℓ+jets channels. The normalisations of the signal templates ($t\bar{t} + 0$, 1, and ≥ 2 additional jets) are free parameters in the fit. For the normalisations of the background processes, Gaussian constraints corresponding to the uncertainties of the background predictions are applied. It has been verified that the use of log-normal constraints gives similar results. The result of the fit is shown in Fig. 5. The QCD multijet and W+jets templates are estimated using the data-based methods described in Sect. 4.

The normalisations for the three signal templates are applied to the predicted differential cross section in the visible phase space, calculated using the simulated $t\bar{t}$ sample from MADGRAPH+PYTHIA. This phase space is defined as in Sect. 6 with the requirement of four particle level jets with $p_T > 30$ GeV. This provides the differential cross section as a function of the number of additional jets, which is finally normalised to the total cross section measured in the same phase space. The results are shown in Fig. 6 and summarised in Table 4.

For each $t\bar{t}$ + additional jet template used in the maximum-likelihood fit, a full correlation is assumed between the rate of events that fulfill the particle-level selection and the rate of events that do not. Therefore, a single template is used for both parts.
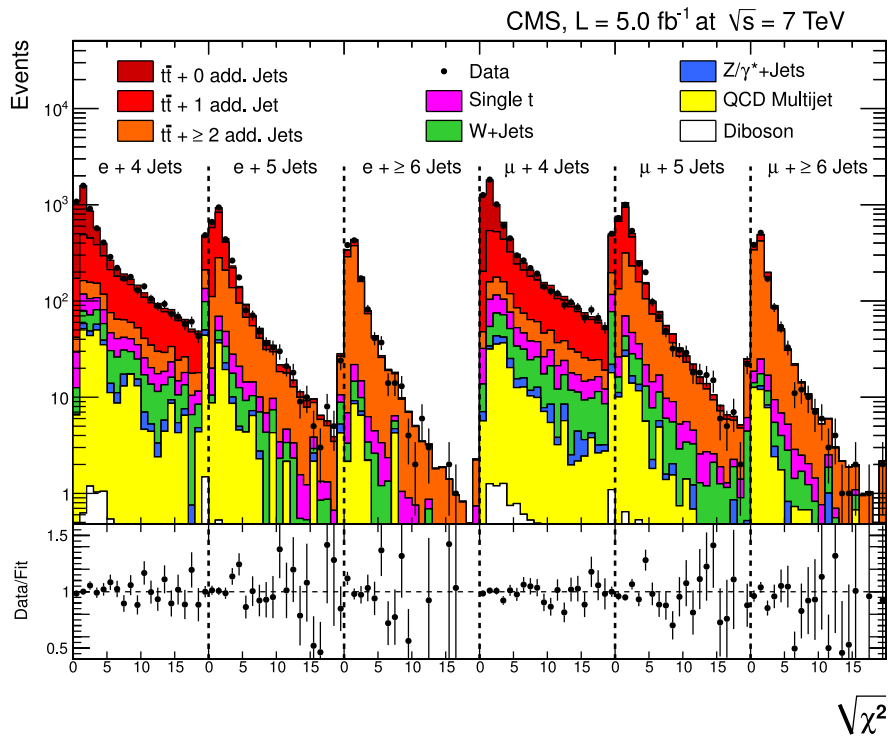
Fig. 5 Result of the simultaneous template fit to the $\sqrt{\chi^2}$ distribution in the ℓ+jets channel. All templates are scaled to the resulting fit parameters

Including an additional template made from events that are not inside the visible phase space leads to fit results that are compatible within the estimated uncertainties. To check the model dependency, the fit is repeated using simulated data from MC@NLO+HERWIG and POWHEG+PYTHIA instead of MADGRAPH+PYTHIA. The results are stable within the uncertainties.

The sources of systematic uncertainties are the same as those discussed in Sect. 5, except for the background normalisations, which are constrained in the fit. Their effect is propagated to the fit uncertainty, which is quoted as the statistical uncertainty. The impact of the systematic uncertainties on the extracted fractions of $t\bar{t}$ + 0, 1, and ≥ 2 additional jets is evaluated using pseudo-experiments. The most important contributions to the systematic uncertainties originate from JES (up to 7 %) and modelling uncertainties: hadronisation (up to 6 %), jet-parton matching threshold (up to 5 %), and renormalisation and factorisation scales (up to 4 %).

The MC@NLO+HERWIG prediction produces fewer events with ≥ 2 additional jets than data, which are well described by MADGRAPH+PYTHIA and POWHEG+PYTHIA. The prediction

from MADGRAPH+PYTHIA with lower renormalisation and factorisation scales provides a worse description of the data. These observations are in agreement with those presented in Sect. 6.

8 Additional jet gap fraction

An alternative way to investigate the jet activity arising from quark and gluon radiation produced in association with the $t\bar{t}$ system is to determine the fraction of events that do not contain additional jets above a given threshold. This measurement is performed using events in the dilepton decay channel after fulfilling the event reconstruction and selection requirements discussed in Sect. 4. The additional jets are defined as those not assigned to the $t\bar{t}$ system by the kinematic reconstruction described in Sect. 4.2.

A threshold observable, referred to as gap fraction [6], is defined as:

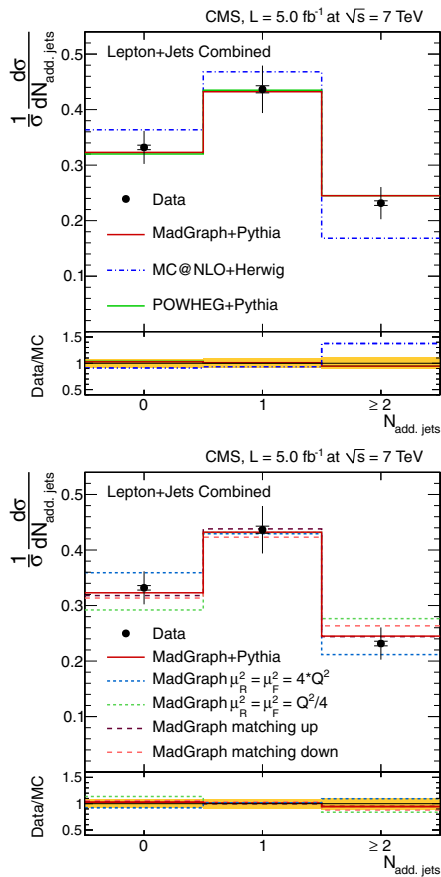$$f(p_\mathrm{T}) = \frac{N(p_\mathrm{T})}{N_\mathrm{total}}, \qquad (2)$$

Fig. 6 Normalised differential t$\bar{\text{t}}$ production cross section as a function of the number of additional jets in the ℓ+jets channel. The measurement is compared to predictions from MADGRAPH+PYTHIA, POWHEG+PYTHIA, and MC@NLO+HERWIG (*top*), as well as from MAD-GRAPH with varied renormalisation and factorisation scales, and jet-parton matching threshold (*bottom*). The *inner (outer) error bars* indicate the statistical (combined statistical and systematic) uncertainty. The *shaded band* corresponds to the combined statistical and systematic uncertainty

where N_{total} is the number of selected events and $N(p_{\text{T}})$ is the number of events that do not contain additional jets above a p_{T} threshold in the whole pseudorapidity range used in the analysis ($|\eta| < 2.4$). The pseudorapidity and p_{T} distributions of the first and second leading (in p_{T}) additional reconstructed jets are presented in Fig. 7. The distributions show good agreement between data and the simulation.

The veto can be extended beyond the additional leading jet criteria by defining the gap fraction as

$$f(H_{\text{T}}) = \frac{N(H_{\text{T}})}{N_{\text{total}}}, \tag{3}$$

where $N(H_{\text{T}})$ is the number of events in which H_{T}, the scalar sum of the p_{T} of the additional jets (with $p_{\text{T}} > 30$ GeV), is less than a certain threshold.

For each value of p_{T} and H_{T} thresholds, the gap fraction is evaluated at particle level in the visible phase space defined in Sect. 6. The additional jets at particle level are defined as all jets within the kinematic acceptance not including the two highest-p_{T} b jets containing the decay products of different b hadrons. They are required to fulfill the condition that they are not within a cone of $\Delta R = 0.4$ from any of the two isolated leptons, as described in Sect. 6.

Given the large purity of the selected events for any value of p_{T} and H_{T}, a correction for detector effects is applied following a simpler approach than the unfolding method used in Sect. 6. Here, the ratio of the particle-level to the simulated gap fraction distributions, obtained with the t$\bar{\text{t}}$ sample from MADGRAPH, provides the correction which is applied to the data.

The measured gap-fraction distribution is compared to predictions from MADGRAPH+PYTHIA, POWHEG+PYTHIA, and MC@NLO+HERWIG, and to the predictions from the MADGRAPH samples with varied renormalisation and factorisation scales and jet-parton matching threshold. In Fig. 8 the gap fraction is measured as a function of the p_{T} of the leading additional jet (left) and as a function of H_{T} (right), with the thresholds (defined at the abscissa where the data point is shown) varied between 35 and 380 GeV.

Table 4 Normalised differential t$\bar{\text{t}}$ production cross section as a function of the jet multiplicity for jets with $p_{\text{T}} > 30$ GeV in the dilepton channel. The statistical, systematic, and total uncertainties are also shown. The main experimental and model systematic uncertainties are displayed: JES and the combination of renormalisation and factorisation scales, jet-parton matching threshold, and hadronisation (in the table "Q^2/Match./Had.")

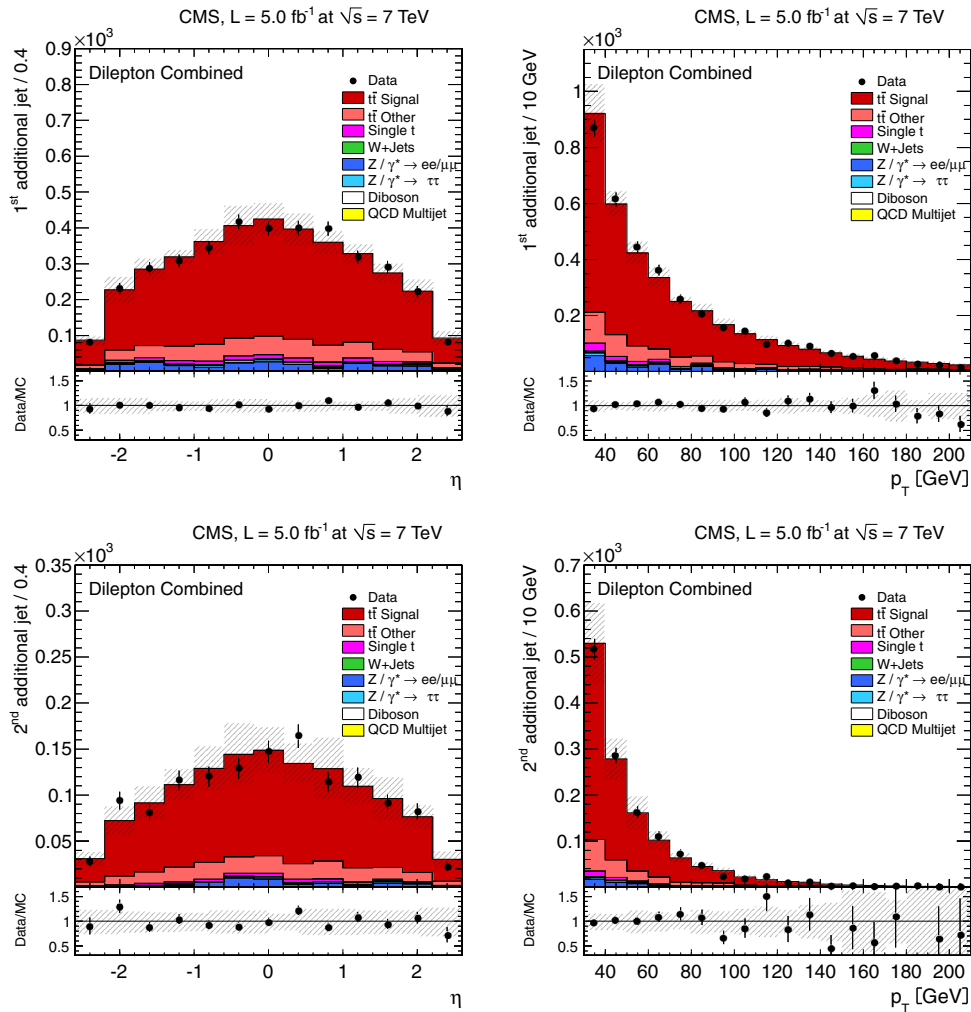| N_{jets}	$1/\sigma \, \text{d}\sigma/\text{d}N_{\text{add. jets}}$	Stat. (%)	Exp. Syst. (%)		Model Syst. (%)		Total (%)
			JES	Other	Q^2/Match./Had.	Other	
t$\bar{\text{t}}$ + 0 add. Jets	0.332	1.2	4.2	1.4	7.5	1.6	9.0
t$\bar{\text{t}}$ + 1 add. Jet	0.436	1.5	0.9	1.0	9.5	1.3	9.8
t$\bar{\text{t}}$ + $\geq$2 add. Jets	0.232	1.8	7.2	1.5	9.6	2.6	12.5

Fig. 7 Distribution of the η (*left*) and the p_T (*right*) of the first (*top*) and second (*bottom*) leading additional reconstructed jets compared to signal and background simulated samples. The *error bars* on the data points indicate the statistical uncertainty. The *hatched band* represents the combined effect of all sources of systematic uncertainty

The results are summarised in Tables 5 and 6, respectively. The measurements are consistent among the three dilepton channels. The gap fraction is lower as a function of H_T showing that the measurement is probing quark and gluon emission beyond the first emission. The gap fraction is better described by MC@NLO +HERWIG compared to MADGRAPH+PYTHIA and POWHEG+PYTHIA. This result is not incompatible with the observation described above, because the gap fraction requires the jets to have a certain p_T above the threshold, which does not imply necessarily large jet multiplicities. Decreasing the renormalisation and factorisation scales or matching threshold in the

MADGRAPH sample worsens the agreement between data and simulation.

The total systematic uncertainty is about 3.5 % for values of the threshold (p_T or H_T) below 40 GeV, and decreases to 0.2 % for values of the thresholds above 200 GeV. Dominant sources of systematic uncertainty arise from the uncertainty in the JES and the background contamination, corresponding to approximately 2 and 1 % systematic uncertainty, respectively, for the smallest p_T and H_T values. Other sources with smaller impact on the total uncertainty are the b-tagging efficiency, JER, pileup, and the procedure used to correct the data to particle level.
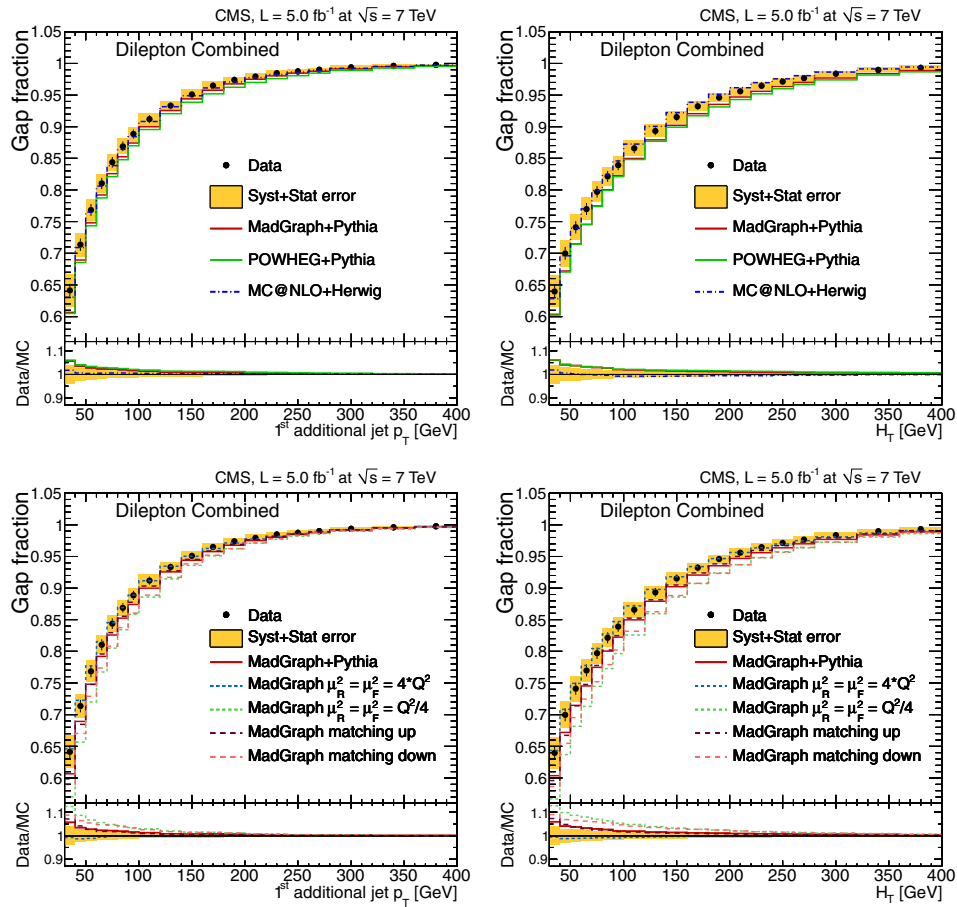
Fig. 8 Measured gap fraction as a function of the additional jet p_T (*left*) and of $H_T = \sum p_T^{\text{add. jets}}$ (*right*) in the dilepton channels. Data are compared to predictions from MADGRAPH+PYTHIA, POWHEG+PYTHIA, and MC@NLO+HERWIG (*top*), as well as from MADGRAPH with var-

ied renormalisation and factorisation scales, and jet-parton matching threshold (*bottom*). The *error bars* on the data points indicate the statistical uncertainty. The *shaded band* corresponds to the combined statistical and total systematic uncertainty (added in quadrature)

9 Summary

Measurements of the normalised differential $t\bar{t}$ production cross section as a function of the number of jets in the dilepton (ee, $\mu\mu$, and eμ) and ℓ+jets (e+jets, μ+jets) channels are presented. The measurements are performed using a data sample corresponding to an integrated luminosity of 5.0 fb^{-1} collected in pp collisions at $\sqrt{s} = 7$ TeV with the CMS detector. The results are presented in the visible phase space and compared with predictions of perturbative quantum chromodynamics from MADGRAPH and POWHEG interfaced with PYTHIA, and MC@NLO interfaced with HERWIG, as well as MADGRAPH with varied renormalisation and factorisation scales, and jet-parton matching threshold. The normalised

differential $t\bar{t}$ production cross section is also measured as a function of the jets radiated in addition to the $t\bar{t}$ decay products in the ℓ+jets channel. The MADGRAPH+PYTHIA and POWHEG+PYTHIA predictions describe the data well up to high jet multiplicities, while MC@NLO+HERWIG predicts fewer events with large number of jets. The gap fraction is measured in dilepton events as a function of the p_T of the leading additional jet and the scalar sum of the p_T of the additional jets, and is also compared to different theoretical predictions. No significant deviations are observed between data and simulation. The MC@NLO+HERWIG model seems to more accurately describe the gap fraction for all values of the thresholds compared to MADGRAPH+PYTHIA and POWHEG+PYTHIA.

Table 5 Measured gap fraction as a function of the additional jet p_T. The statistical, systematic, and total uncertainties are also shown

p_T Threshold (GeV)	Result	Stat. (%)	Syst. (%)	Total (%)
35	0.64	1.7	3.5	3.9
45	0.70	1.4	2.6	3.0
55	0.74	1.3	2.4	2.7
65	0.77	1.2	2.0	2.3
75	0.80	1.1	1.6	2.0
85	0.82	1.0	1.4	1.8
95	0.84	1.0	1.4	1.7
110	0.87	0.9	1.1	1.4
130	0.89	0.8	0.8	1.1
150	0.92	0.7	0.8	1.1
170	0.93	0.6	0.6	0.8
190	0.95	0.6	0.5	0.7
210	0.96	0.5	0.5	0.7
230	0.96	0.4	0.5	0.6
250	0.97	0.4	0.4	0.6
270	0.98	0.4	0.4	0.5
300	0.98	0.3	0.3	0.5
340	0.99	0.3	0.3	0.4
380	0.99	0.2	0.2	0.3

Table 6 Measured gap fraction as a function of $H_T = \sum p_T^{\text{add. jets}}$. The statistical, systematic, and total uncertainties are also shown

H_T Threshold (GeV)	Result	Stat. (%)	Syst. (%)	Total (%)
35	0.64	1.6	3.6	3.9
45	0.71	1.4	2.3	2.6
55	0.77	1.2	1.9	2.3
65	0.81	1.1	1.4	1.8
75	0.84	1.0	1.2	1.5
85	0.87	0.9	1.1	1.4
95	0.89	0.8	1.0	1.3
110	0.91	0.7	0.8	1.1
130	0.93	0.6	0.6	0.8
150	0.95	0.5	0.6	0.8
170	0.96	0.4	0.5	0.7
190	0.97	0.4	0.4	0.6
210	0.98	0.3	0.4	0.5
230	0.98	0.3	0.3	0.4
250	0.99	0.3	0.2	0.3
270	0.99	0.2	0.2	0.3
300	0.99	0.2	0.2	0.3
340	1.00	0.2	0.2	0.2
380	1.00	0.1	0.1	0.2

References

1. S. Dittmaier, P. Uwer, S. Weinzierl, NLO QCD corrections to $t\bar{t}$ + jet production at hadron colliders. Phys. Rev. Lett. **98**, 262002 (2007). doi:10.1103/PhysRevLett.98.262002. arXiv:hep-ph/0703120
2. G. Bevilacqua, M. Czakon, C.G. Papadopoulos, M. Worek, Hadronic top-quark pair production in association with two jets at Next-to-Leading Order QCD. Phys. Rev. D **84**, 114017 (2011). doi:10.1103/PhysRevD.84.114017. arXiv:1108.2851
3. M.I. Gresham, I.-W. Kim, K.M. Zurek, Searching for top flavor violating resonances. Phys. Rev. D **84**, 034025 (2011). doi:10.1103/PhysRevD.84.034025. arXiv:1102.0018
4. CMS Collaboration, The CMS experiment at the CERN LHC. JINST **3**, S08004 (2008). doi:10.1088/1748-0221/3/08/S08004
5. CMS Collaboration, Measurement of differential top-quark-pair production cross sections in pp collisions at $\sqrt{s}$ = 7 TeV. Eur. Phys. J. C **73**, 2339 (2013). doi:10.1140/epjc/s10052-013-2339-4. arXiv:hep-ex/1211.2220
6. ATLAS Collaboration, Measurement of $t\bar{t}$ production with a veto on additional central jet activity in pp collisions at $\sqrt{s}$ = 7 TeV using the ATLAS detector. Eur. Phys. J. C **72** 2043 (2012). doi:10.1140/epjc/s10052-012-2043-9. arXiv:1203.5015

7. J. Alwall et al., The automated computation of tree-level and next-to-leading order differential cross sections, and their matching to parton shower simulations. JHEP **07**, 079 (2014). doi:10.1007/JHEP07(2014)079

8. T. Sjöstrand, S. Mrenna, P.Z. Skands, PYTHIA 6.4 physics and manual. JHEP **05** 026 (2006). doi:10.1088/1126-6708/2006/05/026. arXiv:hep-ph/0603175

9. M.L. Mangano, M. Moretti, F. Piccinini, M. Treccani, Matching matrix elements and shower evolution for top-quark production in hadronic collisions. JHEP **01**, 013 (2007). doi:10.1088/1126-6708/2007/01/013. arXiv:hep-ph/0611129

10. CMS Collaboration, Measurement of the underlying event activity at the LHC with $\sqrt{s} = 7$ TeV and comparison with $\sqrt{s} = 0.9$ TeV. JHEP **09**, 109 (2011). doi:10.1007/JHEP09(2011)109. arXiv:1107.0330

11. J. Pumplin et al., New generation of parton distributions with uncertainties from global QCD analysis. JHEP **07**, 012 (2002). doi:10.1088/1126-6708/2002/07/012. arXiv:hep-ph/0201195

12. P. Nason, A New method for combining NLO QCD with shower Monte Carlo algorithms. JHEP **11**, 040 (2004). doi:10.1088/1126-6708/2004/11/040. arXiv:hep-ph/0409146

13. S. Frixione, P. Nason, C. Oleari, Matching NLO QCD computations with Parton Shower simulations: the POWHEG method. JHEP **11**, 070 (2007). doi:10.1088/1126-6708/2007/11/070. arXiv:0709.2092

14. S. Alioli, P. Nason, C. Oleari, E. Re, NLO single-top production matched with shower in POWHEG: s- and t-channel contributions. JHEP **09**, 111 (2009). doi:10.1088/1126-6708/2009/09/111. arXiv:0907.4076. [Erratum doi:10.1007/JHEP02(2010)011]

15. E. Re, Single-top Wt-channel production matched with parton showers using the POWHEGmethod. Eur. Phys. J. C **71**, 1547 (2011). doi:10.1140/epjc/s10052-011-1547-z. arXiv:1009.2450

16. S. Frixione, B.R. Webber, Matching NLO QCD computations and parton shower simulations. JHEP **06**, 29 (2002). doi:10.1088/1126-6708/2002/06/029. arXiv:hep-ph/0204244

17. G. Corcella et al., HERWIG 6: an event generator for hadron emission reactions with interfering gluons (including supersymmetric processes). JHEP **01**, 010 (2001). doi:10.1088/1126-6708/2001/01/010. arXiv:hep-ph/0011363

18. N. Kidonakis, NNLL resummation for s-channel single top quark production. Phys. Rev. D **81**, 054028 (2010). doi:10.1103/PhysRevD.81.054028. arXiv:1001.5034

19. N. Kidonakis, Next-to-next-to-leading-order collinear and soft gluon corrections for t-channel single top quark production. Phys. Rev. D **83**, 091503 (2011). doi:10.1103/PhysRevD.83.091503. arXiv:1103.2792

20. N. Kidonakis, Two-loop soft anomalous dimensions for single top quark associated production with W^- or H^-. Phys. Rev. D **82**, 054018 (2010). doi:10.1103/PhysRevD.82.054018. arXiv:hep-ph/1005.4451

21. J.M. Campbell, R.K. Ellis, C. Williams, Vector boson pair production at the LHC. JHEP **07**, 018 (2011). doi:10.1007/JHEP07(2011)018. arXiv:1105.0020

22. M. Czakon, A. Mitov, Top++: a program for the calculation of the top-pair cross-section at hadron colliders (2011). arXiv:1112.5675

23. S. Alekhin et al., The PDF4LHC Working Group Interim Report (2011). arXiv:1101.0536

24. M. Botje et al., The PDF4LHC Working Group Interim Recommendations. (2011). arXiv:1101.0538

25. A.D. Martin, W.J. Stirling, R.S. Thorne, G. Watt, Parton distributions for the LHC. Eur. Phys. J. C **63**, 189 (2009). doi:10.1140/epjc/s10052-009-1072-5. arXiv:0901.0002

26. H.-L. Lai et al., New parton distributions for collider physics. Phys. Rev. D **82**, 074024 (2010). doi:10.1103/PhysRevD.82.074024. arXiv:1007.2241

27. J. Gao et al., CT10 next-to-next-to-leading order global analysis of QCD. Phys. Rev. D **89**, 033009 (2014). doi:10.1103/PhysRevD.89.033009. arXiv:1302.6246

28. NNPDF Collaboration, Parton distributions with LHC data. Nucl. Phys. B **867**, 244 (2013). doi:10.1016/j.nuclphysb.2012.10.003. arXiv:1207.1303

29. Nucl. Instrum. Meth. A GEANT4—a simulation toolkit. **506**, 250 (2003). doi:10.1016/S0168-9002(03)01368-8

30. CMS Collaboration, Particle-Flow Event Reconstruction in CMS and Performance for Jets, Taus, and E_T^{miss}. CMS Physics Analysis Summary CMS-PAS-PFT-09-001 (2009). http://cdsweb.cern.ch/record/1194487

31. CMS Collaboration, Commissioning of the Particle-Flow Reconstruction in Minimum-Bias and Jet Events from PP Collisions at 7 TeV. CMS Physics Analysis Summary CMS-PAS-PFT-10-002 (2010). http://cdsweb.cern.ch/record/1279341

32. M. Cacciari, G.P. Salam, G. Soyez, The catchment area of jets. JHEP **04**, 005 (2008). doi:10.1088/1126-6708/2008/04/005. arXiv:0802.1188

33. CMS Collaboration, Electron Reconstruction and Identification at $\sqrt{s} = 7$ TeV. CMS Physics Analysis Summary CMS-PAS-EGM-10-004 (2010). http://cdsweb.cern.ch/record/1299116

34. CMS Collaboration, Performance of CMS muon reconstruction in pp collision events at $\sqrt{s} = 7$ TeV. JINST **7**, P10002 (2012). doi:10.1088/1748-0221/7/10/P10002. arXiv:1206.4071

35. CMS Collaboration, Determination of jet energy calibration and transverse momentum resolution in CMS. JINST **6**, P11002 (2011). doi:10.1088/1748-0221/6/11/P11002. arXiv:1107.4277

36. M. Cacciari, G.P. Salam, Dispelling the N^3 myth for the k_t jet-finder. Phys. Lett. B **641**, 57 (2006). doi:10.1016/j.physletb.2006.08.037. arXiv:hep-ph/0512210

37. M. Cacciari, G.P. Salam, G. Soyez, The anti-k_t jet clustering algorithm. JHEP **04**, 063 (2008). doi:10.1088/1126-6708/2008/04/063. arXiv:0802.1189

38. M. Cacciari, G. P. Salam, and G. Soyez, "FastJet user manual", (2011). arXiv:1111.6097.

39. CMS Collaboration, Identification of b-quark jets with the CMS experiment. JINST **08**, P04013 (2013). doi:10.1088/1748-0221/8/04/P04013. arXiv:1211.4462

40. Particle Data Group, J. Beringer et al., Review of particle physics. Phys. Rev. D **86**, 010001 (2012). doi:10.1103/PhysRevD.86.010001

41. CMS Collaboration, Measurement of the $t\bar{t}$ production cross section and the top quark mass in the dilepton channel in pp collisions at $\sqrt{s} = 7$ TeV. JHEP **07**, 049 (2011). doi:10.1007/JHEP07(2011)049. arXiv:1105.5661

42. CMS Collaboration, Measurement of the electron charge asymmetry in inclusive W production in pp collisions at $\sqrt{s} = 7$ TeV. Phys. Rev. Lett. **109**, 111806 (2012). doi:10.1103/PhysRevLett.109.111806. arXiv:1206.2598

43. CMS Collaboration, Measurement of the $t\bar{t}$ production cross section in pp collisions at $\sqrt{s} = 7$ TeV with lepton + jets final states. Phys. Lett. B **720**, 83 (2013). doi:10.1016/j.physletb.2013.02.021. arXiv:1212.6682

44. CMS Collaboration, Jet Energy Resolution in CMS at $\sqrt{s} = 7$ TeV. CMS Physics Analysis Summary CMS-PAS-JME-10-014 (2010). http://cdsweb.cern.ch/record/1299116

45. P.Z. Skands, D. Wicke, Non-perturbative QCD effects and the top mass at the Tevatron. Eur. Phys. J. C **52**, 133 (2007). doi:10.1140/epjc/s10052-007-0352-1. arXiv:hep-ph/0703081

46. P.Z. Skands, Tuning Monte Carlo generators: The Perugia tunes. Phys. Rev. D **82**, 074018 (2010). doi:10.1103/PhysRevD.82.074018. arXiv:1005.3457

47. CMS Collaboration, Measurement of the $t\bar{t}$ production section in pp collisions at $\sqrt{s}$ = 7TeV using the kinematic properties of events with leptons and jets. Eur. Phys. J. C **71**, 1721 (2011). doi:10.1140/epjc/s10052-011-1721-3. arXiv:1106.0902

48. CMS Collaboration, Measurement of the $t\bar{t}$ production section in the dilepton channel in pp collisions at $\sqrt{s}$ = 7 TeV. JHEP **11**, 067 (2012). doi:10.1007/JHEP11(2012)067. arXiv:1208.2671

49. CMS Collaboration, Absolute Calibration of the Luminosity Measurement at CMS: Winter 2012 Update. CMS Physics Analysis

Summary CMS-PAS-SMP-12-008 (2012). http://cdsweb.cern.ch/record/1434360

50. A. Höcker, V. Kartvelishvili, SVD approach to data unfolding. Nucl. Instrum. Meth. A **372**, 469 (1996). doi:10.1016/0168-9002(95)01478-0. arXiv:hep-ph/9509307

51. V. Blobel, "An unfolding method for high energy physics experiments", (2002). arXiv:hep-ex/0208022

52. F. James, *Statistical Methods in Experimental Physics*, 2nd edn. World (Scientific, Singapore, 2006)

The CMS Collaboration

Yerevan Physics Institute, Yerevan, Armenia
S. Chatrchyan, V. Khachatryan, A. M. Sirunyan, A. Tumasyan

Institut für Hochenergiephysik der OeAW, Wien, Austria
W. Adam, T. Bergauer, M. Dragicevic, J. Erö, C. Fabjan[1], M. Friedl, R. Frühwirth[1], V. M. Ghete, C. Hartl, N. Hörmann, J. Hrubec, M. Jeitler[1], W. Kiesenhofer, V. Knünz, M. Krammer[1], I. Krätschmer, D. Liko, I. Mikulec, D. Rabady[2], B. Rahbaran, H. Rohringer, R. Schöfbeck, J. Strauss, A. Taurok, W. Treberer-Treberspurg, W. Waltenberger, C.-E. Wulz[1]

National Centre for Particle and High Energy Physics, Minsk, Belarus
V. Mossolov, N. Shumeiko, J. Suarez Gonzalez

Universiteit Antwerpen, Antwerpen, Belgium
S. Alderweireldt, M. Bansal, S. Bansal, T. Cornelis, E. A. De Wolf, X. Janssen, A. Knutsson, S. Luyckx, S. Ochesanu, B. Roland, R. Rougny, H. Van Haevermaet, P. Van Mechelen, N. Van Remortel, A. Van Spilbeeck

Vrije Universiteit Brussel, Brussel, Belgium
F. Blekman, S. Blyweert, J. D'Hondt, N. Heracleous, A. Kalogeropoulos, J. Keaveney, T. J. Kim, S. Lowette, M. Maes, A. Olbrechts, D. Strom, S. Tavernier, W. Van Doninck, P. Van Mulders, G. P. Van Onsem, I. Villella

Université Libre de Bruxelles, Bruxelles, Belgium
C. Caillol, B. Clerbaux, G. De Lentdecker, L. Favart, A. P. R. Gay, A. Léonard, P. E. Marage, A. Mohammadi, L. Perniè, T. Reis, T. Seva, L. Thomas, C. Vander Velde, P. Vanlaer, J. Wang

Ghent University, Ghent, Belgium
V. Adler, K. Beernaert, L. Benucci, A. Cimmino, S. Costantini, S. Crucy, S. Dildick, G. Garcia, B. Klein, J. Lellouch, J. Mccartin, A. A. Ocampo Rios, D. Ryckbosch, S. Salva Diblen, M. Sigamani, N. Strobbe, F. Thyssen, M. Tytgat, S. Walsh, E. Yazgan, N. Zaganidis

Université Catholique de Louvain, Louvain-la-Neuve, Belgium
S. Basegmez, C. Beluffi[3], G. Bruno, R. Castello, A. Caudron, L. Ceard, G. G. Da Silveira, C. Delaere, T. du Pree, D. Favart, L. Forthomme, A. Giammanco[4], J. Hollar, P. Jez, M. Komm, V. Lemaitre, J. Liao, O. Militaru, C. Nuttens, D. Pagano, A. Pin, K. Piotrzkowski, A. Popov[5], L. Quertenmont, M. Selvaggi, M. Vidal Marono, J. M. Vizan Garcia

Université de Mons, Mons, Belgium
N. Beliy, T. Caebergs, E. Daubie, G. H. Hammad

Centro Brasileiro de Pesquisas Fisicas, Rio de Janeiro, Brazil
G. A. Alves, M. Correa Martins Junior, T. Martins, M. E. Pol, M. H. G. Souza

Universidade do Estado do Rio de Janeiro, Rio de Janeiro, Brazil
W. L. Aldá Júnior, W. Carvalho, J. Chinellato[6], A. Custódio, E. M. Da Costa, D. De Jesus Damiao, C. De Oliveira Martins, S. Fonseca De Souza, H. Malbouisson, M. Malek, D. Matos Figueiredo, L. Mundim, H. Nogima, W. L. Prado Da Silva, J. Santaolalla, A. Santoro, A. Sznajder, E. J. Tonelli Manganote[6], A. Vilela Pereira

Universidade Estadual Paulista [a], Universidade Federal do ABC [b], São Paulo, Brazil
C. A. Bernardes[b], F. A. Dias[a,7], T. R. Fernandez Perez Tomei[a], E. M. Gregores[b], P. G. Mercadante[b], S. F. Novaes[a], Sandra S. Padula[a]

229

THE EUROPEAN
PHYSICAL JOURNAL C

CrossMark

Measurement of the differential cross section for top quark pair production in pp collisions at $\sqrt{s} = 8\,\mathrm{TeV}$

CMS Collaboration[*]

CERN, 1211 Geneva 23, Switzerland

Abstract The normalized differential cross section for top quark pair ($t\bar{t}$) production is measured in pp collisions at a centre-of-mass energy of 8 TeV at the CERN LHC using the CMS detector in data corresponding to an integrated luminosity of 19.7 fb^{-1}. The measurements are performed in the lepton+jets (e/μ+jets) and in the dilepton (e$^+$e$^-$, $\mu^+\mu^-$, and e$^\pm\mu^\mp$) decay channels. The $t\bar{t}$ cross section is measured as a function of the kinematic properties of the charged leptons, the jets associated to b quarks, the top quarks, and the $t\bar{t}$ system. The data are compared with several predictions from perturbative quantum chromodynamic up to approximate next-to-next-to-leading-order precision. No significant deviations are observed relative to the standard model predictions.

1 Introduction

Understanding the production and properties of top quarks is fundamental for testing the quality of the standard model (SM) and for searching for new physical phenomena beyond its scope. The large top quark data samples produced in proton–proton (pp) collisions at the CERN LHC provide access to precision measurements that are crucial for checking the internal consistency of the SM at the LHC energy scale. In particular, measurements of the top quark pair ($t\bar{t}$) production cross section as a function of $t\bar{t}$ kinematic observables are important for comparing with the state-of-the-art quantum chromodynamic (QCD) predictions within the SM, and thereby constrain QCD parameters. In addition, the top quark plays a relevant role in theories beyond the SM, and such differential measurements are therefore expected to be sensitive to new phenomena [1].

Differential $t\bar{t}$ production cross sections have been measured previously at the Fermilab p$\bar{p}$ Tevatron [2,3], and at the LHC at a centre-of-mass energy $\sqrt{s} = 7$ TeV [4–6]. We present here the first measurement of the normalized differential $t\bar{t}$ production cross section with the CMS detector at $\sqrt{s} = 8$ TeV. The analysis uses data recorded in 2012 corresponding to an integrated luminosity of 19.7 $\pm$ 0.5 fb^{-1}, which is about a factor of four larger than the sample used in the measurement performed by the CMS Collaboration at 7 TeV [5]. The analysis largely follows the procedures of Ref. [5] and benefits from the increase in statistical precision together with improvements in kinematic reconstruction algorithms and extended systematic studies, leading to a significant reduction of the total uncertainties.

The measurements are performed in ℓ+jets channels ($\ell =$ e or μ), which contain a single isolated charged lepton and at least four jets in the final state, and in dilepton channels, with two oppositely charged leptons (e$^+$e$^-$, $\mu^+\mu^-$, e$^\pm\mu^\mp$) and at least two jets. The $t\bar{t}$ cross section is determined as a function of the kinematic properties of the top quarks and of the $t\bar{t}$ system, as well as of the leptons and jets associated with bottom (b) quarks (b jets) from top quark decays.

The kinematic properties of top quarks are obtained through kinematic-fitting and reconstruction algorithms. The normalized differential $t\bar{t}$ cross section is determined by counting the number of $t\bar{t}$ signal events in each bin of a given observable, correcting for detector effects and acceptance, and dividing by the measured total inclusive $t\bar{t}$ event rate. The latter is evaluated by integrating over all bins in each observable.

The results for directly measured quantities, such as kinematic properties of leptons and b jets, are presented in a fiducial phase space defined by the kinematic and geometric acceptance of all selected final-state objects. This avoids extrapolating the measured cross section into regions that are not experimentally accessible. In addition, the top quark and $t\bar{t}$ distributions are determined in the full phase space, in order to facilitate the comparison with higher-order perturbative QCD calculations. The results are compared to sev-

[*] e-mail: cms-publication-committee-chair@cern.ch

Springer

eral predictions obtained with the leading-order (LO) MAD-
GRAPH [7] generator interfaced to PYTHIA [8] for parton evo-
lution and hadronization, the next-to-leading-order (NLO)
generators POWHEG [9–11], interfaced to both PYTHIA and
HERWIG [12], and MC@NLO [13] interfaced to HERWIG, and
the latest NLO calculations with next-to-next-to-leading-
logarithm (NNLL) corrections [14,15], and approximate
next-to-next-to-leading-order (NNLO) predictions [16]. The
approximate NNLO predictions can be computed with the
DIFFTOP [17] program.

This document is structured as follows. A brief descrip-
tion of the CMS detector is provided in Sect. 2. Details of the
event simulation are given in Sect. 3, and event reconstruction
and selection are discussed in Sect. 4. The estimated system-
atic uncertainties on the measurements of the cross section
are described in Sect. 5. The results of the measurement are
discussed in Sect. 6, followed by a summary in Sect. 7.

2 CMS detector

The central feature of the CMS apparatus is a superconduct-
ing solenoid of 13 m length and 6 m inner diameter, which
provides an axial magnetic field of 3.8 T. Within the field
volume are a silicon-pixel and strip tracker, a lead tungstate
crystal electromagnetic calorimeter (ECAL), and a brass and
scintillator hadron calorimeter (HCAL), each composed of
a barrel and two endcap sections. Charged particle trajec-
tories are measured by the inner tracking system, cover-
ing a pseudorapidity range of $|\eta| < 2.5$. The ECAL and
the HCAL surround the tracking volume, providing high-
resolution energy and direction measurements of electrons,
photons, and hadronic jets up to $|\eta| < 3$. Muons are measured
in gas-ionization detectors embedded in the steel flux return
yoke outside the solenoid covering the region $|\eta| < 2.4$.
Extensive forward calorimetry complements the coverage
provided by the barrel and endcap detectors up to $|\eta| < 5.2$.
The detector is nearly hermetic, allowing for energy balance
measurements in the plane transverse to the beam directions.
A two-tier trigger system selects the pp collisions for use in
the analysis. A more detailed description of the CMS detec-
tor, together with a definition of the coordinate system and
the relevant kinematic variables, can be found in Ref. [18].

3 Event simulation and theoretical calculations

Event generators, interfaced with a detailed detector simu-
lation, are used to model experimental effects, such as con-
sequences of event reconstruction and choice of selection
criteria, as well as detector resolution. The $t\bar{t}$ sample is simu-
lated using the LO MADGRAPH event generator (v. 5.1.5.11),
which implements the relevant matrix elements with up to

three additional partons. The MADSPIN [19] package is used
to incorporate spin correlation effects with matrix elements
for up to three additional partons. The value of the top quark
mass is fixed to $m_t = 172.5$ GeV and the proton struc-
ture is described by the parton distribution functions (PDF)
CTEQ6L1 [20]. The generated events are subsequently pro-
cessed with PYTHIA (v. 6.426, referred to as PYTHIA6 in
the following) for parton showering and hadronization, and
the MLM prescription [21] is used for matching of matrix-
element jets to parton showers. The CMS detector response
is simulated using GEANT4 (v. 9.4) [22].

In addition to the MADGRAPH prediction, calculations
obtained with the NLO generators MC@NLO (v. 3.41) and
POWHEG (v. 1.0 r1380) are compared to the results pre-
sented in Sect. 6. While POWHEG and MC@NLO are for-
mally equivalent up to the NLO accuracy, they differ in
the techniques used to avoid double counting of radia-
tive corrections that can arise from interfacing with the
parton showering generators. Two POWHEG samples are
used: one is processed through PYTHIA6 and the other
through HERWIG (v. 6.520, referred to as HERWIG6 in
the following) for the subsequent parton showering and
hadronization. The parton showering in PYTHIA6 is based
on a transverse-momentum-ordered evolution scale, whereas
in HERWIG6 it is angular-ordered. The events generated
with MC@NLO are interfaced with HERWIG6. The HERWIG6
AUET2 tune [23] is used to model the underlying event in
the POWHEG+HERWIG6 sample, while the default tune is used
in the MC@NLO+HERWIG6 sample. The proton structure is
described by the PDF sets CT10 [24] and CTEQ6M [20]
for POWHEG and MC@NLO, respectively. In addition, the lat-
est available NLO+NNLL [14,15] and approximate NNLO
QCD predictions [16] are also used to compare with the
data. The NNLO MSTW2008 [25] PDF set is used for
both the NLO+NNLL and the approximate NNLO calcu-
lations.

Standard model background samples are simulated with
MADGRAPH (without the MADSPIN package), POWHEG, or
PYTHIA6, depending on the process. The main background
contributions originate from the production of W and Z/γ^*
bosons with additional jets (referred to as W+jets and Z+jets,
respectively, in the following), single top quark (s-, t-, and tW
channels), diboson (WW, WZ, and ZZ), $t\bar{t}$ production in asso-
ciation with a Z, W, or γ boson (referred to as $t\bar{t}$+Z/W/γ in the
following), and QCD multijet events. The W+jets, Z+jets,
and $t\bar{t}$+Z/W/γ samples are simulated with MADGRAPH with
up to two additional partons in the final state. The POWHEG
generator is used for simulating single top quark produc-
tion, while PYTHIA6 is used to simulate diboson and QCD
multijet events. Parton showering and hadronization are also
simulated with PYTHIA6 in all the background samples. The
PYTHIA6 Z2* tune [26] is used to characterize the underlying
event in both the $t\bar{t}$ and the background samples.

For comparison with the measured distributions, the event yields in the simulated samples are normalized to an integrated luminosity of 19.7 fb^{-1}, according to their predicted cross sections. These are taken from NNLO (W+jets [27,28] and Z+jets [27]), NLO+NNLL (single top quark s-, t-, and tW channels [16]), NLO (diboson [29], t$\bar{\text{t}}$+W [30], and t$\bar{\text{t}}$+Z [31]), and LO (QCD multijet [8]) calculations. The predicted cross section for the t$\bar{\text{t}}$+γ sample is obtained by scaling the LO cross section obtained with the WHIZARD event generator [32] by an NLO/LO correction K-factor [33]. Correction factors described in Sects. 4 and 5, and subsequently referred to as scale factors, are applied when needed to improve the description of the data by the simulation. The t$\bar{\text{t}}$ simulation is normalized to the data to present the expected rates in the figures in Sect. 4.

4 Event reconstruction and selection

The event selection is similar to that described in Ref. [5] for the measurement of normalized differential t$\bar{\text{t}}$ cross sections at $\sqrt{s} = 7$ TeV, and is based on the final-state topology of t$\bar{\text{t}}$ events. The top quark decays almost exclusively into a W boson and a b quark, and only the subsequent decays of one or two of the W bosons into a charged lepton (electron or muon) and a neutrino are considered. These signatures imply the presence of isolated leptons with high transverse momentum p_T, large p_T imbalance caused by the neutrinos that escape detection, and highly energetic jets. The identification of b jets through b-tagging techniques is used to increase the purity of the selected sample. The event selection in each channel is optimized to maximize the content of t$\bar{\text{t}}$ signal events and background rejection.

4.1 Lepton, jet, and missing transverse energy reconstruction

Events are reconstructed using a particle-flow technique [34, 35], which combines signals from all subdetectors to enhance the reconstruction and identification of individual particles observed in pp collisions. Charged hadrons from pileup events, i.e. those originating from additional pp interactions within the same bunch crossing, are subtracted on an event-by-event basis. Subsequently, the remaining neutral-hadron component from pileup is accounted for through jet energy corrections [36].

Electron candidates are reconstructed from a combination of the track momentum at the main interaction vertex, the corresponding energy deposition in the ECAL, and the energy sum of all bremsstrahlung photons attached to the track [37]. The candidates are required to have $p_\text{T} > 33$ GeV within the pseudorapidity interval $|\eta| < 2.1$ for the ℓ+jets channels, while electron candidates in the dilepton channels are

required to have $p_\text{T} > 20$ GeV and $|\eta| < 2.4$. As an additional quality criterion, a relative isolation $I_\text{rel}(0.3) < 0.10$ in the ℓ+jets channels and $I_\text{rel}(0.3) < 0.15$ in the dilepton channels is required, where $I_\text{rel}(x)$ is defined as the sum of the p_T of all neutral and charged reconstructed particle candidates inside a cone of $\Delta R \equiv \sqrt{(\Delta\eta)^2 + (\Delta\phi)^2} < x$ around the electron (excluding the electron itself) in η-ϕ space, divided by the p_T of the electron.

Muon candidates are reconstructed using the track information from the silicon tracker and the muon system. They are required to have $p_\text{T} > 33$ GeV and $|\eta| < 2.1$ in the ℓ+jets channels, while in the dilepton channels the corresponding selection requires $p_\text{T} > 20$ GeV and $|\eta| < 2.4$. Isolated muon candidates are selected if they fulfill $I_\text{rel}(0.4) < 0.12$ and $I_\text{rel}(0.3) < 0.15$ in the ℓ+jets and dilepton channels, respectively. The same definition of relative isolation described above is also used for muon candidates.

Jets are reconstructed by clustering the particle-flow candidates [38] using the anti-k_T clustering algorithm with a distance parameter of $R = 0.5$ [39]. Electrons and muons passing less stringent selections on lepton kinematic quantities and isolation, relative to the ones specified above, are identified but excluded from clustering. A jet is selected if it has $p_\text{T} > 30$ GeV and $|\eta| < 2.4$ for both the ℓ+jets and dilepton channels. Jets originating from b quarks are identified through a "combined secondary vertex" algorithm [40], which provides a b-tagging discriminant by combining secondary vertices and track-based lifetime information. The chosen working point in the ℓ+jets channels has an efficiency for tagging a b jet of $\approx$60 %, while the probability to misidentify light-flavour jets as b jets (mistag rate) is only $\approx$1.5 %. In the dilepton channels, the working point is selected to provide b-tagging efficiency and mistag rate of $\approx$80–85 and $\approx$10 %, respectively [40]. These requirements are chosen to reduce the background contribution in the corresponding channels while keeping a large fraction of the t$\bar{\text{t}}$ signal.

The missing transverse energy $E\!\!\!/_\text{T}$ is defined as the magnitude of the imbalance in the transverse momentum $\vec{p}\!\!\!/_\text{T}$ in the event, which is the negative of the vectorial sum of the momenta in the transverse plane of all the particles reconstructed with the particle-flow algorithm [41]. To mitigate the effect of contributions from pileup on the resolution in $E\!\!\!/_\text{T}$ we use a multivariate correction where the input is separated into components that originate from the primary and other collision vertices [42]. This correction improves the $E\!\!\!/_\text{T}$ resolution by $\approx$5 %.

4.2 Event selection

Events in the ℓ+jets channels that are triggered by the presence of a single electron (muon) with $p_\text{T} > 27$ GeV ($p_\text{T} > 24$ GeV, $|\eta| < 2.1$), are selected if they contain exactly one reconstructed lepton fulfilling the requirements
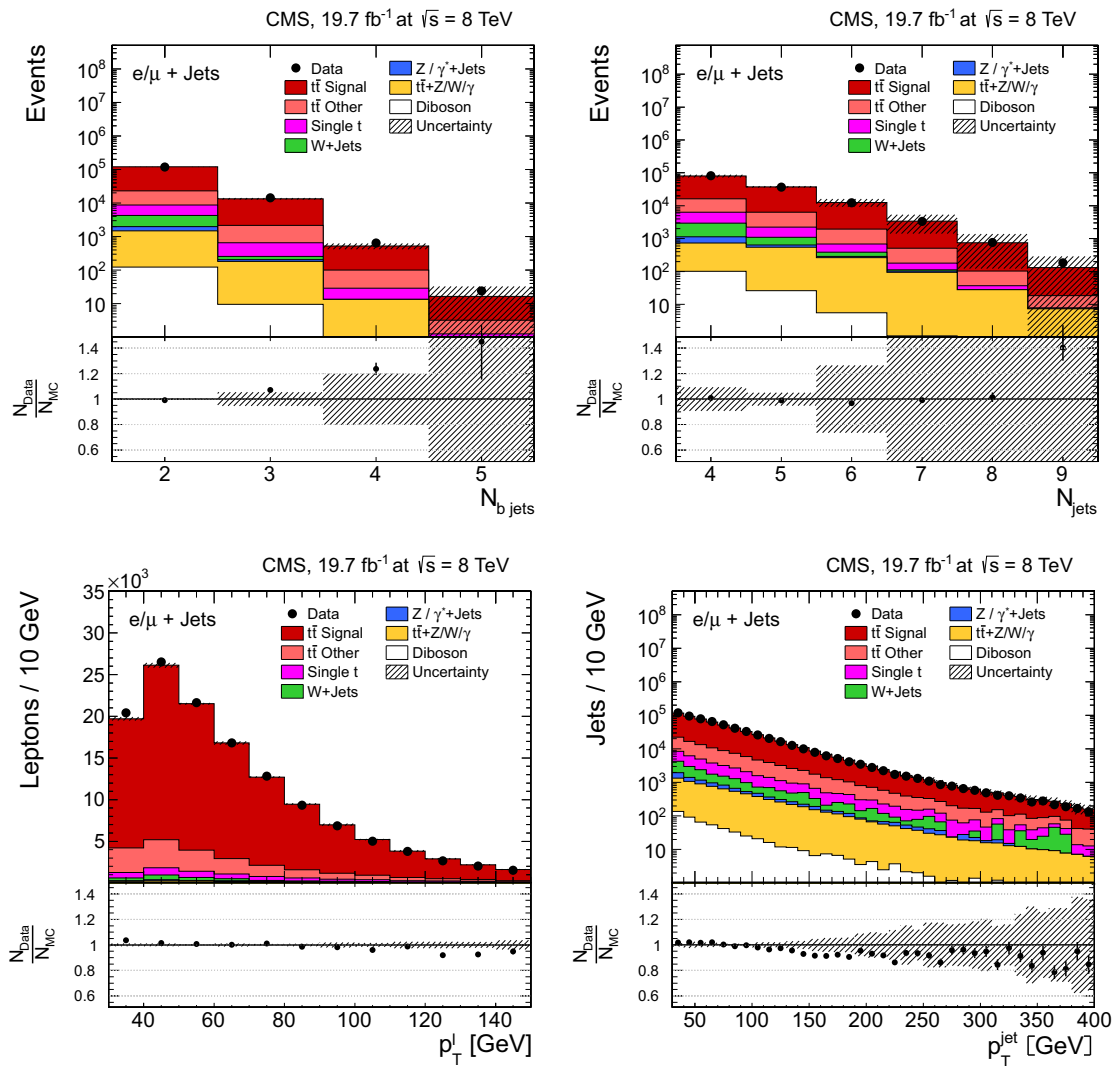
Fig. 1 Kinematic distributions after event selection and before the kinematic reconstruction of the $t\bar{t}$ system in the ℓ+jets channels: the multiplicity in the reconstructed number of b-tagged jets (*top left*), the multiplicity in the reconstructed number of jets (*top right*), the p_T of the selected isolated leptons (*bottom left*), and the p_T of all reconstructed jets (*bottom right*). The QCD multijet background is negligible and not shown. The *hatched regions* correspond to the *shape* uncertainties for the signal and backgrounds (cf. Sect. 5). The *lower part of each plot* shows the ratio of data to the predictions

described in Sect. 4.1. Events are rejected if there are additional electron candidates with $p_T > 20$ GeV, $|\eta| < 2.5$, and $I_{rel}(0.3) < 0.15$, or additional muon candidates with $p_T > 10$ GeV, $|\eta| < 2.5$, and $I_{rel}(0.4) < 0.2$. Additionally, an event must contain at least four reconstructed jets satisfying the criteria described in Sect. 4.1. To suppress background contribution mainly from W+jets events, at least two of these jets are required to be tagged as b jets, and at least

two must not be tagged as b jets, as they are used to reconstruct $W \rightarrow q\bar{q}'$ decays. In the dilepton channels, events are triggered using combinations of two leptons with p_T thresholds of 8 and 17 GeV, and are selected if they contain at least two isolated leptons of opposite electric charge and at least two jets. At least one of the jets is required to be b-tagged. In events with more than two leptons, we choose the lepton pair with opposite charge and largest value in the sum of
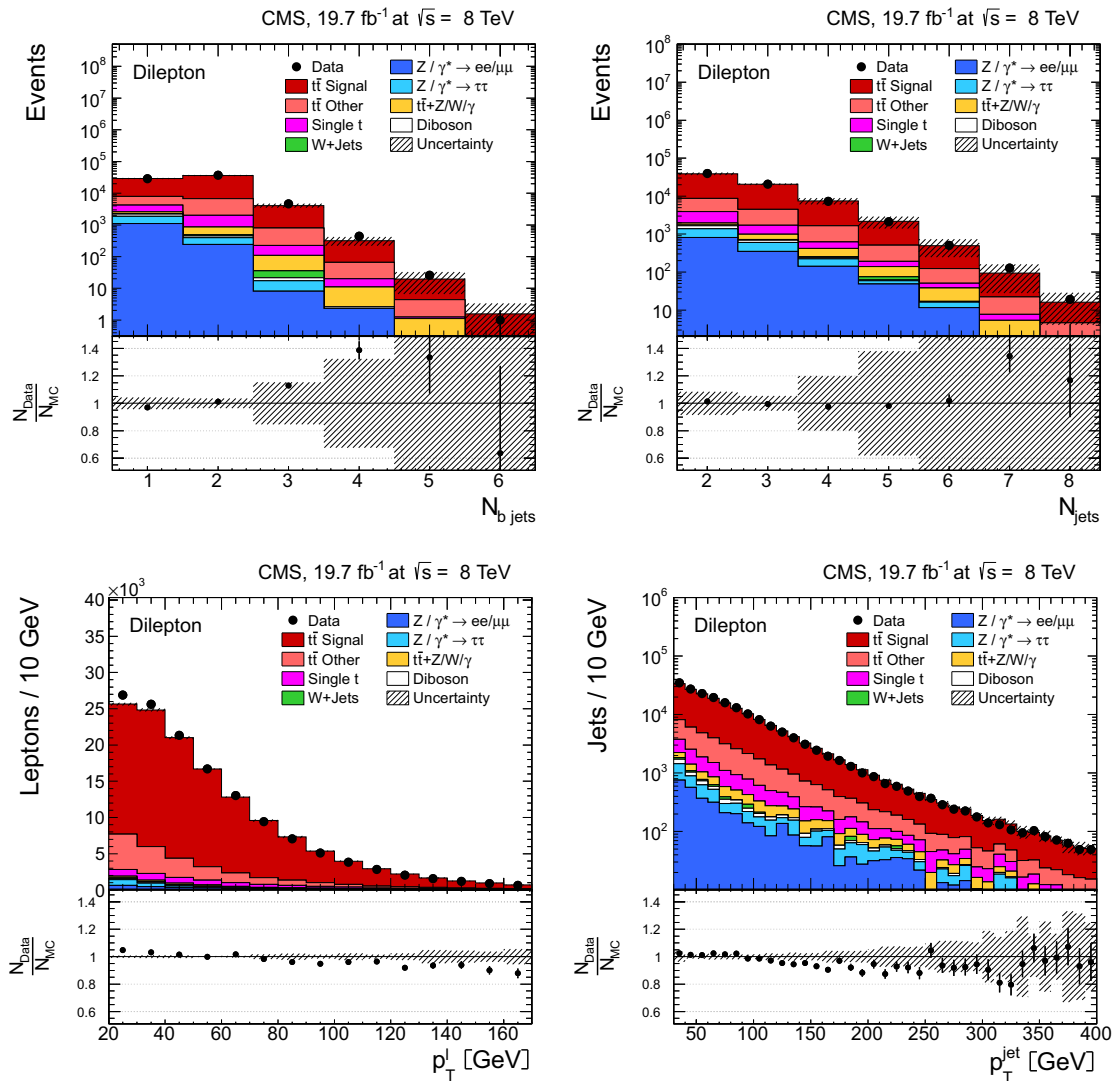
Fig. 2 Kinematic distributions after event selection and before the kinematic reconstruction of the $t\bar{t}$ system for the dilepton channels: the multiplicity in the reconstructed number of b-tagged jets (*top left*), the multiplicity in the number of reconstructed jets (*top right*), the p_T of the selected isolated leptons (*bottom left*), and the p_T of the reconstructed jets (*bottom right*). The QCD multijet background is negligible and not shown. The Z/γ^*+jets background is determined from data [5,43]. The *hatched regions* correspond to the *shape* uncertainties for the signal and backgrounds (cf. Sect. 5). The *lower part of each plot* shows the ratio of data to the predictions

their scalar p_T. Events with an invariant mass of the lepton pair smaller than 20 GeV are removed to suppress events from decays of heavy-flavour resonances and low-mass Drell–Yan processes. Backgrounds from Z+jets processes in the e^+e^- and $\mu^+\mu^-$ channels are also suppressed by requiring the dilepton invariant mass to be outside a Z boson mass window of 91 ± 15 GeV, and to have $\not{E}_T > 40$ GeV.

After these selection steps, several basic distributions in ℓ+jets and dilepton events are shown in Figs. 1 and 2, respectively. The hatched regions correspond to the shape uncertainties for the signal and background (cf. Sect. 5), and are dominated by the former. The data are reasonably well described by the simulation, as shown in the lower part of each plot, where the ratio of data to simulation is presented

to better indicate the level of agreement between data and the default $t\bar{t}$ signal (MADGRAPH+PYTHIA6) and background samples used in the analysis. For both channels, however, data tend to have lower p_T values than predicted by the simulation. It has been verified that the results presented in Sect. 6 are not affected by these remaining differences between data and simulation. A better data-to-simulation agreement in the lepton and jet p_T distributions is obtained by scaling the top quark p_T spectrum in simulation to match the data. However, the impact on the measurement of the cross sections is negligible.

4.3 Kinematic reconstruction of the $t\bar{t}$ system

The kinematic properties of the top quark pair are determined from the four-momenta of all final-state objects through kinematic reconstruction algorithms. These algorithms are improved versions of those described in Ref. [5].

In the ℓ+jets channels, a constrained kinematic fitting algorithm is applied [5,44] to the four-momenta of the selected lepton and up to five leading jets, and the $\vec{p}_T$ representing the transverse momentum of the neutrino, which are changed according to their resolutions. The fit is constrained to reconstruct two W bosons, each with a mass of 80.4 GeV. In addition, the reconstructed top quark and antiquark masses are required to be equal. To reduce the number of permutations in the association of jets to quarks, only b-tagged jets are considered as b quarks, and only untagged jets are considered as light quarks. In events with several combinatorial solutions, only the one with the minimum χ^2 in the fit is accepted. The main improvement relative to the method described in Ref. [5] is the increase in the number of correct assignments of b jets to b quarks. This is achieved by applying the kinematic fit twice, sequentially, in each event. In the first fit, the top quark mass is fixed to a value of 172.5 GeV. The jet combination that provides the minimum χ^2 in the fit is then used as input to the second kinematic fit, in which the top quark mass is not fixed, and the solution to this fit is retained. A further improvement in the method is to require the χ^2-probability of the second kinematic fit to be >2 %. This criterion is chosen to optimize the fraction of correctly reconstructed signal events, without increasing significantly the statistical uncertainty in the data. The efficiency of this requirement is about 87 % for signal events with the correct jet assignment. As a result, the number of correctly reconstructed events is increased by almost a factor of two relative to the method used in Ref. [5], and effects from migration of events across bins, which are relevant for the measurements of the cross section, are reduced. It has been checked that any possible bias in the results that could be introduced by fixing the top quark mass to a specific value in the first kinematic fit is within the assigned systematic uncertainty on

the dependence of the measurement on the top quark mass (cf. Sect. 5.2).

The dilepton channels use an algebraic kinematic reconstruction method [5,45]. The only unknowns are the three-momenta of the two neutrinos, which are reconstructed imposing the following kinematic constraints: p_T conservation in the event; the W bosons, and top quark and antiquark masses. In contrast to the method of Ref. [5], the top quark mass is fixed to a value of 172.5 GeV. Each suitable pair of b jet candidates in the event, and both possible assignments of these two jets to the two selected leptons, are considered in the kinematic reconstruction. Combinations with two b-tagged jets are preferred to using single b-tagged jets. In the new method, events are reconstructed 100 times, each time randomly smearing the measured energies and directions of the reconstructed lepton and b jet candidates by their respective detector resolutions. This smearing recovers events that yielded no solution of the equations for the neutrino momenta, because of measurement fluctuations. The equations for the neutrino momenta can have up to four solutions. For a given smearing, the solution is identified by the one yielding the smallest invariant mass of the $t\bar{t}$ system. For each solution, a weight is calculated based on the expected true lepton-b-jet invariant mass spectrum. The weights are summed over the 100 reconstruction attempts, and the kinematic quantities associated to the top quark and antiquark are calculated as a weighted average. Finally, the two jet and lepton-jet assignments that yield the maximum sum of weights are chosen for analysis. It has been checked that any bias introduced through the use of the lepton-b-jet and $t\bar{t}$ invariant masses is negligible. This method yields on average a reconstruction efficiency of $\approx$94 %, which is 6 % higher than the one described in Ref. [5], and reduces systematic migration effects.

Distributions of the top quark or antiquark and $t\bar{t}$ kinematic observables (the transverse momenta p_T^t, $p_T^{t\bar{t}}$, and the rapidities y_t and $y_{t\bar{t}}$) are presented in Figs. 3 and 4 for the ℓ+jets and dilepton channels, respectively. The hatched regions correspond to the shape uncertainties for the signal and background (cf. Sect. 5), and are dominated by the former. The lower panel in each plot also shows the ratio of data relative to the simulated signal and background samples.

In general, the data are reasonably well described by the simulation within the uncertainties. For both channels, the measured p_T distributions, in particular p_T^t, are somewhat softer than the simulated distributions: the data lie above the simulation for $p_T^t < 60(65)$ GeV in the ℓ+jets (dilepton) channels, while they lie below for $p_T^t > 200$ GeV. This pattern was also observed at 7 TeV [5]. To ensure that the results presented in Sect. 6 are not affected by such small remaining differences between data and simulation, the analysis has been repeated in different kinematic regions, with different selection requirements, and after scaling the top
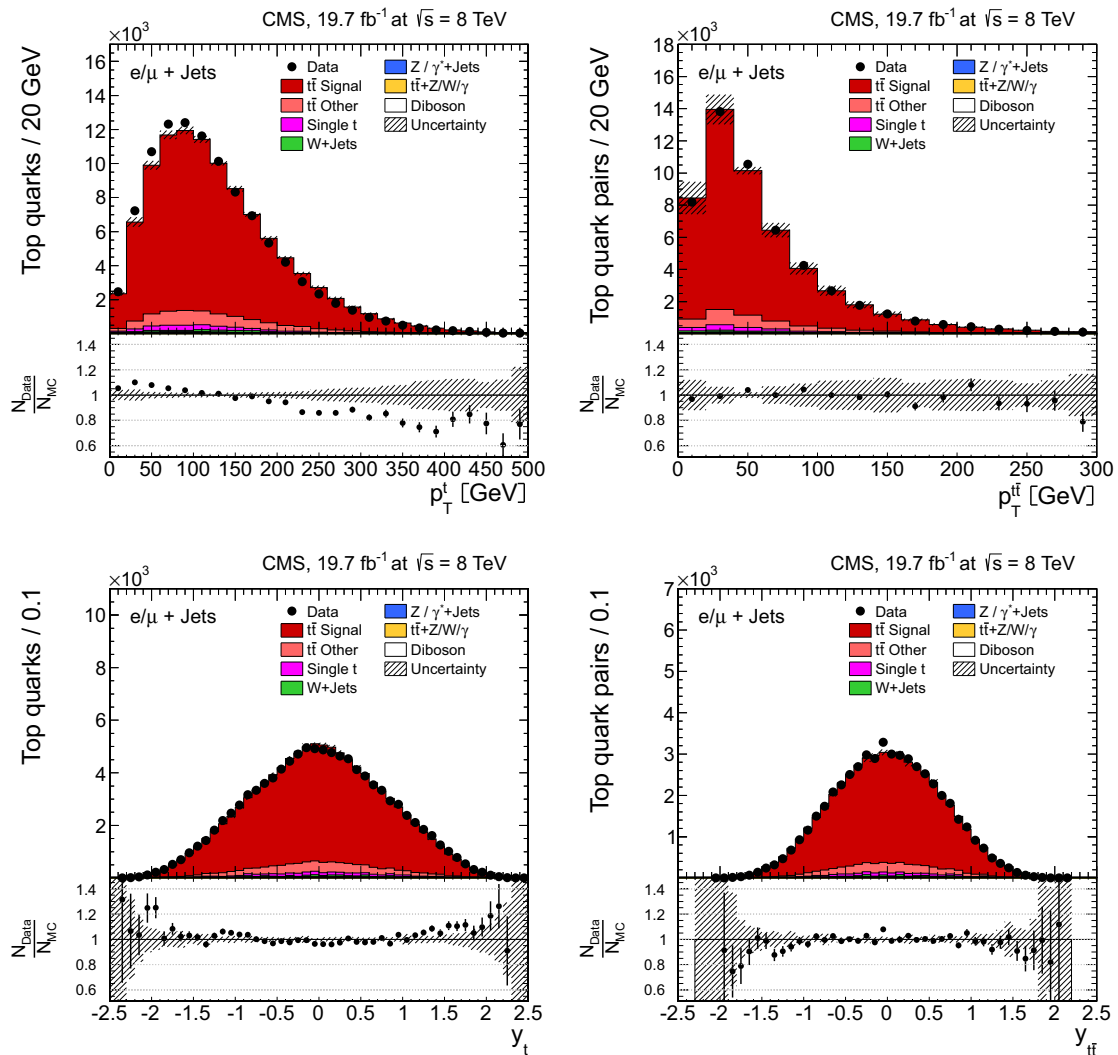
235

Fig. 3 Distribution of top quark or antiquark (*left*) and t$\bar{\text{t}}$ (*right*) quantities as obtained from the kinematic reconstruction in the ℓ+jets channels. The *top row* shows the p_T, and the *bottom row* shows the rapidities. The QCD multijet background is negligible and not shown. The *hatched regions* correspond to the *shape* uncertainties for the signal and backgrounds (cf. Sect. 5). The *lower part of each plot* shows the ratio of data to the predictions

quark p_T spectrum in simulation to match the data. However, the impact on the measurement of the cross sections is negligible.

Following the event selection described in Sect. 4.2 and the kinematic reconstruction of the t$\bar{\text{t}}$ system, the main contributions to the background in the ℓ+jets channels arise from t$\bar{\text{t}}$ decays into channel other than ℓ+jets (including t$\bar{\text{t}}$ decays into τ leptons originating from the primary interaction) and single top quark events. The contribution from W+jets and

QCD multijet events are well suppressed after the b-tagging requirement, while other t$\bar{\text{t}}$ events are somewhat reduced after the χ^2-probability requirement. A total of 24,927 events are found in the e+jets channel and 26,843 events in the μ+jets channel. The contribution from t$\bar{\text{t}}$ signal to the final event sample is 89.0 %. The remaining fraction of events contains 7.3 % t$\bar{\text{t}}$ decays other than the ℓ+jets channels, 2.4 % single top quark events, 0.9 % W+jets and t$\bar{\text{t}}$+Z/W/γ events, and negligible fractions of Z+jets, diboson, and QCD multijet
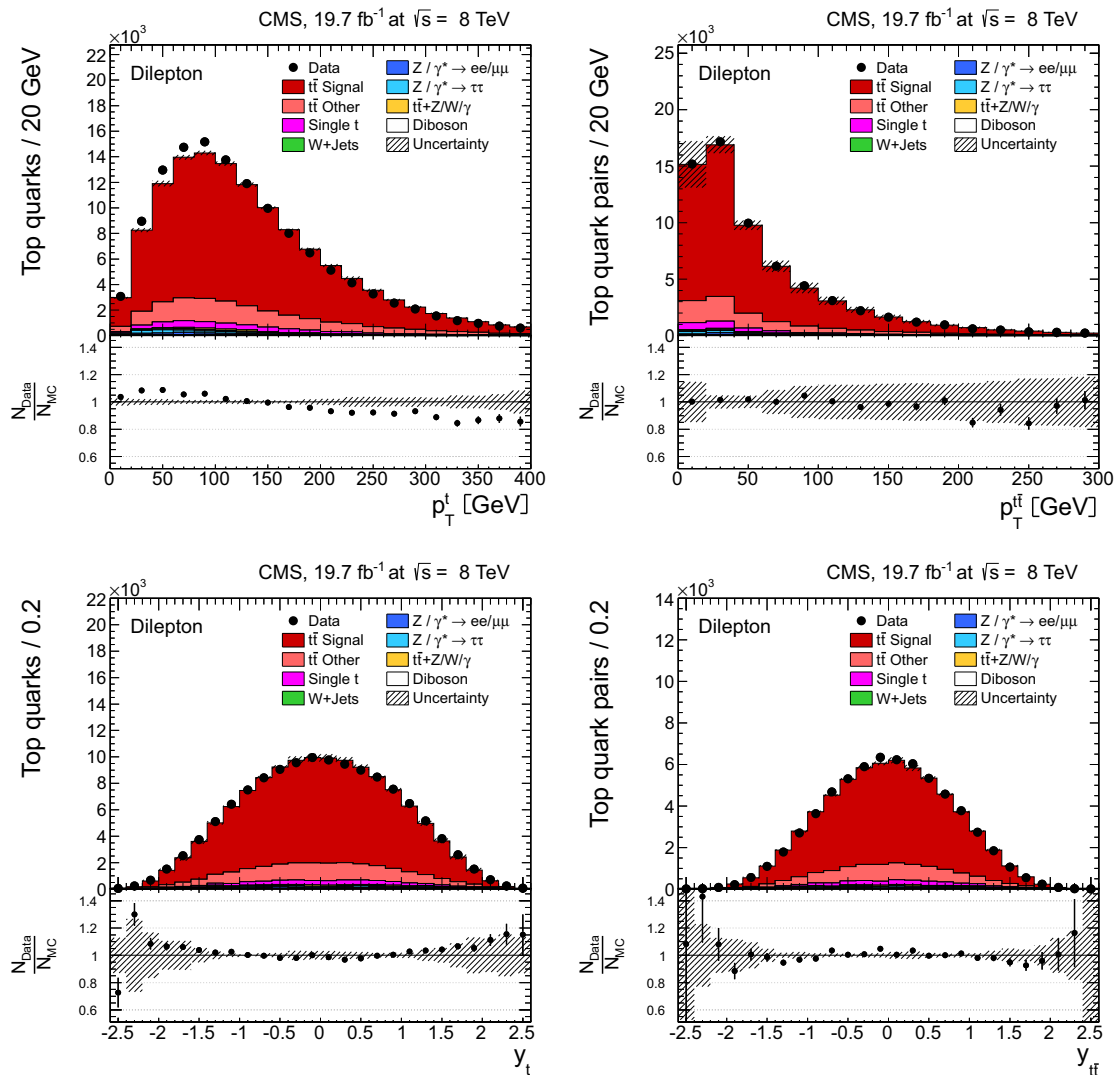
Fig. 4 Distribution of top quark or antiquark (*left*) and $t\bar{t}$ (*right*) quantities as obtained from the kinematic reconstruction in the dilepton channels. The *top row* shows the p_T, and the *bottom row* shows the rapidities. The QCD multijet background is negligible and not shown. The

Z/γ^*+jets background is determined from data [5,43]. The *hatched regions* correspond to the *shape* uncertainties for the signal and backgrounds (cf. Sect. 5). The *lower part of each plot* shows the ratio of data to the predictions

events. All background contributions are determined from simulation.

In the dilepton channels, 10,678 events are found in the e^+e^- channel, 14,403 in the $\mu^+\mu^-$ channel, and 39,640 in the $e^\pm\mu^\mp$ channel. Only $t\bar{t}$ events containing at least two leptons (electrons or muons) from W decays in the final state are considered as signal, and constitute 79.0 % of the final event sample. All other $t\bar{t}$ candidate events, specifi-

cally those originating from decays via τ leptons, are considered as background and amount to 13.3 % of the final event sample. The fraction of Z+jets events is found to be 2.4 %. This background, which is dominant to the e^+e^- and $\mu^+\mu^-$ channels, is estimated from data using the number of events observed within the Z-peak region (which is removed from the candidate sample), and a correction needed for non-Z+jets backgrounds in this same control

Table 1 Breakdown of typical systematic uncertainties for the normalized differential cross sections. The uncertainty in the jet-parton matching threshold is indicated as "ME-PS threshold"; "PS" refers to "parton shower". The medians of the distribution of uncertainties over all bins of the measurement are quoted. For the ℓ+jets channels, the background from Z+jets is negligible and included in the "Background (all other)" category

Source	Relative systematic uncertainty (%)			
	Lepton and b jet observables		Top quark and t$\bar{\text{t}}$ observables	
	ℓ+jets	Dileptons	ℓ+jets	Dileptons
Trigger eff. and lepton selec.	0.1	0.1	0.1	0.1
Jet energy scale	2.3	0.4	1.6	0.8
Jet energy resolution	0.4	0.2	0.5	0.3
Background (Z+jets)	–	0.2	–	0.1
Background (all other)	0.9	0.4	0.7	0.4
b tagging	0.7	0.1	0.6	0.2
Kinematic reconstruction	–	<0.1	–	<0.1
Pileup	0.2	0.1	0.3	0.1
Fact./renorm. scale	1.1	0.7	1.8	1.2
ME-PS threshold	0.8	0.5	1.3	0.8
Hadronization and PS	2.7	1.4	1.9	1.1
Top quark mass	1.5	0.6	1.0	0.7
PDF choice	0.1	0.2	0.1	0.5
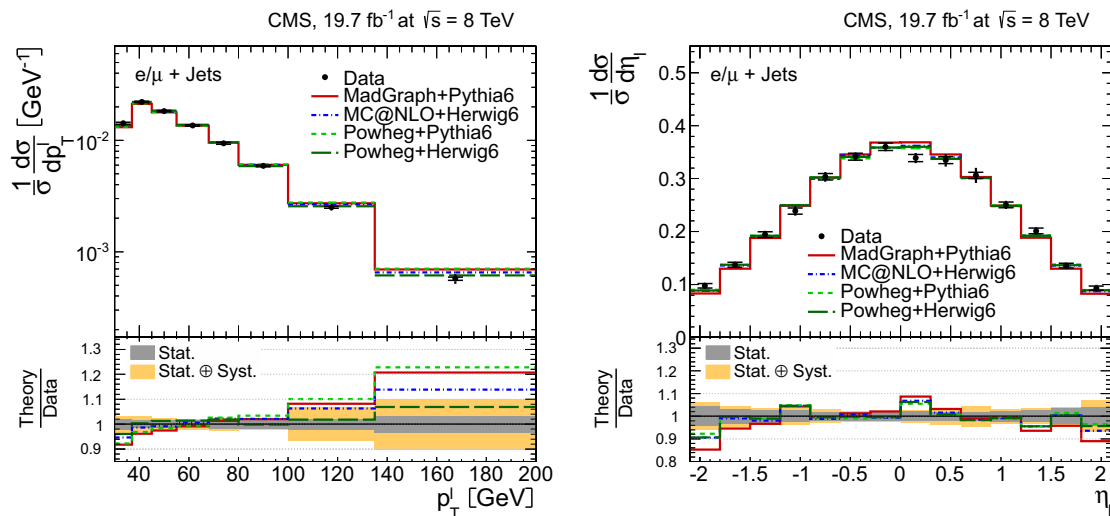
Fig. 5 Normalized differential t$\bar{\text{t}}$ production cross section in the ℓ+jets channels as a function of the p_T^ℓ (*left*) and η_ℓ (*right*) of the charged lepton. The *superscript* 'ℓ' refers to both ℓ^+ and ℓ^-. The data points are placed at the midpoint of the bins. The *inner* (*outer*) *error bars* indicate the statistical (combined statistical and systematic) uncertainties. The measurements are compared to predictions from MADGRAPH+PYTHIA6, POWHEG+PYTHIA6, POWHEG+HERWIG6, and MC@NLO+HERWIG6. The *lower part of each plot* shows the ratio of the predictions to data

region is obtained from data in the $\text{e}^\pm\mu^\mp$ channel [5,43]. Other sources of background, including single top quark production (3.4 %), t$\bar{\text{t}}$+Z/W/γ production (1 %), the contribution arising from misidentified or genuine leptons within jets (0.6 %), or diboson events (0.3 %), are estimated from simulation.

Fig. 6 Normalized differential $t\bar{t}$ production cross section in the ℓ+jets channels as a function of the p_T^b (*top left*) and η_b (*top right*) of the b jets, and the $p_T^{b\bar{b}}$ (*bottom left*) and $m_{b\bar{b}}$ (*bottom right*) of the b jet pair. The *superscript* 'b' refers to both b and $\bar{b}$ jets. The data points are placed at the midpoint of the bins. The *inner* (*outer*) *error bars* indicate the statistical (combined statistical and systematic) uncertainties. The measurements are compared to predictions from MADGRAPH+PYTHIA6, POWHEG+PYTHIA6, POWHEG+HERWIG6, and MC@NLO+HERWIG6. The *lower part of each plot* shows the ratio of the predictions to data

5 Systematic uncertainties

The measurement is affected by systematic uncertainties that originate from detector effects and from theoretical assumptions. Each source of systematic uncertainty is assessed individually by changing the corresponding efficiency, resolution, or scale by its uncertainty, using a prescription similar to the one followed in Ref. [5]. For each change made, the mea-sured normalized differential cross section is recalculated, and the difference of the changed result relative to its nominal value in each bin is taken as the systematic uncertainty. The overall uncertainty on the measurement is obtained by adding all the contributions in quadrature, and is of the order of 3–10 %, depending on the observable and the bin. A detailed description of this is given in Sects. 5.1 and 5.2. The typical representative values of the systematic uncertainties in
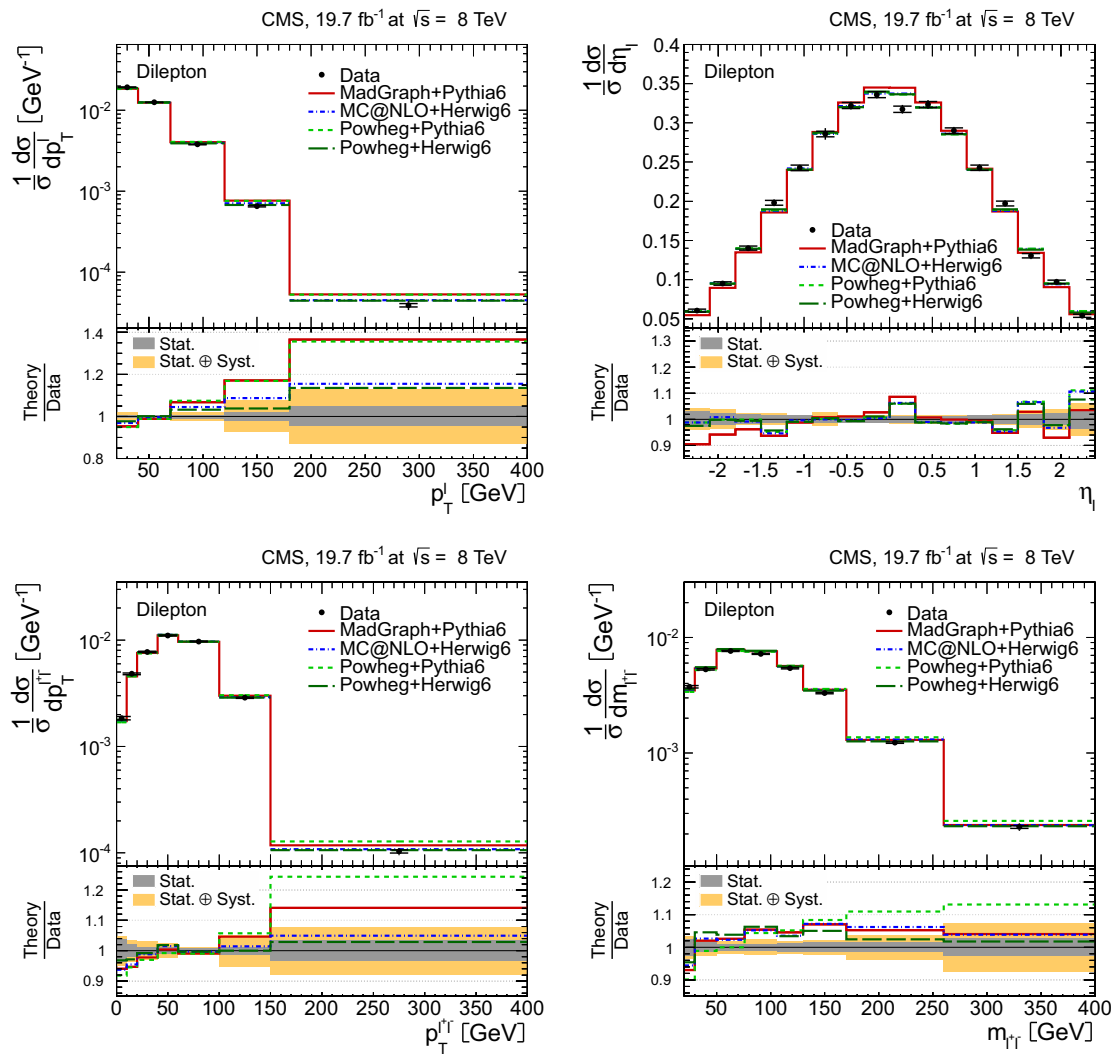
Fig. 7 Normalized differential $t\bar{t}$ production cross section in the dilepton channels as a function of the p_T^ℓ (*top left*) and η_ℓ (*top right*) of the charged leptons, and the $p_T^{\ell^+\ell^-}$ (*bottom left*) and $m_{\ell^+\ell^-}$ (*bottom right*) of the lepton pair. The *superscript* 'ℓ' refers to both ℓ^+ and ℓ^-. The data points are placed at the midpoint of the bins. The *inner* (*outer*) *error bars* indicate the statistical (combined statistical and systematic) uncertainties. The measurements are compared to predictions from MADGRAPH+PYTHIA6, POWHEG+PYTHIA6, POWHEG+HERWIG6, and MC@NLO+HERWIG6. The *lower part of each plot* shows the ratio of the predictions to data

the normalized differential cross sections are summarized in Table 1.

5.1 Experimental uncertainties

The efficiencies of the single-electron and single-muon triggers in the ℓ+jets channels are determined using the "tag-and-probe" method of Ref. [46] using Z boson event samples. Scale factors close to unity within a few percent are extracted to account for the observed dependence on the η and p_T of the lepton. The lepton identification and isolation efficiencies for the ℓ+jets channels obtained with the tag-and-probe method agree well between data and simulation, so that the applied corrections are very close to unity. The systematic uncertainties are determined by shape-dependent changes in trigger and selection efficiencies by their uncer-

Fig. 8 Normalized differential $t\bar{t}$ production cross section in the dilepton channels as a function of the p_T^b (*top left*) and η_b (*top right*) of the b jets, and the $p_T^{b\bar{b}}$ (*bottom left*) and $m_{b\bar{b}}$ (*bottom right*) of the b jet pair. The *superscript* 'b' refers to both b and $\bar{b}$ jets. The data points are placed at the midpoint of the bins. The *inner* (*outer*) *error bars* indicate the statistical (combined statistical and systematic) uncertainties. The measurements are compared to predictions from MADGRAPH+PYTHIA6, POWHEG+PYTHIA6, POWHEG+HERWIG6, and MC@NLO+HERWIG6. The *lower part of each plot* shows the ratio of the predictions to data

tainties. Lepton trigger efficiencies in the dilepton channels are measured using triggers that are only weakly correlated to the dilepton triggers used in the analysis. A dependence on η of a few percent is observed, and scale factors are extracted. The lepton identification and isolation uncertainties in the dilepton channels are also determined using the tag-and-probe method, and are again found to be described very well by the simulation for both electrons and muons.

The overall difference between data and simulation in bins of η and p_T is estimated to be <2 % for electrons, and scale factors for muons are found to be close to unity within 1.0 %.

The uncertainty due to the limited knowledge of the jet energy scale is determined by changes implemented in jet energy in bins of p_T and η [38]. The uncertainty due to the limited accuracy of the jet energy resolution (JER) is deter-

Fig. 9 Normalized differential t̄t production cross section in the ℓ+jets channels as a function of the p_T^t (*top left*), the t̄t rest frame p_T^{t*} (*top right*), and the rapidity y_t (*bottom left*) of the top quarks or antiquarks, and the difference in the azimuthal angle between the top quark and the antiquark $\Delta\phi(t,\bar{t})$ (*bottom right*). The data points are placed at the midpoint of the bins. The *inner (outer) error bars* indicate the sta-
tistical (combined statistical and systematic) uncertainties. The measurements are compared to predictions from MADGRAPH+PYTHIA6, POWHEG+PYTHIA6, POWHEG+HERWIG6, MC@NLO+HERWIG6, and to approximate NNLO [16] calculations, when available. The *lower part of each plot* shows the ratio of the predictions to data

mined by changing the simulated JER by ±1σ in different η regions [38].

The uncertainty in b-tagging efficiency is determined by taking the maximum change in the shape of p_T and η b jet distributions obtained by changing the scale factors. This is achieved by dividing the b jet distributions in p_T and η into two bins at the median of the respective distributions. These correspond to $p_T = 65$ GeV, and $|\eta| = 0.7$ and 0.75

for the ℓ+jets and dilepton channels, respectively. The b-tagging scale factors for b jets in the first bin are scaled up by half of the uncertainties quoted in Ref. [40], while those in the second bin are scaled down, and vice versa, so that a maximum variation is assumed and the difference between the scale factors in the two bins reflects the full uncertainty. The changes are made separately in the p_T and η distributions, and independently for heavy-flavour (b and c)

🙋 Springer

Fig. 10 Normalized differential $t\bar{t}$ production cross section in the ℓ+jets channels as a function of the p_T of the leading (*left*) and trailing (*right*) top quarks or antiquarks. The data points are placed at the midpoint of the bins. The *inner (outer) error bars* indicate the sta- tistical (combined statistical and systematic) uncertainties. The measurements are compared to predictions from MADGRAPH+PYTHIA6, POWHEG+PYTHIA6, POWHEG+HERWIG6, and MC@NLO+HERWIG6. The *lower part of each plot* shows the ratio of the predictions to data

and light (s, u, d, and gluon) jets, assuming that they are all uncorrelated.

The uncertainty in background normalization is determined by changing the background yields. In the ℓ+jets channels, the background normalization for the diboson, QCD multijet, W+jets, and Z+jets samples is conservatively varied by ±50 % [5], since these backgrounds, being very small, are determined from simulation rather than from data. The normalization of the $t\bar{t}$+Z/W/γ samples is changed by ±30 %. For the single top quark sample, the uncertainty is covered by changing the normalization by ±30 %, and the kinematic scales of the event process (renormalization and factorization scales) as described in Sect. 5.2. In the e^+e^- and $\mu^+\mu^-$ channels, the dominant background from Z+jets determined from data [5,43] is changed in normalization by ±30 %. In addition, changes in the background contributions from single top quark, diboson, QCD multijet, $t\bar{t}$+Z/W/γ, and W+jets events of ±30 % are used in dilepton channels [5].

The kinematic reconstruction of top quarks is well described by the simulation, and the resulting uncertainties are small. In the case of the ℓ+jets analysis, the uncertainty of the kinematic fit is included in the changes in jet energy scales and resolutions, and in the uncertainty on the dependence on the top quark mass (cf. Sect. 5.2). In the dilepton analysis, the bin-to-bin uncertainty is determined from the small remaining difference in efficiency between simulation and data.

The pileup model estimates the mean number of additional pp interactions to be about 20 events per bunch crossing for the analyzed data. This estimate is based on the total inelastic proton–proton cross section, which is determined to be 69.4 mb following the measurement described in Ref. [47]. The systematic uncertainty is determined by changing this cross section within its uncertainty of ±5 %.

5.2 Uncertainties in modelling

The impact of theoretical assumptions on the measurement is determined, as indicated previously, by repeating the analysis and replacing the standard MADGRAPH $t\bar{t}$ simulation by dedicated simulation samples with altered parameters.

The uncertainty in modelling of the hard-production process is assessed through changes in the renormalization and factorization scales in the MADGRAPH sample by factors of two and 0.5 relative to their common nominal value, which is set to the Q of the hard process. In MADGRAPH, Q is defined by $Q^2 = m_t^2 + \Sigma p_T^2$, where the sum is over all additional final state partons in the matrix element. The impact of the choice of the scale that separates the description of jet production through matrix elements (ME) or parton shower (PS) in MADGRAPH is studied by changing its reference value of 20 GeV to 40 and 10 GeV. In the ℓ+jets channels, changes in the renormalization and factorization scales are also applied to single top quark events to deter-

Fig. 11 Normalized differential $t\bar{t}$ production cross section in the ℓ+jets channels as a function of the $p_T^{t\bar{t}}$ (*top left*), $y_{t\bar{t}}$ (*top right*), and $m_{t\bar{t}}$ (*bottom*) of the $t\bar{t}$ system. The data points are placed at the midpoint of the bins. The *inner* (*outer*) *error bars* indicate the statistical (combined statistical and systematic) uncertainties. The measurements are com-

pared to predictions from MADGRAPH+PYTHIA6, POWHEG+PYTHIA6, POWHEG+HERWIG6, MC@NLO+HERWIG6, and to NLO+NNLL [14,15] calculations, when available. The *lower part of each plot* shows the ratio of the predictions to data

mine an uncertainty on the shape of this background contribution. The dependence of the measurement on the top quark mass is also estimated from dedicated MADGRAPH simulation samples in which the top quark mass is changed by ±1 GeV relative to the value used in the default simulation. The uncertainty from hadronization and parton showering is assessed by comparing the results obtained from samples simulated with POWHEG and MC@NLO interfaced with PYTHIA6 and HERWIG6, respectively. The uncertainty

from the choice of PDF is determined by reweighting the sample of simulated $t\bar{t}$ signal events according to the 52 CT10 PDF error sets [24], at a 90 % confidence level. The maximum variation is taken as uncertainty. As mentioned in Sects. 4.2 and 4.3, the effect of scaling the top quark p_T spectrum in simulation to match the data has negligible impact on the measured cross sections, therefore no systematic uncertainty is taken into account for this effect.
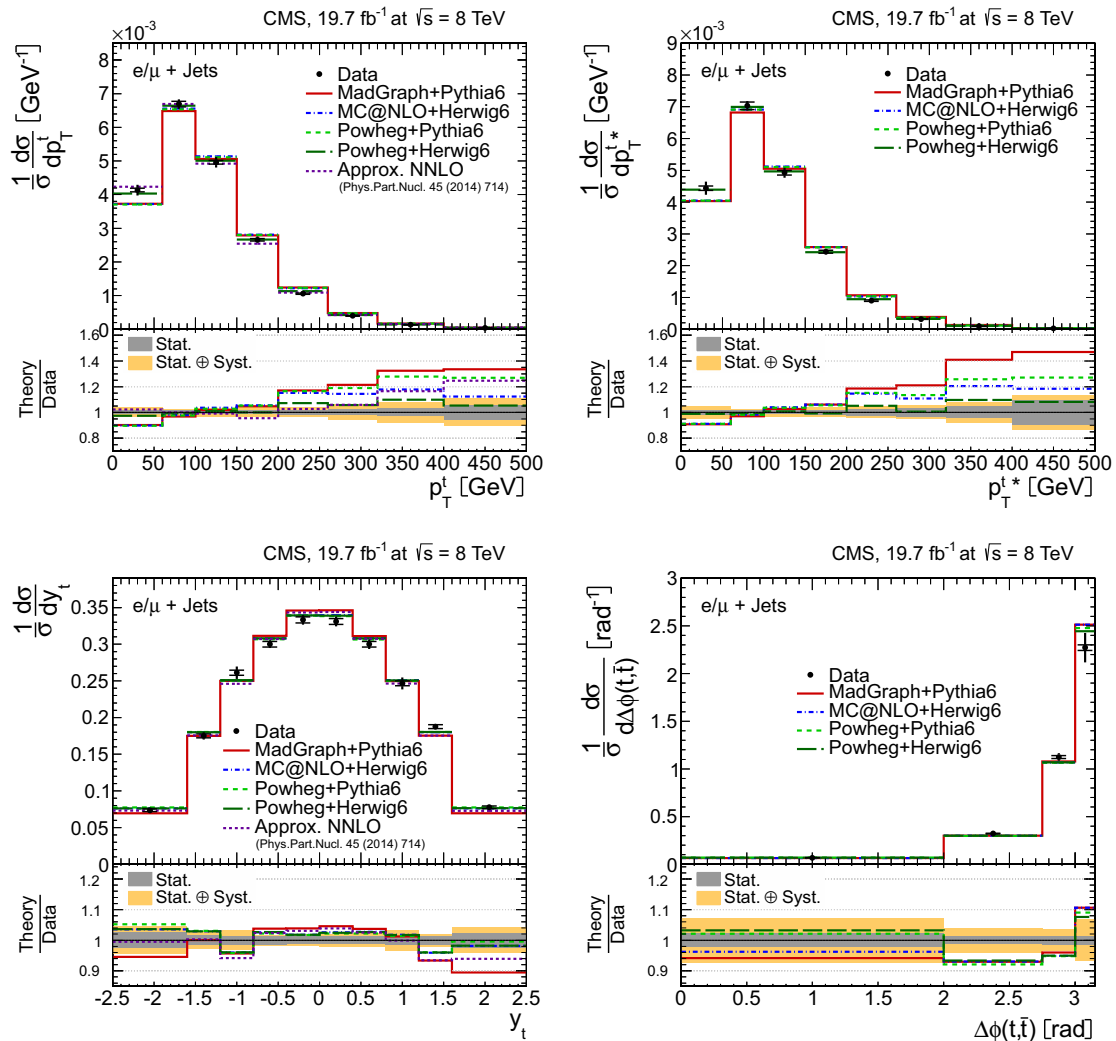
Fig. 12 Normalized differential $t\bar{t}$ production cross section in the dilepton channels as a function of the p_T^t (*top left*), the $t\bar{t}$ rest frame p_T^{t*} (*top right*), and the rapidity y_t (*bottom left*) of the top quarks or antiquarks, and the difference in the azimuthal angle between the top quark and the antiquark $\Delta\phi(t,\bar{t})$ (*bottom right*). The data points are placed at the midpoint of the bins. The *inner* (*outer*) *error bars* indicate the statistical (combined statistical and systematic) uncertainties. The measurements are compared to predictions from MADGRAPH+PYTHIA6, POWHEG+PYTHIA6, POWHEG+HERWIG6, MC@NLO+HERWIG6, and to approximate NNLO [16] calculations, when available. The *lower part of each plot* shows the ratio of the predictions to data

6 Normalized differential cross sections

The normalized $t\bar{t}$ cross section in each bin i of each observable X is determined as a function of the kinematic properties of the leptons, the lepton pair, the b jets, the b jet system, the top quarks, and the $t\bar{t}$ system through the relation [5]:

$$\frac{1}{\sigma}\frac{d\sigma_i}{dX} = \frac{1}{\sum_i x_i}\frac{x_i}{\Delta_i^X} \tag{1}$$

where x_i represents the number of signal events measured in data in bin i after background subtraction and corrected for detector efficiencies, acceptances, and migrations, and Δ_i^X is the bin width. The differential cross section is normalized by the sum of x_i over all bins, as indicated in Eq. (1). The integrated luminosity is omitted, as it cancels in the ratio. Because of the normalization, sources of systematic uncertainty that are correlated across all bins of the measurement, e.g. the uncertainty in the integrated luminosity, also can-

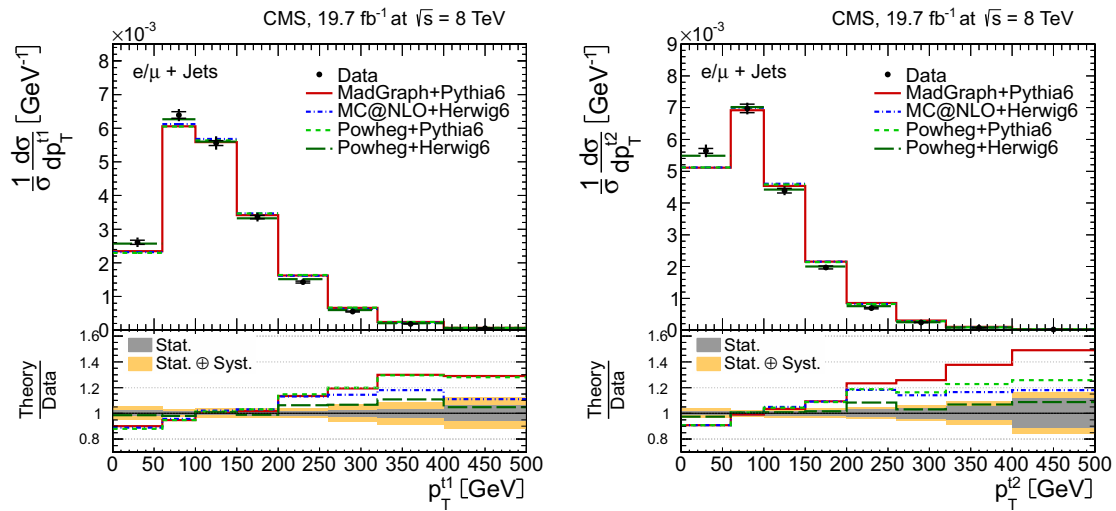**Fig. 13** Normalized differential tt̄ production cross section in the dilepton channels as a function of the p_T of the leading (*left*) and trailing (*right*) top quarks or antiquarks. The data points are placed at the midpoint of the bins. The *inner (outer) error bars* indicate the statistical (combined statistical and systematic) uncertainties. The measurements are compared to predictions from MADGRAPH+PYTHIA6, POWHEG+PYTHIA6, POWHEG+HERWIG6, and MC@NLO+HERWIG6. The *lower part of each plot* shows the ratio of the predictions to data

cel. The contribution to the background from other tt̄ decays is taken into account, after subtracting all other background components, by correcting the number of signal events in data using the expected signal fraction. The expected signal fraction is defined as the ratio of the number of selected tt̄ signal events to the total number of selected tt̄ events (i.e. signal and all other tt̄ events) in simulation. This procedure avoids the dependence on the total inclusive tt̄ cross section used in the normalization of the simulated signal sample.

Effects from trigger and detector efficiencies and resolutions leading to the migration of events across bin boundaries, and therefore to statistical correlations among neighbouring bins, are corrected by using a regularized unfolding method [5,48,49]. For each measured distribution, a response matrix is defined that accounts for migrations and efficiencies using the simulated MADGRAPH+PYTHIA6 tt̄ signal sample. The generalized inverse of the response matrix is used to obtain the unfolded distribution from the measured distribution by applying a χ^2 minimization technique. A smoothing prescription (regularization) is applied to prevent large unphysical fluctuations that can be introduced when directly inverting the response matrix. The strength of the regularization is determined and optimized individually for each distribution using the averaged global correlation method [50]. To keep the bin-to-bin migrations small, the widths of bins in the measurement are chosen according to their purity (ratio of the number of events generated and reconstructed in a particular bin to the total number of events reconstructed in

that bin; this quantity is sensitive to migrations into the bin) and stability (ratio of the number of events generated and reconstructed in a particular bin to the number of events generated in that bin; this is sensitive to migrations out of the bin). The purity and stability of the bins in this analysis are typically 60 % or larger, mainly due to the improvements in the kinematic reconstruction methods discussed in Sect. 4.3.

The performance of the unfolding procedure is tested for possible biases from the choice of the input model (the MADGRAPH+PYTHIA6 tt̄ signal simulation). It is verified that, either by reweighting the signal simulation or injecting a resonant tt̄ peak into the simulation of the signal, the unfolding procedure based on the nominal response matrices still recovers these altered shapes within statistical uncertainties. Moreover, tt̄ samples simulated with POWHEG+PYTHIA6 and MC@NLO+HERWIG6 are used to obtain the response matrices applied in the unfolding when determining the systematic uncertainties of the model (cf. Sect. 5.2). Therefore, possible effects from the unfolding procedure are already taken into account in the systematic uncertainties. The unfolded results are found to be consistent with those obtained using other regularization techniques [49].

The measurement of the normalized differential cross sections proceeds as follows. For each kinematic distribution, the event yields in the separate channels are added together, the background is subtracted, and the unfolding is performed. It is verified that the measurements in separate channels yield results consistent within their uncertainties. The systematic

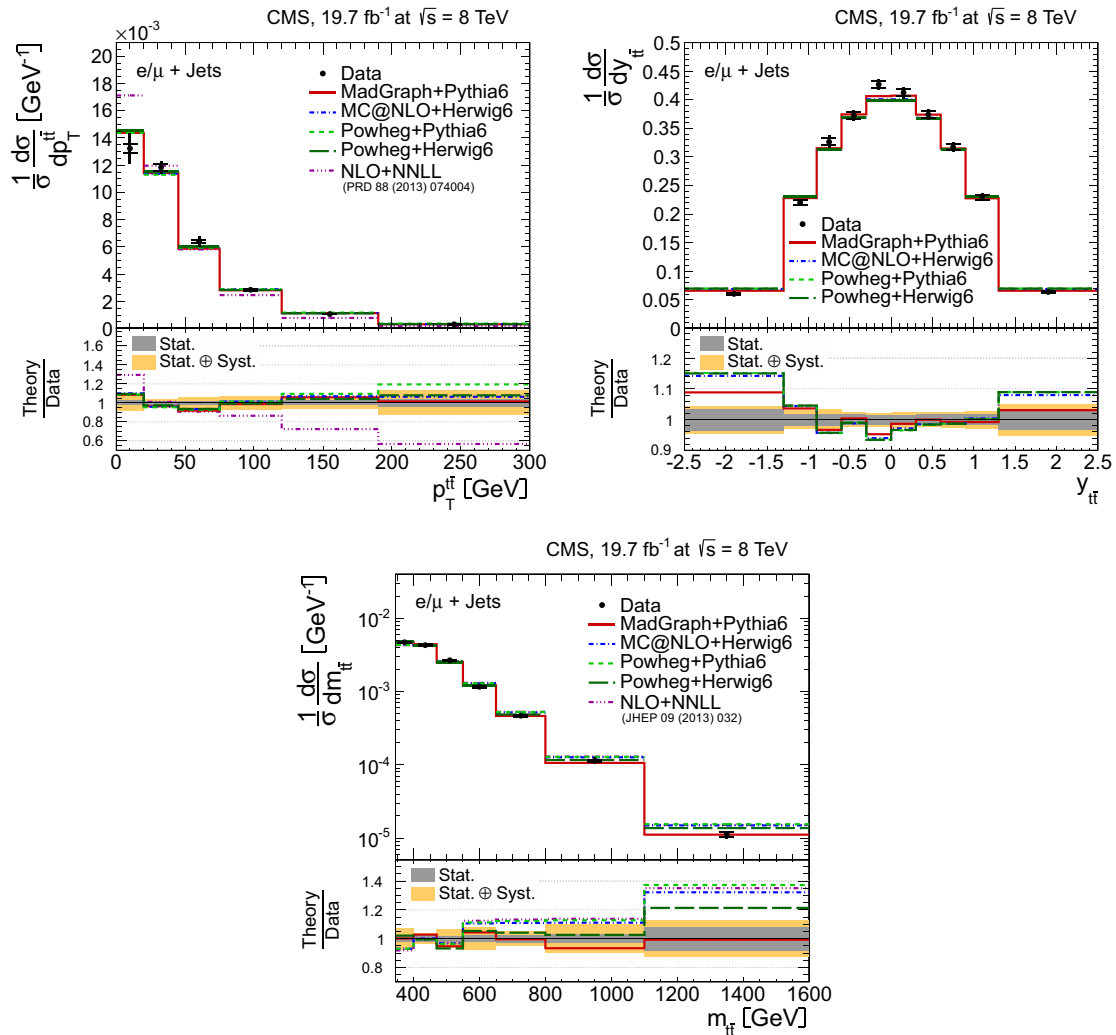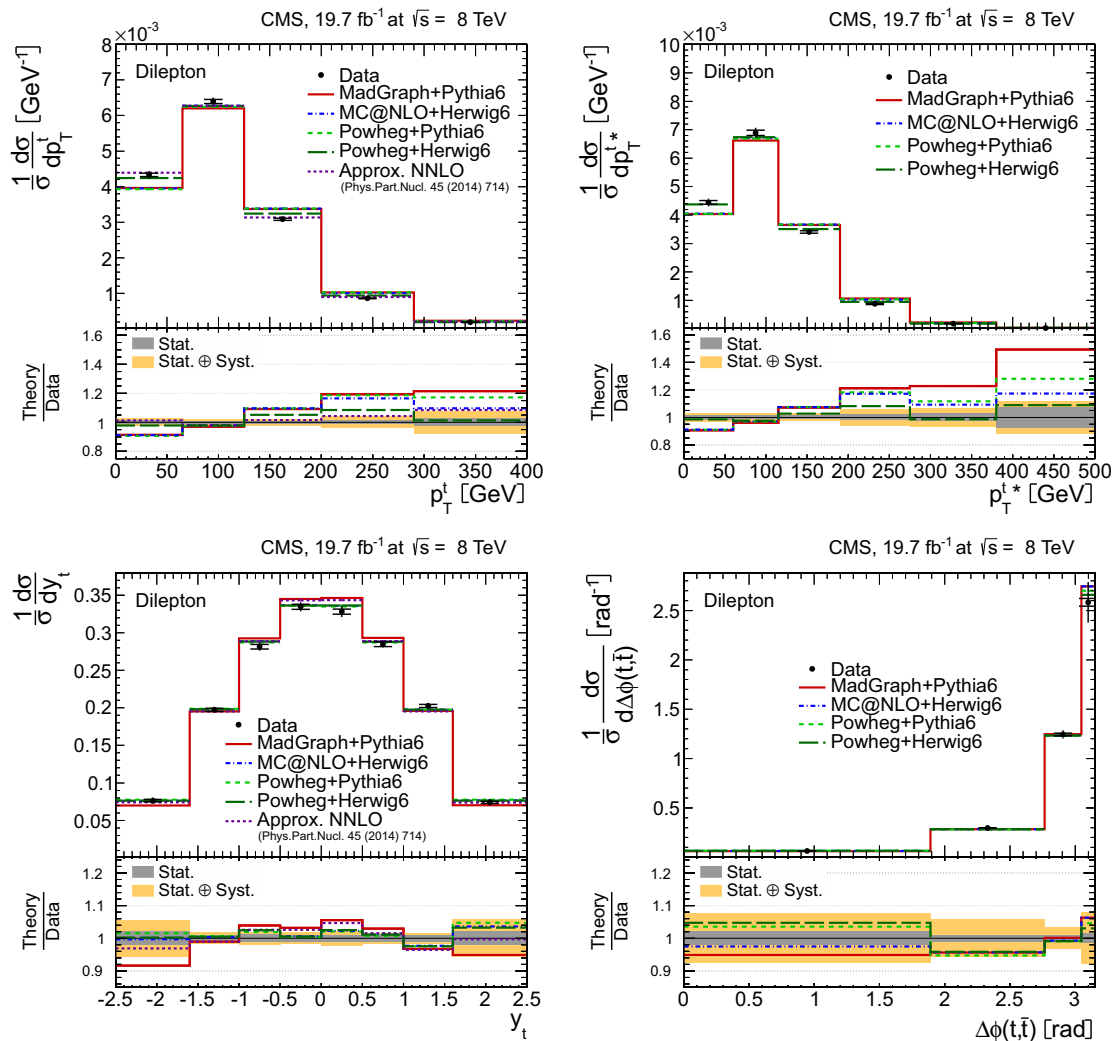**Fig. 14** Normalized differential $t\bar{t}$ production cross section in the dilepton channels as a function of the $p_T^{t\bar{t}}$ (*top left*), $y_{t\bar{t}}$ (*top right*), and $m_{t\bar{t}}$ (*bottom*) of the $t\bar{t}$ system. The data points are placed at the midpoint of the bins. The *inner* (*outer*) *error bars* indicate the statistical (combined statistical and systematic) uncertainties. The measurements are com-

pared to predictions from MADGRAPH+PYTHIA6, POWHEG+PYTHIA6, POWHEG+HERWIG6, MC@NLO+HERWIG6, and to NLO+NNLL [14,15] calculations, when available. The *lower part of each plot* shows the ratio of the predictions to data

uncertainties in each bin are determined from the changes in the combined cross sections. This requires the full analysis to be repeated for every systematic change, and the difference relative to the nominal combined value is taken as the systematic uncertainty for each bin of each observable. This method therefore takes into account the correlation among systematic uncertainties in different channels and bins.

The normalized differential cross sections of leptons and b jets are unfolded to the particle level and determined in a fiducial phase space defined by the kinematic and geometric region in which the final-state leptons and jets are produced within the detector acceptance (cf. Sect. 6.1). This minimizes model uncertainties from the extrapolation of the measurement outside of the experimentally well-described regions of phase space. In addition, the top quark

Fig. 15 Comparison of normalized differential $t\bar{t}$ production cross section in the dilepton and ℓ+jets channels as a function of the p_T^t (*top left*), the $t\bar{t}$ rest frame p_T^{t*} (*top right*), and the rapidity y_t (*bottom left*) of the top quarks or antiquarks, and the difference in the azimuthal angle between the top quark and the antiquark $\Delta\phi(t,\bar{t})$ (*bottom right*). The measurements are presented relative to the MAD-GRAPH+PYTHIA6 prediction. A horizontal bin-centre correction is applied to all data points (cf. Sect. 6.2). The *inner* (*outer*) error bars indicate the statistical (combined statistical and systematic) uncertainties. The predictions from POWHEG+PYTHIA6, POWHEG+HERWIG6, and MC@NLO+HERWIG6, also presented relative to MADGRAPH+PYTHIA6, are shown for comparison

and $t\bar{t}$-system quantities are unfolded to the parton level and presented in the full phase space (cf. Sect. 6.2) to provide easier comparisons with recent QCD calculations. The measurements are compared to predictions from MAD-GRAPH+PYTHIA6, POWHEG+PYTHIA6, POWHEG+HERWIG6, and MC@NLO+HERWIG6. The top quark and $t\bar{t}$ results are also compared to the latest calculations at NLO+NNLL [14,15] and approximate NNLO [16] precision, when available.

In addition to the measurements discussed in Ref. [5], results for the p_T and invariant mass of the b jet pair, the p_T of the top quarks or antiquarks in the $t\bar{t}$ rest frame, the p_T of the highest (*leading*) and second-highest (*trailing*) p_T of the top quark or antiquark, and the difference in the azimuthal angle between the top quark and antiquark are also presented.
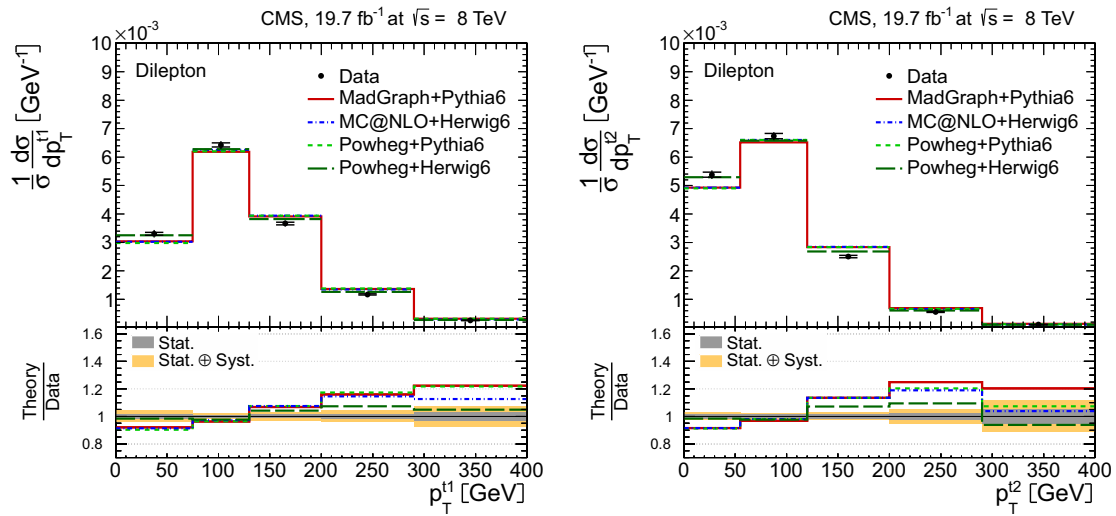
Fig. 16 Comparison of normalized differential $t\bar{t}$ production cross section in the dilepton and ℓ+jets channels as a function of the p_T of the leading (*left*) and trailing (*right*) top quarks or antiquarks. The measurements are presented relative to the MAD-GRAPH+PYTHIA6 prediction. A *horizontal* bin-centre correction is applied to all data points (cf. Sect. 6.2). The *inner* (*outer*) error bars indicate the statistical (combined statistical and systematic) uncertainties. The predictions from POWHEG+PYTHIA6, POWHEG+HERWIG6, and MC@NLO+HERWIG6, also presented relative to MADGRAPH+PYTHIA6, are shown for comparison

All values of normalized differential cross sections, including bin boundaries, are provided in tables in the supplemental material (URL will be inserted by publisher)

6.1 Lepton and b jet differential cross sections

The normalized differential $t\bar{t}$ cross section as a function of the lepton and b jet kinematic properties is measured at the particle level, where the objects are defined as follows. Leptons from W boson decays are defined after final-state radiation. A jet is defined at the particle level, following a procedure similar to that described in Sect. 4.1 for reconstructed jets, by applying the anti-k_T clustering algorithm with a distance parameter of 0.5 to all stable particles (excluding the decay products from W boson decays into $e\nu$, $\mu\nu$, and final states with leptonic τ decays). A jet is defined as a b jet if it contains any of the decay products of a B hadron. Only the two b jets of highest p_T originating from different B hadrons are considered as arising from the top quark decays.

The measurements are presented in a fiducial phase space defined by geometric and kinematic requirements on these particle-level objects as follows. The charged leptons from the W boson decays must have $|\eta| < 2.1$ and $p_T > 33$ GeV in the ℓ+jets channels, and $|\eta| < 2.4$ and $p_T > 20$ GeV in the dilepton channels. Exactly one and two leptons are required, respectively, in the ℓ+jets and the dilepton channels. At least four jets with $|\eta| < 2.4$ and $p_T > 30$ GeV, two of which

are b jets, are required in the ℓ+jets channels. In the dilepton channels, both b jets from the top quark decays must satisfy $|\eta| < 2.4$ and $p_T > 30$ GeV. The fiducial particle-level corrections are determined using simulated $t\bar{t}$ events that fulfill these requirements; all other $t\bar{t}$ events are classified as background and are removed.

Figure 5 presents the normalized differential cross section in the ℓ+jets channels as a function of the lepton transverse momentum p_T^{ℓ} and pseudorapidity η_{ℓ}. The distributions of the transverse momentum of the b jets p_T^b and their pseudorapidity η_b are given in Fig. 6, together with the transverse momentum $p_T^{b\bar{b}}$ and invariant mass $m_{b\bar{b}}$ of the b jet pair. Also shown are predictions from MAD-GRAPH+PYTHIA6, POWHEG+PYTHIA6, POWHEG+HERWIG6, and MC@NLO+HERWIG6. The lower panel in each plot shows the ratio of each of these predictions to data, in order to quantify their level of agreement relative to data.

Figure 7 presents the normalized differential cross sections for the dilepton channels: the transverse momentum p_T^{ℓ} and the pseudorapidity η_{ℓ} of the leptons, and the transverse momentum $p_T^{\ell^+\ell^-}$ and the invariant mass $m_{\ell^+\ell^-}$ of the lepton pair. The distributions in the transverse momentum of the b jets p_T^b and their pseudorapidity η_b are shown in Fig. 8, together with the transverse momentum $p_T^{b\bar{b}}$ and invariant mass $m_{b\bar{b}}$ of the b jet pair. Predictions from MAD-GRAPH+PYTHIA6, POWHEG+PYTHIA6, POWHEG+HERWIG6, and MC@NLO+HERWIG6 are also presented for comparison.
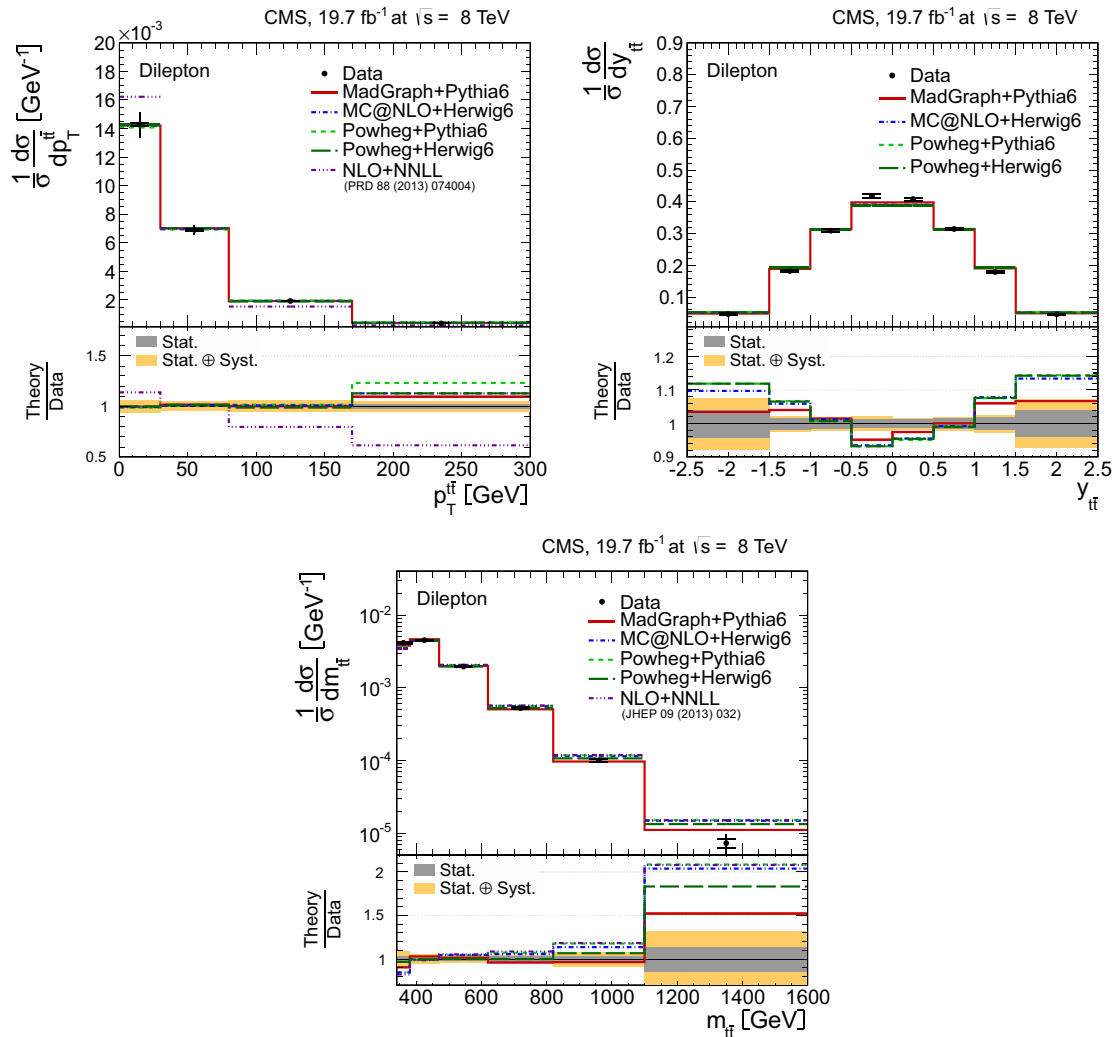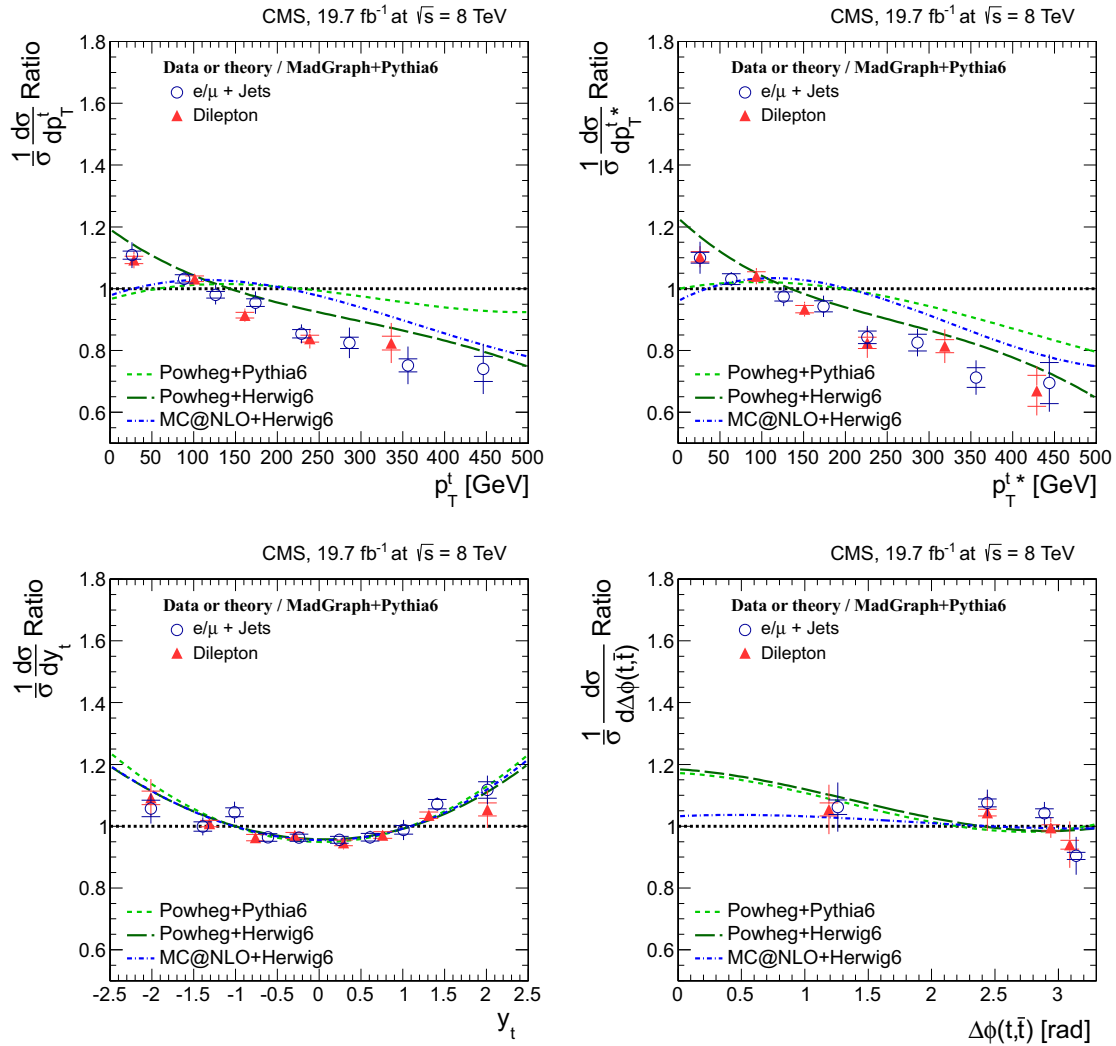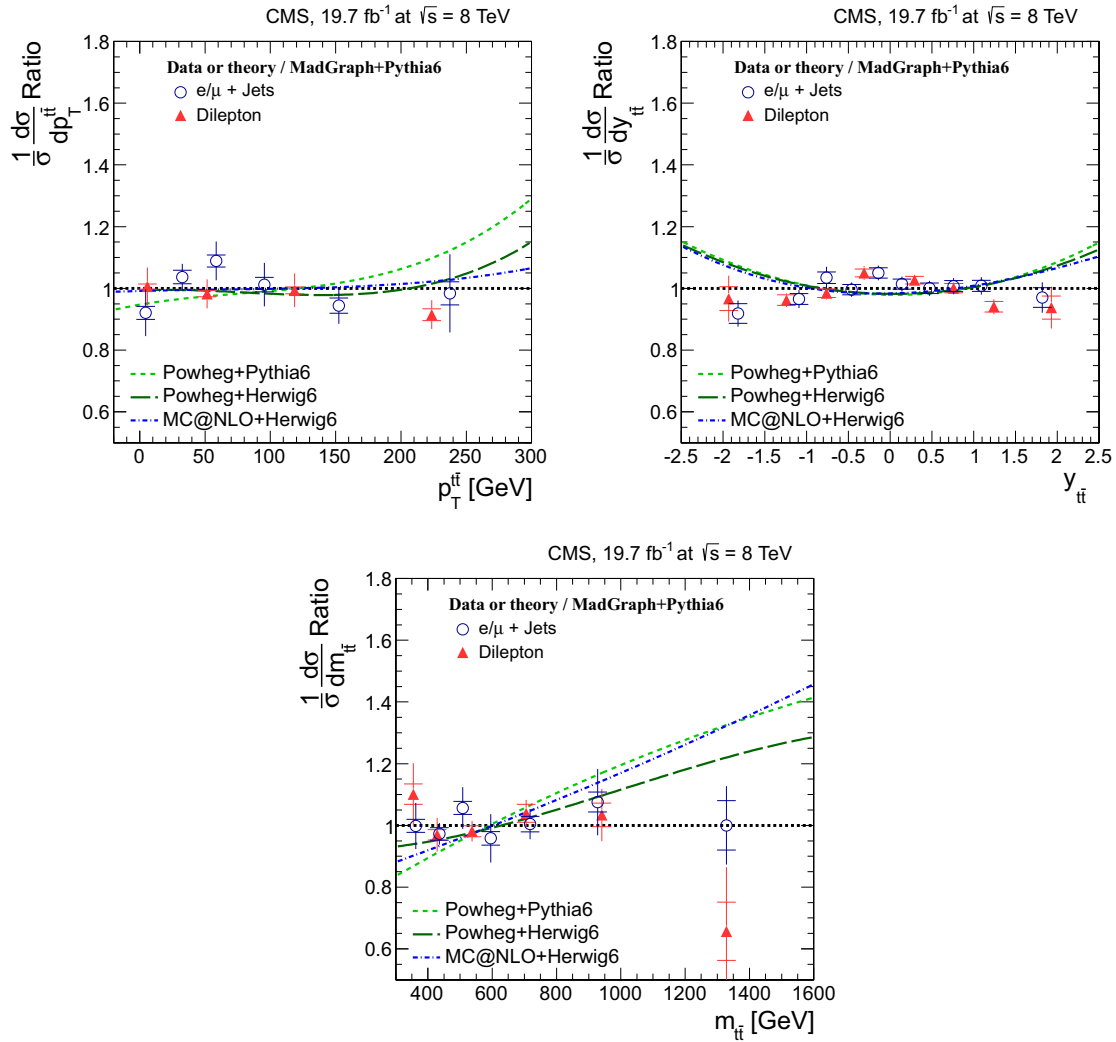
Fig. 17 Comparison of normalized differential $t\bar{t}$ production cross section in the dilepton and ℓ+jets channels as a function of the $p_T^{t\bar{t}}$ (*top left*), $y_{t\bar{t}}$ (*top right*), and $m_{t\bar{t}}$ (*bottom*) of the $t\bar{t}$ system. The measurements are presented relative to the MADGRAPH+PYTHIA6 prediction. A *horizontal* bin-centre correction is applied to all data points (cf. Sect. 6.2). The *inner* (*outer*) *error bars* indicate the statistical (combined statistical and systematic) uncertainties. The predictions from POWHEG+PYTHIA6, POWHEG+HERWIG6, and MC@NLO+HERWIG6, also presented relative to MADGRAPH+PYTHIA6, are shown for comparison. For better visibility, data points with identical bin centres (cf. Supplemental Tables 6, 10) are shifted *horizontally* by a negligible amount

In general, none of the examined predictions provides an accurate description of data for all measured lepton and b jet distributions. A steeper p_T spectrum is observed in data for the lepton and the b jet distributions compared to the predictions in both decay channels, which is best described by POWHEG+HERWIG6. The lepton p_T in data is above the predictions for $p_T^\ell < 40$ GeV, while it is below for $p_T^\ell > 100$ GeV. A similar behaviour is observed for $p_T^{\ell^+\ell^-}$, p_T^b, and $p_T^{b\bar{b}}$. The $m_{\ell^+\ell^-}$ distribution in data is below all predictions for $m_{\ell^+\ell^-} > 30$ GeV. Worse agreement is found for POWHEG+PYTHIA6. The η distributions in data are described by the predictions within the experimental uncertainties. The η_b distributions are slightly less central in data than in the predictions, and are worse described by MADGRAPH+PYTHIA6.
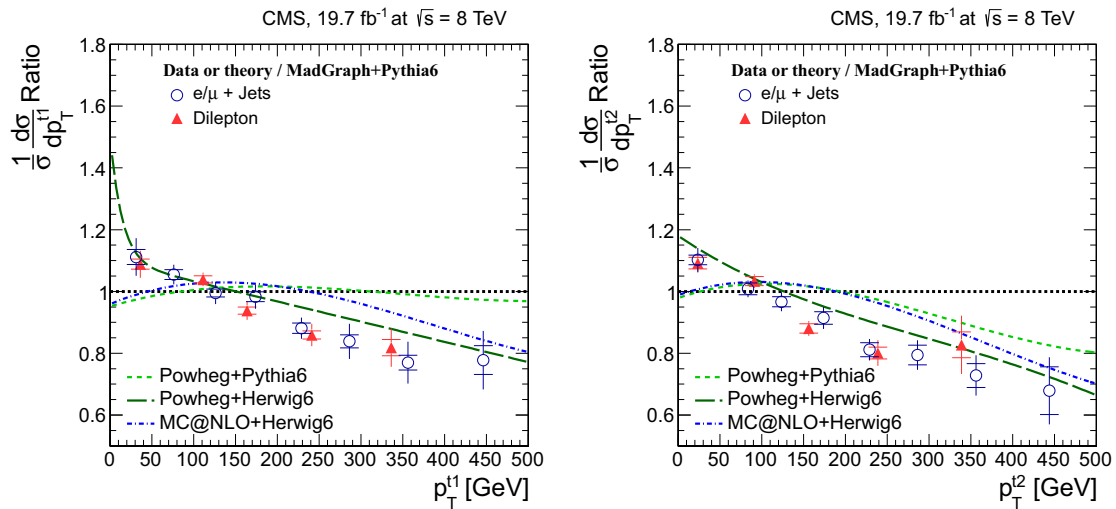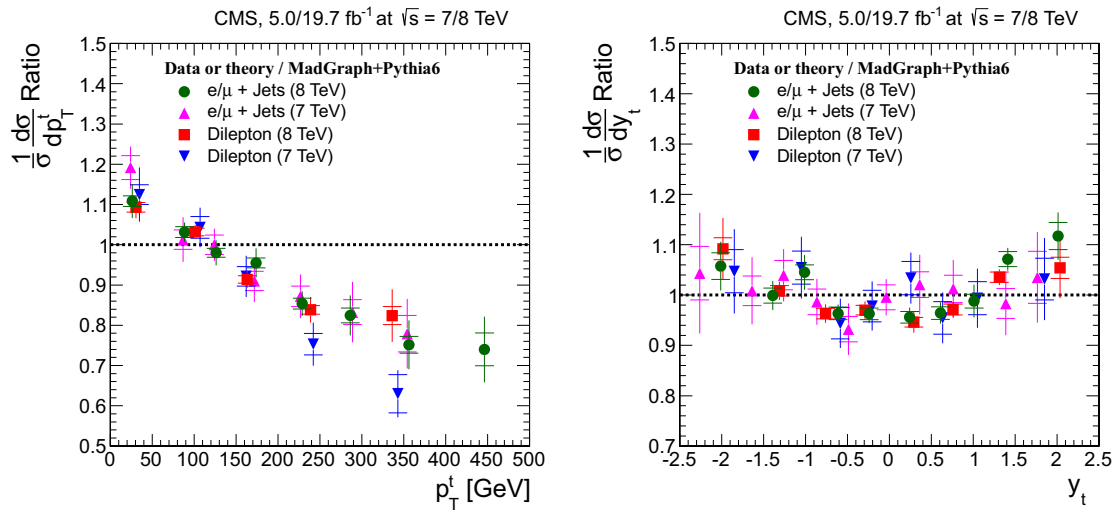
Fig. 18 Comparison of normalized differential $t\bar{t}$ production cross section in the dilepton and ℓ+jets channels at 7 TeV [5] and 8 TeV, as a function of the p_T^t (*left*) and rapidity y_t (*right*) of the top quarks or antiquarks. The measurements are presented relative to the corresponding MADGRAPH+PYTHIA6 predictions. A *horizontal* bin-centre correction is applied to all data points (cf. Sect. 6.2). The *inner* (*outer*) error bars indicate the statistical (combined statistical and systematic) uncertainties. For better visibility, data points with identical bin centres (cf. Supplemental Tables 6, 10) are shifted *horizontally* by a negligible amount

The remaining distributions are described by the predictions within experimental uncertainties.

6.2 Top quark and $t\bar{t}$ differential cross sections

The normalized differential $t\bar{t}$ cross section as a function of the kinematic properties of the top quarks and the $t\bar{t}$ system is defined with respect to the top quarks or antiquarks before the decay (parton level) and after QCD radiation, and extrapolated to the full phase space using the MADGRAPH+PYTHIA6 prediction for the ℓ+jets and dilepton channels.

In Figs. 9, 10 and 11, the following distributions are presented for the ℓ+jets channels: the transverse momentum p_T^t and the rapidity y_t of the top quarks or antiquarks, the transverse momentum p_T^{t*} of the top quarks or antiquarks in the $t\bar{t}$ rest frame, the difference in the azimuthal angle between the top quark and antiquark $\Delta\phi(t,\bar{t})$, the transverse momentum of the leading (p_T^{t1}) and trailing (p_T^{t2}) top quark or antiquark, and the transverse momentum $p_T^{t\bar{t}}$, the rapidity $y_{t\bar{t}}$, and the invariant mass $m_{t\bar{t}}$ of the $t\bar{t}$ system. The data are compared to predictions from MADGRAPH+PYTHIA6, POWHEG+PYTHIA6, POWHEG+HERWIG6, and MC@NLO+HERWIG6. In addition, the approximate NNLO calculation [16] is also shown for the top quark p_T and rapidity results, while the $m_{t\bar{t}}$ and the $p_T^{t\bar{t}}$ distributions are compared to the NLO+NNLL predictions from Refs. [14,15], respectively. Figures 12, 13 and 14

show the corresponding distributions in the dilepton channels. The lower panel in each plot also shows the ratio of each prediction relative to data.

In general, the POWHEG+HERWIG6 prediction provides a good description of data for all measured distributions. The shape of the top quark p_T spectrum is softer in data than in the predictions from MADGRAPH+PYTHIA6, POWHEG+PYTHIA6, and MC@NLO+HERWIG6 in both channels. The data lie above the predictions for $p_T^t < 60\,(65)$ GeV in the ℓ+jets (dilepton) channels, while they lie below for $p_T^t > 200$ GeV. This effect was also observed at 7 TeV [5]. The disagreement between data and predictions in the tail of the distributions is also observed in a measurement by the ATLAS Collaboration [6]. In contrast, the prediction from POWHEG+HERWIG6 and the approximate NNLO calculation provide a better description of the data, as they predict a slightly softer top quark p_T distribution than the three other simulations. The difference between the POWHEG+PYTHIA6 and POWHEG+HERWIG6 distributions is attributed to different treatment of the hardest initial state radiation in PYTHIA6 and HERWIG6. The same pattern is observed for p_T^{t*}, indicating that the softer spectrum in data is not caused by the boost of the $t\bar{t}$ system. It is also present in the p_T^{t1}, and particularly, in the p_T^{t2} distributions. For all these distributions, the POWHEG+HERWIG6 prediction provides a better description of the data. The difference in the shape of the top quark p_T spectrum between data and simulation is
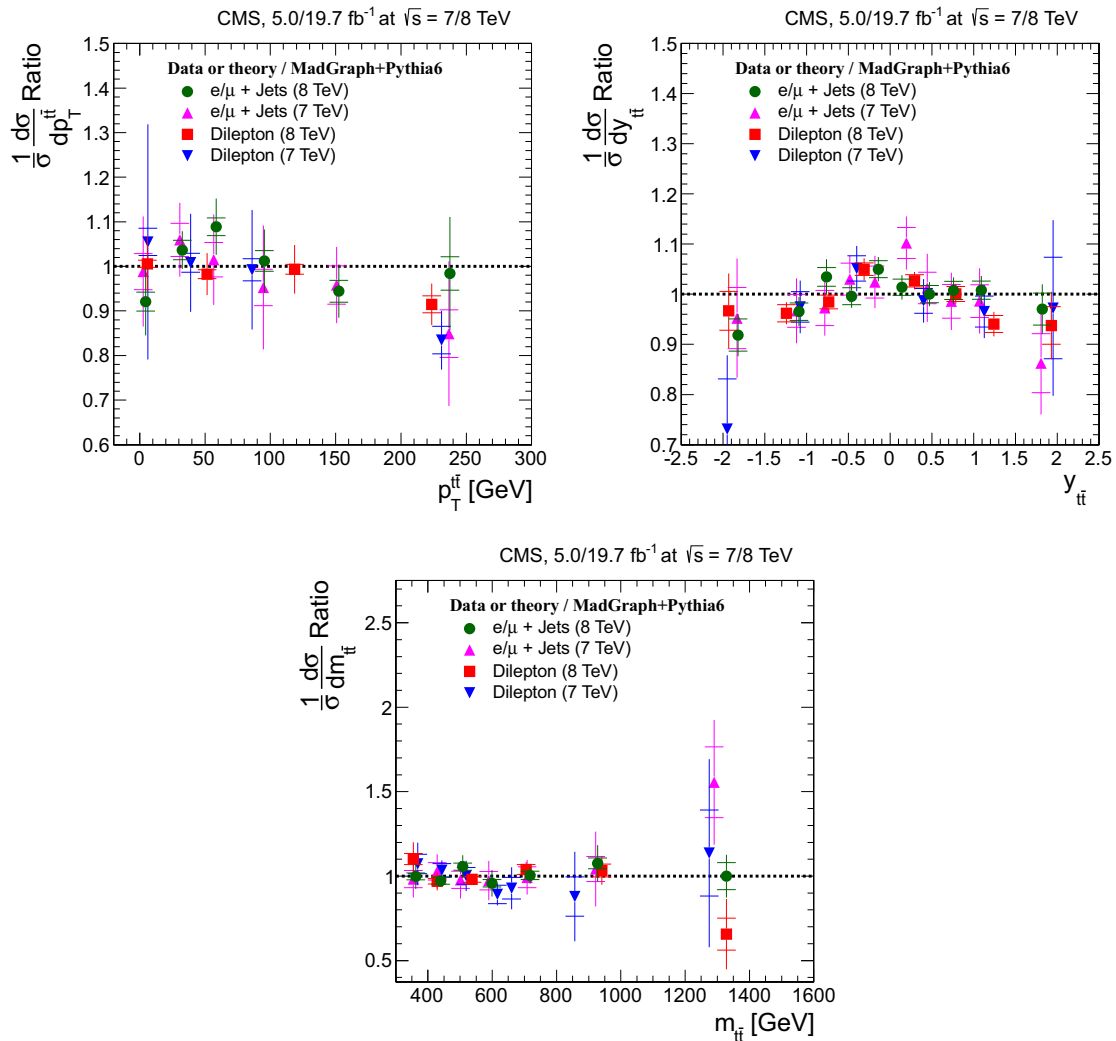
Fig. 19 Comparison of normalized differential t$\bar{\text{t}}$ production cross section in the dilepton and ℓ+jets channels at 7 TeV [5] and 8 TeV, as a function of the $p_T^{t\bar{t}}$ (*top left*), $y_{t\bar{t}}$ (*top right*), and $m_{t\bar{t}}$ (*bottom*) of the t$\bar{\text{t}}$ system. The measurements are presented relative to the corresponding MADGRAPH+PYTHIA6 predictions. A *horizontal* bin-centre correction is applied to all data points (cf. Sect. 6.2). The *inner* (*outer*) *error bars* indicate the statistical (combined statistical and systematic) uncertainties. For better visibility, data points with identical bin centres (cf. Supplemental Tables 9, 12) are shifted *horizontally* by a negligible amount

observed consistently in the analyses using different event selection requirements or different pileup conditions. The y_t distribution is found to be slightly less central in data than in the predictions, particularly in the case of MAD-GRAPH+PYTHIA6 and the approximate NNLO calculation, which are more central than the other predictions. On the contrary, $y_{t\bar{t}}$ is more central in data, and it is slightly better described by MADGRAPH+PYTHIA6. The $m_{t\bar{t}}$ distribution in data tends to be lower than the predictions for large $m_{t\bar{t}}$ values, and is better described by MADGRAPH+PYTHIA6 and POWHEG+HERWIG6. The $p_T^{t\bar{t}}$ spectrum is well described by all the considered predictions, except for the NLO+NNLL calculation, which fails to describe the data for all $p_T^{t\bar{t}}$ values.

The results from the ℓ+jets and dilepton channels are compared to each other in Figs. 15, 16 and 17. This is only feasible for the top quark and t$\bar{\text{t}}$ quantities, since they are

measured in the same phase space (i.e. the full parton level phase space) for both channels. The results are presented relative to the MADGRAPH+PYTHIA6 prediction to highlight the level of agreement between data and the default $t\bar{t}$ simulation. To facilitate the comparison of measurements that are performed using different size and number of bins, a horizontal bin-centre correction is applied to all data points from both channels. In each bin, the measured data points are presented at the horizontal position in the bin where the predicted bin-averaged cross section equals the cross section of the unbinned MADGRAPH+PYTHIA6 calculation (cf. [51]), which is common for both channels. The data are also compared to the predictions from POWHEG+PYTHIA6, POWHEG+HERWIG6, MC@NLO+HERWIG6 relative to MAD-GRAPH+PYTHIA6. The results are consistent between the channels for all quantities, in particular, for all measurements related to the top quark p_T distribution. The softer spectrum in data relative to MADGRAPH+PYTHIA6 is clearly visible.

In addition, a comparison between results obtained at $\sqrt{s} = 7$ [5] and 8 TeV is also performed for both the ℓ+jets and dilepton channels, and presented in Figs. 18 and 19 for p_T^t, y_t, $p_T^{t\bar{t}}$, $y_{t\bar{t}}$, and $m_{t\bar{t}}$. Since the fiducial phase space definition for the normalized differential cross sections is also different for each value of $\sqrt{s}$, the comparison is again only possible for top quark and $t\bar{t}$ quantities. The measurements are presented relative to the corresponding default MADGRAPH+PYTHIA6 predictions at 7 and 8 TeV. A horizontal bin-centre correction with respect to the MAD-GRAPH+PYTHIA6 predictions is applied to all data points from both channels and $\sqrt{s}$ values. The results are consistent between the channels for all quantities, both at 7 and 8 TeV. The uncertainties in almost all bins of the distributions are reduced for the 8 TeV results relative to 7 TeV, mainly due to the improvements discussed in Sect. 4.3. The softer p_T^t in data relative to MADGRAPH+PYTHIA6 is also visible at 7 TeV.

7 Summary

First measurements are presented of normalized differential $t\bar{t}$ production cross sections in pp collisions at $\sqrt{s} = 8$ TeV. The measurements are performed with the CMS detector in the ℓ+jets ($\ell = $ e or μ) and dilepton (e$^+$e$^-$, $\mu^+\mu^-$, and e$^\pm\mu^\mp$) $t\bar{t}$ decay channels. The normalized $t\bar{t}$ cross section is measured as a function of the transverse momentum, rapidity, and invariant mass of the final-state leptons and b jets in the fiducial phase space, and the top quarks and $t\bar{t}$ system in the full phase space. The measurements in the different decay channels are in agreement with each other. In general, the data are in agreement with standard model predictions up to approximate NNLO precision. Among the

examined predictions, POWHEG+HERWIG6 provides the best overall description of the data. However, the p_T spectrum in data for leptons, jets, and top quarks is softer than expected, particularly for MADGRAPH+PYTHIA6, POWHEG+PYTHIA6, and MC@NLO+HERWIG6. The calculation at approximate NNLO precision also provides a good description of the top quark p_T spectrum. The $m_{t\bar{t}}$ distribution in data tends to be lower than the predictions for large $m_{t\bar{t}}$ values. The $p_T^{t\bar{t}}$ spectrum is well described by all the considered predictions, except for the NLO+NNLL calculation, which fails to describe the data for all $p_T^{t\bar{t}}$ values. The results show the same behaviour as the corresponding CMS measurements at $\sqrt{s} = 7$ TeV.

References

1. R. Frederix, F. Maltoni, Top pair invariant mass distribution: a window on new physics. JHEP **01**, 047 (2009). doi:10.1088/1126-6708/2009/01/047. arXiv:0712.2355

2. CDF Collaboration, First measurement of the $t\bar{t}$ differential cross section $d\sigma/dM_{t\bar{t}}$ in $p\bar{p}$ collisions at $\sqrt{s}$ = 1.96 TeV. Phys. Rev. Lett. **102**, 222003 (2009). doi:10.1103/PhysRevLett.102.222003. arXiv:0903.2850

3. D0 Collaboration, Measurement of differential $t\bar{t}$ production cross sections in $p\bar{p}$ collisions. Phys. Rev. D **90**, 092006 (2014). doi:10.1103/PhysRevD.90.092006. arXiv:1401.5785

4. ATLAS Collaboration, Measurements of top quark pair relative differential cross-sections with ATLAS in pp collisions at $\sqrt{s}$ = 7 TeV. Eur. Phys. J. C **73**, 2261 (2013). doi:10.1140/epjc/s10052-012-2261-1. arXiv:1207.5644

5. CMS Collaboration, Measurement of differential top-quark pair production cross sections in pp collisions at $\sqrt{s}$ = 7 TeV. Eur. Phys. J. C **73**, 2339 (2013). doi:10.1140/epjc/s10052-013-2339-4. arXiv:1211.2220

6. ATLAS Collaboration, Measurements of normalized differential cross-sections for $t\bar{t}$ production in pp collisions at $\sqrt{(s)}$ = 7 TeV using the ATLAS detector. Phys. Rev. D **90**, 072004 (2014). doi:10.1103/PhysRevD.90.072004. arXiv:1407.0371

7. J. Alwall et al., MadGraph v5: going beyond. JHEP **06**, 128 (2011). doi:10.1007/JHEP06(2011)128. arXiv:1106.0522

8. T. Sjöstrand, S. Mrenna, P. Skands, PYTHIA 6.4 physics and manual. JHEP **05**, 026 (2006). doi:10.1088/1126-6708/2006/05/026. arXiv:hep-ph/0603175

9. S. Alioli et al., NLO single-top production matched with shower in POWHEG: s- and t-channel contributions. JHEP **09**, 111 (2009). doi:10.1088/1126-6708/2009/09/111. arXiv:0907.4076

10. S. Alioli et al., A general framework for implementing NLO calculations in shower Monte Carlo programs: the POWHEG BOX. JHEP **06**, 043 (2010). doi:10.1007/JHEP06(2010)043. arXiv:1002.2581 [Erratum: doi:10.1007/JHEP02(2010)011]

11. E. Re, Single-top Wt-channel production matched with parton showers using the POWHEG method. Eur. Phys. J. C **71**, 1547 (2011). doi:10.1140/epjc/s10052-011-1547-z. arXiv:1009.2450

12. G. Corcella et al., HERWIG 6: an event generator for hadron emission reactions with interfering gluons (including supersymmetric processes). JHEP **01**, 010 (2001). doi:10.1088/1126-6708/2001/01/010. arXiv:hep-ph/0011363

13. S. Frixione, B.R. Webber, Matching NLO QCD computations and parton shower simulations. JHEP **06**, 29 (2002). doi:10.1088/1126-6708/2002/06/029. arXiv:hep-ph/0204244

14. A. Ferroglia, B.D. Pecjak, L.L. Yang, Top-quark pair production at high invariant mass: an NNLO soft plus virtual approximation. JHEP **09**, 032 (2013). doi:10.1007/JHEP09(2013)032. arXiv:1306.1537

15. H.T. Li et al., Top quark pair production at small transverse momentum in hadronic collisions. Phys. Rev. D **88**, 074004 (2013). doi:10.1103/PhysRevD.88.074004. arXiv:1307.2464

16. N. Kidonakis, NNLL threshold resummation for top-pair and single-top production. Phys. Part. Nuclei **45**, 714 (2014). doi:10.1134/S1063779614040091. arXiv:1210.7813

17. M. Guzzi, K. Lipka, S.-O. Moch, Top-quark pair production at hadron colliders: differential cross section and phenomenological applications with DiffTop. JHEP **01**, 082 (2015). doi:10.1007/JHEP01(2015)082. arXiv:1406.0386

18. CMS Collaboration, The CMS experiment at the CERN LHC. JINST **3**, S08004 (2008). doi:10.1088/1748-0221/3/08/S08004

19. P. Artoisenet, R. Frederix, O. Mattelaer, R. Rietkerk, Automatic spin-entangled decays of heavy resonances in Monte Carlo simulations. JHEP **03**, 015 (2013). doi:10.1007/JHEP03(2013)015. arXiv:1212.3460

20. J. Pumplin et al., New generation of parton distributions with uncertainties from global QCD analysis. JHEP **07**, 012 (2002). doi:10.1088/1126-6708/2002/07/012. arXiv:hep-ph/0201195

21. M.L. Mangano, M. Moretti, F. Piccinini, M. Treccani, Matching matrix elements and shower evolution for top-quark production in hadronic collisions. JHEP **01**, 013 (2007). doi:10.1088/1126-6708/2007/01/013. arXiv:hep-ph/0611129

22. GEANT4 Collaboration, GEANT4 – a simulation toolkit. Nucl. Instrum. Methods A **506**, 250 (2003). doi:10.1016/S0168-9002(03)01368-8

23. ATLAS Collaboration, ATLAS tunes of PYTHIA 6 and Pythia 8 for MC11. ATLAS PUB note ATL-PHYS-PUB-2011-009. https://cdsweb.cern.ch/record/1363300

24. H.-L. Lai et al., New parton distributions for collider physics. Phys. Rev. D **82**, 074024 (2010). doi:10.1103/PhysRevD.82.074024. arXiv:1007.2241

25. A.D. Martin, W.J. Stirling, R.S. Thorne, G. Watt, Parton distributions for the LHC. Eur. Phys. J. C **63**, 189 (2009). doi:10.1140/epjc/s10052-009-1072-5. arXiv:0901.0002

26. CMS Collaboration, Measurement of the underlying event activity at the LHC with $\sqrt{s}$ = 7 TeV and comparison with $\sqrt{s}$ = 0.9 TeV. JHEP **09**, 109 (2011). doi:10.1007/JHEP09(2011)109. arXiv:1107.0330

27. K. Melnikov, F. Petriello, Electroweak gauge boson production at hadron colliders through $\mathcal{O}(\alpha_s^2)$. Phys. Rev. D **74**, 114017 (2006). doi:10.1103/PhysRevD.74.114017. arXiv:hep-ph/0609070

28. K. Melnikov, F. Petriello, W Boson production cross section at the large hadron collider with $\mathcal{O}(\alpha_s^2)$ corrections. Phys. Rev.

254

Lett. **96**, 231803 (2006). doi:10.1103/PhysRevLett.96.231803. arXiv:hep-ph/0603182

29. J.M. Campbell, R.K. Ellis, C. Williams, Vector boson pair production at the LHC. JHEP **07**, 018 (2011). doi:10.1007/JHEP07(2011)018. arXiv:1105.0020

30. J.M. Campbell, R.K. Ellis, t$\bar{\text{t}}$W$^\pm$ production and decay at NLO. JHEP **07**, 052 (2012). doi:10.1007/JHEP07(2012)052. arXiv:1204.5678

31. M.V. Garzelli, A. Kardos, C.G. Papadopoulos, Z. Trócsányi, t$\bar{\text{t}}$W$^\pm$ and t$\bar{\text{t}}$Z hadroproduction at NLO accuracy in QCD with parton shower and hadronization effects. JHEP **11**, 056 (2012). doi:10.1007/JHEP11(2012)056. arXiv:1208.2665

32. W. Kilian, T. Ohl, J. Reuter, WHIZARD: simulating multi-particle processes at LHC and ILC. Eur. Phys. J. C **71**, 1742 (2011). doi:10.1140/epjc/s10052-011-1742-y. arXiv:0708.4233

33. K. Melnikov, M. Schulze, A. Scharf, QCD corrections to top quark pair production in association with a photon at hadron colliders. Phys. Rev. D **83**, 074013 (2011). doi:10.1103/PhysRevD.83.074013. arXiv:1102.1967

34. CMS Collaboration, Particle-flow event reconstruction in CMS and performance for jets, taus, and $E_{\text{T}}^{\text{miss}}$. CMS Physics Analysis Summary CMS-PAS-PFT-09-001 (2009)

35. CMS Collaboration, Commissioning of the particle-flow event reconstruction with the first LHC collisions recorded in the CMS detector. CMS Physics Analysis Summary CMS-PAS-PFT-10-001 (2010)

36. M. Cacciari, G.P. Salam, G. Soyez, The catchment area of jets. JHEP **04**, 005 (2008). doi:10.1088/1126-6708/2008/04/005. arXiv:0802.1188

37. CMS Collaboration, Performance of electron reconstruction and selection with the CMS detector in proton-proton collisions at $\sqrt{s} = 8$ Tev. JINST **10**, P06005 (2015). doi:10.1088/1748-0221/10/06/P06005. arXiv:1502.02701

38. CMS Collaboration, Determination of jet energy calibration and transverse momentum resolution in CMS. JINST **6**, P11002 (2011). doi:10.1088/1748-0221/6/11/P11002. arXiv:1107.4277

39. M. Cacciari, G.P. Salam, G. Soyez, The anti-k_t jet clustering algorithm. JHEP **04**, 063 (2008). doi:10.1088/1126-6708/2008/04/063. arXiv:0802.1189

40. CMS Collaboration, Identification of b-quark jets with the CMS experiment. JINST **8**, P04013 (2013). doi:10.1088/1748-0221/8/04/P04013. arXiv:1211.4462

41. CMS Collaboration, Missing transverse energy performance of the CMS detector. JINST **6**, P09001 (2011). doi:10.1088/1748-0221/6/09/P09001. arXiv:1106.5048

42. CMS Collaboration, Performance of the CMS missing transverse momentum reconstruction in pp data at $\sqrt{s} = 8$ TeV. JINST **10**, P02006 (2015). doi:10.1088/1748-0221/10/02/P02006. arXiv:1411.0511

43. CMS Collaboration, Measurement of the t$\bar{\text{t}}$ production cross section and the top quark mass in the dilepton channel in pp collisions at $\sqrt{s} =$ TeV. JHEP **07**, 049 (2011). doi:10.1007/JHEP07(2011)049. arXiv:1105.5661

44. J. d'Hondt et al., Fitting of event topologies with external kinematic constraints in CMS. CMS Note 2006-023 (2006)

45. D0 Collaboration, Measurement of the top quark mass using dilepton events. Phys. Rev. Lett. **80**, 2063 (1998). doi:10.1103/PhysRevLett.80.2063. arXiv:hep-ex/9706014

46. CMS Collaboration, Measurement of the Drell–Yan cross sections in pp collisions at $\sqrt{s} = 7$ TeV with the CMS experiment. JHEP **10**, 007 (2011). doi:10.1007/JHEP10(2011)007. arXiv:1108.0566

47. TOTEM Collaboration, First measurement of the total proton–proton cross section at the LHC energy of $\sqrt{s} = 7$ TeV. Europhys. Lett. **96**, 21002 (2011). doi:10.1209/0295-5075/96/21002. arXiv:1110.1395

48. A. Hoecker, V. Kartvelishvili, SVD approach to data unfolding. Nucl. Instrum. Methods A **372**, 469 (1996). doi:10.1016/0168-9002(95)01478-0. arXiv:hep-ph/9509307

49. V. Blobel, An unfolding method for high energy physics experiments (2002). arXiv:hep-ex/0208022

50. F. James, *Statistical Methods in Experimental Physics*, 2nd edn. (World Scientific, Singapore, 2006)

51. G.D. Lafferty, T.R. Wyatt, Where to stick your data points: the treatment of measurements within wide bins. Nucl. Instrum. Methods A **355**, 541 (1995). doi:10.1016/0168-9002(94)01112-5

Search for the associated production of the Higgs boson with a top-quark pair

The CMS collaboration

E-mail: cms-publication-committee-chair@cern.ch

ABSTRACT: A search for the standard model Higgs boson produced in association with a top-quark pair ($t\bar{t}H$) is presented, using data samples corresponding to integrated luminosities of up to $5.1\,\mathrm{fb}^{-1}$ and $19.7\,\mathrm{fb}^{-1}$ collected in pp collisions at center-of-mass energies of $7\,\mathrm{TeV}$ and $8\,\mathrm{TeV}$ respectively. The search is based on the following signatures of the Higgs boson decay: $H \to$ hadrons, $H \to$ photons, and $H \to$ leptons. The results are characterized by an observed $t\bar{t}H$ signal strength relative to the standard model cross section, $\mu = \sigma/\sigma_{\mathrm{SM}}$, under the assumption that the Higgs boson decays as expected in the standard model. The best fit value is $\mu = 2.8 \pm 1.0$ for a Higgs boson mass of $125.6\,\mathrm{GeV}$.

JHEP09(2014)087

Contents

1 Introduction

Since the discovery of a new boson by the CMS and ATLAS Collaborations [1, 2] in 2012, experimental studies have focused on determining the consistency of this particle's properties with the expectations for the standard model (SM) Higgs boson [3–8]. To date, all measured properties, including couplings, spin, and parity are consistent with the SM expectations within experimental uncertainties [9–13].

One striking feature of the SM Higgs boson is its strong coupling to the top quark relative to the other SM fermions. Based on its large mass [14] the top-quark Yukawa coupling is expected to be of order one. Because the top quark is heavier than the Higgs boson, its coupling cannot be assessed by measuring Higgs boson decays to top quarks.
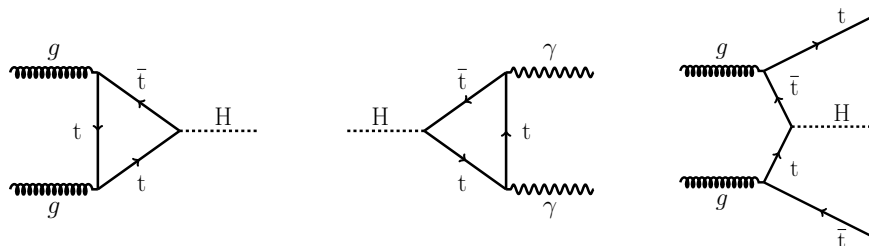
Figure 1. Feynman diagrams showing the gluon fusion production of a Higgs boson through a top-quark loop (left), the decay of a Higgs boson to a pair of photons through a top-quark loop (center), and the production of a Higgs boson in association with a top-quark pair (right). These diagrams are representative of SM processes with sensitivity to the coupling between the top quark and the Higgs boson.

However, the Higgs boson's coupling to top quarks can be experimentally constrained through measurements involving the gluon fusion production mechanism that proceeds via a fermion loop in which the top quark provides the dominant contribution (left panel of figure 1), assuming there is no physics beyond the standard model (BSM) contributing to the loop. Likewise the decay of the Higgs boson to photons involves both a fermion loop diagram dominated by the top-quark contribution (center panel of figure 1), as well as a W boson loop contribution. Current measurements of Higgs boson production via gluon fusion are consistent with the SM expectation for the top-quark Yukawa coupling within experimental uncertainties [9–12].

Probing the top-quark Yukawa coupling directly requires a process that results in both a Higgs boson and top quarks explicitly reconstructed via their final-state decay products. The production of a Higgs boson in association with a top-quark pair (t$\bar{\text{t}}$H) satisfies this requirement (right panel of figure 1). A measurement of the rate of t$\bar{\text{t}}$H production provides a direct test of the coupling between the top quark and the Higgs boson. Furthermore, several new physics scenarios [15–17] predict the existence of heavy top-quark partners, that would decay into a top quark and a Higgs boson. Observation of a significant deviation in the t$\bar{\text{t}}$H production rate with respect to the SM prediction would be an indirect indication of unknown phenomena.

The results of a search for t$\bar{\text{t}}$H production using the CMS detector [18] at the LHC are described in this paper. The small t$\bar{\text{t}}$H production cross section — roughly 130 fb at $\sqrt{s} = 8$ TeV [19–28]—makes measuring its rate experimentally challenging. Therefore, it is essential to exploit every accessible experimental signature. As the top quark decays with nearly 100% probability to a W boson and a b quark, the experimental signatures for top-quark pair production are determined by the decay of the W boson. When both W bosons decay hadronically, the resulting final state with six jets (two of which are b-quark jets) is referred to as the all-hadronic final state. If one of the W bosons decays leptonically, the final state with a charged lepton, a neutrino, and four jets (two of which are b-quark jets) is called lepton + jets. Finally, when both W bosons decay leptonically, the resulting

dilepton final state has two charged leptons, two neutrinos, and two b-quark jets. All three of these top-quark pair signatures are used in the search for t̄tH production in this paper. Although in principle, electrons, muons, and taus should be included as "charged leptons," experimentally, the signatures of a tau lepton are less distinctive than those of the electron or muon. For the rest of this paper, the term "charged lepton" will refer only to electrons or muons, including those coming from tau lepton decays.

Within the SM, the observed mass of the Higgs boson near 125 GeV [9, 29, 30] implies that a variety of Higgs boson decay modes are experimentally accessible. At this mass, the dominant decay mode, $H \rightarrow b\bar{b}$, contributes almost 60% of the total Higgs boson decay width. The next largest contribution comes from $H \rightarrow WW$ with a branching fraction around 20%. Several Higgs boson decay channels with significantly smaller branching fractions still produce experimentally accessible signatures, especially $H \rightarrow \gamma\gamma$, $H \rightarrow \tau\tau$, and $H \rightarrow ZZ$.

The experimental searches for t̄tH production presented here can be divided into three broad categories based on the Higgs boson signatures: $H \rightarrow$ hadrons, $H \rightarrow$ photons, and $H \rightarrow$ leptons. There are two main Higgs boson decay modes that contribute to the $H \rightarrow$ hadrons searches: $H \rightarrow b\bar{b}$ and $H \rightarrow \tau\tau$, where both τ leptons decay hadronically. Note that events with τ pairs include both direct $H \rightarrow \tau\tau$ decays and those where the τ leptons are produced by the decays of W or Z bosons from $H \rightarrow WW$ and $H \rightarrow ZZ$ decays. Events used in the $H \rightarrow$ hadrons searches have one or more isolated charged lepton from the W boson decays from the top quarks, which means these searches focus on the lepton + jets and dilepton t̄t final states, using single-lepton or dilepton triggers, respectively. Multivariate analysis (MVA) techniques are employed to tag the jets coming from b-quark or τ-lepton decays and to separate t̄tH events from the large t̄t+jets backgrounds.

In contrast, the $H \rightarrow$ photons search focuses exclusively on the $H \rightarrow \gamma\gamma$ decay mode. In this case, the photons provide the trigger, and all three t̄t decay topologies are included in the analysis. The CMS detector's excellent $\gamma\gamma$ invariant mass resolution [31] is used to separate the t̄tH signal from the background, and the background model is entirely based on data.

Finally, in the $H \rightarrow$ leptons search, the leptons arise as secondary decay products from $H \rightarrow WW$, $H \rightarrow ZZ$, and $H \rightarrow \tau\tau$ decays, as well as from the W bosons produced in the top quark decays. To optimize the signal-to-background ratio, events are required to have either a pair of same-sign charged leptons, or three or more charged leptons. The events are required to pass the dilepton or trilepton triggers. Multivariate analysis techniques are used to separate leptons arising from W-boson, Z-boson and τ-lepton decays, referred to as signal leptons, from background leptons, which come from b-quark or c-quark decays, or misidentified jets. MVA techniques are also used to distinguish t̄tH signal events from background events that are modeled using a mixture of control samples in data and Monte Carlo (MC) simulation. Table 1 summarizes the main features of each search channel described above.

To characterize the strength of the t̄tH signal relative to the SM cross section ($\mu = \sigma/\sigma_{SM}$) a fit is performed simultaneously in all channels. The fit uses specific discriminating distributions in each channel, either a kinematic variable like the diphoton invariant mass in the $H \rightarrow$ photons channel or an MVA discriminant as in the $H \rightarrow$ hadrons and $H \rightarrow$

– 3 –

Category	Signature	Trigger	Signature
H → Hadrons H → b$\bar{\text{b}}$ H → $\tau_\text{h}\tau_\text{h}$ H → WW	Lepton + Jets (t$\bar{\text{t}}$H → $\ell\nu$jjbbbb)	Single Lepton	1 e/μ, $p_\text{T} > 30\,\text{GeV}$ $\geq$4 jets + $\geq$2 b-tags, $p_\text{T} > 30\,\text{GeV}$
	Dilepton (t$\bar{\text{t}}$H → $\ell\nu\ell\nu$bbbb)	Dilepton	1 e/μ, $p_\text{T} > 20\,\text{GeV}$ 1 e/μ, $p_\text{T} > 10\,\text{GeV}$ $\geq$3 jets + $\geq$2 b-tags, $p_\text{T} > 30\,\text{GeV}$
	Hadronic τ (t$\bar{\text{t}}$H → $\ell\nu\tau_\text{h}[\nu]\tau_\text{h}[\nu]$jjbb)	Single Lepton	1 e/μ, $p_\text{T} > 30\,\text{GeV}$ 2 τ_h, $p_\text{T} > 20\,\text{GeV}$ $\geq$2 jets + 1-2 b-tags, $p_\text{T} > 30\,\text{GeV}$
H → Photons H → $\gamma\gamma$	Leptonic (t$\bar{\text{t}}$H → $\ell\nu$jjbb$\gamma\gamma$, t$\bar{\text{t}}$H → $\ell\nu\ell\nu$bb$\gamma\gamma$)	Diphoton	2 γ, $p_\text{T} > m_{\gamma\gamma}/2\,(25)\,\text{GeV}$ for 1st (2nd) $\geq$1 e/μ, $p_\text{T} > 20\,\text{GeV}$ $\geq$2 jets + $\geq$1 b-tags, $p_\text{T} > 25\,\text{GeV}$
	Hadronic (t$\bar{\text{t}}$H → jjjjbb$\gamma\gamma$)	Diphoton	2 γ, $p_\text{T} > m_{\gamma\gamma}/2\,(25)\,\text{GeV}$ for 1st (2nd) 0 e/μ, $p_\text{T} > 20\,\text{GeV}$ $\geq$4 jets + $\geq$1 b-tags, $p_\text{T} > 25\,\text{GeV}$
H → Leptons H → WW H → $\tau\tau$ H → ZZ	Same-Sign Dilepton (t$\bar{\text{t}}$H → $\ell^\pm\nu\ell^\pm[\nu]$jjj[j]bb)	Dilepton	2 e/μ, $p_\text{T} > 20\,\text{GeV}$ $\geq$4 jets + $\geq$1 b-tags, $p_\text{T} > 25\,\text{GeV}$
	3 Lepton (t$\bar{\text{t}}$H → $\ell\nu\ell[\nu]\ell[\nu]$j[j]bb)	Dilepton, Trielectron	1 e/μ, $p_\text{T} > 20\,\text{GeV}$ 1 e/μ, $p_\text{T} > 10\,\text{GeV}$ 1 e(μ), $p_\text{T} > 7(5)\,\text{GeV}$ $\geq$2 jets + $\geq$1 b-tags, $p_\text{T} > 25\,\text{GeV}$
	4 Lepton (t$\bar{\text{t}}$H → $\ell\nu\ell\nu\ell[\nu]\ell[\nu]$bb)	Dilepton, Trielectron	1 e/μ, $p_\text{T} > 20\,\text{GeV}$ 1 e/μ, $p_\text{T} > 10\,\text{GeV}$ 2 e(μ), $p_\text{T} > 7(5)\,\text{GeV}$ $\geq$2 jets + $\geq$1 b-tags, $p_\text{T} > 25\,\text{GeV}$

Table 1. Summary of the search channels used in the t$\bar{\text{t}}$H analysis. In the description of the signatures, an ℓ refers to any electron or muon in the final state (including those coming from leptonic τ decays). A hadronic τ decay is indicated by τ_h. Finally, j represents a jet coming from any quark or gluon, or an unidentified hadronic τ decay, while b represents a b-quark jet. Any element in the signature enclosed in square brackets indicates that the element may not be present, depending on the specific decay mode of the top quark or Higgs boson. The minimum transverse momentum p_T of various objects is given to convey some sense of the acceptance of each search channel; however, additional requirements are also applied. Jets labeled as b-tagged jets have been selected using the algorithm described in section 4. More details on the triggers used to collect data for each search channel are given in section 3. Selection of final-state objects (leptons, photons, jets, etc.) is described in general in section 4, with further channel-specific details included in sections 5–7. In this table and the rest of the paper, the number of b-tagged jets is always included in the jet count. For example, the notation 4 jets + 2 b-tags means four jets of which two jets are b-tagged.

– 4 –

leptons cases. The uncertainties involved in the background modeling are introduced in the fit as nuisance parameters, so that the best-fit parameters provide an improved description of the background.

This paper is structured as follows. Sections 2 and 3 describe the CMS detector, and the data and simulation samples, respectively. Section 4 discusses the common object reconstruction and identification details shared among the different search channels. Sections 5, 6, and 7 outline the selection, background modeling, and signal extraction techniques for the H → hadrons, H → photons, and H → leptons analyses, respectively. Section 8 details the impact of systematic uncertainties on the searches. Finally, the combination procedure and results are presented in section 9, followed by a summary in section 10.

2 The CMS detector

The central feature of the CMS apparatus is a superconducting solenoid of $6\,\mathrm{m}$ internal diameter, providing an axial magnetic field of $3.8\,\mathrm{T}$ parallel to the beam direction. Within the superconducting solenoid volume, there are a silicon pixel and strip tracker, a lead tungstate crystal electromagnetic calorimeter (ECAL), and a brass/scintillator hadron calorimeter (HCAL). The tracking detectors provide coverage for charged particles within $|\eta| < 2.5$. The ECAL and HCAL calorimeters provide coverage up to $|\eta| < 3.0$. The ECAL is divided into two distinct regions: the barrel region, which covers $|\eta| < 1.48$, and the endcap region, which covers $1.48 < |\eta| < 3.0$. A quartz-fiber forward calorimeter extends the coverage further up to $|\eta| < 5.0$. Muons are measured in gas-ionization detectors embedded in the steel flux-return yoke outside the solenoid. The first level (L1) of the CMS trigger system, composed of custom hardware processors, uses information from the calorimeters and muon detectors to select the most interesting events in a fixed time interval of less than $4\,\mu\mathrm{s}$. The high-level trigger (HLT) processor farm further decreases the event rate from around $100\,\mathrm{kHz}$ to less than $1\,\mathrm{kHz}$, before data storage. A more detailed description of the CMS detector, together with a definition of the coordinate system used and the relevant kinematic variables, can be found in ref. [18].

3 Data and simulation samples

This search is performed with samples of proton-proton collisions at $\sqrt{s} = 7\,\mathrm{TeV}$, collected with the CMS detector in 2011 (referred to as the 7 TeV dataset), and at $\sqrt{s} = 8\,\mathrm{TeV}$, collected in 2012 (referred to as the 8 TeV dataset). All of the search channels make use of the full CMS 8 TeV dataset, corresponding to an integrated luminosity that ranges from $19.3\,\mathrm{fb}^{-1}$ to $19.7\,\mathrm{fb}^{-1}$, with a 2.6% uncertainty [32]. The luminosity used varies slightly because the different search channels have slightly different data quality requirements, depending on the reconstructed objects and triggers used. In addition, the H → photons analysis makes use of data collected at $\sqrt{s} = 7\,\mathrm{TeV}$, corresponding to an integrated luminosity of $5.1\,\mathrm{fb}^{-1}$. Finally, the $t\bar{t}H$ search in the H → $b\bar{b}$ final state based on the 7 TeV dataset with an integrated luminosity of $5.0\,\mathrm{fb}^{-1}$, described in ref. [33], is combined with the 8 TeV analysis to obtain the final $t\bar{t}H$ result. The uncertainty on the 7 TeV luminosity is 2.2% [34].

In the H → hadrons and H → leptons analyses, events are selected by triggering on the presence of one or more leptons. For the H → photons analysis, diphoton triggers are used.

Single-lepton triggers are used for channels with one lepton in the final state. The single-electron trigger requires the presence of an isolated, good-quality electron with transverse momentum $p_T > 27$ GeV. The single-muon trigger requires a muon candidate isolated from other activity in the event with $p_T > 24$ GeV. Dilepton triggers are used for channels with two or more leptons in the final state. The dilepton triggers require any combination of electrons and muons, one lepton with $p_T > 17$ GeV and another with $p_T > 8$ GeV. In the H → leptons analysis, a trielectron trigger is used, with minimum p_T thresholds of 15 GeV, 8 GeV, and 5 GeV. The H → photons analysis uses diphoton triggers with two different photon identification schemes. One requires calorimetric identification based on the electromagnetic shower shape and isolation of the photon candidate. The other requires only that the photon has a high value of the R_9 shower shape variable, where R_9 is calculated as the ratio of the energy contained in a 3×3 array of ECAL crystals centered on the most energetic deposit in the supercluster to the energy of the whole supercluster. The superclustering algorithm for photon reconstruction is explained in more detail in section 4. The E_T thresholds at trigger level are 26 (18) GeV and 36 (22) GeV on the leading (trailing) photon depending on the running period. To maintain high trigger efficiency, all four combinations of thresholds and selection criteria are used.

Expected signal events and, depending on the analysis channel, some background processes are modeled with MC simulation. The t$\bar{\text{t}}$H signal is modeled using the PYTHIA generator [35] (version 6.4.24 for the 7 TeV dataset and version 6.4.26 for the 8 TeV dataset). Separate samples were produced at nine different values of m_H: 110, 115, 120, 122.5, 125, 127.5, 130, 135, and 140 GeV, and are used to interpolate for intermediate mass values. The background processes t$\bar{\text{t}}$W, t$\bar{\text{t}}$Z, t$\bar{\text{t}}$+jets, Drell-Yan+jets, W+jets, ZZ+jets, WW+jets, and WZ+jets are all generated with the MADGRAPH 5.1.3 [36] tree-level matrix element generator, combined with PYTHIA for the parton shower and hadronization. For the H → leptons analysis, the rare WWZ, WWW, t$\bar{\text{t}} + \gamma$+jets, and t$\bar{\text{t}}$WW processes are generated similarly. Single top quark production (t+q, t+b, and t+W) is modeled with the next-to-leading-order (NLO) generator POWHEG 1.0 [37–42] combined with PYTHIA. Samples that include top quarks in the final state are generated with a top quark mass of 172.5 GeV. For the H → photons analysis, the gluon fusion (gg → H) and vector boson fusion (q$\bar{\text{q}}$ → q$\bar{\text{q}}$H) production modes are generated with POWHEG at NLO, and combined with PYTHIA for the parton shower and hadronization. Higgs boson production in association with weak bosons (q$\bar{\text{q}}$ → WH/ZH) is simulated with PYTHIA. Samples generated with a leading order generator use the CTEQ6L1 parton distribution function (PDF) [43] set, while samples generated with NLO generators use the CTEQ6.6M PDF set [44].

The CMS detector response is simulated using the GEANT4 software package [45]. All events from data and simulated samples are required to pass the same trigger conditions and are reconstructed with identical algorithms to those used for collision data. Effects from additional pp interactions in the same bunch crossing (pileup) are modeled by adding simulated minimum bias events (generated with PYTHIA) to the generated hard interactions. The pileup interaction multiplicity distribution in simulation reflects the luminosity

profile observed in pp collision data. Additional correction factors are applied to individual object efficiencies and energy scales to bring the MC simulation into better agreement with data, as described in section 4.

4   Object reconstruction and identification

A global event description is obtained with the CMS particle-flow (PF) algorithm [46, 47], which optimally combines the information from all CMS sub-detectors to reconstruct and identify each individual particle in the pp collision event. The particles are classified into mutually exclusive categories: charged hadrons, neutral hadrons, photons, muons, and electrons. The primary collision vertex is identified as the reconstructed vertex with the highest value of $\sum p_{\mathrm{T}}^2$, where the summation includes all particles used to reconstruct the vertex. Although the separate $t\bar{t}H$ search channels share the same overall object reconstruction and identification approach, there are differences in some of the selection requirements. Generally speaking, the requirements in the $H \rightarrow$ hadrons channel are more stringent than in the $H \rightarrow$ photons or leptons because of the larger backgrounds in the first channel and the smaller amount of signal in the other ones.

Photon candidates are reconstructed from the energy deposits in the ECAL, grouping the individual clusters into a supercluster. The superclustering algorithms achieve an almost complete reconstruction of the energy of photons (and electrons) that convert into electron-positron pairs (emit bremsstrahlung) in the material in front of the ECAL. In the barrel region, superclusters are formed from five-crystal-wide strips in η, centered on the locally most energetic crystal (seed), and have a variable extension in ϕ. In the endcaps, where the crystals are arranged according to an x-y rather than an η-ϕ geometry, matrices of 5×5 crystals (which may partially overlap) around the most energetic crystals are merged if they lie within a narrow ϕ road. The photon candidates are collected within the ECAL fiducial region $|\eta| < 2.5$, excluding the barrel-endcap transition region $1.44 < |\eta| < 1.57$ where photon reconstruction is sub-optimal. Isolation requirements are applied to photon candidates by looking at neighboring particle candidates reconstructed with the PF event reconstruction technique [46]. Additional details on photon reconstruction and identification can be found in ref. [30].

Electrons with $p_{\mathrm{T}} > 7\,\mathrm{GeV}$ are reconstructed within the geometrical acceptance of the tracker, $|\eta| < 2.5$. The reconstruction combines information from clusters of energy deposits in the ECAL and the electron trajectory reconstructed in the inner tracker [48–51]. The track-cluster matching is initiated either "outside-in" from ECAL clusters, or "inside-out" from track candidates. Trajectories in the tracker volume are reconstructed using a dedicated modeling of the electron energy loss and fitted with a Gaussian sum filter [48]. The electron momentum is determined from the combination of ECAL and tracker measurements. Electron identification relies on a multivariate technique that combines observables sensitive to the amount of bremsstrahlung along the electron trajectory, the spatial and momentum matching between the electron trajectory and associated clusters, and shower shape observables. In order to increase the lepton efficiency, the $H \rightarrow$ leptons analysis uses a looser cut on the multivariate discriminant than do the other analysis channels. Al-

though the minimum p_T requirement on electrons is $p_T > 7\,\text{GeV}$, the different $t\bar{t}H$ search channels, particularly the H → hadrons channel, use a higher threshold on some of the selected electrons depending on the trigger requirements and to help control backgrounds (see sections 5–7 for more details).

Muons are reconstructed within $|\eta| < 2.4$ and for $p_T > 5\,\text{GeV}$ [52]. The reconstruction combines information from both the silicon tracker and the muon spectrometer. The matching between the inner and outer tracks is initiated either "outside-in", starting from a track in the muon system, or "inside-out", starting from a track in the silicon tracker. The PF muons are selected among the reconstructed muon track candidates by applying minimal requirements on the track components in the muon and tracker systems and taking into account matching with energy deposits in the calorimeters [53]. Depending on the level of backgrounds in a given analysis channel, different requirements can be placed on the distance of closest approach for the muon to the collision vertex — referred to as the impact parameter (IP)—in both the $z-$direction (d_z) and the $x-y$ plane (d_{xy}) to reject background muons. As in the electron case, the p_T threshold for some or all of the muons is set higher than the $5\,\text{GeV}$ default, depending on the trigger requirements used by a particular search channel and to control backgrounds.

An important quantity for distinguishing signal and background leptons is isolation. Although conceptually similar, isolation is defined slightly differently for muons and electrons depending on the analysis channel. Muon isolation is assessed by calculating the sum of the transverse energy of the other particles in a cone of $\Delta R = \sqrt{(\Delta\eta)^2 + (\Delta\phi)^2} = 0.4$ around the muon direction, excluding the muon itself, where $\Delta\eta$ and $\Delta\phi$ are the angular differences between the muon and the other particles in the η and ϕ directions. To correct for the effects of pileup, charged contributions not originating from the primary collision vertex are explicitly removed from the isolation sum, and the neutral contribution is corrected assuming a ratio of 0.5 for the contribution of neutral to charged objects to the pileup activity. The ratio of the corrected isolation sum to the muon p_T is the relative isolation of the muon. For the H → leptons search, electron isolation is calculated identically to muon isolation. For the H → hadrons and H → photons searches, there are two differences. The first is that the electron isolation sum only takes into account charged and neutral particles in a cone of $\Delta R = 0.3$. Second, the correction for pileup effects to the neutral contribution in the isolation sum is made using the average p_T density calculated from neutral particles multiplied by the effective area of the isolation cone. The relative isolation is the ratio of this corrected isolation sum to the electron p_T.

Jets are reconstructed by clustering the charged and neutral PF particles using the anti-k_T algorithm with a distance parameter of 0.5 [54, 55]. For the H → hadrons search, particles identified as isolated muons and electrons are expected to come from W-boson decays and are excluded from the clustering. Non-isolated muons and electrons are expected to come from b-quark decays and are included in the clustering. The H → leptons and H → photons searches do not exclude the isolated leptons from the jet clustering, but require selected jets to be separated by $\Delta R > 0.5$ from the selected leptons. The choice not to exclude leptons from the clustered jets in the H → leptons search is an integral part of the non-prompt lepton rejection strategy. When a lepton is clustered into a jet, that

information is used to help determine whether the lepton originated from a semileptonic decay of a heavy (bottom or charm) quark (see section 7 for more details).

Jets are required to have at least two PF constituents and more than 1% of their energy in both the electromagnetic and hadronic components to reject jets arising from instrumental effects. For the H → leptons and H → photons searches, additional requirements are applied to remove jets coming from pileup vertices [56]. For the H → hadrons and H → leptons analyses, charged PF particles not associated with the primary event vertex are ignored when clustering the jets to reduce the contribution from pileup. The momentum of the clustered jet is corrected for a variety of effects [57]. The component coming from pileup activity — in the case of H → hadrons or leptons, just the neutral part — is removed by applying a residual energy correction following the area-based procedure described in refs. [58, 59]. Further corrections based on simulation, γ/Z+jets data, and dijet data are then applied, as well as a correction to account for residual differences between data and simulation [57]. Selected jets are required to have $|\eta| < 2.4$, and $p_T > 25\,\text{GeV}$ (H → leptons and H → photons) or $p_T > 30\,\text{GeV}$ (H → hadrons). The higher p_T requirement in the latter case arises from the larger amount of background in that sample.

Jets are identified as originating from a b-quark using the combined secondary vertex (CSV) algorithm [60, 61] that utilizes information about the impact parameter of tracks and reconstructed secondary vertices within the jets in a multivariate algorithm. The CSV algorithm provides a continuous output ranging from 0 to 1; high values of the CSV discriminant indicate that the jet likely originates from a b quark, while low values indicate the jet is more consistent with light-flavor quarks or gluons. The efficiency to tag b-quark jets and the rate of misidentification of non-b-quark jets depend on the working point chosen. For the medium working point of the CSV algorithm, the b-tagging efficiency is around 70% (20%) for jets originating from a b (c) quark and the probability of mistagging for jets originating from light quarks or gluons is approximately 2%. For the loose working point, the efficiency to tag jets from b (c) quarks is approximately 85% (40%) and the probability to tag jets from light quarks or gluons is about 10%. These efficiencies and mistag probabilities vary with the p_T and η of the jets, and the values quoted are indicative of the predominant jets in this analysis.

The hadronic decay of a τ lepton (τ_h) produces a narrow jet of charged and neutral hadrons — almost all pions. Each neutral pion subsequently decays into a pair of photons. The identification of τ_h jets begins with the formation of PF jets by clustering charged hadron and photon objects via the anti-k_T algorithm. Then, the hadron-plus-strips (HPS) [62, 63] algorithm tests each of the most common τ_h decay mode hypotheses using the electromagnetic objects found within rectangular bands along the azimuthal direction. In the general algorithm, combinations of charged hadrons and photons (one charged hadron, one charged hadron + photons, and three charged hadrons) must lead to invariant masses consistent with the appropriate intermediate resonances [63]. For this analysis, only the decays involving exactly one charged hadron are used.

The missing transverse energy vector is calculated as the negative vector p_T sum of all PF candidates identified in the event. The magnitude of this vector is denoted as E_T^{miss}. Since pileup interactions degrade the performance of the E_T^{miss} variable, the H → leptons

– 9 –

search also uses the $H_\mathrm{T}^\mathrm{miss}$ variable. This variable is computed in the same way as the $E_\mathrm{T}^\mathrm{miss}$, but uses only the selected jets and leptons. The $H_\mathrm{T}^\mathrm{miss}$ variable has worse resolution than $E_\mathrm{T}^\mathrm{miss}$ but it is more robust as it does not rely on soft objects in the event. A linear discriminator is computed based on the two variables,

$$L_\mathrm{D} = 0.60 E_\mathrm{T}^\mathrm{miss} + 0.40 H_\mathrm{T}^\mathrm{miss}, \qquad (4.1)$$

exploiting the fact that $E_\mathrm{T}^\mathrm{miss}$ and $H_\mathrm{T}^\mathrm{miss}$ are less correlated in events with missing transverse energy from instrumental mismeasurement than in events with genuine missing transverse energy. The linear discriminant is constructed to optimize separation between $t\bar{t}H$ and Z+jets in simulation.

To match the performance of reconstructed objects between data and simulation, the latter is corrected with the following data-MC scale factors: leptons are corrected for the difference in trigger efficiency, as well as in lepton identification and isolation efficiency. For the H → leptons channel, corrections accounting for residual differences between data and simulation are applied to the muon momentum, as well as to the ECAL energy before combining with the tracking momentum for electrons. All lepton corrections are derived using tag-and-probe techniques [64] based on samples with Z boson and J/ψ decays into two leptons. Jet energy corrections as described above are applied as a function of the jet p_T and η [57]. Standard efficiency scale factors for the medium and loose b-tagging working points [60, 61] are applied for light- and heavy-flavor jets in the H → leptons and H → photons searches, while the H → hadrons search uses a more sophisticated correction to the CSV shape (see section 5 for more details).

5 H → hadrons

5.1 Event selection

Events in the H → hadrons analysis are split into three different channels based on the decay modes of the top-quark pair and the Higgs boson: the lepton+jets channel ($t\bar{t} \to \ell\nu q\bar{q}'b\bar{b}$, H → $b\bar{b}$), the dilepton channel ($t\bar{t} \to \ell^+\nu\ell^-\bar{\nu}b\bar{b}$, H → $b\bar{b}$), and the τ_h channel ($t\bar{t} \to \ell\nu q\bar{q}'b\bar{b}$, H → $\tau_\mathrm{h}\tau_\mathrm{h}$), where a lepton is an electron or a muon. For the lepton+jets channel, events containing an energetic, isolated lepton, and at least four energetic jets, two or more of these jets must be b-tagged, are selected. For the dilepton channel, a pair of oppositely charged leptons and three or more jets, with at least two of the jets being b-tagged, are required. For the τ_h channel, beyond the two identified hadronically decaying τ leptons, at least two jets, one or two of which must be b-tagged, are required. The event selections are designed to be mutually exclusive. For all figures (figures 2–7) and tables (tables 2–4) of the H → hadrons analysis, the b-tagged jets are included in the jet count.

In addition to the baseline selection detailed in section 4, two additional sets of selection criteria are applied to leptons in the H → hadrons analysis: tight and loose, described below. All events are required to contain at least one tight electron or muon. Loose requirements are only applied to the second lepton in the dilepton channel.

Tight and loose muons differ both in the identification and kinematic requirements. For events in the lepton+jets and τ_h channels, tight muons are required to have $p_\mathrm{T} > 30\,\mathrm{GeV}$

and $|\eta| < 2.1$ to ensure that the trigger is fully efficient with respect to the offline selection. Tight muons in the dilepton channel have a lower p_T threshold at $20\,\mathrm{GeV}$. Loose muons must have $p_T > 10\,\mathrm{GeV}$ and $|\eta| < 2.4$. For tight (loose) muons, the relative isolation is required to be less than $0.12\,(0.2)$. Tight muons must also satisfy additional quality criteria based on the number of hits associated with the muon candidate in the pixel, strip, and muon detectors. To ensure the muon is from a W decay, it is required to be consistent with originating from the primary vertex with an impact parameter in the $x - y$ plane $d_{xy} < 0.2\,\mathrm{cm}$ and distance from the primary vertex in the z-direction $d_z < 0.5\,\mathrm{cm}$. For loose muons, no additional requirements beyond the baseline selection are applied.

Tight electrons in the lepton+jets and τ_h channels are required to have $p_T > 30\,\mathrm{GeV}$, while the dilepton channel requires $p_T > 20\,\mathrm{GeV}$. Loose electrons are required to have $p_T > 10\,\mathrm{GeV}$. All electrons must have $|\eta| < 2.5$, and those that fall into the transition region between the barrel and endcap of the ECAL ($1.44 < |\eta| < 1.57$) are rejected. Tight electrons must have a relative isolation less than 0.1, while loose electrons must have a relative isolation less than 0.2. In a manner similar to tight muons, tight electrons are required to have $d_{xy} < 0.02\,\mathrm{cm}$ and $d_z < 1\,\mathrm{cm}$, while loose electrons must have $d_{xy} < 0.04\,\mathrm{cm}$.

For τ leptons decaying hadronically, only candidates with well-reconstructed decay modes [63] that contain exactly one charged pion are accepted. Candidates must have $p_T > 20\,\mathrm{GeV}$ and $|\eta| < 2.1$, and the p_T of the charged pion must be greater than $5\,\mathrm{GeV}$. Candidates are additionally required to fulfill criteria that reject electrons and muons mimicking hadronic τ-lepton decays. These include requirements on the consistency of information from the tracker, calorimeters, and muon detectors, including the absence of large energy deposits in the calorimeters for muons and bremsstrahlung pattern recognition for electrons. A multivariate discriminant, which takes into account the effects of pileup, is used to select loosely isolated τ_h candidates [65]. Finally, the τ_h candidates must be separated from the single tight muon or electron in the event by a distance $\Delta R > 0.25$. Events are required to contain at least one pair of oppositely charged τ_h candidates. In the case that multiple valid pairs exist, the pair with the most isolated τ_h signatures, based on the aforementioned MVA discriminant, is chosen.

While the basic jet p_T threshold is $30\,\mathrm{GeV}$, in the lepton+jets channel, the leading three jets must have $p_T > 40\,\mathrm{GeV}$. Jets originating from b quarks are identified using the CSV medium working point.

5.2 Background modeling

All the backgrounds in the $\mathrm{H} \to$ hadrons analysis are normalized using NLO or better inclusive cross section calculations [66–71]. To determine the contribution of individual physics processes to exclusive final states as well as to model the kinematics, the MC simulations described in section 3 are used. The main background, $t\bar{t}+$ jets, is generated using MadGraph inclusively, with tree-level diagrams for up to $t\bar{t}+3$ extra partons. These extra partons include both b and c quarks. However, as there are significantly different uncertainties in the production of additional light-flavor (lf) jets compared to heavy-flavor (hf), the $t\bar{t}+$jets sample is separated into subsamples based on the quark flavor associated with the reconstructed jets in the event. Events where at least two reconstructed jets are

– 11 –

matched at the generator level to extra b quarks (that is b quarks not originating from a top-quark decay) are labeled as $t\bar{t} + b\bar{b}$ events. If only a single jet is matched to a b quark, the event is classed as $t\bar{t}+b$. These cases typically arise because the second extra b quark in the event is either too far forward or too soft to be reconstructed as a jet, or the two extra b quarks have merged into a single jet. Finally, if at least one reconstructed jet is matched to a c quark at the generator level, the event is labeled as $t\bar{t} + c\bar{c}$. Different systematic uncertainties affecting both rates and shapes are applied to each of the separate subsets of the $t\bar{t}$+jets sample, as described in section 8.

Besides the common corrections to MC samples described in section 4, additional correction factors are applied for samples modeling the backgrounds for this analysis channel. A correction factor to $t\bar{t}$+jets MC samples is applied so that the top-quark p_T spectrum from MADGRAPH agrees with the distribution observed in data and predicted by higher-order calculations. These scale factors, which range from roughly 0.75 to 1.2, were derived from a fully corrected measurement of the $t\bar{t}$ differential cross section as function of the top-quark p_T using the $\sqrt{s} = 8$ TeV dataset obtained using the same techniques as described in ref. [72].

Furthermore, a dedicated correction to the CSV b-tagging rates is applied to all the MC samples. The CSV discriminant is used to identify b-quark jets, and the CSV discriminant shape is used in the signal extraction technique to distinguish between events with additional genuine b-quark jets and those with mistags. Therefore, a correction for the efficiency difference between data and simulation over the whole range of discriminator values is applied. The scale factors — which are between 0.7 and 1.3 for the bulk of the jets — are derived separately for light-flavor (including gluons) and b-quark jets using two independent samples of 8 TeV data in the dilepton channel. Both control samples are also orthogonal to the events used in the signal extraction. The light-flavor scale factor derivation uses a control sample enriched in events with a Z boson, selected by requiring a pair of opposite-charge, same-flavor leptons and exactly two jets. The b-quark scale factor is derived in a sample dominated by dileptonic $t\bar{t}$, a signature that includes exactly two b-quark jets, by selecting events with two leptons that are not consistent with a Z boson decay and exactly two jets. Using these control samples, a tag-and-probe approach is employed where one jet ("tag") passes the appropriate b-tagging requirement for a light-flavor or b-quark jet. The CSV discriminant of the other jet ("probe") is compared between the data and simulation, and the ratio gives a scale factor for each jet as a function of CSV discriminant value, p_T and η. Each light-flavor or b-quark jet is then assigned an appropriate individual scale factor. The CSV output shape for c-quark jets is dissimilar to that of both light-flavor and b-quark jets; hence, in the absence of a control sample of c-quark jets in data, a scale factor of 1 is applied, with twice the relative uncertainty ascertained from b-quark jets (see section 8). These CSV scale factors are applied to simulation on an event-by-event basis where the overall scale factor is the product of the individual scale factors for each jet in the event. This procedure was checked using control samples.

Tables 2, 3, and 4 show the predicted event yields compared to data after the selection in the lepton+jets, dilepton, and τ_h channels, respectively. The tables are sub-divided into the different jet and b-tag categories used in each channel. The signal yield is the SM

– 12 –

	≥6 jets + 2 b-tags	4 jets + 3 b-tags	5 jets + 3 b-tags	≥6 jets + 3 b-tags	4 jets + 4 b-tags	5 jets + ≥4 b-tags	≥6 jets + ≥4 b-tags
$t\bar{t}H(125.6\,\mathrm{GeV})$	28.5 ± 2.5	12.4 ± 1.0	18.1 ± 1.5	18.9 ± 1.5	1.5 ± 0.2	4.4 ± 0.4	6.7 ± 0.6
$t\bar{t}$+lf	7140 ± 310	4280 ± 150	2450 ± 130	1076 ± 74	48.4 ± 10.0	54 ± 12	44 ± 11
$t\bar{t}$+b	570 ± 170	364 ± 94	367 ± 98	289 ± 87	20.0 ± 5.5	28.6 ± 8.0	33 ± 10
$t\bar{t} + b\bar{b}$	264 ± 59	123 ± 29	193 ± 42	232 ± 49	15.8 ± 3.6	45.2 ± 9.7	86 ± 18
$t\bar{t} + c\bar{c}$	2420 ± 300	690 ± 130	800 ± 130	720 ± 110	29.7 ± 5.6	55 ± 11	81 ± 13
$t\bar{t}$+W/Z	85 ± 11	15.0 ± 2.0	20.9 ± 2.8	24.7 ± 3.3	1.0 ± 0.2	2.1 ± 0.4	4.7 ± 0.8
Single t	236 ± 18	213 ± 17	101.7 ± 10.0	47.7 ± 6.7	2.8 ± 1.4	7.5 ± 3.8	6.7 ± 2.6
W/Z+jets	75 ± 27	46 ± 30	13 ± 12	7.7 ± 8.8	1.1 ± 1.2	0.9 ± 1.0	0.3 ± 0.8
Diboson	4.5 ± 1.0	5.4 ± 0.9	2.0 ± 0.5	1.0 ± 0.4	0.2 ± 0.2	0.1 ± 0.1	0.2 ± 0.1
Total bkg	10790 ± 200	5730 ± 110	3935 ± 74	2394 ± 65	119.0 ± 8.2	193.4 ± 10.0	256 ± 16
Data	10724	5667	3983	2426	122	219	260

Table 2. Expected event yields for signal ($m_H = 125.6\,\mathrm{GeV}$) and backgrounds in the lepton+jets channel. Signal and background normalizations used for this table are described in the text.

prediction (μ fixed to 1). In these tables, background yields and uncertainties use the best-fit value of all nuisance parameters, with μ fixed at 1. For more details about the statistical treatment and the definition of μ, see section 9. The expected and observed yields agree well in all final states across the different jet and b-tag categories.

Figures 2, 3, and 4 show the data-to-simulation comparisons of variables that give the best signal-background separation in each of the lepton+jets, dilepton, and τ_h channels, respectively. In these plots, the background is normalized to the SM expectation; the uncertainty band (shown as a hatched band in the stack plot and a green band in the ratio plot) includes statistical and systematic uncertainties that affect both the rate and shape of the background distributions. For the ratio plots shown below each distribution, only the background expectation (and not the signal) is included in the denominator of the ratio. The contribution labeled "EWK" is the sum of the diboson and W/Z+jets backgrounds. The $t\bar{t}H$ signal ($m_H = 125.6\,\mathrm{GeV}$) is not included in the stacked histogram, but is shown as a separate open histogram normalized to 30 times the SM expectation ($\mu = 30$). To calculate the variable second $m(\mathrm{jj,H})$, the invariant masses of all jet pairs with at least one b-tagged jet are calculated and the jet pair whose mass is the second closest to the Higgs boson mass is chosen. Within the uncertainties, the simulation reproduces well the shape and the normalization of the distributions.

5.3 Signal extraction

Boosted decision trees (BDTs) [73] are used to further improve signal sensitivity. In the lepton+jets and dilepton channels, BDTs are trained separately for each category, using the $t\bar{t}H$ sample with $m_H = 125\,\mathrm{GeV}$. The three dilepton categories use a single BDT. Of the seven lepton+jets categories, four categories use a single BDT, while three categories each use two BDTs in a tiered configuration. The tiered configuration includes one BDT that is trained specifically to discriminate between $t\bar{t}H$ and $t\bar{t}b\bar{b}$ events, the output of which

– 13 –
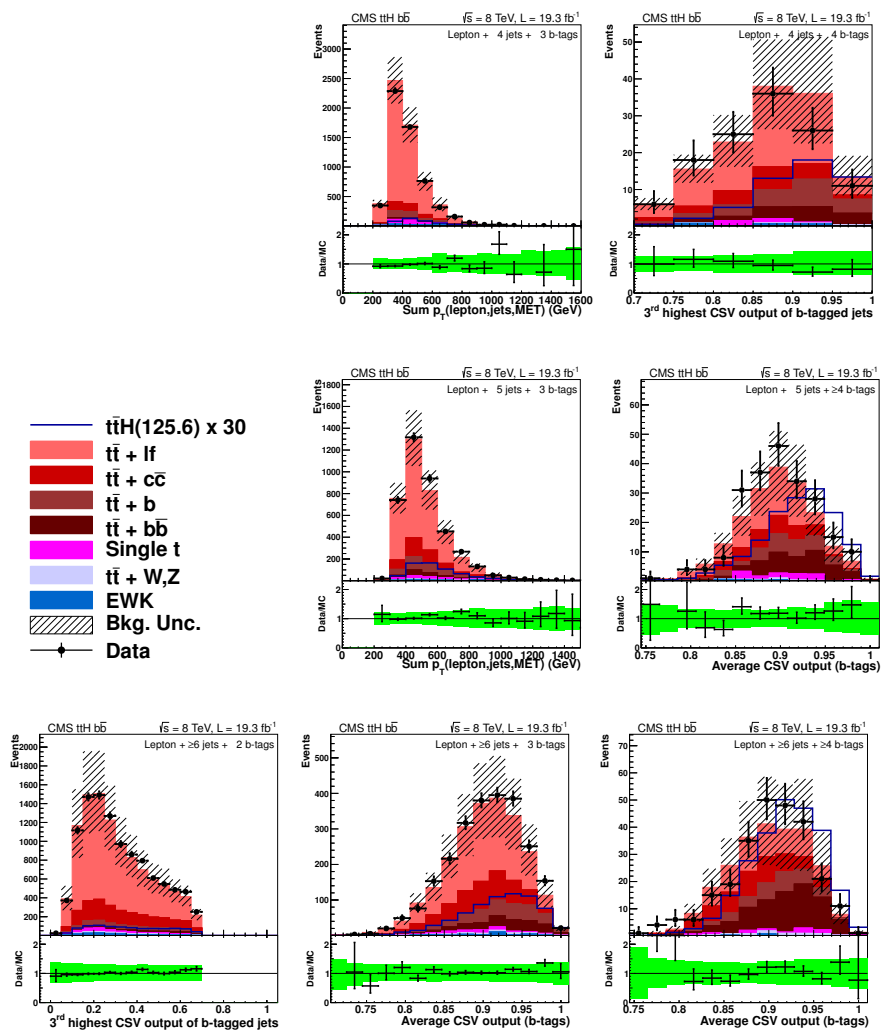
Figure 2. Input variables that give the best signal-background separation for each of the lepton+jets categories used in the analysis at $\sqrt{s} = 8\,\mathrm{TeV}$. The top, middle, and bottom rows show the events with 4, 5, and $\geq$6 jets, respectively, while the left, middle, and right columns are events with 2, 3, and $\geq$4 b-tags, respectively. More details regarding these plots are found in the text.
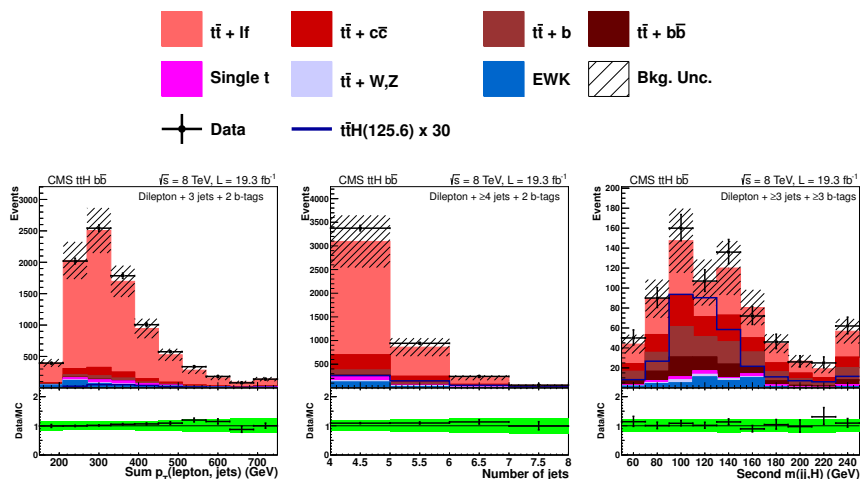
Figure 3. Input variables that give the best signal-background separation for each of the dilepton categories used in the analysis at $\sqrt{s} = 8\,\mathrm{TeV}$. The left, middle, and right panels show the events with 3 jets and 2 b-tags, ≥ 4 jets and 2 b-tags, and ≥ 3 b-tags, respectively. More details regarding these plots are found in the text.
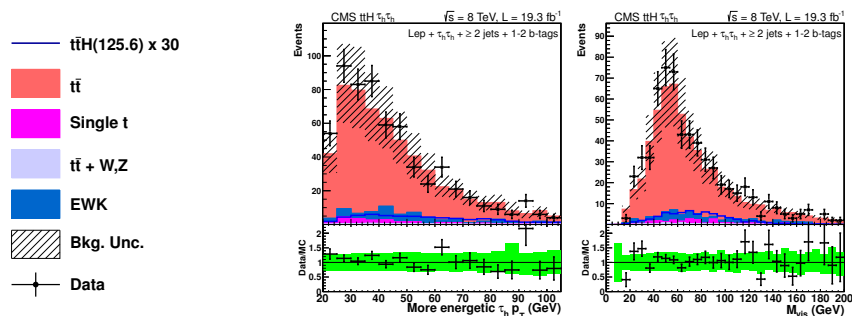
Figure 4. Examples of input variables that give the best signal-background separation in the analysis of the τ_h channels at $\sqrt{s} = 8\,\mathrm{TeV}$. The left plot shows the p_T of the more energetic τ_h, while the right plot displays M_vis, the mass of the visible τ_h decay products. Events of all categories are shown. More details regarding these plots are found in the text.

	3 jets + 2 b-tags	≥4 jets + 2 b-tags	≥3 b-tags
t$\bar{\text{t}}$H(125.6 GeV)	7.4 ± 0.6	14.5 ± 1.2	10.0 ± 0.8
t$\bar{\text{t}}$+lf	7650 ± 170	3200 ± 120	227 ± 35
t$\bar{\text{t}}$+b	210 ± 55	198 ± 57	160 ± 43
t$\bar{\text{t}}$ + b$\bar{\text{b}}$	50 ± 13	76 ± 17	101 ± 21
t$\bar{\text{t}}$ + c$\bar{\text{c}}$	690 ± 110	761 ± 97	258 ± 46
t$\bar{\text{t}}$+W/Z	29.5 ± 3.8	50.5 ± 6.4	10.9 ± 1.5
Single t	218 ± 16	95.2 ± 8.8	14.6 ± 3.6
W/Z+jets	217 ± 52	98 ± 28	21 ± 15
Diboson	9.5 ± 0.9	2.9 ± 0.4	0.6 ± 0.1
Total bkg	9060 ± 130	4475 ± 82	793 ± 28
Data	9060	4616	774

Table 3. Expected event yields for signal (m_H = 125.6 GeV) and backgrounds in the dilepton channel. Signal and background normalizations used for this table are described in the text.

	2 jets + 1 b-tag	3 jets + 1 b-tag	≥4 jets + 1 b-tag	2 jets + 2 b-tags	3 jets + 2 b-tags	≥4 jets + 2 b-tags
t$\bar{\text{t}}$H(125.6 GeV)	0.4 ± 0.1	0.6 ± 0.1	0.5 ± 0.1	0.1 ± 0.0	0.2 ± 0.0	0.3 ± 0.0
t$\bar{\text{t}}$+lf	266 ± 12	144.7 ± 7.1	72.1 ± 4.1	55.0 ± 3.4	45.2 ± 2.8	28.8 ± 2.1
t$\bar{\text{t}}$+W/Z	1.1 ± 0.2	1.3 ± 0.2	1.3 ± 0.3	0.5 ± 0.1	0.6 ± 0.1	0.9 ± 0.2
Single t	12.9 ± 2.1	3.5 ± 1.2	0.7 ± 0.6	2.2 ± 0.9	1.2 ± 0.5	0.4 ± 0.7
W/Z+jets	22.9 ± 6.3	7.7 ± 2.8	2.1 ± 1.2	1.0 ± 0.6	0.3 ± 0.2	0.2 ± 0.4
Diboson	0.9 ± 0.2	0.7 ± 0.2	0.1 ± 0.0	0.0 ± 0.0	0.1 ± 0.0	0.0 ± 0.1
Total bkg	304 ± 14	158.0 ± 7.5	76.4 ± 4.2	58.7 ± 3.6	47.3 ± 2.9	30.4 ± 2.3
Data	292	171	92	41	48	35

Table 4. Expected event yields for signal (m_H = 125.6 GeV) and backgrounds in the τ_h channel. Signal and background normalizations used for this table are described in the text.

is then used as an input variable in the second, more general, t$\bar{\text{t}}$H versus t$\bar{\text{t}}$+jets BDT. This tiered approach allows better discrimination between the t$\bar{\text{t}}$H process and the difficult t$\bar{\text{t}}$b$\bar{\text{b}}$ component of t$\bar{\text{t}}$+jets production, resulting in better control of t$\bar{\text{t}}$+hf systematics and a lower expected limit on μ. In the τ_h channel, due to the low event counts, a single BDT is used for all categories, using an event selection equivalent to the union of all categories with more than one untagged jet.

All BDTs utilize variables involving the kinematics of the reconstructed objects, the event shape, and the CSV b-tag discriminant. Ten variables are used as inputs to the final BDTs in all lepton+jets categories, while 10 or 15 variables are used in the first BDT in

categories employing the tiered-BDT system (the ≥ 6 jets $+$ ≥ 4 b-tags and ≥ 6 jets $+$ 3 b-tags categories use 15 variables, and the 5 jets $+$ ≥ 4 b-tags category uses ten variables due to lower available training statistics in that category). The dilepton channel uses four variables for the 3 jets $+$ 2 b-tags category and six in each of the other categories. In the τ_h channel, almost all variables used to train the BDT are related to the τ_h system, such as the mass of the visible τ decay products, the p_T, the isolation, and the decay mode of both τ_h, and the $|\eta|$ and distance to the lepton of the more energetic τ_h. In addition, the p_T of the most energetic jet, regardless of the b-tagging status, is used in the BDT.

To train the BDTs, the τ_h channel uses simulated $t\bar{t}H$, $H \to \tau\tau$ ($m_H = 125\,\text{GeV}$) events with generator-level matched τ_h pairs as the signal, whereas both the lepton+jets and dilepton channels use $t\bar{t}H$ ($m_H = 125\,\text{GeV}$) events, with inclusive Higgs boson decays. All three channels use $t\bar{t}$+jets events as background when training. An equal number of signal and background events are used for a given category and channel. The signal and background events are evenly divided into two subsamples: one set of events is used to do the actual training, and the other is used as a test sample to monitor against overtraining. The specific BDT method used is a "gradient boost", available as part of the TMVA package [74] in ROOT [75]. The tree architecture consists of five nodes, a few hundred trees form a forest, and the learning rate is set to 0.1.

Figures 5, 6, and 7 show the final BDT output distributions for the lepton+jets, dilepton, and τ_h channels, respectively. Background-like events have a low BDT output value, while signal-like events have a high BDT output value. The background distributions use the best-fit values of all nuisance parameters, with μ fixed at 1, and the uncertainty bands are constructed using the post-fit nuisance parameter uncertainties. The fit is described in section 9. The $t\bar{t}H$ signal ($m_H = 125.6\,\text{GeV}$) is not included in the stacked histogram, but is shown as a separate open histogram normalized to 30 times the SM expectation ($\mu = 30$). For the ratio plots shown below each BDT distribution, only the background expectation (and not the signal) is included in the denominator of the ratio. The final BDT outputs provide better discrimination between signal and background than any of the input variables individually. The BDT output distributions are used to set limits on the Higgs boson production cross section, as described in section 9.

6 H $\to$ photons

The diphoton analysis selects events using the diphoton system to identify the presence of a Higgs boson, and a loose selection on the remaining objects to accept all possible $t\bar{t}$ decays, while rejecting other Higgs boson production modes that are not directly sensitive to the top-quark Yukawa coupling. The background is extracted directly from the diphoton invariant mass distribution $m_{\gamma\gamma}$, exploiting the fact that a signal around $125\,\text{GeV}$ will be characterized by a narrow peak.

The event selection starts from the requirement of two photons, where the leading photon is required to have a $p_T > m_{\gamma\gamma}/2$ and the second photon to have a $p_T > 25\,\text{GeV}$. The variable threshold on the leading photon p_T increases the efficiency while minimizing trigger turn-on effects. The photon identification and energy measurement is the same as
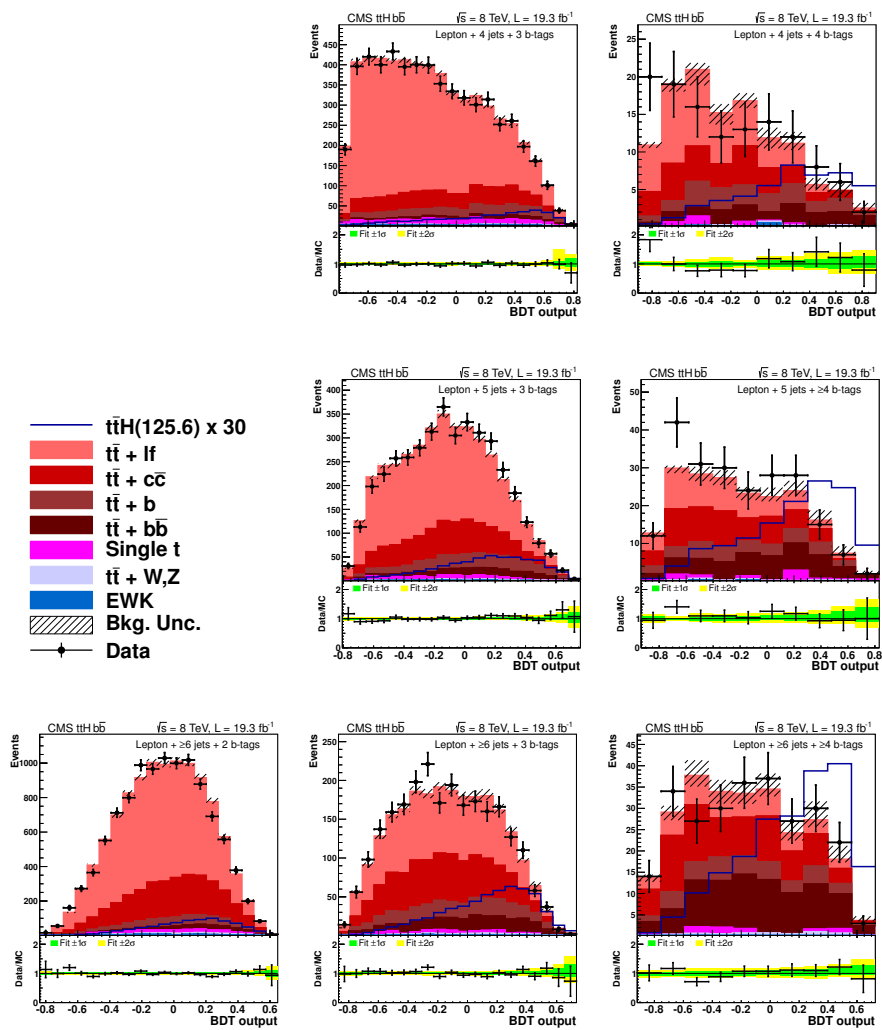
Figure 5. Final BDT output for lepton+jets events. The top, middle and, bottom rows are events with 4, 5, and ≥6 jets, respectively, while the left, middle, and right columns are events with 2, 3, and ≥4 b-tags, respectively. Details regarding signal and background normalizations are described in the text.
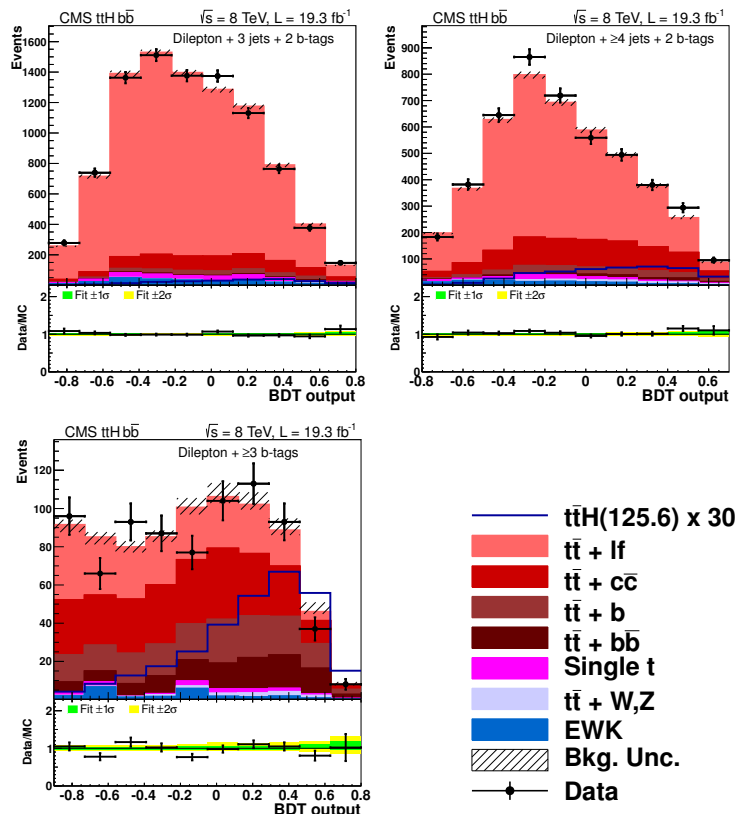
Figure 6. Final BDT output for dilepton events. The upper left, upper right, and lower left plots are events with 3 jets + 2 b-tags, ≥4 jets + 2 b-tags, and ≥3 b-tags, respectively. Details regarding signal and background normalizations are described in the text.

that used in ref. [30] with the only exception being that the primary vertex selection is done as described in section 4 of this paper. The presence of at least one b-tagged jet according to the medium working point of the CSV algorithm is required, consistent with the presence of b jets from top quark decays in the final state. Muons must lie in the pseudorapidity range $|\eta| < 2.4$, and electrons within $|\eta| < 2.5$. Both muons and electrons are required to have p_{T} greater than 20 GeV.

Events are categorized in two subsamples: the leptonic and hadronic channels. The hadronic channel requires, in addition to the two photons in the event, at least four jets of which at least one is b-tagged and no identified high-p_{T} charged leptons, whereas the leptonic channel requires at least two jets of which at least one is b-tagged and at least one charged lepton, where $\ell = \mathrm{e}, \mu$, with $p_{\mathrm{T}} > 20$ GeV. The 7 TeV dataset is too small to perform an optimization on each signal decay mode; thus events passing the hadronic and leptonic selections are combined in a single category.
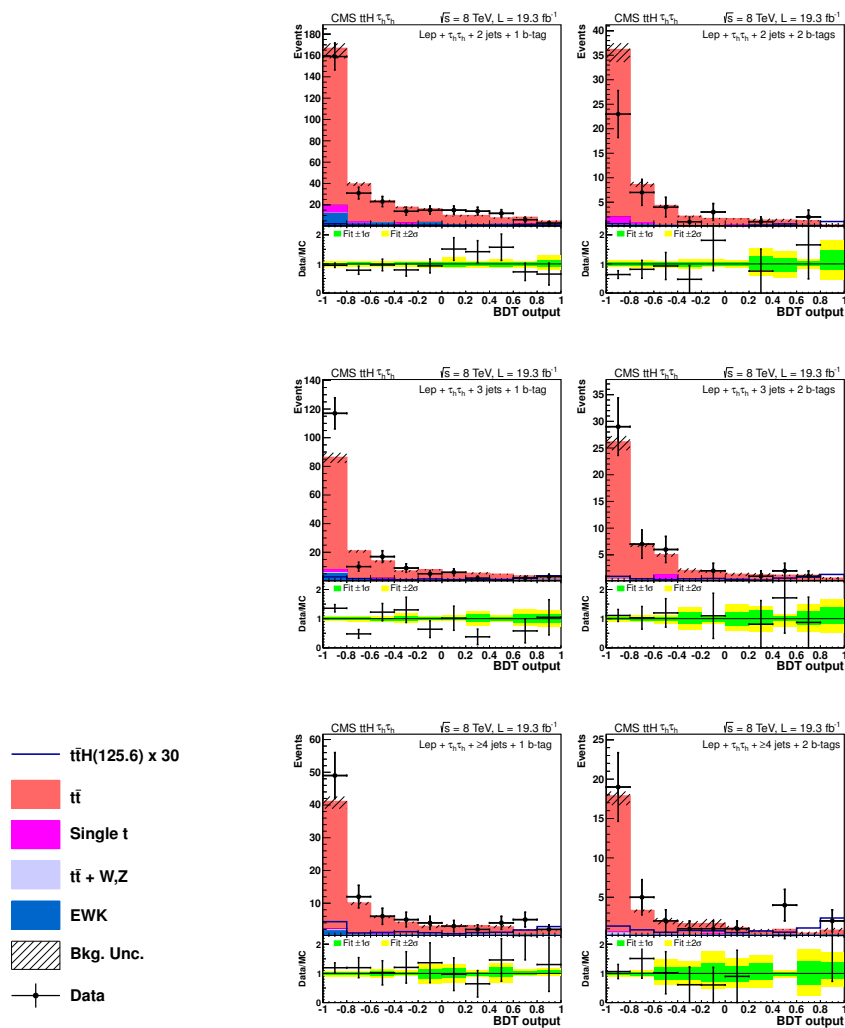
Figure 7. Final BDT output for events in the τ_h channel. The top row is the 2 jet categories, while the second and third rows are for the categories with 3 jets and ≥ 4 jets, respectively. In each row, the columns are for the categories with 1 b-tag (left) and 2 b-tags (right). Details regarding signal and background normalizations are described in the text.

Unlike the H → hadrons and H → leptons channels, the contribution from Higgs boson production modes other than t$\bar{t}$H must be treated with care for this channel. This is because this analysis is designed to have very loose requirements on the jet and lepton activity, and the other Higgs boson production modes will peak at the same location in the diphoton invariant mass distribution as the t$\bar{t}$H signal. This is in contrast with the situation for the H → hadrons and H → leptons analyses, where the non-t$\bar{t}$H production modes tend to populate the most background-rich region of the phase space investigated, thus a very small contamination of non-t$\bar{t}$H Higgs boson production has almost no impact on those analyses. The event selection for the t$\bar{t}$H, H → photons channel is thus designed to minimize the contribution from other Higgs boson production modes. The expected signal yields for the various production processes for the SM Higgs boson of mass 125.6 GeV in this channel are shown in table 5, after selection in the $100 \leq m_{\gamma\gamma} \leq 180$ GeV range. As can be seen, the contribution of production modes other than t$\bar{t}$H is minor. The contribution of single-top-quark-plus-Higgs-boson production has not been explicitly estimated but its cross section is expected to be only about 1/10 of the t$\bar{t}$H cross section and the events have different kinematics [76], so its contribution to the sample is expected to be small.

The main backgrounds are the production of top quarks and either genuine or misidentified photons in the final state, and the production of high-p_{T} photons in association with many jets, including heavy-flavor jets. Because the background will be estimated by fitting the data which is a mixture of these processes, it is useful to test the background modeling in an independent control sample defined using collision data. The control sample is constructed using events that have been recorded with the single-photon trigger paths, and inverting the photon identification requirements on one of the two photons used to reconstruct the Higgs boson signal. To take into account the fact that the efficiency of the photon isolation requirement is not constant as a function of the photon p_{T} and η, a two-dimensional reweighting procedure is applied to the leading and subleading photon candidates in such events. The reweighting is performed so as to match the photon p_{T} and η spectra to the ones of photons populating the signal region. A control sample with similar kinematic properties as the data, yet statistically independent, is thus obtained.

The extent to which the control sample is well-modeled is tested using events passing the photon selections, and the requirement of at least two high-p_{T} jets. The sample is further split into events with and without charged leptons, to test the kinematic properties of the model against data. A few key kinematic distributions are shown in figure 8, where the black markers show the signal sample, the green histogram is the control sample data, and the red line displays the signal kinematics. All distributions are normalized to the number of events observed in data.

Even after the dedicated event selection, the dataset is still largely dominated by backgrounds. The strategy adopted in this analysis is to fit for the amount of signal in the diphoton mass spectrum, as this provides a powerful discriminating variable due to the excellent photon energy resolution, in the region surrounding the Higgs boson mass. The background is obtained by fitting this distribution in each channel (hadronic or leptonic) over the range 100 GeV $< m_{\gamma\gamma} < 180$ GeV. The actual functional form used to fit the background, in any particular channel, is included as a discrete nuisance parameter in the

– 21 –
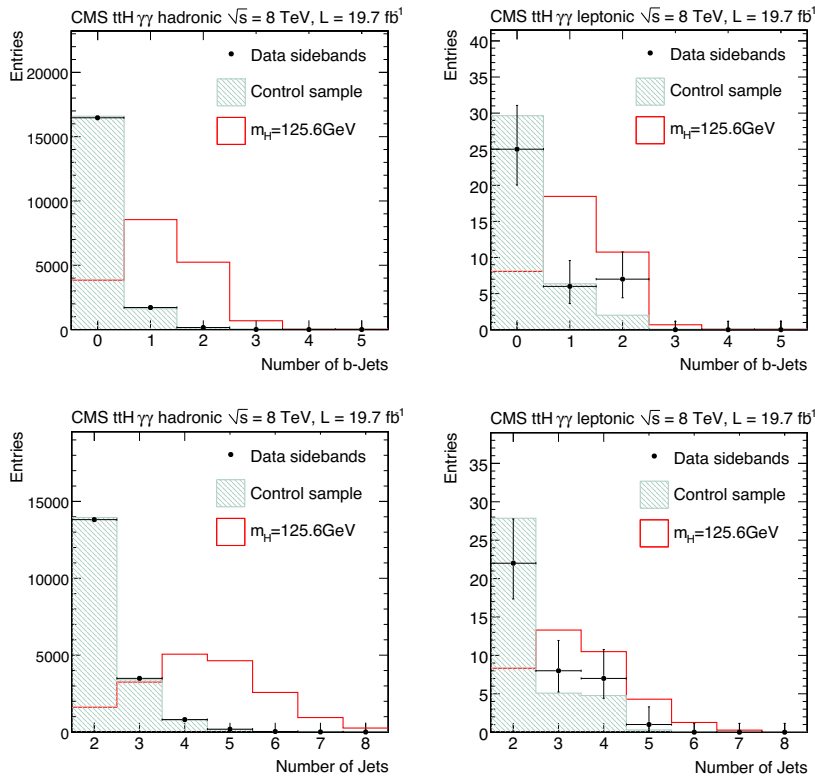
Figure 8. Distributions of the b-tagged jet multiplicity (top row) and jet multiplicity (bottom row) for events passing a relaxed selection in the hadronic (left) and leptonic (right) channels, but removing events where the diphoton invariant mass is consistent with the Higgs boson mass within a 10 GeV window. The relaxed selection applies the standard photon and lepton requirements but allows events with any number of jets. The plots compare the data events with two photons and at least two jets (black markers) and the data from the control sample (green filled histogram) to simulated $t\bar{t}H$ events (red open histogram). Both signal and background histograms are normalized to the total number of data events observed in this region to allow for a shape comparison.

likelihood functions used to extract the results; exponentials, power-law functions, polynomials (in the Bernstein basis), and Laurent series are considered for this analysis. When fitting the background by minimizing the value of twice the negative logarithm of the likelihood (2NLL), all functions in these families are tried, with a penalty term added to 2NLL to account for the number of free parameters in the fitted function. Pseudoexperiments have shown that this "envelope" method provides good coverage of the uncertainty associated with the choice of the function, for all the functions considered for the background, and provides an estimate of the signal strength with negligible bias [30].

	7 TeV	8 TeV	
	All decays	Hadronic channel	Leptonic channel
t̄tH	0.21	0.51	0.45
gg → H	0.01	0.02	0
VBF H	0	0	0
WH/ZH	0.01	0.01	0.01
Total H	0.23	0.54	0.46
Data	9	32	11

Table 5. Expected signal yields after event selections in the $100\,\text{GeV} < m_{\gamma\gamma} < 180\,\text{GeV}$ diphoton mass window. Different Higgs boson production processes are shown separately. The total number of data events present in each channel is displayed at the bottom of the table. A Higgs boson mass of $125.6\,\text{GeV}$ is assumed.
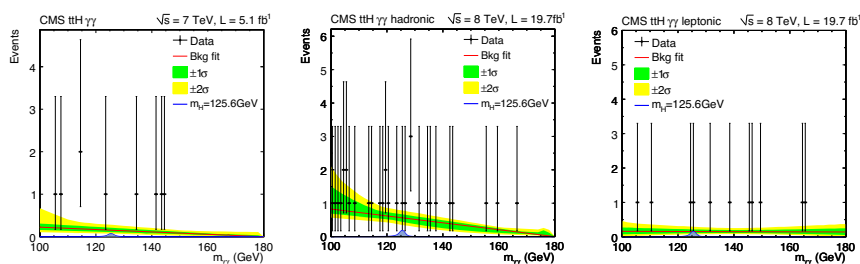
Figure 9. Diphoton invariant mass distribution for $\sqrt{s} = 7\,\text{TeV}$ data events for the combined hadronic and leptonic selections on the left, and for $\sqrt{s} = 8\,\text{TeV}$ data events passing the hadronic (middle), and leptonic (right) selections. The red line represents the fit to the data, while the green (yellow) band show the 1σ (2σ) uncertainty band. The theoretical prediction for the signal contribution (in blue) includes the main Higgs boson production modes.

The diphoton invariant mass spectra for data, the expected signal contribution, and the background estimate from data are shown in figure 9 for the combination of hadronic and leptonic selections on the $\sqrt{s} = 7\,\text{TeV}$ data (left), the hadronic (middle) and leptonic (right) channels separately using $\sqrt{s} = 8\,\text{TeV}$ data. The expected signal contribution of the dominant SM Higgs boson production modes is shown as a blue histogram. The result of the fit is shown in the plots as a red line, together with the uncertainty bands corresponding to 1σ (green) and 2σ (yellow) coverage. The observed diphoton mass spectra agree well with the background estimates.

7   H → leptons

7.1   Object identification

In this channel the signal has multiple prompt leptons from W, Z, or τ decays. The largest backgrounds have at least one non-prompt lepton, usually from the decay of a b hadron (in $t\bar{t}$+jets, Z+jets, and W+jets events). The analysis begins with a preselection of electron and muon objects using loose criteria with very high efficiency for prompt leptons and moderate non-prompt lepton rejection. In addition to the basic cuts from section 4, the lepton is required to be associated with the event vertex. The distance between the lepton track and the event vertex along the z-axis and perpendicular to it (d_z and d_{xy}) must be less than 1 cm and 0.5 cm, respectively. The S_{IP} (defined as the ratio of the IP to its uncertainty) is required to be less than 10, a fairly loose cut intended to retain efficiency for leptons coming from τ decays. Next, a multivariate discriminator based on BDT techniques is used to distinguish prompt from non-prompt leptons. This discriminator, referred to as the lepton MVA, is trained with simulated prompt leptons from the $t\bar{t}$H MC sample and non-prompt leptons from the $t\bar{t}$+jets MC sample, separately for electrons and muons and for several bins in p_T and η.

The lepton MVA input variables relate to the lepton IP, isolation, and the properties of the nearest jet, within $\Delta R < 0.5$. A tight working point on the lepton MVA output is used for the search in the dilepton and trilepton final states, and a loose working point is used for the four-lepton final state. For the tight working point, the efficiency to select prompt electrons is of order 35% for $p_T^e \sim 10\,\mathrm{GeV}$ and reaches a plateau of 85% at $p_T^e \sim 45\,\mathrm{GeV}$; for prompt muons it is of order 55% for $p_T^\mu \sim 10\,\mathrm{GeV}$, and reaches a plateau of about 97% at $p_T^\mu \sim 45\,\mathrm{GeV}$. The efficiency to select electrons (muons) from the decay of b hadrons is between 5–10% (around 5%).

To suppress electrons from photon conversions, tight electrons with missing tracker hits before the first reconstructed hit, or associated with a successfully reconstructed conversion vertex, are rejected [77].

Additional cuts are used to suppress incorrect charge reconstruction in the dilepton final states. For electrons, the tracker and ECAL charge measurements must agree, where the ECAL charge is measured by comparing the position of the energy deposits in the ECAL to a straight-line trajectory formed from the electron hits in the pixel detector [50, 78]. For muons, the relative uncertainty in the track p_T must be less than 20%.

The agreement between data and simulation for the input variables and the final lepton MVA is validated in dedicated control regions. For prompt leptons, high-purity control samples are selected with same-flavor, opposite-sign pairs of leptons with an invariant mass close to that of the Z boson and little E_T^{miss}. In these events, tight isolation and p_T selection are applied to the leading lepton, and the trailing lepton is used to check the agreement between simulation and data. High-purity τ leptons are selected by requiring opposite-flavor, opposite-sign pairs of electrons and muons with an invariant mass between 20 GeV and 80 GeV. In these events, tight isolation, p_T, and S_{IP} cuts are applied to one of the two leptons, and the other lepton is used to compare simulation and data. For non-prompt leptons, samples enriched in leptons from the decay of b hadrons are selected

– 24 –

with three-lepton $Z \to \ell\ell + \ell$ and $t\bar{t} \to \ell\ell + \ell$ control regions. The agreement is good; small corrections to better match the data distributions of the input variables are applied to the simulation before training the MVA discriminant. Efficiency scale factors for the tight and loose lepton MVA working points are computed for prompt leptons with a tag-and-probe technique in the $Z \to \ell\ell$ control region. Backgrounds with non-prompt leptons are estimated directly from data, as described in section 7.3.

7.2 Event selection

The multilepton selection is optimized to accept $t\bar{t}H$ events where the Higgs boson decays into WW, ZZ, or $\tau\tau$, and at least one W boson, Z boson, or τ decays leptonically. With at least one additional lepton from the top decays, the events have one of the following three signatures:

- two same-sign leptons (electrons or muons) plus two b-quark jets;

- three leptons plus two b-quark jets;

- four leptons plus two b-quark jets.

The first three rows in table 6 show the expected distribution of the $t\bar{t}H$ signal among these different signatures. The other rows in the table will be discussed below.

Candidate events that match one of these signal signatures are selected by requiring combinations of reconstructed objects. Three features are common to all three decay signatures:

- Each event is required to have one lepton with $p_T > 20\,\text{GeV}$ and another with $p_T > 10\,\text{GeV}$ to satisfy the dilepton trigger requirements.

- If an event has any pair of leptons, regardless of charge or flavor, that form an invariant mass less than $12\,\text{GeV}$, that event is rejected. This requirement reduces contamination from Υ and J/ψ, as well as very low-mass Drell-Yan events that are not included in the simulation.

- Since signal events have two top quarks, each event is required to have at least two jets, where at least two jets satisfy the loose CSV working point or one jet satisfies the medium CSV working point.

In addition, pairs of leptons with the same flavor whose invariant mass is within $10\,\text{GeV}$ of the Z boson mass are rejected to suppress background events with a Z boson decay. Same-sign dielectron events are rejected if they contain any such pair. Events in the 3ℓ and 4ℓ categories are rejected only if the two leptons in the pair have opposite charges.

Same-sign dilepton events are required to have exactly two leptons with identical charges and at least four hadronic jets. Each lepton must pass the lepton preselection, the tight working point of the lepton MVA discriminant, and the charge quality requirements. To reject events from backgrounds with a Z boson, $L_D > 30\,\text{GeV}$ is required for

	ee	eμ	μμ	3ℓ	4ℓ
t̄tH, H → WW	1.0 ± 0.1	3.2 ± 0.4	2.4 ± 0.3	3.4 ± 0.5	0.29 ± 0.04
t̄tH, H → ZZ	—	0.1 ± 0.0	0.1 ± 0.0	0.2 ± 0.0	0.09 ± 0.02
t̄tH, H → ττ	0.3 ± 0.0	1.0 ± 0.1	0.7 ± 0.1	1.1 ± 0.2	0.15 ± 0.02
t̄t W	4.3 ± 0.6	16.5 ± 2.3	10.4 ± 1.5	10.3 ± 1.9	—
t̄t Z/γ*	1.8 ± 0.4	4.9 ± 0.9	2.9 ± 0.5	8.4 ± 1.7	1.12 ± 0.62
t̄t WW	0.1 ± 0.0	0.4 ± 0.1	0.3 ± 0.0	0.4 ± 0.1	0.04 ± 0.02
t̄t γ	1.3 ± 0.3	1.9 ± 0.5	—	2.6 ± 0.6	—
WZ	0.6 ± 0.6	1.5 ± 1.7	1.0 ± 1.1	3.9 ± 0.7	—
ZZ	—	0.1 ± 0.1	0.1 ± 0.0	0.3 ± 0.1	0.47 ± 0.10
Rare SM bkg.	0.4 ± 0.1	1.6 ± 0.4	1.1 ± 0.3	0.8 ± 0.3	0.01 ± 0.00
Non-prompt	7.6 ± 2.5	20.0 ± 4.4	11.9 ± 4.2	33.3 ± 7.5	0.43 ± 0.22
Charge misidentified	1.8 ± 0.5	2.3 ± 0.7	—	—	—
All signals	1.4 ± 0.2	4.3 ± 0.6	3.1 ± 0.4	4.7 ± 0.7	0.54 ± 0.08
All backgrounds	18.0 ± 2.7	49.3 ± 5.4	27.7 ± 4.7	59.8 ± 8.0	2.07 ± 0.67
Data	19	51	41	68	1

Table 6. Expected and observed yields after the selection in all five final states. For the expected yields, the total systematic uncertainty is also indicated. The rare SM backgrounds include triboson production, tbZ, $W^{\pm}W^{\pm}$qq, and WW produced in double parton interactions. A '-' indicates a negligible yield. Non-prompt and charge-misidentification backgrounds are described in section 7.3.

dielectron events, where L_D is defined in section 4, equation (4.1). To further suppress reducible backgrounds, especially non-t̄t backgrounds, the threshold on the p_T of the second lepton is raised to 20 GeV, and the scalar sum of the p_T of the two leptons and of the E_T^{miss} is required to be above 100 GeV.

The three-lepton candidate selection requires exactly three leptons that pass the lepton preselection and the tight working point for the lepton MVA discriminant. To further reject events from backgrounds with a Z boson, an L_D requirement is applied, with a tighter threshold if the event has a pair of leptons with the same flavor and opposite charge. For events with large jet multiplicity (≥ 4 jets), where contamination from the Z-boson background is smaller, the L_D requirement is not applied.

The four-lepton candidate selection requires exactly four leptons that each pass the lepton preselection and the loose working point of the lepton MVA discriminant.

The observed event yields in data for each final state and the expectations from the different physical processes after event selection are summarized in table 6. The details of the calculations of the signal and background yields are discussed in the next section.

– 26 –

7.3 Signal and background modeling

Three categories of backgrounds are identified in this search: $t\bar{t}V$ backgrounds from the associated production of a $t\bar{t}$ pair and one or more W or Z bosons; diboson or multiboson production associated with multiple hadronic jets; and reducible backgrounds from events with non-prompt leptons, or opposite-sign dilepton events in which the charge of one of the leptons is misidentified. These three background classes are estimated separately with different methods, described below. The systematic uncertainties associated with each background estimate are discussed in section 8.

The $t\bar{t}H$ signal and backgrounds from $t\bar{t}W$ and $t\bar{t}Z$, as well as minor backgrounds like $t\bar{t}WW$ and triboson processes, are estimated from simulation, normalized to the NLO inclusive cross sections for each process [15, 19–28, 67, 68, 79, 80]. The combined cross section of $t\bar{t}W$ and $t\bar{t}Z$ has been measured by the CMS Collaboration in 7 TeV data [81]. The results are consistent with theory but have larger uncertainties. The prediction for the $t\bar{t}Z$ process is also tested directly in a trilepton control region requiring two of the leptons to have the same flavor, opposite charge, and invariant mass within 10 GeV of the nominal Z boson mass [82]. Agreement is observed in this control region, though the precision of the test is dominated by the statistical uncertainty of about 35%. Agreement was also observed in a $t\bar{t} \rightarrow e^{\pm}\mu^{\mp} b\bar{b} \nu\bar{\nu}$ sample, indicating good simulation of prompt leptons and real b-quark jets.

The WZ and ZZ production processes with the gauge bosons decaying to electrons, muons, or taus can yield the same leptonic final states as the signal. These processes are predicted theoretically at NLO accuracy, but the uncertainty in the production cross section of diboson with additional partons can be large. To reduce this uncertainty, a low-signal control sample of WZ or ZZ plus at least two jets is selected by vetoing any event with a loose b tag, as well as inverting the $Z \rightarrow \ell\ell$ veto. The diboson background in the signal region is normalized according to the event yield observed in this control region times an extrapolation factor, taken from MC simulation, associated with going from the control region to the signal region.

The expected flavor composition in simulation for WZ events after the full selection in the trilepton final state is approximately 50% from WZ production in association with mistagged jets from light quarks or gluons, 35% from events with one jet originating from a c quark, and 15% from events with b quarks. For ZZ in the four-lepton final state, the expectation is about 40% events with jets from gluons or light quarks, 35% from events with b quarks and 25% from events with c quarks.

The reducible backgrounds with at least one non-prompt lepton are estimated from data. A control region dominated by reducible backgrounds is defined by selecting events with the same kinematics as the signal region, but for which at least one of the leptons fails the requirement on the lepton MVA. The kinematic distributions for data in this region are consistent with MC, mostly $t\bar{t}$+jets with one non-prompt lepton, as shown in figure 10. Extrapolation to the signal region is then performed by weighting events in the control region by the probability for non-prompt leptons to pass the lepton MVA selection, measured from same-sign dilepton and lepton+b-tagged jet data in control regions with fewer jets than the signal region, as a function of the lepton p_T and η, separately for muons and electrons.

– 27 –
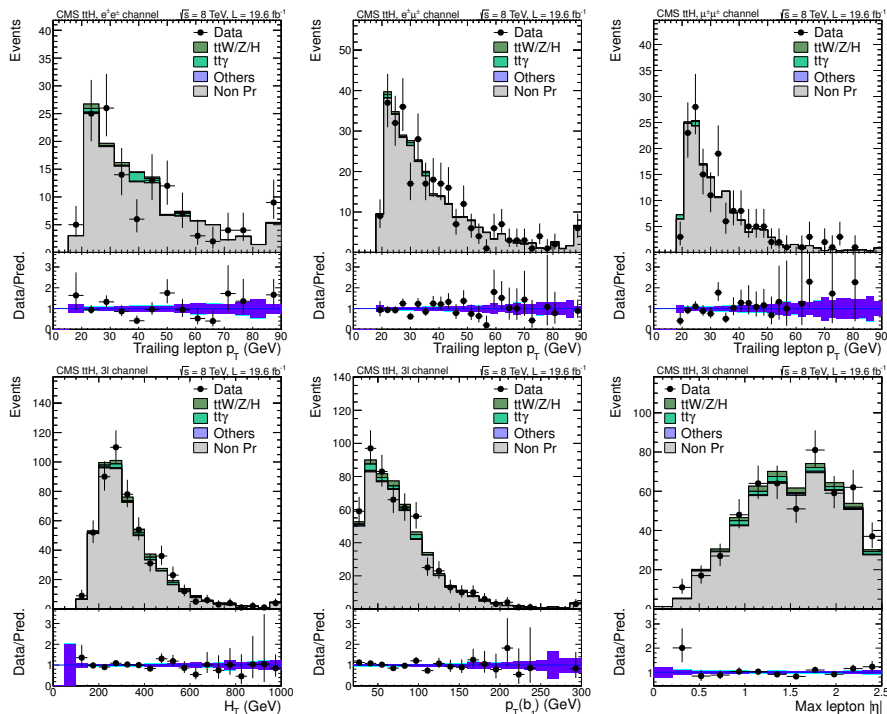
Figure 10. These plots show the distribution of key discriminating variables for events where one lepton fails the lepton MVA requirement. The expected distribution for the non-prompt background is taken from simulation (mostly $t\bar{t}$+jets), and the yield is fitted from the data. The bottom panel of each plot shows the ratio between data and predictions as well as the overall uncertainties after the fit (blue). In the first row the distributions of the trailing lepton p_T for the $e^{\pm}e^{\pm}$ (left), $e^{\pm}\mu^{\pm}$ (center), and $\mu^{\pm}\mu^{\pm}$ (right) final states are shown. In the second row the distributions of the H_T (left), the p_T of the jet with highest b-tagging discriminator (center), and the lepton maximum $|\eta|$ (right) are shown for the trilepton channel.

Events in which a single lepton fails the lepton MVA requirement enter the signal region prediction with weight $\epsilon/(1-\epsilon)$, where ϵ denotes the aforementioned probability computed for the p_T, η, and flavor of the lepton failing the selection. Events with two leptons failing the requirement are also used, but with a negative weight $-\epsilon_1\epsilon_2/[(1-\epsilon_1)(1-\epsilon_2)]$; this small correction is necessary to account for events with two background-like leptons contaminating the sample of events with a single lepton failing the requirement.

The measurement of the probability for non-prompt leptons to pass the lepton MVA cuts, and the weighting of events in the control region, are performed separately for events with at most one jet satisfying the medium CSV requirement and for events with at least two, to account for the different flavor composition and kinematics of the two samples.

Charge misidentification probabilities are determined as function of the lepton p_T and η from the observed yields of same-sign and opposite-sign dilepton pairs with mass within $10\,\mathrm{GeV}$ of the Z-boson mass. For electrons, this probability varies from 0.03% in the barrel to 0.3% in the endcaps, while for muons the probability is found to be negligible.

The prediction for background dilepton events with misidentified electron charge in the signal region is computed from opposite-sign dilepton events passing the full selection, except for the charge requirement: events with a single electron enter the prediction with a weight equal to the charge misidentification probability for that electron, while dielectron events enter the prediction with a weight equal to the sum of the charge misidentification probabilities for the two electrons.

7.4 Signal extraction

After the event selection, overall yields are still dominated by background. The strategy adopted in this search is to fit for the amount of signal in the distribution of a suitable discriminating variable.

In the dilepton analysis, a BDT output is used as discriminating variable. The BDT is trained with simulated $t\bar{t}H$ signal and $t\bar{t}$+jets background events, with six input variables: the p_T and $|\eta|$ of the trailing lepton, the minimal angular separation between the trailing lepton and the closest jet, the transverse mass of the leading lepton and E_T^{miss}, H_T, and H_T^{miss}. The same training is used for the ee, eμ, and $\mu\mu$ final states, as the gain in performance from dedicated trainings in each final state is found to be negligible.

In the trilepton analysis, a BDT output is also used as the final discriminant. The BDT is trained with simulated $t\bar{t}H$ signal and a mix of $t\bar{t}$+jets, $t\bar{t}W$, and $t\bar{t}Z$ background events, with seven discriminating variables: the number of hadronic jets, the p_T of the jet with the highest b-tagging discriminant value, the scalar sum of lepton and jet p_T (H_T), the fraction of H_T from jets and leptons with $|\eta| < 1.2$, the maximum of the $|\eta|$ values of the three leptons, the minimum ΔR separation between any pair of opposite-sign leptons, and the mass of three jets, two close to the W-boson mass and a b-tagged jet, closest to the nominal top quark mass [82].

As a cross-check in both the dilepton and the trilepton final states, the number of hadronic jets was used instead of the BDT as the discriminating variable. The gain in signal strength precision from the multivariate analysis compared to this simpler cross-check is about 10%.

In the four-lepton analysis, only the number of hadronic jets is used: the sensitivity of this channel is limited by the very small branching fraction, and the estimation of the kinematic distributions of the reducible backgrounds from data is also challenging due to the low event yields.

In the dilepton and trilepton final states, events are divided into categories by the sum of the electrical charges of the leptons, to exploit the charge asymmetry present in several SM background cross sections in pp collisions ($t\bar{t}W$, WZ, single top quark t-channel, W+jets). The gain in signal strength precision from this categorization is approximately 5%.

The expected and observed distributions of the number of selected jets and the BDT output, for the different final states of the dilepton analysis, are shown in figure 11. The same distributions are shown for the trilepton analysis in figure 12. The distribution of the number of selected jets is also shown for the four-lepton channel in figure 12. The t$\bar{\text{t}}$H signal yield in the stack is the SM prediction ($\mu = 1$); additionally, the signal yield for $\mu = 5$ is shown as a dotted line. The background distributions use the best-fit values of all nuisance parameters, with μ fixed at 1, and the uncertainty bands are constructed using the nuisance parameter uncertainties.

The dilepton data are in good agreement with the predictions in the ee and eμ channels, while an excess of signal-like events is visible in the $\mu\mu$ final state. The details of this excess are discussed below. In the trilepton channel the overall data yield matches expectations. The jet multiplicity in data is a bit higher, but the distribution of the BDT discriminator matches the prediction. In the four-lepton channel only one event is observed with respect to an overall SM prediction (including expected t$\bar{\text{t}}$H contribution) of about three events.

Because the excess of signal-like events is most pronounced in the dimuon channel, additional cross-checks were performed. The agreement between expected and observed yields in the ee and eμ channels suggests that the background estimates are reasonable. Detailed studies of various single-muon and dimuon distributions did not reveal any potential additional source of background. Moreover, the analysis of the dimuon final state has been repeated with different lepton selections, using looser working points for the lepton MVA and also with traditional selections on individual variables. These approaches have sensitivities 10–50% worse than the nominal analysis and give compatible results. The consistency of these checks suggests this excess does not arise from a deficiency in the estimation of the backgrounds.

8 Systematic uncertainties

There are a number of systematic uncertainties that impact the estimated signal or background rates, the shape of the final discriminant, or both. This section describes the various sources of systematic uncertainty. Section 9 will explain how the effects of these uncertainties are accounted for in the likelihood function used to set limits and extract the best-fit Higgs boson signal.

Different systematic uncertainties are relevant for different parts of the overall t$\bar{\text{t}}$H analysis. Uncertainties related to MC modeling affect all analysis channels, whereas systematic uncertainties related to the background estimation or object identification can be specific to particular channels. Table 7 summarizes the impact of systematic uncertainties on this analysis. For each broad category, table 7 shows the range of effects the systematic uncertainties have on the signal and background rates, and notes whether the uncertainty also has an effect on the shape of the final discriminant. Cases for which a systematic category only applies to one analysis channel are noted in parentheses. Further details are given below.

Global event uncertainties affect all the analysis channels. The integrated luminosity is varied by $\pm 2.2\%$ for the 7 TeV dataset [34] and by $\pm 2.6\%$ for the 8 TeV dataset [32] from its nominal value. The effect of finite background MC statistics in the analysis is accounted

– 30 –
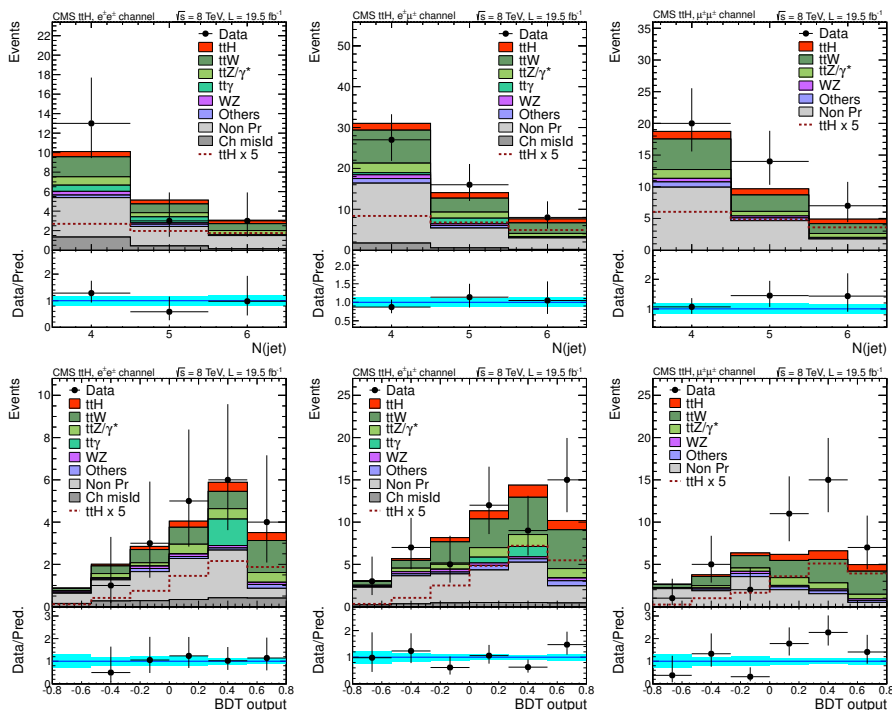
Figure 11. Distribution of the jet multiplicity (top row) and the BDT discriminant (bottom row) for the same-sign dilepton search, for the final states ee (left), eμ (center), and μμ (right). Signal and background normalizations are explained in the text. The b-tagged jets are included in the jet multiplicity.

for using the approach described in refs. [83, 84]. To avoid including thousands of nuisance parameters that have no effect on the result, this uncertainty is not evaluated for any bin in the BDT shapes for which the MC statistical uncertainty is negligible compared to the data statistics or where there is no appreciable contribution from signal. Tests show that the effect on the final result of neglecting the MC statistical uncertainty for these bins is smaller than 2%. In total, there are 190 nuisance parameters used to describe the fluctuations in the bins of the BDT outputs.

The reconstructed objects in each event come with their own uncertainties. The uncertainty from the jet energy scale [57] is evaluated by varying the energy scale for all jets in the signal and background simulation simultaneously either up or down by one standard deviation as a function of jet p_T and η, and reevaluating the yields and discriminant shapes of all processes. These variations have a negligible effect on the $m_{\gamma\gamma}$ distribution, and shape effects for the H → photons channel are ignored. The jet energy resolution uncertainty is found to have a negligible impact for all channels. The corrections for the b-tagging efficiencies for light-flavored, c-, and b-quark jets have associated uncertainties [60]. These
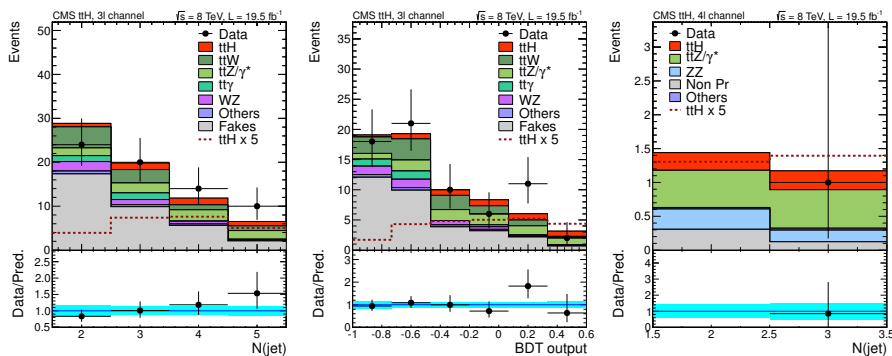
Figure 12. Distribution of the jet multiplicity (left) and BDT discriminant (center) for the trilepton search. Events with positive and negative charge are merged in these plots, but they are used separately in the signal extraction. The plot on the right shows the jet multiplicity for the four-lepton search. Signal and background normalizations are explained in the text. The b-tagged jets are included in the jet multiplicity.

uncertainties are parameterized as a function of the p_T, η, and flavor of the jets. Their effect on the analysis is evaluated by shifting the correction factor of each jet up and down by one standard deviation of the appropriate uncertainty. Because the CSV distribution for jets in the H $\rightarrow$ hadrons channel receives shape corrections, it requires a different set of shape uncertainties. In deriving the CSV shape corrections, there are uncertainties from background contamination, jet energy scales, and limited size of the data samples. The statistical uncertainty in the CSV shape corrections has the potential to modify the shape of the CSV distribution in complicated ways. To parameterize this, the shape uncertainties are broken down into two orthogonal components: one component can vary the overall slope of the CSV distribution, while the other component changes the center of the distribution relative to the ends. These uncertainties are evaluated separately for light-flavor and b-quark jets. Twice the b-quark jet uncertainties are also applied to c-quark jets, whose nominal scale factor is 1.

Electron and muon identification and trigger efficiency uncertainties are estimated by comparing variations in the difference in performance between data and MC simulation using a high-purity sample of Z-boson decays. These uncertainties vary between 1% and 6%. The systematic uncertainty associated with the MVA selection of prompt leptons in the H $\rightarrow$ leptons channel uses tag-and-probe measurements comparing data and simulation in dilepton Z-boson events in the dilepton channel. The overall uncertainty amounts to about 5% per lepton. The uncertainty in the misidentification probabilities for non-prompt leptons is estimated from simulation. The misidentification rate is estimated following the same approach and parameterization used in the QCD dominated control region, but instead using only MC samples with a similar composition. This simulation-based misidentification rate is then applied to MC samples with the expected background composition in the signal region, and the amount of disagreement between the number of non-prompt leptons predicted by the parameterized misidentification rate and those actually observed in this collection of MC samples is used to estimate the systematic uncertainty. The uncer-

Source	Rate uncertainty		Shape
	Signal	Backgrounds	
Experimental			
Integrated luminosity	2.2–2.6%	2.2–2.6%	No
Jet energy scale	0.0–8.4%	0.1–11.5%	Yes
CSV b-tagging	0.9–21.7%	3.0–29.0%	Yes
Lepton reco. and ID	0.3–14.0%	1.4–14.0%	No
Lepton misidentification rate (H → leptons)	—	35.1–45.7%	Yes
Tau reco. and ID (H → hadrons)	11.3–14.3%	24.1–28.8%	Yes
Photon reco. and ID (H → photons)	1.6–3.2%	—	Yes
MC statistics	—	0.2–7.0%	Yes
Theoretical			
NLO scales and PDF	9.7–14.8%	3.4–14.7%	No
MC modeling	2.3–5.1%	0.9–16.8%	Yes
Top quark p_{T}	—	1.4–6.9%	Yes
Additional hf uncertainty (H → hadrons)	—	50%	No
H contamination (H → photons)	36.7–41.2%		No
WZ (ZZ) uncertainty (H → leptons)	—	22% (19%)	No

Table 7. Summary of systematic uncertainties. Each row in the table summarizes a category of systematic uncertainties from a common source or set of related sources. In the statistical implementation, most of these uncertainties are treated via multiple nuisance parameters. The table summarizes the impact of these uncertainties both in terms of the overall effect on signal and background rates, as well as on the shapes of the signal and background distributions. The rate columns show a range of uncertainties, since the size of the rate effect varies both with the analysis channel as well as the specific event selection category within a channel. The uncertainties quoted here are *a priori* uncertainties; that is they are calculated prior to fitting the data, which leads to a reduction in the impact of the uncertainties as the data helps to constrain them.

tainty is assessed separately for different p_{T}, η and b-tagged jet multiplicity bins for each flavor. The overall uncertainty amounts to about 40%, which is applied using linear and quadratic deformations of the p_{T}- and η-dependent misidentification rate.

The uncertainties in the τ_{h} identification consist of electron and jet misidentification rates, as well as the uncertainty in the τ_{h} identification itself. The last is applied to the generator-level matched τ_{h}, and estimated to be 6% per object, using a tag-and-probe technique with a $Z \to \tau\tau \to \mu\tau_{\mathrm{h}}$ process. The jet misidentification rate uncertainty is determined to be 20% by comparing τ_{h} misidentification rates in data and simulated W+jets events, where the W boson decays to $\mu\nu$. Likewise, the electron misidentification rate uncertainty is found to be 5% from $Z \to ee$ events using a tag-and-probe technique. The τ_{h} energy scale systematics are obtained from studies involving $Z \to \tau\tau$ [65].

– 33 –

For photon identification, the uncertainty in the data-MC efficiency scale factor from the fiducial region determines the overall uncertainty, as measured using a tag-and-probe technique applied to $Z \to$ ee events (3.0% in the ECAL barrel, 4.0% in ECAL endcap). For the uncertainties related to the photon scale and resolution, the photon energy is shifted and smeared respectively within the known uncertainty for both photons.

Theoretical uncertainties may affect the yield of signal and background contributions as well as the shape of distributions. Signal and background rates are estimated using cross sections of at least NLO accuracy, which have uncertainties arising primarily from the PDFs and the choice of the factorization and renormalization scales. The cross section uncertainties are each separated into their PDF and scale components and correlated, where appropriate, between processes. For example, the PDF uncertainty for processes originating primarily from gluon-gluon initial states, e.g., $t\bar{t}$ and $t\bar{t}H$ production, are treated as completely correlated.

In addition to the rate uncertainties coming from the NLO or better cross section calculations, the modeling of the $t\bar{t}$+jets (including $t\bar{t} + b\bar{b}$ and $t\bar{t} + c\bar{c}$), $t\bar{t}V$, diboson+jets and the W/Z+jets processes are subject to MC modeling uncertainties arising from the extrapolation from the inclusive rates to exclusive rates for particular jet or tag categories using the MADGRAPH tree-level matrix element generator matched to the PYTHIA parton shower MC program. Although MADGRAPH incorporates contributions from higher-order diagrams, it does so only at tree-level, and is subject to fairly large uncertainties arising from the choice of scales. These uncertainties are evaluated using samples for which the factorization and renormalization scales have been varied up and down by a factor of two. Scale variations are propagated to both the rate and (where significant) the final discriminant shape. Scale variations are treated as uncorrelated for the $t\bar{t}$+light flavor, $t\bar{t} + b\bar{b}$, and $t\bar{t} + c\bar{c}$ components. The scale variations for W+jets and Z+jets are treated as correlated; all other scale variations are treated as uncorrelated.

A systematic uncertainty on the top quark p_T reweighting for the $t\bar{t}$+jets simulation is assessed using the uncorrected MC shapes as a -1 standard deviation systematic uncertainty, and overcorrected MC shapes as a $+1$ standard deviation uncertainty. The overcorrected shapes are calculated by doubling the deviation of the top-quark p_T scale factors from 1. The $t\bar{t} + b\bar{b}$ and $t\bar{t} + c\bar{c}$ processes represent an important source of irreducible background for the H $\to$ hadrons analysis. Neither control region studies nor higher-order theoretical calculations [85] can currently constrain the normalization of these contributions to better than 50% accuracy. Therefore, an extra 50% uncorrelated rate uncertainty is conservatively assigned to the $t\bar{t} + b\bar{b}$, $t\bar{t} + b$ and $t\bar{t} + c\bar{c}$ processes.

In the H $\to$ photons analysis, to assess the contamination from Higgs boson production from mechanisms other than $t\bar{t}H$, it is necessary to extrapolate MC predictions to final states with several jets beyond those included in the matrix elements used for the calculation. As these jets are modeled primarily with parton shower techniques, the uncertainty in these predictions should be carefully assessed. As POWHEG is used to model gg $\to$ H production, the uncertainty on the rate of additional jets is estimated by taking the observed difference between the POWHEG predictions and data in $t\bar{t}$ events which are dominated by gluon fusion production, gg $\to t\bar{t}$ [86]. This uncertainty amounts to at most 30%, which

– 34 –

includes the uncertainty in the fraction of gg → H plus heavy-flavor jets. Furthermore, the fraction of gg → H plus heavy-flavor jets is scaled by the difference observed between data and the POWHEG predictions [87] in t$\bar{\text{t}}$b$\bar{\text{b}}$ and t$\bar{\text{t}}$q$\bar{\text{q}}$/gg. These large uncertainties apply to a very small subset of the events falling into the signal region, thus resulting in a very small uncertainty on the final sensitivity to the signal itself.

In the H → leptons analysis, the normalization uncertainty in the WZ (ZZ) process comes from a variety of sources. Several uncertainties are related to the control region used to estimate the normalization, as described in section 7.3. The statistical uncertainty in the control region estimate results in 10% (12%) uncertainty in the normalization, while residual backgrounds in the control region account for another 10% (4%). Uncertainties in the b-tagging efficiencies result in a 15% (7.5%) normalization uncertainty. While uncertainties in the PDFs [88, 89] and on the extrapolation from the control region to the signal region cause normalization uncertainties of 4% (3%) and 5% (12%) respectively. Taken together, the uncertainties described above result in an overall WZ (ZZ) normalization uncertainty of 22% (19%).

9 Results

The statistical methodology employed for these results is identical to that used for other CMS Higgs boson analyses. More details can be found in ref. [9]. In brief, a binned likelihood spanning all analysis channels included in a given result is constructed. The amount of signal is characterized by the signal strength parameter μ, which is the ratio of the observed cross section for t$\bar{\text{t}}$H production to the SM expectation. In extracting μ some assumption must be made about the branching fractions of the Higgs boson. Unless stated otherwise, μ is extracted assuming SM branching fractions. Under some circumstances the branching fractions are parameterized in a more sophisticated fashion, for example allowing separate scaling for the Higgs boson's couplings to different particles in the SM. Uncertainties in the signal and background predictions are incorporated by means of nuisance parameters. Each distinct source of uncertainty is accounted with its own nuisance parameter, and in the case where a given source of uncertainty impacts more than one analysis channel, a single nuisance parameter is used to capture the correlation in this uncertainty between channels. Nuisance parameters are profiled, allowing high-statistics but signal-poor regions in the data to constrain certain key nuisance parameters.

To assess the consistency of the data with different hypotheses, a profile likelihood ratio test statistic is used: $q(\mu) = -2\ln\left[\mathcal{L}(\mu, \hat{\theta}_\mu)/\mathcal{L}(\hat{\mu}, \hat{\theta})\right]$, where θ represents the full suit of nuisance parameters. The parameters $\hat{\mu}$ and $\hat{\theta}$ represent the values that maximize the likelihood function globally, while the parameters $\hat{\theta}_\mu$ are the nuisance parameter values that maximize the likelihood function for a given μ. Results are reported both in terms of the best-fit value for μ and its associated uncertainty and in terms of upper limits on μ at 95% confidence level (CL). Limits are computed using the modified frequentist CL$_\text{S}$ method [90, 91]. Results are obtained both independently for each of the distinct t$\bar{\text{t}}$H signatures (b$\bar{\text{b}}$, $\tau_\text{h}\tau_\text{h}$, $\gamma\gamma$, same-sign $2l$, $3l$, and $4l$) as well as combined over all channels.

The best-fit signal strengths from the individual channels and from the combined fit are given in table 8 and figure 13. The internal consistency of the six results with a common signal strength has been evaluated to be 29%, estimated from the asymptotic behavior of the profile likelihood function [9]. Combining all channels, the best fit value of the common signal strength is $\mu = 2.8^{+1.0}_{-0.9}$ (68% CL). For this fit, the rates of Higgs boson production from mechanisms other than t$\bar{\text{t}}$H production are fixed to their SM expectations; however, allowing all Higgs boson contributions to float with a common signal strength produces a negligible change in the fit result. Although the fit result shows an excess, within uncertainties, the result is consistent with SM expectations. The p-value under the SM hypothesis ($\mu = 1$) is 2.0%. The p-value for the background-only hypothesis ($\mu = 0$) is 0.04%, corresponding to a combined local significance of 3.4 standard deviations. Assuming SM Higgs boson production with $m_\text{H} = 125.6$ GeV [29], the expected local significance is 1.2 standard deviations.

Throughout this paper, whenever a specific choice for Higgs boson mass has been required, a mass of 125.6 GeV has been used, corresponding to the most precise Higgs boson mass measurement by CMS at the time these results were obtained [29]. However, the recent CMS measurement of inclusive Higgs boson production with the Higgs boson decaying to a pair of photons [30], obtains a lower Higgs boson mass value. The combination of CMS Higgs boson mass measurements is expected to be very close to 125 GeV. The combined t$\bar{\text{t}}$H measurement is not very sensitive to the Higgs boson mass value. The combined best-fit signal strength obtained assuming a Higgs boson mass of 125 GeV is $\mu = 2.9^{+1.1}_{-0.9}$. This result corresponds to a 3.5 standard deviation excess over the background-only ($\mu = 0$) hypothesis, and represents a 2.1 standard deviation upward fluctuation on the SM t$\bar{\text{t}}$H ($\mu = 1$) expectation. These values are very close to the values quoted above for $m_\text{H} = 125.6$ GeV.

Although the observed signal strength is consistent with SM expectations, it does represent a roughly 2 standard deviation upward fluctuation. Therefore, it is interesting to look more closely at how the different channels contribute to the observed excess. From figure 13, it can be seen that the same-sign dilepton channel yields the largest signal strength. Within that channel, the same-sign dimuon subsample has the largest signal strength, with $\mu = 8.5^{+3.3}_{-2.7}$ compared with $\mu = 2.7^{+4.6}_{-4.1}$ for the same-sign dielectron channel and $\mu = 1.8^{+2.5}_{-2.3}$ for the same-sign electron-muon channel. The internal consistency of these three channels, along with the three and four lepton channels, is 16%. To characterize the impact of the same-sign dimuon channel on the combined fit, the fit was repeated with that channel omitted, resulting in a signal strength of $\mu = 1.9^{+1.0}_{-0.9}$. This fit result corresponds to a p-value under the SM hypothesis ($\mu = 1$) of 17%. The p-value under the background-only hypothesis for this fit is 1.6% corresponding to a local significance of 2.2 standard deviations. Although removing the same-sign dimuon channel does result in a lower fitted signal strength, the overall conclusion is unchanged.

In the above, consistency with SM expectations is assessed by varying the t$\bar{\text{t}}$H signal strength. An alternative approach would be to vary individual couplings between the Higgs boson and other particles. The collected statistics are currently insufficient to allow individual couplings to each SM particle to be probed. However, it is feasible to scale the couplings to vector bosons and fermions separately. This is a useful approach for testing whether the excess observed is consistent with expectations from SM t$\bar{\text{t}}$H production. Fol-

– 36 –

t$\bar{\text{t}}$H channel	Best-fit μ	95% CL upper limits on $\mu = \sigma/\sigma_{\text{SM}}$ ($m_{\text{H}} = 125.6\,\text{GeV}$)				
				Expected		
	Observed	Observed	Median signal-injected	Median	68% CL range	95% CL range
$\gamma\gamma$	$+2.7^{+2.6}_{-1.8}$	7.4	5.7	4.7	[3.1, 7.6]	[2.2, 11.7]
$b\bar{b}$	$+0.7^{+1.9}_{-1.9}$	4.1	5.0	3.5	[2.5, 5.0]	[1.9, 6.7]
$\tau_{\text{h}}\tau_{\text{h}}$	$-1.3^{+6.3}_{-5.5}$	13.0	16.2	14.2	[9.5, 21.7]	[6.9, 32.5]
4l	$-4.7^{+5.0}_{-1.3}$	6.8	11.9	8.8	[5.7, 14.3]	[4.0, 22.5]
3l	$+3.1^{+2.4}_{-2.0}$	7.5	5.0	4.1	[2.8, 6.3]	[2.0, 9.5]
Same-sign 2l	$+5.3^{+2.1}_{-1.8}$	9.0	3.6	3.4	[2.3, 5.0]	[1.7, 7.2]
Combined	$+2.8^{+1.0}_{-0.9}$	4.5	2.7	1.7	[1.2, 2.5]	[0.9, 3.5]

Table 8. The best-fit values of the signal strength parameter $\mu = \sigma/\sigma_{\text{SM}}$ for each t$\bar{\text{t}}$H channel at m_{H} = 125.6 GeV. The signal strength in the four-lepton final state is not allowed to be below approximately -6 by the requirement that the expected signal-plus-background event yield must not be negative in either of the two jet multiplicity bins. The observed and expected 95% CL upper limits on the signal strength parameter $\mu = \sigma/\sigma_{\text{SM}}$ for each t$\bar{\text{t}}$H channel at m_{H} = 125.6 GeV are also shown.

lowing the methodology used to study the properties of the new boson in the global CMS Higgs boson analysis [9], the scale factors κ_{V} and κ_{f} are introduced to modify the coupling of the Higgs boson to vector bosons and fermions, respectively. Figure 14 shows the 2D likelihood scan over the (κ_{V},κ_{f}) phase space using only the t$\bar{\text{t}}$H analysis channels. The best-fit values of the coupling modifiers are at (κ_{V},κ_{f}) = (2.2,1.5), which is compatible at the 95% CL with the expectation from the SM Higgs boson (1,1).

As BSM physics can enhance the production rate for the t$\bar{\text{t}}$H and t$\bar{\text{t}}$H+X final states, it is also useful to characterize the upper limit on t$\bar{\text{t}}$H production. Furthermore, the expected limit serves as a convenient gauge of the sensitivity of the analysis. The 95% CL expected and observed upper limits on μ are shown in table 8 for $m_{\text{H}} = 125.6\,\text{GeV}$ and as a function of m_{H} in figure 15, when combining all channels. Both the expected limit in the background-only hypothesis and the hypothesis including the SM Higgs boson signal, assuming the SM cross section, are quoted. In addition to the median expected limit under the background-only hypothesis, the bands that contain the one and two standard deviation ranges around the median are also quoted. In the absence of a t$\bar{\text{t}}$H signal, the median expected upper limit on μ from the combination of all channels is 1.7; the corresponding median expectation under the hypothesis of SM t$\bar{\text{t}}$H production with $m_{\text{H}} = 125.6\,\text{GeV}$ is 2.7. The observed upper limit on μ is 4.5, larger than both expectations, compatible with the observation that the best fit value of the signal strength modifier μ is greater than one. The limits for the individual channels at $m_{\text{H}} = 125.6\,\text{GeV}$ are given in the right panel of figure 15.
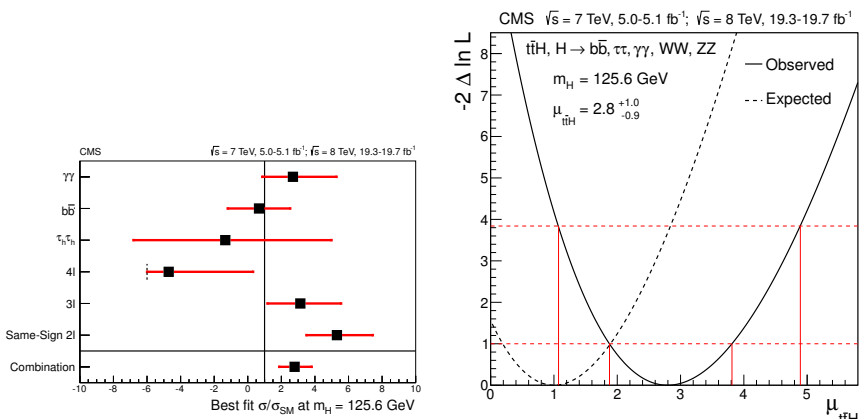
Figure 13. Left: the best-fit values of the signal strength parameter $\mu = \sigma/\sigma_{\rm SM}$ for each $t\bar{t}H$ channel at $m_{\rm H} = 125.6\,{\rm GeV}$. The signal strength in the four-lepton final state is not allowed to be below approximately -6 by the requirement that the expected signal-plus-background event yield must not be negative in either of the two jet multiplicity bins. Right: the 1D test statistic $q(\mu_{t\bar{t}H})$ scan vs. the signal strength parameter for $t\bar{t}H$ processes $\mu_{t\bar{t}H}$, profiling all other nuisance parameters. The lower and upper horizontal lines correspond to the 68% and 95% CL, respectively. The $\mu_{t\bar{t}H}$ values where these lines intersect with the $q(\mu_{t\bar{t}H})$ curve are shown by the vertical lines.
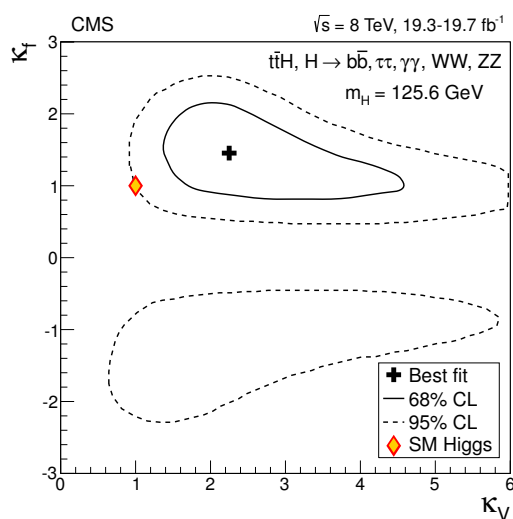
Figure 14. The 2D test statistic $q(\kappa_{\rm V}, \kappa_{\rm f})$ scan vs. the modifiers to the coupling of the Higgs boson to vector bosons ($\kappa_{\rm V}$) and fermions ($\kappa_{\rm f}$), profiling all other nuisances, extracted using only the $t\bar{t}H$ analysis channels. The contour lines at 68% CL (solid line) and 95% CL (dashed line) are shown. The best-fit and SM predicted values of the coupling modifiers ($\kappa_{\rm V}$, $\kappa_{\rm f}$) are given by the black cross and the open diamond, respectively.
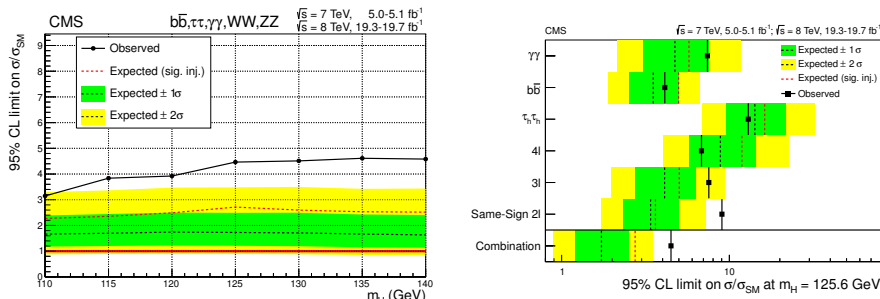
Figure 15. The 95% CL upper limits on the signal strength parameter $\mu = \sigma/\sigma_{\mathrm{SM}}$. The black solid and dotted lines show the observed and background-only expected limits, respectively. The red dotted line shows the median expected limit for the SM Higgs boson with $m_{\mathrm{H}} = 125.6\,\mathrm{GeV}$. The green and yellow areas show the 1σ and 2σ bands, respectively. Left: limits as a function of m_{H} for all channels combined. Right: limits for each channel at $m_{\mathrm{H}} = 125.6\,\mathrm{GeV}$.

10 Summary

The production of the standard model Higgs boson in association with a top-quark pair has been investigated using data recorded by the CMS experiment in 2011 and 2012, corresponding to integrated luminosities of up to $5.1\,\mathrm{fb}^{-1}$ and $19.7\,\mathrm{fb}^{-1}$ at $\sqrt{s} = 7\,\mathrm{TeV}$ and $8\,\mathrm{TeV}$ respectively. Signatures resulting from different combinations of decay modes for the top-quark pair and the Higgs boson have been analyzed. In particular, the searches have been optimized for the $\mathrm{H} \to \mathrm{b}\overline{\mathrm{b}}$, $\tau_{\mathrm{h}}\tau_{\mathrm{h}}$, $\gamma\gamma$, WW, and ZZ decay modes. The best-fit value for the signal strength μ is 2.8 ± 1.0 at 68% confidence level. This result represents an excess above the background-only expectation of 3.4 standard deviations. Compared to the SM expectation including the contribution from $\mathrm{t}\overline{\mathrm{t}}\mathrm{H}$, the observed excess is equivalent to a 2-standard-deviation upward fluctuation. These results are obtained assuming a Higgs boson mass of $125.6\,\mathrm{GeV}$ but they do not vary significantly for other choices of the mass in the vicinity of $125\,\mathrm{GeV}$. These results are more consistent with the SM $\mathrm{t}\overline{\mathrm{t}}\mathrm{H}$ expectation than with the background-only hypothesis.

Acknowledgments

– 39 –

– 40 –

by EU-ESF and the Greek NSRF; and the National Priorities Research Program by Qatar National Research Fund.

References

[1] CMS collaboration, *Observation of a new boson at a mass of* 125 *GeV with the CMS experiment at the LHC*, *Phys. Lett.* **B 716** (2012) 30 [`arXiv:1207.7235`] [ɪɴSPIRE].

[2] ATLAS collaboration, *Observation of a new particle in the search for the standard model Higgs boson with the ATLAS detector at the LHC*, *Phys. Lett.* **B 716** (2012) 1 [`arXiv:1207.7214`] [ɪɴSPIRE].

[3] F. Englert and R. Brout, *Broken symmetry and the mass of gauge vector mesons*, *Phys. Rev. Lett.* **13** (1964) 321 [ɪɴSPIRE].

[4] P.W. Higgs, *Broken symmetries, massless particles and gauge fields*, *Phys. Lett.* **12** (1964) 132 [ɪɴSPIRE].

[5] P.W. Higgs, *Broken symmetries and the masses of gauge bosons*, *Phys. Rev. Lett.* **13** (1964) 508 [ɪɴSPIRE].

[6] G.S. Guralnik, C.R. Hagen and T.W.B. Kibble, *Global conservation laws and massless particles*, *Phys. Rev. Lett.* **13** (1964) 585 [ɪɴSPIRE].

[7] P.W. Higgs, *Spontaneous symmetry breakdown without massless bosons*, *Phys. Rev.* **145** (1966) 1156 [ɪɴSPIRE].

[8] T.W.B. Kibble, *Symmetry breaking in non-Abelian gauge theories*, *Phys. Rev.* **155** (1967) 1554 [ɪɴSPIRE].

[9] CMS collaboration, *Observation of a new boson with mass near* 125 *GeV in pp collisions at* $\sqrt{s} = 7$ *and* 8 *TeV*, *JHEP* **06** (2013) 081 [`arXiv:1303.4571`] [ɪɴSPIRE].

[10] CMS collaboration, *Study of the mass and spin-parity of the Higgs boson candidate via its decays to Z boson pairs*, *Phys. Rev. Lett.* **110** (2013) 081803 [`arXiv:1212.6639`] [ɪɴSPIRE].

[11] ATLAS collaboration, *Measurements of Higgs boson production and couplings in diboson final states with the ATLAS detector at the LHC*, *Phys. Lett.* **B 726** (2013) 88 [`arXiv:1307.1427`] [ɪɴSPIRE].

[12] ATLAS collaboration, *Evidence for the spin-0 nature of the Higgs boson using ATLAS data*, *Phys. Lett.* **B 726** (2013) 120 [`arXiv:1307.1432`] [ɪɴSPIRE].

[13] CDF and D0 collaborations, T. Aaltonen et al., *Higgs boson studies at the Tevatron*, *Phys. Rev.* **D 88** (2013) 052014 [`arXiv:1303.6346`] [ɪɴSPIRE].

[14] CDF and D0 collaborations, T. Aaltonen et al., *Combination of the top-quark mass measurements from the Tevatron collider*, *Phys. Rev.* **D 86** (2012) 092003 [`arXiv:1207.1069`] [ɪɴSPIRE].

[15] N. Arkani-Hamed, A.G. Cohen and H. Georgi, *Electroweak symmetry breaking from dimensional deconstruction*, *Phys. Lett.* **B 513** (2001) 232 [`hep-ph/0105239`] [ɪɴSPIRE].

[16] N. Arkani-Hamed, A.G. Cohen, E. Katz and A.E. Nelson, *The littlest Higgs*, *JHEP* **07** (2002) 034 [`hep-ph/0206021`] [ɪɴSPIRE].

– 41 –

[17] R. Contino, L. Da Rold and A. Pomarol, *Light custodians in natural composite Higgs models*, *Phys. Rev.* **D 75** (2007) 055014 [hep-ph/0612048] [ɪɴSPIRE].

[18] CMS collaboration, *The CMS experiment at the CERN LHC*, 2008 *JINST* **3** S08004 [ɪɴSPIRE].

[19] R. Raitio and W.W. Wada, *Higgs boson production at large transverse momentum in QCD*, *Phys. Rev.* **D 19** (1979) 941 [ɪɴSPIRE].

[20] J.N. Ng and P. Zakarauskas, *A QCD parton calculation of conjoined production of Higgs bosons and heavy flavors in pp̄ collision*, *Phys. Rev.* **D 29** (1984) 876 [ɪɴSPIRE].

[21] Z. Kunszt, *Associated production of heavy Higgs boson with top quarks*, *Nucl. Phys.* **B 247** (1984) 339 [ɪɴSPIRE].

[22] W. Beenakker et al., *Higgs radiation off top quarks at the Tevatron and the LHC*, *Phys. Rev. Lett.* **87** (2001) 201805 [hep-ph/0107081] [ɪɴSPIRE].

[23] W. Beenakker et al., *NLO QCD corrections to tt̄H production in hadron collisions*, *Nucl. Phys.* **B 653** (2003) 151 [hep-ph/0211352] [ɪɴSPIRE].

[24] S. Dawson, L.H. Orr, L. Reina and D. Wackeroth, *Associated top quark Higgs boson production at the LHC*, *Phys. Rev.* **D 67** (2003) 071503 [hep-ph/0211438] [ɪɴSPIRE].

[25] S. Dawson, C. Jackson, L.H. Orr, L. Reina and D. Wackeroth, *Associated Higgs production with top quarks at the Large Hadron Collider: NLO QCD corrections*, *Phys. Rev.* **D 68** (2003) 034022 [hep-ph/0305087] [ɪɴSPIRE].

[26] M.V. Garzelli, A. Kardos, C.G. Papadopoulos and Z. Trócsányi, *Standard model Higgs boson production in association with a top anti-top pair at NLO with parton showering*, *Europhys. Lett.* **96** (2011) 11001 [arXiv:1108.0387] [ɪɴSPIRE].

[27] LHC Hɪɢɢs Cʀoss sᴇᴄᴛɪoɴ Woʀᴋɪɴɢ Gʀoᴜᴘ, S. Dittmaier et al., *Handbook of LHC higgs cross sections: 1. Inclusive observables*, CERN report CERN-2011-002, CERN, Geneva Switzerland (2011) [arXiv:1101.0593] [ɪɴSPIRE].

[28] LHC Hɪɢɢs Cʀoss sᴇᴄᴛɪoɴ Woʀᴋɪɴɢ Gʀoᴜᴘ, S. Heinemeyer et al., *Handbook of LHC Higgs cross sections: 3. Higgs properties*, CERN report CERN-2013-004, CERN, Geneva Switzerland (2013) [arXiv:1307.1347] [ɪɴSPIRE].

[29] CMS collaboration, *Measurement of the properties of a Higgs boson in the four-lepton final state*, *Phys. Rev.* **D 89** (2014) 092007 [arXiv:1312.5353] [ɪɴSPIRE].

[30] CMS collaboration, *Observation of the diphoton decay of the Higgs boson and measurement of its properties*, submitted to *Eur. Phys. J.* **C** [arXiv:1407.0558] [ɪɴSPIRE].

[31] CMS collaboration, *Energy calibration and resolution of the CMS electromagnetic calorimeter in pp collisions at $\sqrt{s} = 7$ TeV*, 2013 *JINST* **8** P09009 [arXiv:1306.2016] [ɪɴSPIRE].

[32] CMS collaboration, *CMS luminosity based on pixel cluster counting — summer* 2013 *update*, CMS-PAS-LUM-13-001, CERN, Geneva Switzerland (2013).

[33] CMS collaboration, *Search for the standard model Higgs boson produced in association with a top-quark pair in pp collisions at the LHC*, *JHEP* **05** (2013) 145 [arXiv:1303.0763] [ɪɴSPIRE].

[34] CMS collaboration, *Absolute calibration of the luminosity measurement at CMS — winter* 2012 *update*, CMS-PAS-SMP-12-008, CERN, Geneva Switzerland (2012).

[35] T. Sjöstrand, S. Mrenna and P.Z. Skands, *PYTHIA* 6.4 *physics and manual*, *JHEP* **05** (2006) 026 [hep-ph/0603175] [INSPIRE].

[36] J. Alwall, M. Herquet, F. Maltoni, O. Mattelaer and T. Stelzer, *MadGraph* 5*: going beyond*, *JHEP* **06** (2011) 128 [arXiv:1106.0522] [INSPIRE].

[37] P. Nason, *A new method for combining NLO QCD with shower Monte Carlo algorithms*, *JHEP* **11** (2004) 040 [hep-ph/0409146] [INSPIRE].

[38] S. Frixione, P. Nason and C. Oleari, *Matching NLO QCD computations with parton shower simulations: the POWHEG method*, *JHEP* **11** (2007) 070 [arXiv:0709.2092] [INSPIRE].

[39] S. Alioli, P. Nason, C. Oleari and E. Re, *A general framework for implementing NLO calculations in shower Monte Carlo programs: the POWHEG BOX*, *JHEP* **06** (2010) 043 [arXiv:1002.2581] [INSPIRE].

[40] E. Re, *Single-top Wt-channel production matched with parton showers using the POWHEG method*, *Eur. Phys. J.* **C 71** (2011) 1547 [arXiv:1009.2450] [INSPIRE].

[41] S. Alioli, P. Nason, C. Oleari and E. Re, *NLO single-top production matched with shower in POWHEG: s- and t-channel contributions*, *JHEP* **09** (2009) 111 [*Erratum ibid.* **02** (2010) 011] [arXiv:0907.4076] [INSPIRE].

[42] T. Melia, P. Nason, R. Rontsch and G. Zanderighi, W^+W^-, WZ *and* ZZ *production in the POWHEG BOX*, *JHEP* **11** (2011) 078 [arXiv:1107.5051] [INSPIRE].

[43] J. Pumplin et al., *New generation of parton distributions with uncertainties from global QCD analysis*, *JHEP* **07** (2002) 012 [hep-ph/0201195] [INSPIRE].

[44] P.M. Nadolsky et al., *Implications of CTEQ global analysis for collider observables*, *Phys. Rev.* **D 78** (2008) 013004 [arXiv:0802.0007] [INSPIRE].

[45] GEANT4 collaboration, S. Agostinelli et al., *Geant4: a simulation toolkit*, *Nucl. Instrum. Meth.* **A 506** (2003) 250 [INSPIRE].

[46] CMS collaboration, *Commissioning of the particle-flow event reconstruction with the first LHC collisions recorded in the CMS detector*, CMS-PAS-PFT-10-001, CERN, Geneva Switzerland (2010).

[47] CMS collaboration, *Commissioning of the particle-flow reconstruction in minimum-bias and jet events from pp collisions at* 7 *TeV*, CMS-PAS-PFT-10-002, CERN, Geneva Switzerland (2010).

[48] S. Baffioni et al., *Electron reconstruction in CMS*, *Eur. Phys. J.* **C 49** (2007) 1099 [INSPIRE].

[49] CMS collaboration, *Electron reconstruction and identification at* $\sqrt{s} = 7$ *TeV*, CMS-PAS-EGM-10-004, CERN, Geneva Switzerland (2010).

[50] CMS collaboration, *Electron commissioning results at* $\sqrt{s} = 7$ *TeV*, CMS-DP-2011-003, CERN, Geneva Switzerland (2011).

[51] CMS collaboration, *Electron performance with* 19.6 fb^{-1} *of data collected at* $\sqrt{s} = 8$ *TeV with the CMS detector*, CMS-DP-2013-003, CERN, Geneva Switzerland (2013).

[52] CMS collaboration, *Performance of CMS muon reconstruction in pp collision events at* $\sqrt{s} = 7$ *TeV*, 2012 *JINST* **7** P10002 [arXiv:1206.4071] [INSPIRE].

[53] CMS collaboration, *Particle-flow commissioning with muons and electrons from* J/Ψ *and* W *events at* 7 *TeV*, CMS-PAS-PFT-10-003, CERN, Geneva Switzerland (2010).

[54] M. Cacciari and G.P. Salam, *Dispelling the N^3 myth for the k_t jet-finder*, *Phys. Lett.* **B 641** (2006) 57 [hep-ph/0512210] [INSPIRE].

[55] M. Cacciari, G.P. Salam and G. Soyez, *The anti-k_t jet clustering algorithm*, *JHEP* **04** (2008) 063 [arXiv:0802.1189] [INSPIRE].

[56] CMS collaboration, *Pileup jet identification*, CMS-PAS-JME-13-005, CERN, Geneva Switzerland (2013).

[57] CMS collaboration, *Determination of jet energy calibration and transverse momentum resolution in CMS*, 2011 *JINST* **6** P11002 [arXiv:1107.4277] [INSPIRE].

[58] M. Cacciari, G.P. Salam and G. Soyez, *The catchment area of jets*, *JHEP* **04** (2008) 005 [arXiv:0802.1188] [INSPIRE].

[59] M. Cacciari and G.P. Salam, *Pileup subtraction using jet areas*, *Phys. Lett.* **B 659** (2008) 119 [arXiv:0707.1378] [INSPIRE].

[60] CMS collaboration, *Identification of b-quark jets with the CMS experiment*, 2013 *JINST* **8** P04013 [arXiv:1211.4462] [INSPIRE].

[61] CMS collaboration, *Performance of b tagging at $\sqrt{s} = 8\,TeV$ in multijet, $t\bar{t}$ and boosted topology events*, CMS-PAS-BTV-13-001, CERN, Geneva Switzerland (2013).

[62] CMS collaboration, *CMS technical design report, volume II: physics performance*, *J. Phys.* **G 34** (2007) 995 [INSPIRE].

[63] CMS collaboration, *Performance of τ-lepton reconstruction and identification in CMS*, 2012 *JINST* **7** P01001 [arXiv:1109.6034] [INSPIRE].

[64] CMS collaboration, *Measurement of the inclusive W and Z production cross sections in pp collisions at $\sqrt{s} = 7\,TeV$*, *JHEP* **10** (2011) 132 [arXiv:1107.4789] [INSPIRE].

[65] CMS collaboration, *Evidence for the 125 GeV Higgs boson decaying to a pair of τ leptons*, *JHEP* **05** (2014) 104 [arXiv:1401.5041] [INSPIRE].

[66] M. Czakon, P. Fiedler and A. Mitov, *Total top-quark pair-production cross section at hadron colliders through $O(\alpha_S^4)$*, *Phys. Rev. Lett.* **110** (2013) 252004 [arXiv:1303.6254] [INSPIRE].

[67] J.M. Campbell and R.K. Ellis, *$t\bar{t}W^\pm$ production and decay at NLO*, *JHEP* **07** (2012) 052 [arXiv:1204.5678] [INSPIRE].

[68] M.V. Garzelli, A. Kardos, C.G. Papadopoulos and Z. Trócsányi, *$t\bar{t}W^\pm$ and $t\bar{t}Z$ hadroproduction at NLO accuracy in QCD with parton shower and hadronization effects*, *JHEP* **11** (2012) 056 [arXiv:1208.2665] [INSPIRE].

[69] N. Kidonakis, *NNLL threshold resummation for top-pair and single-top production*, *Phys. Part. Nucl.* **45** (2014) 714 [arXiv:1210.7813] [INSPIRE].

[70] J.M. Campbell and R.K. Ellis, *MCFM for the Tevatron and the LHC*, *Nucl. Phys. Proc. Suppl.* **205-206** (2010) 10 [arXiv:1007.3492] [INSPIRE].

[71] Y. Li and F. Petriello, *Combining QCD and electroweak corrections to dilepton production in FEWZ*, *Phys. Rev.* **D 86** (2012) 094034 [arXiv:1208.5967] [INSPIRE].

[72] CMS collaboration, *Measurement of differential top-quark pair production cross sections in pp colisions at $\sqrt{s} = 7\,TeV$*, *Eur. Phys. J.* **C 73** (2013) 2339 [arXiv:1211.2220] [INSPIRE].

[73] B.P. Roe et al., *Boosted decision trees, an alternative to artificial neural networks*, *Nucl. Instrum. Meth.* **A 543** (2005) 577 [physics/0408124] [INSPIRE].

Measurement of the $t\bar{t}$ production cross section in the dilepton channel in pp collisions at $\sqrt{s} = 8\,\text{TeV}$

The CMS collaboration

E-mail: cms-publication-committee-chair@cern.ch

ABSTRACT: The top-antitop quark ($t\bar{t}$) production cross section is measured in proton-proton collisions at $\sqrt{s} = 8\,\text{TeV}$ with the CMS experiment at the LHC, using a data sample corresponding to an integrated luminosity of $5.3\,\text{fb}^{-1}$. The measurement is performed by analysing events with a pair of electrons or muons, or one electron and one muon, and at least two jets, one of which is identified as originating from hadronisation of a bottom quark. The measured cross section is $239\pm2\,(\text{stat.})\pm11\,(\text{syst.})\pm6\,(\text{lum.})\,\text{pb}$, for an assumed top-quark mass of $172.5\,\text{GeV}$, in agreement with the prediction of the standard model.

JHEP02(2014)024

Contents

1   Introduction

A precise measurement of the $t\bar{t}$ production cross section can be used to test the theory of quantum chromodynamics (QCD) at next-to-next-to-leading-order (NNLO) level. It can be also used in global fits of the parton distribution functions (PDF) at NNLO, and allows an estimation of $\alpha_s(M_Z)$ as described in [1, 2]. Furthermore, top-quark production is an important source of background in many searches for physics beyond the standard model (SM). A large sample of top-quark events has been collected at the Large Hadron Collider (LHC), and studies of top-quark production have been conducted in various decay channels as well as searches for deviations from the SM predictions [3–9].

This paper presents a measurement of the $t\bar{t}$ production cross section, $\sigma_{t\bar{t}}$, based on the dilepton channel (e^+e^-, $\mu^+\mu^-$, and $e^\pm\mu^\mp$) in a data sample of proton-proton collisions at $\sqrt{s} = 8\,\text{TeV}$ corresponding to an integrated luminosity of $5.3\,\text{fb}^{-1}$ recorded by the Compact Muon Solenoid (CMS) experiment. In the SM, top quarks are predominantly produced in $t\bar{t}$ pairs via the strong interaction and decay almost exclusively to a W boson and a bottom quark. We measure the $t\bar{t}$ production cross section selecting final states that contain two leptons of opposite electric charge, momentum imbalance associated to the neutrinos from the W boson decays, and two jets of particles resulting from the hadronisation of two b quarks.

2   The CMS detector and simulation

The CMS detector [10] has a superconducting solenoid occupying the central region that provides an axial magnetic field of 3.8 T. The silicon pixel and the strip tracker cover $0 <$

$\phi < 2\pi$ in azimuth and $|\eta| < 2.5$ in pseudorapidity, where η is defined as $\eta = -\ln[\tan(\theta/2)]$, with θ being the polar angle measured with respect to the anticlockwise-beam direction. The lead-tungstate crystal electromagnetic calorimeter and the brass/scintillator hadron calorimeter are located inside the solenoid. Muons are measured in gas-ionisation detectors embedded in the steel flux return yoke outside the solenoid. The detector is nearly hermetic, thereby providing reliable measurement of momentum imbalance in the plane transverse to the beams. A two-tier trigger system selects the most interesting pp collisions for offline analysis.

Several MC event generators are used to simulate signal and background events: MAD-GRAPH (v. 5.1.4.8) [11], POWHEG (r1380) [12] and PYTHIA (v. 6.424) [13], depending on the process considered. The MADGRAPH generator with spin correlations is used to model $t\bar{t}$ events with a top-quark mass of 172.5 GeV and combined with PYTHIA to simulate parton showering, hadronisation, and the underlying event. The MADGRAPH generator is also used to simulate the W+jets and Drell-Yan (DY) processes. Single-top-quark events are simulated using POWHEG. Inclusive production of the WZ and ZZ diboson final states is simulated with PYTHIA. Production of WW fully leptonic final states is simulated with MADGRAPH. Decays of τ leptons are handled with TAUOLA (v. 2.75) [14]. The contributions from WW, WZ and ZZ (referred to as "VV") and single-top-quark production are taken from MC simulations with appropriate next-to-leading order (NLO) cross sections. All other backgrounds are estimated from control samples extracted from collision data.

The $t\bar{t}$ production cross section amounts to $\sigma_{t\bar{t}} = 252.9^{+6.4}_{-8.6}\,(\text{scale}) \pm 11.7\,(\text{PDF} + \alpha_s)\,\text{pb}$ as calculated with the TOP++ program [15] at NNLO in perturbative QCD, including soft-gluon resummation at next-to-next-to-leading-log order [16], and assuming a top-quark mass $m_t = 172.5$ GeV. The first uncertainty comes from the independent variation of the factorisation and renormalisation scales, μ_F and μ_R, while the second one is associated to variations in the PDF and α_s following the PDF4LHC prescriptions [17]. Expected signal yields in figures and tables are normalised to that value unless otherwise stated.

The simulated samples include additional interactions per bunch crossing (pileup), with the distribution matching that observed in data.

3 Event selection

Event selection is similar to that used for the measurement of the $t\bar{t}$ dilepton cross section at $\sqrt{s} = 7$ TeV [4]. At trigger level, events are required to have two electrons, two muons, or one electron and one muon, where one of these leptons has transverse momentum $p_T > 17$ GeV and the other has $p_T > 8$ GeV. Events are then selected with two oppositely charged leptons reconstructed with the CMS particle-flow (PF) algorithm [18], both with $p_T > 20$ GeV and $|\eta| < 2.5$ for electrons and $|\eta| < 2.1$ for muons. In events with more than one pair of leptons passing these selections, the pair of opposite-sign leptons with the largest value of total transverse momentum is selected. Events with τ leptons contribute to the measurement only if they decay to electrons or muons that satisfy the selection requirements. The efficiency for dilepton triggers is measured in data through triggers based on transverse momentum imbalance. The trigger efficiency is approximately 90% to

93% for the three final states. Using the measured dilepton trigger efficiency in data, the corresponding efficiencies in the simulation are corrected by p_{T} and η multiplicative data-to-simulation scale factors (SFs), which have an average value of 0.96 and uncertainties in the range 1 to 2%.

Charged-lepton candidates from W-boson decays are usually isolated from other particles in the event. For each electron or muon candidate, a cone of $\Delta R < 0.3$ is constructed around the track direction at the event vertex, where ΔR is defined as $\Delta R = \sqrt{(\Delta \eta)^2 + (\Delta \phi)^2}$, and $\Delta \eta$ and $\Delta \phi$ are the differences in pseudorapidity and azimuthal angle between any energy deposit and the axis of the lepton track. The scalar sum of the p_{T} of all particles reconstructed with the PF algorithm, consistent with the chosen primary vertex and contained within the cone, is calculated, excluding the contribution from the lepton candidate itself. The relative isolation discriminant, I_{rel}, is defined as the ratio of this sum to the p_{T} of the lepton candidate. The neutral component is corrected for pileup based on the average energy density deposited by neutral particles in the event: an average transverse energy due to pileup is determined event by event and is subtracted from the transverse energy in the isolation cone. A lepton candidate is rejected if $I_{\mathrm{rel}} > 0.15$. The efficiency of the lepton selection is measured using a "tag-and-probe" method in dilepton events enriched in Z-boson candidates, as described in [4, 19]. The measured values for the combined identification and isolation efficiencies are typically of 96% for muons and 90% for electrons. Based on a comparison of lepton selection efficiencies in data and simulation, the event yield in simulation is corrected by p_{T}-and η-dependent SFs, which have an average value of 0.99 and uncertainties in the range 1 to 2% to provide consistency with data. Considering also the dilepton trigger, the combined factors have an average value of 0.96 and uncertainties around 2% for the three $t\bar{t}$ final states.

Dilepton candidate events with an invariant mass $M_{\ell\ell} < 20\,\mathrm{GeV}$ ($\ell = \mathrm{e}$ or μ) are removed to suppress backgrounds from heavy-flavour resonances, as well as contributions from low-mass DY processes. Events with dilepton invariant masses within $\pm 15\,\mathrm{GeV}$ of the Z mass are also rejected in the same-flavour channels.

Jets are reconstructed from the PF particle candidates using the anti-k_{T} clustering algorithm [20] with a distance parameter of 0.5. The jet energy is corrected for pileup in a manner similar to the correction of the energy inside the lepton isolation cone. Jet energy corrections are also applied as a function of the jet p_{T} and η [21]. Events are required to have at least two reconstructed jets with $p_{\mathrm{T}} > 30\,\mathrm{GeV}$ and $|\eta| < 2.5$.

The missing transverse energy, $\not{E}_{\mathrm{T}}$, is defined as the magnitude of the momentum imbalance, which is the negative sum of the momenta of all reconstructed particles in the plane transverse to the beams. A value of $\not{E}_{\mathrm{T}} > 40\,\mathrm{GeV}$ is required in the $\mathrm{e}^+\mathrm{e}^-$ and $\mu^+\mu^-$ channels while no $\not{E}_{\mathrm{T}}$ requirement is imposed for the $\mathrm{e}^{\pm}\mu^{\mp}$ mode, as there is very little contamination from DY events in this channel.

Since $t\bar{t}$ events contain jets from hadronisation of b quarks, requiring their presence can reduce background from events without b quarks. Jets are identified as b jets using the combined secondary vertex algorithm (CSV) [22]. The operating point chosen for CSV corresponds to an identification efficiency of about 85% and a misidentification (mistag) probability of about 10% [23] for light-flavour jets (u, d, s and gluons). The selection requires the presence of at least one b jet in the event.

– 3 –
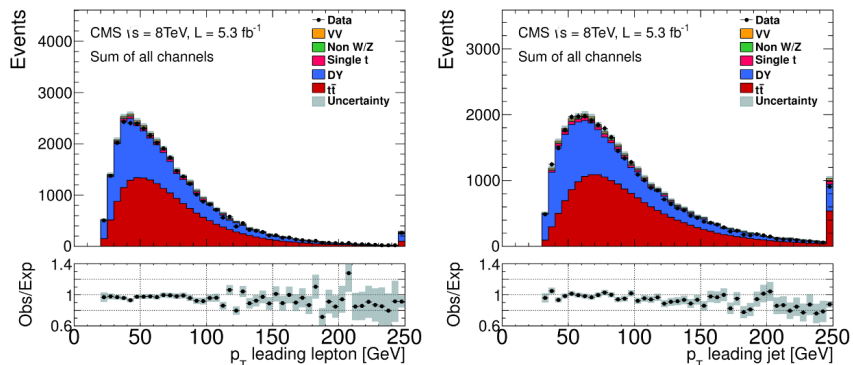
Figure 1. The p_T distributions of the highest-p_T lepton (left) and jet (right) after the jet multiplicity selection, for all three final states. The expected distributions for $t\bar{t}$ signal and individual backgrounds are shown after data-based corrections are applied; the last bin contains the overflow events. The hatched bands correspond to the total statistical uncertainty in the event yields for the sum of the $t\bar{t}$ and background predictions. The ratios of data to the sum of the expected yields are given at the bottom.

Figure 1 shows the p_T distributions of the highest-p_T lepton and jet after jet multiplicity selection, for all three final states combined. In this and the following figures the signal yields refer to an assumed top-quark mass of 172.5 GeV. The hatched regions correspond to the total statistical uncertainties in the predicted event yields. The ratio of the data to the sum of simulations and data-based predictions for the signal and backgrounds is shown in the bottom panels. A detailed description of the different background estimates is given in section 4. The multiplicities of selected jets and b jets are shown in figure 2 for the $e^{\pm}\mu^{\mp}$ channel, which is expected to have less background contamination. A similar level of agreement is obtained with the e^+e^- and $\mu^+\mu^-$ channels.

4 Background determination

Backgrounds in this analysis arise from single-top-quark, DY and VV events, in which at least two prompt leptons are produced from Z or W decays. Other background sources, such as $t\bar{t}$ or W+jets events with decays into lepton+jets and where at least one jet is incorrectly reconstructed as a lepton (which mainly happens for electrons) or a lepton from the decay of bottom or charm hadrons (which mainly happens for muons), are grouped into the non-W/Z lepton category. Background yields from single-top-quark and VV events are estimated from simulation, while all other backgrounds are estimated from data.

The DY background is estimated using the "$R_{\text{out/in}}$" method [3, 4, 24] in which the events outside of the Z mass window are obtained by normalising the event yield from simulation to the observed number of events inside the Z mass window. The data-to-simulation scale factor is found to be 1.3±0.4 for the $e^{\pm}\mu^{\mp}$ channel. This value is compatible
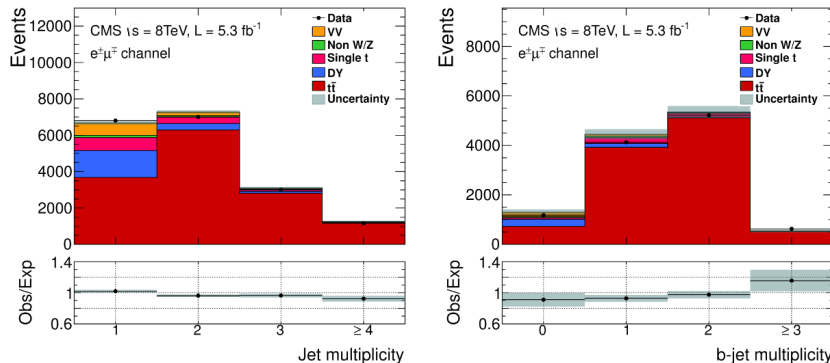
Figure 2. Jet multiplicity (left) in events passing the dilepton criteria, and (right) b-jet multiplicity in events passing the full event selections but before the b-jet requirement, for the $e^{\pm}\mu^{\mp}$ channel. In the right figure, the hatched bands show the total statistical and b-jet systematic uncertainties in the event yields for the sum of the $t\bar{t}$ and background predictions. The hatched bands in the left figure show only the total statistical uncertainty on the predicted event yields. The ratios of data to the sum of the expected yields are given at the bottom.

with 1.5 ± 0.5, which is estimated using a template fit as described in [4]. For the e^+e^- and $\mu^+\mu^-$ channels the factors are found to be 1.7 ± 0.5 and 1.6 ± 0.5, respectively.

Non-prompt leptons can arise from decays of mesons or heavy-flavour quarks, jet misidentification, photon conversions, or finite resolution detector effects whereas prompt leptons usually originate from decays of W or Z bosons and are isolated and well identified. Backgrounds with non-prompt leptons are estimated [25] from a control sample of collision data in which leptons are selected with relaxed identification and isolation requirements defining the loose lepton candidate, while the set of signal selection cuts described in section 3 defines the tight lepton candidate. The prompt and non-prompt lepton ratios are defined as the ratio of the number of tight candidates to the number of loose ones as measured from samples enriched in leptonic decays of Z bosons or in QCD dijet events, respectively. These ratios, parametrized as a function of p_T and η of the lepton, are then used to weight the events in the loose-loose dilepton sample, to obtain the estimated contribution from the non-prompt lepton background in the signal region. The systematic uncertainty comes from the jet p_T spectrum in dijet events and amounts, together with the statistical one, to 40% of the estimated yield.

5 Sources of systematic uncertainty

Simulated events are scaled according to the lepton efficiency correction factors, which are typically close to one, measured using control samples in data, leading to a 1 to 2% uncertainty in the $t\bar{t}$ selection efficiency.

The impact of uncertainty in the jet energy scale (JES) and jet energy resolution (JER) are estimated from the change observed in the number of selected MC $t\bar{t}$ events

after varying the jet momenta within the JES uncertainties [21], and in the case of JER by an η-dependent correction with an average of $\pm 10\%$. For the e^+e^- and $\mu^+\mu^-$ channels these uncertainties are also propagated to $\not{E}_T$ resulting in a larger uncertainty than for the $e^\pm\mu^\mp$ channel.

The uncertainties on the b jet scale factors in $t\bar{t}$ signal events are approximately 2% for b jets and 10% for mistagged jets [22, 23], depending on the p_T of the jets. They are propagated to the $t\bar{t}$ selection efficiency in simulated events.

The uncertainty assigned to the pileup simulation amounts to 0.8%, as obtained by varying the inelastic cross section by 5%. The uncertainty in the integrated luminosity is 2.6% [26].

The systematic effects related to the missing higher-order diagrams in MADGRAPH are estimated with two different methods. The uncertainty in the signal acceptance is determined by varying the renormalisation and factorisation scales simultaneously up and down by a factor of two using MADGRAPH, and the uncertainty is taken as the maximum difference after the final event selection. The effect on the calculated $t\bar{t}$ production cross section is 2.3%, which is the value used in the analysis for this uncertainty. This estimate is cross-checked by comparing the predictions of the leading-order and NLO generators MADGRAPH and POWHEG, where both use PYTHIA for hadronisation and extra radiation. The systematic uncertainty is found to be 2.2%, comparable with the above estimate.

The matching between the matrix elements (ME) and the parton shower (PS) evolution is done by applying the MLM prescription [27]. Changing the thresholds that control the matching of partons from the matrix element with those from PS by factors of 0.5 and 2.0 for one of the parameters (minimum k_T measure between partons) and 0.75 and 1.5 for the other (jet matching threshold for the k_T-MLM scheme) compared to the default thresholds, produces a 1.6% variation in the $t\bar{t}$ event selection efficiency.

The uncertainty arising from the hadronisation model affects mainly the JES and the fragmentation of b jets. As the b-jet efficiencies and mistagging rates are taken from data, no additional uncertainty is expected from this source. The uncertainty in the JES already contains a contribution from the uncertainty in the hadronisation. The hadronisation uncertainty is also determined by comparing samples of events generated with POWHEG where the hadronisation is modelled with PYTHIA or HERWIG, and the effect on the calculated $t\bar{t}$ cross section is 1.4%, which is well within the JES uncertainty.

Uncertainties in the selected number of single-top-quark and VV events are calculated following the same prescription as for the signal yield. In addition, an uncertainty in the cross sections for single-top-quark and VV backgrounds, taken from measurements and estimated to be approximately 20% [28–36], is added in quadrature.

Table 1 summarizes the magnitude of the systematic uncertainties on the $t\bar{t}$ production cross section from the different sources.

6   Results

The $t\bar{t}$ production cross section is measured by counting events after applying the selection criteria described in section 3. Table 2 shows the total number of events observed in data

Source	e^+e^-	$\mu^+\mu^-$	$e^\pm\mu^\mp$
Trigger efficiencies	4.1	3.0	3.6
Lepton efficiencies	5.8	5.6	4.0
Lepton energy scale	0.6	0.3	0.2
Jet energy scale	10.3	10.8	5.2
Jet energy resolution	3.2	4.0	3.0
b-jet tagging	1.9	1.9	1.7
Pileup	1.7	1.5	2.0
Scale (μ_F and μ_R)	5.7	5.5	5.6
Matching partons to showers	3.9	3.8	3.8
Single top quark	2.6	2.4	2.3
VV	0.7	0.7	0.5
Drell-Yan	10.8	10.3	1.5
Non-W/Z leptons	0.9	3.2	1.9
Total systematic	18.6	18.6	11.4
Integrated luminosity	6.4	6.1	6.2
Statistical	5.2	4.5	2.6

Table 1. Summary of the individual contributions to the systematic uncertainty on the $\sigma_{t\bar{t}}$ measurement. The uncertainties are given in pb. The statistical uncertainty on the result is given for comparison.

and the number of signal and background events expected from simulation or estimates from data. Table 3 lists the mean acceptance (which contains contributions from $W \rightarrow \tau\nu_\tau$, with leptonic τ decays) multiplied by the selection efficiency and the branching fraction in the dilepton final state, and the measured cross section for each of the three final states, e^+e^-, $\mu^+\mu^-$, and $e^\pm\mu^\mp$, which give compatible results. The e^+e^- and $\mu^+\mu^-$ channels have two additional sources of uncertainty, arising from the DY background estimation and from the propagation of the JES to the $\not{E}_T$ estimation, which limit the precision of the measurement of $\sigma_{t\bar{t}}$ in those final states.

A combination of the three final states using the BLUE method [37] yields a measured cross section of $\sigma_{t\bar{t}} = 239.0 \pm 2.1\,(\text{stat.}) \pm 11.3\,(\text{syst.}) \pm 6.2\,(\text{lum.})$ pb for a top-quark mass of 172.5 GeV. In the combination, the systematic uncertainties are 100% correlated across channels, except those associated to the lepton efficiencies, which have a correlation coefficient of 0.64 for e^+e^- with $e^\pm\mu^\mp$ and 0.55 for $\mu^+\mu^-$ with $e^\pm\mu^\mp$. Finally, the uncertainties associated with the data-based estimates and the statistical uncertainties are taken as uncorrelated.

In this analysis the dependence of the acceptance on the top-quark mass is found to be quadratic within the present uncertainty of the top-quark mass [38]. The cross-section
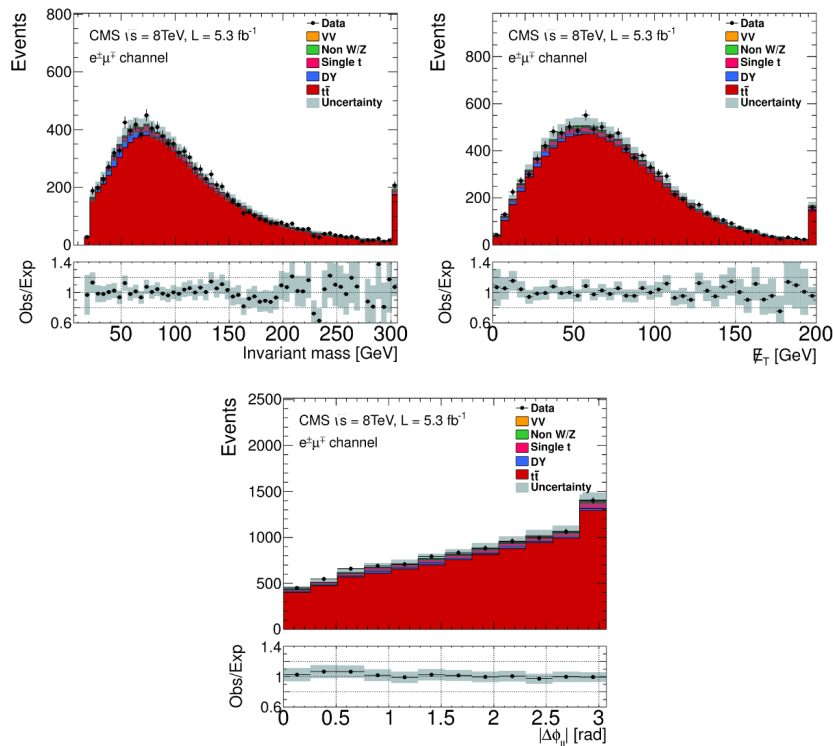
Figure 3. Distributions of (upper left) the dilepton invariant-mass, (upper right) the $\not{E}_T$, and (lower) the difference of the azimuthal angle between the two selected leptons, after the b-jet multiplicity selection and for the $e^{\pm}\mu^{\mp}$ channel. For the first two plots the last bin contains the overflow events. The expected distributions for $t\bar{t}$ signal, in this case, are normalised to the measured $t\bar{t}$ cross section. The hatched bands correspond to the total uncertainty in the predicted event yields for the sum of the $t\bar{t}$ and background predictions. The ratios of data to the sum of the expected yields are given at the bottom.

dependence in the range 160–185 GeV can be parametrized as

$$\sigma_{t\bar{t}}/\sigma_{t\bar{t}}\left(m_t = 172.5\right) = 1.00 - 0.009 \times \left(m_t - 172.5\right) - 0.000168 \times \left(m_t - 172.5\right)^2 \qquad (6.1)$$

where m_t is given in GeV. Assuming a top-quark mass value of 173.2 GeV [38], a cross section value $\sigma_{t\bar{t}} = 237.5 \pm 13.1$ pb is obtained.

Figure 3 shows the distributions of $M_{\ell\ell}$, $\not{E}_T$ and the difference of the azimuthal angle between the two selected leptons ($\Delta\phi_{\ell\ell}$) and their ratios to expectations for the $e^{\pm}\mu^{\mp}$ channel, which dominates the combination.

	Number of events		
Source	e^+e^-	$\mu^+\mu^-$	$e^\pm\mu^\mp$
Drell-Yan	386 ± 116	492 ± 148	194 ± 58
Non-W/Z leptons	25 ± 10	114 ± 46	185 ± 72
Single top quark	127 ± 28	157 ± 34	413 ± 88
VV	30 ± 8	39 ± 10	94 ± 21
Total background	569 ± 120	802 ± 159	886 ± 130
$t\bar{t}$ dilepton signal	2728 ± 182	3630 ± 250	9624 ± 504
Data	3204	4180	9982

Table 2. Number of dilepton events after applying the event selection and requiring at least one b jet. The results are given for the individual sources of background, $t\bar{t}$ signal with a top-quark mass of $172.5\,\mathrm{GeV}$ and $\sigma_{t\bar{t}} = 252.9\,\mathrm{pb}$, and data. The uncertainties correspond to the statistical and systematic components added in quadrature.

	e^+e^-	$\mu^+\mu^-$	$e^\pm\mu^\mp$
$\epsilon_{\mathrm{total}}$ (%)	0.203 ± 0.012	0.270 ± 0.017	0.717 ± 0.033
$\sigma_{t\bar{t}}$ (pb)	$244.3 \pm 5.2 \pm 18.6 \pm 6.4$	$235.3 \pm 4.5 \pm 18.6 \pm 6.1$	$239.0 \pm 2.6 \pm 11.4 \pm 6.2$

Table 3. The total efficiencies $\epsilon_{\mathrm{total}}$, i.e. the products of event acceptance, selection efficiency and branching fraction for the respective $t\bar{t}$ final states, as estimated from simulation for a top-quark mass of $172.5\,\mathrm{GeV}$, and the measured $t\bar{t}$ production cross sections, where the uncertainties are from statistical, systematic and integrated luminosity components, respectively.

7 Summary

A measurement of the $t\bar{t}$ production cross section in proton-proton collisions at $\sqrt{s} = 8\,\mathrm{TeV}$ is presented for events containing a lepton pair (e^+e^-, $\mu^+\mu^-$, $e^\pm\mu^\mp$), at least two jets with at least one tagged as b jet, and a large imbalance in transverse momentum in the final state. The measurement is obtained through an event-counting analysis based on a data sample corresponding to $5.3\,\mathrm{fb}^{-1}$. The result obtained by combining the three final states is $\sigma_{t\bar{t}} = 239 \pm 2\,\mathrm{(stat.)} \pm 11\,\mathrm{(syst.)} \pm 6\,\mathrm{(lum.)}\,\mathrm{pb}$, in agreement with the prediction of the standard model for a top-quark mass of $172.5\,\mathrm{GeV}$.

References

[1] CMS collaboration, *Determination of the top-quark pole mass and strong coupling constant from the $t\bar{t}$ production cross section in pp collisions at $\sqrt{s} = 7$ TeV, Phys. Lett.* **B 728** (2014) 496 [arXiv:1307.1907] [INSPIRE].

[2] M. Czakon, M.L. Mangano, A. Mitov and J. Rojo, *Constraints on the gluon PDF from top quark pair production at hadron colliders, JHEP* **07** (2013) 167 [arXiv:1303.7215] [INSPIRE].

[3] CMS collaboration, *Measurement of the $t\bar{t}$ production cross section and the top quark mass in the dilepton channel in pp collisions at $\sqrt{s} = 7$ TeV, JHEP* **07** (2011) 049 [arXiv:1105.5661] [INSPIRE].

[4] CMS collaboration, *Measurement of the $t\bar{t}$ production cross section in the dilepton channel in pp collisions at $\sqrt{s} = 7$ TeV, JHEP* **11** (2012) 067 [arXiv:1208.2671] [INSPIRE].

[5] ATLAS collaboration, *Measurement of the cross section for top-quark pair production in pp collisions at $\sqrt{s} = 7$ TeV with the ATLAS detector using final states with two high-p_T leptons, JHEP* **05** (2012) 059 [arXiv:1202.4892] [INSPIRE].

[6] CMS collaboration, *Measurements of $t\bar{t}$ spin correlations and top-quark polarization using dilepton final states in pp collisions at $\sqrt{s} = 7$ TeV,* arXiv:1311.3924 [INSPIRE].

[7] CMS collaboration, *Measurement of the charge asymmetry in top-quark pair production in proton-proton collisions at $\sqrt{s} = 7$ TeV*, *Phys. Lett.* **B 709** (2012) 28 [arXiv:1112.5100] [INSPIRE].

[8] ATLAS collaboration, *Search for new phenomena in $t\bar{t}$ events with large missing transverse momentum in proton-proton collisions at $\sqrt{s} = 7$ TeV with the ATLAS detector*, *Phys. Rev. Lett.* **108** (2012) 041805 [arXiv:1109.4725] [INSPIRE].

[9] ATLAS collaboration, *Search for anomalous production of prompt like-sign muon pairs and constraints on physics beyond the Standard Model with the ATLAS detector*, *Phys. Rev.* **D 85** (2012) 032004 [arXiv:1201.1091] [INSPIRE].

[10] CMS collaboration, *The CMS experiment at the CERN LHC*, 2008 *JINST* **3** S08004 [INSPIRE].

[11] J. Alwall, M. Herquet, F. Maltoni, O. Mattelaer and T. Stelzer, *MadGraph 5: going beyond*, *JHEP* **06** (2011) 128 [arXiv:1106.0522] [INSPIRE].

[12] S. Frixione, P. Nason and C. Oleari, *Matching NLO QCD computations with parton shower simulations: the POWHEG method*, *JHEP* **11** (2007) 070 [arXiv:0709.2092] [INSPIRE].

[13] T. Sjöstrand, S. Mrenna and P.Z. Skands, *PYTHIA 6.4 physics and manual*, *JHEP* **05** (2006) 026 [hep-ph/0603175] [INSPIRE].

[14] N. Davidson, G. Nanava, T. Przedzinski, E. Richter-Was and Z. Was, *Universal interface of TAUOLA technical and physics documentation*, *Comput. Phys. Commun.* **183** (2012) 821 [arXiv:1002.0543] [INSPIRE].

[15] M. Czakon and A. Mitov, *Top++, a program for the calculation of the top-pair cross-section at hadron colliders*, arXiv:1112.5675 [INSPIRE].

[16] M. Czakon, P. Fiedler and A. Mitov, *The total top quark pair production cross-section at hadron colliders through $O(\alpha_S^4)$*, *Phys. Rev. Lett.* **110** (2013) 252004 [arXiv:1303.6254] [INSPIRE].

[17] M. Botje et al., *The PDF4LHC working group interim recommendations*, arXiv:1101.0538 [INSPIRE].

[18] CMS collaboration, *Commissioning of the particle-flow reconstruction in minimum-bias and jet events from pp collisions at 7 TeV*, CMS-PAS-PFT-10-002 (2010).

[19] CMS collaboration, *Measurements of inclusive W and Z cross sections in pp collisions at $\sqrt{s} = 7$ TeV*, *JHEP* **01** (2011) 080 [arXiv:1012.2466] [INSPIRE].

[20] M. Cacciari, G.P. Salam and G. Soyez, *The anti-k_t jet clustering algorithm*, *JHEP* **04** (2008) 063 [arXiv:0802.1189] [INSPIRE].

[21] CMS collaboration, *Determination of jet energy calibration and transverse momentum resolution in CMS*, 2011 *JINST* **6** P11002 [arXiv:1107.4277] [INSPIRE].

[22] CMS collaboration, *Identification of b-quark jets with the CMS experiment*, 2013 *JINST* **8** P04013 [arXiv:1211.4462] [INSPIRE].

[23] CMS collaboration, *Results on b-tagging identification in 8 TeV pp collisions*, CMS-DP-2013-005 (2013).

[24] CMS collaboration, *First measurement of the cross section for top-quark pair production in proton-proton collisions at $\sqrt{s} = 7$ TeV*, *Phys. Lett.* **B 695** (2011) 424 [arXiv:1010.5994] [INSPIRE].

[25] CMS collaboration, *Measurement of Higgs boson production and properties in the WW decay channel with leptonic final states*, *JHEP* **01** (2014) 096 [arXiv:1312.1129] [InSPIRE].

[26] CMS collaboration, *CMS luminosity based on pixel cluster counting — Summer 2013 update*, CMS-PAS-LUM-13-001 (2013).

[27] M.L. Mangano, M. Moretti, F. Piccinini and M. Treccani, *Matching matrix elements and shower evolution for top-quark production in hadronic collisions*, *JHEP* **01** (2007) 013 [hep-ph/0611129] [InSPIRE].

[28] CMS collaboration, *Measurement of W^+W^- and ZZ production cross sections in pp collisions at $\sqrt{s} = 8$ TeV*, *Phys. Lett.* **B 721** (2013) 190 [arXiv:1301.4698] [InSPIRE].

[29] CMS collaboration, *Measurement of the W^+W^- cross section in pp collisions at $\sqrt{s} = 7$ TeV and limits on anomalous $WW\gamma$ and WWZ couplings*, *Eur. Phys. J.* **C 73** (2013) 2610 [arXiv:1306.1126] [InSPIRE].

[30] CMS collaboration, *Measurement of W^+W^- production and search for the Higgs boson in pp collisions at $\sqrt{s} = 7$ TeV*, *Phys. Lett.* **B 699** (2011) 25 [arXiv:1102.5429] [InSPIRE].

[31] CMS collaboration, *Measurement of the sum of WW and WZ production with W + dijet events in pp collisions at $\sqrt{s} = 7$ TeV*, *Eur. Phys. J.* **C 73** (2013) 2283 [arXiv:1210.7544] [InSPIRE].

[32] CMS collaboration, *Measurement of the ZZ production cross section and search for anomalous couplings in $2\ell 2\ell'$ final states in pp collisions at $\sqrt{s} = 7$ TeV*, *JHEP* **01** (2013) 063 [arXiv:1211.4890] [InSPIRE].

[33] CMS collaboration, *Measurement of the single-top-quark t-channel cross section in pp collisions at $\sqrt{s} = 7$ TeV*, *JHEP* **12** (2012) 035 [arXiv:1209.4533] [InSPIRE].

[34] ATLAS collaboration, *Measurement of the WW cross section in $\sqrt{s} = 7$ TeV pp collisions with the ATLAS detector and limits on anomalous gauge couplings*, *Phys. Lett.* **B 712** (2012) 289 [arXiv:1203.6232] [InSPIRE].

[35] ATLAS collaboration, *Measurement of the WZ production cross section and limits on anomalous triple gauge couplings in proton-proton collisions at $\sqrt{s} = 7$ TeV with the ATLAS detector*, *Phys. Lett.* **B 709** (2012) 341 [arXiv:1111.5570] [InSPIRE].

[36] ATLAS collaboration, *Measurement of the ZZ production cross section and limits on anomalous neutral triple gauge couplings in proton-proton collisions at $\sqrt{s} = 7$ TeV with the ATLAS detector*, *Phys. Rev. Lett.* **108** (2012) 041804 [arXiv:1110.5016] [InSPIRE].

[37] L. Lyons, D. Gibaut and P. Clifford, *How to combine correlated estimates of a single physical quantity*, *Nucl. Instrum. Meth.* **A 270** (1988) 110 [InSPIRE].

[38] Particle Data Group, J. Beringer et al., *Review of particle physics*, *Phys. Rev.* **D 86** (2012) 010001 [InSPIRE].

– 12 –

CMS Physics Analysis Summary

Investigations of the impact of the parton shower tuning in Pythia 8 in the modelling of $t\bar{t}$ at $\sqrt{s} = 8$ and 13 TeV

The CMS Collaboration

Abstract

Studies are presented comparing top quark pair differential distribution data collected with the CMS detector at $\sqrt{s} = 8$ and 13 TeV to state-of-the-art theoretical predictions. A tuning of POWHEG v2+PYTHIA8 through jet kinematics in top quark pair events and global variables is described and the studies validating the new settings along with the new event tune are presented. With the new event tune, the description of top quark pair and jet kinematics in top quark pair events, as well as the overall description of observables are improved. Studies of independent matrix element and parton shower scale variations along with initial-state and final-state radiation variations with several differential cross section measurements are also presented and the effects of these variations on particular observables are identified.

1 Introduction

Extracting the most information from top-quark measurements at hadron colliders requires a dedicated effort in theoretical modelling. In the Run 1 of the LHC, it was observed that the leading order (LO) generator MADGRAPH 5.1.3.30 [1] with up to three additional partons interfaced with PYTHIA 6.426 [2] using the Z2* event tune[1] [5] described reasonably well most of the differential $t\bar{t}$ distributions obtained from data, except for the transverse momentum of the top quark, p_T^t [6]. A new generation of next-to-leading order (NLO) matrix element (ME) event generators interfaced with new parton-shower (PS) codes are expected to provide better modelling of the signal and backgrounds, and reduce the dominant theoretical uncertainties with respect to the Run 1. These new codes used in conjunction with a new event tune are assessed using LHC Run 1 data and with a new set of differential distributions at $\sqrt{s}$=13 TeV using different final states [7–10]. The uncertainties assigned to the choice of the renormalization and factorization scales at the ME level are observed to provide good coverage with respect to most of the discrepancies observed so far. An exception is however made regarding the modelling of the extra jet multiplicity in $t\bar{t}$ events. The description of high jet multiplicities in $t\bar{t}$ events is not only important in top quark physics, but also in Higgs physics and searches for new physics. In this study, to improve the high jet multiplicities in $t\bar{t}$ events, a number of parameters have been tested and the most sensitive ones to jet kinematics in $t\bar{t}$ events are determined and optimized. We report on investigations carried out to tune the PS and matching parameters in the POWHEG v2 + PYTHIA 8 [11–13] setup using Run 1 data on jet activity in $t\bar{t}$ events. The jet activity mainly constrains those parameters that control the probability for parton emission and the interplay between hard and soft parton emission. The jet activity, however, does not strongly constrain the global production of hadrons known colloquially as "the underlying event." The sensitive parameters are then used as an input to derive a new event tune based on other data that is sensitive to the global production of hadrons. The final tune is tested against the results of several $t\bar{t}$ and other indepedent analyses performed in both Run 1 and Run 2. Based on our positive results, this tune will serve as the nominal setup to calibrate the top quark physics analyses in CMS in Run 2. The comparisons between theory predictions and unfolded data are accomplished using the RIVET [14] framework. The top-quark final state at particle-level (see [15]) is implemented in RIVET analysis modules that are available in the code repository. The RIVET framework is designed to run on any MC generator by allowing only final state particles in the HepMC [16] data format. This ensures independence from unphysical information in the generators and direct theory versus data comparisons. The top-quark final state at particle level (see [15]) is implemented in RIVET analysis modules that are available in the code repository.

This document is organized as follows: Section 2 summarizes the $t\bar{t}$ input data used in our analysis, as well as the RIVET routines employed. Comparisons are made between data and predictions from POWHEG v2 and MG5_aMC@NLO [17] in different configurations. Section 3 describes the procedure and results on tuning POWHEG v2 + PYTHIA 8 PS. A new event tune is derived which is used for comparisons throughout the rest of the document. Section 4 reports on the comparisons of the improved tuning with different data, and the summary is given in Section 5.

---

[1]Z2* tune is based on the Z1 tune[3] but using the CTEQ6L Parton Distribution Function (PDF) set [4] instead of the CTEQ5L PDF set.

2 Input Data

The data samples used correspond to an integrated luminosity of 19.7 fb^{-1} at $\sqrt{s} = 8$ TeV and 2.3 fb^{-1} at $\sqrt{s} = 13$ TeV. The list of analyses and distributions used for the comparisons in this note is shown in Table 1. In the table, p_T and y designate transverse momentum and rapidity, t_h and t_ℓ denote respectively the reconstructed top quark in the hadronic and leptonic legs, $t\bar{t}$ represents the top-anti-top quark system, and $j1$ and $j2$ are the leading additional and sub-leading additional jets. The symbols N, m, ΔR, H_T, S_T, and GF denote the number of jets, invariant mass, distance in $\eta - \phi$ space, the scalar sum of jet transverse momenta, the scalar sum of the transverse momenta of all objects, and gap fraction. The latter is defined as the fraction of events that do not contain additional jets above a given threshold. Finally, tj refers to the top quark jet defined in Section 2.4.

Table 1: List of analyses and distributions used for the comparisons in this manuscript. The columns list the final state (channel) analyzed, the quantities compared in this note and the level (parton or particle) to which they correspond, the center-of-mass energy, the integrated luminosity, and the designation assigned in this note to the RIVET repository when available.

Channel	Quantities	$\sqrt{s}$ (TeV)	Int. Lum. (fb^{-1})	Analysis [RIVET] [Reference]
lepton+jets	$p_T(t_h)$, $\lvert y(t_h)\rvert$, $p_T(t_\ell)$, $\lvert y(t_\ell)\rvert$ $p_T(t\bar{t})$, $\lvert y(t\bar{t})\rvert$, $M(t\bar{t})$, N_{add-j}	13	2.3	A [CMS_2016_I1434354] [8]
dilepton	$N_j >30, 60, 100$ GeV p_T^{j1}, p_T^{j2} $m(jj)$, $\Delta R(jj)$ p_T^{bj1}, p_T^{bj2} $m(b\bar{b})$, $\Delta R(b\bar{b})$ **** $(p_T^{j1}, p_T^{j2}, H_T)$ vs GF(inclusive) GF($\lvert\eta\rvert < 0.8$) GF($0.8 < \lvert\eta\rvert < 1.5$) GF($1.5 < \lvert\eta\rvert < 2.4$)	8	19.7	B [CMS_2015_I1397174] [18]
lepton+jets	MET, H_T, S_T, p_T^W	8	19.7	C [CMS_2016_I1473674] [19]
lepton+jets	p_T^t, y_t, p_T^{tj}, y_{tj}	8	19.7	D [CMS_2015_I1388555] [20]
lepton+jets	$N_j >30$ GeV	8	19.7	E [21]

2.1 Analysis A

The measurements reported in [8] are performed in the lepton+jets decay channels with a single muon or electron in the final state. The differential cross sections are presented at particle level,

relative to a phase space close to the experimental acceptance. The particle-level phase space is defined using the following definitions:

- Lepton: an electron or muon with $p_T > 30$ GeV and $|\eta| < 2.5$, with photons within a cone of radius 0.1 around the lepton included in the definition,

- Jet: a jet is reconstructed with the anti-k_t [22] clustering algorithm with a distance parameter of 0.4, after removing the neutrinos and the constituents of the leptons as defined above. To identify b jets at the generator level ghost B-hadrons [15] are included in the jet clustering. Jets are required to have $p_T > 25$ GeV and $|\eta| < 2.5$,

- b-jet: a jet that contains a ghost B-hadron as part of its constituents.

A W boson is reconstructed from a lepton and the sum of the neutrino energies, while another W boson is reconstructed from a light jet pair. The two top quarks are reconstructed by combining b jets to these W bosons. A check based on the W boson and top quark masses is performed to choose the proper combinations.

In this note, the distributions are normalized with a conservative approach, neglecting the correlations of uncertainties between the cross section in bins of a selected variable and the total cross section.

2.2   Analysis B

The measurement reported in [18] shows jet multiplicity distributions in $t\bar{t}$ events measured in 19.7 fb^{-1} of proton-proton collision data at a centre-of-mass energy of 8 TeV. The $t\bar{t}$ pairs are reconstructed in the dilepton decay channel with two oppositely charged isolated leptons (electrons or muons) and at least two jets of which at least one must be tagged as a b jet. The analysis follows, to a large extent, the strategy used in the measurement of normalized $t\bar{t}$ differential cross sections in the same decay channel described in Ref. [6]. The absolute and normalized differential cross sections for $t\bar{t}$ production are measured as a function of the jet multiplicity in the event for different jet transverse momentum thresholds and the kinematic properties of the leading additional jets, in order to probe the momentum dependence of the hard-gluon emission. The results are presented in a visible phase space in which all selected final-state objects are produced within the detector acceptance and are thus measurable experimentally. The absolute and normalized tt+jets production cross sections are also measured as a function of the p_T and pseudorapidity (η) of the leading additional jets, ordered by p_T. In cases with at least two additional jets or two b jets, the cross section is also measured as a function of the angular distance between the two jets and their dijet invariant mass. The results are reported both in the visible phase space and extrapolated to the full phase space of the $t\bar{t}$ system (corrected for acceptance and branching fractions) to facilitate the comparison with theoretical calculations. Furthermore, the fraction of events without additional jets above a threshold (gap fraction) is measured as a function of the transverse momenta of the leading additional jets and the scalar sum of the transverse momenta of all additional jets. The analysis combines particle-level information with decay mode selection at parton level using the following object definitions:

- Lepton: an electron or muon with $p_T > 20$ GeV and $|\eta| < 2.4$, from the W boson decay after final state radiation

- Jet: a jet is reconstructed with the anti-k_t clustering algorithm with a distance parameter of 0.5, using all stable particles but removing the constituents of the leptons as defined above. Jets are required to have $p_T > 20$ GeV and $|\eta| < 2.4$,

- b-jet: a jet that contains a matched B-hadron as part of its constituents coming from

a top quark decay. To identify b jets at the generator level, ghost B-hadrons are included in the jet clustering.

In addition to the visible phase-space definitions described above, the extrapolation to the full phase-space includes corrections to dilepton branching fractions and no requirements on top quark decay products, however any other additional jet must fulfill the above jet selection. In this note, only gap fraction and normalized differential cross sections are used.

2.3 Analysis C

The measurements reported in [19] comprise normalized differential cross sections for top quark pair production with respect to four kinematic event variables: the missing transverse energy, the scalar sum of the jet transverse momentum, the scalar sum of the p_T of all objects in the event, and the p_T of leptonically decaying W bosons from top quark decays.

The data sample consists of 5.0 fb^{-1} of proton-proton collisions at $\sqrt{s} = 7$ TeV and 19.7 fb^{-1} at $\sqrt{s}= 8$ TeV, however this note only uses 8 TeV distributions. Top quark pair events containing exactly one electron or muon are selected vetoing events with additional lepton candidates, and the event must have at least four jets with $p_T > 30$GeV, of which at least two are tagged as containing b hadrons. The results are presented after correcting for detector effects to allow direct comparison with theoretical predictions.

The analysis for this note implements the above selection and observables using particle level with the following definitions:

- Lepton: an electron or muon with photons within a cone of radius 0.1 around the lepton included in the definition. A veto on events where W boson decayed to τ is applied.

- Jet: a jet is reconstructed with the anti-k_t clustering algorithm with a distance parameter of 0.5, after removing the constituents of the leptons as defined above.

A W boson is reconstructed from a lepton and the sum of the neutrino energies.

The results from this analysis are complementary, since the $t\bar{t}$ production cross section is measured as a function of variables that do not require the reconstruction of the top quarks from their decay products.

2.4 Analysis D

The cross section for pair production of top quarks with high transverse momenta ($p_T > 400$ GeV) is measured. The measurement is performed for lepton+jets events, where one top quark decays according to $t \rightarrow Wb \rightarrow \ell\nu b$, with ℓ denoting an electron or muon, and the second top quark decays to an hadronic final state and is reconstructed as a single, large-radius jet and identified as a top quark candidate using jet substructure techniques. Differential cross sections as a function of the top quark p_T and rapidity, are measured at particle level within a fiducial region resembling the detector-level selections and at parton level. In this analysis, the particle level phase space is defined using the following object definitions:

- Lepton: An electron or muon originating from the decay of a W boson. The lepton is required to have $p_T > 45$ GeV and $|\eta| <2.1$.

- b-Jet: AK5 jets are formed by clustering the final state particles in the event using the anti-k_t algorithm with distance parameter R = 0.5. Here, final state particles refers to all status 1 particles in the event, excepting neutrinos and particles originating from

the decay of the muon defined above. The gen AK5 jet is required to have $p_T > 30$ GeV and $|\eta| <2.4$. AK5 jets in the same hemisphere as the lepton ($\Delta R(e/\mu, jet) < \pi/2$) are defined as b-jet candidates.

- Top Jet Candidate: CA8 jets are formed by clustering the final state particles in the event using the Cambridge-Aachen algorithm [23, 24] with distance parameter R=0.8. Here, final state particles refers to all status 1 particles in the event, excepting neutrinos and particles originating from the decay of the muon defined above. The gen CA8 jet is required to have $p_T > 30$ GeV and $|\eta| <2.4$. CA8 jets which have $p_T > 400$ GeV, 140 GeV $<$ mass $<$ 250 GeV, and are in the opposite hemisphere from the lepton ($\Delta R(e/\mu, jet) > \pi/2$) are defined as top jet candidates.

The particle-level phase space is defined by requiring $\geq$1 b jet candidate, $\geq$1 top jet candidate, and exactly one lepton. This is in addition to the parton-level semileptonic requirement. The highest-p_T top jet candidate is defined as the particle-level top jet, tj.

2.5 Analysis E

The measurement reported in [21] includes a differential $t\bar{t}$ cross section in bins of jet multiplicity at $\sqrt{s} = 8$ TeV in the lepton+jets (e/μ+jets) final state. The cross section is presented in the visible phase-space that follows closely the requirements and detector acceptance, and was implemented using particle level with the following definitions:

- Lepton: an electron or muon with $p_T > 30$ GeV and $|\eta| < 2.4$, with photons within a cone of radius 0.1 around the lepton included in the definition. A veto on events with additional loose leptons of $p_T > 15$ and $|\eta| < 2.5$ is applied.

- Jet: a jet is reconstructed with the anti-k_t clustering algorithm with a distance parameter of 0.5, after removing the neutrinos and the constituents of the leptons as defined above, but clustering also decay-photons and removing afterwards all leptons with $p_T > 5$ GeV from jet clustering. To identify b jets at the generator level, ghost B-hadrons are included in the jet clustering. Four jets are required to have $p_T > 30$ GeV and $|\eta| < 2.5$,

- b-jet: a jet that contains a B-hadron as part of its constituents. At least one b-jet is required.

3 Monte Carlo Settings, and α_s+hdamp Tuning with POWHEG + PYTHIA 8

The initial measurements of the additional jet multiplicity in $t\bar{t}$ events using 13 TeV data have shown poor agreement with the POWHEG v2+ PYTHIA 8 CUETP8M1 tune [7–9]. In order to improve the agreement, investigations have been carried on which parameters could be tuned. The following parameters have been found to be the most relevant to tune the jet measured in $t\bar{t}$ dilepton events at 8 TeV [18]:

- POWHEG: `hdamp` (h_{damp}) is the model parameter that controls ME/PS matching and effectively regulates the high-p_T radiation by damping real emissions generated by POWHEG with a factor of $h_{\mathrm{damp}}^2 / \left(p_T^2 + h_{\mathrm{damp}}^2 \right)$. The default value is equal to the top-quark mass $m_t = 172.5$ GeV used in simulation.

- PYTHIA 8: `SpaceShower:alphaSvalue` (α_s^{ISR}) is the value of the strong coupling at m_Z used for the initial-state shower. LEP event shapes [25] yielded $\alpha_s^{\mathrm{FSR}} = 0.1365$ for the final state shower. The default for both α_s^{FSR} and α_s^{ISR} are taken to be this value.

We have tuned the values of the two parameters described above using the jet multiplicity (N_{jets}) and leading additional jet multiplicity distributions in the dilepton final state obtained at $\sqrt{s}$=8 TeV. The information on the input data for tuning is also shown in Table 2. For tuning, we used the PROFESSOR tool [26]. In the tuning procedure all other PYTHIA 8 values are fixed to those found in the derivation of the CUETP8M1 tune using minimum bias data [27].

Table 2: The input data and distributions used in the $alpha_s^{ISR} + h_{damp}$ tuning.

Channel	Quantities	$\sqrt{s}$ (TeV)	Int. Lum. (fb^{-1})	Analysis [RIVET] [Reference]
dilepton	$N_j >30$ GeV p_T^{j1}	8	19.7	B [CMS_2015_I1397174] [18]

Samples of $t\bar{t}$ events at 8 TeV are generated with different combinations of $0.25m_t \leq h_{damp} \leq 4m_t$ and $0.05 \leq \alpha_s^{ISR} \leq 0.15$, resulting in 55 "anchor points" leading to an envelope of predictions covering the jet multiplicity and jet p_T data and their uncertainties. The h_{damp} values considered are $(0.25, 0.5, 1.0, 2.0, 4.0) \times m_t$, and the α_s^{ISR} values are 0.05, 0.06, 0.07, up to 0.15.

The PROFESSOR tuning software uses the generated anchor points to create an interpolation of the observable values in each bin as a function of the tuning parameters. The interpolation (and the tuning results) has been checked to be stable when using either all anchor points or a randomly selected sub-set of 25 anchor points.

The impact of the tuning parameters on N_{jets} and leading additional jet p_T can be quantified through the bin-wise sensitivity $S = \frac{dMC(p)}{dp} \times \frac{p_c}{MC(p_c)}$, where MC denotes the bin value for a parameter value p, and p_c is a reference parameter point. As shown in Fig. 1, α_s^{ISR} impacts mostly the higher jet multiplicities, while h_{damp} has a high influence on the ratio of 2-jet to 3-jet events and the leading additional jet p_T. This is in agreement with the expectation that the leading additional jet stems from the real radiation, estimated by the POWHEG generator.
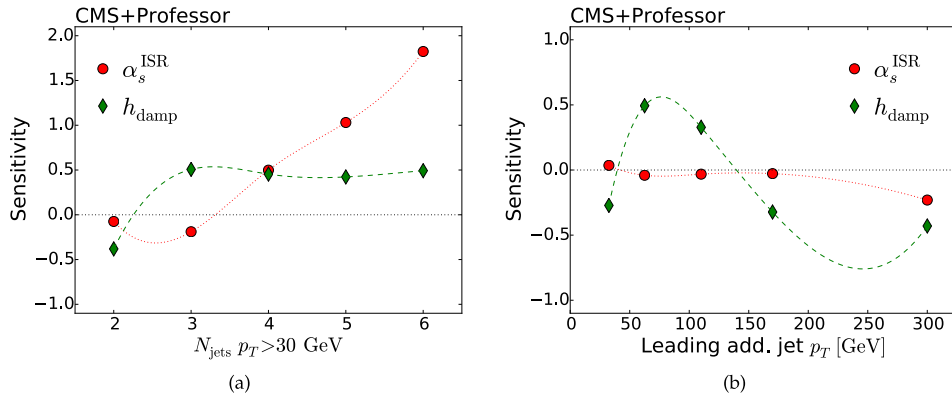
Figure 1: Sensitivity of (a) the multiplicity of jets with $p_T > 30$ GeV and (b) the leading additional jet p_T to the tuning parameters.

The tuning is performed by minimizing a χ^2 function

$$\chi^2(\vec{p}) = [\vec{x} - \vec{\mu}(\vec{p})]^T C^{-1} [\vec{x} - \vec{\mu}(\vec{p})], \tag{1}$$

where $\vec{x}$ denotes the data values, $\vec{\mu}$ the MC prediction for parameter values $\vec{p}$, and C the co-variance matrix. When calculating Eq. 1, we assume full correlation for each individual source of systematic uncertainty across all bins and observables. The statistical uncertainties are assumed to be uncorrelated for simplicity.

The χ^2 minimization yields a result of

$$h_{\text{damp}} = 1.581^{+0.658}_{-0.585} \times m_t, \qquad \alpha_s^{\text{ISR}} = 0.1108^{+0.0145}_{-0.0142} \tag{2}$$

for the new tune, CUETP8M1T4. A retuning of α_s alone to the same $t\bar{t}$ data yields $\alpha_s^{\text{ISR}} = 0.115^{+0.021}_{-0.019}$ (CUETP8M1T1 [28]). The predictions obtained with these optimized settings are shown in Fig. 2. Both yield a significantly lower value of α_s^{ISR}, curing the overshoot of CUETP8M1 at high jet multiplicities.
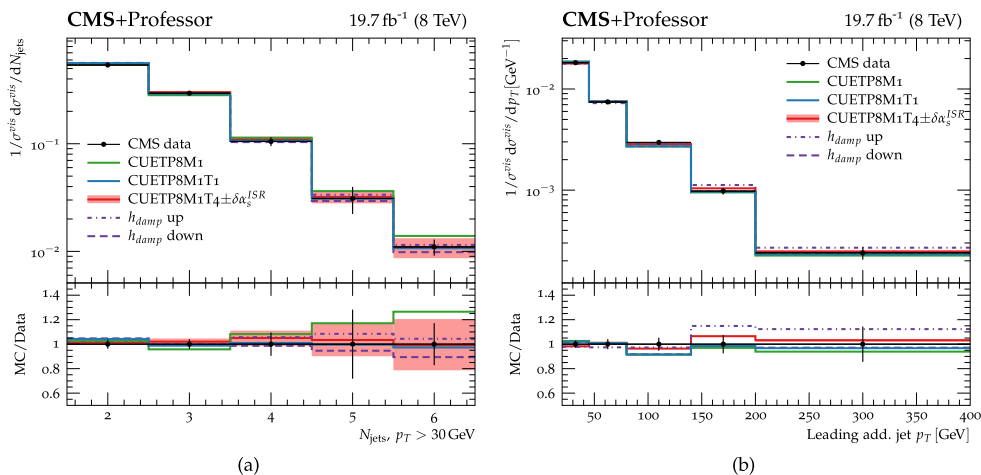
Figure 2: Different tunes compared to (a) the multiplicity of jets with $p_T > 30\,\text{GeV}$ and (b) the leading additional jet p_T. The uncertainty band shows the α_s^{ISR} uncertainty on the tuned prediction, while the dashed lines indicate the h_{damp} uncertainty.

Once the ISR α_s is extracted from the aforementioned measurements, using independent data sets a new event tune is derived accordingly, fixing the α_s value to the optimized one. The parameters considered for the event tune are related to the amount of multi-parton interactions (MPI), of proton overlap in the hadronic collisions and of colour reconnection, according to the event modelling used in PYTHIA 8 [29]. Indeed, a change of the event parameters is expected, if a different value of ISR α_s is chosen; this is due to the complex interplay between the MPI and PS contributions. Other parameters of the simulation that affect, for example, the PS, the fragmentation, and the intrinsic-parton p_T are fixed to the values of the CUETP8M1 [27, 30]. The new event tune is extracted again using PROFESSOR software [26] and RIVET [14], by generating sets of MC predictions in an automatized way with a 100 different choices of

parameters values related to the event simulation. The set of tuned parameters that best fits the input measurements defines the new event tune. The new event tunes are determined by fitting event observables measured at 13 TeV [31], which are the charged-particle multiplicity and p_T sum (Σp_T) in the MIN and MAX regions, as defined in [27], as a function of the leading track p_T. The charged-particle multiplicity as a function of η at 13 TeV [32] is also included in the fit. The adopted procedure is similar to the one described in [27]. Since only measurements performed at 13 TeV are considered, the parameter relative to the energy dependence of the partonic cross section cutoff (ECMPOW) is fixed to the value of CUETP8M1. The resulting event tune parameters are listed in Table 3. Note that the main changes between the parameters of the two tunes are α_s, PDF set, MPI p_{T0}^{ref} infrared regularization scale and the amount of color reconnection. The large change in the amount of color reconnection is a result of the different PDF set and the α_s value used in the different tunes.

Table 3: The parameters of the old tune (CUETP8M1) and the new tune (CUETP8M2T4). The parameter (in italic) relative to the energy dependence of the partonic cross section cutoff (ECMPOW) is fixed to the value of CUETP8M1 in the fit of the new tune. In the new tune, the ISR α_s is fixed to the value extracted from the $t\bar{t}$ events described previously.

	CUETP8M1	CUETP8M2T4
Tune	pp 14	pp 14
Tune	ee 7	ee 7
MultipartonInteractions ecmPow	0.2521	0.2521
SpaceShower:alphaSvalue	0.1365	0.1108
PDF pSet LHAPDF6	NNPDF23_lo_qed_as_0130	NNPDF30_lo_as_0130
MultipartonInteractions:pT0Ref	2.40	2.20
MultipartonInteractions:expPow	1.6	1.6
ColourReconnection:range	1.8	6.6

Predictions obtained with the new tunes are compared to other measurements which are not used in the tuning procedure. This helps to give a more general picture of the performance of the energy-dependent tune. The following observables, measured in pp collisions at 13 TeV by the CMS experiment, are investigated:

- Forward energy flow as a function of η, dE/dη [33];
- Central charged-particle multiplicity as a function of η, dN/dη [34];
- Underlying event observables, i.e. charged-particle multiplicity and Σp_T, in MIN and MAX regions, as a function of the leading jet p_T [31].

In addition to these, exclusive and inclusive number of jets, jet p_T, η, and H_T in 1 to 6 N_{jets} bins in Z+jets events measured at $\sqrt{s} = 8$ TeV [35] are used to check the effects of the new tune. A very good agreement is achieved by the predictions of the new tune for most of the compared measurement within systematic uncertainties.

4 Comparisons

In the following, we evaluate how the new CUETP8M2T4 PYTHIA 8 tune, obtained from the procedure described in the previous section, affects the modelling of CMS $t\bar{t}$ data, when different ME generators are employed. The primary settings used in the MC sample generation are given in Table 4. The ME mode hvq represents the heavy quark production for the POWHEG hard event generator [11–13]. The top-quark mass value used in all the simulations is 172.5 GeV and the corresponding PDF (shown in Table 4) at ME is used again for the PYTHIA 8 showering. The factorization and renormalization scales are denoted by μ_F and μ_R, respectively. In the definition of these scales, the transverse mass is used as $m_T = \sqrt{m_t^2 + p_T^2}$. The transverse mass of the top quark is shown with m_T^t. The q_{cut} parameter is the matching scale while x_{qcut} is the cutoff scale value for MLM matching in the k_T scheme. The smallest q_{cut} value is restricted to be above x_{qcut}. The q_{cut}^{ME} parameter is the cut applied to regulate multi-jet MEs in the FXFX mathing procedure. The q_{cut} parameters are optimized for each pp collision center of mass energy. The minimum p_T for the emission of light quarks is represented by $ptsqmin$. The data distributions are compared to four different settings, namely, POWHEG v2+PYTHIA 8, MG5_aMC@NLO+PYTHIA 8 [FXFX] [36], MG5_aMC@NLO+PYTHIA 8 [MLM] [37], and MC@NLO [38] except for Analysis D for which solely POWHEG v2+PYTHIA 8 comparison is reported. For all analyses, in addition to the new tune, comparisons with the previous tune (CUETP8M1) are also reported. Additional comparison for analysis A and B can be found in the Appendix.

Table 4: The MC samples used in the comparisons performed in this manuscripts.

ME generator	POWHEG v2	aMC@NLO	MG5_aMC@NLO	MG5_aMC@NLO
ME mode	hvq	Inclusive	FXFX Merging	MLM
ME pQCD level	$t\bar{t}$ [NLO]	$t\bar{t}$ [NLO]	$t\bar{t}$ +0,1,2 jets [NLO]	$t\bar{t}$ + 0, 1, 2, 3 jets
	1 jet [LO]	1 jet [LO]	3 jets [LO]	[LO]
$\mu_R = \mu_F$	m_T^t	$\sum_{t,\bar{t}} m_T/2$	$\sum_{t,\bar{t},\text{jets}} m_T/2$	$\sum_{t,\bar{t},\text{jets}} m_T/2$
PS	PYTHIA 8.219	PYTHIA 8.219	PYTHIA 8.219	PYTHIA 8.219
Tune	CUETP8M2T4	CUETP8M2T4	CUETP8M2T4	CUETP8M2T4
Tune	CUETP8M1			
ME PDF	NNPDF3.0 [39]	NNPDF3.0	NNPDF3.0	NNPDF23 [40]
ME α_s	0.118	0.118	0.118	0.130
Other	$h_{damp} = 1.581 m_t$			
	$h_{damp} = m_t$			
	$ptsqmin = 0.8$ GeV			
	$pThard = 0$			
	$pTdef = 1$			
q_{cut} (8 TeV)	-	-	30 GeV	60 GeV
q_{cut} (13 TeV)	-	-	40 GeV	80 GeV
Other (8 TeV)	-	-	$q_{cut}^{ME} = 10$ GeV	$x_{qcut} = 20$ GeV
Other (13 TeV)	-	-	$q_{cut}^{ME} = 20$ GeV	$x_{qcut} = 20$ GeV

4.1 Top quark and t̄t Kinematics

Figure 3 displays the normalized t̄t cross section in bins of p_T ^{t} in data and MC in the lepton+jets channel at $\sqrt{s}$ =13 TeV. Comparisons of the normalized t̄t cross section have been made for hadronically decaying top quarks (t_h) and leptonically decaying top quarks (t_l) separately. Data is compared to the predictions of POWHEG, MG5_aMC@NLO (either with MLM matching or FXFX merging), and aMC@NLO matched with the parton shower (PS) simulation PYTHIA 8 with the old (CUETP8M1) as well as the new (CUETP8M2T4) event tunes. Comparisons are also made using the predictions of POWHEG with different h_{damp} values with h_{damp}=1.581m_{top} being the central value obtained from the tuning. For t_h, it is observed that the predictions of the NLO MC generators matched with PYTHIA 8 with the old and new tunes agree with data within uncertainties. The LO order predictions of MG5_aMC@NLO, i.e. MLM configuration, does not agree with data. Using the new tune MG5_aMC@NLO[MLM] predictions become even worse. Fot t_l, the agreement with data is in general worse than t_h. At a bin-by-bin level, the new tune makes the predictions for t_l a bit worse for all except POWHEG[2]. It is also observed that the tuned h_{damp} value with its uncertainties still do not provide a good description of top quark p_T.

Normalized t̄t cross section data in bins of p_T ^{t} for the hadronically decaying top quarks (t_h) for 0, 1, 2, and 3 or more additional jets are compared to the different MC configurations in Figure 4. It is observed that the 0-additional jets case has the worst agreement between data and theory predictions, while the top-p_T discrepancy gets reduced starting from the 1-additional jet case when scale uncertainties are considered.

To have a more complete assessment of uncertainties due to the scale choices, we considered ME and PS scale variations. The lower and upper bounds for ME and PS scale variations considered are 0.5 and 2.0, respectively. The following independent FSR and ISR variations for the PS have been considered in PYTHIA 8:

- 'TimeShower:renormMultFac = 4.0', # FSR up
- 'SpaceShower:renormMultFac = 4.0',# ISR up
- 'TimeShower:renormMultFac = 0.25', # FSR down
- 'SpaceShower:renormMultFac = 0.25',# ISR down

Figure 5 displays the normalized cross sections in bins of p_T ^{t}, p_T (t̄t), and M(t̄t) with the bands representing the envelopes of maximum and minimum bin-by-bin deviations from the nominal scenario in which the scales are set to 1. In the figure, the envelopes are shown separately for ME+PS normalization scale factor and shape, ME+PS shape, ME normalization scale factor and shape, PS normalization scale factor and shape variations. The PS envelope is calculated with simultaneous variations of ISR and FSR in opposite directions to yield maximal effect, i.e. ISR up/FSR down and ISR down/FSR up. It is observed that the effects of the ME normalization scale factor and shape variations are larger than that of PS variations. The combined ME+PS normalization scale factor and shape variations are the highest ones and compared to them the ME+PS shape variations alone are quite small.

For boosted top quarks, normalized t̄t cross section in bins of parton-level top quark p_T and y as well as particle-level t jet p_T and y in the lepton+jets channel at $\sqrt{s}$ =8 TeV are displayed in Figure 6. The boosted distributions shown are normalized to the integrated cross section

---

[2]We note however that we did not compute the complete χ^2, including the full covariance matrix, in order to give a more quantitative statement supporting this statement. The same applies for other, following, comparisons in this manuscript.

for events with top quark p_T >400 GeV. The cross section is compared to the predictions of POWHEG combined with PYTHIA 8 with the old (CUETP8M1) and the new (CUETP8M2T4) event tunes. The data points are shown with the error bars. The systematic discrepancy observed at lower boosts of the top quark is also observed for top quark p_T > 400 GeV at the parton level, while for particle-level t jet p_T, the predictions agree well with data. The predictions with the old and the new tunes have no significant difference in the distributions in Figure 6.

Figure 7 displays the normalized t̄t cross section in bins of p_T (t̄t) and of M(t̄t) in data and MC in the lepton+jets channel at $\sqrt{s}$ =13 TeV. The cross sections are compared to the predictions of POWHEG, MG5_aMC@NLO either with MLM matching or FXFX merging, and aMC@NLO. For each case the PS simulation is done by PYTHIA 8 with the old (CUETP8M1) and the new (CUETP8M2T4) event tunes. Except for MG5_aMC@NLO[MLM] and aMC@NLO with the new tune, all predictions agree reasonably well with data. Comparisons are also made using the predictions of POWHEG with different h_{damp} values with h_{damp}=1.581m_{top} corresponding to the central value obtained from the tuning. The variations of h_{damp} around the tuned value induce variations of ≈ 10% in both distributions. From the comparison of the p_T (t̄t) distribution, it is clear that data disfavors the case with vanishing h_{damp}.

Figure 3: Normalized $t\bar{t}$ cross section in bins of $p_T{}^t$ in data and MC in the lepton+jets channel at $\sqrt{s}$ =13 TeV (Analysis A). The upper plots (a and b) show the hadronically decaying top quarks (t_h) and the lower plots (c and d) the leptonically decaying top quarks t_l. In plots a and c, the cross sections are compared to the predictions of POWHEG, MG5_aMC@NLO either with MLM mathing or FXFX merging, and aMC@NLO. For each case the PS simulation is done by PYTHIA 8 with the old (CUETP8M1) and the new (CUETP8M2T4) event tunes. In plots b and d, the cross sections are compared to the predictions of POWHEG with different h_{damp} values with h_{damp}=1.581m_{top} corresponding to the central value obtained from the tuning. Below each panel, the ratios of the predictions to data are shown with the yellow band indicating the total data uncertainties.

Figure 4: Normalized t̄t cross section in bins of $p_T{}^t$ for the hadronically decaying top quarks (t_h) in data and MC in the lepton+jets channel at $\sqrt{s} =$ 13 TeV (Analysis A). Panels a to d display $p_T{}^t$ in events with no, one, two, and three additional jets, respectively. The cross sections are compared to the predictions of POWHEG, MG5_aMC@NLO either with MLM mathing or FXFX merging, and aMC@NLO. For each case the PS simulation is done by PYTHIA 8 with the old (CUETP8M1) and the new (CUETP8M2T4) event tunes. Below each panel, the ratios of the predictions to data are shown with the yellow band indicating the total data uncertainties.
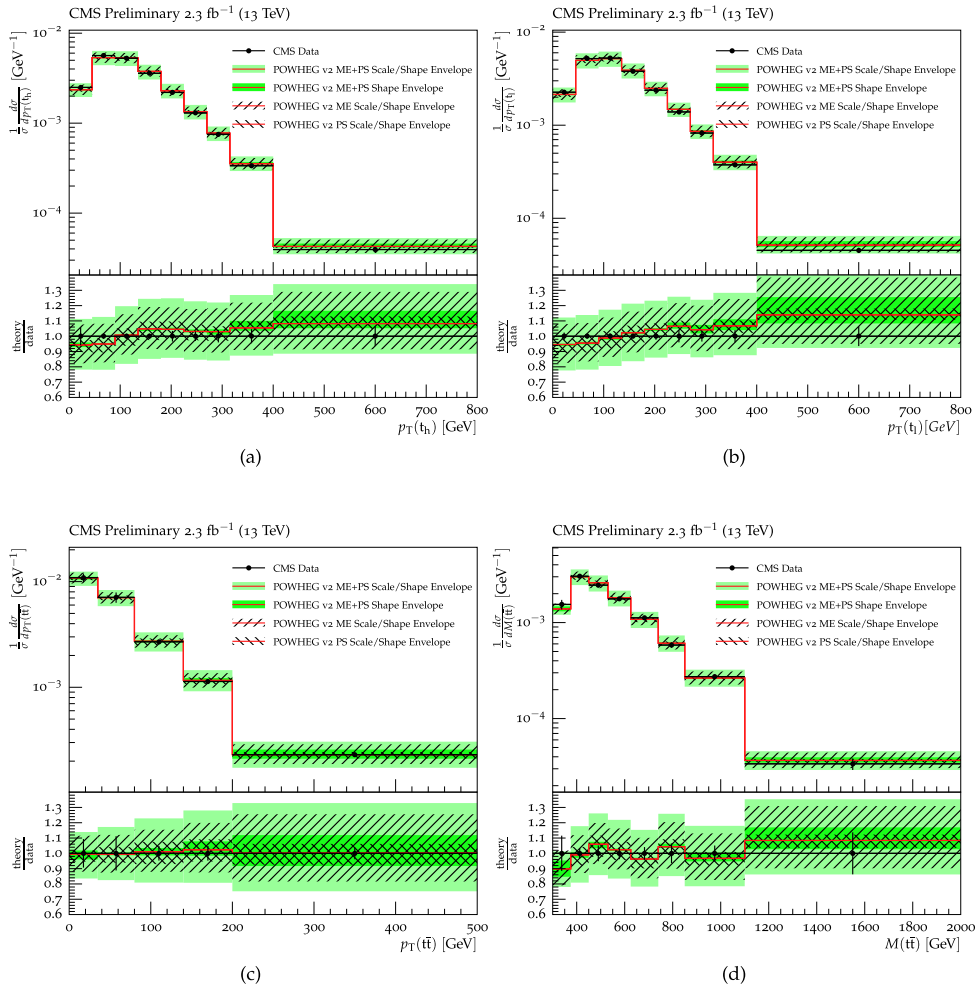
Figure 5: Normalized $t\bar{t}$ cross section in bins of $p_T{}^t$ for the hadronically decaying top quarks (t_h) (a), for the leptonically decaying top quarks (t_l) (b), in bins of p_T ($t\bar{t}$) (c), and in bins of M($t\bar{t}$) (d) in data and MC along with ME+PS normalization scale factor + shape and shape envelopes in the lepton+jets channel at $\sqrt{s}$ =13 TeV (Analysis A).
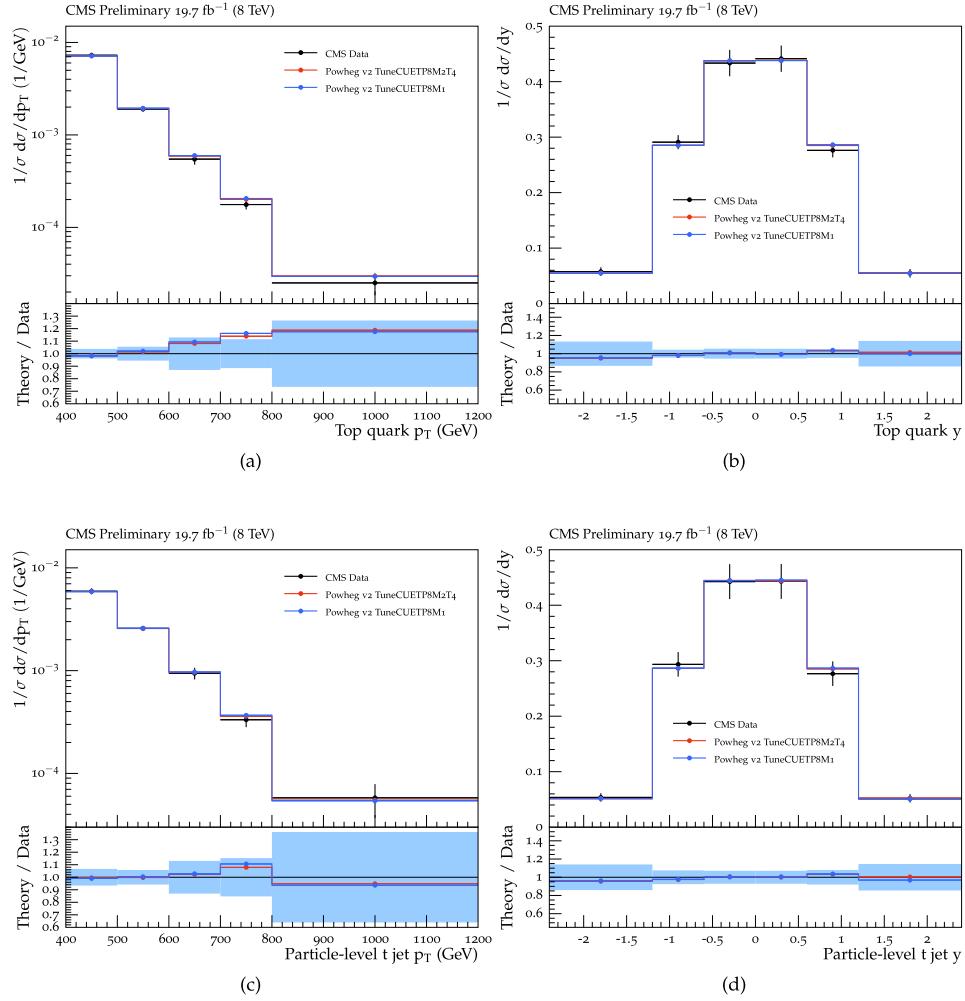
Figure 6: Normalized t$\bar{\text{t}}$ cross section in bins of parton-level top quark p_T (a) and rapidity (b), particle-level t jet p_T (c) and y (d) in the lepton+jets channel at $\sqrt{s}$ =8 TeV (Analysis D). The boosted distributions shown are normalized to the integrated cross section for events with top quark p_T >400 GeV. The cross section is compared to the predictions of POWHEG combined with PYTHIA 8 with the old (CUETP8M1) and the new (CUETP8M2T4) event tunes. The data points are shown with the total uncertainties. In the lower plot, the ratios of the predictions to data are shown with the blue band indicating the total data uncertainties.
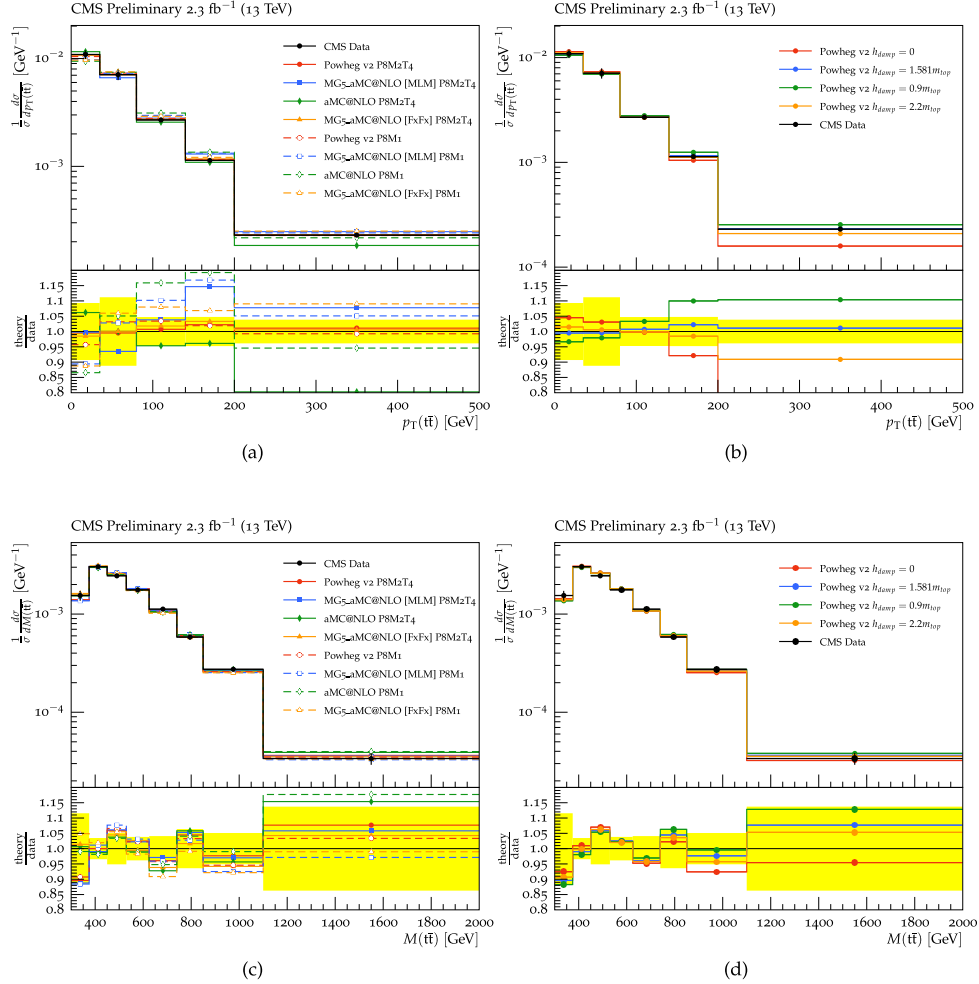
Figure 7: Normalized t$\bar{\text{t}}$ cross section in bins of p_T (t$\bar{\text{t}}$) (top) and of M(t$\bar{\text{t}}$) (bottom) in data and MC in the lepton+jets channel at $\sqrt{s}$ =13 TeV (Analysis A). The cross sections are compared to the predictions of POWHEG, MG5_aMC@NLO either with MLM mathing or FXFX merging, and aMC@NLO. For each case the PS simulation is done by PYTHIA 8 with the old (CUETP8M1) and the new (CUETP8M2T4) event tunes. In the lower panel of each plot, the ratios of the predictions to data are shown with the yellow band indicating the total data uncertainties.

4.2   **Global Event Variables**

Figure 8 displays the normalized $t\bar{t}$ cross section in bins of missing E_T, H_T, S_T, and $p_T{}^W$ in data and MC in the lepton+jets channel at $\sqrt{s} = 8$ TeV. All predictions agree well with data within uncertainties except MG5_aMC@NLO[MLM] and aMC@NLO with the new tune. The similarity of the predicition of MG5_aMC@NLO[FxFx] and POWHEG with the old and the new tunes assure that tuning α_s^{ISR} do not bias the results in searches that involves high missing E_T in the final states, and modelling $t\bar{t}$ from simulation. In the ratio of the predictions to data in the $p_T{}^W$ variable, a clear slope is visible and unlike other comparisons, this comparison shows that the new tune does not describe well data both for POWHEG and MG5_aMC@NLO[FxFx]. The result is not surprising given its correlation with the modelling of the top quark p_T, discussed in the previous section.
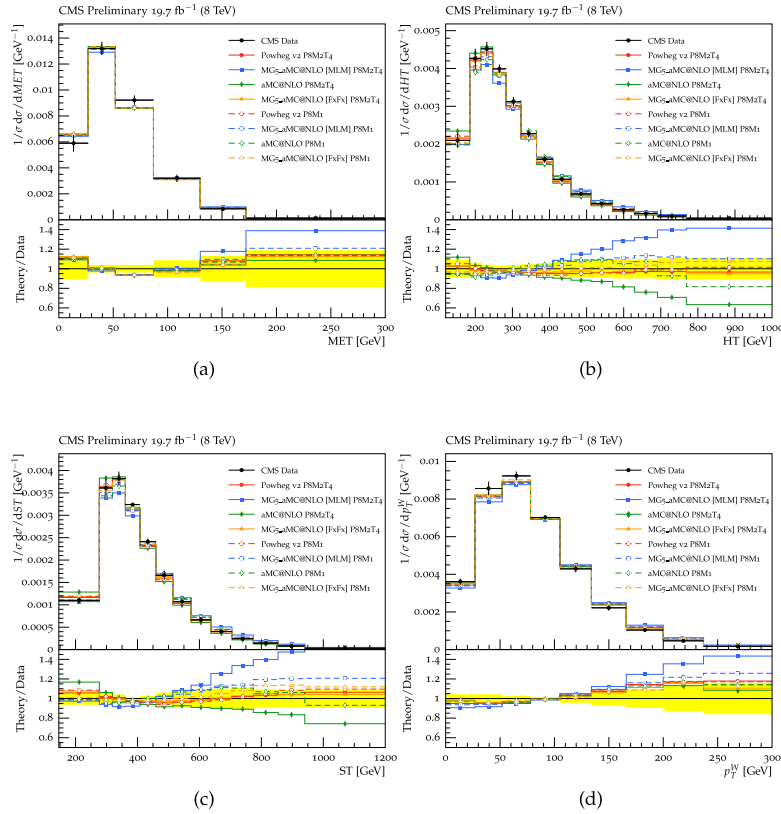
Figure 8: Normalized $t\bar{t}$ cross section in bins of missing E_T (a), H_T (b), S_T (c), and $p_T{}^W$ (d) in data and MC in the lepton+jets channel at $\sqrt{s} = 8$ TeV (Analysis C). The cross sections are compared to the predictions of POWHEG, MG5_aMC@NLO either with MLM mathing or FXFX merging, and aMC@NLO. For each case the PS simulation is done by PYTHIA 8 with the old (CUETP8M1) and the new (CUETP8M2T4) event tunes. In the lower panel of each plot, the ratios of the predictions to data are shown with the yellow band indicating the total data uncertainties.

4.3   Jet Activity

Normalized $t\bar{t}$ cross sections in bins of p_T of the leading additional jet in the visible phase space and in the full $t\bar{t}$ phase space in the dilepton channel are shown in Figure 9. The cross sections are compared to the predictions of POWHEG, MG5_aMC@NLO either with [MLM] mathing or [FXFX] merging, and aMC@NLO. For each case the PS simulation is done by PYTHIA 8 with the old (CUETP8M1) and the new (CUETP8M2T4) event tunes. Apart from MG5_aMC@NLO[MLM] with the new tune and aMC@NLO with both tunes, all theory predictions agree well with the data both in the visible as well as in the full phase space.

Jet activity is also investigated through comparisons using gap fraction in bins of p_T of the leading additional jet (Figure 10) and in bins of H_T (Figure 11). The best agreement with data is provided by POWHEG with the new tune. Significant discrepancies with respect to data are observed with all other settings.
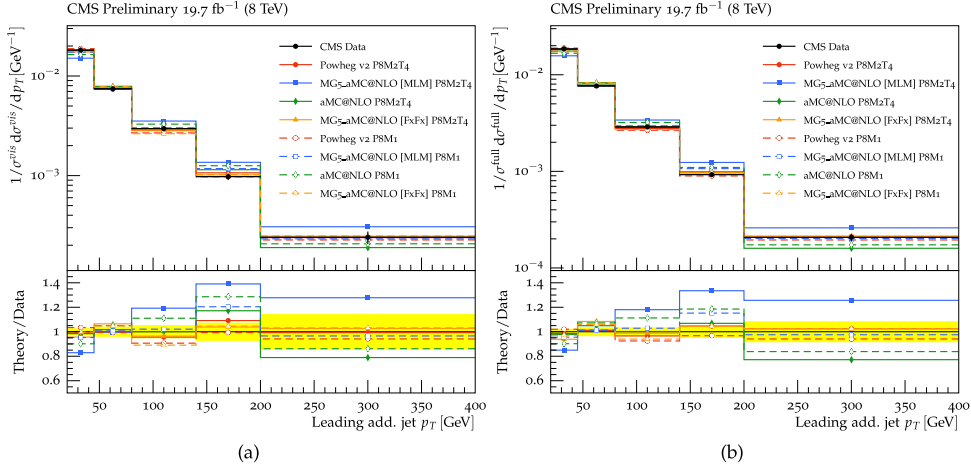
Figure 9: Normalized $t\bar{t}$ cross section in bins of p_T of the leading additional jet in the visible phase space (a) and in the full $t\bar{t}$ phase space (b) in the dilepton channel at $\sqrt{s}$=8 TeV (Analysis B). The cross sections are compared to the predictions of POWHEG, MG5_aMC@NLO either with [MLM] mathing or [FXFX] merging, and aMC@NLO. For each case the PS simulation is done by PYTHIA 8 with the old (CUETP8M1) and the new (CUETP8M2T4) event tunes. In the lower panel of each plot, the ratios of the predictions to data are shown with the yellow band indicating the total data uncertainties.
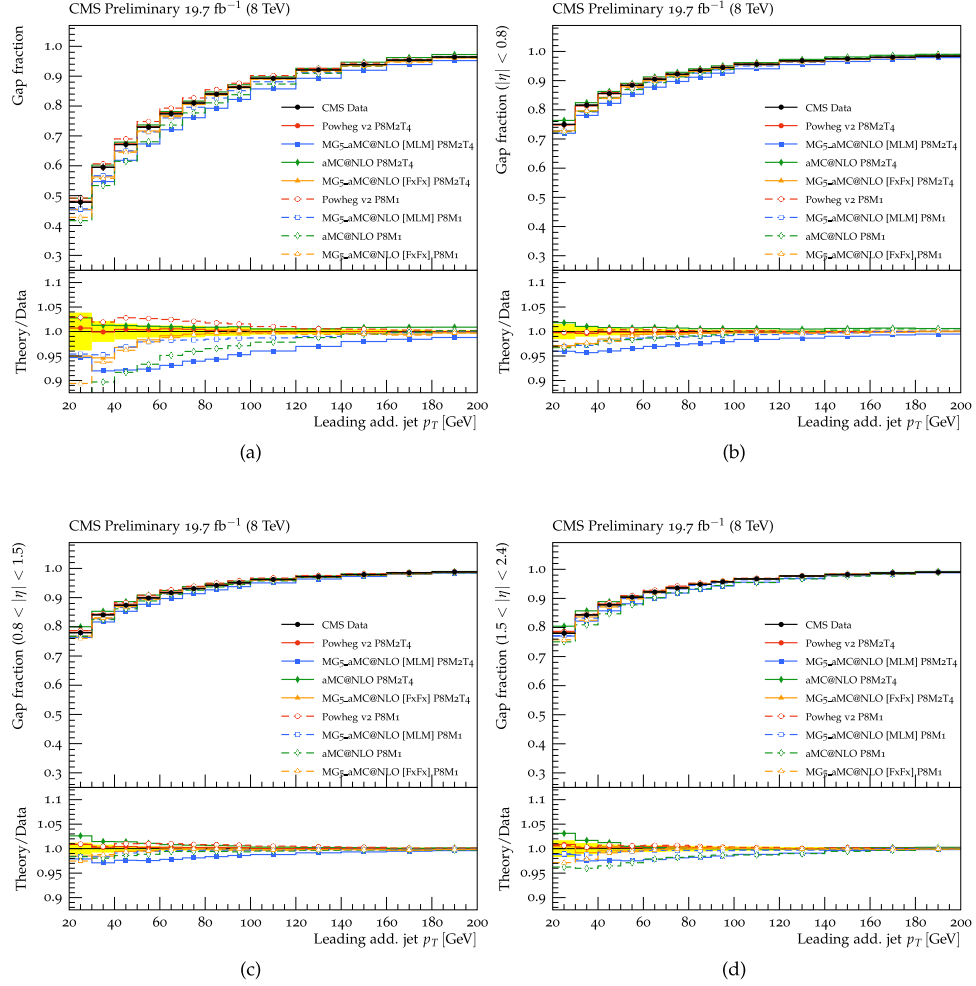
Figure 10: Gap fraction in bins of p_T of the leading additional jet in the dilepton channel at $\sqrt{s}$=8 TeV (Analysis B). Panel a displays the gap fraction without any requirements on η. Panel b to d display the gap fraction in different η regions of the additional jets.
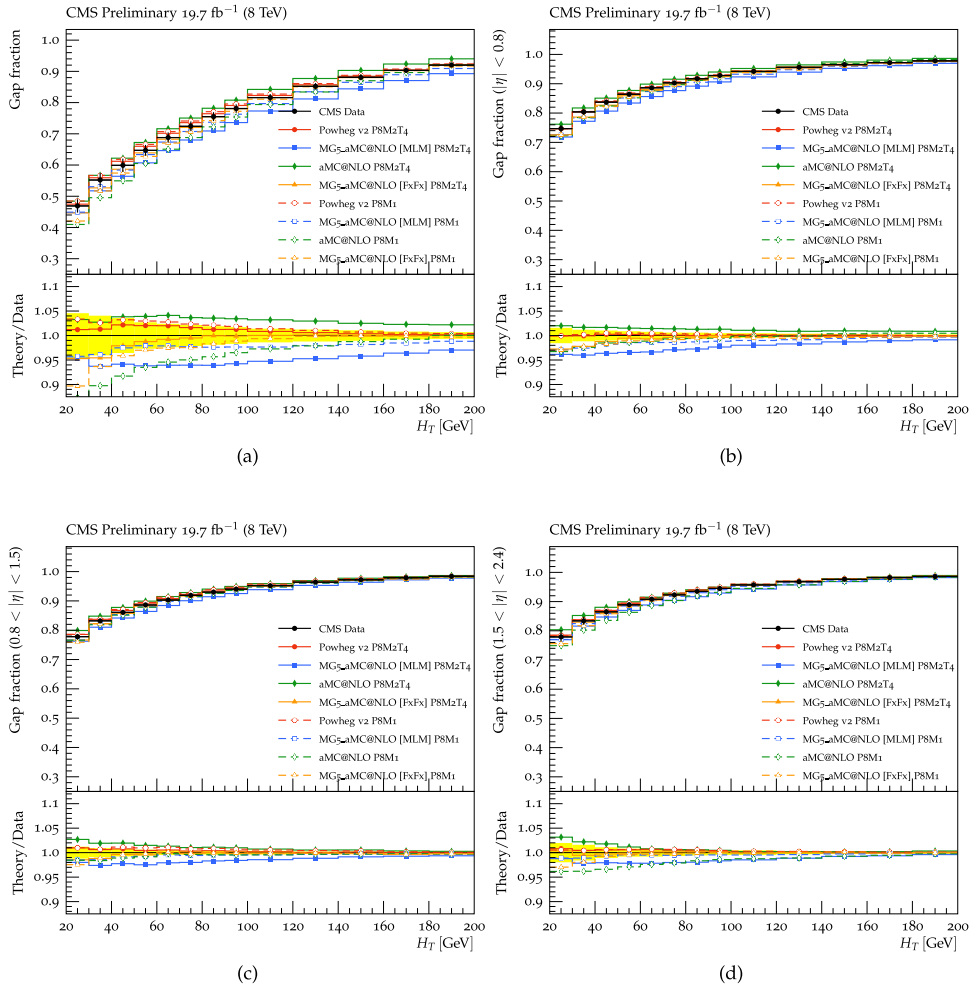
Figure 11: Gap fraction in bins of H_T in the dilepton channel at $\sqrt{s}$=8 TeV (Analysis B). Panel a displays the gap fraction without any requirements on η. Panel b to d display the gap fraction in different η regions of the additional jets.

4.4   Jet Multiplicity

Normalized $t\bar{t}$ cross sections in bins of number of additional jets in data and MC in the lepton+jets channel at $\sqrt{s}$ =13 TeV are shown in Figure 12. The cross sections are compared to the predictions of POWHEG, MG5_aMC@NLO either with MLM mathing or FXFX merging, and aMC@NLO. For each case the PS simulation is done by PYTHIA 8 with the old (CUETP8M1) and the new (CUETP8M2T4) event tunes. By using the new tune, both POWHEG and MG5_aMC@NLO[FxFx] predictions are in signifcantly better agreement with the data with respect to the previous tune which overestimated the jet multiplicity. It is important to note that the predictions of neither MG5_aMC@NLO[MLM] nor aMC@NLO with the new tune agree with data. The cross sections are also compared to the predictions of POWHEG with different h_{damp} values. The predictions using the tuned h_{damp} with its uncertainties agree within the data uncertainties, while the predictions with $h_{damp} = 0$ do not agree with data.

Jet multiplicity distributions measured at $\sqrt{s}$ =8 TeV in the dilepton channel and lepton+jets channels are displayed in Figure 13. In the dilepton channel, comparisons have been made at three different jet p_T thresholds, namely, 30, 60, and 100 GeV. Although there is some threshold dependence, the predictions with the new tune agree well with data. As in other distributions, MG5_aMC@NLO[MLM] and aMC@NLO with the new tune give the worst predictions.

Normalized $t\bar{t}$ cross section in bins of number of additional jets in data and MC along with normalization scale factor and shape envelopes of ME, PS, and ME+PS ME+ISR variations in the lepton+jets channel at $\sqrt{s}$ =13 TeV and 8 TeV are shown in Figures 14 and 15, respectively. In Figure 15, some of the high jet multiplicity bins contain low number of events and some of the downward and upward variations go in the same direction. Therefore, the central value in some bins are not contained within the envelope. For such bins, we forced the envelope to include the central values in Figure 15. As in Figure 5 the PS envelope is calculated with simultaneous variations of ISR and FSR in opposite directions. Also in this case, it is observed that the effects of the ME normalization scale factor and shape variations are larger than that of PS variations.

Figure 12: Normalized $t\bar{t}$ cross section in bins of number of additional jets in data and MC in the lepton+jets channel at $\sqrt{s}$ =13 TeV (Analysis A). In plot a, the cross sections are compared to the predictions of POWHEG, MG5_aMC@NLO either with MLM mathing or FXFX merging, and aMC@NLO. For each case the PS simulation is done by PYTHIA 8 with the old (CUETP8M1) and the new (CUETP8M2T4) event tunes. In plot b, the cross sections are compared to the predictions of POWHEG with different h_{damp} values with h_{damp}=1.581m_{top} corresponding to the central value obtained from the tuning. Below each panel, the ratios of the predictions to data are shown with the yellow band indicating the total data uncertainties.
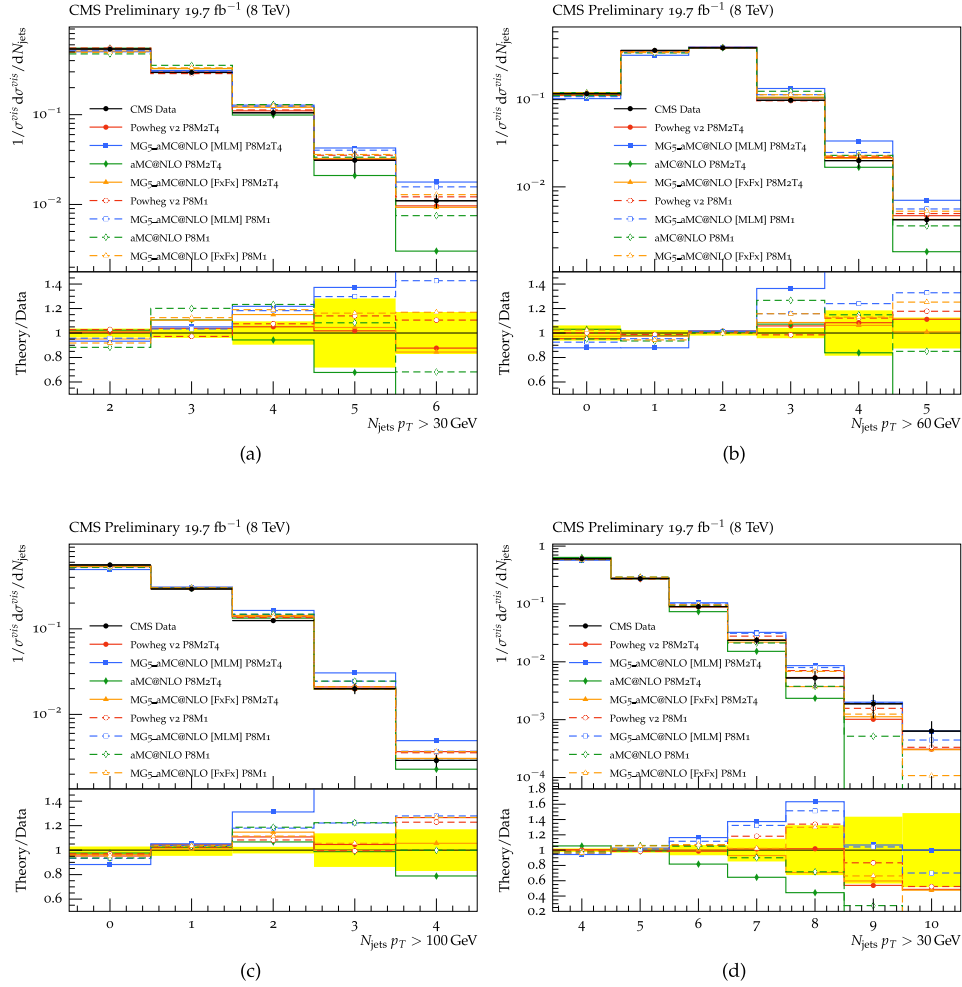
Figure 13: Normalized $t\bar{t}$ cross section in bins of number of jets in data and MC in the dilepton channel (a to c) (Analysis B) and lepton+jets channel (d) (Analysis E) at $\sqrt{s}$ =8 TeV. Figures a to c show normalized $t\bar{t}$ cross sections with a jet p_T cut of 30, 60, and 100 GeV, respectively. Figure d shows normalized $t\bar{t}$ cross sections with a jet p_T cut of 30 GeV. The cross sections are compared to the predictions of POWHEG, MG5_aMC@NLO either with MLM mathing or FXFX merging, and aMC@NLO. For each case the PS simulation is done by PYTHIA 8 with the old (CUETP8M1) and the new (CUETP8M2T4) event tunes. Below each panel, the ratios of the predictions to data are shown with the yellow band indicating the total data uncertainties.
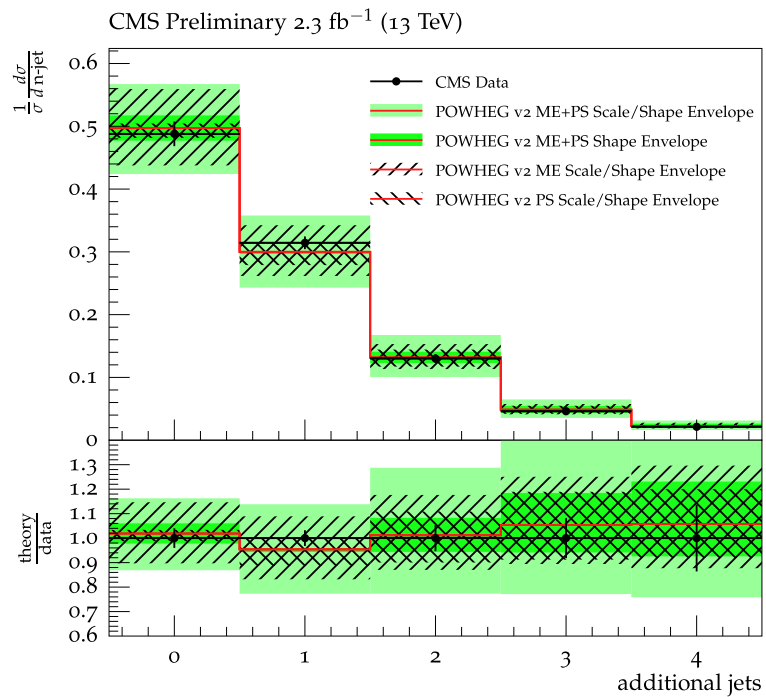
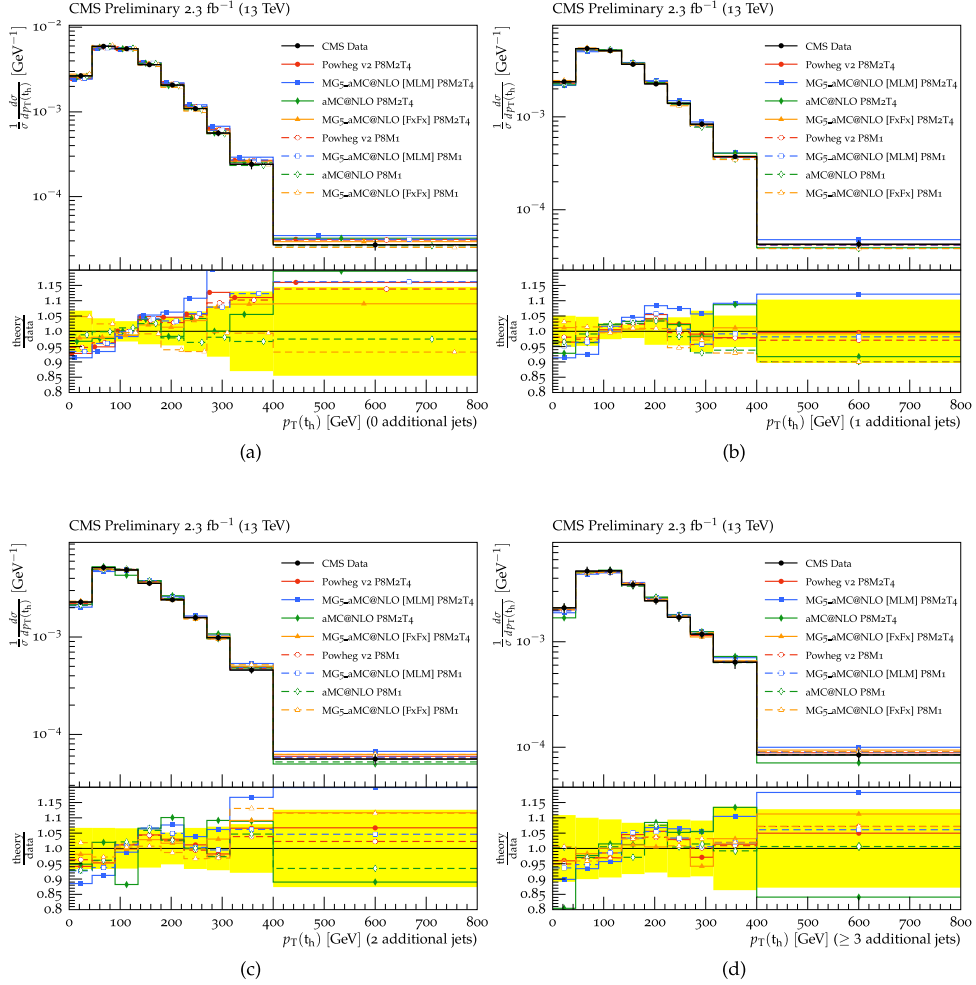Figure 14: Normalized $t\bar{t}$ cross section in bins of number of additional jets in data and MC along with ME, PS, and ME+PS normalization scale factor and shape envelopes in the lepton+jets channel at $\sqrt{s} =$ 13 TeV (Analysis A).
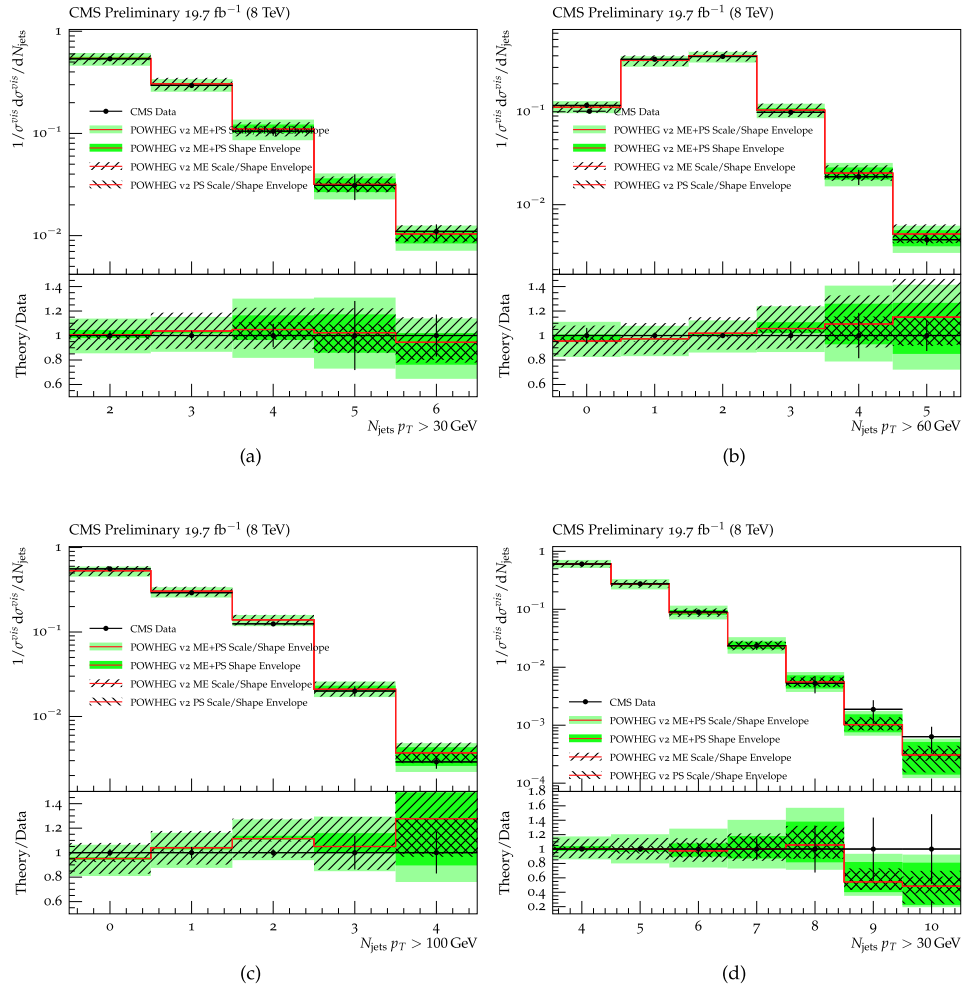
Figure 15: Normalized $t\bar{t}$ cross section in bins of number of jets in data and MC in the dilepton channel (a, b, and c) (Analysis B) and lepton+jets channel (d) (Analysis E) at $\sqrt{s} =8$ TeV along with ME, PS, and ME+PS normalization scale factor and shape envelopes.

5 Summary and Conclusions

A new PYTHIA 8 tune with a lower parton shower α_s, with respect to the one used in the CUETP8M1 [27, 30] tune along with a new h_{damp} value in POWHEG v2 is found to improve the description of $t\bar{t}$ kinematics, as well as the overall description of observables at $\sqrt{s} = 8$ and 13 TeV. The tuned α_s and h_{damp} values are found to be consistent with the ATLAS optimized values [41, 42]. POWHEG v2+PYTHIA 8 with the new tune agrees well with all considered distributions and the new tune applied to MG5_aMC@NLO in FxFx configuration gives consistent results with data as well. In most of the distributions, the new tune does not improve MG5_aMC@NLO[MLM] or aMC@NLO +PYTHIA 8 predictions.

Tuning a parameter in the parton shower can potentially bias particular new physics searches, in particular if the tune is based on the dataset where the search is performed. In this study we have shown that tuning $\alpha_s + h_{damp}$ using N_{jets} and p_T of the leading additional jet in $t\bar{t}$ events does not change the predictions of POWHEG +PYTHIA 8 and MG5_aMC@NLO+PYTHIA 8. In particular, the fact that global event variables such as missing E_T and H_T are not changed by the new tune gives us confidence that searches involving missing E_T will not be biased. However, one should pay particular attention if the new physics search relies on N_{jets}, p_T ($t\bar{t}$) or p_T of leading additional jets in $t\bar{t}$-like processes.

In the Run 1 of the LHC it was observed that the leading order (LO) generator MADGRAPH 5.1.3.30 with up to three additional partons interfaced with PYTHIA 6.426 using the Z2* underlying event tune describes well most of the differential $t\bar{t}$ distributions obtained from data, except for top quark p_T. The α_s^{ISR} value used for the MG5_aMC@NLO+PYTHIA 6 in Run I was 0.1273 and the α_s used in the ME was 0.130. In Run II, when the ME α_s is 0.118 (as in MG5_aMC@NLO+PYTHIA 8 [FxFx] and POWHEG +PYTHIA 8) and the parton shower value, α_s^{ISR}, is 0.1108, all differential $t\bar{t}$ distributions are described well as with the Run I configuration. In addition, using $\alpha_s^{ISR} = 0.1108$ in the MG5_aMC@NLO+PYTHIA 8 [MLM] configuration which uses $\alpha_s=0.130$ in the ME does not describe the data well. The observations above point that the consistency of the α_s value between the parton shower and the ME may be particularly important for emissions which are matched or merged (see e.g. [43] for MLM matching). For POWHEG +PYTHIA this does not apply since POWHEG almost exclusively handles the first emission, while PYTHIA exclusively handles all the subsequent emissions. For aMC@NLO +PYTHIA (i.e. no merging), this applies to the first emission, and for MG5_aMC@NLO+PYTHIA FxFx and MLM configurations this applies to approximately the first three emissions. Considering these, it may be desirable to set different values for matched/merged and unmatched emissions. The hypotheses above will be tested in more detailed studies.

We have also studied independent ME scale variations along with ISR and FSR variations with several different differential cross section measurements. We have observed that ME scale variations affect the normalization scale factor more than the shape and they are larger than PS variations.

A Appendix: Additional Comparisons

A.1 Analysis A
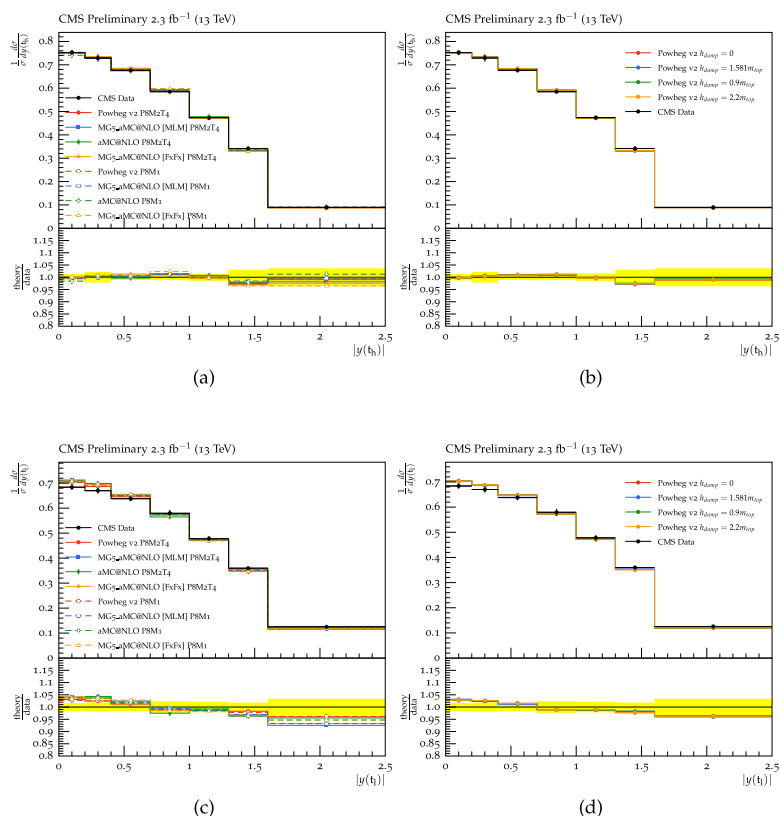
Figure 16: Normalized tt̄ cross section in bins of y^t in data and MC in the lepton+jets channel at $\sqrt{s}$ =13 TeV (Analysis A). The upper plots (a and b) show the hadronically decaying top quarks (t_h) and the lower plots (c and d) the leptonically decaying top quarks t_l. In plots a and c, the cross sections are compared to the predictions of POWHEG, MG5_aMC@NLO either with [MLM] mathing or [FXFX] merging, and aMC@NLO. For each case the PS simulation is done by PYTHIA 8 with the old (CUETP8M1) and the new (CUETP8M2T4) event tunes. In plots b and d, the cross sections are compared to the predictions of POWHEG with different h_{damp} values with h_{damp}=1.581m_{top} corresponding to the central value obtained from the tuning. Below each panel, the ratios of the predictions to data are shown with the yellow band indicating the total data uncertainties.

Figure 17: Normalized tt̄ cross section in bins of y(tt̄) in data and MC in the lepton+jets channel at $\sqrt{s}$ =13 TeV (Analysis A). The cross sections are compared to the predictions of POWHEG, MG5_aMC@NLO either with MLM mathing or FXFX merging, and aMC@NLO (left). For each case the PS simulation is done by PYTHIA 8 with the old (CUETP8M1) and the new (CUETP8M2T4) event tunes. The cross sections are also compared to the predictions of POWHEG with different h_{damp} values with h_{damp}=1.581m_{top} corresponding to the central value obtained from the tuning (right). In the lower panel of each plot, the ratios of the predictions to data are shown with the yellow band indicating the total data uncertainties.
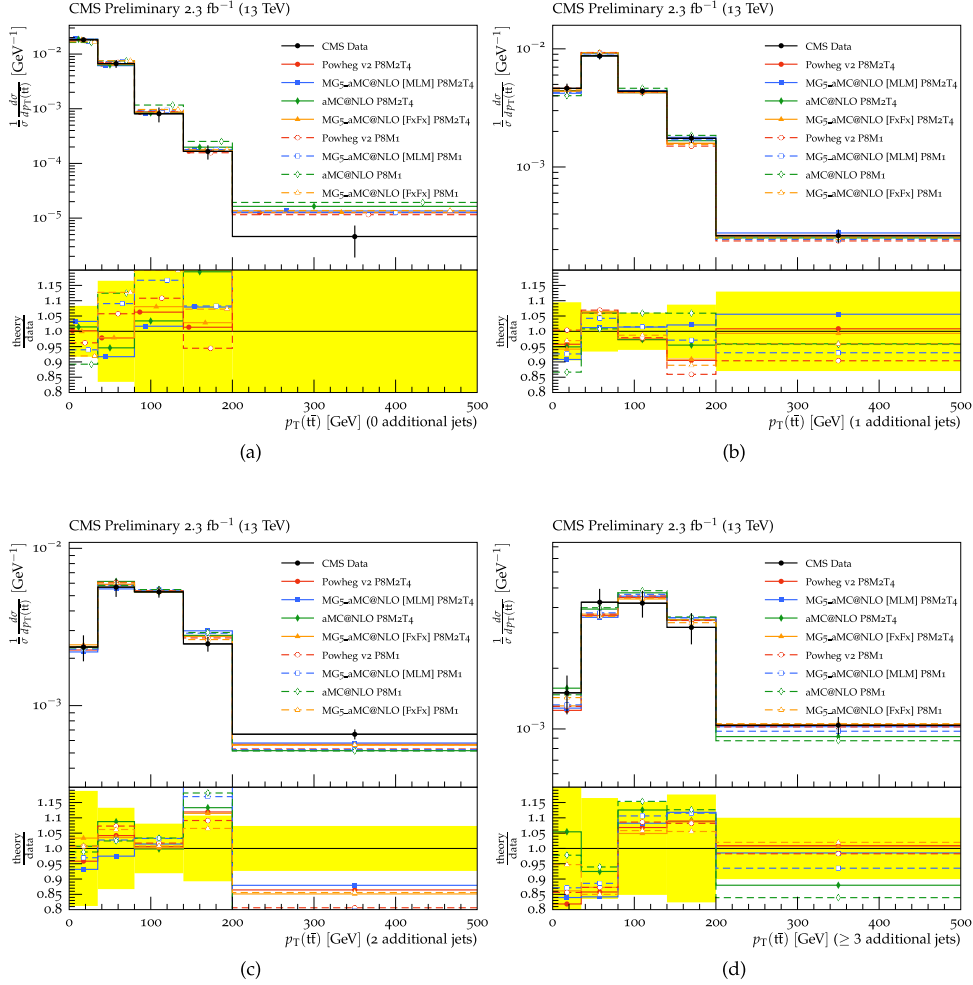
Figure 18: Normalized t$\bar{\text{t}}$ cross section in bins of p_T (t$\bar{\text{t}}$) for 0,1,2 and 3 or more additional jets in data and MC in the lepton+jets channel at $\sqrt{s}$ =13 TeV (Analysis A). The cross sections are compared to the predictions of POWHEG, MG5_aMC@NLO either with MLM mathing or FXFX merging, and aMC@NLO. For each case the PS simulation is done by PYTHIA 8 with the old (CUETP8M1) and the new (CUETP8M2T4) event tunes. In the lower panel of each plot, the ratios of the predictions to data are shown with the yellow band indicating the total data uncertainties.
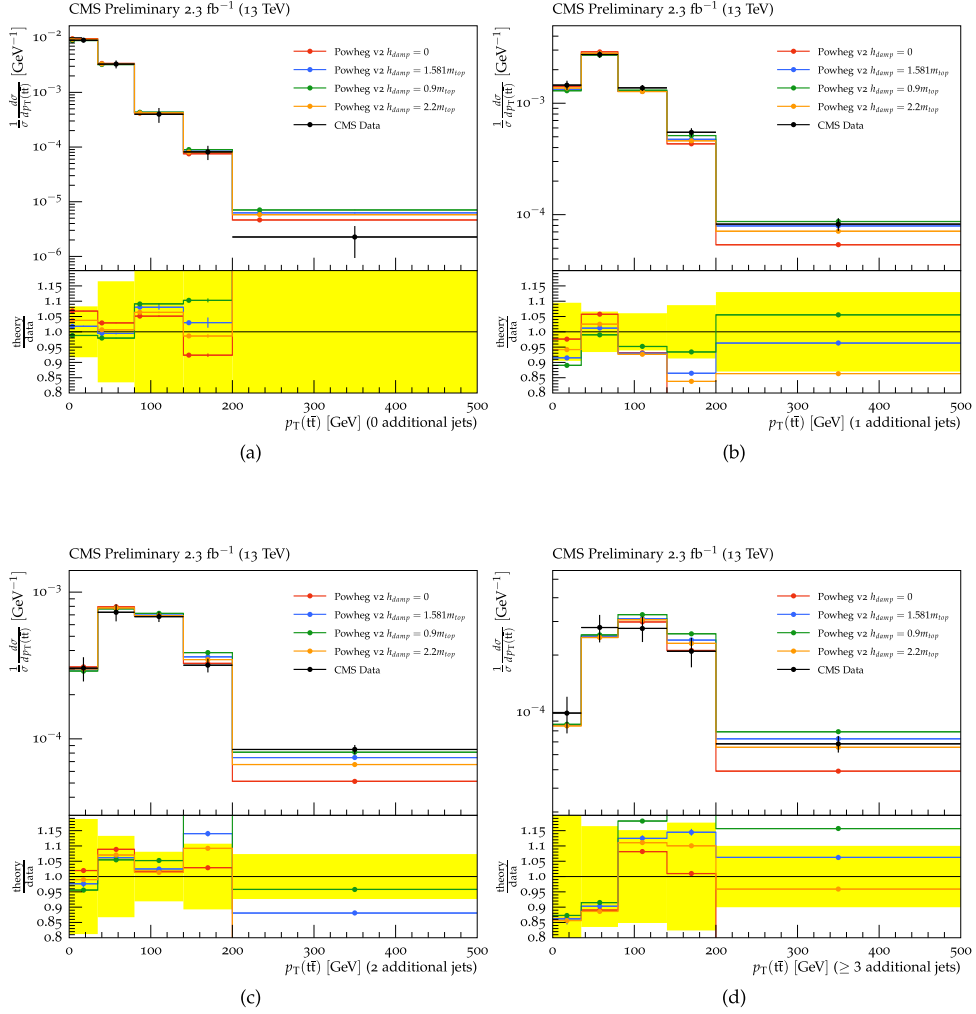
Figure 19: Normalized t$\bar{\text{t}}$ cross section in bins of p_{T} (t$\bar{\text{t}}$) for 0,1,2 and 3 or more additional jets in data and MC in the lepton+jets channel at $\sqrt{s}$ =13 TeV (Analysis A). The cross sections are compared to the predictions of POWHEG with different h_{damp} values with h_{damp}=1.581m_{top} corresponding to the central value obtained from the tuning. In the lower panel of each plot, the ratios of the predictions to data are shown with the yellow band indicating the total data uncertainties.
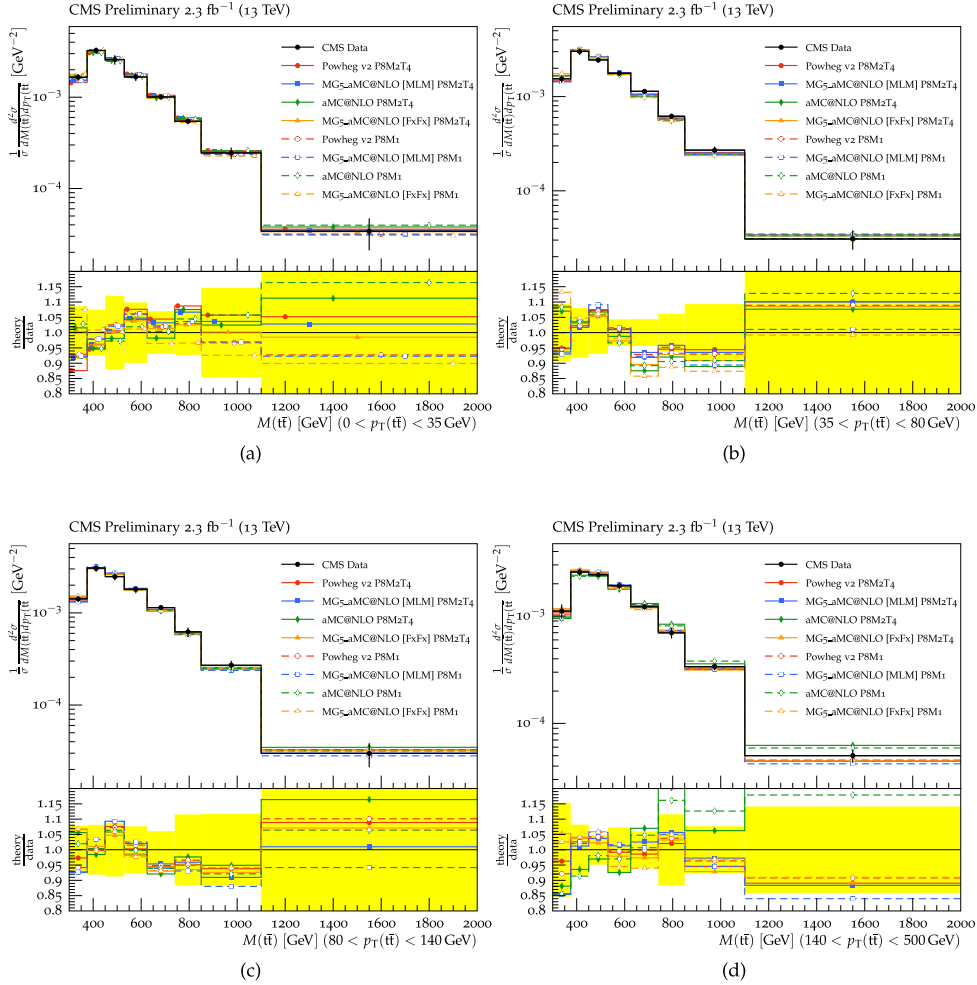
Figure 20: Normalized t$\bar{\text{t}}$ cross section in bins of M(t$\bar{\text{t}}$) for different p_T (t$\bar{\text{t}}$) bins in data and MC in the lepton+jets channel at $\sqrt{s}$ =13 TeV (Analysis A). The cross sections are compared to the predictions of POWHEG, MG5_aMC@NLO either with MLM mathing or FXFX merging, and aMC@NLO. For each case the PS simulation is done by PYTHIA 8 with the old (CUETP8M1) and the new (CUETP8M2T4) event tunes. In the lower panel of each plot, the ratios of the predictions to data are shown with the yellow band indicating the total data uncertainties.

(a)

(b)

(c)

(d)
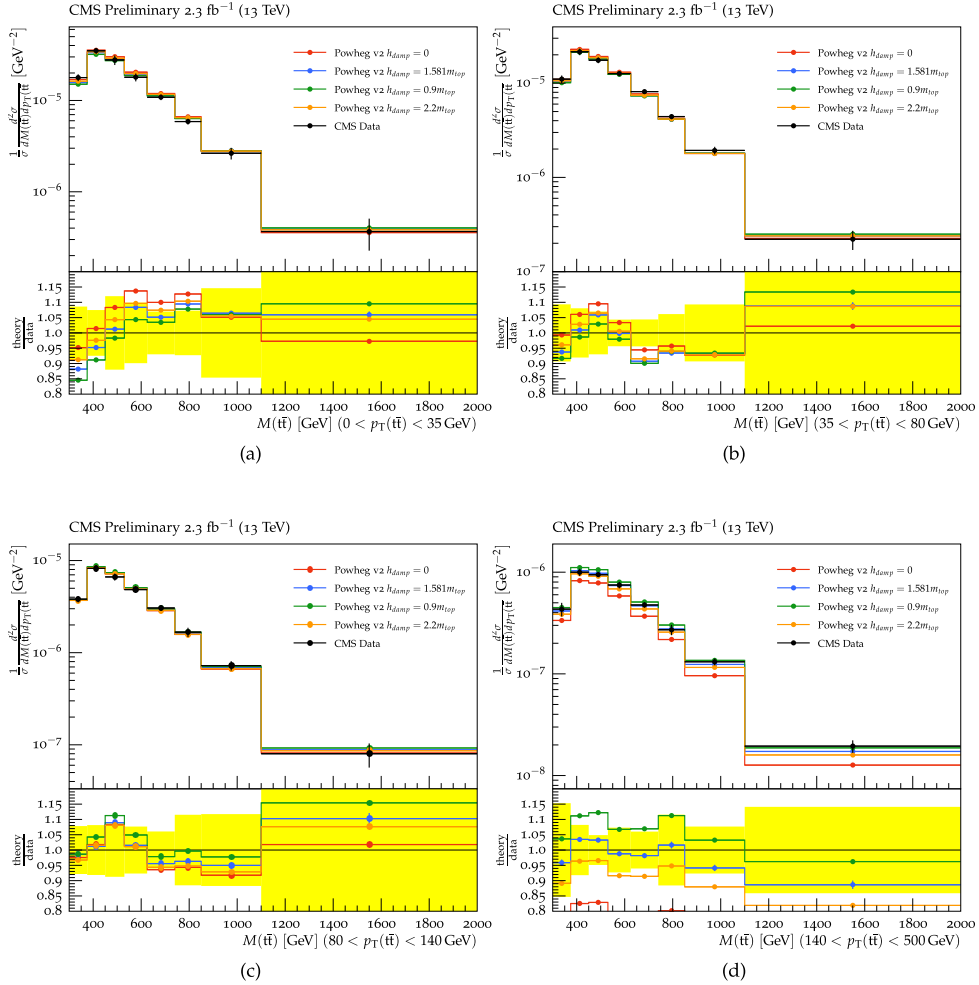
Figure 21: Normalized $t\bar{t}$ cross section in bins of M($t\bar{t}$) for different p_T ($t\bar{t}$) bins in data and MC in the lepton+jets channel at $\sqrt{s}$ =13 TeV (Analysis A). The cross sections are compared to the predictions of POWHEG with different h_{damp} values with h_{damp}=1.581m_{top} corresponding to the central value obtained from the tuning. In the lower panel of each plot, the ratios of the predictions to data are shown with the yellow band indicating the total data uncertainties.
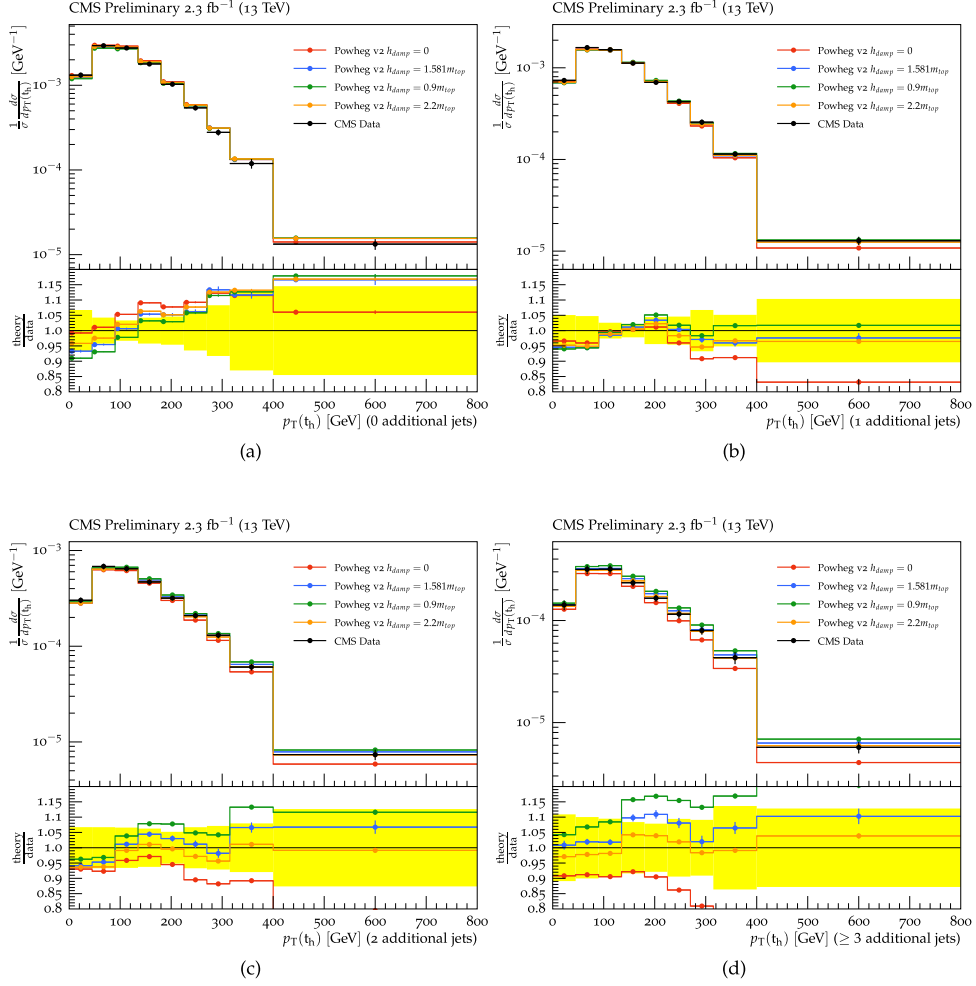
Figure 22: Normalized $t\bar{t}$ cross section in bins of $p_T{}^t$ for the hadronically decaying top quarks (t_h) in data and MC in the lepton+jets channel at $\sqrt{s}$ =13 TeV (Analysis A). Panels a to d display $p_T{}^t$ in events with no, one, two, and three additional jets, respectively. The cross sections are compared to the predictions of POWHEG combined with PYTHIA 8 with the new (CUETP8M2T4) event tune with different h_{damp} values with h_{damp}=1.581m_{top} corresponding to the central value obtained from the tuning.
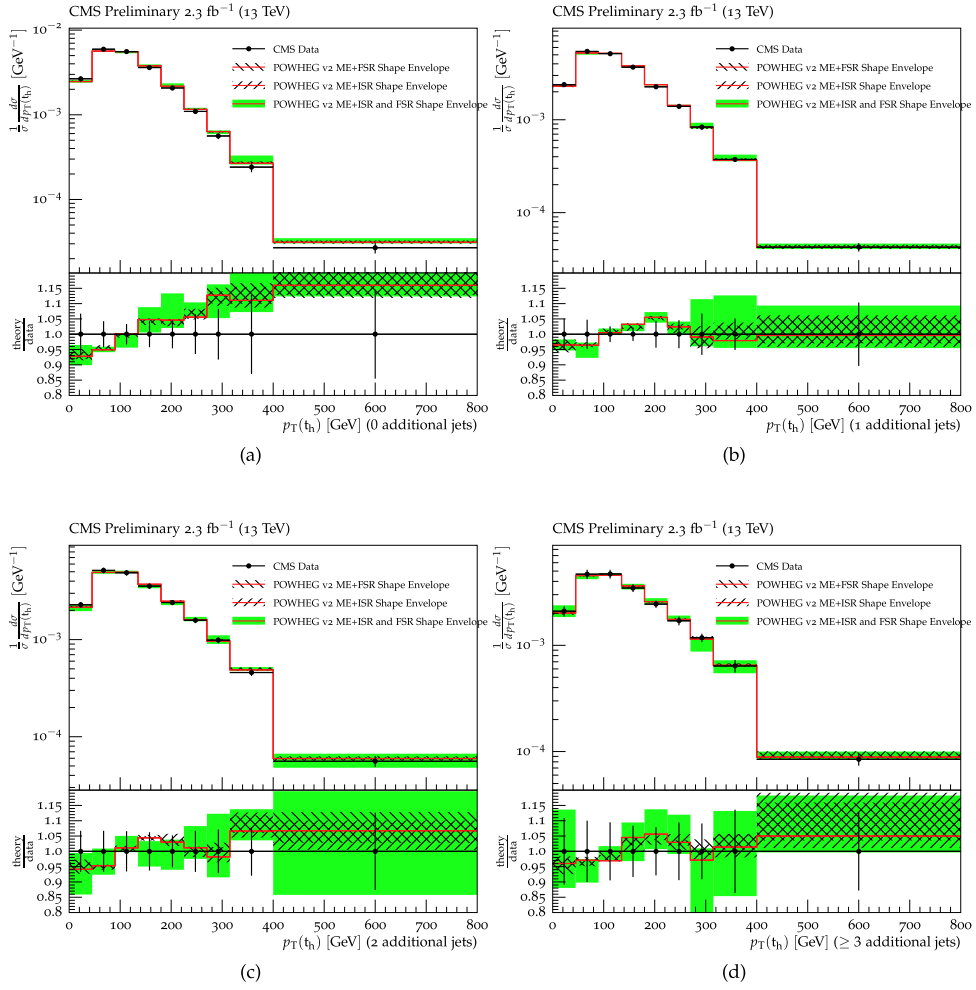
Figure 23: Normalized $t\bar{t}$ cross section in bins of $p_T{}^t$ for the hadronically decaying top quarks (t_h) in data and MC along with ME+FSR, ME+ISR and ME+ISR and FSR variations shape envelopes in the lepton+jets channel at $\sqrt{s} =13$ TeV (Analysis A). Panels a to d display $p_T{}^t$ in events with 0, 1, 2, and 3 or more additional jets, respectively.

A.2   **Analysis B**
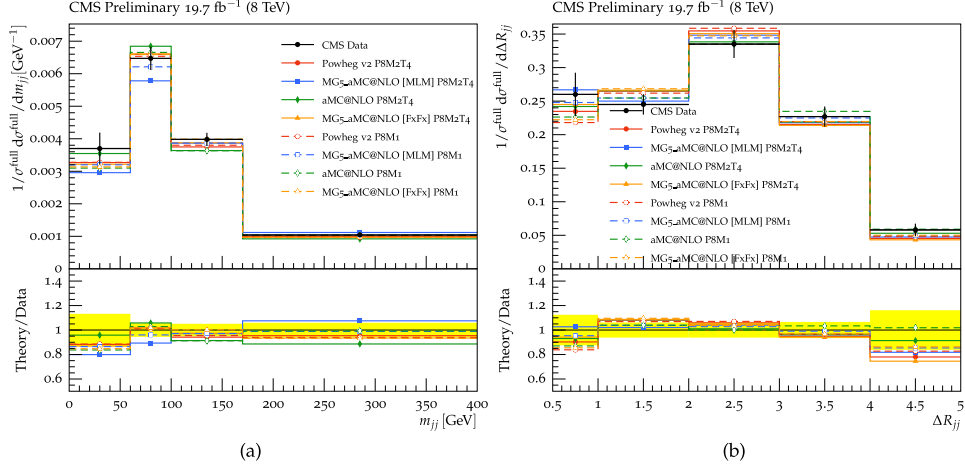
Figure 24: Normalized $t\bar{t}$ cross section in bins of invariant mass (left) and the angular distance (right) of the leading and subleading additional jets in the dilepton channel at $\sqrt{s} = 8$ TeV (Analysis B). The cross sections are compared to the predictions of POWHEG, MG5_aMC@NLO either with MLM mathing or FXFX merging, and aMC@NLO. In the lower panel of each plot, the ratios of the predictions to data are shown with the yellow band indicating the total data uncertainties.
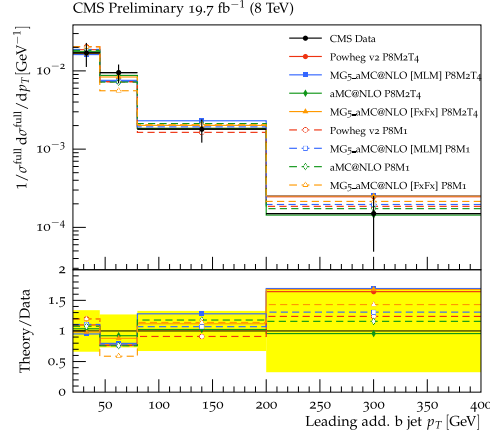
Figure 25: Normalized $t\bar{t}$ cross section in bins of leading additional b jet p_T in the dilepton channel at $\sqrt{s} = 8$ TeV (Analysis B). The cross sections are compared to the predictions of POWHEG, MG5_aMC@NLO either with MLM mathing or FXFX merging, and aMC@NLO. In the lower panel, the ratios of the predictions to data are shown with the yellow band indicating the total data uncertainties.
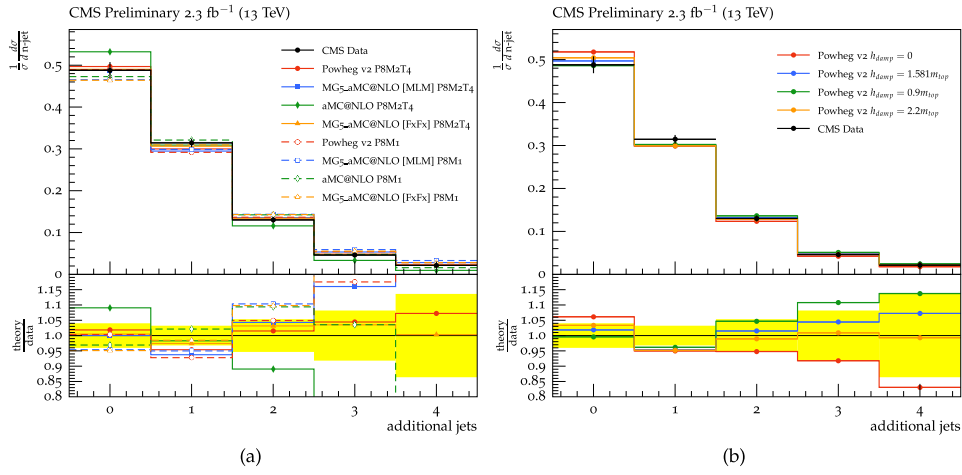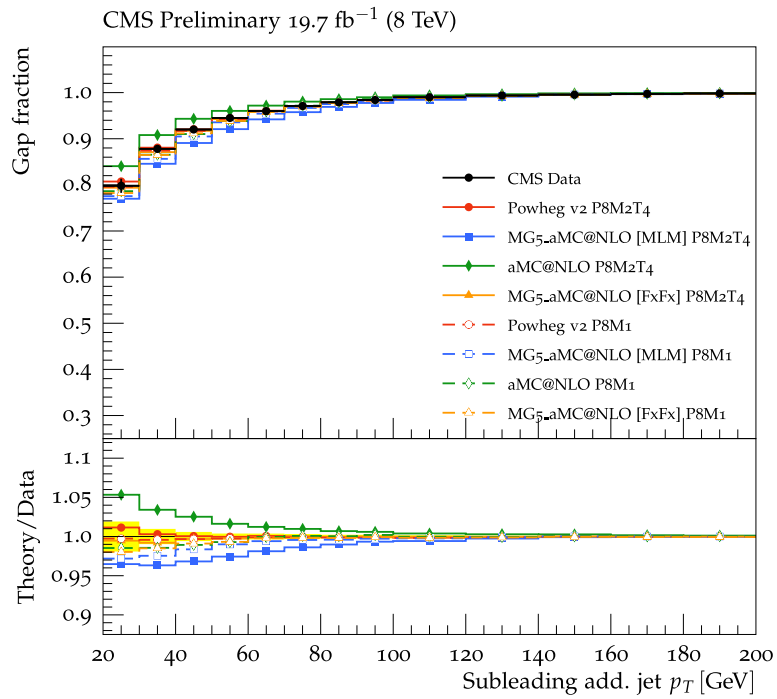
Figure 26: Normalized $t\bar{t}$ cross section in bins of subleading additional jet p_T in the dilepton channel at $\sqrt{s} = 8$ TeV (Analysis B). The cross sections are compared to the predictions of POWHEG, MG5_aMC@NLO either with MLM mathing or FXFX merging, and aMC@NLO. In the lower panel, the ratios of the predictions to data are shown with the yellow band indicating the total data uncertainties.

References

[1] J. Alwall, M. Herquet, and F. Maltoni, "MadGraph 5: Going Beyond", *JHEP* **6** (2011) 128, `doi:10.1007/JHEP06(2011)128`.

[2] T. Sjöstrand, S. Mrenna, and P. Skands, "PYTHIA 6.4 physics and manual", *JHEP* **05** (2006) 026, `doi:10.1088/1126-6708/2006/05/026`, `arXiv:hep-ph/0603175`.

[3] R. Field, "Early LHC Underlying Event Data - Findings and Surprises", in *Hadron collider physics. Proceedings, 22nd Conference, HCP 2010, Toronto, Canada, August 23-27, 2010*. 2010. `arXiv:1010.3558`.

[4] J. Pumplin et al., "New generation of parton distributions with uncertainties from global QCD analysis", *JHEP* **07** (2002) 012, `doi:10.1088/1126-6708/2002/07/012`, `arXiv:hep-ph/0201195`.

[5] CMS Collaboration, "Event generator tunes obtained from underlying event and multiparton scattering measurements", *Eur. Phys. J.* **C76** (2016), no. 3, 155, `doi:10.1140/epjc/s10052-016-3988-x`, `arXiv:1512.00815`.

[6] CMS Collaboration, "Measurement of the differential cross section for top quark pair production in pp collisions at $\sqrt{s} = 8\,\text{TeV}$", *Eur. Phys. J.* **C75** (2015), no. 11, 542, `doi:10.1140/epjc/s10052-015-3709-x`, `arXiv:1505.04480`.

[7] CMS Collaboration, "Measurement of particle level differential $t\bar{t}$ cross sections in the dilepton channel at $\sqrt{s} = 13$ TeV", Technical Report CMS-PAS-TOP-16-007, 2016.

[8] CMS Collaboration, "Measurement of differential cross sections for top quark pair production using the lepton+jets final state in proton-proton collisions at 13 TeV", (2016). `arXiv:1610.04191`. Submitted to *Phys. Rev. D*.

[9] CMS Collaboration, "Measurement of the differential cross section for $t\bar{t}$ production in the dilepton final state at $\sqrt{s} = 13$ TeV", CMS Physics Analysis Summary CMS-PAS-TOP-16-011, 2016.

[10] CMS Collaboration, "Measurement of the $t\bar{t}$ production cross section at 13 TeV in the all-jets final state", CMS Physics Analysis Summary CMS-PAS-TOP-16-013, 2016.

[11] P. Nason, "A New method for combining NLO QCD with shower Monte Carlo algorithms", *JHEP* **11** (2004) 040, `doi:10.1088/1126-6708/2004/11/040`, `arXiv:0409146`.

[12] S. Frixione, P. Nason, and C. Oleari, "Matching NLO QCD computations with Parton Shower simulations: the POWHEG method", *JHEP* **11** (2007) 070, `doi:10.1088/1126-6708/2007/11/070`, `arXiv:0709.2092`.

[13] S. Alioli, P. Nason, C. Oleari, and E. Re, "A general framework for implementing NLO calculations in shower Monte Carlo programs: the POWHEG BOX ", *JHEP* **06** (2010) 043, `doi:10.1007/JHEP06(2010)043`, `arXiv:1002.2581`.

[14] A. Buckley, J. Butterworth, D. Grellscheid et al., "Rivet user manual", *Comput. Phys. Commun.* **184** (2013) 2803, `doi:10.1016/j.cpc.2013.05.021`, `arXiv:1003.0694`.

[15] CMS Collaboration, "Comparisons of Theory Predictions for the $t\bar{t}$ Process with Data from pp Collisions at $\sqrt{s}= 8$ TeV", CMS Physics Analysis Summary CMS-PAS-TOP-15-011, 2015.

[16] M. Dobbs and J. Hansen, "The HepMC C++ Monte Carlo event record for High Energy Physics", *Comput. Phys. Commun.* **134** (2001) 41.

[17] J. Alwall, R. Frederix, S. Frixione et al., "The automated computation of tree-level and next-to-leading order differential cross sections, and their matching to parton shower simulations", *JHEP* **07** (2014) 079, `doi:10.1007/JHEP07(2014)079`, `arXiv:1405.0301`.

[18] CMS Collaboration, "Measurement of $t\bar{t}$ production with additional jet activity, including b quark jets, in the dilepton decay channel using pp collisions at $\sqrt{s} = 8$ TeV", *Eur. Phys. J.* **C76** (2016), no. 7, 379, `doi:10.1140/epjc/s10052-016-4105-x`, `arXiv:1510.03072`.

[19] CMS Collaboration, "Measurement of the differential cross sections for top quark pair production as a function of kinematic event variables in pp collisions at $\sqrt{s}$=7 and 8 TeV", *Phys. Rev.* **D94** (2016), no. 5, 052006, `doi:10.1103/PhysRevD.94.052006`, `arXiv:1607.00837`.

[20] CMS Collaboration, "Measurement of the integrated and differential t-tbar production cross sections for high-pt top quarks in pp collisions at $\sqrt{s} = 8$ TeV", *Phys. Rev. D.* (2016) `doi:10.1103/PhysRevD.94.072002`, `arXiv:1605.00116`. [Phys. Rev.D94,072002(2016)].

[21] CMS Collaboration, "Measurement of the differential production cross section for top-quark pairs as a function of jet multiplicity in the lepton+jets final state at $\sqrt{s} = 8$ TeV with the CMS detector", Technical Report CMS-PAS-TOP-15-006, 2016.

[22] C. Matteo, S. G. P., and S. Gregory, "The anti-k_t jet clustering algorithm", *JHEP* **04** (2008) 063, `doi:10.1088/1126-6708/2008/04/063`, `arXiv:0802.1189`.

[23] M. Wobisch and T. Wengler, "Hadronization corrections to jet cross-sections in deep inelastic scattering", in *Monte Carlo generators for HERA physics. Proceedings, Workshop, Hamburg, Germany, 1998-1999*. 1998. `arXiv:hep-ph/9907280`.

[24] Y. L. Dokshitzer, G. D. Leder, S. Moretti, and B. R. Webber, "Better jet clustering algorithms", *JHEP* **08** (1997) 001, `doi:10.1088/1126-6708/1997/08/001`, `arXiv:hep-ph/9707323`.

[25] L3 Collaboration, "Studies of hadronic event structure in e^+e^- annihilation from 30-GeV to 209-GeV with the L3 detector", *Phys. Rept.* **399** (2004) 71–174, `doi:10.1016/j.physrep.2004.07.002`, `arXiv:hep-ex/0406049`.

[26] A. Buckley et al., "Systematic event generator tuning for the LHC", *Eur. Phys. J.* **C65** (2010) 331–357, `doi:10.1140/epjc/s10052-009-1196-7`, `arXiv:0907.2973`.

[27] CMS Collaboration, "Event generator tunes obtained from underlying event and multiparton scattering measurements", *Eur. Phys. J. C* **76** (2016), no. 3, 155, `doi:10.1140/epjc/s10052-016-3988-x`, `arXiv:1512.00815`.

[28] CMS Collaboration, "Measurement of $t\bar{t}$ production with additional jet activity, including b quark jets, in the dilepton decay channel using pp collisions at $\sqrt{s} = 8$ TeV", *Eur. Phys. J.* **C76** (2016), no. 7, `doi:10.1140/epjc/s10052-016-4105-x`, `arXiv:1510.03072`. http://cms-results.web.cern.ch/cms-results/public-results/publications/TOP-12-041/index.html#AddFig.

[29] T. Sjostrand, S. Mrenna, and P. Skands, "A Brief Introduction to PYTHIA 8.1", *Comput. Phys. Commun.* **178** (2008) 852, `doi:10.1016/j.cpc.2008.01.036`, `arXiv:0710.3820`.

[30] P. Skands, S. Carrazza, and J. Rojo, "Tuning PYTHIA 8.1: the Monash 2013 Tune", *Eur. Phys. J.* **C74** (2014), no. 8, 3024, `doi:10.1140/epjc/s10052-014-3024-y`, `arXiv:1404.5630`.

[31] CMS Collaboration, "Underlying Event Measurements with Leading Particles and Jets in pp collisions at $\sqrt{s} = 13$ TeV", Technical Report CMS-PAS-FSQ-15-007, 2015.

[32] CMS Collaboration, "Pseudorapidity distribution of charged hadrons in proton-proton collisions at $\sqrt{s} = 13$ TeV", *Phys. Lett.* **B751** (2015) 143–163, `doi:10.1016/j.physletb.2015.10.004`, `arXiv:1507.05915`.

[33] CMS Collaboration, "Measurement of the pseudorapidity dependence of the energy and transverse energy density in pp collisions at $\sqrt{s} = 13$ TeV with CMS", Technical Report CMS-PAS-FSQ-15-006, 2016.

[34] CMS Collaboration, "Measurement of pseudorapidity distributions of charged particles in proton-proton collisions at $\sqrt{s} = 13$ TeV by the CMS experiment.", Technical Report CMS-PAS-FSQ-15-008, 2016.

[35] CMS Collaboration, "Z+jets differential cross section at 8 TeV", CMS Physics Analysis Summary CMS-PAS-SMP-13-007, 2014.

[36] R. Frederix and S. Frixione, "Merging meets matching in MC@NLO", *JHEP* **12** (2012) 061, `doi:10.1007/JHEP12(2012)061`, `arXiv:1209.6215`.

[37] J. Alwall et al., "Comparative study of various algorithms for the merging of parton showers and matrix elements in hadronic collisions", *Eur. Phys. J.* **C53** (2008) 473–500, `doi:10.1140/epjc/s10052-007-0490-5`, `arXiv:0706.2569`.

[38] S. Frixione and B. R. Webber, "Matching NLO QCD computations and parton shower simulations", *JHEP* **06** (2002) 029, `doi:10.1088/1126-6708/2002/06/029`, `arXiv:hep-ph/0204244`.

[39] R. D. Ball et al., "Parton distributions for the LHC Run II", *JHEP* **04** (2015) 040, `doi:10.1007/JHEP04(2015)040`, `arXiv:1410.8849`.

[40] R. D. Ball et al., "Parton distributions with LHC data", *Nucl.Phys. B* **867** (2013) 244, `doi:10.1016/j.nuclphysb.2012.10.003`, `arXiv:1207.1303`.

[41] ATLAS Collaboration, "A study of the sensitivity to the Pythia8 parton shower parameters of $t\bar{t}$ production measurements in pp collisions at $\sqrt{s} = 7$ TeV with the ATLAS experiment at the LHC",. ATL-PHYS-PUB-2015-007, 2015.

[42] ATLAS Collaboration, "Studies on top-quark Monte Carlo modelling for Top2016",. ATL-PHYS-PUB-2016-020, 2016.

[43] B. Cooper et al., "Importance of a consistent choice of α_s in the matching of AlpGen and Pythia", *Eur. Phys. J.* **C72** (2012) 2078, `doi:10.1140/epjc/s10052-012-2078-y`, `arXiv:1109.5295`.

CMS PAS HIG-16-038

CMS Physics Analysis Summary

Search for ttH production in the H → bb decay channel with 2016 pp collision data at $\sqrt{s} = 13$ TeV

The CMS Collaboration

Abstract

The results of the search for the associated production of a Higgs boson with a top quark-antiquark pair (ttH) in proton-proton collisions at a center-of-mass energy of $\sqrt{s} = 13$ TeV are presented. The data correspond to an integrated luminosity of up to 12.9 fb^{-1} recorded with the CMS experiment in 2016. Candidate ttH events are selected with criteria enhancing the lepton+jets or dilepton decay-channels of the tt system and the decay of the Higgs boson into a bottom quark-antiquark pair (H → bb). In order to increase the sensitivity of the search, selected events are split into several categories with different expected signal and background rates. In each category signal and background events are separated using a multivariate approach that combines a matrix element method with boosted decision trees. The results are characterized by an observed ttH signal strength relative to the standard model cross section, $\mu = \sigma/\sigma_{\mathrm{SM}}$, under the assumption of $m_H = 125$ GeV. A combined fit of multivariate discriminant distributions in all categories results in an observed (expected) upper limit of $\mu < 1.5$ (1.7) at the 95% confidence level, and a best fit value of $\mu = -0.19^{+0.45}_{-0.44}$(stat.) $^{+0.66}_{-0.68}$(syst.).

1 Introduction

The observation of a Higgs boson with a mass of approximately 125 GeV [1, 2] at the Large Hadron Collider (LHC) marked the starting point of a broad experimental program to determine the properties of the newly discovered particle. To date, the results of all measurements performed at the LHC are consistent with the expectations for a standard model (SM) Higgs boson. Decays into $\gamma\gamma$, ZZ and WW final states have been observed and there is evidence for the direct decay of the particle to fermions from the $\tau\tau$ and $b\bar{b}$ decay channels [3, 4]. The measured rates of various production and decay channels agree with the SM expectations [5, 6] and the hypothesis of a spin-0 particle is favored over other hypotheses [7, 8].

In the SM the coupling of the Higgs boson to fermions is of Yukawa type, with a coupling strength proportional to the fermion mass. Probing the coupling of the Higgs boson to the heaviest known fermion, the top quark, is hence very important for testing the SM and for constraining models of physics beyond the SM (BSM). Indirect constraints on the top–Higgs coupling are available from processes including top-quark loops, for example Higgs boson production through gluon-gluon fusion [5, 6]. On the other hand, the associated production of a Higgs boson and a top quark-antiquark pair ($t\bar{t}H$ production) is a direct probe of the top–Higgs coupling, as illustrated by the Feynman diagrams in Fig. 1. If observed it would prove the coupling of the Higgs boson to fermions with weak isospin $+1/2$ ("up-type") in addition to couplings to τ and b, which carry a weak isospin of $-1/2$ ("down-type"). The Higgs boson decay into bottom quark-antiquark pairs ($b\bar{b}$), also shown in Fig. 1, is attractive as a final state because it features the largest branching fraction of 0.58 ± 0.02 for a 125 GeV Higgs boson [9].

Figure 1: Exemplary leading-order Feynman diagrams for $t\bar{t}H$ production, including the subsequent decays of the top quark-antiquark pair in the lepton+jets channel (left) and the dilepton channel (right) as well as the decay of the Higgs boson into a bottom quark-antiquark pair.

Several BSM physics models predict a significantly enhanced $t\bar{t}H$ production rate while not modifying the branching fractions of Higgs boson decays by a measurable amount. For example, a number of BSM physics models predict vector-like partners of the top-quark (T) that decay into tH, bW and tZ final states [10–19]. The production and decay of $T\bar{T}$ pairs would lead to final states indistinguishable from those of $t\bar{t}H$ production. In this context, a measurement of the $t\bar{t}H$ production cross section has the potential to distinguish the SM Higgs mechanism from alternative mechanisms to generate fermion mass.

Various dedicated searches for $t\bar{t}H$ production have been conducted during Run I of the LHC. The CMS searches employ pp collision data corresponding to an integrated luminosity of $5\,\text{fb}^{-1}$ at a center-of-mass energy of $\sqrt{s} = 7\,\text{TeV}$ and $19.5\,\text{fb}^{-1}$ at $\sqrt{s} = 8\,\text{TeV}$. These searches have been

performed studying Higgs boson decays to hadrons, photons, and leptons using multivariate analysis (MVA) techniques, showing a mild excess of the observed $t\bar{t}H$ cross section relative to the SM expectation of $\mu = \sigma/\sigma_{SM} = 2.8 \pm 1.0$ [20]. A similar excess of $\mu = 2.1^{+1.4}_{-1.2}$ is observed in a search for $t\bar{t}H$ production in multilepton final states with $20.3\,\text{fb}^{-1}$ of ATLAS data at $\sqrt{s} = 8\,\text{TeV}$ [21].

The CMS search results have also entered a comprehensive test of the compatibility of the Higgs boson couplings with SM predictions [6]. The sensitivity for the $t\bar{t}H$ process in the $H \rightarrow b\bar{b}$ decay channel was further increased by employing the matrix element method (MEM) [22], resulting in an observed (expected) upper limit of $\mu < 4.2\,(3.3)$ at 95% confidence level [23]. ATLAS obtained an observed (expected) upper limit on $t\bar{t}H$ production in the $H \rightarrow b\bar{b}$ decay channel of $\mu < 3.4\,(2.2)$ using $20.3\,\text{fb}^{-1}$ of pp collision data at $\sqrt{s} = 8\,\text{TeV}$ [24].

Observation of $t\bar{t}H$ production is one of the major goals in Higgs boson physics for the LHC Run II. The increased center-of-mass energy of $\sqrt{s} = 13\,\text{TeV}$ results in a $t\bar{t}H$ production cross section 3.9 times larger than at $\sqrt{s} = 8\,\text{TeV}$ based on next-to-leading (NLO) calculations, while the cross section for the most important background, $t\bar{t}$ production, is only increased by a factor of 3.3 [25], resulting in a more favorable signal-to-background ratio. Latest CMS searches for $t\bar{t}H$ production with Run-II data in the diphoton and multilepton final-states of the Higgs boson observe signal strengths of $\mu = 1.9^{+1.5}_{-1.2}$ [26] and $\mu = 2.0^{+0.8}_{-0.7}$ [27], respectively. ATLAS finds $\mu = -0.3^{+1.3}_{-1.0}$ [28] and $\mu = 2.5^{+1.3}_{-1.1}$ [29], respectively.

In the $H \rightarrow b\bar{b}$ final state, CMS has performed a search for $t\bar{t}H$ production using $2.7\,\text{fb}^{-1}$ of data recorded in 2015 [30]. Analysis methods established in Run I have been significantly improved, and novel methods have been added. In particular, the two multivariate techniques – namely MEM and boosted decision trees (BDT) [31–35] – using different information from each event and aiming at separating different background components, have both been employed to obtain a better performance than using one technique alone. The analysis obtains a value of $\mu = -2.0^{+1.8}_{-1.8}$. A new result by ATLAS in $H \rightarrow b\bar{b}$ channel, based on $13.2\,\text{fb}^{-1}$, measures $\mu = 2.1^{+1.0}_{-0.9}$ [29].

This document summarizes a search for the $t\bar{t}H$ production in the $H \rightarrow b\bar{b}$ final state performed with up to $12.9\,\text{fb}^{-1}$ of data recorded with the CMS detector in 2016. It is an update of the above mentioned search [30]. One improvement is due to a refined Monte Carlo (MC) modeling, leading to a more accurate description of the data, in particular the jet-multiplicity spectrum. The event selection is adapted to $t\bar{t}H$ events with the decay of the Higgs boson into a $b\bar{b}$ pair and lepton+jets as well as dilepton decays of the $t\bar{t}$ pair, resulting in the final state $\ell\nu\,q\bar{q}'\,b\bar{b}$ ($\ell^+\nu\,\ell^-\bar{\nu}\,b\bar{b}$) for lepton+jets (dilepton) $t\bar{t}$ decays, where $\ell = e, \mu$. Events are split into mutually exclusive categories according to the number of reconstructed jets and the number of jets identified as coming from the hadronization of b quarks (b tagging). In each category, signal and background processes are separated employing BDTs which use the kinematic properties of jets and charged leptons, the b tagging probability, invariant masses and angular correlations of combinations of jets and leptons, as well as observables characterizing the event shape as inputs. Those categories with high number of jets or number of b-tagged jets are further subdivided into two sub-categories depending on the BDT discriminant output, and in each sub-category the MEM discriminant is used as final discriminant. From a combined profile-likelihood fit of the final discriminant output distributions to data in all categories, a best-fit value of the signal-strength modifier μ is obtained. In absence of a signal, an upper limit on μ is set.

This document is structured as follows: in Section 3, the data samples and MC simulated sam-

ples are described. The basic selection of analysis objects and events is discussed in Section 4. The general analysis strategy and background estimation methods are introduced in Section 5. The effect of systematic uncertainties is studied in Section 6. Results of the studies are presented in Section 7, followed by conclusions in Section 8.

2 The CMS Detector

The central feature of the CMS apparatus is a superconducting solenoid of 6 m internal diameter, providing a magnetic field of 3.8 T. Within the superconducting solenoid volume are a silicon pixel and strip tracker, a lead tungstate crystal electromagnetic calorimeter (ECAL), and a brass and scintillator hadron calorimeter (HCAL), each composed of a barrel and two endcap sections. Forward calorimeters extend the pseudorapidity coverage provided by the barrel and endcap detectors. Muons are measured in gas-ionization detectors embedded in the steel flux-return yoke outside the solenoid. A more detailed description of the CMS detector, together with a definition of the coordinate system used and the relevant kinematic variables, can be found in Ref. [36].

3 Data and Simulation Samples

This analysis is performed using proton-proton (pp) collision data at a center-of-mass energy of $\sqrt{s} = 13$ TeV, which were collected with the CMS detector in 2016 and correspond to a total integrated luminosity of 12.9 fb^{-1} and $11.4 - 12.9$ fb^{-1} for the lepton+jets and dilepton channels, respectively. The different (lower) luminosity in the dilepton channel only affects the e^+e^- channel and is due to disabled trigger paths during parts of the data taking.

MC event generators, interfaced with a detailed detector simulation, are used to model experimental effects, such as reconstruction and selection efficiencies, as well as detector resolutions. The CMS detector response is simulated using GEANT4 (v. 9.4) [37].

For the simulation of the reference $t\bar{t}H$ signal sample, the next-to-leading-order (NLO) event generator POWHEG (v. 2) [38, 39] is used. The value of the Higgs boson mass is assumed to be 125 GeV, while the top quark mass value is set to 172.5 GeV. The proton structure is described by the parton distribution functions (PDF) NNPDF3.0 [40]. The generated events are subsequently processed with PYTHIA (v. 8.2) [41] for parton showering and hadronization.

Standard model backgrounds are simulated using POWHEG, MG5_aMC@NLO (v. 2.2.2) [42], or PYTHIA, depending on the process. The main background contribution originates from $t\bar{t}$ production, the production of W and Z/γ^* bosons with additional jets (referred to as W+jets and Z+jets or commonly as V+jets in the following), single top quark production (tW channel), and diboson (WW, WZ, and ZZ) processes, and $t\bar{t}$ production in association with a W or Z boson (referred to as $t\bar{t}$+W and $t\bar{t}$+Z or commonly as $t\bar{t}$+V in the following). Both the $t\bar{t}$ and the single top quark samples are simulated with POWHEG. The V+jets and $t\bar{t}$+V samples are simulated with the NLO generator MG5_aMC@NLO, where for the V+jets samples the matching of matrix-element jets to parton showers is performed using the FXFX [43] prescription. PYTHIA is used to simulate diboson events. Parton showering and hadronization are also simulated with PYTHIA in all the background samples. The PYTHIA CUETP8M1 tune [44, 45] was used in the past to characterize the underlying event in both the $t\bar{t}H$ signal and the background samples. However, our $t\bar{t}H$ search based on the 2015 data has shown that this tune results in a much harder jet-multiplicity spectrum in simulation with respect to data. Since $t\bar{t}H$ events typically show a high jet multiplicity, this data-simulation discrepancy will have a big impact on our

search. In order to improve the modeling, a custom tune has been derived by CMS. For this new tune, the (mostly uncorrelated) parameters α_S^{ISR} and h_{damp} are optimized based on several measurements at $\sqrt{s} = 8\,\mathrm{TeV}$. The latter is the parameter that controls the matrix element and parton shower matching in POWHEG and effectively regulates the high-p_T radiation. Validation studies show that this new tune significantly improves the jet-multiplicity modeling. For this analysis, we used the $t\bar{t}H$ signal and $t\bar{t}$ background samples produced with this new tune.

For comparison with the measured distributions, the events in the simulated samples are normalized to the same integrated luminosity of the data according to their predicted cross sections. These are taken from theoretical calculations at next-to-next-to-leading order (NNLO, for V+jets production), approximate NNLO (single top quark tW channel [46]), and NLO (diboson production [47] and $t\bar{t}$+V production [48]). The $t\bar{t}H$ cross section [25, 49–52] and Higgs boson branching fractions [53–56] used in the analysis also have NLO accuracy. The $t\bar{t}$ simulated sample is normalized to the full NNLO calculation with resummation to next-to-next-to-leading-logarithmic (NNLL) accuracy [57–63], assuming a top quark mass value of 172.5 GeV and using the NNPDF3.0 PDF set. This sample is further separated into the following processes based on the flavor of additional jets that do not originate from the top quark decays in the event: $t\bar{t}+b\bar{b}$, defined at generator level as the events in which two additional b jets are generated within the acceptance requirements (cf. Section 4) and originate from one or more B hadrons; $t\bar{t}+b$, for which only one additional b jet originates from a single B hadron; $t\bar{t}+2b$, which corresponds to events with two additional B hadrons that are close enough in direction to produce a single b jet; $t\bar{t}+c\bar{c}$, for which events have at least one c jet within acceptance and no additional b jets; $t\bar{t}$ + light flavor ($t\bar{t}+LF$), which correspond to events that do not belong to any of the above processes. The separation is motivated by the fact that different sub-samples originate from different physics processes and have different systematic uncertainties. A similar separation strategy has been followed by the ATLAS collaboration [24].

Effects from additional pp interactions in the same bunch crossing (pileup) are modeled by adding simulated minimum-bias events (generated with PYTHIA) to all simulated processes. The pileup multiplicity distribution in simulation is reweighted to reflect the luminosity profile of the observed pp collisions. Correction factors described in Section 4 are applied where necessary to improve the description of the data by the simulation.

4 Object and Event Selection

The event selection aims at selecting events from the production of a Higgs boson in association with a top quark-antiquark pair, where only the case in which the Higgs boson decays into a bottom quark-antiquark pair is considered. In the SM, the top quark is expected to decay into a W boson and a b quark nearly 100% of the time. Hence different $t\bar{t}$ decay modes can be identified according to the subsequent decays of the W bosons. Two $t\bar{t}$ decay modes are considered: the lepton+jets mode ($t\bar{t} \rightarrow \ell\nu\, q\bar{q}'\, b\bar{b}$), where one W boson decays into a charged lepton and a neutrino, and the dilepton mode ($t\bar{t} \rightarrow \ell^+\nu\, \ell^-\bar{\nu}\, b\bar{b}$), where both W bosons decay into a charged lepton and a neutrino. These signatures imply the presence of isolated leptons ($\ell = e, \mu$), missing transverse momentum owing to the neutrinos from W boson decays, and highly energetic jets originating from the final-state quarks. The heavy-quark content of the jets is identified through b tagging techniques.

At trigger level, events in the lepton+jets channel are required to contain an electron (muon) with transverse momentum (p_T) threshold of $p_T > 27\,\mathrm{GeV}$ ($p_T > 22\,\mathrm{GeV}$). For electrons a pseudorapidity range of $|\eta| < 2.1$ is required. Events in the dilepton channel are required to

contain two leptons fulfilling the requirement of p_T thresholds between 8 GeV and 23 GeV and isolation criteria.

Events are reconstructed using a particle-flow (PF) technique [64, 65], which combines signals from all sub-detectors to enhance the reconstruction performance by identifying individual particle candidates in pp collisions. Charged hadrons from pileup events are omitted in the subsequent event reconstruction.

The electron and muon candidates are required to be sufficiently isolated from nearby jet activity as follows. For each electron (muon) candidate, a cone of $\Delta R = 0.3$ ($\Delta R = 0.4$) is constructed around the direction of the track at the event vertex, where ΔR is defined as $\sqrt{(\Delta \eta)^2 + (\Delta \phi)^2}$, and $\Delta \eta$ and $\Delta \phi$ are the distances in pseudorapidity and azimuthal angle. Excluding the contribution from the lepton candidate, the scalar sum of the p_T of all particle candidates inside the cone consistent with arising from the chosen primary event vertex is calculated. The neutral component from pileup events is subtracted event-by-event based on the average transverse energy deposited by neutral particles in the event, which is removed from the transverse energy in the isolation cone. A relative isolation discriminant, I_{rel}, is defined as the ratio of this sum to the p_T of the lepton candidate. Electron candidates are selected if they have values of $I_{rel} < 0.15$, while muons are selected if they fulfill the requirement of $I_{rel} < 0.15$ in the lepton+jets channel and $I_{rel} < 0.25$ in the dilepton channel. In addition, electrons from identified photon conversions are rejected. To further increase the purity of muons originating from the primary interaction and to suppress misidentified muons or muons from decay-in-flight processes, additional quality criteria, such as a minimal number of hits associated with the muon track, are required in both the silicon tracker and the muon system.

For the lepton+jets channel, events are selected containing exactly one energetic, isolated lepton (e or μ), which is required to have $p_T > 25$ GeV or $p_T > 30$ GeV in the case of the μ or e, respectively, and $|\eta| < 2.1$ (but excluding electrons within a small region of $|\eta|$ between the barrel and endcap sections of the ECAL). For the dilepton channel, events are required to have a pair of oppositely charged energetic leptons (e$^+$e$^-$, $\mu^+\mu^-$, $\mu^\pm$e$^\mp$). The leading lepton is required to have $p_T > 25$ GeV and the subleading lepton $p_T > 15$ GeV, and both leptons are required to fulfill the requirement of $|\eta| < 2.4$. The invariant mass of the selected lepton pair is required to be larger than 20 GeV to suppress events from heavy-flavor resonance decays and low-mass Drell-Yan processes. In the same-flavor channels, events are rejected if the dilepton invariant mass is within the region 76 GeV $< m^{\ell\ell} < 106$ GeV, thereby suppressing further contribution from Z+jets processes.

Jets are reconstructed from the PF particle candidates using the anti-k_T clustering algorithm [66] implemented in FASTJET [67] with a distance parameter of 0.4. The jet energy is corrected for the remaining neutral-hadron pileup component in a manner similar to that used to find the energy within the lepton isolation cone [68]. Jet energy corrections are also applied as a function of jet p_T and η [69] to data and simulation. Events in the lepton+jets channel are required to have at least four reconstructed jets with $p_T > 30$ GeV and $|\eta| < 2.4$. In the dilepton channels, at least three jets with $p_T > 20$ GeV and $|\eta| < 2.4$ are required, from which the two leading jets must satisfy $p_T > 30$ GeV.

Jets originating from the hadronization of b quarks are identified using a combined secondary vertex algorithm (CSVv2) [70], which provides a b tagging discriminant by combining identified secondary vertices and track-based lifetime information. A discriminant value is chosen such that the probability of tagging jets originating from light-flavor quarks (u, d, or s) or gluons is around 1%, and the corresponding efficiency for tagging jets from b (c) quarks is $\approx$70% (20%). The shape of the CSVv2 discriminant distribution in simulation is corrected by scale fac-

tors to better describe the jet CSVv2 shape observed in the data [71]. This correction is derived separately for light-flavor and b jets from a "tag-and-probe" approach using control samples enriched in events with a Z boson and exactly two jets, and $t\bar{t}$ events with no additional jets.

The missing transverse momentum vector $\vec{p}_T^{\,\mathrm{miss}}$ is defined as the projection of the negative vector sum of the momenta of all reconstructed particles in an event on the plane perpendicular to the beams. Its magnitude is referred to as E_T^{miss}. In the dilepton same-flavor channels, events are required to fulfill the requirement of $E_T^{\mathrm{miss}} > 40\,\mathrm{GeV}$.

Events from $t\bar{t}H$ are generally characterized by having more jets and more b-tags than the background processes. Events are divided into categories based on the number of jets and the number of b-tagged jets. For the lepton+jets channel, events are separated into the following four categories: $\geq 6\,\text{jets}, 3\,\text{b-tags}$; $4\,\text{jets}, 4\,\text{b-tags}$; $5\,\text{jets}, \geq 4\,\text{b-tags}$ and $\geq 6\,\text{jets}, \geq 4\,\text{b-tags}$. For the dilepton channel, events are divided into three categories: $3\,\text{jets}, 3\,\text{b-tags}$; $\geq 4\,\text{jets}, 3\,\text{b-tags}$ and $\geq 4\,\text{jets}, \geq 4\,\text{b-tags}$.

Tables 1 and 2 show the predicted and observed event yields after the event selection in the lepton+jets and dilepton channels, respectively. The tables are sub-divided into the different jet and b-tag categories used in each channel. The expected and observed yields agree well in all final states across the different categories of jets and b-tags.

Table 1: $t\bar{t}H$ and background event yields for lepton+jets categories. The processes and the separation of the $t\bar{t}$ +jets sample are described in Section 3. The uncertainties in the expected yields include the statistical as well as all the systematic contributions. Cases where no events pass the event selection are marked as "—".

Process	$\geq 6\,\text{jets}, 3\,\text{b-tags}$	$4\,\text{jets}, 4\,\text{b-tags}$	$5\,\text{jets}, \geq 4\,\text{b-tags}$	$\geq 6\,\text{jets}, \geq 4\,\text{b-tags}$
$t\bar{t}$+LF	2710.6 ± 1027.1	91.4 ± 69.9	96.9 ± 75.8	86.2 ± 71.9
$t\bar{t}$+$c\bar{c}$	1771.9 ± 1099.0	59.3 ± 47.0	112.5 ± 88.9	175.8 ± 141.6
$t\bar{t}$+b	717.6 ± 406.8	37.6 ± 23.1	69.6 ± 42.4	86.3 ± 57.0
$t\bar{t}$+2b	401.4 ± 237.1	16.0 ± 9.9	33.8 ± 20.6	54.9 ± 37.3
$t\bar{t}$+$b\bar{b}$	777.0 ± 468.4	42.2 ± 23.8	126.5 ± 71.6	306.3 ± 183.2
Single t	331.9 ± 77.2	19.2 ± 7.8	29.5 ± 11.4	30.0 ± 10.8
V+jets	79.5 ± 30.9	5.7 ± 6.8	7.7 ± 5.1	7.2 ± 3.9
$t\bar{t}$+V	81.4 ± 17.0	2.2 ± 0.6	6.3 ± 1.7	18.1 ± 5.2
Diboson	4.3 ± 2.3	0.5 ± 0.5	—	—
Total bkg.	6875.6 ± 2776.8	274.1 ± 153.0	482.9 ± 239.7	764.8 ± 365.3
$t\bar{t}H$	74.2 ± 9.7	4.0 ± 0.8	11.7 ± 2.2	26.9 ± 5.6
Data	6811	376	551	787

5   Analysis Strategy and Background Estimation

The BDT and MEM techniques are used to further improve the signal-to-background separation in both lepton+jets and dilepton channels of the analysis. The information of both techniques are used to derive a single discriminant, this way exploiting the strength of both methods.

The BDTs utilize information related to object kinematics, event shape, and the jet CSVv2 b-tag discriminant. A separate BDT is trained for each category, resulting in four BDTs in the lepton+jets and three in the dilepton channel. The training is performed using simulated $t\bar{t}H$

Table 2: t̄tH and background event yields for dilepton categories. The processes and the separation of the t̄t +jets sample are described in Section 3. The uncertainties in the expected yields include the statistical as well as all the systematic contributions. Cases where no events pass the event selection are marked as "—".

Process	3 jets, 3 b-tags	$\geq$ 4 jets, 3 b-tags	$\geq$ 4 jets, $\geq$ 4 b-tags
t̄t+LF	179.0 ± 68.7	390.1 ± 167.9	7.6 ± 3.6
t̄t+c$\bar{c}$	117.5 ± 73.8	382.6 ± 237.7	19.4 ± 15.5
t̄t+b	94.2 ± 51.9	228.0 ± 127.7	14.4 ± 9.2
t̄t+2b	31.7 ± 17.3	99.1 ± 54.3	6.2 ± 3.8
t̄t+b$\bar{b}$	17.1 ± 9.4	172.5 ± 92.9	57.9 ± 32.6
Single t	16.0 ± 4.6	38.4 ± 11.9	2.4 ± 1.2
V+jets	1.6 ± 2.2	1.6 ± 4.1	0.7 ± 0.5
t̄t+V	1.4 ± 0.5	16.6 ± 3.4	2.6 ± 0.8
Diboson	—	0.4 ± 0.4	—
Total bkg.	458.3 ± 197.0	1329.3 ± 503.1	111.2 ± 49.8
t̄tH	1.8 ± 0.4	16.5 ± 3.4	4.4 ± 1.3
Data	498	1469	146

and t̄t+jets events as signal and background, respectively, which are weighted to achieve equal yields of signal and background events in each category. In order to avoid a biased performance estimate, the signal and background events are split in half: one half is used to perform the training, and the other half is used in the final analysis to monitor the performance and derive the final limits. The specific BDT boosting method used is the stochastic gradient boost [31, 72], available as part of the TMVA package [33] in ROOT. The choice of BDT input variables as well as the tree architecture are optimized separately in each category with a procedure based on the particle swarm algorithm [73]. A description of the input variables is provided in Appendices A and B for each category of the lepton+jets and the dilepton channel, respectively.

Within the MEM, each event is assigned a probability density value computed from the four-momenta of the reconstructed particles, which is based on the differential cross section of the signal or background process. The MEM discriminant is constructed as ratio of the probability density values of the signal and background hypothesis. The deployed algorithm is an improved version of the method described in [23]. The probability density functions are constructed at LO, assuming gluon-gluon fusion production both for signal and background processes. The t̄t + b$\bar{b}$ matrix elements have been found to provide comparable discrimination power against all background subprocesses and are solely used to model the background. Hadronization and detector effects are taken into account via transfer functions derived from simulation, which map the measured four-momenta to the final-state particles in the matrix element. In each event, the four jets that most likely originate from b quarks are considered explicitly as candidates for the b-quarks from the decay of the Higgs boson and the top quark, whereas light jets, if present, are permuted over as the candidates for the light quarks from the hadronic decay of the W-boson. All permutations are considered when associating the b-like jets to top quark or Higgs boson decays in the matrix element, similarly we permute over up to 4 additional light jets for the W decay candidates. The four b-like jets are selected using the likelihood ratio between the hypotheses that four or two jets in the event arose from b quarks and the rest from light quarks, based on the expected b tagging discriminant probability densities from simulation.

The BDT and MEM discriminants perform differently in terms of signal and background separation. While the BDT achieves a slightly better separation against the inclusive $t\bar{t}$ background, the MEM is by construction especially powerful in separating against the challenging $t\bar{t} + b\bar{b}$ background. The correlation between the BDT and MEM discriminants have been studied in different control regions in data and found to be well-modeled by the simulation. In this analysis, the two discriminants are utilized with the scheme described below. This results in the best sensitivity, and it is robust against effects due to the binning of the templates and overoptimization of the multivariate discriminants.

In the dilepton 3 jets, 3 b-tags category, a BDT output distribution is used as final discriminant that enters the fit. This category contains a relatively large number of events, which is a desirable situation for training the BDT. In the lepton+jets categories, as well as dilepton ≥ 4 jets, 3 b-tags and ≥ 4 jets, ≥ 4 b-tags categories, events are further separated into two subcategories, one with low (background-like) and one with high (signal-like) BDT output, divided by the median of the BDT output distribution for simulated signal events. In each sub-category, the MEM is used as final discriminant. The high BDT output sub-category is expected to be enhanced with signal events, and the MEM discriminant achieves additional separation against the residual $t\bar{t} + b\bar{b}$ background contributions. The choice of the median contributes to a robust result by ensuring a sufficient number of events in each sub-category. Including the low BDT output sub-category constrains the background contributions and systematic uncertainties for each of the different event topologies.

The final discriminant outputs provide better discrimination between signal and background than any of the input variables individually. Utilizing both the BDT and MEM information also leads to better signal and background separation than using BDT-only or MEM-only information. The output distributions of the background and signal processes are fit to the data simultaneously in all channels and categories to set limits on the Higgs boson production cross section, as described in Section 7.

6 Systematic Uncertainties

In Table 3, all sources of systematic uncertainties considered in the analysis are listed. They affect either the yields of the signal or background processes, or the discriminant shape, or both. In the last case, the yield and shape effects are treated as entirely correlated and are varied simultaneously. The uncertainties are taken into account via nuisance parameters in the final fit procedure described in Section 7.

The effect of the uncertainties is evaluated individually in each category of each analysis channel, where the effects from the same source are treated as fully correlated. The impact of the systematic variations differs among the categories. As an example, the change in background and signal event yield due to the different uncertainties is listed in Table 4 for the ≥ 6 jets, 3 b-tags category of the lepton+jets channel, which shows high sensitivity and at the same time contains a relatively large number of events such that the variations are statistically significant.

The uncertainty in the luminosity estimate is 6.2% [74]. Electron and muon identification and trigger efficiency uncertainties were estimated by comparing variations in measured efficiency between data and MC simulation using a high-purity sample of Z-boson decays and are found to be 2–4%. Effects of the uncertainty in the distribution of the number of pileup interactions are evaluated by varying the cross section used to predict the number of pileup interactions in MC by $\pm 5\%$ from its nominal value. The uncertainty of the jet energy scale [69] (resolution) is evaluated by varying the energy scale (resolution) correction of all jets in the signal and background

Table 3: Systematic uncertainties considered in the analysis.

Source	Type	Remarks
Luminosity	rate	Signal and all backgrounds
Lepton ID/Iso	shape	Signal and all backgrounds
Trigger efficiency	shape	Signal and all backgrounds
Pileup	shape	Signal and all backgrounds
Jet energy scale	shape	Signal and all backgrounds
Jet energy resolution	shape	Signal and all backgrounds
b-tag HF fraction	shape	Signal and all backgrounds
b-tag HF stats (linear)	shape	Signal and all backgrounds
b-tag HF stats (quadratic)	shape	Signal and all backgrounds
b-tag LF fraction	shape	Signal and all backgrounds
b-tag LF stats (linear)	shape	Signal and all backgrounds
b-tag LF stats (quadratic)	shape	Signal and all backgrounds
b-tag charm (linear)	shape	Signal and all backgrounds
b-tag charm (quadratic)	shape	Signal and all backgrounds
QCD scale ($t\bar{t}H$)	rate	Scale uncertainty of NLO $t\bar{t}H$ prediction
QCD scale ($t\bar{t}$)	rate	Scale uncertainty of NLO $t\bar{t}$ prediction
QCD scale ($t\bar{t}$+HF)	rate	Additional 50% rate uncertainty of $t\bar{t}$+HF predictions
QCD scale (t)	rate	Scale uncertainty of NLO single t prediction
QCD scale (V)	rate	Scale uncertainty of NNLO W and Z prediction
QCD scale (VV)	rate	Scale uncertainty of NLO diboson prediction
pdf (gg)	rate	PDF uncertainty for gg initiated processes except $t\bar{t}H$
pdf (gg $t\bar{t}H$)	rate	PDF uncertainty for $t\bar{t}H$
pdf ($q\bar{q}$)	rate	PDF uncertainty of $q\bar{q}$ initiated processes ($t\bar{t}$ W, W, Z)
pdf (qg)	rate	PDF uncertainty of qg initiated processes (single t)
Q^2 scale ($t\bar{t}$)	shape	Renormalization and factorization scale uncertainties of the $t\bar{t}$ ME generator, independent for additional jet flavors
PS Scale ($t\bar{t}$)	rate	Renormalization and factorization scale uncertainties of the parton shower (for $t\bar{t}$ events), independent for additional jet flavors
Bin-by-bin statistics	shape	statistical uncertainty of the signal and background prediction due to the limited sample size

Table 4: Specific effect of systematic uncertainties that affect the discriminant shape on the predicted background and signal yields for events in the ≥ 6 jets, 3 b-tags category of the lepton+jets channel. Here, only the sum of the largest background processes, $t\bar{t}$+LF, $t\bar{t}$+b, $t\bar{t}$+2b, $t\bar{t}$+b$\bar{b}$, and $t\bar{t}$+c$\bar{c}$, are considered.

Process	$t\bar{t}$ rate up/down [%]	$t\bar{t}$H rate up/down [%]
Jet energy scale	+12.6/ − 11.8	+8.4/ − 8.0
Jet energy resolution	+0.2/ − 0.3	−0.0/ − 0.1
Pile-up	+0.1/ − 0.1	−0.2/ + 0.1
Electron efficiency	+0.5/ − 0.5	+0.5/ − 0.5
Muon efficiency	+0.4/ − 0.4	+0.4/ − 0.4
Electron trigger efficiency	+1.2/ − 1.2	+1.3/ − 1.3
Muon trigger efficiency	+0.8/ − 0.8	+0.9/ − 0.9
b-Tag HF contamination	−9.4/ + 9.8	−2.6/ + 2.8
b-Tag HF stats (linear)	−3.1/ + 3.3	−2.5/ + 2.7
b-Tag HF stats (quadratic)	+2.6/ − 2.4	+2.4/ − 2.2
b-Tag LF contamination	+7.1/ − 5.2	+5.8/ − 4.5
b-Tag LF stats (linear)	−2.0/ + 4.4	+0.5/ + 1.5
b-Tag LF stats (quadratic)	+2.1/ + 0.2	+1.5/ + 0.5
b-Tag charm Uncertainty (linear)	−11.1/ + 14.9	−3.1/ + 4.1
b-Tag charm Uncertainty (quadratic)	+0.5/ − 0.5	−0.0/ + 0.0
Q^2 scale ($t\bar{t}$+LF)	−6.2/ + 7.5	−
Q^2 scale ($t\bar{t}$+b)	−1.7/ + 2.0	−
Q^2 scale ($t\bar{t}$+2b)	−1.1/ + 1.4	−
Q^2 scale ($t\bar{t}$+b$\bar{b}$)	−2.0/ + 2.5	−
Q^2 scale ($t\bar{t}$+c$\bar{c}$)	−4.3/ + 5.4	−
PS scale ($t\bar{t}$+LF)	+4.8/ − 9.0	−
PS scale ($t\bar{t}$+b)	−0.9/ + 0.7	−
PS scale ($t\bar{t}$+2b)	−0.8/ + 0.9	−
PS scale ($t\bar{t}$+b$\bar{b}$)	−1.5/ + 2.7	−
PS scale ($t\bar{t}$+c$\bar{c}$)	−3.9/ + 3.0	−

predictions by one standard deviation. The uncertainty of the CSVv2 b-tagging scale factors is evaluated by applying alternative scale factors based on varying the following systematic effects by one standard deviation, separately for the different jet flavors: the contamination of background processes in the control samples, the jet energy scale uncertainty — which is correlated with the overall jet energy scale uncertainty — and the statistical uncertainty in the scale factor evaluation. The impact of the latter is parametrized as the sum of two orthogonal contributions: a linear and a quadratic term, which allow an overall tilt and a shift of the center of the b-tagging discriminant distribution, respectively. Both for the jet energy scale and for the b-tagging scale factor uncertainties, the event categorization and successive evaluation of the discriminant is re-evaluated after applying the systematic variations to account for migration effects between categories.

Theoretical uncertainties of the cross sections used to predict the rates of various processes are propagated to the yield estimates. All rates are estimated using cross sections of at least NLO accuracy, which have uncertainties arising primarily from PDFs and the choice of factorization and renormalization scales (both in the matrix element and the parton shower). The cross section uncertainties are each separated into their PDF and scale components and correlated where appropriate between processes. For example, the PDF uncertainty for processes originating primarily from gluon-gluon initial states, such as $t\bar{t}$ and $t\bar{t}H$ production, are treated as 100% correlated. The $t\bar{t}+b\bar{b}$ process, and to lesser extent the $t\bar{t}+2b$, $t\bar{t}+b$, and $t\bar{t}+c\bar{c}$ production, represent important sources of irreducible background. Neither control region studies nor higher-order theoretical calculations can currently constrain the normalization of these contributions to better than 50% accuracy; therefore a conservative extra 50% rate uncertainty is assigned to the $t\bar{t}$ +heavy-flavor processes. This rate uncertainty has the largest impact on the median expected limit; omitting it in the computation improves the limit by approximately 10%. The effect of the scale uncertainties on the discriminant output shape is also taken into account for the $t\bar{t}$+jets production using event weights obtained directly from the MC generator in case of the matrix element and dedicated samples generated with different scale choices in case of the parton shower. The factorization and renormalization scales of the matrix element generator and also the scales of the initial-state radiation and the final-state radiation of the parton shower of the general-purpose MC event generator are varied simultaneously by a factor of 0.5 and 2. These scale variations are treated as uncorrelated between the matrix element generator and the general-purpose MC event generator. Possible shape variations of the final discriminant distributions due to the PDF uncertainty have been evaluated by comparing the results to those obtained when using the PDF replicas provided with the NNPDF set. The replicas parametrize the PDF uncertainties and are derived from re-sampling of the experimental data that are used to fit the nominal PDF [40]. The impact on the discriminant distributions has been found to be negligible, and therefore, is not propagated into the final analysis.

The impact of statistical fluctuations in the signal and background prediction due to the limited number of simulated events is accounted for using the approach described in [75, 76].

7   Results

The signal strength modifier $\mu = \sigma/\sigma_{\mathrm{SM}}$ of the $t\bar{t}H$ production cross section is determined in a simultaneous binned maximum-likelihood fit to the data across all analysis categories, cf. Section 5. The fit procedure takes into account systematic uncertainties that modify the shape and normalization of the final discriminant distributions, as described in Section 6. The final discriminants in all categories before and after the fit to data are displayed in Figs. 2 to 5 and Figs. 6 to 9, respectively.
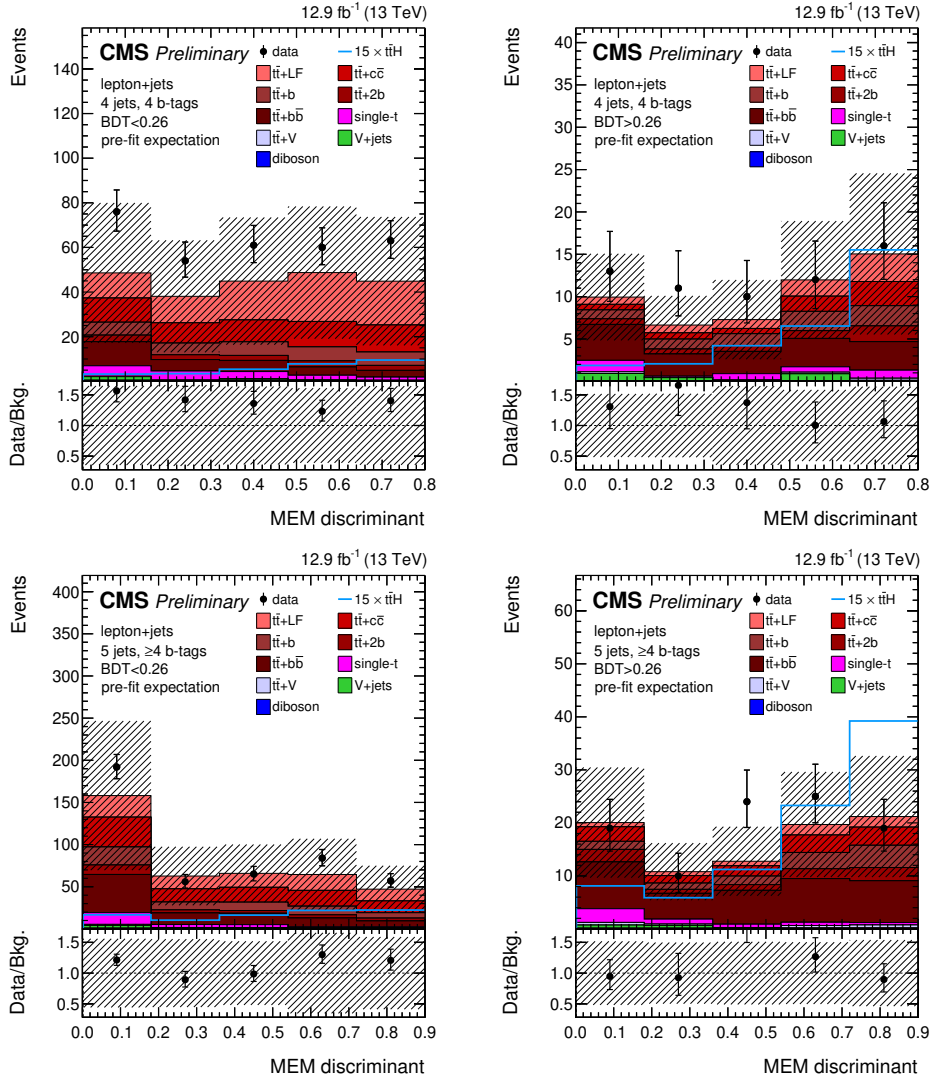
Figure 2: Final discriminant (MEM) shapes in the lepton+jets channel before the fit to data, in the analysis categories with 4 jets, 4 b-tags (top row) and 5 jets, $\geq$ 4 b-tags (bottom row) with low (left) and high (right) BDT output. The expected background contributions (filled histograms) are stacked, and the expected signal distribution (line) for a Higgs-boson mass of $m_H = 125$ GeV is superimposed. Each contribution is normalized to an integrated luminosity of 12.9 fb^{-1}, and the signal distribution is additionally scaled by a factor of 15 for better readability. The error bands include the total uncertainty of the fit model. The distributions observed in data (markers) are also shown.
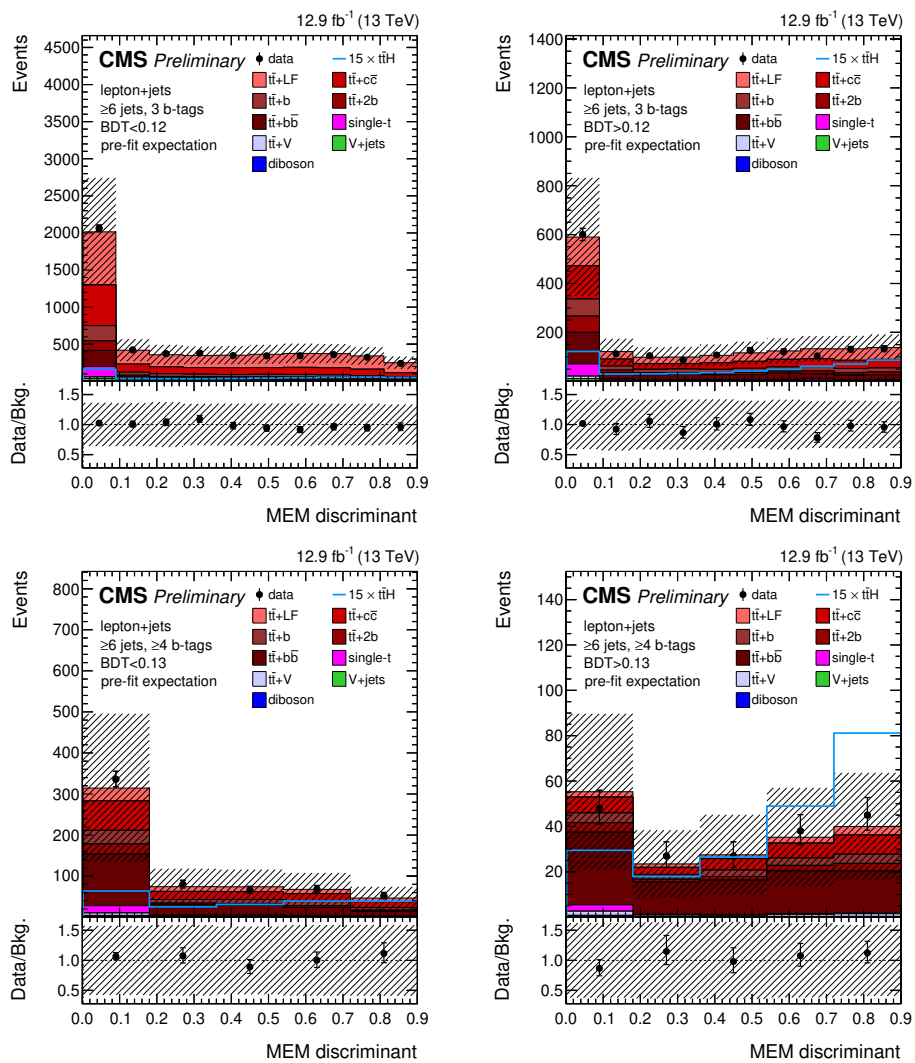
Figure 3: Final discriminant (MEM) shapes in the lepton+jets channel before the fit to data, in the analysis categories with ≥ 6 jets, 3 b-tags (top row) and ≥ 6 jets, ≥ 4 b-tags (bottom row) with low (left) and high (right) BDT output (continued from Fig. 2).
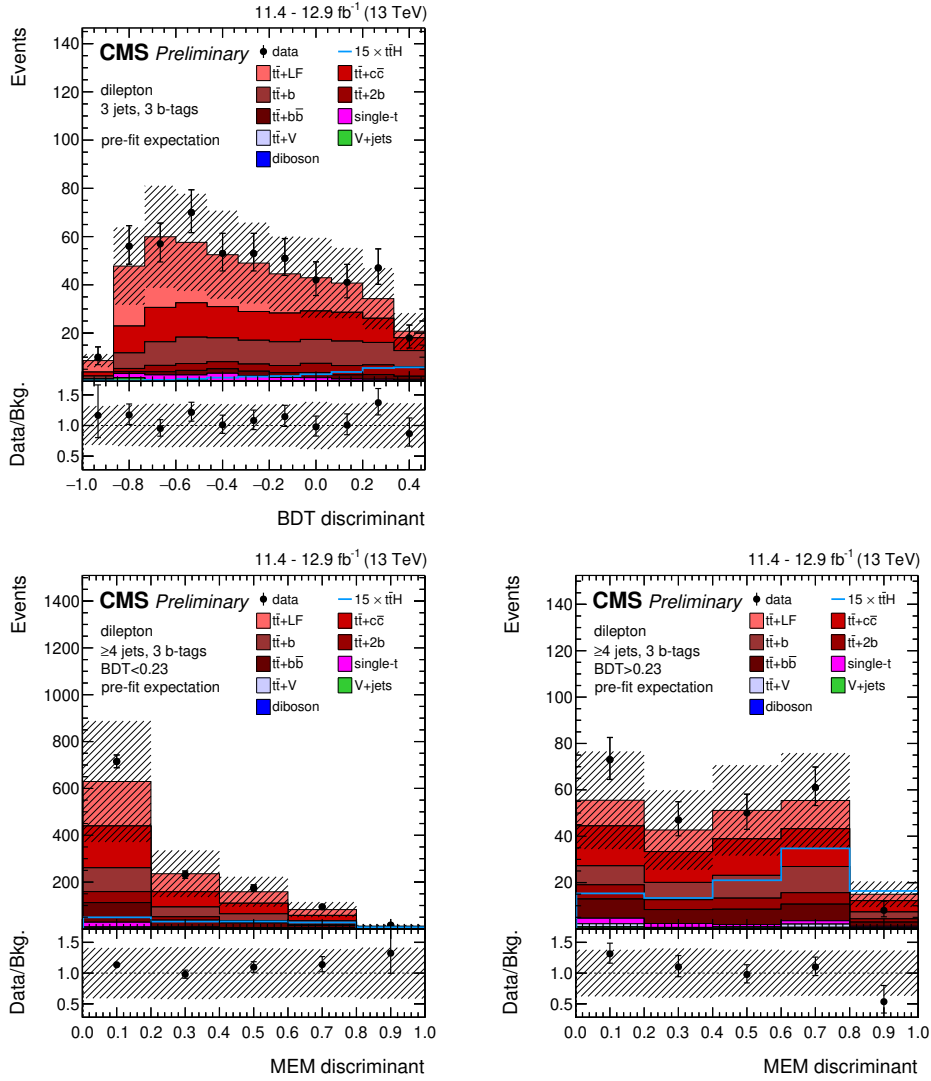
Figure 4: Final discriminant shapes (BDT or MEM) in the dilepton channel before the fit to data, in the analysis categories with 3 jets, 3 b-tags (top row) and ≥ 4 jets, 3 b-tags (bottom row) with low (left) and high (right) BDT output. The expected background contributions (filled histograms) are stacked, and the expected signal distribution (line) for a Higgs-boson mass of $m_H = 125\,\mathrm{GeV}$ is superimposed. Each contribution is normalized to an integrated luminosity of $11.4 - 12.9\,\mathrm{fb}^{-1}$, and the signal distribution is additionally scaled by a factor of 15 for better readability. The error bands include the total uncertainty of the fit model. The distributions observed in data (markers) are also shown.
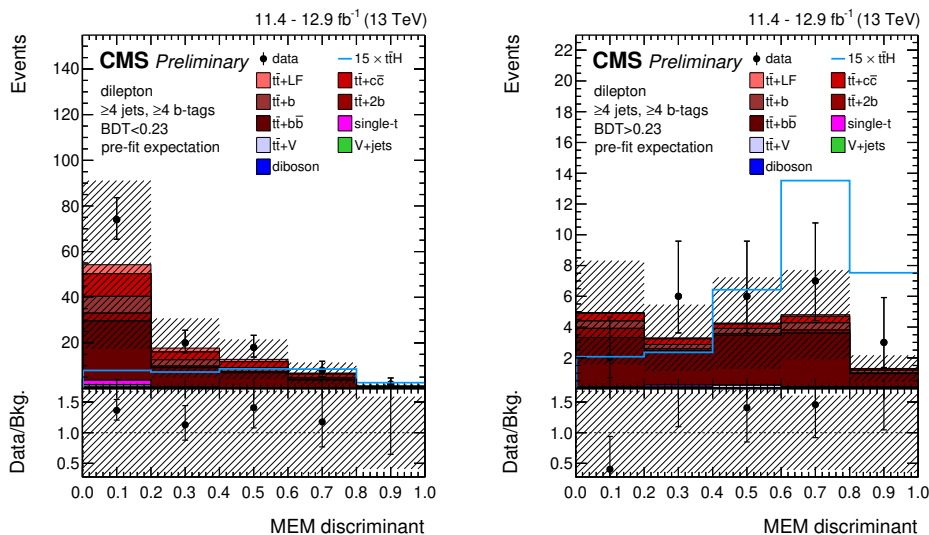
Figure 5: Final discriminant (MEM) shapes in the dilepton channel before the fit to data, in the analysis categories with ≥ 4 jets, ≥ 4 b-tags with low (left) and high (right) BDT output (continued from Fig. 4).

The best-fit value of μ is $-0.19 \,^{+0.45}_{-0.44}(\text{stat.}) \,^{+0.66}_{-0.68}(\text{syst.})$ with a total uncertainty of $^{+0.80}_{-0.81}$. This is 1.5 standard deviations from the standard model expectation of $\mu = 1$. The best-fit values in each analysis channel and in the combination are listed in Table 5 and displayed in Fig. 10 (left).

The value obtained for μ is both compatible with the SM expectation and no signal: an upper limit at 95% confidence level (CL) is determined using a modified frequentist CL_s method [77, 78]. When combining all categories and channels, an observed (expected) upper limit of $\mu < 1.5$ (1.7) at the 95% CL is obtained. The expected and observed upper limits in each channel and in the combination are listed in Table 5 and visualized in Figure 10 (right). The limits in each individual category are listed in Appendices A and B for the lepton+jets and the dilepton channel, respectively.

Table 5: Best-fit value of the signal strength modifier μ and the median expected and observed 95% CL upper limits (UL) in the dilepton and the lepton+jets channels as well as the combined results. The one standard deviation ($\pm 1\sigma$) confidence intervals of the expected limit and the best-fit value are also quoted, split into the statistical and systematic components in the latter case. Expected limits are calculated with the asymptotic method [79].

Channel	Observed UL	Expected UL	Best-fit μ
Dilepton	3.2	$3.4^{+1.5}_{-1.0}$	$-0.04^{+1.50}_{-1.39}(\text{tot.}) \,^{+1.05}_{-0.96}(\text{stat.}) \,^{+1.01}_{-1.06}(\text{syst.})$
Lepton+jets	1.8	$2.1^{+1.0}_{-0.6}$	$-0.43^{+1.02}_{-1.02}(\text{tot.}) \,^{+0.51}_{-0.52}(\text{stat.}) \,^{+0.88}_{-0.87}(\text{syst.})$
Combined	1.5	$1.7^{+0.7}_{-0.5}$	$-0.19^{+0.80}_{-0.81}(\text{tot.}) \,^{+0.45}_{-0.44}(\text{stat.}) \,^{+0.66}_{-0.68}(\text{syst.})$
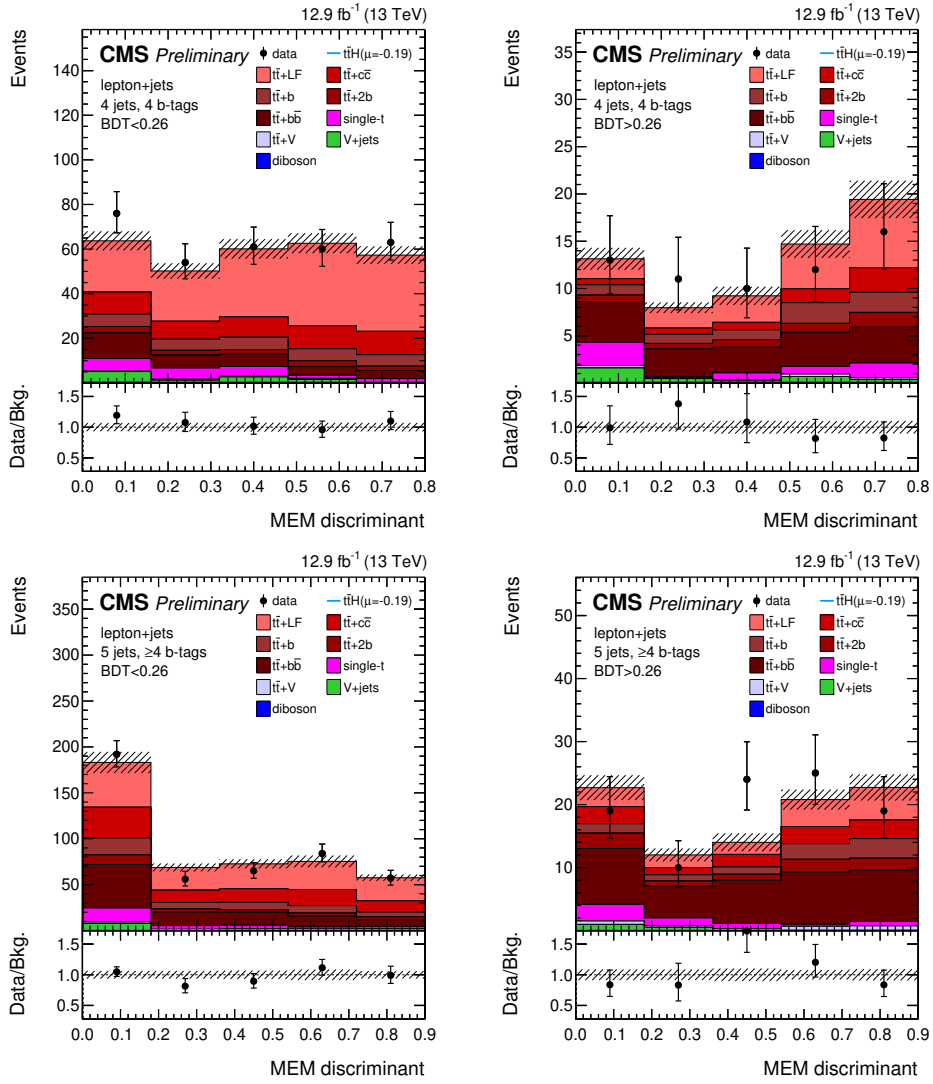
Figure 6: Final discriminant shapes (MEM) in the analysis categories with 4 jets, 4 b-tags (top row) and 5 jets, ≥ 4 b-tags (bottom row) with low (left) and high (right) BDT output in the lepton+jets channel after the fit to data.
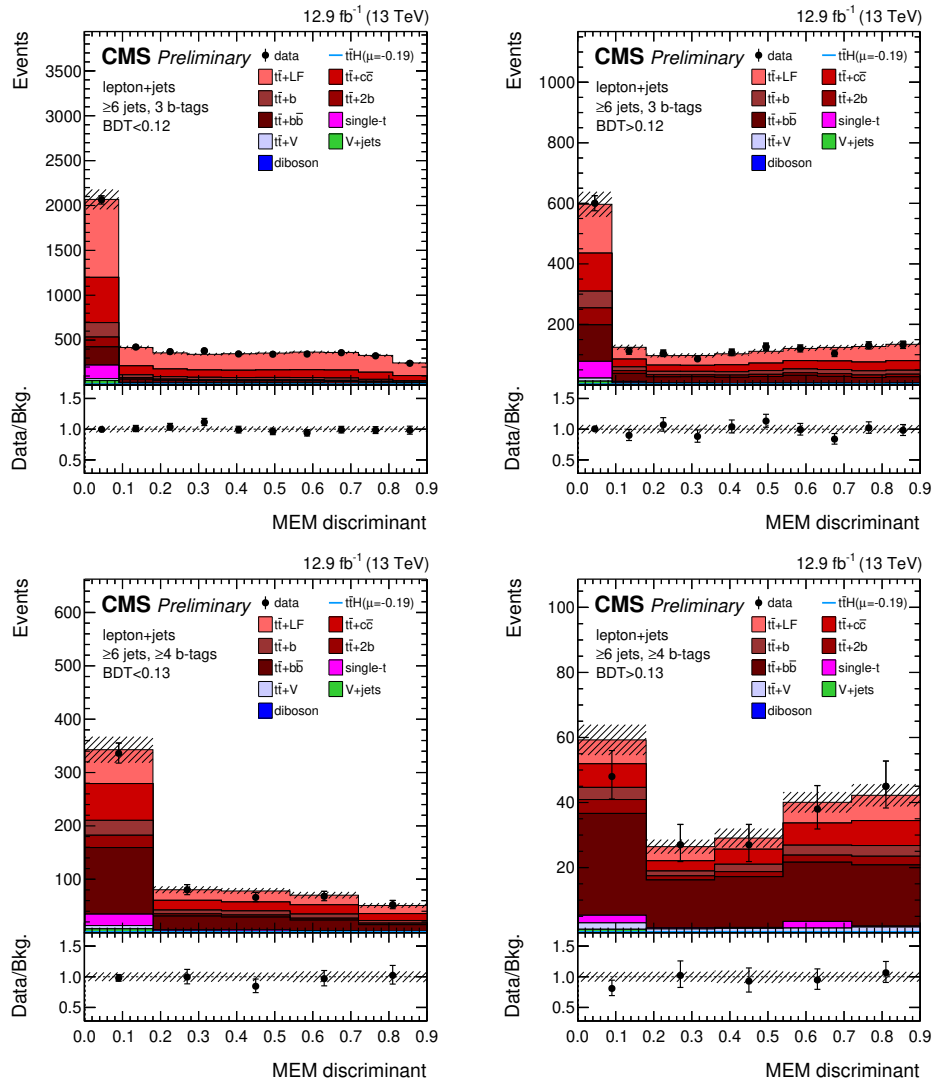
Figure 7: Final discriminant shapes (MEM) in the analysis categories with ≥ 6 jets, 3 b-tags (top row) and ≥ 6 jets, ≥ 4 b-tags (bottom row) with low (left) and high (right) BDT output in the lepton+jets channel after the fit to data (continued from Fig. 6).
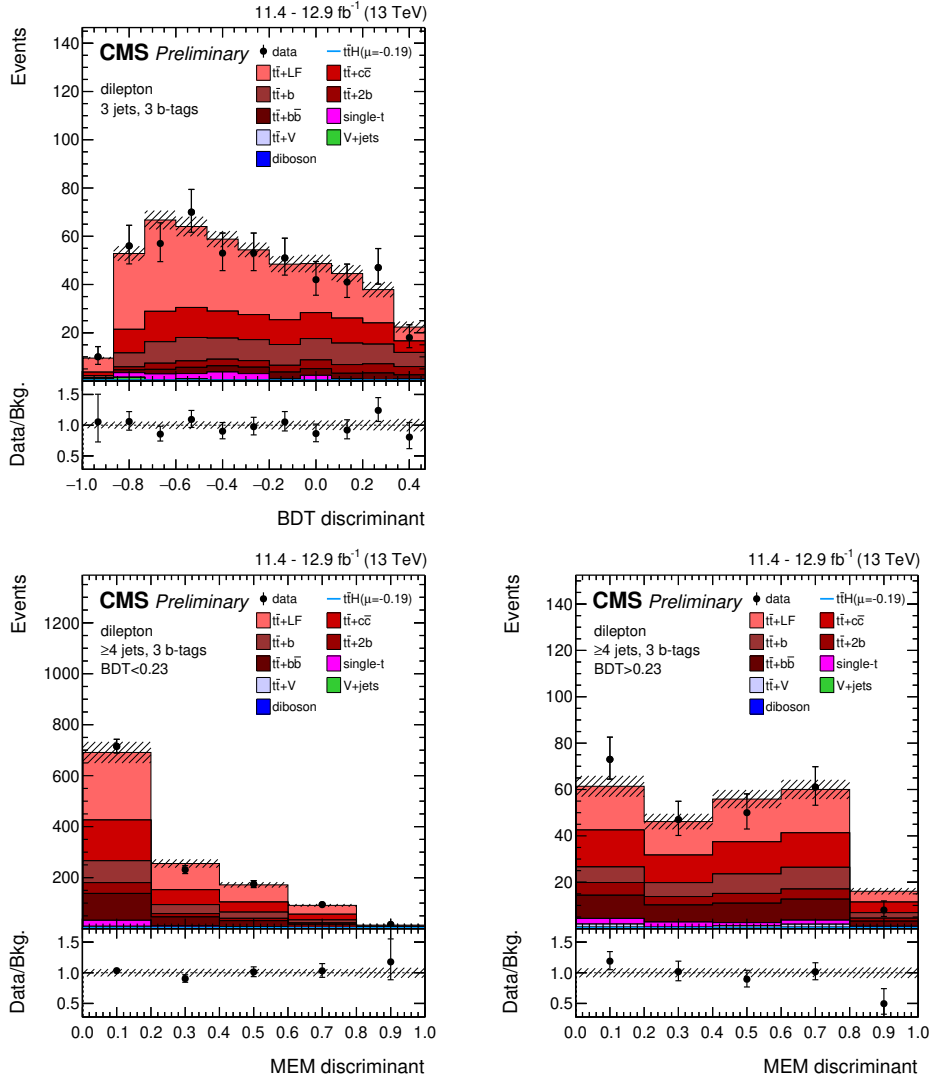
Figure 8: Final discriminant shapes (BDT or MEM) in the analysis categories with 3 jets, 3 b-tags (top row) and ≥ 4 jets, 3 b-tags (bottom row) with low (left) and high (right) BDT output in the dilepton channel after the fit to data.
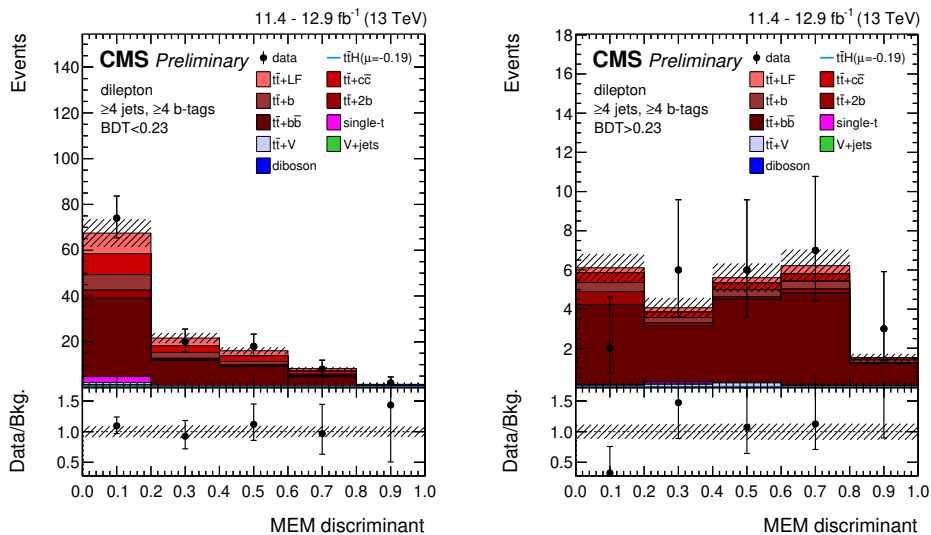
Figure 9: Final discriminant shapes (MEM) in the analysis categories with ≥ 4 jets, ≥ 4 b-tags with low (left) and high (right) BDT output in the dilepton channel after the fit to data (continued from Fig. 8).
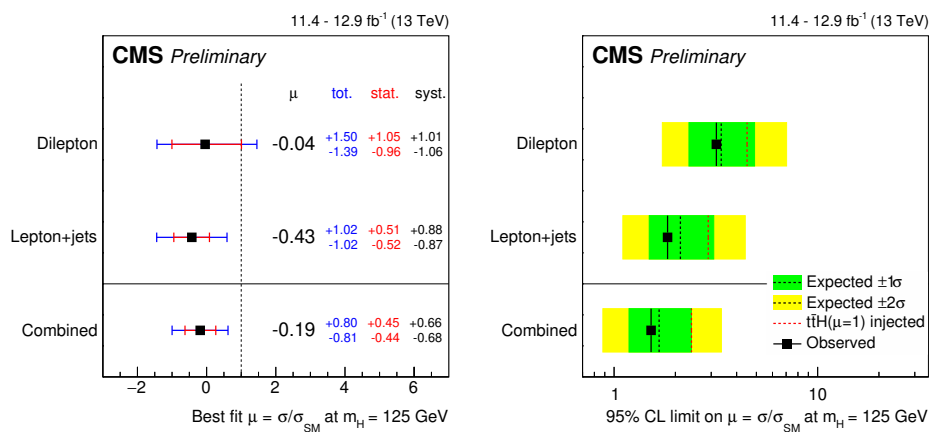
Figure 10: Best-fit values of the signal strength modifiers μ with their $\pm 1\sigma$ confidence intervals, also split into their statistical and systematic components (left), and median expected and observed 95% CL upper limits on μ (right). The expected limits are displayed together with $\pm 1\sigma$ and $\pm 2\sigma$ confidence intervals. Also shown are the limits in case of an injected signal of $\mu = 1$.

8 Summary

A search for the associated production of a Higgs boson and a top quark-antiquark pair is performed using up to $12.9\,\mathrm{fb}^{-1}$ of pp collision data recorded with the CMS detector at a center-of-mass energy of 13 TeV in 2016. Candidate events are selected in final states compatible with the Higgs boson decay $H \to b\bar{b}$ and the lepton+jets or dilepton decay channel of the $t\bar{t}$ pair. Selected events are split into mutually exclusive categories according to their $t\bar{t}$ decay channel and jet content. In each category a powerful discriminant is constructed to separate the $t\bar{t}H$ signal from the $t\bar{t}$-dominated background, based on boosted decision trees and the matrix element method. An observed (expected) upper limit on the $t\bar{t}H$ production cross section relative to the SM expectations of $\mu = 1.5\,(1.7)$ at the 95% confidence level is obtained. The best-fit value of μ is $-0.19\,^{+0.45}_{-0.44}(\text{stat.})\,^{+0.66}_{-0.68}(\text{syst.})$. These results are compatible with SM expectations at the level of 1.5 standard deviations.

A   Lepton+Jets Additional Material

In the following, the input variables used to train the BDTs in each category of the lepton+jets channel are presented. In Table 6, all variables used in any of the categories are described, and in Table 7, the variables used per category are listed. The observed and expected upper limits at 95% CL on the signal strength modifier μ under the background-only hypothesis in the lepton+jets channel are listed in Table 8 and displayed in Fig. 11 for the individual categories and for the combined fit in all categories.
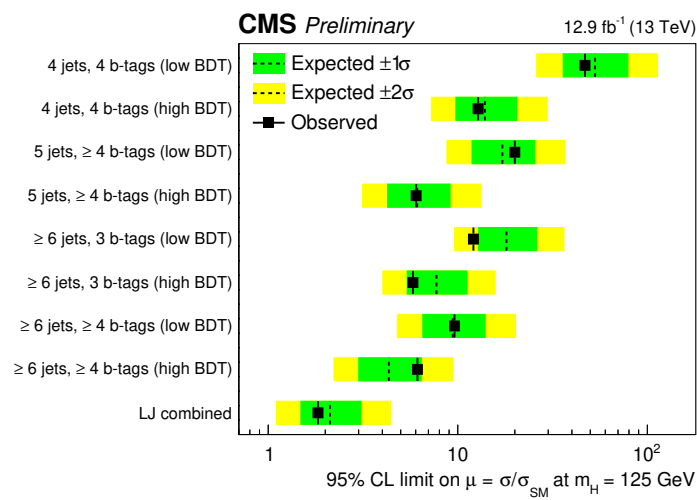
Figure 11: Observed and expected upper limits at 95% CL on μ in the lepton+jets channel. The limits are calculated with the asymptotic method.

Table 6: Variables used in the BDT training in the lepton+jets channel.

Object and event kinematics	
$p_T(\text{jet } i)$	Transverse momentum of i-th jet, jets ordered in p_T
HT	Scalar sum of transverse momenta for all jets with $p_T > 30 \text{ GeV}/c$
MET	Missing transverse energy
$\sum p_T(\text{jets}, \text{lepton}, \text{MET})$	Sum of the p_T of all jets, leptons, and MET
$M(\text{jets}, \text{lepton}, \text{MET})$	Invariant mass of the 4-vector sum of all jets, leptons, and MET
avg. $\Delta R(\text{tag}, \text{tag})$	Average ΔR between b-tagged jets
avg. $\Delta \eta(\text{jet}, \text{jet})$	Average $\Delta \eta$ between jets
max $\Delta|\eta|$ (jet, avg. jet $|\eta|$)	Maximal $\Delta|\eta|$ between any jet and the average $|\eta|$ of all jets
max $\Delta|\eta|$ (tag, avg. jet $|\eta|$)	Maximal $\Delta|\eta|$ between any b-tagged jet and the average $|\eta|$ of all jets
max $\Delta|\eta|$ (tag, avg. tag $|\eta|$)	Maximal $\Delta|\eta|$ between any b-tagged jet and the average $|\eta|$ of all b-tagged jets
min $\Delta R(\text{tag}, \text{tag})$	ΔR between the two closest b-tagged jets
M_3	Invariant mass of the 3-jet system with largest transverse momentum
min $\Delta R(\text{lepton}, \text{jet})$	ΔR between the lepton and the closest jet
M_2 of min $\Delta R(\text{tag}, \text{tag})$	Invariant mass of the two b-tagged jets that are closest in ΔR
$M_2(\text{tag}, \text{tag})$ closest to 125	Invariant mass of the two b-tagged jets with an invariant mass closest to 125 GeV/c^2
best Higgs mass	A minimum-chi-squared fit to event kinematics is used to select two b-tagged jets as top-decay products. Of the remaining b-tagged jets, the invariant mass of the two with highest E_T is saved as this quantity.
$\sqrt{\Delta \eta(t^{\text{lep}}, b\bar{b}) \times \Delta \eta(t^{\text{had}}, b\bar{b})}$	Square root of the product of $|\Delta \eta|(\text{leptonic top}, b\bar{b})$ and $|\Delta \eta|(\text{hadronic top}, b\bar{b})$, where the $b\bar{b}$-system and the candidates for the leptonically and hadronically decaying top quarks are found with the best Higgs mass algorithm
$(\Sigma p_T(\text{jet}))/(\Sigma E(\text{jet}))$	Ratio of the sum of the transverse momenta of all jets and the sum of the energies of all jets
CSVv2 b-tag	
1st- to 5th-highest CSVv2	First- to fifth-highest highest b-tag discriminant value of all jets
avg. CSVv2 of b-tagged jets	Average b-tag discriminant value of all b-tagged jets
2nd moment of b-tagged jets' CSVv2	Squared difference between the b-tag discriminant value of a given b-tagged jet and the average CSVv2 discriminant value of all b-tagged jets, summed over all b-tagged jets
b-tagging likelihood ratio	Ratio of the likelihood that the event contains four b-jets to the likelihood that it contains two b-jets. The likelihoods are constructed from the b-tag discriminant, the p_T and the η of the jets.
Event shape	
sphericity	The sphericity is defined as $\frac{3}{2}(\lambda_2 + \lambda_3)$ where the λ_i are the eigenvalues of the sphericity tensor as defined in [80]
aplanarity	The aplanarity is defined as $\frac{3}{2}\lambda_3$ where the λ_i are the eigenvalues of the sphericity tensor as defined in [80]
$H_1 - H_4$	The first four Fox-Wolfram moments as defined in [81]

Table 7: BDT input variable assignment per category in the lepton+jets channel.

4 jets, 4 tags	5 jets, ≥ 4 tags
$\sum p_{\mathrm{T}}(\text{jets, lepton, MET})$	avg. $\Delta\eta(\text{jet, jet})$
avg. CSVv2 of b-tagged jets	HT
aplanarity	avg. CSVv2 of b-tagged jets
H_3	$M_2(\text{tag, tag})$ closest to 125
$(\Sigma p_{\mathrm{T}}(\text{jet}))/(\Sigma E(\text{jet}))$	M_3
M_2 of min ΔR(tag, tag)	$\sum p_{\mathrm{T}}(\text{jets, lepton, MET})$
	M_2 of min ΔR(tag, tag)
	aplanarity
	avg. ΔR(tag, tag)
≥ 6 jets, 3 tags	≥ 6 jets, ≥ 4 tags
aplanarity	best Higgs mass
$\sqrt{\Delta\eta(\mathrm{t^{lep}, bb}) \times \Delta\eta(\mathrm{t^{had}, bb})}$	$M_2(\text{tag, tag})$ closest to 125
$(\Sigma p_{\mathrm{T}}(\text{jet}))/(\Sigma E(\text{jet}))$	$M(\text{jets, lepton, MET})$
min ΔR(tag, tag)	4th highest CSVv2
2nd moment of b-tagged jets' CSVv2	$\sum p_{\mathrm{T}}(\text{jets, lepton, MET})$
$\sum p_{\mathrm{T}}(\text{jets, lepton, MET})$	5th highest CSVv2
b-tagging likelihood ratio	

Table 8: Observed and median expected 95% CLs upper limits on μ in the lepton+jets channel, calculated with the asymptotic method. The upper and lower range of the 1σ confidence interval is also quoted.

Category	Observed	Expected
4 jets, 4 b-tags (low BDT)	46.9	$53.0^{+26.0}_{-17.0}$
4 jets, 4 b-tags (high BDT)	12.8	$13.9^{+6.6}_{-4.1}$
5 jets, ≥ 4 b-tags (low BDT)	20.0	$17.2^{+8.3}_{-5.3}$
5 jets, ≥ 4 b-tags (high BDT)	6.0	$6.1^{+3.0}_{-1.8}$
≥ 6 jets, 3 b-tags (low BDT)	12.1	$18.1^{+8.0}_{-5.2}$
≥ 6 jets, 3 b-tags (high BDT)	5.8	$7.7^{+3.5}_{-2.3}$
≥ 6 jets, ≥ 4 b-tags (low BDT)	9.6	$9.4^{+4.5}_{-2.9}$
≥ 6 jets, ≥ 4 b-tags (high BDT)	6.1	$4.3^{+2.1}_{-1.3}$
lepton+jets combined	1.8	$2.1^{+1.0}_{-0.6}$

B   Dilepton Additional Material

In the following, the input variables used to train the BDTs in each category of the dilepton channel are presented. In Table 9, all variables used in any of the categories are described, and in Table 10, the variables used per category are listed. The observed and expected upper limits at 95% CL on the signal strength modifier μ under the background-only hypothesis in the dilepton channel are listed in Table 11 and displayed in Fig. 12 for the individual categories and for the combined fit in all categories.
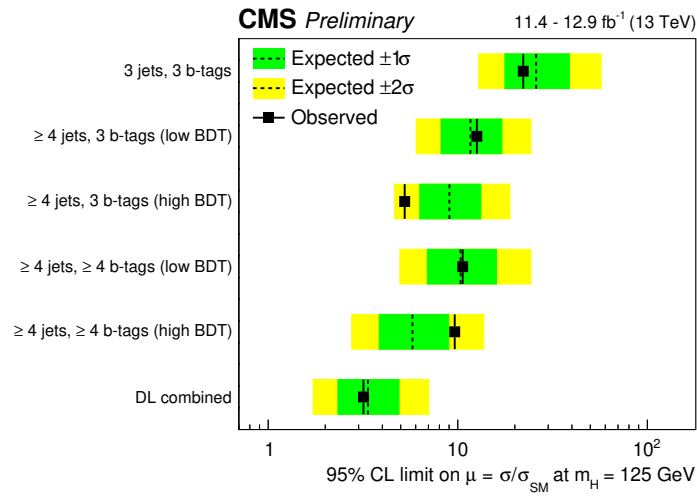
Figure 12: Observed and expected and upper limits at 95% CL on μ in the dilepton channel. The limits are calculated with the asymptotic method.

Table 9: Variables used in the BDT training in the dilepton channel.

Event variable	Description
Object and event kinematics	
$\langle \Delta R_{\text{tag,tag}} \rangle$	Average ΔR between b-tagged jets
$\sum p_{T\text{jets,leptons}}$	Sum of the p_T of all jets and leptons
$\tau_{\text{jet,jet}}^{\text{max mass}}$	Twist angle between jet pair
$\min \Delta R_{\text{tag,tag}}$	ΔR between the two closest b-tagged jets
$\max \Delta \eta_{\text{tag,tag}}$	$\Delta \eta$ between the two furthest b-tagged jets
$M_{\text{jet,jet}}^{\min \Delta R}$	Invariant mass of jet pair with minimum ΔR
$M_{\text{higgs-like}}^{\text{jj}}$	Invariant mass of a jet pair ordered in closeness to the Higgs mass
$M_{\text{tag,tag}}^{\min \Delta R}$	Mass of b-tagged jet pair with minimum ΔR
$p_{T \text{ tag,tag}}^{\min \Delta R}$	Sum of the p_T of b-tagged jet pair with minimum ΔR
Centrality (tags)	Ratio of the sum of the transverse momentum of all b-tagged jets and the sum of the energy of all b-tagged jets
Centrality (jets, leptons)	Ratio of the sum of the transverse momentum of all jets and leptons, and the sum of the energy of all jets and leptons
H_T	Scalar sum of transverse momentum for all jets
$\min \Delta R_{\text{jet,jet}}$	ΔR between the two closest jets
median $M_{\text{jet,jet}}$	Median invariant mass of all combinations of jet pairs
$M_{\text{tag,tag}}^{\text{max mass}}$	Mass for b-tagged jet pair with maximum invariant mass combination
$\langle \Delta R_{jet,tag} \rangle$	Average ΔR between jets (with at least one b-tagged jet)
$p_{T \ jet,tag}^{\min \Delta R}$	Sum of the p_T of jet pair with minimum ΔR (with at least one b-tagged jet)
$\tau_{\text{jet,tag}}^{\text{max mass}}$	Twist angle between jet pair (with at least one b-tagged jet)
$m_{\text{jet,jet,jet}}^{\text{max } p_T}$	Invariant mass of the 3-jet system with the largest transverse momentum.
$M_{\text{higgs-like}}^{\text{bj}}$	Invariant mass of a jet pair (with at least one b-tagged jet) ordered in closeness to the Higgs mass
CSVv2 b-tag	
$\langle d \rangle_{\text{tagged/untagged}}$	Average CSVv2 b-tag discriminant value for b-tagged/un-b-tagged jets
Event shape	
H_0, H_1, H_2, H_3, H_4	Fox-Wolfram moments [81]
C(jets)	$3 \left(\lambda_1 \lambda_2 + \lambda_1 \lambda_3 + \lambda_2 \lambda_3 \right)$ [80]

Table 10: BDT input variable assignment per category in the dilepton channel.

3 jets, 3 tags	$\geq$4 jets, 3 tags	$\geq$4 jets, $\geq$4 tags
$\langle d \rangle_{\text{tagged}}$	Centrality(jets & leptons)	Centrality(jets & leptons)
$H_1(\text{jets})$	C(jets)	Centrality(tags)
$M^{\text{bj}}_{\text{higgs-like}}$	$H_2(\text{tags})$	H_T^{tags}
$M^{\text{max mass}}_{\text{tag,tag}}$	$M^{\text{jj}}_{\text{higgs-like}}$	$M^{\text{jj}}_{\text{higgs-like}}$
$\min \Delta R_{\text{tag,tag}}$	$M^{\max p_T}_{\text{jet,jet,jet}}$	$\min \Delta R_{\text{jet,jet}}$
$\max \Delta \eta_{\text{jet,jet}}$	$M^{\min \Delta R}_{\text{tag,tag}}$	$M^{\min \Delta R}_{jet,tag}$
$\min \Delta R_{\text{jet,jet}}$	$\min \Delta R_{\text{tag,tag}}$	$M^{\text{max mass}}_{\text{tag,tag}}$
$\sum p_{T\text{jets,leptons}}$	$\max \Delta \eta_{\text{tag,tag}}$	$M^{\min \Delta R}_{\text{tag,tag}}$
$H_4/H_0(\text{tags})$	$\tau^{\text{max mass}}_{\text{tag,tag}}$	$\max \Delta \eta_{\text{jet,jet}}$
		$\max \Delta \eta_{\text{tag,tag}}$
		median $M_{\text{jet,jet}}$

Table 11: Observed and median expected and 95% CLs upper limits on μ in the dilepton channel, calculated with the asymptotic method. The upper and lower range of the 1σ confidence interval is also quoted.

Category	Observed	Expected
3 jets, 3 b-tags	22.2	$25.9^{+12.9}_{-8.2}$
$\geq$ 4 jets, 3 b-tags (low BDT)	12.6	$11.7^{+5.4}_{-3.5}$
$\geq$ 4 jets, 3 b-tags (high BDT)	5.2	$9.0^{+4.2}_{-2.7}$
$\geq$ 4 jets, $\geq$ 4 b-tags (low BDT)	10.6	$10.3^{+5.6}_{-3.4}$
$\geq$ 4 jets, $\geq$ 4 b-tags (high BDT)	9.6	$5.8^{+3.2}_{-1.9}$
dilepton combined	3.2	$3.4^{+1.5}_{-1.0}$

References

[1] ATLAS Collaboration, "Observation of a new particle in the search for the Standard Model Higgs boson with the ATLAS detector at the LHC", *Phys. Lett. B* **716** (2012), no. 1, 1–29, `doi:10.1016/j.physletb.2012.08.020`, `arXiv:1207.7214`.

[2] CMS Collaboration, "Observation of a new boson at a mass of 125 GeV with the CMS experiment at the LHC", *Phys. Lett. B* **716** (2012), no. 1, 30–61, `doi:10.1016/j.physletb.2012.08.021`, `arXiv:1207.7235`.

[3] CMS Collaboration, "Evidence for the direct decay of the 125 GeV Higgs boson to fermions", *Nature Phys.* **10** (2014), no. 5, 557–560, `doi:10.1038/nphys3005`, `arXiv:1401.6527`.

[4] ATLAS Collaboration, "Evidence for the Higgs-boson Yukawa coupling to tau leptons with the ATLAS detector", *JHEP* **04** (2015) 117, `doi:10.1007/JHEP04(2015)117`, `arXiv:1501.04943`.

[5] ATLAS Collaboration, "Measurements of Higgs boson production and couplings in diboson final states with the ATLAS detector at the LHC", *Phys. Lett. B* **726** (2013), no. 1-3, 88–119, `doi:10.1016/j.physletb.2014.05.011`, `10.1016/j.physletb.2013.08.010`, `arXiv:1307.1427`. [Erratum: Phys. Lett.B734,406(2014)].

[6] CMS Collaboration, "Precise determination of the mass of the Higgs boson and tests of compatibility of its couplings with the standard model predictions using proton collisions at 7 and 8 TeV", *Eur. Phys. J. C.* **75** (2015), no. 5, 212, `doi:10.1140/epjc/s10052-015-3351-7`, `arXiv:1412.8662`.

[7] ATLAS Collaboration, "Evidence for the spin-0 nature of the Higgs boson using ATLAS data", *Phys. Lett. B* **726** (2013), no. 1-3, 120–144, `doi:10.1016/j.physletb.2013.08.026`, `arXiv:1307.1432`.

[8] CMS Collaboration, "Constraints on the spin-parity and anomalous HVV couplings of the Higgs boson in proton collisions at 7 and 8 TeV", *Phys. Rev. D* **92** (2015), no. 1, 012004, `doi:10.1103/PhysRevD.92.012004`, `arXiv:1411.3441`.

[9] LHC Higgs Cross Section Working Group Collaboration, "Handbook of LHC Higgs Cross Sections: 4. Deciphering the Nature of the Higgs Sector", `arXiv:1610.07922`.

[10] G. Burdman, M. Perelstein, and A. Pierce, "Large Hadron Collider tests of a little Higgs model", *Phys. Rev. Lett.* **90** (2003), no. 24, 241802, `doi:10.1103/PhysRevLett.90.241802`, `arXiv:hep-ph/0212228`. [Erratum: Phys. Rev. Lett.92,049903(2004)].

[11] T. Han, H. E. Logan, B. McElrath, and L.-T. Wang, "Phenomenology of the little Higgs model", *Phys. Rev. D* **67** (2003), no. 9, 095004, `doi:10.1103/PhysRevD.67.095004`, `arXiv:hep-ph/0301040`.

[12] M. Perelstein, M. E. Peskin, and A. Pierce, "Top quarks and electroweak symmetry breaking in little Higgs models", *Phys. Rev. D* **69** (2004), no. 7, 075002, `doi:10.1103/PhysRevD.69.075002`, `arXiv:hep-ph/0310039`.

[13] H.-C. Cheng, I. Low, and L.-T. Wang, "Top partners in little Higgs theories with T-parity", *Phys. Rev. D* **74** (2006), no. 5, 055001, `doi:10.1103/PhysRevD.74.055001`, `arXiv:hep-ph/0510225`.

[14] H.-C. Cheng, B. A. Dobrescu, and C. T. Hill, "Electroweak symmetry breaking and extra dimensions", *Nucl. Phys. B.* **589** (2000), no. 1-3, 249–268, `doi:10.1016/S0550-3213(00)00401-6`, `arXiv:hep-ph/9912343`.

[15] M. Carena, E. Ponton, J. Santiago, and C. E. M. Wagner, "Light Kaluza Klein States in Randall-Sundrum Models with Custodial SU(2)", *Nucl. Phys. B.* **759** (2006), no. 1-2, 202–227, `doi:10.1016/j.nuclphysb.2006.10.012`, `arXiv:hep-ph/0607106`.

[16] R. Contino, L. Da Rold, and A. Pomarol, "Light custodians in natural composite Higgs models", *Phys. Rev. D* **75** (2007), no. 5, 055014, `doi:10.1103/PhysRevD.75.055014`, `arXiv:hep-ph/0612048`.

[17] G. Burdman and L. Da Rold, "Electroweak Symmetry Breaking from a Holographic Fourth Generation", *JHEP* **12** (2007) 086, `doi:10.1088/1126-6708/2007/12/086`, `arXiv:0710.0623`.

[18] C. T. Hill, "Topcolor: Top quark condensation in a gauge extension of the standard model", *Phys. Lett. B* **266** (1991), no. 3, 419–424, `doi:10.1016/0370-2693(91)91061-Y`.

[19] A. Carmona, M. Chala, and J. Santiago, "New Higgs Production Mechanism in Composite Higgs Models", *JHEP* **07** (2012) 049, `doi:10.1007/JHEP07(2012)049`, `arXiv:1205.2378`.

[20] CMS Collaboration, "Search for the associated production of the Higgs boson with a top-quark pair", *JHEP* **09** (2014) 087, `doi:10.1007/JHEP09(2014)087`, `10.1007/JHEP10(2014)106`, `arXiv:1408.1682`. [Erratum: JHEP10,106(2014)].

[21] ATLAS Collaboration, "Search for the associated production of the Higgs boson with a top quark pair in multilepton final states with the ATLAS detector", *Phys. Lett. B* **749** (2015) 519–541, `doi:10.1016/j.physletb.2015.07.079`, `arXiv:1506.05988`.

[22] J. M. Campbell et al., "The Matrix Element Method at Next-to-Leading Order", *JHEP* **11** (2012) 043.

[23] CMS Collaboration, "Search for a standard model Higgs boson produced in association with a top-quark pair and decaying to bottom quarks using a matrix element method", *Eur. Phys. J. C.* **75** (2015), no. 6, 251, `doi:10.1140/epjc/s10052-015-3454-1`, `arXiv:1502.02485`.

[24] ATLAS Collaboration, "Search for the Standard Model Higgs boson produced in association with top quarks and decaying into $b\bar{b}$ in pp collisions at $\sqrt{s} = 8$ TeV with the ATLAS detector", *Eur. Phys. J. C.* **75** (2015), no. 7, 349, `doi:10.1140/epjc/s10052-015-3543-1`, `arXiv:1503.05066`.

[25] LHC Higgs Cross Section Working Group Collaboration, "Handbook of LHC Higgs Cross Sections: 1. Inclusive Observables", `doi:10.5170/CERN-2011-002`, `arXiv:1101.0593`.

[26] CMS Collaboration, "Updated measurements of Higgs boson production in the diphoton decay channel at $\sqrt{s} = 13$ TeV in pp collisions at CMS.", CMS Physics Analysis Summary CMS-PAS-HIG-16-020, 2016.

[27] CMS Collaboration, "Search for associated production of Higgs bosons and top quarks in multilepton final states at $\sqrt{s} = 13$ TeV", CMS Physics Analysis Summary CMS-PAS-HIG-16-022, 2016.

[28] ATLAS Collaboration, "Measurement of fiducial, differential and production cross sections in the $H \to \gamma\gamma$ decay channel with 13.3 fb^{-1} of 13 TeV proton-proton collision data with the ATLAS detector", Technical Report ATLAS-CONF-2016-067, 2016.

[29] ATLAS Collaboration, "Search for the Associated Production of a Higgs Boson and a Top Quark Pair in Multilepton Final States with the ATLAS Detector", Technical Report ATLAS-CONF-2016-058, 2016.

[30] CMS Collaboration, "Search for t$\bar{\text{t}}$H production in the H $\to$ b$\bar{\text{b}}$ decay channel with $\sqrt{s} = 13$ TeV pp collisions at the CMS experiment", CMS Physics Analysis Summary CMS-PAS-HIG-16-004, 2016.

[31] T. J. Hastie, R. J. Tibshirani, and J. H. Friedman, "The elements of statistical learning : data mining, inference, and prediction". Springer series in statistics. Springer, New York, NY, 2. ed., corr. at 10. print. edition, 2013. ISBN 978-0-387-84857-0.

[32] P. C. Bhat, "Multivariate Analysis Methods in Particle Physics", *Annual Review of Nuclear and Particle Science* **61** (2011), no. 1, 281, `doi:10.1146/annurev.nucl.012809.104427`.

[33] A. Höcker et al., "TMVA: Toolkit for Multivariate Data Analysis", *PoS* **ACAT** (2007) 040, `arXiv:physics/0703039`.

[34] K. Kondo, "Dynamical Likelihood Method for Reconstruction of Events With Missing Momentum. 1: Method and Toy Models", *J. Phys. Soc. Jap.* **57** (1988) 4126–4140, `doi:10.1143/JPSJ.57.4126`.

[35] D0 Collaboration, "A precision measurement of the mass of the top quark", *Nature* **429** (2004) 638–642, `doi:10.1038/nature02589`, `arXiv:hep-ex/0406031`.

[36] CMS Collaboration, "The CMS experiment at the CERN LHC", *JINST* **3** (2008), no. 8, S08004, `doi:10.1088/1748-0221/3/08/S08004`.

[37] GEANT4 Collaboration, "GEANT4—a simulation toolkit", *Nucl. Instrum. Meth. A* **506** (2003), no. 3, 250, `doi:10.1016/S0168-9002(03)01368-8`.

[38] S. Frixione, P. Nason, and C. Oleari, "Matching NLO QCD computations with parton shower simulations: the POWHEG method", *JHEP* **11** (2007) 070, `doi:10.1088/1126-6708/2007/11/070`, `arXiv:0709.2092`.

[39] E. Re, "Single-top Wt-channel production matched with parton showers using the POWHEG method", *Eur. Phys. J. C* **71** (2011) 1547, `doi:10.1140/epjc/s10052-011-1547-z`, `arXiv:1009.2450`.

[40] NNPDF Collaboration, "Parton distributions for the LHC Run II", *JHEP* **04** (2015) 040, `doi:10.1007/JHEP04(2015)040`, `arXiv:1410.8849`.

[41] T. Sjöstrand et al., "An introduction to PYTHIA 8.2", *Comput. Phys. Commun.* **191** (2015) 159, `doi:10.1016/j.cpc.2015.01.024`, `arXiv:1410.3012`.

[42] J. Alwall et al., "The automated computation of tree-level and next-to-leading order differential cross sections, and their matching to parton shower simulations", *JHEP* **07** (2014) 079, `doi:10.1007/JHEP07(2014)079`, `arXiv:1405.0301`.

[43] R. Frederix and S. Frixione, "Merging meets matching in MC@NLO", *JHEP* **12** (2012) 061, `doi:10.1007/JHEP12(2012)061`, `arXiv:1209.6215`.

[44] CMS Collaboration, "Underlying event tunes and double parton scattering", CMS Physics Analysis Summary CMS-PAS-GEN-14-001, 2014.

[45] P. Skands, S. Carrazza, and J. Rojo, "Tuning PYTHIA 8.1: the Monash 2013 Tune", *Eur. Phys. J. C* **74** (2014), no. 8, 3024, `doi:10.1140/epjc/s10052-014-3024-y`, `arXiv:1404.5630`.

[46] N. Kidonakis, "Two-loop soft anomalous dimensions for single top quark associated production with W⁻ or H⁻", *Phys. Rev. D* **82** (2010), no. 5, 054018, `doi:10.1103/PhysRevD.82.054018`, `arXiv:hep-ph/1005.4451`.

[47] J. M. Campbell, R. K. Ellis, and C. Williams, "Vector boson pair production at the LHC", *JHEP* **07** (2011) 018, `doi:10.1007/JHEP07(2011)018`, `arXiv:1105.0020`.

[48] F. Maltoni, D. Pagani, and I. Tsinikos, "Associated production of a top-quark pair with vector bosons at NLO in QCD: impact on $t\bar{t}H$ searches at the LHC", `arXiv:1507.05640`.

[49] W. Beenakker et al., "Higgs radiation off top quarks at the Tevatron and the LHC", *Phys. Rev. Lett.* **87** (2001), no. 20, 201805, `doi:10.1103/PhysRevLett.87.201805`, `arXiv:hep-ph/0107081`.

[50] W. Beenakker et al., "NLO QCD corrections to t t̄H production in hadron collisions", *Nucl. Phys. B* **653** (2003), no. 1-2, 151, `doi:10.1016/S0550-3213(03)00044-0`, `arXiv:hep-ph/0211352`.

[51] S. Dawson, L. H. Orr, L. Reina, and D. Wackeroth, "Associated top quark Higgs boson production at the LHC", *Phys. Rev. D* **67** (2003), no. 7, 071503, `doi:10.1103/PhysRevD.67.071503`, `arXiv:hep-ph/0211438`.

[52] S. Dawson et al., "Associated Higgs production with top quarks at the large hadron collider: NLO QCD corrections", *Phys. Rev. D* **68** (2003), no. 3, 034022, `doi:10.1103/PhysRevD.68.034022`, `arXiv:hep-ph/0305087`.

[53] A. Djouadi, J. Kalinowski, and M. Spira, "HDECAY: A program for Higgs boson decays in the standard model and its supersymmetric extension", *Comput. Phys. Commun.* **108** (1998), no. 1, 56, `doi:10.1016/S0010-4655(97)00123-9`, `arXiv:hep-ph/9704448`.

[54] A. Djouadi, M. M. Mühlleitner, and M. Spira, "Decays of supersymmetric particles: The Program SUSY-HIT (SUspect-SdecaY-Hdecay-InTerface)", *Acta Phys. Polon. B* **38** (2007) 635, `arXiv:hep-ph/0609292`.

[55] A. Bredenstein, A. Denner, S. Dittmaier, and M. M. Weber, "Precise predictions for the Higgs-boson decay H → WW/ZZ → 4 leptons", *Phys. Rev. D* **74** (2006), no. 1, 013004, `doi:10.1103/PhysRevD.74.013004`, `arXiv:hep-ph/0604011`.

[56] A. Bredenstein, A. Denner, S. Dittmaier, and M. M. Weber, "Radiative corrections to the semileptonic and hadronic Higgs-boson decays H → WW/ZZ → 4 fermions", *JHEP* **02** (2007) 080, `doi:10.1088/1126-6708/2007/02/080`, `arXiv:hep-ph/0611234`.

[57] M. Cacciari et al., "Top-pair production at hadron colliders with next-to-next-to-leading logarithmic soft-gluon resummation", *Phys. Lett. B* **710** (2012), no. 4-5, 612, `doi:10.1016/j.physletb.2012.03.013`, `arXiv:1111.5869`.

[58] P. Baernreuther et al., "Percent Level Precision Physics at the Tevatron: First Genuine NNLO QCD Corrections to $q\bar{q} \to t\bar{t} + X$", *Phys. Rev. Lett.* **109** (2012), no. 13, 132001, `doi:10.1103/PhysRevLett.109.132001`, `arXiv:1204.5201`.

[59] M. Czakon and A. Mitov, "NNLO corrections to top-pair production at hadron colliders: the all-fermionic scattering channels", *JHEP* **12** (2012) 054, `arXiv:1207.0236`.

[60] M. Czakon and A. Mitov, "NNLO corrections to top-pair production at hadron colliders: the quark-gluon reaction", *JHEP* **01** (2013) 080, `arXiv:1210.6832`.

[61] M. Beneke et al., "Hadronic top-quark pair production with NNLL threshold resummation", *Nucl. Phys. B* **855** (2012), no. 3, 695, `doi:10.1016/j.nuclphysb.2011.10.021`, `arXiv:1109.1536`.

[62] M. Czakon, P. Fiedler, and A. Mitov, "Total Top-Quark Pair-Production Cross Section at Hadron Colliders Through $O(\alpha_S^4)$", *Phys. Rev. Lett.* **110** (2013), no. 25, 252004, `doi:10.1103/PhysRevLett.110.252004`, `arXiv:1303.6254`.

[63] M. Czakon and A. Mitov, "Top++: A Program for the Calculation of the Top-Pair Cross-Section at Hadron Colliders", *Comput. Phys. Commun.* **185** (2014), no. 11, 2930, `doi:10.1016/j.cpc.2014.06.021`, `arXiv:1112.5675`.

[64] CMS Collaboration, "Particle–flow event reconstruction in CMS and performance for jets, taus, and E_T^{miss}", CMS Physics Analysis Summary CMS-PAS-PFT-09-001, 2009.

[65] CMS Collaboration, "Commissioning of the particle-flow event reconstruction with the first LHC collisions recorded in the CMS detector", CMS Physics Analysis Summary CMS-PAS-PFT-10-001, 2010.

[66] M. Cacciari, G. P. Salam, and G. Soyez, "The anti-k_t jet clustering algorithm", *JHEP* **04** (2008) 063, `doi:10.1088/1126-6708/2008/04/063`, `arXiv:0802.1189`.

[67] M. Cacciari, G. P. Salam, and G. Soyez, "FastJet User Manual", *Eur. Phys. J.* **C72** (2012) 1896, `doi:10.1140/epjc/s10052-012-1896-2`, `arXiv:1111.6097`.

[68] M. Cacciari, G. P. Salam, and G. Soyez, "The catchment area of jets", *JHEP* **04** (2008) 005, `doi:10.1088/1126-6708/2008/04/005`, `arXiv:0802.1188`.

[69] CMS Collaboration, "Determination of jet energy calibration and transverse momentum resolution in CMS", *JINST* **6** (2011), no. 11, P11002, `doi:10.1088/1748-0221/6/11/P11002`, `arXiv:1107.4277`.

[70] CMS Collaboration, "Identification of b-quark jets with the CMS experiment", *JINST* **8** (2013), no. 4, P04013, `doi:10.1088/1748-0221/8/04/P04013`, `arXiv:1211.4462`.

[71] CMS Collaboration, "Identification of b quark jets at the CMS Experiment in the LHC Run 2", CMS Physics Analysis Summary CMS-PAS-BTV-15-001, 2016.

[72] J. H. Friedman, "Stochastic gradient boosting", *Computational Statistics & Data Analysis* **38** (2002), no. 4, 367,
`doi:http://dx.doi.org/10.1016/S0167-9473(01)00065-2`. Nonlinear Methods and Data Mining.

[73] J. Kennedy and R. Eberhart, "Particle swarm optimization", in *Proceedings of the IEEE International Conference on neural networks*, volume 4, pp. 1942–1948. Nov, 1995. `doi:10.1109/ICNN.1995.488968`.

[74] CMS Collaboration, "CMS Luminosity Measurement for the 2015 Data Taking Period", CMS Physics Analysis Summary CMS-PAS-LUM-15-001, 2016.

[75] R. J. Barlow and C. Beeston, "Fitting using finite Monte Carlo samples", *Comput. Phys. Commun.* **77** (1993), no. 2, 219–228, `doi:10.1016/0010-4655(93)90005-W`.

[76] J. S. Conway, "Incorporating Nuisance Parameters in Likelihoods for Multisource Spectra", in *Proceedings, PHYSTAT 2011 Workshop on Statistical Issues Related to Discovery Claims in Search Experiments and Unfolding, CERN,Geneva, Switzerland 17-20 January 2011.* 2011. `arXiv:1103.0354`.

[77] A. Read, "Modified frequentist analysis of search results (the CL_s method)", Technical Report CERN-OPEN-2000-005, CERN, 2000.

[78] T. Junk, "Confidence level computation for combining searches with small statistics", *Nucl. Instrum. Meth. A* **434** (1999), no. 2-3, 435,
`doi:10.1016/S0168-9002(99)00498-2`, `arXiv:hep-ex/9902006`.

[79] G. Cowan, K. Cranmer, E. Gross, and O. Vitells, "Asymptotic formulae for likelihood-based tests of new physics", *Eur. Phys. J.* **C71** (2011) 1554, `doi:10.1140/epjc/s10052-011-1554-0`, `10.1140/epjc/s10052-013-2501-z`, `arXiv:1007.1727`. [Erratum: Eur. Phys. J.C73,2501(2013)].

[80] J. D. Bjorken and S. J. Brodsky, "Statistical Model for Electron-Positron Annihilation into Hadrons", *Phys. Rev. D* **1** (Mar, 1970) 1416–1420, `doi:10.1103/PhysRevD.1.1416`.

[81] G. Fox and S. Wolfram, "Event shapes in e^+e^- annihilation", *Nuclear Physics B* **157** (1979), no. 3, 543–544, `doi:10.1016/0550-3213(79)90120-2`.

CMS Physics Analysis Summary

Determination of the normalised invariant mass distribution of tt̄+jet and extraction of the top quark mass

The CMS Collaboration

Abstract

A measurement of the top quark mass from top quark pair (tt̄) events produced in association with additional hard jets is performed in pp collisions at $\sqrt{s} = 8$ TeV with the CMS detector using data recorded in 2012, corresponding to an integrated luminosity of 19.7 fb^{-1}. The mass is extracted from the normalised invariant mass distribution of the tt̄+jet system at reconstruction level as well as from the related normalised differential cross section. Both measurements are performed in the dileptonic decay channels (e$^+$e$^-$, $\mu^+\mu^-$ and e$^\pm\mu^\pm$) of the tt̄ quark pairs.

1 Introduction

The mass of the top quark (m_t) is an important parameter for precision tests of the standard model and is either measured directly, based on the kinematic reconstruction of the decay products of the quark, or based on the mass dependency of the inclusive $t\bar{t}$ production cross section. Direct determinations of the top quark mass have been performed at the Tevatron and LHC colliders and the current world average of direct measurements is $m_t = 173.34 \pm 0.27\,\text{(stat)} \pm 0.71\,\text{(syst)}$ GeV [1], while the most precise combination of direct measurements by CMS yields $m_t = 172.44 \pm 0.13\,\text{(stat)} \pm 0.41\,\text{(syst)}$ GeV [2].

In this note an alternative approach to measure the mass is presented, following a method proposed in [3] using the normalised differential cross section as a function of the invariant mass of the $t\bar{t}$ system and the leading additional jet in the event, which does not stem from the top quark decays. The observable is defined as

$$\rho_s = \frac{2 \cdot m_0}{\sqrt{s_{t\bar{t}+\text{jet}}}} \, ,$$

where m_0 is a scale of the order of the top quark mass and $\sqrt{s_{t\bar{t}+\text{jet}}}$ denotes the invariant mass of the two top quark candidates and the additional leading jet.

First the measurement of the reconstructed ρ_s distribution is described and the extraction of the top quark mass using a traditional template technique is presented. For this, the observed ρ_s distribution is compared to simulations at reconstruction level generated with different top quark masses. Then the normalised differential cross section is derived by unfolding the distribution of ρ_s in order to correct for detector effects. Finally, the extraction of the top quark mass from the measured differential cross section is performed using theoretical predictions assuming different top quark masses. The extraction of the top quark mass from this differential cross section has been previously measured by the ATLAS Collaboration in the lepton+jets decay channel [4].

The measurements are performed using $t\bar{t}$ events in pp collisions recorded at $\sqrt{s} = 8$ TeV with the CMS detector [5], corresponding to an integrated luminosity of 19.7 fb^{-1}. The events are selected in the dileptonic decay channel with two oppositely charged isolated leptons (electrons or muons) and at least two jets and one b-tagged jet. The analysis presented in this document follows the strategy of other CMS measurements of differential $t\bar{t}$ cross sections and the $t\bar{t}$+jet studies in the same decay channel [6, 7]. This note focuses on the sensitivity of the method proposed, studying in detail the experimental and model uncertainties associated to the measurements.

The document is organized as follows. In Section 2 the process of event simulation and the employed MC simulations are described, the event selection is outlined in Section 3, and the sources of systematic uncertainties are discussed in Section 4. The extraction of the top quark mass from the ρ_s distribution is presented in Section 5. In Section 6, the calculation of the normalised differential cross section as function of ρ_s is described, and Section 7 details the top quark mass extraction from the cross section. A summary of the measurements is given in Section 8.

2 Event Simulation

In this analysis, the reference $t\bar{t}$ sample is simulated using the MADGRAPH event generator (v. 5.1.5.11) with the MADSPIN [8] package to account for spin correlation effects. The $t\bar{t}$ signal

was generated with up to three additional partons. The value of the top quark mass in the reference sample is chosen to be $m_t = 172.5$ GeV and the proton structure is described by the CTEQ6L1 [9] set of parton density functions (PDFs). The generated events are subsequently processed with PYTHIA (v. 6.424) [10] for fragmentation and hadronization using the MLM prescription for the matching of jets with parton showers [11]. The PYTHIA Z2* tune [12] is used to describe the underlying event. The CMS detector response is simulated using GEANT4 (v. 9.4) [13]. In addition to the reference sample, MADGRAPH+PYTHIA samples generated with m_t values of 166.5, 169.5, 171.5, 173.5, 175.5, and 178.5 GeV are used to evaluate the dependence of the measurement on the top quark mass and to extract the result.

Standard model backgrounds are simulated with MADGRAPH, POWHEG or PYTHIA, depending on the process. The main background contributions stem from Z/γ^* (referred to as Drell–Yan, DY in the following), single top quark (tW-channel) and W-boson production with additional jets (W+jets in the following). Smaller background contributions arise from diboson (WW, WZ and ZZ), $t\bar{t}$ production in association with a Z, W, or γ boson (referred to as $t\bar{t}+Z/W/\gamma$ in the following), and QCD multijet events. For comparison with the measured distributions, the events in the simulated samples are normalised to an integrated luminosity of $19.7\,\text{fb}^{-1}$ according to their cross section predictions. They are taken from NNLO (W+jets and DY), NLO+NNLL (single top quark tW-channel [14]), NLO (diboson [15], $t\bar{t}+W$ [16]) and LO (QCD multijet [10]) calculations. The predicted cross section for the $t\bar{t}+\gamma$ sample is obtained by scaling the LO cross section as obtained with the WHIZARD event generator [17] with an NLO k-factor [18].

The top quark mass is extracted through a fit to the data using the predicted normalised differential $t\bar{t}+$jet cross section from a NLO calculation combined with parton showering. The samples are generated using POWHEG (POWHEGBOX ttJ) with the PYTHIA (v. 8.205) 4C tune [19] for hadronization, and the proton structure is described by the CT10 PDF set. The values of the top quark mass for the different samples are $m_t = 172.5\,\text{GeV}$ and $\pm1\,\text{GeV}$, $\pm3\,\text{GeV}$, $\pm6\,\text{GeV}$, and an additional sample is provided at $m_t = 163.5\,\text{GeV}$.

3   Event Selection

The events are reconstructed using a particle-flow technique in which signals from all subdetectors are combined [20]. Charged hadron candidates from pileup events, i.e. originating from a vertex other than the one of the hard interaction, are removed before jet clustering on an event by event basis. Subsequently, the remaining component of neutral particle candidates from pileup events is evaluated [21]. Electron candidates are reconstructed from a combination of their charged track and their energy deposition in the ECAL, while electrons from identified photon conversions are rejected. Muon candidates are reconstructed from tracks which can be linked to both the silicon tracker and the muon system. The leptons, both electrons and muons, are required to have a transverse momentum of $p_T > 20\,\text{GeV}$ within the pseudorapidity region $|\eta| < 2.4$, and to be isolated with $I_{rel} < 0.15$. I_{rel} is defined as the sum of the transverse momenta of all neutral and charged reconstructed particle candidates, excluding the lepton itself, inside a cone of $\Delta R \equiv \sqrt{(\Delta\eta)^2 + (\Delta\phi)^2} < 0.3$ in the $\eta - \phi$ space, divided by the transverse momentum of the lepton under consideration. Jets are reconstructed by clustering the particle-flow candidates [22] using the anti-k_T clustering algorithm with size parameter $R = 0.5$ [23]. Muons and electrons passing less stringent selection criteria compared to the ones mentioned above have been identified and are excluded from the clustering process. Jets are selected in the pseudorapidity interval $|\eta| < 2.4$ and with a requirement of $p_T > 30\,\text{GeV}$. Jets originating from bottom quarks are identified using combined secondary vertex and track-based lifetime

information. The b-tagging efficiency for the working point chosen for this analysis is about 80–85% and the mis-tag rate around 10% [24]. The missing transverse energy E_T^{miss} is defined as the magnitude of the imbalance of the transverse momentum of all reconstructed particle candidates [25].

Events are selected if they contain at least two isolated leptons (electrons or muons) of opposite charge and two jets of which at least one is identified as b jet. These events are triggered using combinations of two leptons fulfiling transverse momentum thresholds and isolation criteria. Events with a lepton pair invariant mass smaller than 20 GeV are removed in order to suppress events from heavy flavour resonance decays and DY processes. In the $\mu\mu$ and ee channels, the dilepton invariant mass is required to be outside a Z-boson mass window of 91 ± 15 GeV and E_T^{miss} is required to be larger than 40 GeV.

A kinematic reconstruction method [26] is used to determine the $t\bar{t}$ kinematic properties and to identify the two b jets originating from the decays of the top quarks. This allows to unambigously assign the additional jets in the event. This method has previously been used in [27, 28]. In the kinematic reconstruction the following constraints are imposed: the balance of the transverse momentum of the two neutrinos; the W-boson invariant mass of 80.4 GeV; and the equality of the top and antitop quark masses. The remaining ambiguities are resolved by prioritising those event solutions with two or one b-tagged jets over solutions using jets without b tags. The top quark mass can be experimentally reconstructed in a broad range due to resolution effects. In order to account for this in the reconstruction, the assumed top quark mass for each lepton-jet combination is varied between 100 GeV and 300 GeV in steps of 1 GeV. Among the physical solutions, the solution of highest priority according to the aforementioned criteria and with the most probable neutrino energies according to a simulated neutrino energy spectrum is chosen. The efficiency of the method is about 90% and only events with a valid solution for the kinematic reconstruction are used for the subsequent analysis.

Events are finally selected if they contain at least one additional jet which has not been selected by the kinematic reconstruction and features a $p_T > 50$ GeV within $|\eta| < 2.4$, following the criteria described in [3].

Dominant backgrounds to the e^+e^- and $\mu^+\mu^-$ channels originate from DY+jets processes. Their contribution is estimated from data following the procedure described in [27, 29] using events rejected by the Z-boson veto. The contributions are scaled by the ratio of events failing and passing the selection criteria as estimated from simulation ($R_{out/in}$) [29]. The remaining backgrounds, including tW, W+jets, diboson, and QCD multijet events, are estimated from simulation.

Figure 1 shows the invariant mass of the $t\bar{t}$ system, the transverse momentum of the leading additional jet, and the ρ_s observable with $m_0 = 170$ GeV [3] for the dilepton event sample. The distributions are compared to the standard model predictions. Only $t\bar{t}$ events with two leptons (electron or muon) in the final state are considered as signal. All other $t\bar{t}$ events, specifically the dominant contribution originating from decays via τ leptons, are considered as background.

4 Systematic Uncertainties

Systematic uncertainties in the measurement arise from detector effects, background modelling, and theoretical assumptions. Each systematic uncertainty is investigated separately and estimated for each bin of the measurement by varying the corresponding efficiency, resolution, or scale within its uncertainty. The different sources of systematic uncertainty described in the
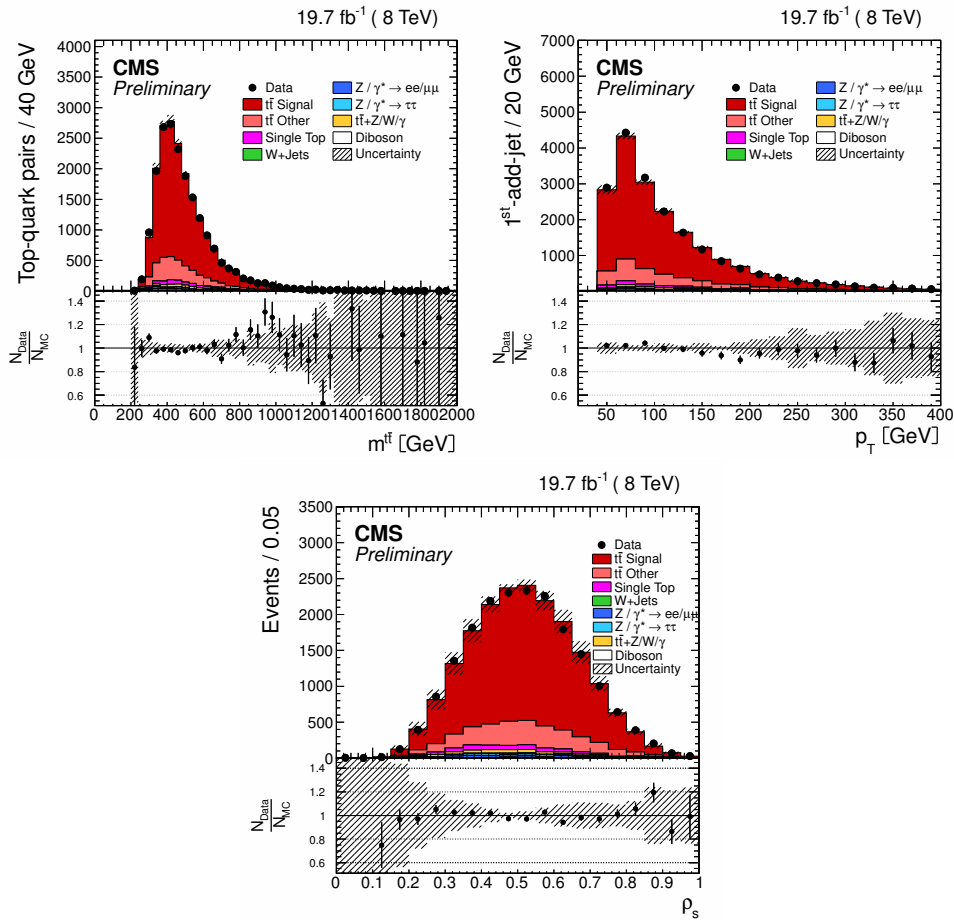
Figure 1: Invariant mass of the $t\bar{t}$ system (top left), transverse momentum of the leading additional jet (top right) and ρ_s (bottom) at reconstruction level for the combined dilepton channel. The $t\bar{t}$ sample is simulated using MADGRAPH and is assuming a top mass of $m_t = 172.5\,\text{GeV}$. The label "$t\bar{t}$ signal" refers to the events decaying dileptonically, while "$t\bar{t}$ other" refers to the other decay modes including $t\bar{t}$ decays into prompt τ-leptons. The hatched regions correspond to all shape uncertainties of the simulation (cf. Section 5).

following are assumed to be uncorrelated.

Experimental Uncertainties

The experimental sources considered are jet energy scale (JES) and jet energy resolution (JER), background normalisation, b-tag efficiency, pileup modeling and the kinematic reconstruction. The experimental uncertainty on the JES [30] is determined by varying the reconstructed energy scale as a function of the transverse momentum and the pseudorapidity of the jet, typically by a few percent. The uncertainty on the JER [31] is estimated by varying the simulated JER within its uncertainty for different pseudorapidity regions.

The impact of the background normalisation is obtained by scaling the background contributions by $\pm 30\%$ [29, 32].

The shape uncertainty on the b-tag efficiency is determined by dividing the b jet distributions for transverse momentum and pseudorapidity into two bins at their respective median value. The b-tag scale factors for the b jets in the first bin are scaled up by half of the assigned uncertainties [24], while those in the second bin are scaled down and vice versa. The difference between the scale factors in the two bins amounts to the full uncertainty.

The effect of pileup events is evaluated by weighting the simulation to the minimum bias cross section determined from data. The pileup model estimates the mean number of additional pp interactions to be about 20 events for the data analysed, based on the total inelastic proton-proton cross section which is determined to be 69.4 mb [33]. The systematic uncertainty is evaluated by varying this cross section within its uncertainty of $\pm 5\%$.

Other uncertainties taken into account stem from lepton trigger and identification efficiencies and the kinematic reconstruction efficiency, which have a negligible impact on the normalised measurements presented. The dependence of the result on the MC top quark mass used as reference for the measurement is found to be negligible.

Modelling Uncertainties

Modelling uncertainties originating from theoretical assumptions on the renormalisation and factorization scales, the jet-parton matching threshold, the hadronization model, the colour reconnection [34] and the underlying event (UE) modelling are determined by repeating the analysis, replacing the reference MADGRAPH signal simulation by dedicated simulation samples.

In particular, the impact of the first source is assessed with MADGRAPH samples with the renormalisation and factorisation scales simultaneously varied from the nominal values of μ_R and μ_F, which are defined by the Q^2 scale in the event as $\mu_R^2 = \mu_F^2 = Q^2 = m_t^2 + \sum p_T^2(\text{jet})$, where the sum runs over all the additional jets in the event not stemming from the $t\bar{t}$ decay. The samples with varied scales use $\mu_R = \mu_F = 4Q^2$ and $Q^2/4$, respectively. For the nominal MADGRAPH sample, a jet-parton matching threshold of 20 GeV is chosen, while for the varied samples, values of 40 and 10 GeV are employed, respectively.

The UE modeling is evaluated by comparing the two different Perugia 11 (P11) PYTHIA tunes `mpHi` and `TeV` to the standard P11 tune.

The uncertainties from ambiguities in modeling colour reconnection effects are estimated by comparing simulations of an underlying event tune including colour reconnection to a tune without the effect (the P11 and P11 `noCR` tunes described in [35]).

The hadronisation model uncertainty is estimated by comparing samples simulated with POWHEG

and MC@NLO, using PYTHIA and HERWIG, respectively, for hadronisation.

The uncertainty arising from the PDFs is assessed by reweighting the $t\bar{t}$ signal sample according to the CT10 error PDF sets at 68% confidence level. The effects of these variations are added in quadrature.

5   Extraction of m_t from ρ_s using a Template Technique

The top quark mass value is determined by comparison of the experimentally observed yields in individual bins of the normalized ρ_s distribution as presented in Fig. 1 with the predicted yields for different values of m_t. Each of the $t\bar{t}$ samples employed for the comparison are normalized such that the total number of expected events including backgrounds corresponds to the events selected in data.

The most probable value of top quark mass is extracted by means of a χ_i^2 distribution for each bin i. For each of them, the predicted yields for the different top quark masses are fitted using a second order polynomial function, $f(m_t)$, in order to obtain a continuous distribution as a function of m_t. The χ_i^2 distributions are then calculated as

$$\chi_i^2(m_t) = \frac{(N_i^{\text{data}} - f_i^{\text{sim}}(m_t))^2}{(\delta N_i^{\text{data}})^2 + (\delta f_i^{\text{sim}}(m_t))^2} \, , \tag{1}$$

where $f_i^{sim}(m_t)$ represents the polynomial fit to the simulation distributions, δf_i^{sim} corresponds to the statistical errors on the simulation obtained from the confidence interval of the fit, and N_i^{data} is the number of selected events in each bin with δN_i^{data} being the corresponding statistical uncertainty. The χ_i^2 does not include the systematic uncertainties, which are treated as external variations as described below. The binning chosen corresponds to the one in Fig. 1 except for the regions $\rho_s < 0.2$ and $\rho_s > 0.85$ which are integrated into two bins in order to increase statistics.

The global χ^2 is calculated by summing all bins to $\chi^2 = \sum_i \chi_i^2(m_t)$ since the individual bins are statistically uncorrelated. The number of degrees of freedom is reduced by one owing to the normalisation of the utilized distributions. In order to accommodate for this in the global χ^2, the bin with the lowest statistical significance is removed from the calculation, i.e., the first bin of the ρ_s distribution. The resulting χ^2 distribution is presented in Fig. 2. The minimum of the distribution is taken as the measured top quark mass value, the statistical uncertainty is calculated as the $\pm 1\sigma$ deviation from the minimum by applying a $\chi^2 + 1$ variation.

The systematic uncertainties described in Section 4 are propagated to the mass measurement by repeating the extraction with each varied input distributions, either by replacing the reference simulation with the dedicated samples, or by varying the corresponding efficiency, resolution, or scale within the respective uncertainties. For each source of uncertainty, the altered simulation is used as input for the χ^2 distribution from which the top quark mass is obtained. The difference between the mass extracted for each source and the nominal measurement is taken as the systematic uncertainty. In the case of the model uncertainties, the reference MADGRAPH $t\bar{t}$ sample with nominal top quark mass is replaced by the corresponding systematic samples, for instance P11 or varied jet-parton matching sample. The same model uncertainty is then assigned to all varied mass MADGRAPH samples.

The breakdown of the systematic uncertainties for the top quark mass is presented in Table 1. All systematic uncertainties quoted are statistically significant, the statistical uncertainties are

19.7 fb^{-1} (8 TeV)
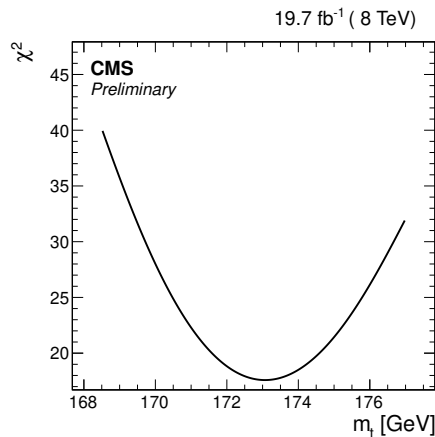
Figure 2: Global χ^2 distribution obtained as the sum of the χ_i^2 distributions of the individual bins for the dilepton combined channel. The most probable top quark mass is extracted from the minimum, the statistical uncertainty from a $\chi^2 + 1$ variation around the minimum.

found to be below 0.1 GeV. The size of the uncertainties is in agreement with the expected values from the blinded analysis, performed using simulated samples as pseudo-data.

The total uncertainty amounts to 2.2 GeV and is calculated as the quadratic sum of all individual contributions. It is dominated by the renormalisation and factorization scales and jet-parton matching uncertainties, while the most relevant experimental contribution arises from uncertainties in the b-tagging. The top quark mass results to $m_{\mathrm{t}} = 173.1 \pm 1.0\,(\mathrm{stat})\,^{+2.0}_{-2.3}\,(\mathrm{syst})$ GeV, including both the statistical uncertainty of data and the MADGRAPH samples used to extract the mass.

In order to calibrate the mass extraction technique, the measurement has been repeated with pseudo data generated from the simulated samples with different top quark masses. The measured top quark masses are compared to the true mass used to generate the input samples as shown in Fig. 3. The measured top quark mass agrees with the input mass within the statistical uncertainty, which indicates that the method does not favour certain values of the mass or introduces a bias toward higher or lower mass values. Propagating the uncertainty of a linear regression to the measured top quark mass would yield an effect of below 0.1 GeV for a mass shift of 1 GeV and can thus be neglected.

6 Differential Cross Section Measurement

The normalized differential $t\bar{t}$ production cross section as a function of ρ_s is measured from the event yields determined in Section 3. In order to avoid additional uncertainties due to the extrapolation of the measurement outside of the phase space region probed experimentally, the differential cross section is determined in a visible phase space defined at particle level by the kinematic and geometrical acceptance of the final-state leptons and jets. The charged leptons from the $t\bar{t}$ decay are selected with $|\eta| < 2.4$ and $p_{\mathrm{T}} > 20$ GeV. A jet is defined at particle level by applying the anti-k_t clustering algorithm to all stable particles except leptons and neutrinos stemming from the W boson decays. A jet is defined as b jet if it has at least one b hadron

Table 1: Breakdown of the systematic uncertainties for the top quark mass extracted from the normalized event yield for the dilepton combined channels. All systematic uncertainties are found to be statistically significant. For the asymmetric uncertainties due to scale variations, the first reported value corresponds to an increase of the corresponding scale and the second one to a decrease.

Source	Δm_t [GeV]
Jet-Parton Matching	$^{-1.3}_{+0.1}$
Q^2 Scale	± 2.0
ME/Showering	$^{+0.2}_{-0.3}$
Color Reconnection	< 0.1
Underlying Event	± 0.1
PDF	± 0.1
Background	± 0.4
Jet Energy Scale	± 0.1
Jet Energy Resolution	± 0.1
Pile-Up	± 0.1
Trigger Eff.	< 0.1
Kinematic Reconstruction	< 0.1
Lepton Eff.	< 0.1
B-Tagging	± 0.2
Total syst.	$^{+2.0}_{-2.3}$
Stat.	± 1.0
Total unc.	$^{+2.2}_{-2.5}$

19.7 fb⁻¹ (8 TeV)
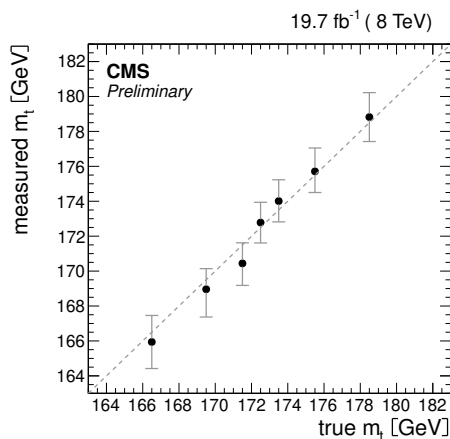
Figure 3: Top quark mass obtained from pseudo data generated from each of the MADGRAPH samples with varied mass values. Neither a favoured mass value nor a bias towards higher or lower masses can be observed.

associated to it, which can be assigned to the corresponding original b quark. The two b jets from the $t\bar{t}$ decay have to fulfill the kinematic requirements $|\eta| < 2.4$ and $p_T > 30$ GeV, while the additional jet is required to have $|\eta| < 2.4$ and $p_T > 50$ GeV.

The differential cross section in each bin is defined as

$$\frac{1}{\sigma}\frac{d\sigma^i}{d\rho_s} = \frac{1}{\sigma}\frac{\sum_j A_{ij}^{-1}(N_{\text{data}}^j - N_{\text{non}-t\bar{t}\text{bkg}}^j) \cdot f^{\text{signal}}}{\Delta_x^i \mathcal{L}},$$ (2)

where j indicates the bin index of the reconstructed variable x, while i denotes the index of the corresponding generator-level bin. N_{data}^j and $N_{\text{non}-t\bar{t}\text{bkg}}^j$ represent the number of data events and estimated background events from processes different than $t\bar{t}$ in bin j, respectively, while $\mathcal{L}$ is the integrated luminosity and Δ_x^i denotes the bin width. The contribution from non-signal $t\bar{t}$ decays is taken into account by correcting $N_{\text{data}} - N_{\text{non}-t\bar{t}\text{bkg}}$ with the signal fraction, f^{signal}, defined as the ratio of selected $t\bar{t}$ signal events to the total number of selected $t\bar{t}$ events. This avoids the dependence on the inclusive $t\bar{t}$ cross section used for normalisation. The distribution is normalized by the sum of the differential cross section per bin σ^i over all bins, $\sigma = \sum \sigma^i$.

Effects from detector efficiency and resolution in each bin i of the measurement are corrected are corrected using a regularized unfolding method [27, 36, 37]. The generalized inverse of the response matrix, denoted as A_{ij}^{-1}, is used to obtain the unfolded values from the measured distribution. In order to avoid nonphysical fluctuations, a smoothing prescription (regularization) is applied. The regularization level is determined using the averaged global correlation method [38].

The binning was chosen such that the purity and stability are above 40% and the sensitivity of the distribution on the top quark mass is enhanced. The purity p^i denotes the number of events generated and correctly reconstructed in a given bin i relative to the number of events that are reconstructed in bin i but generated anywhere. The stability s^i represents the number of events which are generated and correctly reconstructed in a given bin i relative to the number of events

that are generated in bin *i* but reconstructed anywhere. In particular for this observable, p^i is between 40% and 60% for all bins, while s^i ranges between 60% to 80%.

All systematic sources described in Section 4 are propagated to the measured differential cross section by replacing the nominal simulation samples used for the unfolding matrix, determination of the background etc. by the samples with the systematic effect applied. For each systematic variation the differential cross section is evaluated. In each bin, the systematic variations are added in quadrature. Due to the normalisation, systematic uncertainties which are correlated across all bins of the measurement, such as the uncertainty on the integrated luminosity as well as all other normalisation uncertainties, cancel out. The final result is obtained as the weighted average of the normalized differential cross sections measured in each of the individual dileptonic channels.

The simulation used to extract the cross sections is the reference sample with a top quark mass of 172.5 GeV. Figure 4 shows the unfolded distribution together with the predicted values for different top quark masses (± 1, 3 and 6 GeV from the nominal value). The total systematic uncertainty is displayed as yellow band, while the statistical uncertainty is represented as grey band. The distribution shows a discriminating power between the different top quark masses, except for the region $\rho_s = 0.5$ where the curves intersect due to the normalisation. The distribution is most sensitive to mass variations in the regions around $\rho_s = 0.4$ and $\rho_s \geq 0.6$ as expected according to the reference [3].
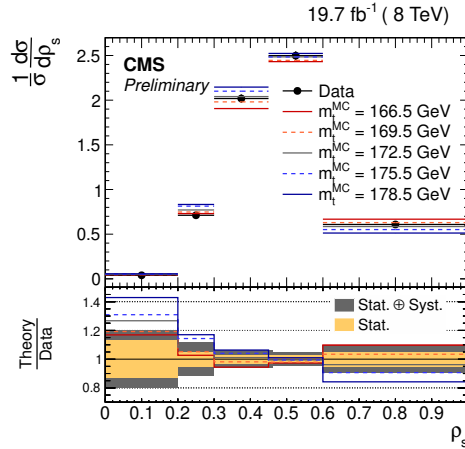
Figure 4: Normalized differential $t\bar{t}$ cross section in the visible phase space after unfolding as a function of the observable ρ_s in the dilepton channels, compared to the predictions from POWHEG $t\bar{t}$+jet simulated with a top quark mass of 172.5 GeV as well as ± 3 and 6 GeV variations with respect to the central value. The grey band represents the statistical uncertainty, the yellow band corresponds to the total systematic uncertainty.

7   Extraction of m_t from the Differential Cross Section

The unfolded differential cross section obtained in Section 6 is used to measure the top quark mass by comparing it to theoretical predictions of the ρ_s distribution. Following the approach described in Section 5, the measured differential cross section is compared to the predicted

cross sections for each bin of the ρ_s distribution using different top quark masses as shown in Fig. 5, and the most probable top quark mass is extracted from a global χ^2 estimator.
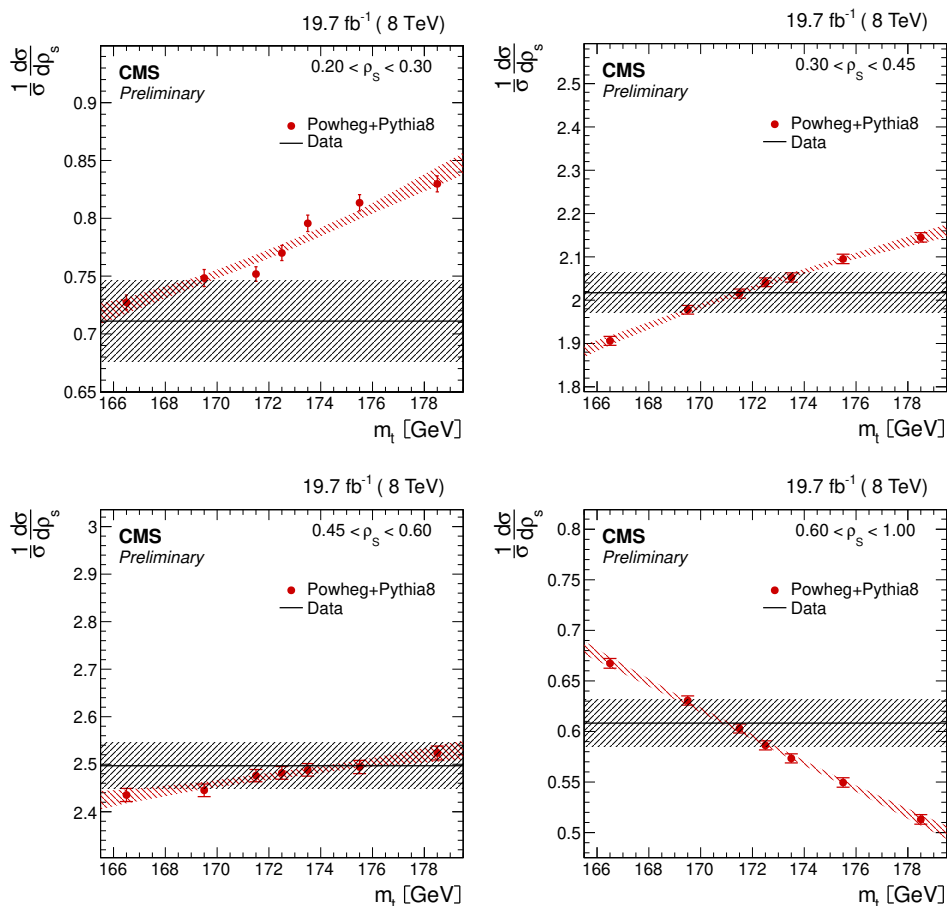
Figure 5: Distributions of the differential cross section for simulation and data for all mass samples in the different bins of the ρ_s distribution, shown for the three dilepton final states combined. The error bands correspond to the statistical error on data and the confidence interval of the second order polynomial for the simulation.

However, owing to the unfolding procedure the individual bins of the ρ_s cross section distribution are correlated and these bin-to-bin correlations need to be taken into account in the global χ^2 distribution via the covariance matrices obtained from the unfolding procedure. Since the individual bins of the simulation samples are uncorrelated, the corresponding statistical uncertainties only contribute to the diagonal elements of the covariance matrix. The global χ^2 estimator is thus obtained as

$$\chi^2(m_t) = V^T(m_t) \times \boldsymbol{COV}(m_t)^{-1} \times V(m_t), \tag{3}$$

where COV^{-1} denotes the inverted and normalized unfolding covariance matrix including the statistical uncertainties from simulation. The vector $V_i(m_t) = f_i^{\text{data}}(m_t) - f_i^{\text{sim}}(m_t)$ represents the difference between the measured cross section and the cross section function obtained by a second order polynomial fit to the simulations with different top quark masses.

The first bin ($0 < \rho_s < 0.2$) is excluded from the global χ^2 in order to satisfy the reduced number of degrees of freedom from the normalisation of the differential cross section. The resulting global χ^2 distribution is presented in Fig. 6. The minimum of the global χ^2 corresponds to the most probable top quark mass with the statistical uncertainty taken as the $\pm 1\,\sigma$ deviation from the minimum by applying a $\chi^2 + 1$ variation.
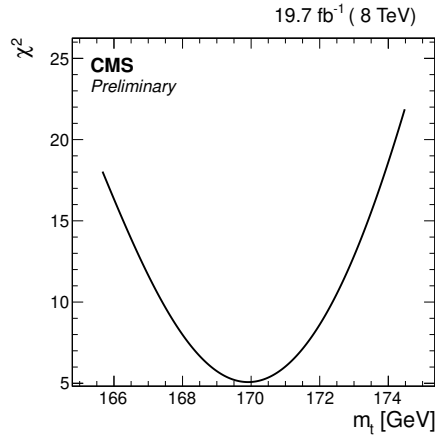
Figure 6: Global χ^2 distribution for the normalized differential cross section as a function of ρ_s in the dilepton combined channel.

Possible biases of the mass extraction have been studied by repeating the measurement using each of the available MADGRAPH samples with different top quark masses as pseudo data, and by confronting the measurement with the MC truth, following the approach presented in Section 5. The values of the top quark mass obtained from the global χ^2 distribution are compared to the mass of the sample used as input as shown Fig. 7. A good agreement within the statistical uncertainty can be observed, indicating that the method is unbiased. Considering a variation of the top quark mass of 1 GeV, the effect would correspond to a ± 0.05 GeV deviation in the final result, which is well below the statistical uncertainty of the measurement. The dependence of the result on the MC top quark mass used to evaluate the background contribution and to unfold the distribution is found to be negligible.

The systematic uncertainties are propagated to the mass measurement as follows. For each uncertainty source the normalized differential cross section is evaluated replacing the simulated samples by the corresponding variations as well as changing the correlation matrix for unfolding accordingly. For each of the obtained cross sections, the χ^2 distribution is calculated and the top quark mass is extracted. The difference between the mass obtained for each source of uncertainty and the nominal mass value is taken as systematic uncertainty. This difference is found to be statistically significant for each source of systematic uncertainty considered.

Additionally, the uncertainty in modelling of the hard-production process is assessed through a simultaneous variation of the renormalisation and factorisation scales in the POWHEG $t\bar{t}$+jet
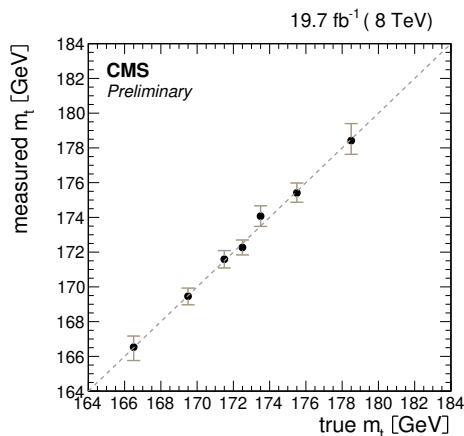
Figure 7: Top quark mass obtained by using each of the MADGRAPH samples with varied mass values as pseudo data, for the dilepton combined channel.

simulation ("POWHEG t$\bar{\text{t}}$+jet modelling") with respect to their common nominal value, which is set to m_t. For each top quark mass value considered in the mass measurement, two dedicated samples have been produced with $\mu_R = \mu_F$ varied coherently by factors of 2 and 0.5. The systematic uncertainty is then evaluated by repeating the mass measurement using the dedicated samples as theoretical prediction.

The breakdown of systematic uncertainties for the top quark mass is shown in Table 2. The first row represents the POWHEG t$\bar{\text{t}}$+jet modelling uncertainty while the other uncertainties are related to the measurement of the cross section. The total systematic uncertainty is dominated by model uncertainty sources, in particular, jet-parton matching and Q^2 and theoretical uncertainties in the POWHEG t$\bar{\text{t}}$+jet simulation. The most relevant experimental uncertainties arise from the background and JES sources.

The top quark mass obtained is 169.9 ± 1.1 (stat) $^{+2.5}_{-3.1}$ (syst) $^{+3.6}_{-1.6}$ (theo) GeV, where the systematic uncertainty is calculated as the quadratic sum of all sources. The systematic uncertainty corresponds to $^{+1.5}_{-1.8}$ %, while the theoretical uncertainty on the modelling assumptions arising from the POWHEG t$\bar{\text{t}}$+jet simulations yields an additional $^{+2.1}_{-0.9}$ %.

8 Summary

The top quark mass is measured from the inverse of the invariant mass of the t$\bar{\text{t}}$+jet system, an observable proposed in [3]. The mass extraction has been performed with a global template fit using the shape of the distribution at reconstruction level as well as using the normalised differential cross section in the visible phase space. The first approach avoids statistical correlations and uncertainties arising from the unfolding procedure, however it cannot be compared to predictions given at generator level, while the second eases the comparisons with theory models.

The top quark mass obtained from the normalized differential t$\bar{\text{t}}$+jet cross section using an NLO calculation interfaced with parton shower yields 169.9 ± 1.1 (stat) $^{+2.5}_{-3.1}$ (syst) $^{+3.6}_{-1.6}$ (theo) GeV. The

Table 2: Breakdown of the systematic uncertainties for the top quark mass measured from the dileptonic channel. All systematic uncertainties are found to be statistically significant. For the asymmetric uncertainties due to scale variations, the first reported value corresponds to an increase of the corresponding scale and the second one to a decrease.

Source	Δm_{t} [GeV]
POWHEG $t\bar{t}$+jet modelling	$^{-1.6}_{+3.6}$
Jet-Parton Matching	$^{-0.1}_{+1.6}$
Q^2 Scale	$^{+1.0}_{-2.8}$
ME/Showering	± 0.4
Color Reconnection	± 0.7
Underlying Event	± 0.3
PDF	$^{+0.9}_{-0.1}$
Background	± 1.0
Jet Energy Scale	± 0.1
Jet Energy Resolution	± 0.1
Pile-Up	± 0.3
Trigger Eff.	< 0.1
Kinematic Reconstruction	< 0.1
Lepton Eff.	± 0.1
B-Tagging	± 0.3
Syst. uncertainty	$^{+2.5}_{-3.1}$
Stat. untertainty	± 1.1

precision is mostly limited by the systematic uncertainties arising from modelling sources and the theory uncertainties in the POWHEG $t\bar{t}$+jet simulation. The result is in agreement within the uncertainties with other measurements performed following the same approach [4] as well as complementary measurements of the mass from the inclusive $t\bar{t}$ production cross section [39–41].

References

[1] ATLAS, CDF, CMS, and D0 Collaborations, "First combination of Tevatron and LHC measurements of the top-quark mass", (2014). `arXiv:1403.4427`.

[2] CMS Collaboration, "Measurement of the top quark mass using proton-proton data at $\sqrt{s}$ = 7 and 8 TeV", `arXiv:1509.04044`.

[3] S. Alioli et al., "A new observable to measure the top-quark mass at hadron colliders", *Eur.Phys.J.* **C73** (2013) 2438, `doi:10.1140/epjc/s10052-013-2438-2`, `arXiv:1303.6415`.

[4] ATLAS Collaboration, "Determination of the top-quark pole mass using $t\bar{t}$ + 1-jet events collected with the ATLAS experiment in 7 TeV pp collisions", *JHEP* **10** (2015) 121, `doi:10.1007/JHEP10(2015)121`, `arXiv:1507.01769`.

[5] CMS Collaboration, "The CMS experiment at the CERN LHC", *JINST* **03** (2008) S08004, `doi:10.1088/1748-0221/3/08/S08004`.

[6] CMS Collaboration, "Measurement of Top Quark Pair Differential Cross Sections at sqrt(s) = 8 TeV", *CMS Physics Analysis Summary* **TOP-12-028** (2013).

[7] CMS Collaboration, "Measurement of the Jet Multiplicity in dileptonic Top Quark Pair Events at 8 TeV", Technical Report CMS-PAS-TOP-12-041, CERN, Geneva, 2013.

[8] P. Artoisenet et al., "Automatic spin-entangled decays of heavy resonances in Monte Carlo simulations", *JHEP* **03** (2013) 015, `doi:10.1007/JHEP03(2013)015`, `arXiv:1212.3460`.

[9] J. Pumplin et al., "New generation of parton distributions with uncertainties from global QCD analysis", *JHEP* **07** (2002) 012, `doi:10.1088/1126-6708/2002/07/012`, `arXiv:hep-ph/0201195`.

[10] T. Sjöstrand, S. Mrenna, and P. Skands, "PYTHIA 6.4 physics and manual", *JHEP* **05** (2006) 026, `doi:10.1088/1126-6708/2006/05/026`, `arXiv:hep-ph/0603175`.

[11] M. L. Mangano, M. Moretti, F. Piccinini, and M. Treccani, "Matching matrix elements and shower evolution for top-quark production in hadronic collisions", *JHEP* **0701** (2007) 013, `doi:10.1088/1126-6708/2007/01/013`, `arXiv:hep-ph/0611129`.

[12] CMS Collaboration, "Measurement of the underlying event activity at the LHC with $\sqrt{s}$ =7 TeV and comparison with $\sqrt{s}$ =0.9 TeV", *JHEP* **09** (2011) 109, `doi:10.1007/JHEP09(2011)109`, `arXiv:1107.0330`.

[13] S. Agostinelli et al., "GEANT4– a simulation toolkit", *Nucl. Instrum. Meth. A* **506** (2003) 250, `doi:10.1016/S0168-9002(03)01368-8`.

[14] N. Kidonakis, "Two-loop soft anomalous dimensions for single top quark associated production with W- or H-", *Phys. Rev.* **D82** (2010) 054018, `doi:10.1103/PhysRevD.82.054018`, `arXiv:hep-ph/1005.4451`.

[15] J. M. Campbell, R. K. Ellis, and C. Williams, "Vector boson pair production at the LHC", *JHEP* **1107** (2011) 018, `doi:10.1007/JHEP07(2011)018`, `arXiv:1105.0020`.

[16] J. Campbell and R. Ellis, "$t\bar{t}W^{+-}$ production and decay at NLO", *JHEP* **07** (2012) 052, `doi:10.007/JHEP07(2012)052`, `arXiv:1204.5678`.

[17] W. Kilian, T. Ohl, and J. Reuter, "WHIZARD: Simulating multi-particle processes at LHC and ILC", *Eur. Phys. J. C* **71** (2011) 1742, `doi:10.1140/epjc/s10052-011-1742-y`, `arXiv:hep-ph/9905386`.

[18] K. Melnikov, M. Schulze, and A. Scharf, "QCD corrections to top quark pair production in association with a photon at hadron colliders", *Phys. Rev. D* **83** (2011) 074013, `doi:10.1103/epjc/PhysRevD.83.074013`, `arXiv:hep-ph/1102.1967`.

[19] R. Corke and T. Sjostrand, "Interleaved Parton Showers and Tuning Prospects", *JHEP* **03** (2011) 032, `doi:10.1007/JHEP03(2011)032`, `arXiv:1011.1759`.

[20] CMS Collaboration, "Commissioning of the Particle-Flow Reconstruction in Minimum-Bias and Jet Events from pp Collisions at 7 TeV", *CMS Physics Analysis Summary* **PFT-10-002** (2010).

[21] M. Cacciari, G. P. Salam, and G. Soyez, "The Catchment Area of Jets", *JHEP* **04** (2008) 005, `doi:10.1088/1126-6708/2008/04/005`, `arXiv:0802.1188`.

[22] CMS Collaboration, "Determination of the jet energy scale in CMS with pp Collisions at $\sqrt{s} = 7$ TeV", *CMS Physics Analysis Summary* **JME-10-010** (2010).

[23] M. Cacciari, G. P. Salam, and G. Soyez, "The anti-k_t jet clustering algorithm", *JHEP* **04** (2008) 063, `doi:10.1088/1126-6708/2008/04/063`, `arXiv:hep-ph/0802.1189`.

[24] CMS Collaboration, "Identification of b-quark jets with the CMS experiment", *JINST* **08** (2013) P04013, `doi:10.1088/1748-0221/8/04/P04013`, `arXiv:hep-ex/1211.4462`.

[25] CMS Collaboration, "Missing transverse energy performance of the CMS detector", *JINST* **06** (2011) P09001, `doi:10.1088/1748-0221/6/09/P09001`, `arXiv:1106.5048`.

[26] D0 Collaboration, "Measurement of the top quark mass using dilepton events", *Phys. Rev. Lett.* **80** (1998) 2063, `doi:10.1103/PhysRevLett.80.2063`, `arXiv:hep-ex/9706014`.

[27] CMS Collaboration, "Measurement of differential top-quark pair production cross sections in pp collisions at $\sqrt{s} = 7$ TeV", *Eur. Phys. J. C* **73** (2013) 2339, `doi:10.1140/epjc/s10052-013-2339-4`, `arXiv:hep-ph/1211.2220`.

[28] CMS Collaboration, "Measurement of jet multiplicity distributions in $t\bar{t}$ production in pp collisions at $\sqrt{s} = 7$ TeV", *Eur. Phys. J. C* **74** (Apr, 2014) 3014, `doi:10.1140/epjc/s10052-014-3014-0`, `arXiv:1404.3171`.

[29] CMS Collaboration, "Measurement of the $t\bar{t}$ production cross section and the top quark mass in the dilepton channel in pp collisions at $\sqrt{s} = 7$ TeV", *JHEP* **07** (2011) 049, `doi:10.1007/JHEP07(2011)049`, `arXiv:hep-ex/1105.5661`.

[30] CMS Collaboration, "Determination of jet energy calibration and transverse momentum resolution in CMS", *JINST* **06** (2011) P11002, `doi:10.1088/1748-0221/6/11/P11002`, `arXiv:1107.4277`.

[31] CMS Collaboration, "Jet energy resolution in CMS at $\sqrt{s} = 7$ TeV", *CMS Physics Analysis Summary* **JME-10-014** (2010).

[32] CMS Collaboration, "Measurement of the $t\bar{t}$ production cross section in the dilepton channel in pp collisions at $\sqrt{s} = 7$ TeV", *JHEP* **1211** (2012) 067, `doi:10.1007/JHEP11(2012)067`, `arXiv:1208.2671`.

[33] TOTEM Collaboration, "First measurement of the total proton-proton cross section at the LHC energy of $\sqrt{s}$ =7 TeV", *Europhys. Lett.* **96** (2011) 21002, `doi:10.1209/0295-5075/96/21002`, `arXiv:hep-ex/1110.1395`.

[34] P. Z. Skands and D. Wicke, "Non-perturbative QCD effects and the top mass at the Tevatron", *Eur. Phys. J. C* **52** (2007) 133, `doi:10.1140/epjc/s10052-007-0352-1`, `arXiv:hep-ph/0703081`.

[35] P. Z. Skands, "Tuning Monte Carlo generators: The Perugia tunes", *Phys. Rev. D* **82** (2010) 074018, `doi:10.1103/PhysRevD.82.074018`, `arXiv:1005.3457`.

[36] A. Hoecker and V. Kartvelishvili, "SVD approach to data unfolding", *Nucl. Instrum. Meth. A* **372** (1996) 469, `doi:10.1016/0168-9002(95)01478-0`, `arXiv:hep-ph/9509307`.

[37] V. Blobel, "An unfolding method for high energy physics experiments", (2002). `arXiv:hep-ex/0208022`.

[38] F. James, "Statistical methods in experimental physics". World Scientific, 2nd edition, 2006.

[39] CMS Collaboration Collaboration, "Measurement of the ttbar production cross section in the emu channel in pp collisions at 7 and 8 TeV", Technical Report CMS-PAS-TOP-13-004, CERN, Geneva, 2015.

[40] R. Astalos et al., "Proceedings of the sixth international workshop on multiple partonic interactions at the Large Hadron Collider", (2015). `arXiv:1506.05829`.

[41] CMS Collaboration, "Determination of the top-quark pole mass and strong coupling constant from the tbart production cross section in pp collisions at $\sqrt{s} = 7$ TeV", *Phys. Lett. B* **728** (2014) 496–517, `doi:10.1016/j.physletb.2014.08.040,10.1016/j.physletb.2013.12.009`, `arXiv:1307.1907`. [Erratum: Phys. Lett.B728,526(2014)].

CMS Physics Analysis Summary

Search for $t\bar{t}H$ production in the $H \rightarrow b\bar{b}$ decay channel with $\sqrt{s} = 13$ TeV pp collisions at the CMS experiment

The CMS Collaboration

Abstract

First results of the search for the associated production of a Higgs boson with a top quark-antiquark pair ($t\bar{t}H$) in proton-proton collisions at a center-of-mass energy of $\sqrt{s} = 13$ TeV are presented. The data correspond to an integrated luminosity of 2.7 fb^{-1} recorded with the CMS experiment in 2015. Candidate $t\bar{t}H$ events are selected with criteria enhancing the lepton+jets or dileptonic decay channels of the $t\bar{t}$ system and the decay of the Higgs boson into a bottom quark-antiquark pair ($H \rightarrow b\bar{b}$). In order to increase the sensitivity of the search, selected events are split into several categories with different expected signal and background rates. In each category signal and background events are separated using a multivariate approach that combines a physics-motivated method (matrix element method, MEM) with methods from machine learning (boosted decision trees, BDTs). The result is presented in terms of the $t\bar{t}H$ signal strength modifier μ, the ratio of the observed $t\bar{t}H$ production cross section relative to the value expected for a 125 GeV standard model Higgs boson. A combined fit of multivariate discriminant templates in all categories to data results in an observed (expected) upper limit of $\mu < 2.6$ (3.6) at the 95% confidence level.

1 Introduction

The observation of a Higgs boson with a mass of approximately 125 GeV [1, 2] at the Large Hadron Collider (LHC) marked the starting point of a broad experimental program to determine the properties of the newly discovered particle. To date, the results of all measurements performed at the LHC are consistent with the expectations for a standard model (SM) Higgs boson. Decays into $\gamma\gamma$, ZZ and WW final states have been observed and there is evidence for the direct decay of the particle to fermions from the $\tau\tau$ and $b\bar{b}$ decay channels [3, 4]. The measured rates of various production and decay channels agree with the SM expectations [5, 6] and the hypothesis of a spin-0 particle is favored over other hypotheses [7, 8].

In the SM the coupling of the Higgs boson to fermions is of Yukawa type, with a coupling strength proportional to the fermion mass. Probing the coupling of the Higgs boson to the heaviest known fermion, the top quark, is hence very important for testing the SM and for constraining models of physics beyond the SM (BSM). Indirect constraints on the top–Higgs coupling are available from processes including top-quark loops, for example Higgs boson production through gluon-gluon fusion [5, 6]. On the other hand, the associated production of a Higgs boson and a top quark-antiquark pair ($t\bar{t}H$ production) is a direct probe of the top–Higgs coupling, as illustrated by the Feynman diagrams in Fig. 1. If observed it would prove the coupling of the Higgs boson to fermions with weak isospin $+1/2$ ("up-type") in addition to couplings to τ and b, which carry a weak isospin of $-1/2$ ("down-type"). The Higgs boson decay into bottom quark-antiquark pairs ($b\bar{b}$), also shown in Fig. 1, is attractive as a final state because it features the largest branching fraction of 0.58 ± 0.02 for a 125 GeV Higgs boson [9]. In addition, both $t\bar{t}H$ production and the decay $H \rightarrow b\bar{b}$ only involve third-generation quarks, which facilitates the theoretical interpretation of the results.

Figure 1: Exemplary leading-order Feynman diagrams for $t\bar{t}H$ production, including the subsequent decays of the top quark-antiquark pair in the lepton+jets channel (left) and the dilepton channel (right) as well as the decay of the Higgs boson into a bottom quark-antiquark pair.

Several BSM physics models predict a significantly enhanced $t\bar{t}H$ production rate while not modifying the branching fractions of Higgs boson decays by a measurable amount. For example, a number of BSM physics models predict vector-like partners of the top-quark (T) that decay into tH, bW and tZ final states [10–19]. The production and decay of $T\bar{T}$ pairs would lead to final states indistinguishable from those of $t\bar{t}H$ production. In this context, measurement of the $t\bar{t}H$ production cross section has the potential to distinguish the SM Higgs mechanism from alterative mechanisms to generate fermion masses.

Various dedicated searches for $t\bar{t}H$ production have been conducted during Run I of the LHC.

The CMS searches employ pp collision data corresponding to an integrated luminosity of $5\,\mathrm{fb}^{-1}$ at a center-of-mass energy of $\sqrt{s} = 7\,\mathrm{TeV}$ and $19.5\,\mathrm{fb}^{-1}$ at $\sqrt{s} = 8\,\mathrm{TeV}$. These searches have been performed studying Higgs boson decays to hadrons, photons, and leptons using multivariate analysis (MVA) techniques, showing a mild excess of the observed $t\bar{t}H$ signal strength relative to the SM expectation of $\mu = \sigma/\sigma_{\mathrm{SM}} = 2.8 \pm 1.0$ [20]. A similar excess of $\mu = 2.1^{+1.4}_{-1.2}$ is observed in a search for $t\bar{t}H$ production in multilepton final states with $20.3\,\mathrm{fb}^{-1}$ of ATLAS data at $\sqrt{s} = 8\,\mathrm{TeV}$ [21].

The CMS search results have also entered a comprehensive test of the compatibility of the Higgs boson couplings with SM preditions [6]. The sensitivity for the $t\bar{t}H$ process in the $H \to b\bar{b}$ decay channel was further increased by employing the matrix element method (MEM) [22], resulting in an observed (expected) upper limit of $\mu = 4.3\,(3.3)$ at 95% confidence level. The current best observed (expected) upper limit on $t\bar{t}H$ production in the $H \to b\bar{b}$ decay channel amounts to $\mu = 3.4\,(2.2)$. It was obtained by the ATLAS collaboration using $20.3\,\mathrm{fb}^{-1}$ of pp collision data at $\sqrt{s} = 8\,\mathrm{TeV}$ [23].

The observation of $t\bar{t}H$ production is one of the major goals in Higgs boson physics for Run II. The increased center-of-mass energy of $\sqrt{s} = 13\,\mathrm{TeV}$ results in a $t\bar{t}H$ production cross section 3.9 times larger than at $\sqrt{s} = 8\,\mathrm{TeV}$, while the cross section for the most important background, $t\bar{t}$ production, is only increased by a factor of 3.3 [24], resulting in a more favorable signal-to-background ratio. In addition, a larger fraction of events contains top quarks or Higgs bosons with transverse momenta above $200\,\mathrm{GeV}$, making "boosted" jet reconstruction techniques increasingly attractive for $t\bar{t}H$ studies [25].

This document summarizes a search for $t\bar{t}H$ production performed with $2.7\,\mathrm{fb}^{-1}$ of data recorded with the CMS detector during the first data-taking period of LHC Run II in 2015. Analysis methods established in Run I have been significantly improved, and novel methods have been added. In particular, the strengths of two multivariate techniques, one physics-motivated (matrix element method, MEM), and one from machine learning (boosted decision trees, BDT), have been combined to obtain a more powerful discriminant.

The event selection is adapted to $t\bar{t}H$ events with the decay of the Higgs boson into a $b\bar{b}$ pair and lepton+jets as well as dilepton decays of the $t\bar{t}$ pair, resulting in the final state $\ell\nu\,q\bar{q}'\,b\bar{b}$ ($\ell^+\nu\,\ell^-\bar{\nu}\,b\bar{b}$) for lepton+jets (dilepton) $t\bar{t}$ decays, where $\ell = \mathrm{e}, \mu$. Events are split into mutually exclusive categories according to the number of reconstructed jets and the number of jets identified as coming from the hadronization of b quarks (b tagging). A further category is added with events in which "boosted" jets are identified as coming from hadronic top quark or $H \to b\bar{b}$ decays. In each category signal and background processes are separated employing BDTs which use the kinematic properties of jets and charged leptons, the b tagging probability, invariant masses and angular correlations of combinations of jets and leptons, as well as observables characterizing the event shape as inputs. The MEM discriminants are either used as input to the BDTs or the BDTs are employed to define categories in which the MEM output is used as the final discriminant. From a combined profile-likelihood fit of discriminant templates to data in all categories, an upper limit on the signal strength modifier μ is obtained.

This document is structured as follows: in Section 3, the data samples and simulated data samples are described. The basic selection of analysis objects and events is discussed in Section 4. The general analysis strategy and background estimation methods are introduced in Section 5. The influence of systematic uncertainties is studied in Section 6. Results of the studies are presented and their statistical interpretation is given in Section 7, followed by conclusions in Section 8.

2 The CMS Detector

The central feature of the CMS apparatus is a superconducting solenoid of 6 m internal diameter, providing a magnetic field of 3.8 T. Within the superconducting solenoid volume are a silicon pixel and strip tracker, a lead tungstate crystal electromagnetic calorimeter (ECAL), and a brass and scintillator hadron calorimeter (HCAL), each composed of a barrel and two endcap sections. Forward calorimeters extend the pseudorapidity coverage provided by the barrel and endcap detectors. Muons are measured in gas-ionization detectors embedded in the steel flux-return yoke outside the solenoid. A more detailed description of the CMS detector, together with a definition of the coordinate system used and the relevant kinematic variables, can be found in Ref. [26].

3 Data and Simulation Samples

This analysis is performed using samples of proton-proton (pp) collisions at $\sqrt{s} = 13$ TeV, which are collected with the CMS detector in 2015 and correspond to a total integrated luminosity of 2.7 fb^{-1}.

Monte Carlo (MC) event generators, interfaced with a detailed detector simulation, are used to model experimental effects, such as reconstruction and selection efficiencies, as well as detector resolutions. The CMS detector response is simulated using GEANT4 (v. 9.4) [27].

For the simulation of the reference tt̄H signal sample, the next-to-leading-order (NLO) event generator POWHEG (v. 2) [28, 29] is used. The value of the Higgs boson mass is assumed to be 125 GeV, while the top quark mass value is set to 172.5 GeV. The proton structure is described by the parton distribution functions (PDF) NNPDF3.0 [30]. The generated events are subsequently processed with PYTHIA (v. 8.2) [31] for parton showering and hadronization.

Standard model backgrounds are simulated using POWHEG, MG5_aMC@NLO (v. 2.2.2) [32], or PYTHIA, depending on the process. The main background contribution originates from tt̄ production, the production of W and Z/γ^* bosons with additional jets (referred to as W+jets and Z+jets or commonly as V+jets in the following), single top quark production (tW channel), and diboson (WW, WZ, and ZZ) processes, and tt̄ production in association with a W or Z boson (referred to as tt̄ +W and tt̄ +Z or commonly as tt̄ +V in the following). Both the tt̄ and the single top quark samples are simulated with POWHEG. The V+jets and tt̄ +V samples are simulated with the NLO generator MG5_aMC@NLO, where for the V+jets samples the matching of matrix-element jets to parton showers is performed using the FxFx [33] prescription. In contrast, PYTHIA is used to simulate diboson events. Parton showering and hadronization are also simulated with PYTHIA in all the background samples. The PYTHIA CUETP8M1 tune [34, 35] is used to characterize the underlying event in both the tt̄H signal and the background samples.

For comparison with the measured distributions, the events in the simulated samples are normalized to an integrated luminosity of 2.7 fb^{-1}, according to their predicted cross sections. These are taken from theoretical calculations at next-to-next-to-leading order (NNLO, for V+jets production), approximate NNLO (single top quark tW channel [36]), and NLO (diboson production [37] and tt̄ +V production [38]). The tt̄H cross section [24, 39–42] and Higgs boson branching fractions [43–46] used in the analysis also have NLO accuracy. The tt̄ simulated sample is normalized to the full NNLO calculation with resummation to next-to-next-to-leading-logarithmic accuracy (NNLL) [47–53], assuming a top quark mass value of 172.5 GeV and using the NNPDF3.0 PDF set. This sample is further separated into the following processes based on the flavor of additional jets that do not orginate from the top quark decays in the event: tt̄+bb̄,

defined at generator level as the events in which two additional b jets are generated within the acceptance requirements (cf. Section 4) and originate from one or more overlapping B hadrons; t$\bar{\text{t}}$+b, for which only one additional b jet originates from a single B hadron; t$\bar{\text{t}}$+2b, which corresponds to events with two additional B hadrons that are close enough in direction to produce a single b jet; t$\bar{\text{t}}$+c$\bar{\text{c}}$, for which events have at least one c jet within acceptance and no additional b jets; t$\bar{\text{t}}$ +light flavor (lf), which correspond to events that do not belong to any of the above processes. The separation is motivated by the fact that different sub-samples originate from different physics processes and have different systematic uncertainties. A similar separation strategy has been followed by the ATLAS collaboration [23].

Effects from additional pp interactions in the same bunch crossing (pileup) are modeled by adding simulated minimum-bias events (generated with PYTHIA) to all simulated processes. The pileup multiplicity distribution in simulation is reweighted to reflect the luminosity profile of the observed pp collisions. Correction factors described in Section 4 are applied where necessary to improve the description of the data by the simulation.

4   Object and Event Selection

The event selection is consistent with the production of a Higgs boson in association with a top quark-antiquark pair. In this analysis, only the cases in which the Higgs boson decays into a bottom quark-antiquark pair are considered. In the SM, the top quark is expected to decay into a W boson and a b quark nearly 100% of the time. Hence different t$\bar{\text{t}}$ decay modes can be identified according to the subsequent decays of the W bosons. Two t$\bar{\text{t}}$ decay modes are considered: the lepton+jets mode (t$\bar{\text{t}} \to \ell \nu \, \text{q} \overline{\text{q}}' \, \text{b} \overline{\text{b}}$), where one W boson decays into a charged lepton and a neutrino, and the dilepton mode (t$\bar{\text{t}} \to \ell^+ \nu \, \ell^- \overline{\nu} \, \text{b} \overline{\text{b}}$), where both W bosons decay into a charged lepton and a neutrino. These signatures imply the presence of isolated leptons (ℓ = e, μ), missing transverse momentum owing to the neutrinos from W boson decays, and highly energetic jets originating from the final-state quarks. The heavy-quark content of the jets is identified through b tagging techniques.

At trigger level, events in the lepton+jets channel are required to contain an electron (muon) with transverse momentum (p_T) threshold of $p_\text{T} > 27 \, \text{GeV}$ ($p_\text{T} > 20 \, \text{GeV}$). For electrons a pseudorapidity range of $|\eta| < 2.1$ is required. Events in the dilepton channel are required to contain two leptons fulfilling p_T thresholds between $8 \, \text{GeV}$ and $17 \, \text{GeV}$ and isolation criteria. Events are reconstructed using a particle-flow (PF) technique [54, 55], which combines signals from all sub-detectors to enhance the reconstruction performance by identifying individual particle candidates in pp collisions. Charged hadrons from pileup events are subtracted event-by-event. Subsequently, the remaining neutral-hadron pileup component is subtracted at the level of jet energy corrections [56].

The electron and muon candidates are required to be sufficiently isolated from nearby jet activity as follows. For each electron (muon) candidate, a cone of $\Delta R = 0.3$ ($\Delta R = 0.4$) is constructed around the direction of the track at the event vertex, where ΔR is defined as $\sqrt{(\Delta \eta)^2 + (\Delta \phi)^2}$, and $\Delta \eta$ and $\Delta \phi$ are the distances in pseudorapidity and azimuthal angle. Excluding the contribution from the lepton candidate, the scalar sum of the p_T of all particle candidates inside ΔR consistent with arising from the chosen primary event vertex is calculated to define a relative isolation discriminant, I_rel, through the ratio of this sum to the p_T of the lepton candidate. Electron candidates are selected if they have values of $I_\text{rel} < 0.15$, while muons are selected if they fulfill $I_\text{rel} < 0.15$ in the lepton+jets channel and $I_\text{rel} < 0.25$ in the dilepton channel. In addition, electrons from identified photon conversions are rejected. To further increase the pu-

rity of muons originating from the primary interaction and to suppress misidentified muons or muons from decay-in-flight processes, additional quality criteria, such as a minimal number of hits associated with the muon track, are required in both the silicon tracker and the muon system. The neutral component from pileup events is subtracted event-by-event based on the average transverse energy deposited by neutral particles in the event, which is removed from the transverse energy in the isolation cone.

For the lepton+jets channel, events are selected containing exactly one energetic, isolated lepton (e or μ), which is required to have $p_T > 25\,\text{GeV}$ or $p_T > 30\,\text{GeV}$ in the case of the μ or e, respectively, and $|\eta| < 2.1$ (but excluding electrons within a small region of $|\eta|$ between the barrel and endcap sections of the ECAL). For the dilepton channel, events are required to have a pair of oppositely charged energetic leptons (e^+e^-, $\mu^+\mu^-$, $\mu^\pm e^\mp$). The leading lepton is required to have $p_T > 20\,\text{GeV}$ and the subleading lepton $p_T > 15\,\text{GeV}$, and both leptons are required to fulfill $|\eta| < 2.4$. The invariant mass of the selected lepton pair is required to be larger than 20 GeV to suppress events from heavy-flavor resonance decays and low-mass Drell–Yan processes. In the same-flavor channels, events are rejected if the dilepton invariant mass is within the region $76\,\text{GeV} < m^{\ell\ell} < 106\,\text{GeV}$, thereby suppressing further contribution from Z+jets processes.

Jets are reconstructed from the PF particle candidates using the anti-k_T clustering algorithm [57] with a distance parameter of 0.4, optimized for the running conditions at the higher center-of-mass energy in LHC Run II. The jet energy is corrected for pileup in a manner similar to that used to find the energy within the lepton isolation cone. Jet energy corrections are also applied as a function of jet p_T and η [58] to data and simulation. Events in the lepton+jets channel are required to have at least four reconstructed jets with $p_T > 30\,\text{GeV}$ and $|\eta| < 2.4$. In the dilepton channels, at least three jets with $p_T > 20\,\text{GeV}$ and $|\eta| < 2.4$ are required, from which the two leading jets must satisfy $p_T > 30\,\text{GeV}$.

Jets originating from the hadronization of b quarks are identified using a combined secondary vertex algorithm (CSV) [59], which provides a b tagging discriminant by combining identified secondary vertices and track-based lifetime information. A discriminant value is chosen such that the efficiency for tagging jets from b (c) quarks is $\approx 70\%$ (20%), while the probability of tagging jets originating from light-flavor quarks (u, d, or s) or gluons is around 1%. The shape of the CSV discriminant distribution in simulation is corrected by scale factors to better describe the efficiency observed in the data [60]. This correction is derived separately for light-flavor and b jets from a "tag-and-probe" approach using control samples enriched in events with a Z boson and exactly two jets, and $t\bar{t}$ events in the eμ channel with no additional jets. At least two b-tagged jets are required.

In the lepton+jets channel, a dedicated reconstruction of the hadronically decaying top quark and the H boson is performed, targeting at the case of high p_T where their decay products are strongly collimated and potentially clustered within one jet (referred to as 'boosted' in the following). The reconstruction is based on the HEP Top Tagger [61–63] and subjet-filterjet algorithm [64] techniques, respectively. All PF particle candidates in the event except the one identified as lepton are clustered into large-radius jets with the Cambridge/Aachen algorithm [65] with a cone-size parameter of 1.5. The presence of the t $\to$ bqq and H $\to$ b$\bar{\text{b}}$ decay products within the jet is inferred by successively reverting the clustering sequence and searching for a significant decrease of the invariant mass when splitting into two subjets, and the subjets eventually obtained are assigned to the t and H $\to$ b$\bar{\text{b}}$ final state particles depending on their CSV discriminant value and their p_T. For the final selection, the boosted t and H candidates are required to have $p_T > 200\,\text{GeV}$ and to fulfil a multivariate selection criterion constructed

from kinematic and secondary-vertex information of the subjets, which assesses the agreement of the candidate with the boosted object hypothesis.

The missing transverse momentum vector $\vec{p}_T^{\text{miss}}$ is defined as the projection on the plane perpendicular to the beams of the negative vector sum of the momenta of all reconstructed particles in an event. Its magnitude is referred to as E_T^{miss}. In the dilepton same-flavor channels, events are required to fulfill $E_T^{\text{miss}} > 40\,\text{GeV}$.

Signal $t\bar{t}H$ events are generally characterized by having more jets and more b-tags than the background processes. Events are then divided into categories based on the number of jets, the number of b-tagged jets, and the presence of boosted objects to improve the sensitivity of the analyses. For the lepton+jets channel, events are separated into the following seven categories: if both a boosted t and H are selected, events are assigned to the 'boosted category', else events are assigned to either of the $\geq 6\,\text{jets}, 2\,\text{b-tags}$; $4\,\text{jets}, 3\,\text{b-tags}$; $5\,\text{jets}, 3\,\text{b-tags}$; $\geq 6\,\text{jets}, 3\,\text{b-tags}$; $4\,\text{jets}, \geq 4\,\text{b-tags}$; $5\,\text{jets}, \geq 4\,\text{b-tags}$ and $\geq 6\,\text{jets}, \geq 4\,\text{b-tags}$ categories. For the dilepton channel, events are divided into five categories: $3\,\text{jets}, 2\,\text{b-tags}$; $3\,\text{jets}, 3\,\text{b-tags}$; $\geq 4\,\text{jets}, 2\,\text{b-tags}$; $\geq 4\,\text{jets}, 3\,\text{b-tags}$ and $\geq 4\,\text{jets}, \geq 4\,\text{b-tags}$.

Tables 1 and 2 show the predicted and observed event yields after the event selection in the lepton+jets and dilepton channels, respectively. The tables are sub-divided into the different jet and b-tag categories used in each channel. The expected and observed yields agree well in all final states across the different categories of jets and b-tags.

5   Analysis Strategy and Background Estimation

Boosted decision trees and a matrix element method are used to further improve the signal-to-background separation in all channels of the analysis. Both techniques are combined into one single discriminant, which exploits the strenghts of both methods. This is a new feature of this analysis compared to previous CMS results [20, 22].

The BDTs utilize information related to object kinematics, event shape, the CSV b-tag discriminant, variables specific to the boosted object reconstruction, and in some cases also the output of the MEM described below. A separate BDT is trained for each category, resulting in eight BDTs in the lepton+jets and five in the dilepton channel. The training is performed using simulated $t\bar{t}H$ and $t\bar{t}$+jets events as signal and background, respectively, which are weighted to achieve equal yields of signal and background events in each category. In order to avoid overoptimization, the signal and background events are split in half: one half is used to perform the training, and the other half is used in the final analysis to monitor the performance and derive the expected limits. The specific BDT method used is the stochastic Gradient Boost, available as part of the TMVA package in ROOT [66]. The choice of BDT input variables as well as the tree architecture is optimized separately in each category with a procedure based on the particle swarm algorithm [67]. A description of the input variables is provided in Appendices A and B for each category of the lepton+jets and the dilepton channel, respectively.

Within the MEM, each event is assigned a probability density value computed from the four-momenta of the reconstructed particles, which is based on the differential cross section of the signal or background process. The MEM discriminant is constructed as ratio of the probability density values of the signal and background hypothesis. The deployed algorithm is an improved version of the method described in [22]. The probability density functions are constructed at LO, assuming gluon-gluon fusion production both for signal and background processes. The $t\bar{t} + b\bar{b}$ matrix elements have been found to provide similar discrimination power

Table 1: t$\bar{\text{t}}$H and background event yields for the lepton+jets categories. The processes and the separation of the t$\bar{\text{t}}$ +jets sample are described in Section 3.

Process	≥ 6 jets, 2 b-tags	4 jets, 3 b-tags	5 jets, 3 b-tags	≥ 6 jets, 3 b-tags
t$\bar{\text{t}}$+lf	5359.3 ± 1226.3	2026.1 ± 651.4	1000.2 ± 352.9	589.5 ± 199.7
t$\bar{\text{t}}$ + c$\bar{\text{c}}$	1722.2 ± 849.5	363.2 ± 190.9	368.1 ± 191.3	396.6 ± 209.5
t$\bar{\text{t}}$+b	393.7 ± 188.2	203.1 ± 92.5	199.6 ± 90.8	170.8 ± 81.4
t$\bar{\text{t}}$+2b	165.2 ± 81.2	78.9 ± 38.0	87.2 ± 40.7	97.3 ± 46.8
t$\bar{\text{t}}$ + b$\bar{\text{b}}$	226.4 ± 113.2	75.8 ± 35.3	114.1 ± 52.3	183.7 ± 86.7
Single Top	283.0 ± 49.0	115.3 ± 30.8	76.2 ± 19.5	47.5 ± 12.7
V+jets	130.5 ± 35.2	38.6 ± 17.8	22.8 ± 10.4	13.6 ± 6.4
t$\bar{\text{t}}$+V	43.5 ± 8.2	4.3 ± 1.2	6.4 ± 1.8	10.0 ± 2.7
Diboson	2.8 ± 1.3	2.1 ± 1.3	0.9 ± 0.5	0.2 ± 0.3
Total bkg	8326.7 ± 1788.6	2907.4 ± 836.5	1875.5 ± 534.7	1509.1 ± 423.7
t$\bar{\text{t}}$H	29.6 ± 2.1	7.4 ± 1.0	10.9 ± 1.2	16.7 ± 2.1
Data	7185	2793	1914	1386
S/B	0.0036	0.0026	0.0059	0.011
Data/B	0.9 ± 0.2	1.0 ± 0.3	1.0 ± 0.3	0.9 ± 0.3

Process	4 jets, ≥ 4 b-tags	5 jets, ≥ 4 b-tags	≥ 6 jets, ≥ 4 b-tags	boosted
t$\bar{\text{t}}$+lf	17.8 ± 10.8	17.7 ± 10.9	17.6 ± 11.3	45.1 ± 9.4
t$\bar{\text{t}}$ + c$\bar{\text{c}}$	11.6 ± 8.2	22.1 ± 15.4	35.9 ± 24.9	21.8 ± 12.0
t$\bar{\text{t}}$+b	8.4 ± 4.4	14.8 ± 7.7	20.0 ± 10.9	10.3 ± 5.5
t$\bar{\text{t}}$+2b	3.5 ± 1.9	6.9 ± 3.7	12.3 ± 6.9	12.3 ± 6.6
t$\bar{\text{t}}$ + b$\bar{\text{b}}$	10.1 ± 4.9	28.8 ± 13.9	73.4 ± 36.6	17.0 ± 8.4
Single Top	2.5 ± 1.1	4.3 ± 1.4	5.5 ± 2.0	7.0 ± 1.7
V+jets	1.0 ± 0.8	0.9 ± 0.8	1.4 ± 0.7	2.5 ± 0.8
t$\bar{\text{t}}$+V	0.3 ± 0.1	0.7 ± 0.3	1.6 ± 0.6	0.9 ± 0.3
Diboson	0.0 ± 0.0	0.1 ± 0.1	0.0 ± 0.0	0.1 ± 0.1
Total bkg	55.2 ± 23.0	96.5 ± 37.6	167.6 ± 65.7	117.0 ± 24.9
t$\bar{\text{t}}$H	0.9 ± 0.2	2.7 ± 0.6	5.9 ± 1.4	2.2 ± 0.3
Data	75	104	150	104
S/B	0.017	0.028	0.035	0.019
Data/B	1.4 ± 0.5	1.1 ± 0.4	0.9 ± 0.4	0.9 ± 0.2

Table 2: t$\bar{\text{t}}$H and background event yields for dilepton categories. The processes and the separation of the t$\bar{\text{t}}$ +jets sample are described in Section 3.

	3 jets, 2 b-tags	3 jets, 3 b-tags	≥ 4 jets, 2 b-tags	≥ 4 jets, 3 b-tags	≥ 4 jets, ≥ 4 b-tags
t$\bar{\text{t}}$+lf	2558.6 ± 542.7	26.6 ± 10.5	2271.6 ± 505.0	60.3 ± 25.6	0.9 ± 0.8
t$\bar{\text{t}}$ + c$\bar{\text{c}}$	220.9 ± 103.4	22.7 ± 13.6	478.4 ± 234.4	78.4 ± 45.4	3.4 ± 2.9
t$\bar{\text{t}}$+b	65.4 ± 28.5	21.4 ± 10.2	126.2 ± 57.7	52.2 ± 25.1	2.7 ± 1.6
t$\bar{\text{t}}$+2b	16.9 ± 7.6	6.6 ± 3.1	42.9 ± 20.2	22.3 ± 10.7	1.2 ± 0.7
t$\bar{\text{t}}$ + b$\bar{\text{b}}$	8.6 ± 4.2	3.6 ± 1.8	48.9 ± 23.7	39.8 ± 18.8	13.4 ± 7.1
Single Top	93.2 ± 16.7	3.0 ± 1.0	87.6 ± 15.8	7.3 ± 2.5	0.4 ± 0.4
V+jets	14.5 ± 11.0	1.3 ± 0.8	16.0 ± 7.4	0.0 ± 0.0	0.0 ± 0.0
t$\bar{\text{t}}$+V	3.6 ± 0.9	0.3 ± 0.2	16.4 ± 3.2	3.2 ± 0.9	0.5 ± 0.2
Diboson	1.7 ± 0.9	0.0 ± 0.0	1.2 ± 1.0	0.1 ± 0.0	0.0 ± 0.0
Total bkg	2983.4 ± 590.4	85.6 ± 25.6	3089.2 ± 650.6	263.6 ± 79.9	22.5 ± 9.8
t$\bar{\text{t}}$H	1.4 ± 0.2	0.4 ± 0.1	8.1 ± 1.1	3.6 ± 0.6	1.0 ± 0.3
Data	3123	115	2943	319	27
S/B	0.00047	0.0051	0.0026	0.014	0.046
Data/B	1.0 ± 0.2	1.3 ± 0.4	1.0 ± 0.2	1.2 ± 0.3	1.2 ± 0.5

against all background subprocesses and are solely used to model the background. Hadronization and detector effects are taken into account via transfer functions derived from simulation, which map the measured four-momenta to the final-state particles in the matrix element. In each event, only the four jets that most likely originate from b quarks are considered explicitly when evaluating the probability densities; contributions from further jets are marginalized by integration. The four jets are selected using the likelihood ratio between the hypotheses that four or two jets in the event arose from b quarks and the rest from light quarks, based on the expected b-tagging probability densities from simulation.

The BDT and MEM discriminants perform slightly differently in terms of signal and background separation. While the BDT achieves in a slightly better separation against the inclusive $t\bar{t}$ background, the MEM is by construction especially powerful in separating against the challenging $t\bar{t} + b\bar{b}$ background. The correlation between the BDT and MEM discriminants have been studied in different control regions in data and found to be well-modeled by the simulation. In the lepton+jets channel, the two discrinants are combined with the scheme described below. This results in the best sensitivity, and it is robust against binning effects and overoptimization.

In the two and three b-tag categories, a BDT is used as final discriminant, which includes the MEM as input variable (in the three b-tags categories). These categories contain a relatively large number of events, which is favourable for training the BDT.

In the categories with four or more b-tags, events are further separated into two sub-categories, one with low and one with high BDT output, defined by the median of the BDT output distribution. In each sub-category, the MEM is used as final discriminant. The high BDT output sub-category is expected to be enhanced with signal events, and the MEM discriminant achieves additional separation against the residual $t\bar{t} + b\bar{b}$ background contributions. The choice of the median contributes to a robust result by ensuring a sufficient number of events in each sub-category.

In the boosted category, which contains the events in which both a boosted top quark and a boosted Higgs boson candidate are reconstructed and identified, a BDT is used as final discriminant. Important input variables are derived from the reconstructed $t\bar{t}$ and $H \rightarrow b\bar{b}$ system, for example the invariant mass of the two b jets assigned to the Higgs boson decay. The sensitivity in the boosted category benefits from reduced combinatorics when assigning reconstructed objects to the top quark and Higgs boson decay products.

The final discriminant outputs provide better discrimination between signal and background than any of the input variables individually. The output distributions of the background and signal processes are fit to the data simultaneously in all channels and categories to set limits on the Higgs boson production cross section, as described in Section 7.

6   Systematic Uncertainties

In Table 3, all sources of systematic uncertainties considered in the analysis are listed. They affect either the yields of the signal or background processes, or the discriminant shape, or both. In the last case, the yield and shape effects are treated as entirely correlated and are varied simultaneously. The uncertainties are taken into account via nuisance parameters in the final fit procedure described in Section 7.

The effect of the uncertainties is evaluated individually in each category of each analysis channel, where the effects from the same source are treated as fully correlated. The impact of the sys-

Table 3: Systematic uncertainties considered in the analysis.

Source	Type	Remarks
Luminosity	rate	Signal and all backgrounds
Lepton ID/trigger efficiency	shape	Signal and all backgrounds
Pileup	shape	Signal and all backgrounds
Jet energy scale	shape	Signal and all backgrounds
b-tag HF fraction	shape	Signal and all backgrounds
b-tag HF stats (linear)	shape	Signal and all backgrounds
b-tag HF stats (quadratic)	shape	Signal and all backgrounds
b-tag LF fraction	shape	Signal and all backgrounds
b-tag LF stats (linear)	shape	Signal and all backgrounds
b-tag LF stats (quadratic)	shape	Signal and all backgrounds
b-tag charm (linear)	shape	Signal and all backgrounds
b-tag charm (quadratic)	shape	Signal and all backgrounds
QCD scale ($t\bar{t}H$)	rate	Scale uncertainty of NLO $t\bar{t}H$ prediction
QCD scale ($t\bar{t}$)	rate	Scale uncertainty of NLO $t\bar{t}$ prediction
QCD scale ($t\bar{t}$+hf)	rate	Additional scale uncertainty of NLO $t\bar{t}$+hf predictions
QCD scale (t)	rate	Scale uncertainty of NLO single t prediction
QCD scale (V)	rate	Scale uncertainty of NNLO W and Z prediction
QCD scale (VV)	rate	Scale uncertainty of NLO diboson prediction
pdf (gg)	rate	Pdf uncertainty for gg initiated processes except $t\bar{t}H$
pdf (gg $t\bar{t}H$)	rate	Pdf uncertainty for $t\bar{t}H$
pdf ($q\bar{q}$)	rate	PDF uncertainty of $q\bar{q}$ initiated processes ($t\bar{t}$ W, W, Z)
pdf (qg)	rate	PDF uncertainty of qg initiated processes (single t)
Q^2 scale ($t\bar{t}$)	shape	Renormalization and factorization scale uncertainties of the $t\bar{t}$ ME generator, independent for additional jet flavors
PS Scale ($t\bar{t}$)	shape	Renormalization and factorization scale uncertainties of the parton shower (for $t\bar{t}$ events), independent for additional jet flavors

tematic variations differ between the categories. As an example, the change in background and signal event yield due to the different uncertainties is listed in Table 4 for the ≥ 6 jets, 3 b-tags category of the lepton+jets channel, which shows high sensitivity and at the same time contains a relatively large number of events such that the variations are statistically significant.

Table 4: Specific effect of systematic uncertainties that affect the discriminant shape on the predicted background and signal yields for events in the ≥ 6 jets, 3 b-tags category of the lepton+jets channel. Here, only the sum of the largest background processes, $t\bar{t}$+lf, $t\bar{t}$+b, $t\bar{t}$+2b, $t\bar{t}$+b$\bar{b}$, and $t\bar{t}$+c$\bar{c}$, are considered.

Process	$t\bar{t}$ rate up/down [%]	$t\bar{t}$H rate up/down [%]
Jet energy Scale	$+11.3/-10.1$	$+7.7/-7.0$
Jet energy Resolution	$-0.1/+0.1$	$-0.1/+0.1$
Pile-Up	$-0.1/+0.0$	$+0.1/-0.2$
Electron Efficiency	$+1.6/-1.6$	$+1.6/-1.6$
Muon Efficiency	$+1.2/-1.2$	$+1.2/-1.2$
b-Tag HF contamination	$-3.5/+8.4$	$+0.2/+0.6$
b-Tag HF stats (linear)	$-6.4/+6.2$	$-5.3/+4.9$
b-Tag HF stats (quadratic)	$+4.2/-4.4$	$+3.3/-3.6$
b-Tag LF contamination	$+7.1/-5.1$	$+5.5/-4.2$
b-Tag LF stats (linear)	$-3.2/+6.5$	$-0.6/+1.1$
b-Tag LF stats (quadratic)	$+0.5/+1.2$	$-0.8/+1.1$
b-Tag charm Uncertainty (linear)	$-12.6/+16.9$	$-0.6/+0.7$
b-Tag charm Uncertainty (quadratic)	$+1.4/-1.4$	$+0.0/-0.0$
Q2 scale ($t\bar{t}$+lf)	$-1.9/+2.8$	$-$
Q2 scale ($t\bar{t}$+b)	$-0.6/+0.9$	$-$
Q2 scale ($t\bar{t}$+2b)	$-0.5/+0.8$	$-$
Q2 scale ($t\bar{t}$+b$\bar{b}$)	$-0.9/+1.3$	$-$
Q2 scale ($t\bar{t}$+c$\bar{c}$)	$-1.6/+2.4$	$-$
PS scale ($t\bar{t}$+lf)	$4.4/-8.7$	$-$
PS scale ($t\bar{t}$+b)	$-1.3/+0.8$	$-$
PS scale ($t\bar{t}$+2b)	$-1.0/+0.4$	$-$
PS scale ($t\bar{t}$+b$\bar{b}$)	$-2.0/+1.3$	$-$
PS scale ($t\bar{t}$+c$\bar{c}$)	$-4.3/+2.3$	$-$

The uncertainty in the luminosity estimate is 2.7% [68]. Electron and muon identification and trigger efficiency uncertainties were estimated by comparing variations in measured efficiency between data and MC simulation using a high-purity sample of Z-boson decays and are found to be 2–4%. Effects of the uncertainty in the distribution of the number of pileup interactions are evaluated by varying the cross section used to predict the number of pileup interactions in MC by ±5% from its nominal value. The uncertainty of the jet energy scale [58] (resolution) are evaluated by varying the energy scale (resolution) correction of all jets in the signal and background predictions by one standard deviation. The uncertainty of the CSV b-tagging scale factors is evaluated by applying alternative scale factors based on varying the following systematic effects by one standard deviation, separately for the different jet flavors: the contamination of background processes in the control samples, the jet energy scale uncertainty — which is correlated with the overall jet energy scale uncertainty — and the statistical uncertainty in the scale factor evaluation. The impact of the latter one is parameterized as the sum of two orthogonal contributions: a linear and a quadratic term, which allow an overall tilt and a shift of the center of CSV distribution, respectively. Both for the jet energy scale and for the b-tagging scale factor uncertainties, the event categorization and successive evaluation of the discriminant is re-evaluated after applying the systematic variations to account for migration effects.

Theoretical uncertainties of the cross sections used to predict the rates of various processes are propagated to the yield estimates. All rates are estimated using cross sections of at least NLO accuracy, which have uncertainties arising primarily from PDFs and the choice of factorization and renormalization scales (both in the matrix element and the parton shower). The cross section uncertainties are each separated into their PDF and scale components and correlated where appropriate between processes. For example, the PDF uncertainty for processes originating primarily from gluon-gluon initial states, such as $t\bar{t}$ and $t\bar{t}H$ production, are treated as 100% correlated. The $t\bar{t}+b\bar{b}$ process, and to lesser extent the $t\bar{t}+2b$, $t\bar{t}+b$, and $t\bar{t}+c\bar{c}$ production, represent important sources of irreducible background. Neither control region studies nor higher-order theoretical calculations can currently constrain the normalization of these contributions to better than 50% accuracy; therefore a conservative extra 50% rate uncertainty is assigned to the $t\bar{t}$ +heavy-flavor processes. This rate uncertainty has the largest impact on the median expected limit; omitting it in the computation improves the limit by approximately 10%. The effect of the scale uncertainties on the discriminant output shape is also taken into account for the $t\bar{t}$+jets production using event weights obtained directly from the MC generator in case of the matrix element and dedicated samples generated with different scale choices in case of the parton shower. The factorization and renormalization scales of the matrix element generator and also the scales of the initial-state radiation and the final-state radiation of the parton shower of the general-purpose MC event generator are varied simultaneously by a factor of 0.5 and 2. These scale variations are treated as uncorrelated between the matrix element generator and the general-purpose MC event generator. The rate and shape variation due to the PDF uncertainty has been evaluated by comparing the results to those obtained when using the sub-PDFs of the NNPDF set and taking into account that the sub-PDFs should have Gaussian-distributed deviations from the nominal PDF. Since the rate and shape uncertainties due to the used NNPDF PDF set have been found to be negligible for the final discriminants and output variables, these uncertainties have not been propagated into the final analysis.

The impact of statistical fluctuations in the signal and background prediction due to the limited number of simulated events is accounted for using the approach described in [69, 70].

7 Results and Statistical Interpretation

The signal strength modifier $\mu = \sigma/\sigma_{SM}$ for the $t\bar{t}H$ production cross section is determined in a simultaneous binned maximum-likelihood fit to data in all analysis categories. The distributions of the final discriminant in all analysis categories before the fit to data are displayed in Figs. 2 to 4. The fit procedure takes into account sytematic uncertainties that modify the shape and normalization of the distribution, as described in Section 6. The distributions of the final discriminant after the fit are shown in Figs. 5 to 7. The value obtained for μ is both compatible with the SM expectation and no signal, therefore an upper limit at 95% confidence level (CL) is determined using a modified frequentist CL_s method [71, 72].

The expected and observed upper limits at the 95% CL on μ under the background-only hypothesis in each channel are listed in Table 5. A Higgs-boson mass of $m_H = 125\,\text{GeV}$ has been assumed in the signal model. The limits in each individual category are listed in Appendices A and B for the lepton+jets and the dilepton channel, respectively.

When combining all categories and channels, we obtain an observed (expected) upper limit of $\mu < 2.6\,(3.6)$ at the 95% confidence level. The best-fit value of μ is $-2.0^{+1.8}_{-1.8}$, which is 1.7 standard deviations from the standard model expectation of $\mu = 1$. The upper limits and best-fit values are illustrated in Fig. 8.

Figure 2: Final discriminant shapes in the different analysis categories in the lepton+jets channel before the fit to data. The expected background contributions (filled histograms) are stacked, and the expected signal distribution (line) for a Higgs-boson mass of $m_H = 125\,\text{GeV}$ is superimposed. Each contribution is normalized to an integrated luminosity of $2.7\,\text{fb}^{-1}$, and the signal contribution is additionally scaled by a factor of 15 for better readability. The distributions in data (markers) are also shown. In the top row the ≥ 6 jets 2 b-tag, the 4 jets 3 b-tag, and the 5 jets 3 b-tag category are shown. Below are the ≥ 6 jets 3 b-tag category, the 4 jets 4 b-tag category with low BDT output, and the 4 jets 4 b-tag category with high BDT output.

Table 5: Best-fit value of the signal strength modifier μ and expected and observed 95% CL upper limits (UL) in the lepton+jets and dilepton channels as well as the combined results. The one standard deviation ($\pm 1\sigma$) confidence intervals of the best-fit value and the expected limit is also quoted. Expected limits are calculated with the asymptotic method [73].

Channel	Best-fit μ	Observed UL	Expected UL
Lepton+jets	$-0.4^{+2.1}_{-2.1}$	4.0	$4.1^{+1.8}_{-1.2}$
Dilepton	$-4.7^{+3.7}_{-3.8}$	5.2	$7.7^{+3.6}_{-2.3}$
Combined	$-2.0^{+1.8}_{-1.8}$	2.6	$3.6^{+1.6}_{-1.1}$

Figure 3: Final discriminant shapes in the different analysis categories in the lepton+jets channel before the fit to data. The expected background contributions (filled histograms) are stacked, and the expected signal distribution (line) for a Higgs-boson mass of $m_H = 125\,\text{GeV}$ is superimposed. Each contribution is normalized to an integrated luminosity of $2.7\,\text{fb}^{-1}$, and the signal contribution is additionally scaled by a factor of 15 for better readability. The distributions in data (markers) are also shown. In the top row the 5 jets 4 b-tag with low BDT output, the 5 jets 4 b-tag category with high BDT output, and the 6 jet category with low BDT output is shown. Below are the 6 jets 4 b-tag category with high BDT output, and the boosted category.

Figure 4: Final discriminant shapes in all analysis categories in the dilepton channel before the fit to data. In the top row the 3 jets, 2 b-tags, 3 jets, 3 b-tags, and $\geq$ 4 jets, 2 b-tags are shown. Below are the $\geq$ 4 jets, 3 b-tags and $\geq$ 4 jets, $\geq$ 4 b-tags categories. The expected background contributions (filled histograms) are stacked, and the expected signal distribution (line) for a Higgs-boson mass of $m_H = 125$ GeV is superimposed. Each contribution is normalized to an integrated luminosity of 2.7 fb^{-1}, and the signal contribution is additionally scaled by a factor of 15 for better readability. The distributions in data (markers) are also shown.
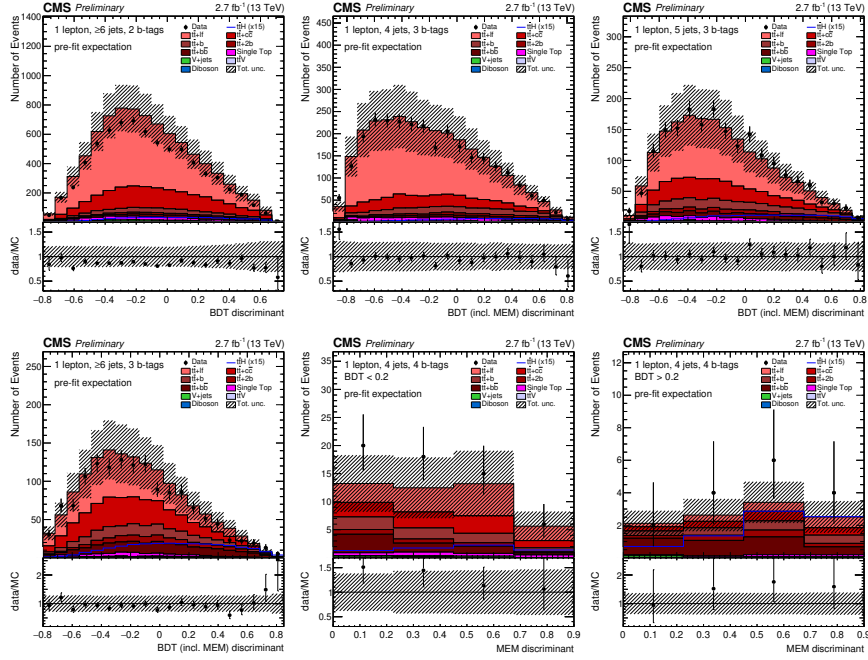
Figure 5: Final discriminant shapes in the different analysis categories in the lepton+jets channel after the fit to data. The expected background contributions (filled histograms) are stacked, and the expected signal distribution (line) for a Higgs-boson mass of $m_H = 125\,\text{GeV}$ is superimposed. Each contribution is normalized to an integrated luminosity of $2.7\,\text{fb}^{-1}$, and the signal contribution is additionally scaled by a factor of 15 for better readability. The distributions in data (markers) are also shown. In the top row the 5 jets 4 b-tag with low BDT output, the 5 jets 4 b-tag category with high BDT output, and the 6 jet category with low BDT output is shown. Below are the 6 jets 4 b-tag category with high BDT output, and the boosted category.
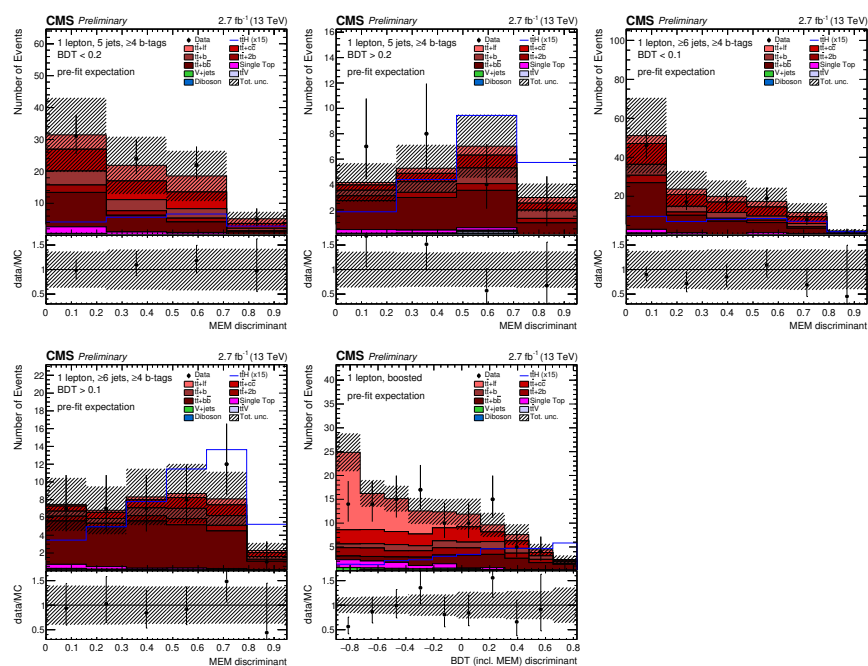
Figure 6: Final discriminant shapes in the different analysis categories in the lepton+jets channel after the fit to data. The expected background contributions (filled histograms) are stacked, and the expected signal distribution (line) for a Higgs-boson mass of $m_H = 125\,\text{GeV}$ is superimposed. Each contribution is normalized to an integrated luminosity of $2.7\,\text{fb}^{-1}$, and the signal contribution is additionally scaled by a factor of 15 for better readability. The distributions in data (markers) are also shown. In the top row the 5 jets 4 b-tag with low BDT output, the 5 jets 4 b-tag category with high BDT output, and the 6 jet category with low BDT output is shown. Below are the 6 jets 4 b-tag category with high BDT output, and the boosted category.
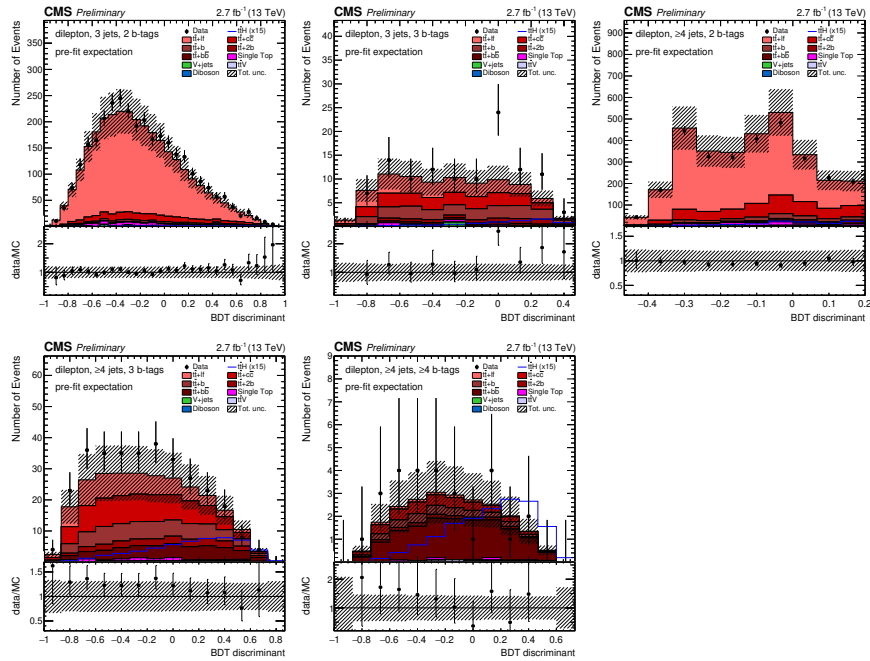
Figure 7: Final discriminant shapes in all analysis categories in the dilepton channel after the fit to data. In the top row the 3 jets, 2 b-tags, 3 jets, 3 b-tags, and $\geq$ 4 jets, 2 b-tags are shown. Below are the $\geq$ 4 jets, 3 b-tags and $\geq$ 4 jets, $\geq$ 4 b-tags categories. The expected background contributions (filled histograms) are stacked, and the expected signal distribution (line) for a Higgs-boson mass of $m_H = 125$ GeV is superimposed. Each contribution is normalized to an integrated luminosity of $2.7\,\text{fb}^{-1}$, and the signal contribution is additionally scaled by a factor of 15 for better readability. The distributions in data (markers) are also shown.
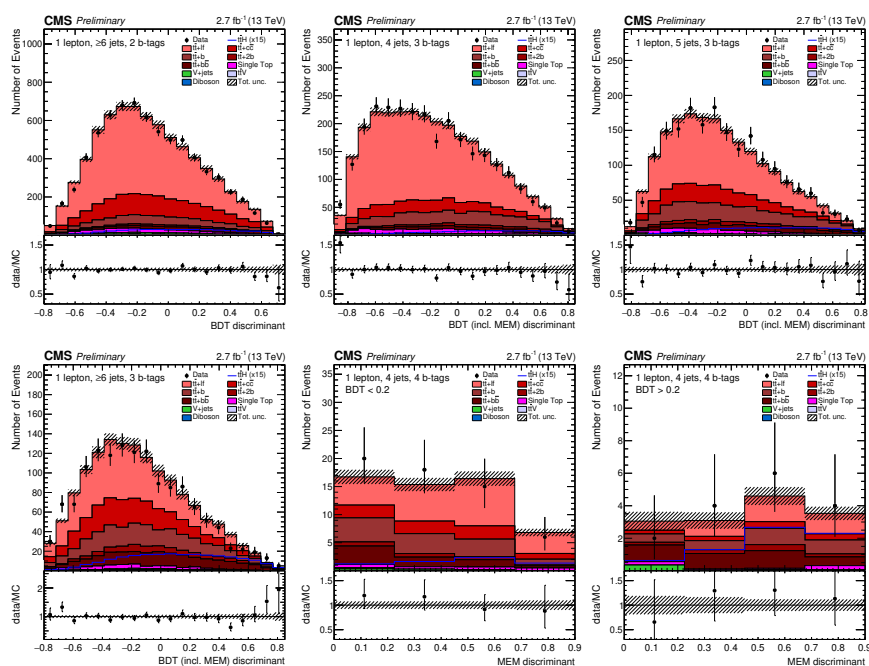
Figure 8: (left) Best-fit values of the signal strength modifiers μ with their $\pm 1\sigma$ confidence intervals. (right) Median expected and observed 95% CL upper limits on μ. The expected limits are displayed together with $\pm 1\sigma$ and $\pm 2\sigma$ confidence intervals.

8   Conclusions

A search for the associated production of a Higgs boson and a top quark-antiquark pair (t$\bar{\text{t}}$H) is performed using the first data recorded with the CMS detector at a center-of-mass energy of 13 TeV in 2015. Candidate events are selected in final states compatible with the Higgs boson decay H $\rightarrow$ b$\bar{\text{b}}$ and the lepton+jets or dilepton decay channel of the t$\bar{\text{t}}$ pair. Selected events are split into mutually exclusive categories according to their t$\bar{\text{t}}$ decay channel and jet content, including a category for "boosted" jets from hadronic decays of top quarks or H $\rightarrow$ b$\bar{\text{b}}$ decays with large transverse momenta. In each category a powerful discriminant is constructed to separate the t$\bar{\text{t}}$H signal from the t$\bar{\text{t}}$-dominated background, based on boosted decision trees and the matrix element method. Using 2.7 fb^{-1} of pp collsion data an observed (expected) upper limit on the t$\bar{\text{t}}$H production cross section relative to the SM expectations of $\mu = 2.6 \, (3.6)$ at the 95% confidence level is obtained.

A Lepton+Jets Additional Material

In the following, the input variables used to train the BDTs in each category of the lepton+jets channel are presented. In Tables 6 and 7, all variables used in any of the categories are described, and in Table 8, the variables used per category are listed. The expected upper limits at 95% CL on the signal strength modifier μ under the background-only hypothesis in the lepton+jets channel are listed in Table 9 and displayed in Fig. 9 for the individual categories and for the combined fit in all categories.

Table 6: Variables used in the BDT training in the lepton+jets channel (continued in Table 7).

Event variable	Description
Object and event kinematics	
jet 1, 2, 3, 4 p_T	Jet transverse momenta, jets ordered in p_T
HT	Scalar sum of transverse momentum for all jets with $p_T > 30\,\mathrm{GeV}/c$
MET	Missing transverse energy
$\sum p_T$(jets,leptons,MET)	Sum of the p_T of all jets, leptons, and MET
mass(lepton,jet,MET)	Invariant mass of the 4-vector sum of all jets, leptons, and MET
avg ΔR(tag,tag)	Average ΔR between b-tagged jets
avg $\Delta\eta$(jet,jet)	Average $\Delta\eta$ between jets
max $\Delta\lvert\eta\rvert$ (jet, avg jet $\lvert\eta\rvert$)	max difference between jet $\lvert\eta\rvert$ and avg $\lvert\eta\rvert$ of jets
max $\Delta\lvert\eta\rvert$ (tag, avg jet $\lvert\eta\rvert$)	max difference between tag $\lvert\eta\rvert$ and avg $\lvert\eta\rvert$ of jets
max $\Delta\lvert\eta\rvert$ (tag, avg tag $\lvert\eta\rvert$)	max difference between tag $\lvert\eta\rvert$ and avg η of tags
min ΔR(tag,tag)	ΔR between the two closest b-tagged jets
M3	Invariant mass of the 3-jet system with largest transverse momentum
min ΔR(lepton,jet)	ΔR between the lepton and the closest jet (LJ channel)
mass(lepton,closest tag)	Invariant mass of the lepton and the closest b-tagged jet in ΔR (LJ channel)
closest tagged dijet mass	Invariant mass of the two b-tagged jets that are closest in ΔR
tagged dijet mass closest to 125	Invariant mass of the b-tagged pair closest to 125 GeV/c^2
best Higgs mass	A minimum-chi-squared fit to event kinematics is used to select two b-tagged jets as top-decay products. Of the remaining b-tagged jets, the invariant mass of the two with highest E_T is saved.
$\sqrt{\Delta\eta(t^{lep},bb) \times \Delta\eta(t^{had},bb)}$	Square root of the product of abs $\Delta\eta$ (leptonic top, bb) and abs $\Delta\eta$ (hadronic top, bb), where the bb-system and the candidates for the leptonic and hadronic tops are found with the best higgs mass algorithm
$(\Sigma$ jet $p_T)/(\Sigma$ jet E)	Ratio of the sum of the transverse momentum of all jets and the sum of the energy of all jets
CSVv2IVF b-tag	
first- to fifth-highest CSV	First- to fifth-highest highest CSVv2IVF discriminator value of all jets
avg CSV (tags/all)	Average b-tag discriminator value for b-tagged/all jets
dev from avg CSV (tags)	Squared difference between the CSVv2IVF discriminator value of a given b-tagged jet and the average CSVv2IVF discriminator value among b-tagged jets, summed over all b-tagged jets
sphericity	Sphericity: $3/2(\lambda_2 + \lambda_3)$ (λ_i: eigenvalues of momentum tensor)
aplanarity	Aplanarity: $3/2\lambda_1$ (λ_i: eigenvalues of momentum tensor)
H_1, H_2, H_3, H_4	Fox-Wolfram moments [74]

Table 7: continued from Table 6.

Event variable	Description
MEM discriminator	
MEM discriminator	MEM discriminator
Boosted object and event reconstruction	
τ_2/τ_1 Higgs cand.	2-subjettiness to 1-subjettiness ratio of Higgs candidate fat jet [75]
m(Higgs, di-filterjet)	Invariant mass of boosted Higgs candidate reconstructed from filtered subjets B1 and B2
$\Delta\eta$(top,Higgs)	Pseudo rapidity difference between boosted top candidate and boosted Higgs candidate
MEM discriminator (using subjets)	MEM discriminator using the subjets from the boosted top candidate

Table 8: BDT input variable assignment per category in the lepton+jets channel.

≥ 4 jets, ≥ 2 b-tags boosted	4 jets, 3 b-tags	4 jets, ≥ 4 b-tags
avg ΔR(tag,tag)	H_1	closest tagged dijet mass
τ_2/τ_1 of Higgs cand.	b-tagging likelihood ratio	b-tagging likelihood ratio
third-highest CSV	$\sum p_T$(jets,leptons,MET)	$\sum p_T$(jets,lepton,MET)
fourth-highest CSV	MEM discriminator	avg ΔR(tag,tag)
$\Delta\eta$(top,Higgs)	avg CSV (tags)	H_3
aplanarity	avg CSV (all)	jet 1 p_T
m(Higgs, di-filterjet)	jet 2 p_T	
min ΔR(tag,tag)	jet 4 p_T	
avg CSV (all)		
MEM discriminator (using subjets)		
b-tagging likelihood ratio		
	5 jets, 3 b-tags	**5 jets, ≥ 4 b-tags**
	MEM discriminator	b-tagging likelihood ratio
	avg ΔR(tag,tag)	jet 3 p_T
	min ΔR(lepton,jet)	tagged dijet mass closest to 125
	b-tagging likelihood ratio	avg $\Delta\eta$(jet,jet)
	fourth-highest CSV	avg ΔR(tag,tag)
	H_1	H_1
	dev from avg CSV (tags)	fifth-highest CSV
	avg $\Delta\eta$(jet,jet)	$(\Sigma$ jet $p_T)/(\Sigma$ jet E$)$
	avg CSV (tags)	
	avg CSV (all)	
	max $\Delta|\eta|$ (tag, avg jet $|\eta|$)	
≥ 6 jets, 2 b-tags	**≥ 6 jets, 3 b-tags**	**≥ 6 jets, ≥ 4 b-tags**
avg $\Delta\eta$(tag,tag)	b-tagging likelihood ratio	$\sum p_T$(jets,leptons,MET)
avg ΔR(tag,tag)	$\sqrt{\Delta\eta(t^{lep},bb)\times\Delta\eta(t^{had},bb)}$	H_3
ΔR(jet1, jet2)	HT	best Higgs mass
b-tagging likelihood ratio	MEM discriminator	b-tagging likelihood ratio
max $\Delta|\eta|$ (tag, avg tags $|\eta|$)	$\sum p_T$(jets,lepton,MET)	tagged dijet mass closest to 125
third-highest CSV	H_1	fifth-highest CSV
sphericity	fourth-highest CSV	$(\Sigma$ jet $p_T)/(\Sigma$ jet E$)$
fourth-highest CSV	avg CSV (tags)	jet 4 p_T
max $\Delta|\eta|$ (tag, avg jet $|\eta|$)	max $\Delta|\eta|$ (tag, avg jet $|\eta|$)	sphericity
min ΔR(tag,tag)		max $\Delta|\eta|$ (tag, avg tag $|\eta|$)
		second-highest CSV

Table 9: Median expected 95% CLs upper limits on μ in the lepton+jets channel, calculated with the asymptotic method. The upper and lower range of one standard deviation is also quoted.

| Category	Observed	Expected
4 jets, 3 b-tags	14.5	$18.6^{+8.2}_{-5.5}$
4 jets, $\geq$ 4 b-tags high BDT output	35.7	$25.6^{+13.4}_{-8.1}$
4 jets, $\geq$ 4 b-tags low BDT output	86.6	$84.2^{+41.3}_{-25.8}$
5 jets, 3 b-tags	16.0	$12.3^{+5.5}_{-3.6}$
5 jets, $\geq$ 4 b-tags high BDT output	7.5	$10.3^{+5.6}_{-3.4}$
5 jets, $\geq$ 4 b-tags low BDT output	35.2	$31.9^{+16.1}_{-9.9}$
$\geq$ 6 jets, 2 b-tags	25.4	$41.1^{+21.1}_{-13.1}$
$\geq$ 6 jets, 3 b-tags	9.6	$7.6^{+3.3}_{-2.2}$
$\geq$ 6 jets, $\geq$ 4 b-tags high BDT output	9.2	$8.3^{+4.4}_{-2.7}$
$\geq$ 6 jets, $\geq$ 4 b-tags low BDT output	15.4	$18.3^{+9.6}_{-5.8}$
$\geq$ 4 jets, $\geq$ 2 b-tags, boosted	7.5	$10.7^{+5.9}_{-3.5}$
lepton+jets combined	4.0	$4.1^{+1.8}_{-1.2}$
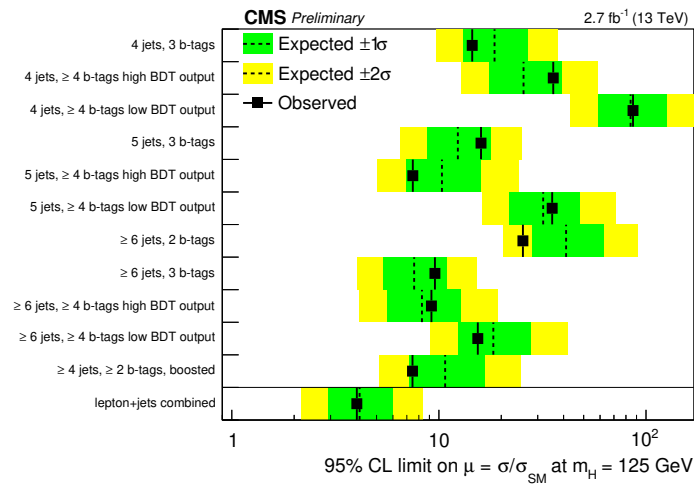
Figure 9: Visualisation of 95% CL upper limits on μ in the lepton+jets channel. The limits are calculated with the asymptotic method and displayed as the median and the $\pm1\sigma$ and $\pm2\sigma$ confidence intervals.

B Dilepton Additional Material

In the following, the input variables used to train the BDTs in each category of the dilepton channel are presented. In Table 10, all variables used in any of the categories are described, and in Table 11, the variables used per category are listed. The expected upper limits at 95% CL on the signal strength modifier μ under the background-only hypothesis in the dilepton channel are listed in Table 12 and displayed in Fig. 10 for the individual categories and for the combined fit in all categories.

Table 10: Variables used in the BDT training in the dilepton channel.

Event variable	Description
Object and event kinematics	
$\langle \Delta R_{tag,tag} \rangle$	Average ΔR between b-tagged jets
$\sum p_{T\,jets,leptons}$	Sum of the p_T of all jets and leptons
$\tau_{jet,jet}^{max\ mass}$	Twist angle between jet pair
$\min \Delta R_{tag,tag}$	ΔR between the two closest b-tagged jets
$\max \Delta \eta_{tag,tag}$	$\Delta \eta$ between the two furthest b-tagged jets
$m_{jet,jet}^{min\Delta R}$	Invariant mass of jet pair ΔR
$M_{higgs-like}^{jj}$	Invariant mass of a jet pair ordered in closeness to a Higgs mass
$m_{tag,tag}^{min\ \Delta R}$	Invariant mass of b-tag jet pair with minimum ΔR
$p_{T\,tag,tag}^{min\ \Delta R}$	Sum p_T of b-tag jet pair with minimum ΔR
Centrality (tags)	Ratio of the sum of the transverse momentum of all b-tagged jets and the sum of the energy of all b-tagged jets
H_T	Scalar sum of transverse momentum for all jets
$\min \Delta R_{jet,jet}$	ΔR between the two closest jets
median $m_{jet,jet}$	Median invariant mass of all combinations of jet pairs
$m_{tag,tag}^{max\ mass}$	Invariant mass of b-tagged jet pair with maximum invariant mass combination
$\langle \Delta R_{jet,tag} \rangle$	Average ΔR between jets (with at least one b-tagged)
$p_{T\,jet,tag}^{min\ \Delta R}$	Sum p_T of jet pair with minimum ΔR between them (with at least one b-tag jet)
$\tau_{jet,tag}^{max\ mass}$	Twist angle between jet pair (with at least one b-tagged)
$m_{jet,tag,tag}^{max\ p_T}$	Invariant mass of the 3-jet system with the largest transverse momentum where at least two jets are b-tagged.
$M_{higgs-like}^{bj}$	Invariant mass of a jet pair (with at least one b-tagged) ordered in closeness to a Higgs mass.
CSVv2IVF b-tag	
$\langle d \rangle_{tagged/untagged}$	Average CSV b-tag discriminant value for b-tagged/un-b-tagged jets
Event shape	
H_0, H_1, H_2, H_3, H_4	Fox-Wolfram moments [74]

Table 11: BDT input variable assignment per category in the dilepton channel.

3 jets, 2 b-tags	3 jets, 3 b-tags	≥ 4 jets, 2 b-tags	≥ 4 jets, 3 b-tags	≥ 4 jets, ≥ 4 b-tags
$\langle d \rangle_{untagged}$	$\langle d \rangle_{tagged}$	median m$_{jet,jet}$	min $\Delta R_{tag,tag}$	min $\Delta R_{tag,tag}$
$\sum p_{T\,jets,leptons}$	$m_{tag,tag}^{min\Delta R}$	$H_1 / H_0 (tags)$	$\langle d \rangle_{untagged}$	median m$_{jet,jet}$
$\tau_{jet,jet}^{\text{max mass}}$	m$_{tag,tag}^{\text{max mass}}$	$m_{jet,jet}^{min\Delta R}$	$\langle d \rangle_{tagged}$	max $\Delta \eta_{tag,tag}$
min $\Delta R_{tag,tag}$	max $\Delta \eta_{jet,jet}$	$\langle d \rangle_{untagged}$	$m_{tag,tag}^{min\Delta R}$	$M_{higgs-like}^{jj}$
max $\Delta \eta_{tag,tag}$	$H_4 / H_0 (tags)$	$H_2 (jets)$	$M_{higgs-like}^{jj}$	H_T^{tags}
$m_{jet,jet}^{min\Delta R}$	$H_1 (jets)$	$\sum p_{T\,jets,leptons}$	max $\Delta \eta_{tag,tag}$	$\langle d \rangle_{tagged}$
$M_{higgs-like}^{jj}$	$\tau_{jet,jet}^{\text{max mass}}$	$\langle \Delta R_{jet,tag} \rangle$	$\langle \Delta R_{jet,tag} \rangle$	$m_{jet,tag}^{min\Delta R}$
$m_{tag,tag}^{min\Delta R}$	$\sum p_{T\,jets,leptons}$	H_T^{jets}	$H_2 (tags)$	$m_{jet,jet}^{min\Delta R}$
	min $\Delta R_{jet,jet}$	$m_{tag,tag}^{min\Delta R}$	$\sum p_{T\,jets,leptons}$	m$_{tag,tag}^{\text{max mass}}$
	$M_{higgs-like}^{bj}$	$p_{T\,jet,tag}^{min\,\Delta R}$	$\tau_{tag,tag}^{\text{max mass}}$	max $\Delta \eta_{jet,jet}$
			Centrality(jets & leptons)	Centrality(jets & leptons)
			m$_{jet,jet,jet}^{\text{max } p_T}$	Centrality(tags)

Table 12: Median expected 95% CLs upper limits on μ in the dilepton channel, calculated with the asymptotic method. The upper and lower range of one standard deviation is also quoted.

Category	Observed	Expected
3 jets, 2 b-tags	186.0	$114.8_{-34.1}^{+52.6}$
≥ 3 jets, 3 b-tags	104.9	$48.6_{-15.9}^{+26.2}$
≥ 4 jets, 2 b-tags	32.4	$40.1_{-11.3}^{+16.8}$
≥ 4 jets, 3 b-tags	7.4	$10.8_{-3.3}^{+5.2}$
≥ 4 jets, ≥ 4 b-tags	9.1	$12.2_{-4.3}^{+7.5}$
dilepton combined	5.2	$7.7_{-2.3}^{+3.6}$
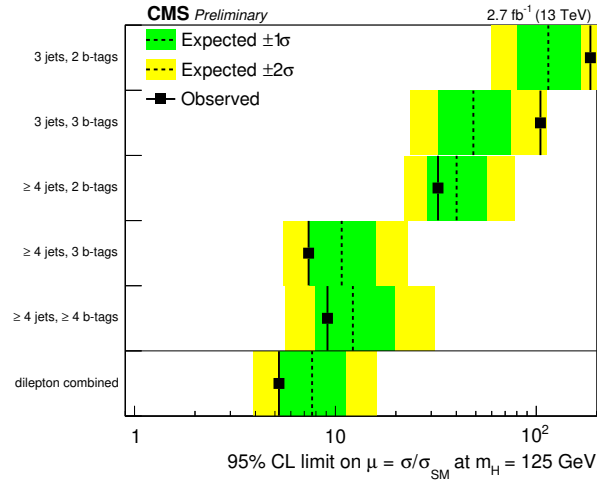
Figure 10: Visualisation of 95% CL upper limits on μ in the dilepton channel. The limits are calculated with the asymptotic method and displayed as the median and the $\pm1\sigma$ and $\pm2\sigma$ confidence intervals.

References

[1] ATLAS Collaboration, "Observation of a new particle in the search for the Standard Model Higgs boson with the ATLAS detector at the LHC", *Phys. Lett. B* **716** (2012), no. 1, 1–29, `doi:10.1016/j.physletb.2012.08.020`, `arXiv:1207.7214`.

[2] CMS Collaboration, "Observation of a new boson at a mass of 125 GeV with the CMS experiment at the LHC", *Phys. Lett. B* **716** (2012), no. 1, 30–61, `doi:10.1016/j.physletb.2012.08.021`, `arXiv:1207.7235`.

[3] CMS Collaboration, "Evidence for the direct decay of the 125 GeV Higgs boson to fermions", *Nature Phys.* **10** (2014), no. 5, 557–560, `doi:10.1038/nphys3005`, `arXiv:1401.6527`.

[4] ATLAS Collaboration, "Evidence for the Higgs-boson Yukawa coupling to tau leptons with the ATLAS detector", *JHEP* **04** (2015) 117, `doi:10.1007/JHEP04(2015)117`, `arXiv:1501.04943`.

[5] ATLAS Collaboration, "Measurements of Higgs boson production and couplings in diboson final states with the ATLAS detector at the LHC", *Phys. Lett. B* **726** (2013), no. 1-3, 88–119, `doi:10.1016/j.physletb.2014.05.011,10.1016/j.physletb.2013.08.010`, `arXiv:1307.1427`. [Erratum: Phys. Lett.B734,406(2014)].

[6] CMS Collaboration, "Precise determination of the mass of the Higgs boson and tests of compatibility of its couplings with the standard model predictions using proton collisions at 7 and 8 TeV", *Eur. Phys. J. C.* **75** (2015), no. 5, 212, `doi:10.1140/epjc/s10052-015-3351-7`, `arXiv:1412.8662`.

[7] ATLAS Collaboration, "Evidence for the spin-0 nature of the Higgs boson using ATLAS data", *Phys. Lett. B* **726** (2013), no. 1-3, 120–144, `doi:10.1016/j.physletb.2013.08.026`, `arXiv:1307.1432`.

[8] CMS Collaboration, "Constraints on the spin-parity and anomalous HVV couplings of the Higgs boson in proton collisions at 7 and 8 TeV", *Phys. Rev. D* **92** (2015), no. 1, 012004, `doi:10.1103/PhysRevD.92.012004`, `arXiv:1411.3441`.

[9] LHC Higgs Cross Section Working Group Collaboration, "Handbook of LHC Higgs Cross Sections: 3. Higgs Properties", `doi:10.5170/CERN-2013-004`, `arXiv:1307.1347`.

[10] G. Burdman, M. Perelstein, and A. Pierce, "Large Hadron Collider tests of a little Higgs model", *Phys. Rev. Lett.* **90** (2003), no. 24, 241802, `doi:10.1103/PhysRevLett.90.241802`, `arXiv:hep-ph/0212228`. [Erratum: Phys. Rev. Lett.92,049903(2004)].

[11] T. Han, H. E. Logan, B. McElrath, and L.-T. Wang, "Phenomenology of the little Higgs model", *Phys. Rev. D* **67** (2003), no. 9, 095004, `doi:10.1103/PhysRevD.67.095004`, `arXiv:hep-ph/0301040`.

[12] M. Perelstein, M. E. Peskin, and A. Pierce, "Top quarks and electroweak symmetry breaking in little Higgs models", *Phys. Rev. D* **69** (2004), no. 7, 075002, `doi:10.1103/PhysRevD.69.075002`, `arXiv:hep-ph/0310039`.

[13] H.-C. Cheng, I. Low, and L.-T. Wang, "Top partners in little Higgs theories with T-parity", *Phys. Rev. D* **74** (2006), no. 5, 055001, `doi:10.1103/PhysRevD.74.055001`, `arXiv:hep-ph/0510225`.

[14] H.-C. Cheng, B. A. Dobrescu, and C. T. Hill, "Electroweak symmetry breaking and extra dimensions", *Nucl. Phys. B.* **589** (2000), no. 1-3, 249–268, `doi:10.1016/S0550-3213(00)00401-6`, `arXiv:hep-ph/9912343`.

[15] M. Carena, E. Ponton, J. Santiago, and C. E. M. Wagner, "Light Kaluza Klein States in Randall-Sundrum Models with Custodial SU(2)", *Nucl. Phys. B.* **759** (2006), no. 1-2, 202–227, `doi:10.1016/j.nuclphysb.2006.10.012`, `arXiv:hep-ph/0607106`.

[16] R. Contino, L. Da Rold, and A. Pomarol, "Light custodians in natural composite Higgs models", *Phys. Rev. D* **75** (2007), no. 5, 055014, `doi:10.1103/PhysRevD.75.055014`, `arXiv:hep-ph/0612048`.

[17] G. Burdman and L. Da Rold, "Electroweak Symmetry Breaking from a Holographic Fourth Generation", *JHEP* **12** (2007) 086, `doi:10.1088/1126-6708/2007/12/086`, `arXiv:0710.0623`.

[18] C. T. Hill, "Topcolor: Top quark condensation in a gauge extension of the standard model", *Phys. Lett. B* **266** (1991), no. 3, 419–424, `doi:10.1016/0370-2693(91)91061-Y`.

[19] A. Carmona, M. Chala, and J. Santiago, "New Higgs Production Mechanism in Composite Higgs Models", *JHEP* **07** (2012) 049, `doi:10.1007/JHEP07(2012)049`, `arXiv:1205.2378`.

[20] CMS Collaboration, "Search for the associated production of the Higgs boson with a top-quark pair", *JHEP* **09** (2014) 087, `doi:10.1007/JHEP09(2014)087,10.1007/JHEP10(2014)106,` `arXiv:1408.1682`. [Erratum: JHEP10,106(2014)].

[21] ATLAS Collaboration, "Search for the associated production of the Higgs boson with a top quark pair in multilepton final states with the ATLAS detector", *Phys. Lett. B* **749** (2015) 519–541, `doi:10.1016/j.physletb.2015.07.079,arXiv:1506.05988`.

[22] CMS Collaboration, "Search for a standard model Higgs boson produced in association with a top-quark pair and decaying to bottom quarks using a matrix element method", *Eur. Phys. J. C.* **75** (2015), no. 6, 251, `doi:10.1140/epjc/s10052-015-3454-1,` `arXiv:1502.02485`.

[23] ATLAS Collaboration, "Search for the Standard Model Higgs boson produced in association with top quarks and decaying into $b\bar{b}$ in pp collisions at $\sqrt{s} = 8$ TeV with the ATLAS detector", *Eur. Phys. J. C.* **75** (2015), no. 7, 349, `doi:10.1140/epjc/s10052-015-3543-1,arXiv:1503.05066`.

[24] LHC Higgs Cross Section Working Group Collaboration, "Handbook of LHC Higgs Cross Sections: 1. Inclusive Observables", `doi:10.5170/CERN-2011-002,` `arXiv:1101.0593`.

[25] T. Plehn, G. P. Salam, and M. Spannowsky, "Fat Jets for a Light Higgs", *Phys. Rev. Lett.* **104** (2010), no. 11, 111801, `doi:10.1103/PhysRevLett.104.111801,` `arXiv:0910.5472`.

[26] CMS Collaboration, "The CMS experiment at the CERN LHC", *JINST* **3** (2008), no. 8, S08004, `doi:10.1088/1748-0221/3/08/S08004`.

[27] GEANT4 Collaboration, "GEANT4—a simulation toolkit", *Nucl. Instrum. Meth. A* **506** (2003), no. 3, 250, `doi:10.1016/S0168-9002(03)01368-8`.

[28] S. Frixione, P. Nason, and C. Oleari, "Matching NLO QCD computations with parton shower simulations: the POWHEG method", *JHEP* **11** (2007) 070, `doi:10.1088/1126-6708/2007/11/070,arXiv:0709.2092`.

[29] E. Re, "Single-top Wt-channel production matched with parton showers using the POWHEG method", *Eur. Phys. J. C* **71** (2011) 1547, `doi:10.1140/epjc/s10052-011-1547-z,arXiv:1009.2450`.

[30] NNPDF Collaboration, "Parton distributions for the LHC Run II", *JHEP* **04** (2015) 040, `doi:10.1007/JHEP04(2015)040,arXiv:1410.8849`.

[31] T. Sjöstrand et al., "An introduction to PYTHIA 8.2", *Comput. Phys. Commun.* **191** (2015) 159, `doi:10.1016/j.cpc.2015.01.024,arXiv:1410.3012`.

[32] J. Alwall et al., "The automated computation of tree-level and next-to-leading order differential cross sections, and their matching to parton shower simulations", *JHEP* **07** (2014) 079, `doi:10.1007/JHEP07(2014)079,arXiv:1405.0301`.

[33] R. Frederix and S. Frixione, "Merging meets matching in MC@NLO", *JHEP* **12** (2012) 061, `doi:10.1007/JHEP12(2012)061,arXiv:1209.6215`.

[34] CMS Collaboration, "Underlying event tunes and double parton scattering", CMS Physics Analysis Summary CMS-PAS-GEN-14-001, CMS Collaboration, 2014.

[35] P. Skands, S. Carrazza, and J. Rojo, "Tuning PYTHIA 8.1: the Monash 2013 Tune", *Eur. Phys. J. C* **74** (2014), no. 8, 3024, `doi:10.1140/epjc/s10052-014-3024-y`, `arXiv:1404.5630`.

[36] N. Kidonakis, "Two-loop soft anomalous dimensions for single top quark associated production with W$^-$ or H$^-$", *Phys. Rev. D* **82** (2010), no. 5, 054018, `doi:10.1103/PhysRevD.82.054018`, `arXiv:hep-ph/1005.4451`.

[37] J. M. Campbell, R. K. Ellis, and C. Williams, "Vector boson pair production at the LHC", *JHEP* **07** (2011) 018, `doi:10.1007/JHEP07(2011)018`, `arXiv:1105.0020`.

[38] F. Maltoni, D. Pagani, and I. Tsinikos, "Associated production of a top-quark pair with vector bosons at NLO in QCD: impact on $t\bar{t}H$ searches at the LHC", `arXiv:1507.05640`.

[39] W. Beenakker et al., "Higgs radiation off top quarks at the Tevatron and the LHC", *Phys. Rev. Lett.* **87** (2001), no. 20, 201805, `doi:10.1103/PhysRevLett.87.201805`, `arXiv:hep-ph/0107081`.

[40] W. Beenakker et al., "NLO QCD corrections to $t\bar{t}H$ production in hadron collisions", *Nucl. Phys. B* **653** (2003), no. 1-2, 151, `doi:10.1016/S0550-3213(03)00044-0`, `arXiv:hep-ph/0211352`.

[41] S. Dawson, L. H. Orr, L. Reina, and D. Wackeroth, "Associated top quark Higgs boson production at the LHC", *Phys. Rev. D* **67** (2003), no. 7, 071503, `doi:10.1103/PhysRevD.67.071503`, `arXiv:hep-ph/0211438`.

[42] S. Dawson et al., "Associated Higgs production with top quarks at the large hadron collider: NLO QCD corrections", *Phys. Rev. D* **68** (2003), no. 3, 034022, `doi:10.1103/PhysRevD.68.034022`, `arXiv:hep-ph/0305087`.

[43] A. Djouadi, J. Kalinowski, and M. Spira, "HDECAY: A program for Higgs boson decays in the standard model and its supersymmetric extension", *Comput. Phys. Commun.* **108** (1998), no. 1, 56, `doi:10.1016/S0010-4655(97)00123-9`, `arXiv:hep-ph/9704448`.

[44] A. Djouadi, M. M. Mühlleitner, and M. Spira, "Decays of supersymmetric particles: The Program SUSY-HIT (SUspect-SdecaY-Hdecay-InTerface)", *Acta Phys. Polon. B* **38** (2007) 635, `arXiv:hep-ph/0609292`.

[45] A. Bredenstein, A. Denner, S. Dittmaier, and M. M. Weber, "Precise predictions for the Higgs-boson decay H → WW/ZZ → 4 leptons", *Phys. Rev. D* **74** (2006), no. 1, 013004, `doi:10.1103/PhysRevD.74.013004`, `arXiv:hep-ph/0604011`.

[46] A. Bredenstein, A. Denner, S. Dittmaier, and M. M. Weber, "Radiative corrections to the semileptonic and hadronic Higgs-boson decays H → WW/ZZ → 4 fermions", *JHEP* **02** (2007) 080, `doi:10.1088/1126-6708/2007/02/080`, `arXiv:hep-ph/0611234`.

[47] M. Cacciari et al., "Top-pair production at hadron colliders with next-to-next-to-leading logarithmic soft-gluon resummation", *Phys. Lett. B* **710** (2012), no. 4-5, 612, `doi:10.1016/j.physletb.2012.03.013`, `arXiv:1111.5869`.

[48] P. Baernreuther et al., "Percent Level Precision Physics at the Tevatron: First Genuine NNLO QCD Corrections to $q\bar{q} \to t\bar{t} + X$", *Phys. Rev. Lett.* **109** (2012), no. 13, 132001, `doi:10.1103/PhysRevLett.109.132001`, `arXiv:1204.5201`.

[49] M. Czakon and A. Mitov, "NNLO corrections to top-pair production at hadron colliders: the all-fermionic scattering channels", *JHEP* **12** (2012) 054, `arXiv:1207.0236`.

[50] M. Czakon and A. Mitov, "NNLO corrections to top-pair production at hadron colliders: the quark-gluon reaction", *JHEP* **01** (2013) 080, `arXiv:1210.6832`.

[51] M. Beneke et al., "Hadronic top-quark pair production with NNLL threshold resummation", *Nucl. Phys. B* **855** (2012), no. 3, 695, `doi:10.1016/j.nuclphysb.2011.10.021`, `arXiv:1109.1536`.

[52] M. Czakon, P. Fiedler, and A. Mitov, "Total Top-Quark Pair-Production Cross Section at Hadron Colliders Through $O(\alpha_S{}^4)$", *Phys. Rev. Lett.* **110** (2013), no. 25, 252004, `doi:10.1103/PhysRevLett.110.252004`, `arXiv:1303.6254`.

[53] M. Czakon and A. Mitov, "Top++: A Program for the Calculation of the Top-Pair Cross-Section at Hadron Colliders", *Comput. Phys. Commun.* **185** (2014), no. 11, 2930, `doi:10.1016/j.cpc.2014.06.021`, `arXiv:1112.5675`.

[54] CMS Collaboration, "Particle–flow event reconstruction in CMS and performance for jets, taus, and $E_{\mathrm{T}}^{\mathrm{miss}}$", CMS Physics Analysis Summary CMS-PAS-PFT-09-001, CMS Collaboration, 2009.

[55] CMS Collaboration, "Commissioning of the particle-flow event reconstruction with the first LHC collisions recorded in the CMS detector", CMS Physics Analysis Summary CMS-PAS-PFT-10-001, CMS Collaboration, 2010.

[56] M. Cacciari, G. P. Salam, and G. Soyez, "The catchment area of jets", *JHEP* **04** (2008) 005, `doi:10.1088/1126-6708/2008/04/005`, `arXiv:0802.1188`.

[57] M. Cacciari, G. P. Salam, and G. Soyez, "The anti-k_t jet clustering algorithm", *JHEP* **04** (2008) 063, `doi:10.1088/1126-6708/2008/04/063`, `arXiv:0802.1189`.

[58] CMS Collaboration, "Determination of jet energy calibration and transverse momentum resolution in CMS", *JINST* **6** (2011), no. 11, P11002, `doi:10.1088/1748-0221/6/11/P11002`, `arXiv:1107.4277`.

[59] CMS Collaboration, "Identification of b-quark jets with the CMS experiment", *JINST* **8** (2013), no. 4, P04013, `doi:10.1088/1748-0221/8/04/P04013`, `arXiv:1211.4462`.

[60] CMS Collaboration, "Identification of b quark jets at the CMS Experiment in the LHC Run 2", CMS Physics Analysis Summary CMS-PAS-BTV-15-001, CMS Collaboration, 2016.

[61] T. Plehn, M. Spannowsky, M. Takeuchi, and D. Zerwas, "Stop Reconstruction with Tagged Tops", *JHEP* **10** (2010) 078, `doi:10.1007/JHEP10(2010)078`, `arXiv:1006.2833`.

[62] C. Anders et al., "Benchmarking an even better top tagger algorithm", *Phys. Rev.* **D89** (2014), no. 7, 074047, `doi:10.1103/PhysRevD.89.074047`, `arXiv:1312.1504`.

[63] G. Kasieczka et al., "Resonance Searches with an Updated Top Tagger", *JHEP* **06** (2015) 203, `doi:10.1007/JHEP06(2015)203`, `arXiv:1503.05921`.

[64] J. M. Butterworth, A. R. Davison, M. Rubin, and G. P. Salam, "Jet substructure as a new Higgs search channel at the LHC", *Phys. Rev. Lett.* **100** (2008), no. 24, 242001, `doi:10.1103/PhysRevLett.100.242001`, `arXiv:0802.2470`.

[65] G. P. Salam, "Towards Jetography", *Eur. Phys. J.* **C67** (2010) 637–686, `doi:10.1140/epjc/s10052-010-1314-6`, `arXiv:0906.1833`.

[66] A. Höcker et al., "TMVA: Toolkit for Multivariate Data Analysis", *PoS* **ACAT** (2007) 040, `arXiv:physics/0703039`.

[67] J. Kennedy and R. Eberhart, "Particle swarm optimization", in *Proceedings of the IEEE International Conference on neural networks*, volume 4, pp. 1942–1948. Nov, 1995. `doi:10.1109/ICNN.1995.488968`.

[68] CMS Collaboration, "CMS Luminosity Measurement for the 2015 Data Taking Period", CMS Physics Analysis Summary CMS-PAS-LUM-15-001, CMS Collaboration, 2016.

[69] R. J. Barlow and C. Beeston, "Fitting using finite Monte Carlo samples", *Comput. Phys. Commun.* **77** (1993), no. 2, 219–228, `doi:10.1016/0010-4655(93)90005-W`.

[70] J. S. Conway, "Incorporating Nuisance Parameters in Likelihoods for Multisource Spectra", in *Proceedings, PHYSTAT 2011 Workshop on Statistical Issues Related to Discovery Claims in Search Experiments and Unfolding, CERN,Geneva, Switzerland 17-20 January 2011.* 2011. `arXiv:1103.0354`.

[71] A. Read, "Modified frequentist analysis of search results (the CL_s method)", Technical Report CERN-OPEN-2000-005, CERN, 2000.

[72] T. Junk, "Confidence level computation for combining searches with small statistics", *Nucl. Instrum. Meth. A* **434** (1999), no. 2-3, 435, `doi:10.1016/S0168-9002(99)00498-2`, `arXiv:hep-ex/9902006`.

[73] G. Cowan, K. Cranmer, E. Gross, and O. Vitells, "Asymptotic formulae for likelihood-based tests of new physics", *Eur. Phys. J.* **C71** (2011) 1554, `doi:10.1140/epjc/s10052-011-1554-0`, `10.1140/epjc/s10052-013-2501-z`, `arXiv:1007.1727`. [Erratum: Eur. Phys. J.C73,2501(2013)].

[74] G. Fox and S. Wolfram, "Event shapes in e^+e^- annihilation", *Nuclear Physics B* **157** (1979), no. 3, 543–544, `doi:10.1016/0550-3213(79)90120-2`.

[75] J. Thaler and K. Tilburg, "Identifying boosted objects with N-subjettiness", *Journal of High Energy Physics* **2011** (2011), no. 3, 1–28, `doi:10.1007/JHEP03(2011)015`.

CMS PAS TOP-15-010

CMS Physics Analysis Summary

First measurement of the differential cross section for tt̄ production in the dilepton final state at $\sqrt{s}$ = 13 TeV

The CMS Collaboration

Abstract

Normalized differential top quark pair (tt̄) production cross sections are measured in proton-proton collisions at a centre-of-mass energy of 13 TeV at the CERN LHC. The data were recorded in 2015 with the CMS detector and correspond to an integrated luminosity of 42 pb^{-1}. The measurements are performed in the dilepton decay channels (e$^+$e$^-$, $\mu^+\mu^-$, and $\mu^\pm$e$^\mp$). The tt̄ production cross section is measured as a function of kinematic properties of the top quarks and the tt̄ system, as well as of the jet multiplicity in the event. Several predictions from perturbative QCD calculations are confronted with the data and are found to describe them well within large statistical uncertainties.

1 Introduction

Differential top quark pair (t$\bar{\text{t}}$) production cross sections have been measured at the LHC at proton-proton (pp) centre-of-mass energies of 7 and 8 TeV [1–4]. Here, a measurement is presented of the normalized differential t$\bar{\text{t}}$ production cross section in pp collisions at a centre-of-mass energy $\sqrt{s}$ of 13 TeV. The analysis follows to a large extent the previous measurement at $\sqrt{s} = 8$ TeV, making use of a data sample recorded in 2015 corresponding to an integrated luminosity of 42 pb^{-1}. This result complements the recent CMS measurement of the t$\bar{\text{t}}$ inclusive production cross section [5], and it is based on the same set of data.

The measurement is performed in the dilepton channels, with two oppositely charged leptons (e$^+$e$^-$, $\mu^+\mu^-$, $\mu^\pm$e$^\mp$) and at least two jets. The t$\bar{\text{t}}$ cross section is determined as a function of the jet multiplicity in the event, as well as of the kinematic properties of the top quarks and the t$\bar{\text{t}}$ system. The kinematic properties of top quarks are obtained through a kinematic reconstruction algorithm [3]. The normalized differential t$\bar{\text{t}}$ production cross section is determined by counting the number of t$\bar{\text{t}}$ signal events in each bin of the measurement, correcting for the detector effects and dividing by the total cross section measured in the corresponding phase space. The latter is obtained by integrating over all bins in each observable. Correlations between the bins of the measurement are taken into account by the use of regularized unfolding techniques.

The jet multiplicity, which is a directly measured observable, is presented in a fiducial phase space defined by the kinematic and geometric acceptance of all selected final-state objects. This avoids extrapolating the measured cross section into regions that are not experimentally accessible. The top quark and t$\bar{\text{t}}$ distributions are determined in the full phase space, in order to facilitate the comparison with higher-order perturbative QCD calculations.

The results are compared to several predictions obtained with the generators MG5_aMC@NLO [6] and MADGRAPH [7] interfaced with PYTHIA [8] for parton evolution and hadronization, and the POWHEG [9–12] generator, interfaced to both PYTHIA and HERWIG++ [13].

2 Event simulation

Event generators, interfaced with a detailed detector simulation, are used to model experimental effects, such as reconstruction and selection efficiencies, as well as detector resolutions. The CMS detector response is simulated using GEANT4 (v. 9.4) [14].

For the simulation of the reference t$\bar{\text{t}}$ signal sample, the next-to-leading-order (NLO) POWHEG (v. 2) [9, 12] event generator is used. The proton structure is described by the parton distribution functions (PDF) NNPDF3.0 [15]. The generated events are subsequently processed with PYTHIA (v. 8.2) [8] (referred to as PYTHIA8 in the following) for parton showering and hadronization.

In addition to the POWHEG + PYTHIA8 simulation, alternative samples of t$\bar{\text{t}}$ events obtained with the NLO MG5_aMC@NLO (v. 2.2.2) [6] generator including MADSPIN [16], and the LO multileg generator MADGRAPH (v. 5.1.5.11) [7] are compared, when available, to the final results presented in Section 5. These samples are interfaced with PYTHIA8 for parton showering and hadronization. The matching of matrix-element jets to parton showers is performed using the FxFx [17] and MLM [18] prescriptions in the MG5_aMC@NLO and MADGRAPH samples, respectively. The proton structure is described by the PDF sets NNPDF3.0 for MG5_aMC@NLO, while the PDF set NNPDF2.3 [15] is used for MADGRAPH. A sample of t$\bar{\text{t}}$ events generated with POWHEG and interfaced with HERWIG++ (v. 2.7.1) [13] is also used to determine determine the

uncertainty on the modelling of the hadronization and parton fragmentation (cf. Section 4).

In all $t\bar{t}$ simulated samples, the value of the top quark mass is assumed to be $m_t = 172.5$ GeV.

Standard model background samples are simulated using MG5_aMC@NLO, Powheg, or Pythia8, depending on the process. The main background contributions originate from Z/γ^* bosons produced with additional jets (refered to as Z+jets in the following), single top quark (tW channel), W boson production with additional jets (W+jets in the following), diboson (WW, WZ, and ZZ), and QCD multijet events. The W+jets and Z+jets samples are simulated with MG5_aMC@NLO. Powheg [10, 12] is used for single top quark production, while Pythia8 is used to simulate diboson and QCD multijet events. Parton showering and hadronization are also simulated with Pythia8 in all the background samples. The Pythia8 CUETP8M1 tune [19, 20] is used to characterize the underlying event in both the $t\bar{t}$ signal and the background samples, except for the $t\bar{t}$ Powheg + Herwig++sample, where the EE5C tune [21] was used.

For comparison with the measured distributions, the events in the simulated samples are normalized to an integrated luminosity of 42 pb^{-1}, according to their predicted cross sections. These are taken from NNLO (W+jets and Z+jets), approximate NNLO (single top quark tW channel [22]), NLO (diboson [23]) and leading-order (LO) (QCD multijet [8]) calculations. Correction factors described in Sections 3 and 4 are applied where necessary to improve the description of the data by the simulation. The $t\bar{t}$ simulated sample is normalized to the full NNLO+NNLL calculation [24–29], which is performed with the Top++2.0 program [30]. The PDF and α_S uncertainties are estimated using the PDF4LHC prescription [31, 32] with the MSTW2008nnlo68cl [33], CT10 NNLO [34, 35], and NNPDF2.3 [36] PDF sets, and added in quadrature to the scale uncertainty to obtain a $t\bar{t}$ production cross section of $831.8 \pm^{19.8}_{29.2}$ (scale) $\pm$ 35.1(PDF + α_s) pb assuming a top quark mass value of 172.5 GeV. Since normalized differential $t\bar{t}$ cross sections are measured in this analysis, the normalization of the $t\bar{t}$ sample is only relevant to present the expected rates in figures in Section 3.

3   Event selection

The event selection is based on the decay topology of the top quark and antiquark, where both decay into a W boson and a b quark, and each of the two W bosons decays into a muon or an electron. At trigger level, events are required to contain two leptons fulfilling transverse momentum (p_T) thresholds and isolation criteria, and are further selected if they contain at least two isolated leptons of opposite electric charge and at least two jets. At least one of the jets is required to be b-tagged. The events are reconstructed using a particle-flow technique [37, 38], which combines signals from all sub-detectors to enhance the reconstruction performance by identifying individual particle candidates in pp collisions. Charged hadrons from pileup events, i.e. those originating from a vertex other than the one of the hard interaction, are subtracted event-by-event. Subsequently, the remaining neutral-hadron pileup component is subtracted at the level of jet energy corrections [39].

The electron candidates are required to have $p_T > 20$ GeV and pseudorapidity $|\eta| < 2.4$, as reconstructed from a combination of the track momentum at the main interaction vertex and the corresponding energy deposition in the ECAL. A relative isolation criterion $I_{rel} < 0.11$ is required, where I_{rel} is defined as the sum of the p_T of all neutral and charged reconstructed particle candidates inside a cone around the electron in $\eta - \phi$ space of $\Delta R \equiv \sqrt{(\Delta\eta)^2 + (\Delta\phi)^2} < 0.3$, divided by the p_T of the electron. In addition, electrons from identified photon conversions are rejected. Muon candidates are reconstructed using the track information from the silicon

tracker and the muon system. They are required to have $p_T > 20\,\text{GeV}$ and $|\eta| < 2.4$. Isolated muon candidates are selected if they fulfill $I_{\text{rel}} < 0.12$ within a cone of $\Delta R < 0.4$ around the muon. To further increase the purity of muons originating from the primary interaction and to suppress misidentified muons or muons from decay-in-flight processes, additional quality criteria, such as a minimal number of hits associated with the muon track, are required in both the silicon tracker and the muon system. The neutral component from pileup events is subtracted event-by-event based on the average transverse energy deposited by neutral particles in the event, which is removed from the transverse energy in the isolation cone.

Jets are reconstructed by clustering the particle-flow candidates using the anti-k_t clustering algorithm with a distance parameter of 0.4 [40]. Jets are selected if they have $p_T > 30\,\text{GeV}$ and $|\eta| < 2.4$. A jet-lepton cleaning procedure is applied, which excludes jets overlapping with fully selected leptons if $\Delta R(jet, lepton) < 0.4$. Jets originating from b quarks are identified by a combined secondary-vertex algorithm [41], which provides a b-tagging discriminant by combining secondary vertices and track-based lifetime information. The working point is chosen to provide b-tagging efficiency of ≈ 80–85% and a probability to misidentify light-flavour jets as b jets (mistag rate) of $\approx 10\%$.

The missing transverse momentum vector $\vec{p}_T^{\text{miss}}$ is defined as the projection on the plane perpendicular to the beams of the negative vector sum of the momenta of all reconstructed particles in an event. Its magnitude is referred to as E_T^{miss}, and is required to have $|\eta| < 3$.

In events with more than two leptons, only the lepton pair with the highest scalar p_T sum is considered. Events with an invariant mass of the lepton pair smaller than $20\,\text{GeV}$ are removed in order to suppress events from heavy-flavour resonance decays and low-mass Drell–Yan processes. Backgrounds from Z+jets processes in the $\mu^+\mu^-$ and e^+e^- channels are further suppressed by requiring the dilepton invariant mass to be outside a Z boson mass window of $91 \pm 15\,\text{GeV}$ and E_T^{miss} to be larger than $40\,\text{GeV}$.

Only $t\bar{t}$ events with two leptons (electrons or muons) in the final state are considered as signal. All other $t\bar{t}$ events, specifically those originating from decays via τ leptons, are considered as background. The background contribution from Z+jets events, which is dominant in the e^+e^- and $\mu^+\mu^-$ channels, is determined from data following the procedure described in Refs. [5, 42]. The background normalization is determined using the number of events inside the Z-peak region, and a correction needed for non-Z+jets backgrounds in this control region is derived from the $\mu^\pm e^\mp$ channel. Other sources of background, including single top quark production, diboson events, or the contribution arising from misidentified or genuine leptons within jets, are estimated from simulation.

Basic distributions of the event sample are shown in Fig. 1 for the leptons, jets, and b jets. The data are generally well described by the simulation, also for the individual channels separately. The QCD multijet background is negligible and not shown.

The kinematic properties of the top quarks and antiquarks are determined from the four-momenta of all final-state objects by means of an algebraic kinematic reconstruction method [3]. The following constraints are imposed: the balance of p_T of the two neutrinos; the W boson invariant mass of 80.4 GeV; and the equality of the top quark and antiquark masses, which are fixed to a value of $172.5\,\text{GeV}$. Each suitable pair of jets and lepton-jet assignment is considered in the kinematic reconstruction. Effects of detector resolution are accounted for by randomly smearing the measured energies and directions of the reconstructed lepton and b jet candidates by their resolutions. For a given smearing, the solution of equations for the neutrino momenta yielding the smallest invariant mass of the $t\bar{t}$ system is chosen. For each solution, a weight is
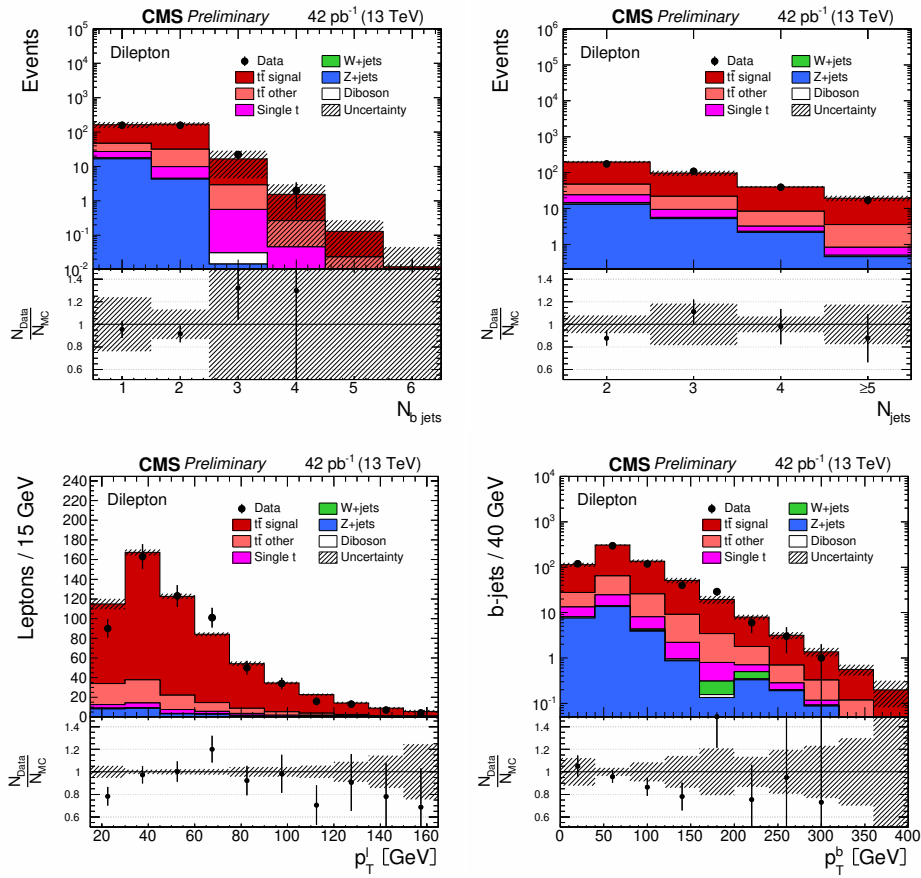
Figure 1: Kinematic distributions after event selection and before the kinematic reconstruction of the $t\bar{t}$ system: the multiplicity in the reconstructed number of b-tagged jets (top left), the multiplicity in the number of reconstructed jets (top right), the p_T of the selected isolated leptons (bottom left), and the p_T of the reconstructed jets (bottom right). The hatched regions correspond to the shape uncertainties for the signal and backgrounds (cf. Section 4). The lower part of each plot shows the ratio of data to the predictions.

calculated based on the expected true invariant mass spectrum of the lepton and b jet from top quark decays. The weights are summed over 100 reconstruction attempts, and the kinematics of the top quark and antiquark are calculated as a weighted average. Finally, the two jet and lepton-jet assignments that yield the maximum sum of weights are used. Combinations with two b-tagged jets are preferred to using single b-tagged jets. The efficiency of the kinematic reconstruction, defined as the number of events with solution over the total number of selected $t\bar{t}$ events, is about 94%. Events with no valid solution are excluded from further analysis. The performance in data and simulation is similar for all measured observables.

The distributions of the top quark or antiquark and $t\bar{t}$ kinematic observables (p_T^t, $|y_t|$, $p_T^{t\bar{t}}$, and $|y_{t\bar{t}}|$) are presented in Fig. 2. In general, the data are well described by the simulation within the statistical uncertainties.

After applying the full event selection and the kinematic reconstruction of the $t\bar{t}$ system, 179 events are found in the $\mu^\pm e^\mp$ channel, 83 events in the $\mu^+\mu^-$ channel, and 44 events in the e^+e^- channel. In all decay channels, the dilepton signal contribution to the final event sample is about 80%. The remaining fraction of events contains around 13% $t\bar{t}$ decays other than the dilepton channels, including $t\bar{t}$ decays into τ leptons originating from the primary interaction, about 4% single top tW events, around 3% Z+jets events, and negligible fractions of W+jets, diboson, and QCD multijet events.

4 Systematic uncertainties

Systematic uncertainties on the measurement arise from detector effects as well as from theoretical uncertainties. Each systematic uncertainty is investigated separately, and determined individually in each bin of the measurement, by variation of the corresponding efficiency, resolution, or scale within its uncertainty, using a prescription similar to the one followed in Ref. [3]. Correction factors, subsequently referred to as scale factors, are applied where necessary to improve the description of the data by the simulation. For each variation, the measured normalized differential cross section is recalculated, and the difference of the varied result to the nominal one in each bin is taken as the systematic uncertainty. The overall uncertainty on the measurement is derived by adding the individual contributions in quadrature.

Lepton trigger efficiencies are measured using triggers that are only weakly correlated to the dilepton triggers used in the analysis [5]. A dependence on η of a few percent is observed and scale factors are derived. The lepton identification and isolation uncertainties are determined using the 'tag-and-probe' method [5, 43] with Z boson event samples, and are found to be described very well by the simulation for both electrons and muons. The overall difference between data and simulation in bins of η and p_T is estimated to be less than 4% for electrons, while scale factors for muons are found to be close to unity.

The uncertainty on the jet energy scale (JES) is determined by variation of the jet energy in bins of p_T and η [44]. The uncertainty on the jet energy resolution (JER) is determined by the variation of the simulated JER by $\pm 1\sigma$ in different η regions [44].

The uncertainty on the b-tagging efficiency is determined by dividing the b-jet distributions for p_T and η into two bins at the median of the respective distributions. The b-tagging scale factors for the b jets in the first bin are scaled up by half of the uncertainties quoted in Ref. [41], while those in the second bin are scaled down and vice versa, so that a maximum variation is assumed and the difference between the scale factors in the two bins reflects the full uncertainty. The variations are performed separately for the p_T and η distributions, and independently for
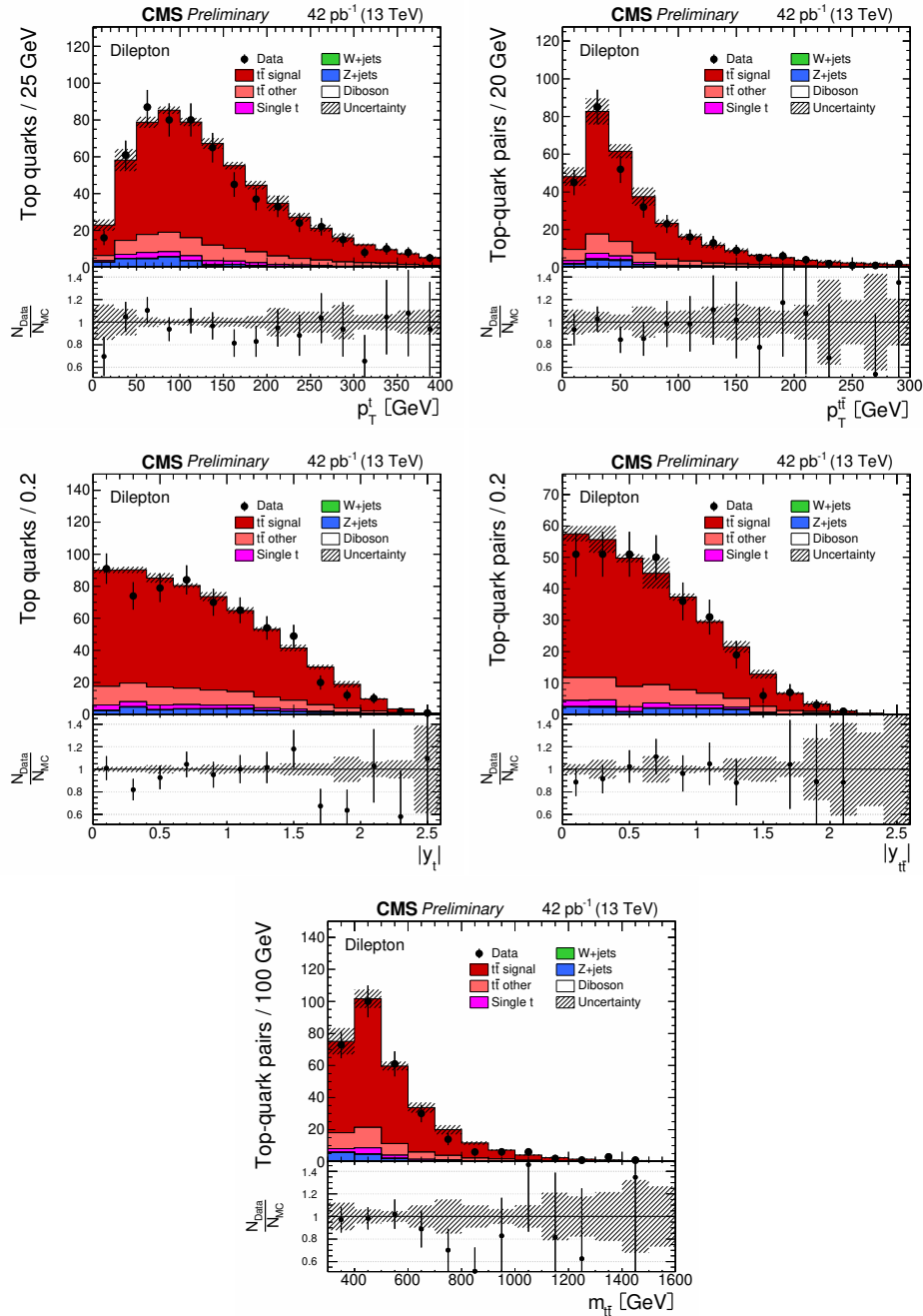
Figure 2: Distribution of top quark or antiquark (left) and $t\bar{t}$ (right) observables as obtained from the kinematic reconstruction: the p_T (top row), the absolute rapidities (middle row), and the invariant mass of the $t\bar{t}$ system (bottom row). The hatched regions correspond to the shape uncertainties for the signal and backgrounds (cf. Section 4). The lower part of each plot shows the ratio of data to the predictions.

heavy-flavour (b and c) and light (s, u, d, and gluon) jets, assuming that they are all uncorrelated.

The background from Z+jets processes as determined from the data is varied in normalization by ±30%. In addition, variations of the background contributions from single top quark and diboson events up and down by ±30% are performed [3].

The kinematic reconstruction of the top quarks is generally found to be well described by the simulation within statistical uncertainties. The uncertainty on the modelling of the number of pileup events is obtained by changing the inelastic cross section by ±5%.

The uncertainty on the modelling of the hard-production process is assessed by variation of the renormalization and factorization scale in the POWHEG signal sample up and down by a factor of two with respect to its nominal value, equal to the Q of the hard process. For the POWHEG sample, Q is defined via $Q^2 = m_t^2 + p_{T,t}^2$, where $p_{T,t}^2$ denotes the p_T of the top quark in the $t\bar{t}$ zero-momentum frame.

The dependence of the measurement on the top quark mass is estimated from dedicated POWHEG simulated samples in which the top quark mass is varied with respect to the value used for the default simulation.

The uncertainty due to the hadronization and parton showering model is estimated by comparing samples simulated with POWHEG using PYTHIA8 and HERWIG++ for hadronization. In addition, the flavor-dependent hadronization uncertainty is part of the JES uncertainty and comes from differences in the energy response for different jet flavours and flavour mixtures. It originates in differences between the Lund fragmentation model (PYTHIA8) and cluster fragmentation (HERWIG++), and is evaluated for each jet flavour independently.

The uncertainty on the choice of the generator to model the $t\bar{t}$ process is evaluated by comparing samples generated with POWHEG and MG5_aMC@NLO, both interfaced to PYTHIA8.

The effect of the uncertainty from the choice of PDF is assessed by reweighting the sample of simulated $t\bar{t}$ signal events according to the NNPDF3.0 PDF sets [15].

The total systematic uncertainty on the normalized differential cross sections is typically around 8.5%. This value is calculated as the median of the distribution of the total systematic uncertainties over all bins of all measured observables. Typical values for the dominant contributions to the systematic uncertainty for rapidity observables (all other observables) are: generator, with 3.4% (1.6%); hadronization and parton showering, with 2.3% (2.9%); PDF, with 1.5% (0.5%); JES, with 1.2% (1.2%); JER, with 0.7% (0.8%); b-tagging, with 0.6% (0.9%).

The total uncertainty on the measurement is typically 19.2%, dominated by the statistical uncertainty.

5 Normalized differential cross section

The normalized differential $t\bar{t}$ cross section $1/\sigma \cdot d\sigma/dX$ is determined as a function of the jet multiplicity and of the kinematic properties of the the top quarks and the $t\bar{t}$ system, through the relation [3, 4]:

$$\frac{1}{\sigma}\frac{d\sigma_i}{dX} = \frac{1}{\sigma}\frac{x_i}{\Delta_i^X}$$

(1)

where x_i represents the number of signal events measured in data after background subtraction and corrected for detector efficiencies, acceptances, and migrations, and Δ_i^X is the bin width. The normalized differential cross section is obtained by dividing this quantity by the measured total cross section σ in the same phase space, which is evaluated by integrating over all bins for each observable X. The contribution to the background from other $t\bar{t}$ decays is taken into account, after subtracting all other background components, by correcting the number of signal events in data using the expected signal fraction. The expected signal fraction is defined as the ratio of the number of selected $t\bar{t}$ signal events to the total number of selected $t\bar{t}$ events (i.e. signal and all other $t\bar{t}$ events) in simulation. This procedure avoids the dependence on the total inclusive $t\bar{t}$ cross section used in the normalization of the simulated signal sample.

Effects from trigger and detector efficiencies and resolutions leading to the migration of events across bin boundaries, and therefore to statistical correlations among neighbouring bins, are corrected by using a regularized unfolding method [3, 45, 46]. For each measured distribution, a response matrix that accounts for migrations and efficiencies is calculated from the simulated POWHEG $t\bar{t}$ signal sample. The generalized inverse of the response matrix is used to obtain the unfolded distribution from the measured distribution by applying a χ^2 technique. To avoid non-physical fluctuations, a regularization prescription is applied. The regularization level is determined individually for each distribution using the averaged global correlation method [47]. To keep the bin-to-bin migrations small, the width of the bins of the measurement are chosen according to their purity (sensitive to migrations into the bin) and stability (sensitive to migrations out of the bin). In this analysis, the purity and stability of the bins are typically 50% or larger.

The unfolding is performed separately for each decay channel, and the final result is obtained by combination of the three channels. For every systematic variation the full analysis, including the combination, is repeated, and the difference with respect to the nominal value is taken as the systematic uncertainty. This way, systematic correlations between the three decay channels are taken into account. Due to the normalization, those systematic uncertainties that are correlated across all bins of the measurement, and therefore only affect the normalization, cancel out.

The normalized differential cross section as a function of the jet multiplicity is determined at the particle level, where the physics objects are defined as follows. Leptons from the W boson decays are defined at the matrix element level. A jet is defined at the particle level by applying the anti-k_T clustering algorithm with distance parameter of $R = 0.4$ [40] to all stable particles, excluding both neutrinos and prompt electrons and muons from W boson decays. A jet is defined as a b jet if it has at least one B hadron associated to it, which is matched to the corresponding original b quark. In order to avoid additional model uncertainties due to the extrapolation of the measurement outside experimentally well-described phase space regions, the cross section for the measured jet multiplicity is presented in a fiducial phase space where the leptons have $|\eta_\ell| < 2.4$ and $p_T^\ell > 20\,\text{GeV}$, and the jets (including both b jets from the top quark decays) lie within the range $|\eta| < 2.4$ and $p_T > 30\,\text{GeV}$.

In addition, the top quark and $t\bar{t}$-system observables are defined with respect to the top quarks or antiquarks before the decay (parton level) and after QCD radiation, and extrapolated to the full phase space using the POWHEG + PYTHIA8 prediction. This allows for comparison with recent QCD calculations.

The measurements are compared to the predictions from POWHEG + PYTHIA8, MG5_aMC@NLO + PYTHIA8, MADGRAPH + PYTHIA8, and POWHEG + HERWIG++.

The multiplicity distribution of jets with p_T thresholds above $30\,\text{GeV}$, N_{jets}, is shown in Fig. 3.

Within uncertainties, data and theoretical predictions agree, also for the individual channels. The measurement is dominated by statistical uncertainties.
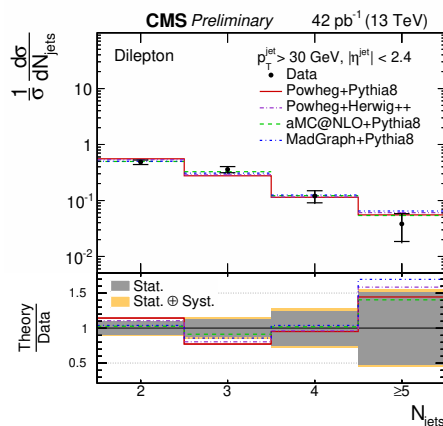

Figure 3: Normalized differential $t\bar{t}$ production cross section as a function of the jet multiplicity N_{jets}. The inner (outer) error bars indicate the statistical (combined statistical and systematic) uncertainty. The measurements are compared to predictions from POWHEG + PYTHIA8, MG5_aMC@NLO + PYTHIA8, MADGRAPH + PYTHIA8, and POWHEG + HERWIG++.

The normalized differential $t\bar{t}$ cross section as a function of the kinematic properties of the top quarks and the $t\bar{t}$ system is presented at parton level and extrapolated to the full phase space using the POWHEG + PYTHIA8 prediction. In Figs. 4 and 5 the distributions for the top quark and the $t\bar{t}$ observables are presented. Those are the transverse momentum p_T^t and the absolute rapidity $|y_t|$ of the top quarks and antiquarks, and the transverse momentum $p_T^{t\bar{t}}$, the absolute rapidity $|y_{t\bar{t}}|$, and the invariant mass $m_{t\bar{t}}$ of the $t\bar{t}$ system.

Also shown are predictions from MG5_aMC@NLO, and MADGRAPH, interfaced to PYTHIA8, and from POWHEG interfaced to both PYTHIA8 and HERWIG++. Good agreement is observed between data and theoretical predictions within uncertainties, also for the individual channels. The measurement is dominated by statistical uncertainties for all observables.

6 Summary

A first measurement of normalized differential top quark pair production cross sections in pp collisions at $\sqrt{s} = 13$ TeV with the CMS detector is presented. The measurement is performed in the dilepton (e^+e^-, $\mu^+\mu^-$, and $\mu^{\pm}e^{\mp}$) $t\bar{t}$ decay channels. The normalized $t\bar{t}$ cross section is measured as a function of the jet multiplicity in the event in the fiducial phase space, and of the transverse momentum, absolute rapidity, and invariant mass of the top quarks and $t\bar{t}$ system in the full phase space. The measurements are in agreement with standard model predictions.
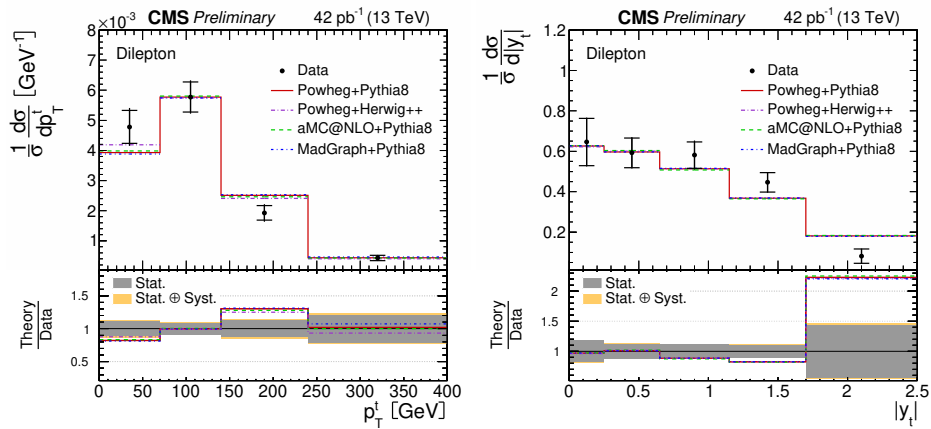
Figure 4: Normalized differential $t\bar{t}$ production cross section as a function of the p_T^t (left) and $|y_t|$ (right) of the top quarks or antiquarks. The inner (outer) error bars indicate the statistical (combined statistical and systematic) uncertainty. The measurements are compared to predictions from POWHEG + PYTHIA8, MG5_aMC@NLO + PYTHIA8, MADGRAPH + PYTHIA8, and POWHEG + HERWIG++.

Figure 5: Normalized differential t$\bar{\text{t}}$ production cross section as a function of the $p_\text{T}^\text{t\bar{t}}$ (top left), $|y_\text{t\bar{t}}|$ (top right), and $m_\text{t\bar{t}}$ (bottom) of the top quark pairs. The inner (outer) error bars indicate the statistical (combined statistical and systematic) uncertainty. The measurements are compared to predictions from POWHEG + PYTHIA8, MG5_aMC@NLO + PYTHIA8, MADGRAPH + PYTHIA8, and POWHEG+ HERWIG++.
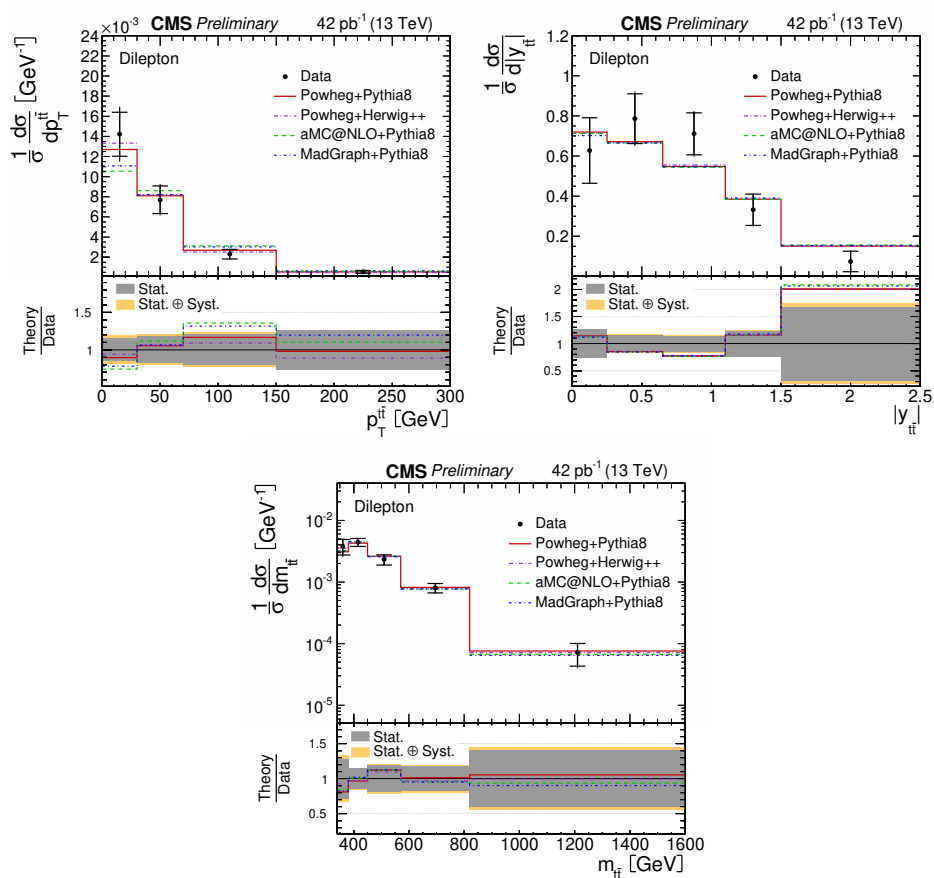
References

[1] ATLAS Collaboration, "Measurements of top quark pair relative differential cross-sections with ATLAS in pp collisions at $\sqrt{s} = 7$ TeV", *Eur. Phys. J. C* **73** (2013) 2261, `doi:10.1140/epjc/s10052-012-2261-1`, `arXiv:1207.5644`.

[2] CMS Collaboration, "Measurement of differential top-quark pair production cross sections in pp collisions at $\sqrt{s} = 7$ TeV", *Eur. Phys. J. C* **73** (2013) 2339, `doi:10.1140/epjc/s10052-013-2339-4`, `arXiv:1211.2220`.

[3] CMS Collaboration, "Measurement of differential cross section for top quark pair production in pp collisions at $\sqrt{s} = 8$ TeV", (2015). `arXiv:hep-ex/1505.04480`. Submitted to EPJC.

[4] CMS Collaboration, "Measurement of ttbar production with additional jet activity and properties of the additional jets, including ttbar bbbar, in the dilepton channel at $\sqrt{s} = 8$ TeV", (2015). TOP-12-041 (2015) in preparation.

[5] CMS Collaboration, "Measurement of the top quark pair production cross section in proton-proton collisions at $\sqrt{s} = 13$ TeV with the CMS detector", CMS Physics Analysis Summary CMS-PAS-TOP-15-003, 2015.

[6] J. Alwall et al., "The automated computation of tree-level and next-to-leading order differential cross sections, and their matching to parton shower simulations", *JHEP* **07** (2014) 079, `doi:10.1007/JHEP07(2014)079`, `arXiv:1405.0301`.

[7] J. Alwall et al., "MadGraph v5: going beyond", *JHEP* **06** (2011) 128, `doi:10.1007/JHEP06(2011)128`, `arXiv:1106.0522`.

[8] T. Sjöstrand et al., "An introduction to PYTHIA 8.2", *Comput. Phys. Commun.* **191** (2015) 159, `doi:10.1016/j.cpc.2015.01.024`, `arXiv:1410.3012`.

[9] S. Frixione, P. Nason, and C. Oleari, "Matching NLO QCD computations with parton shower simulations: the POWHEG method", *JHEP* **11** (2007) 070, `doi:10.1088/1126-6708/2007/11/070`, `arXiv:0709.2092`.

[10] S. Alioli et al., "NLO single-top production matched with shower in POWHEG: *s*- and *t*-channel contributions", *JHEP* **09** (2009) 111, `doi:10.1088/1126-6708/2009/09/111`, `arXiv:0907.4076`.

[11] S. Alioli et al., "A general framework for implementing NLO calculations in shower Monte Carlo programs: the POWHEG BOX", *JHEP* **06** (2010) 043, `doi:10.1007/JHEP06(2010)043`, `arXiv:1002.2581`.

[12] E. Re, "Single-top Wt-channel production matched with parton showers using the POWHEG method", *Eur. Phys. J. C* **71** (2011) 1547, `doi:10.1140/epjc/s10052-011-1547-z`, `arXiv:1009.2450`.

[13] M. Bahr et al., "Herwig++ Physics and Manual", *Eur. Phys. J. C* **58** (2008) 639–707, `doi:10.1140/epjc/s10052-008-0798-9`, `arXiv:0803.0883`.

[14] GEANT4 Collaboration, "GEANT4—a simulation toolkit", *Nucl. Instrum. Meth. A* **506** (2003) 250, `doi:10.1016/S0168-9002(03)01368-8`.

[15] NNPDF Collaboration, "Unbiased global determination of parton distributions and their uncertainties at NNLO and LO", *Nucl. Phys. B* **855** (2012) 153, `doi:10.1016/j.nuclphysb.2011.09.024`, `arXiv:1107.2652`.

[16] P. Artoisenet et al., "Automatic spin-entangled decays of heavy resonances in Monte Carlo simulations", *JHEP* **03** (2013) 015, `doi:10.1007/JHEP03(2013)015`, `arXiv:1212.3460`.

[17] R. Frederix and S. Frixione, "Merging meets matching in MC@NLO", *JHEP* **12** (2012) 061, `doi:10.1007/JHEP12(2012)061`, `arXiv:1209.6215`.

[18] M. L. Mangano, M. Moretti, F. Piccinini, and M. Treccani, "Matching matrix elements and shower evolution for top-quark production in hadronic collisions", *JHEP* **01** (2007) 013, `doi:10.1088/1126-6708/2007/01/013`, `arXiv:hep-ex/0611129`.

[19] CMS Collaboration, "Underlying event tunes and double parton scattering", CMS Physics Analysis Summary CMS-PAS-GEN-14-001, 2014.

[20] P. Skands, S. Carrazza, and J. Rojo, "Tuning PYTHIA 8.1: the Monash 2013 Tune", *Eur. Phys. J. C* **74** (2014), no. 8, 3024, `doi:10.1140/epjc/s10052-014-3024-y`, `arXiv:1404.5630`.

[21] M. H. Seymour and A. Siodmok, "Constraining MPI models using σ_{eff} and recent Tevatron and LHC Underlying Event data", *JHEP* **10** (2013) 113, `doi:10.1007/JHEP10(2013)113`, `arXiv:1307.5015`.

[22] N. Kidonakis, "Two-loop soft anomalous dimensions for single top quark associated production with W^- or H^-", *Phys. Rev. D* **82** (2010) 054018, `doi:10.1103/PhysRevD.82.054018`, `arXiv:hep-ph/1005.4451`.

[23] J. M. Campbell, R. K. Ellis, and C. Williams, "Vector boson pair production at the LHC", *JHEP* **07** (2011) 018, `doi:10.1007/JHEP07(2011)018`, `arXiv:1105.0020`.

[24] M. Cacciari et al., "Top-pair production at hadron colliders with next-to-next-to-leading logarithmic soft-gluon resummation", *Phys. Lett. B* **710** (2012) 612, `arXiv:1111.5869`.

[25] P. Baernreuther et al., "Percent Level Precision Physics at the Tevatron: First Genuine NNLO QCD Corrections to $q\bar{q} \to t\bar{t} + X$", *Phys. Rev. Lett.* **109** (2012) 132001, `doi:10.1103/PhysRevLett.109.132001`, `arXiv:1204.5201`.

[26] M. Czakon and A. Mitov, "NNLO corrections to top-pair production at hadron colliders: the all-fermionic scattering channels", *JHEP* **12** (2012) 054, `arXiv:1207.0236`.

[27] M. Czakon and A. Mitov, "NNLO corrections to top-pair production at hadron colliders: the quark-gluon reaction", *JHEP* **01** (2013) 080, `arXiv:1210.6832`.

[28] M. Beneke et al., "Hadronic top-quark pair production with NNLL threshold resummation", *Nucl. Phys. B* **855** (2012) 695, `doi:10.1016/j.nuclphysb.2011.10.021`, `arXiv:1109.1536`.

[29] M. Czakon, P. Fiedler, and A. Mitov, "Total Top-Quark Pair-Production Cross Section at Hadron Colliders Through $O(\alpha_S^4)$", *Phys.Rev.Lett.* **110** (2013) 252004, `doi:10.1103/PhysRevLett.110.252004`, `arXiv:1303.6254`.

[30] M. Czakon and A. Mitov, "Top++: A Program for the Calculation of the Top-Pair Cross-Section at Hadron Colliders", *Comput.Phys.Commun.* **185** (2014) 2930, `doi:10.1016/j.cpc.2014.06.021`, `arXiv:1112.5675`.

[31] S. Alekhin et al., "The PDF4LHC Working Group Interim Report", `arXiv:1101.0536`.

[32] M. Botje et al., "The PDF4LHC Working Group Interim Recommendations", `arXiv:1101.0538`.

[33] A. D. Martin, W. J. Stirling, R. S. Thorne, and G. Watt, "Parton distributions for the LHC", *Eur. Phys. J. C* **63** (2009) 189, `doi:10.1140/epjc/s10052-009-1072-5`, `arXiv:0901.0002`.

[34] H.-L. Lai et al., "New parton distributions for collider physics", *Phys. Rev. D* **82** (2010) 074024, `doi:10.1103/PhysRevD.82.074024`, `arXiv:1007.2241`.

[35] J. Gao et al., "CT10 next-to-next-to-leading order global analysis of QCD", *Phys. Rev. D* **89** (2014) 033009, `doi:10.1103/PhysRevD.89.033009`, `arXiv:1302.6246`.

[36] NNPDF Collaboration, "Parton distributions with LHC data", *Nucl. Phys. B* **867** (2013) 244, `doi:10.1016/j.nuclphysb.2012.10.003`, `arXiv:1207.1303`.

[37] CMS Collaboration, "Particle–flow event reconstruction in CMS and performance for jets, taus, and $E_\mathrm{T}^\mathrm{miss}$", CMS Physics Analysis Summary CMS-PAS-PFT-09-001, 2009.

[38] CMS Collaboration, "Commissioning of the particle-flow event reconstruction with the first LHC collisions recorded in the CMS detector", CMS Physics Analysis Summary CMS-PAS-PFT-10-001, 2010.

[39] M. Cacciari, G. P. Salam, and G. Soyez, "The catchment area of jets", *JHEP* **04** (2008) 005, `doi:10.1088/1126-6708/2008/04/005`, `arXiv:0802.1188`.

[40] M. Cacciari, G. P. Salam, and G. Soyez, "The anti-k_t jet clustering algorithm", *JHEP* **04** (2008) 063, `doi:10.1088/1126-6708/2008/04/063`, `arXiv:0802.1189`.

[41] CMS Collaboration, "Identification of b-quark jets with the CMS experiment", *JINST* **8** (2013) P04013, `doi:10.1088/1748-0221/8/04/P04013`, `arXiv:1211.4462`.

[42] CMS Collaboration, "Measurement of the $t\bar{t}$ production cross section in the dilepton channel in pp collisions at $\sqrt{s} = 8$ TeV", *JHEP* **02** (2014) 024, `doi:10.1007/JHEP02(2014)024`, `arXiv:1312.7582`.

[43] CMS Collaboration, "Measurement of the Drell-Yan cross sections in pp collisions at $\sqrt{s} = 7$ TeV with the CMS experiment", *JHEP* **10** (2011) 007, `doi:10.1007/JHEP10(2011)007`, `arXiv:1108.0566`.

[44] CMS Collaboration, "Determination of jet energy calibration and transverse momentum resolution in CMS", *JINST* **6** (2011) P11002, `doi:10.1088/1748-0221/6/11/P11002`, `arXiv:1107.4277`.

[45] A. Hoecker and V. Kartvelishvili, "SVD Approach to Data Unfolding", *Nucl.Instrum.Meth.* **A372** (1996) 469–481, `doi:10.1016/0168-9002(95)01478-0`, `arXiv:hep-ph/9509307v2`.

[46] V. Blobel, "An unfolding method for high energy physics experiments", `arXiv:0208022`.

[47] F. James, "Statistical methods in experimental physics". World Scientific, second edition, 2006.